

A WIDE FIELD CAMERA FOR X-RAY ASTRONOMY

by

MARK RAYNER SIMS

Thesis submitted to the University of Leicester  
for the degree of Doctor of Philosophy

May 1981

X-ray Astronomy Group  
Department of Physics  
University of Leicester

UMI Number: U355519

All rights reserved

INFORMATION TO ALL USERS

The quality of this reproduction is dependent upon the quality of the copy submitted.

In the unlikely event that the author did not send a complete manuscript and there are missing pages, these will be noted. Also, if material had to be removed, a note will indicate the deletion.



UMI U355519

Published by ProQuest LLC 2015. Copyright in the Dissertation held by the Author.  
Microform Edition © ProQuest LLC.

All rights reserved. This work is protected against  
unauthorized copying under Title 17, United States Code.



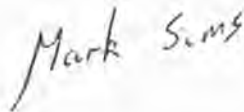
ProQuest LLC  
789 East Eisenhower Parkway  
P.O. Box 1346  
Ann Arbor, MI 48106-1346



024611054x

# DECLARATION

I hereby declare that no part of this thesis has been previously submitted to this or any other University as part of the requirement for a higher degree. The work described here was conducted by the undersigned except for the contributions from colleagues and other workers acknowledged in the text, references, and in the following note on publications.

A handwritten signature in dark ink, reading "Mark Sims". The signature is written in a cursive style, with the first letters of "Mark" and "Sims" being capitalized and prominent.

Mark Sims

May 1981



### Note on Publications

Some of the work reported here has been published  
(in full or in part) elsewhere as follows:

Chapter 1   Sims, M.R., & Fraser, G.W., IAU Circ. No.3339, 1979.

Chapters 2 and 3   Sims, M., Turner, M.J.L., & Willingale, R.  
Space Sci. Instrum., 5, 109, 1980.

Chapters 5 and 6   Sims, M.R., Thomas, H.D., & Turner, M.J.L., IEEE  
Trans. Nucl. Sci, in press, 1981.

## ACKNOWLEDGEMENTS

The work described in this thesis has benefited from advice and discussions with many members of the X-ray Astronomy Group, and Physics Department. I would like, however, to especially thank the following people for the stated reasons: Dr. Martin Turner for supervising this work, for his continuous encouragement and criticism throughout three and a half years; Huw Thomas who provided all the 50/50 gas mix data described in Chapter 6 of this thesis, and allowed me to plot, analyse and generally criticise this work; Dr. Richard Willingale for his continuous encouragement, advice, and software without which much of the computer simulation work would have been impossible; Dr. Graham Smith, Dr. Ernie Mathieson, Phil Gilvin for many discussions over Argon/Methane counter data, detector physics, and electronics; John Spragg, who designed the prototype detector and components, and enlightened me in many aspects of engineering and spacecraft design; the Mechanical and both Electronic Workshops of the Physics Department who constructed most of the detector and electronics; in particular Roger Cooper who built the signal processing electronics and Professor Ken Pounds, FRS, who tolerated my research programme, made many constructive criticisms of the programme and the first draft of this thesis.

I would like to thank Dr. A.C. Brinkman and J. Heise of the University of Utrecht, Holland, for many illuminating discussions on the shadow camera and X-80 mission.

I would also like to thank the U.K. S.R.C. for providing a studentship for my research. Finally, special thanks to Helen Townsend and Lorna Friel for typing this thesis, and John Kerruish for enclosed photographs. All original drawings were done by the author.

## CONTENTS

	<u>Page</u>
CHAPTER 1 : VARIABILITY IN X-RAY SOURCES	
1.1 Introduction	1
1.2 Brief Review of X-ray Astronomy	1
1.3 X-ray Sources and their Scales of Variability	5
1.4 X-ray Burst and Transient Sources	7
1.5 Other Sources of Extreme Variability	13
1.6 Instrumentation to Study Variability	15
1.7 The Shadow or Dicke Camera	17
CHAPTER 2 : THE SHADOW CAMERA	
2.1 Introduction	19
2.2 Principle of the Shadow Camera	19
2.3 Sensitivity of the Shadow Camera	25
2.4 Parameters of the Shadow Camera	29
2.5 The Shadow Camera: A Detector Limited System	32
2.6 Mask Patterns; Required Characteristics	34
2.7 A One- or Two-Dimensional System	37
2.8 The Shadow Camera: Sky Background Limited Case	38
2.9 Practical Design Considerations for the Shadow Camera	40
2.10 Review of a Shadow Camera Design	47
2.11 Other Designs for the Shadow Camera	51
2.12 Summary	57
CHAPTER 3 : DECONVOLUTION AND SIMULATION OF THE SHADOW CAMERA	
3.1 Introduction	59
3.2 Deconvolution: Advanced Methods	59
3.3 Computer Simulation Method	69
3.4 Simulation Deconvolution, Display and Analysis	82
3.5 Simulation Results I : The Perfect Camera	88

3.6	Simulation Results II : Disturbing Effects	99
3.7	Summary	107
CHAPTER 4 : THE IMAGING PROPORTIONAL COUNTER		
4.1	Introduction	111
4.2	Advantages and Disadvantages of the IPC	111
4.3	Basic Principles of the IPC	114
4.4	Gas Choice for the IPC	116
4.5	Position Sensing in an IPC	123
4.6	IPC Mechanical Design Considerations	134
4.7	Readout Electronics: Design Considerations	140
4.8	Future/Other Detectors for the Shadow Camera	144
CHAPTER 5 : A PROTOTYPE IPC FOR THE SHADOW CAMERA		
5.1	Introduction	149
5.2	Mechanical Construction	150
5.3	Detector Filling	157
5.4	Prototype Electronics	160
5.5	IPC Configurations: Parameters; Evaluation Method	165
5.6	Results from the One-Dimensional Position Sensitive Detector	170
CHAPTER 6 : RESULTS OF A TWO-DIMENSIONAL IMAGING PROPORTIONAL COUNTER		
6.1	Introduction	175
6.2	Basic Counter Parameters	176
6.3	Position Resolution versus Position Encoding Method; Along Anode	179
6.4	Across the Anode Wire Modulation Effects	190
6.5	The Limits of Position Resolution	211
6.6	Conclusion	227

CHAPTER 7 :	CONCLUSION/FUTURE WORK	
7.1	Introduction	231
7.2	The Shadow Camera	231
7.3	The IPC for the Shadow Camera	235
7.4	Future Work	236
APPENDIX A :	$f(\theta, \phi)$ AND THE CALCULATION OF EFFECTIVE AND TOTAL SOLID ANGLE	
A.1	Derivation of $f(\theta, \phi)$	238
A.2	Calculation of Effective Solid Angle	239
A.3	Calculation of Total Solid Angle	240
APPENDIX B :	THE DETECTOR RESPONSE AND SAMPLING RATE REQUIRED FOR THE SHADOW CAMERA	
B.1	Detector Response	241
B.2	Required Sampling Rate	243
APPENDIX C :	THE MAXIMUM ENTROPY METHOD OF DECONVOLUTION	244
REFERENCES		246

## CHAPTER 1

### VARIABILITY IN X-RAY SOURCES

#### 1.1. Introduction

This thesis relates the development and practical design of an X-ray astronomy experiment, a wide field camera to detect and investigate X-ray burst and transient sources, and monitor general variability of celestial X-ray sources. First in this chapter a review of X-ray astronomy and types of instrumentation will be given, followed by a brief review of X-ray sources and their known scales of variability. Finally the previous work in the field will be described leading to definition of the required characteristics of an experiment to monitor general variability of X-ray sources, and the need, and work required for its development.

#### 1.2. Brief Review of X-ray Astronomy

##### 1.2.1. Historical Perspective

Practical X-ray astronomy has been a science since June 1962 when an experiment built by the group of American Science and Engineering Inc., found the first non-solar X-ray source, Sco X-1 (Giacconi et al., 1962). However even in the mid 1950's there was speculation concerning possible high energy photons from celestial sources and the new discoveries that would result from studies of the X-ray region of the electro-magnetic spectrum. The galactic interstellar medium is strongly absorbing throughout most of the ultra-violet part of the spectrum and it is not until soft X-ray wavelengths that it becomes transparent again. However, the earth's atmosphere is itself opaque at X-ray energies, so serious observations had to wait until the rocket became available.

Throughout the 1960's many sounding rocket observations took place giving a first picture of a number of discrete point-like X-ray sources clustered mainly along the galactic plane, along with a uniform background emission. During this early period and indeed until the present day, high altitude balloons were used for high energy studies ( $\geq 30$  keV) of sources.

In December 1970 the first satellite dedicated to X-ray astronomy was launched by NASA, Small Astronomy Satellite A or Uhuru. The prime objective of the mission was to conduct an all sky survey to a sensitivity of about  $10^{-2}$  to  $10^{-3}$  times the flux of the strong source associated with the Crab Nebula supernova remnant, in the 2 to 6 keV energy range. The observing time of Uhuru soon exceeded all other X-ray observations up to its launch, and in 1973 the third Uhuru catalogue of sources was published listing 161 sources.

Since Uhuru, many other satellites devoted in part or totally to non-solar X-ray astronomy have been launched; Copernicus (USA/UK 1972); Ariel 5 (UK 1974); SAS-3 (USA 1975); OSO-7 (USA 1971); ANS (Netherlands 1974); OSO-8 (USA 1975); HEAO-A (USA 1977); HEAO-B or the Einstein Observatory as it is now known (USA 1978); Ariel 6 (UK 1979); and Hakucho (Japan 1979).

As a result of these satellites, balloon, and rocket programs, approximately 650 celestial X-ray sources are known at present, many of these being optically identified. The sources can be divided into two types, galactic and extragalactic. Figure 1.2.1 shows the sky distribution of sources in galactic co-ordinates ( $l_2, b_2$ ) from the 3A catalogue (McHardy et al., 1981). The identified galactic sources include single stars and associations, binary systems, pulsators, supernova remnants, and planetary nebulae. The extragalactic sources include normal galaxies, active galaxies, quasi-stellar objects and clusters of galaxies.



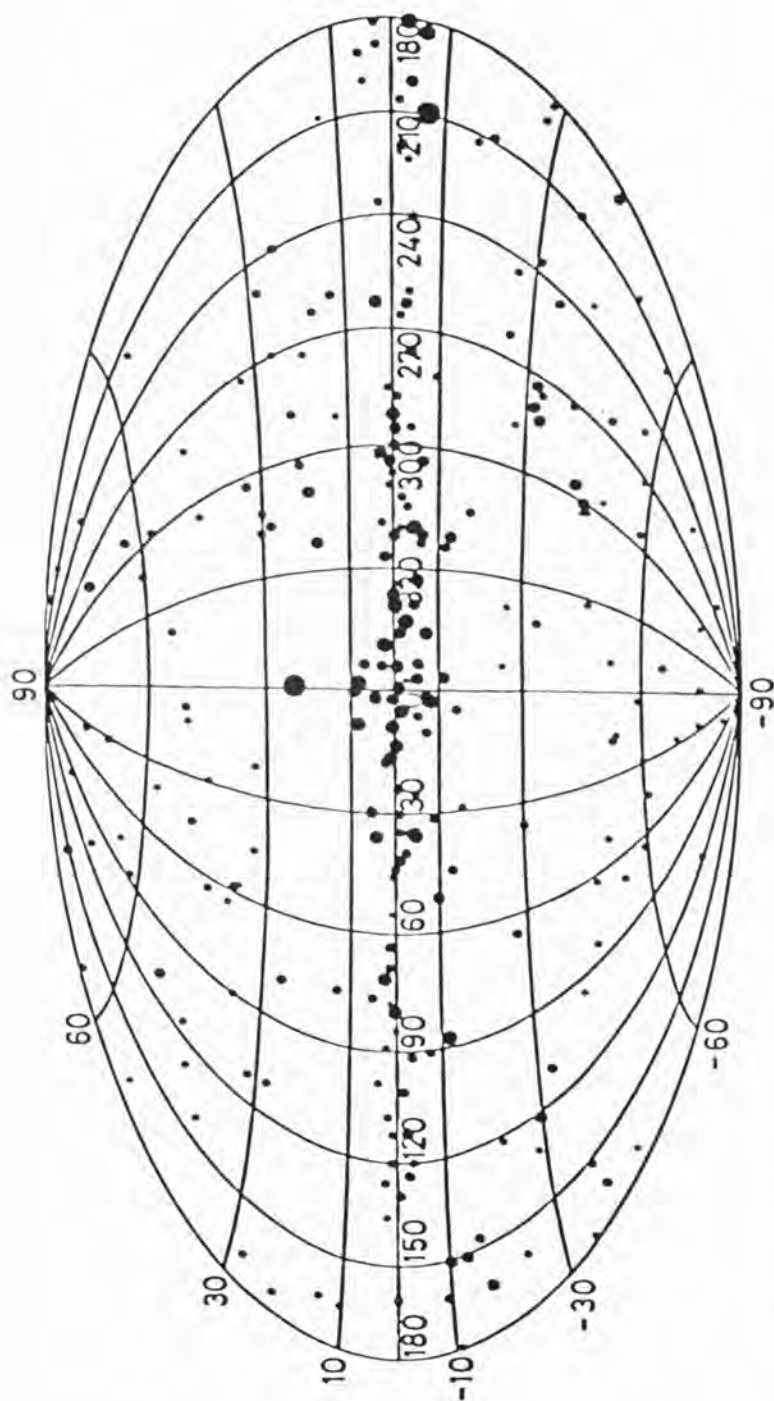


Figure 1.2.1. The celestial distribution of X-ray sources listed in the 3A Catalogue (McHardy et al., 1981). The sky is shown in galactic co-ordinates  $(l_2, b_2)$ , with the galactic centre at the centre of the map.



### 1.2.2. X-ray Astronomy Instrumentation to Date

X-ray astronomy can be divided into three energy ranges (the energy range defining the instrumentation design); the soft energy  $\sim .0125 - 1.5$  keV; the medium energy  $\sim 1.5 - 20$  keV; and the hard energy  $\sim 20 - 100$  keV . Detailed reviews of the history, instrumentation, and results of X-ray astronomy can be found in Schreier 1978, Murray 1977, Peterson 1975, Jagoda and Antrim 1975. The wide field camera is designed to operate in the medium energy range.

Until recently the main instruments used for observations in this energy range have been the proportional counter, and, for medium to high energy work, the scintillation counter. Pulse height distributions from each instrument providing some energy information about the source under observation.

Simple collimators, slit or tubular, limit the fields of view of the experiment and provide angular resolution of the order of a degree. Fine resolving power has been achieved, however, in the medium energy range by use of the modulation collimator developed by Oda 1965, this technique giving a substantial field of view, yet with an angular resolution of approximately an arc minute.

True imaging payloads are now becoming important along with other forms of detector to improve the spatial, temporal and spectral resolution and extend the energy range; CCD's; Gas Scintillation Proportional Counters; microchannel plate cameras; solid state spectrometers; and crystal spectrometers. Two methods of imaging are possible in the X-ray region. At energies smaller than  $\sim 4$  keV grazing incidence telescopes are used, but at energies greater than this transform imaging or the pin-hole camera must be used.

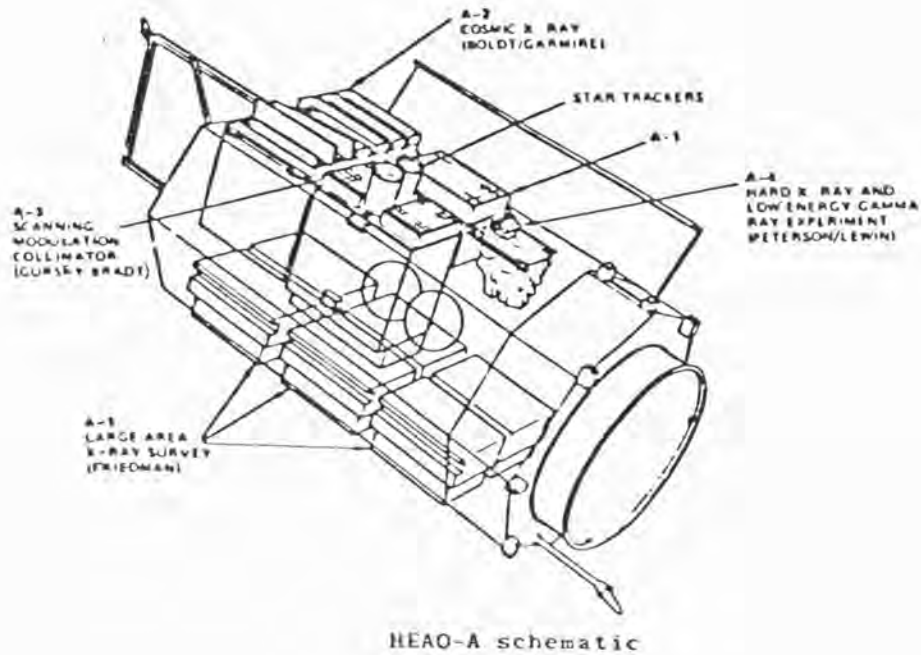
Grazing incidence, that is the use of total external reflection of X-rays under grazing incidence produces direct images of X-ray sources, see

Franks 1977 and references contained therein, while transform imaging produces a 'coded' picture which must be deconvolved, that is decoded to produce an image of the source field. HEAO-B or the Einstein Observatory was the first satellite designed to carry a grazing incidence system to image celestial X-ray sources, whilst at present apart from one sounding rocket experiment, as discussed in Chapter 2, and modulation collimators, no large area wide field transform imaging experiment has flown.

Detailed reviews of HEAO-A and Einstein the largest X-ray astronomy experiments flown to date are given by Friedman, and Schreier 1978. HEAO-A and Einstein are shown schematically in Figure 1.2.2.

HEAO-A had four X-ray astronomy experiments on board, all non-imaging. The A-1 experiment was a large area array comprising of seven modular proportional counters. All were of the gas flow type using xenon-methane and operating in the energy range .2 - 20 keV . A variety of mechanical collimators were used giving fields of view from  $8^\circ \times 2^\circ$  to  $1^\circ \times 0.5^\circ$  . The total open area of A-1 was  $14000 \text{ cm}^2$ . The A-2 experiment consisted of a set of detectors, all proportional counters mechanically collimated, with an overall energy range 0.15 to 60 keV . Each set of two covering a different range, .15 to 3 keV , 1.5 to 15 keV , and 3 to 60 keV . The effective areas were 600, 800 and  $900 \text{ cm}^2$  respectively. The A-3 experiment was a modulation collimator providing positioning to approximately 5 arc seconds for sources in the range 1.5 to 15 keV . Finally the A-4 experiment was an array of seven phoswich scintillators covering the range 10 keV to 10 MeV .

The Einstein Observatory carries 5 focal plane instruments and one monitor proportional counter. The focal plane instrumentation being a focal plane spectrometer, solid state spectrometer, objective grating spectrometer, imaging proportional counter and high resolution imager, that is a microchannel plate detector.



#### HEAO-B EXPERIMENT CONFIGURATION

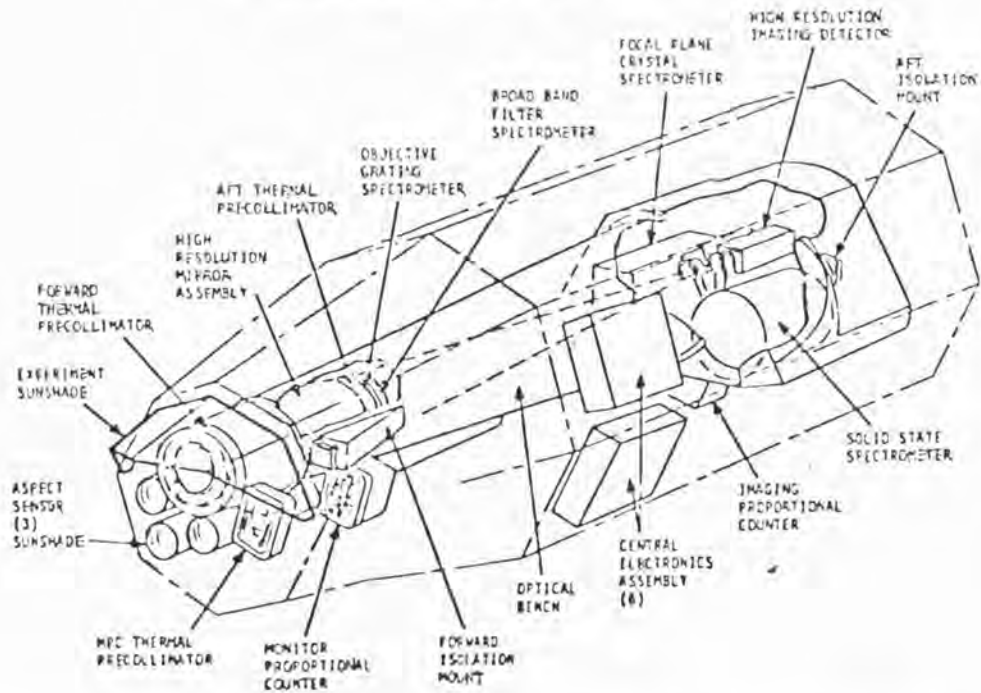


Figure 1.2.2. Schematics of HEAO-A and HEAO-B (now renamed The Einstein Observatory) spacecraft showing experiment configuration. (From Schreier, Friedman 1978).

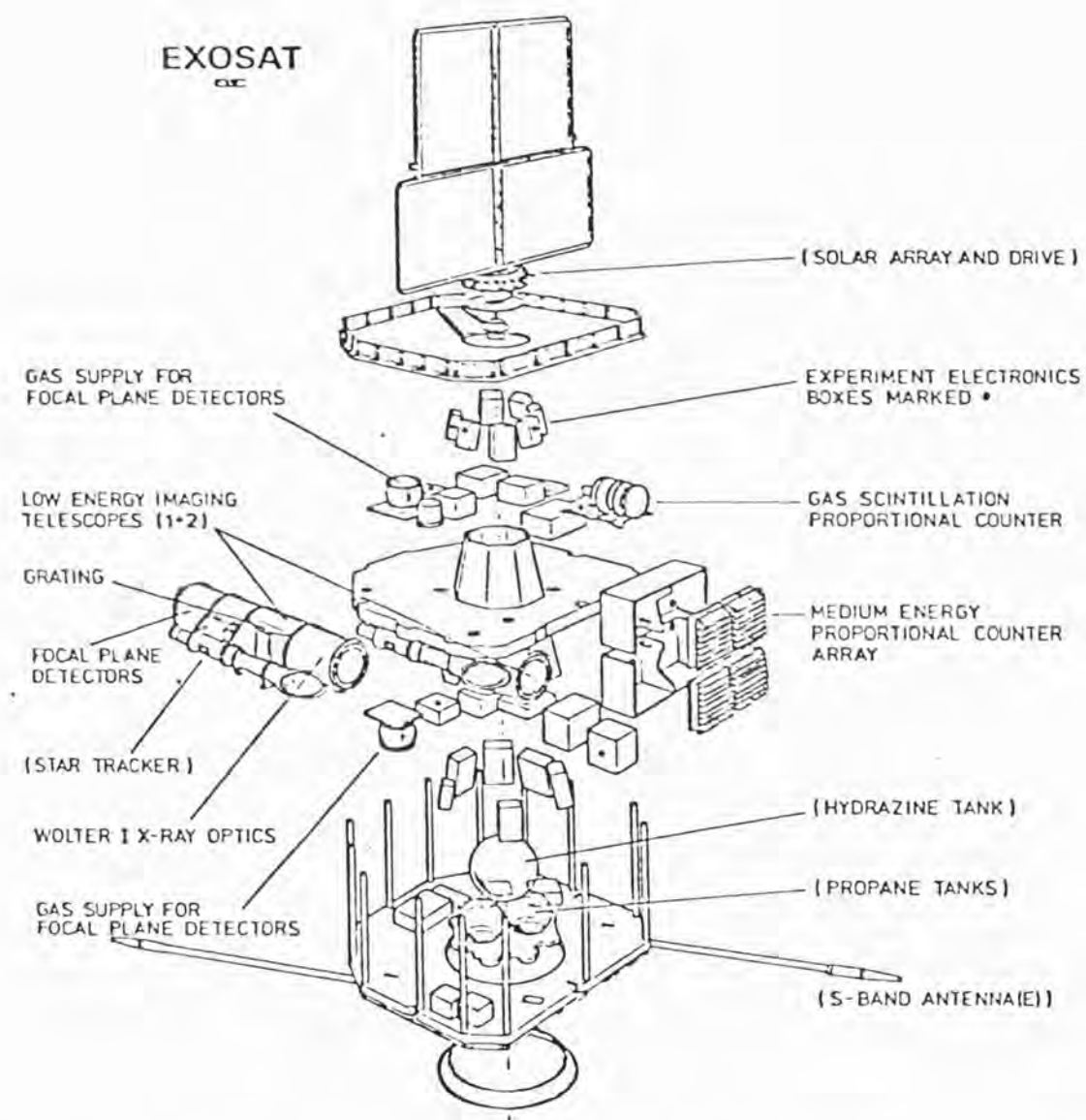


Figure 1.2.3. Schematic of the construction of the EXOSAT spacecraft. The spacecraft is three axis stabilised and currently scheduled for launch in 1982. (From Pounds 1981)

Both satellites have been reasonably successful. Problems with the A-1 experiment of HEAO-A were encountered due to hardware failures of the proportional counters, and analysis software problems. All other experiments have produced their expected amounts of data. HEAO-A re-entered in 1979.

Einstein is still in orbit, at present several thousand images of the X-ray sky have been produced. The only experiment no longer working is the solid state spectrometer which has spent all its available cyrogen. Lack of attitude control gas, after control problems will limit the remaining life of the satellite to a few months.

The only approved European X-ray astronomy mission in the future is the European Space Agency satellite EXOSAT, launch date 1982. (Astro C a Japanese satellite was approved late 1980). The satellite construction is shown schematically in Figure 1.2.3. The satellite will carry four experiments, two low energy imaging telescopes 0.05 to 2 keV geometric area  $100 \text{ cm}^2$  spatial resolution  $\approx 8$  arc seconds, a large area medium energy proportional counter array 1 to 60 keV and a gas scintillation proportional counter. The medium energy experiment has a total effective area  $\approx 1600 \text{ cm}^2$ , and field of view of 45 arc minutes FWHM. The energy range of the gas scintillator detector is 1.5 to 80 keV with an effective area of  $\sim 170 \text{ cm}^2$ . The aim of the mission is to study temporal and spectral variations of all known types of celestial X-ray sources. A detailed description is given in the paper by Pounds 1981.

### 1.3. X-ray Sources and their Scales of Variability

Sco X-1, the first celestial X-ray source to be discovered is the brightest 'steady' source known, the weakest yet detected is approximately  $10^{-7}$  times fainter. All types of sources apart from supernova remnants



show some variability on time scales from milliseconds to months. Indeed the variability in many cases leading to a better understanding of the nature of the sources, comparison of X-ray variability with observations at other energies for example optical and radio having lead to identifications of many sources. Reviews of the nature of X-ray sources, their identifications and variability are given by Rossi 1978, Bradt 1978, and Murray 1977.

Each type of source can in fact be characterised by its variability. Table 1.3.1 gives the source type, characteristic variability and suggested mechanism, for the common variable X-ray sources.

Apart from supernova remnants, many galactic X-ray sources are thought to be binary in nature, and hence should, and do exhibit variability. Extragalactic sources, that is active galaxies, also show variability, however, generally on a much longer time scale, hours to days, the characteristic timescale being  $\sim 1$  day, the X-ray origin being deep in the galactic nucleus. However not all sources have obvious temporal signatures and not all have been identified with known objects. To date only one gamma ray burst source has been tentatively identified. Although some sources lack obvious temporal signatures, such features could require much higher sensitivity than available from present and past experiments. For example, the galactic bulge sources, while being highly variable, at present only one has shown the characteristic variation of binary systems (Marshall 1981). Data from the Ariel V Sky Survey Instrument (SSI) shows 3A1658-293 the most regular X-ray burst source to have a  $1.82 \pm .05$  day period.

The sources with the most obvious temporal signatures are the transients and burst sources. Transient sources differ from most other sources, in mostly being seen on one occasion only (although some are known to recur), in a region of sky where no source has been detected in the past.

TABLE 1.3.1

## X-RAY SOURCES AND THEIR SCALES OF VARIABILITY

<u>Source Type</u>	<u>Typical Variability</u>	<u>X-Ray Production Mechanism</u>
X-ray pulsators e.g. Cen X-3, Her X-1.	Pulsations at a period of a few seconds to hundreds of seconds.	Plasma accretion from a companion onto or spinning neutron star or white dwarf
Binary systems (High mass) e.g. Cyg X-1	With quasi-periodic millisecond bursts of X-rays	Plasma accretion from a companion into a black hole
X-ray bursters	Bursts lasting a few to tens of seconds	Thermonuclear flash on surface of a neutron star or unstable accretion flow
Active galaxies	Irregular on time scales of hours to months	Galactic nuclei: Accretion into massive black holes?
Transients	Short lived, time scale minutes to hours	Origin unknown
	Long lived, time scale days to months	Binary systems with either high eccentricity or variable mass transfer from companion onto compact object, neutron star, white dwarf.
Gamma-ray bursts	Bursts in both X-ray and Gamma-ray bands lasting a few seconds, sub second time structure	Origin unknown

Two transients were in fact discovered before any satellite observations, by sounding rocket experiments (Harries 1967, Evans 1970). Transients are characterised by a rapid rise in intensity over either a period of approximately a week, or minutes to hours, and then a gradual decay back to invisibility. X-ray burst sources or bursters have also been observed, a burst being a very rapid increase in X-ray flux in a few to fractions of a second, with a subsequent decay over tens of seconds.

The prime purpose in development and construction of a wide field camera for X-ray astronomy is to observe and study X-ray bursts and transient sources.

#### 1.4. X-ray Burst and Transient Sources

##### 1.4.1. X-ray Transients

Transient sources can be divided into two distinct classes, the bright long lived type and the weak short time scale ones. The brighter long lived transients are confined mainly to the galactic plane, whilst the weak brief transients are distributed widely over the sky mainly at high galactic latitudes (an experiment selection effect). Because of their short duration, tens of seconds to hours, very little information is known about the second class. Some transients are known to be recurrent, however the majority of them have only been seen once.

The bright galactic transients are almost certainly binary systems with variable mass transfer onto compact objects; these have been reviewed in detail by Pounds 1976, Kaluzienski 1977 and Rossi 1978. Among these sources there are three which have regular pulsations, and hard spectra; 0535 + 26 (104 second period); 0115 + 634 (3.61 second period); and 1118 - 615 (405 second period). Five of the bright transients have been identified with stars which underwent an optical brightening coincident in time with the X-ray outburst, and have a soft spectrum, these are commonly



called X-ray novae.

Table 1.4.1 adapted from Bradt 1978, lists the galactic transients and summarised properties given in that publication. This table is not comprehensive due to the problems of definition between publications but shows the general properties of the source type.

Both 0535 + 26 and 0115 + 63 are known to be recurrent transients. 0115 + 63 which was last seen to flare in December 1977 reached approximately the brightness of Sco X-1. The brightness lead to an accurate measurement of the Doppler effect in its pulsations by SAS-3 (Rappaport et al., 1978). This revealed a strong elliptical orbit motion with a period of 24.3 days and an eccentricity of 0.34. Figure 1.4.1 shows the combined light curve of the transient 0535 + 26 in which 9 flares (arrowed) have been observed. This curve is a combination of data from Ariel V, SAS-3, and Hakucho, by the author. (Oda 1980 (a),(b), Rosenberg et al., 1975, Ricketts et al., 1975, Sims and Fraser 1979, Clark and Chartres 1978, Chartres and Li 1977, Ricker and Primini 1977, Rappaport et al., 1976(a), Li et al., 1979). All data being normalised to Ariel V SSI counts. (A full description of the Ariel V experiment being given in Villa et al., 1976). Figure 1.4.2 gives the residuals from an assumed period of 105 days, starting Epoch 42535 MJD. As can be seen a possible delay of ~110 days occurs between outbursts of the source. A problem is to explain the scatter. Oda has suggested a systematic trend could exist and currently the Japanese group are analysing the above combined light curve in detail. The recurrent behaviour of many bright galactic transients suggest long period eccentric orbit binary systems with variable mass transfer between the pair of stars.

All the coincident X-ray/optical novae have been identified with low mass stars, which brighten optically due to reprocessed X-rays. The

TABLE 1.4.1  
TRANSIENT X-RAY SOURCES

Source	Common Name	X-ray Properties	Flux Density		(2-11 keV)	Optical Properties
			Max	Min $\mu$ Jy		
0042 + 327		Transient 1977 11.6 day period?	5.5	< 0.5	Star	Variable $\lambda$ 4686 V = 19.2.
0050 - 727	SMC X-3		5	$\leq 1$	Star OB Emission Lines V = 15	
0052 - 739	SMC X-2		7	$\leq 1$	Star OB Variable ?	V = 14.8
0115 + 634		Binary period = 24.3d Pulsing P = 3.61 sec.	15000	$\leq 2$	Star B type V = 15.6 H $\alpha$ emission	
0449 - 55		Fast ~ 200 min high galactic latitude transient	140	$\leq 5$	M dwarf?	
0535 - 668	LMC	Recurrent transient Probable 16.7d period	180	$\leq 1$	Star B type V = 12.8	
0535 - 262		Recurrent pulsator P = 104 sec, 110 day period?	2000	3	Star B type V = 9.1	
0620 - 003	Nova Mon '75	Very bright X-ray Nova	> 50000	$\leq 5$	Star - optical brightening to V = 10.4	
1118 - 615		Pulsating P = 405 sec	70	< 5	Be star? V = 12.1 Mira Variable?	
1524 - 617	Tra X-1	X-ray Nova	225	10	Coincident optical nova	
1543 - 475		Bright transient July '71 to Sept. '72	2240	< 1.2		
1608 - 522		'Steady' and recurrent nova Burster?	1100	< 1.0	Optical nova	
1630 - 472		Recurrent transient	1400	< 2	Star UV excess V = 18.3	
1658 - 298		Burster with transient behaviour	80	< 5		
1705 - 250	Nova Oph '77	X-ray Nova	3500	< 1.5	Coincident optical nova	
1715 - 321		10 min. Flare	2000	15		
1742 - 289		Nova near galactic centre Burster MXB 1743 - 29?	2000	< 9		
1743 - 322		Very long decay Aug '77 to Mar '78	770	$\leq 10$		
1743 - 288	GX+0.2-0.2		90	< 7		
1744 - 361			275	< 25		
1745 - 203	NGC 6440		181	17	Globular Cluster	
1803 - 245			850	$\leq 10$		
1908 + 005	Aql X-1	Recurrent	1000	< 11	Star Coincident optical brightening V = 19.2	

Note Crab - 1000  $\mu$  Jy (2-11 keV)

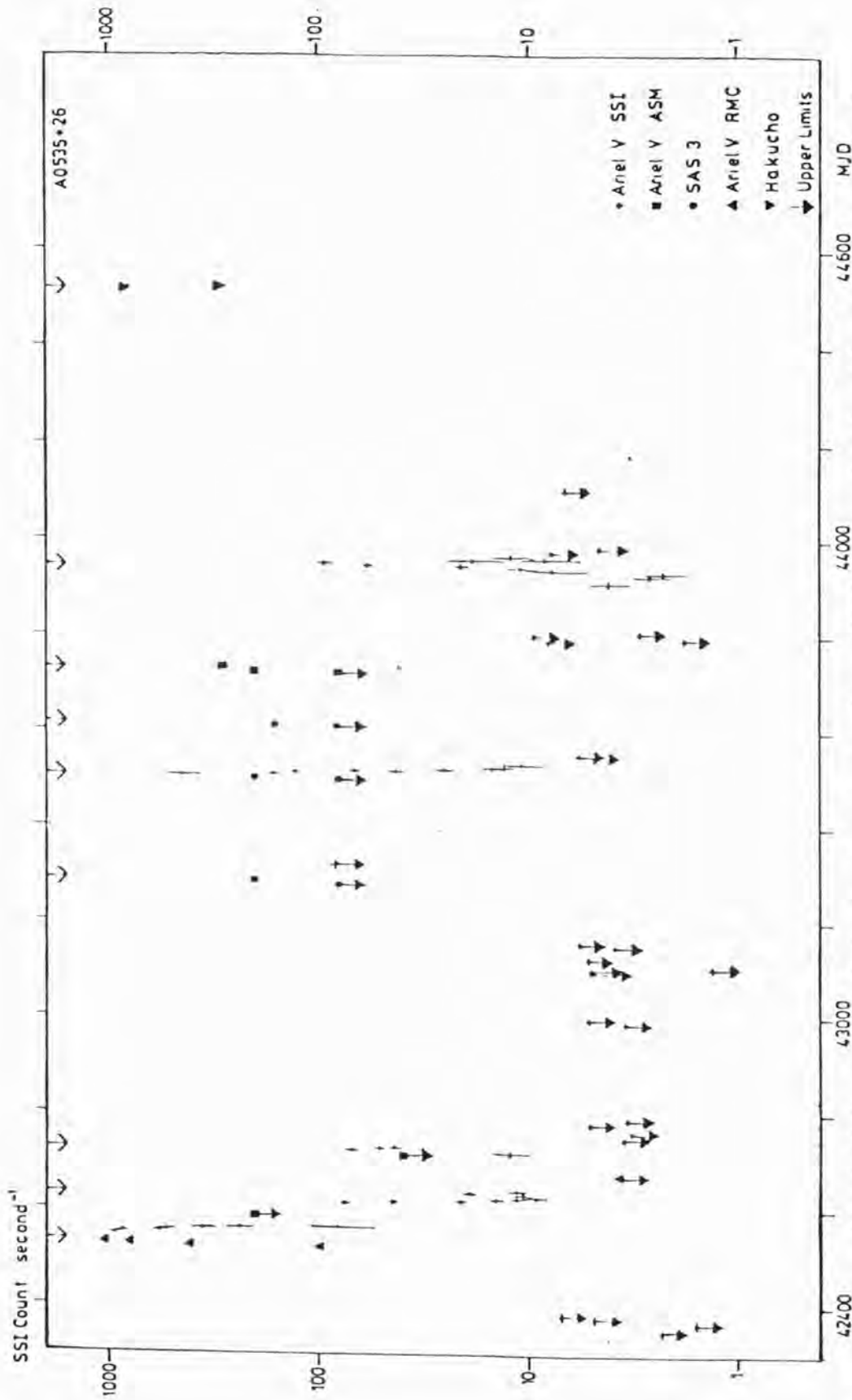


Figure 1.4.1. The combined light curve of the recurrent transient A0535 + 26 using data from three spacecraft, Ariel V, SAS-3, and Hakucho. Nine separate peaks in the observed flux are visible (arrowed). Peak No.2 from the left is many times smaller than the others and may not represent a true outburst from the transient. The time is given in MJD and covers approximately ~ 7 years.

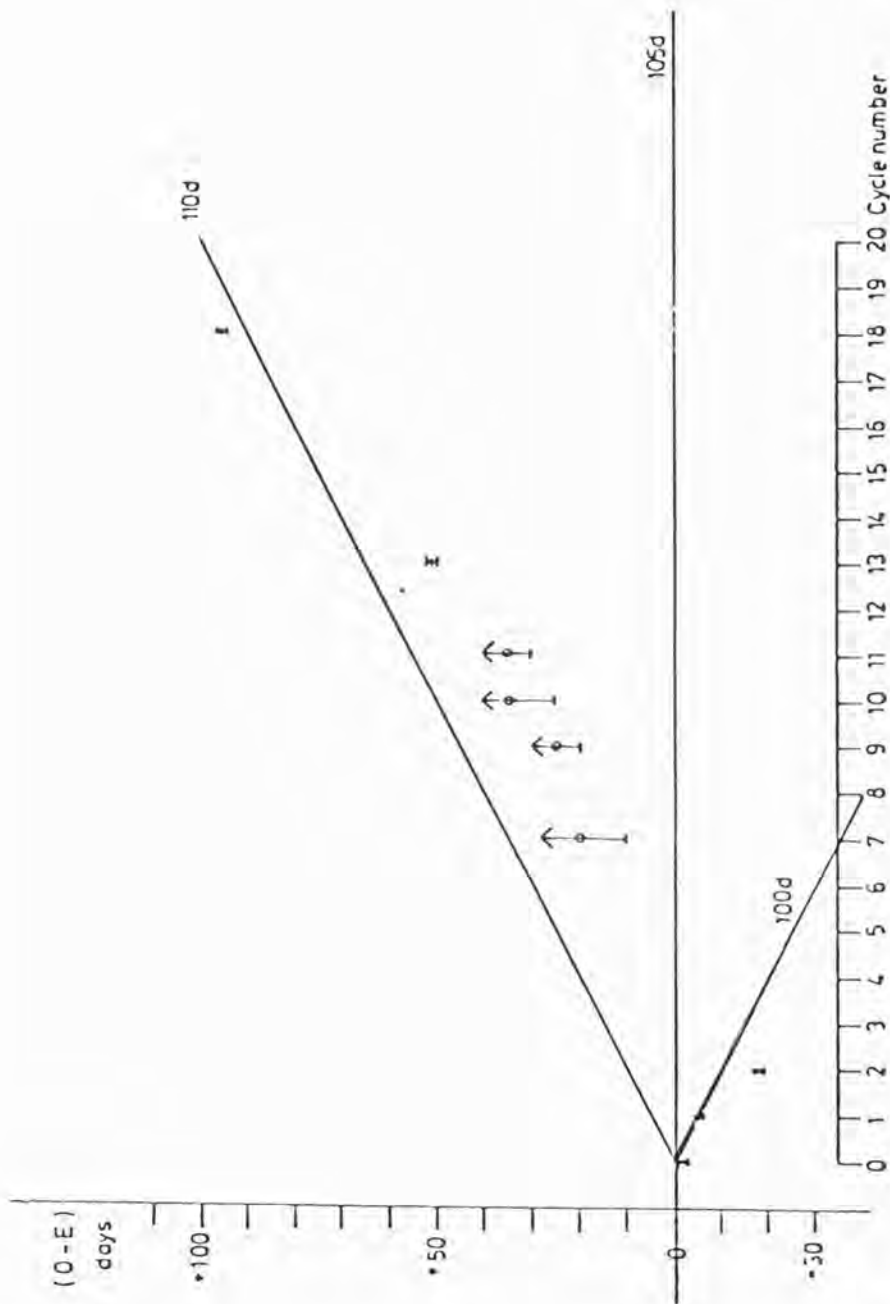


Figure 1.4.2.

This figure shows the residuals from an assumed period between outbursts from A0535 + 26. The difference between observed time and expected time in days is plotted against cycle number for an assumed period of 105 days, phase zero being MJD 42535. For the outbursts where near exact dates of peak flux are known, a dot with maximum error bars is used. For all other outbursts a horizontal bar represents the minimum difference and a circle the most likely date of maximum flux, taking the other outbursts as a model. The expected lines of deviation for periods of 100 and 110 days are marked. Note a delay of approximately 110 days exists between outbursts; not all cycles are however covered by the available data.

peak intensities in optical and X-ray are seen to occur simultaneously, the X-ray luminosities being over 100 times greater than the optical. In contrast none of the optical novae have yet been found to emit X-rays.

No recent adequate survey of transients however exists, due to the difficulty of definition and comparison between experiments. Little at present is known about the weak brief transients seen by Ariel V, SAS-3, and HEAO-1 (Ricketts 1978, Rappaport 1976(b), Kaluzienski 1978), their time scales of outburst running from several minutes to hours. So far approximately 30 such transients have been detected. As shown in Figure 1.4.3 these transients appear to obey a number intensity index of  $-1.5$ , the data and analysis being provided by Turner, Ricketts and the author. Figure 1.4.4 shows the typical time profiles of high latitude transients taken from a Spacelab. Proposal to NASA by the University of Leicester and the Center for Space Research of MIT. This proposal will be discussed in detail in Chapter 2.

Three have been identified, the transient A1103 + 38 decayed slowly enough for Ariel V to be repositioned yielding a cross scan, giving a position close to Mk 421 a BL.Lac object (Ricketts 1976). A1353 - 40 decayed over a few hours, but recurred 200 days later and has been identified with NGC 5367 a local region of star formation (Cooke 1976), finally A0711 + 01 has been associated with the  $\gamma$ -ray burst of 5 March 1979 (Cline et al., 1980, Evans et al., 1980). The celestial distribution of the remaining brief transients suggests they may be extragalactic, halo objects, or nearly main sequence stars. However a mixture of origins is very possible, including extreme variability of active galaxies, flare stars or low luminosity stellar X-ray sources. Rappaport 1976 has suggested that the sources may be nearby, intrinsically weak white dwarf binaries.

Detection and accurate positioning, hence optical identification of a large number of these sources, would enable questions of their origin to

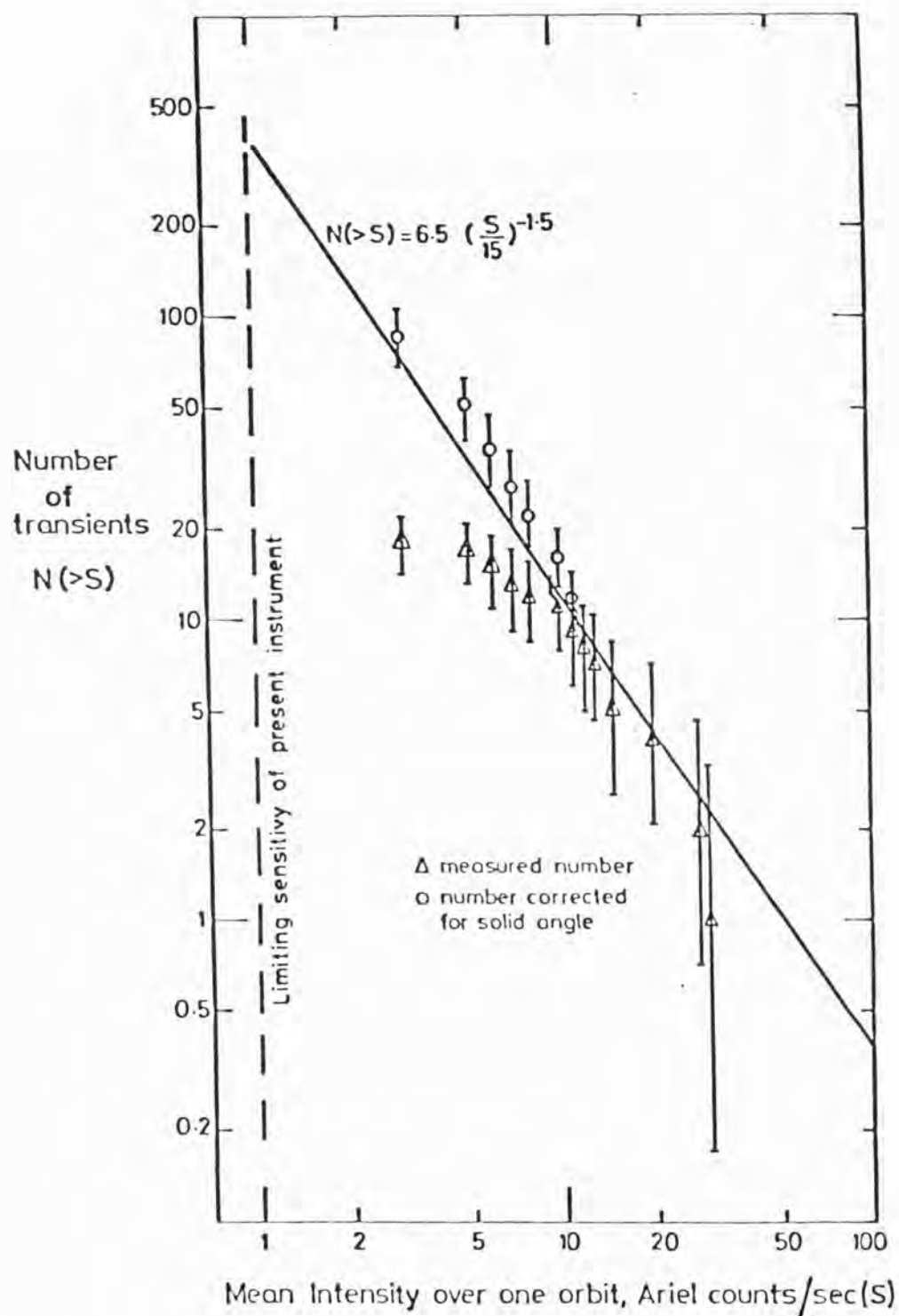


Figure 1.4.3. Estimated source counts of the X-ray high latitude transients. The estimate is based on Ariel V observations and is corrected for the decrease in effective solid angle of the Ariel V Sky Survey Instrument near its limiting sensitivity.

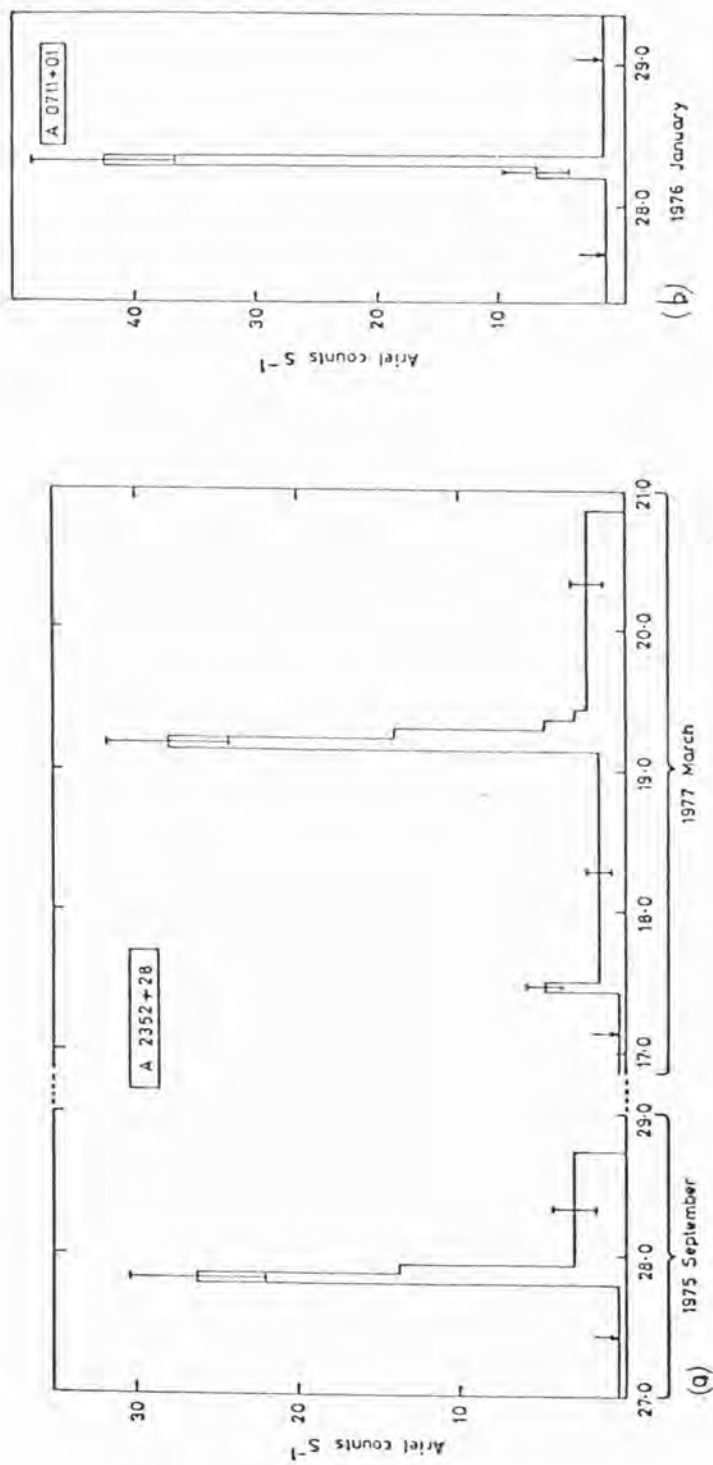


Figure 1.4.4. Typical time profiles of transients:

- (a) Observations with Ariel V of two flares of the short lived transient source A2352 + 28. Error bars are  $\pm 1\sigma$ .
- (b) The short lived X-ray transient sources A0711 + 01 as observed by Ariel V. This has been provisionally identified with  $\gamma$ -ray burst 76 - 2. Error bars are again  $\pm 1\sigma$ .



be settled. Light curves along with spectra would enable the basic emission mechanisms to be understood.

#### 1.4.2. X-ray Burst Sources

X-ray burst sources are characterised by a sudden increase in X-ray flux with a rise time of a few seconds or smaller decaying over tens of seconds. The peak intensities are comparable with the strongest 'steady' X-ray sources. Not all burst sources have been associated with sources of 'steady' X-ray emission; most but not all have been observed more than once. The first two bursts were detected arising from the globular cluster NGC 6624 in 1975 by ANS, these bursts being separated by 8 hours (Grindlay and Heise 1975). Intensive searches for bursts have been carried out since, by several satellites; however SAS-3 and Hakucho have produced most data in this field. The most comprehensive review to date is given by Lewin and Joss 1980. Figure 1.4.5 shows the initial burst discovery as given in Grindlay et al., 1976.

At present approximately 30 burst sources are known, most confined to the galactic plane, with a distinct concentration towards the galactic centre. Figure 1.4.6 shows the sky distribution in galactic co-ordinates of confirmed burst sources taken from Lewin and Joss.

Bursts can be classified into two distinct types (Hoffman, Marshall, Lewin 1978): Type I bursts at intervals of hours to days which show distinct spectral softening during their decay, and Type II bursts at intervals of seconds to minutes, showing no spectral evolution during the decay. Type I bursts are probably thermonuclear flashes on the surface of a neutron star whilst Type II are thought to represent instabilities in the accretion flow onto a neutron star. Nearly all sources are Type I burst sources, although some Type II bursts have been seen from some Type I sources. Only the burst source MXB 1730 - 335, the Rapid Burster is seen to emit both



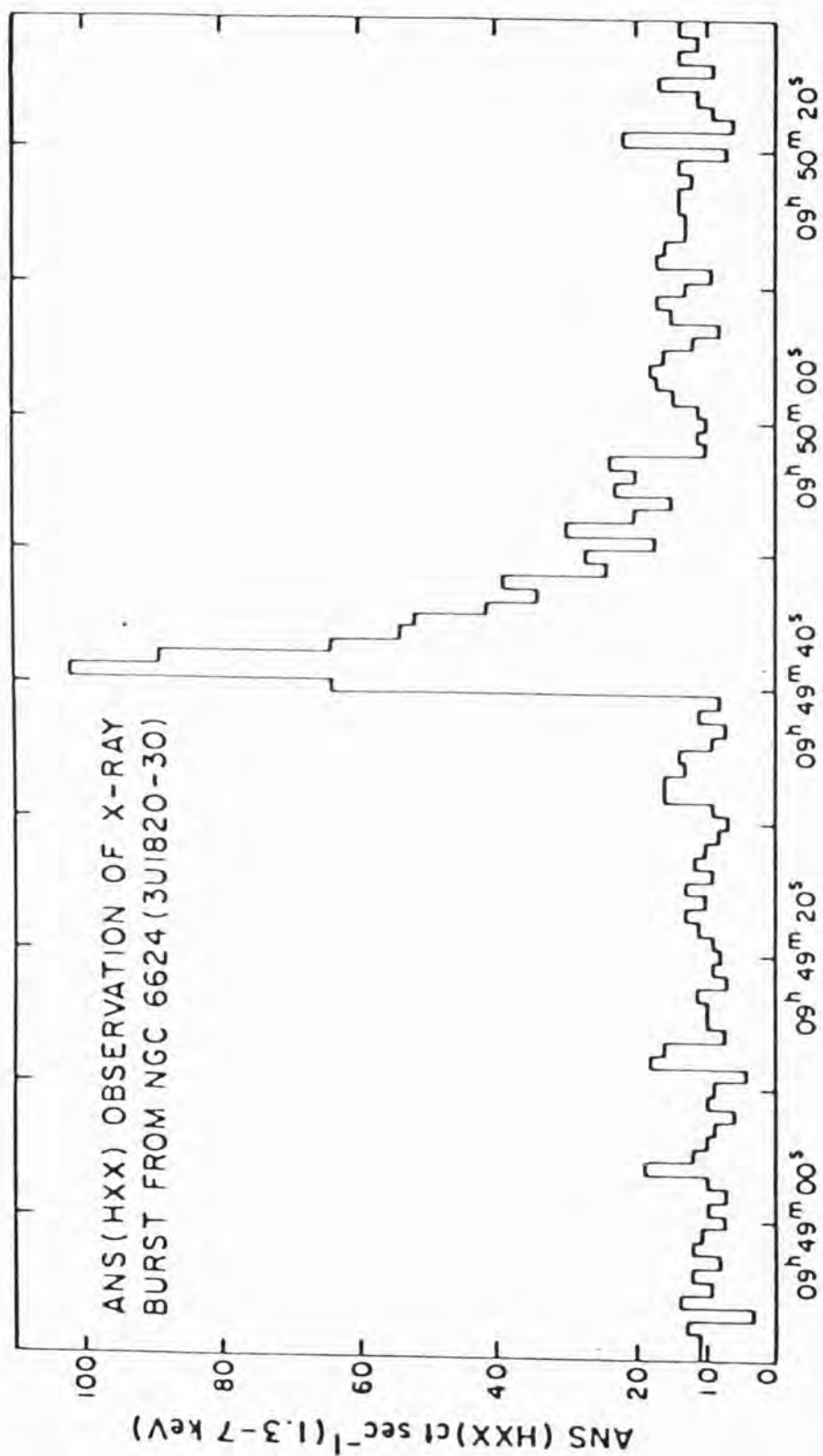


Figure 1.4.5. The discovery of X-ray bursts. This is one of two bursts observed, from the source located in the globular cluster NGC 6624, with the Astronomical Netherlands Satellite on 28 September 1975. The integration intervals are 1s. (From Grindlay et al., 1976)

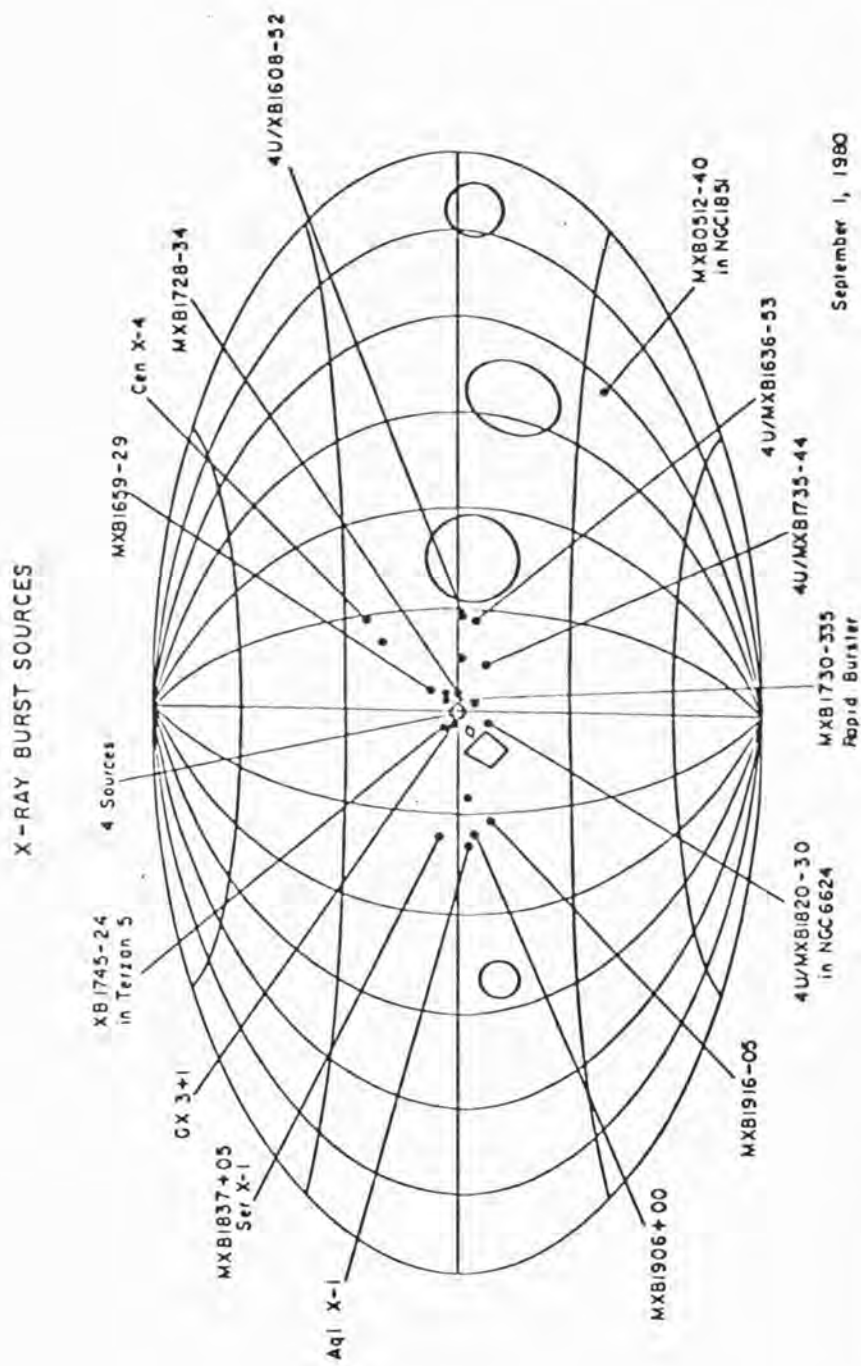


Figure 1.4.6. Celestial distribution of 31 confirmed X-ray burst sources (1 September 1980) in galactic coordinates. All poorly defined burst sources are not shown. At least 26 of the shown sources emit Type I bursts. (From Lewin and Joss 1980)

regularly, A full comprehensive list of burst sources and their respective properties is given in Lewin and Joss.

Table 1.4.2 summarises the known observational parameters of the various types of X-ray burst, a third peculiar variety observed only from the rapid burster being included for completeness.

Most Type I burst sources have an associated source of steady X-ray emission, and are believed to be members of the Galactic Bulge Sources, population II. Six of these sources have been optically identified with faint blue stars, five of the burst sources being identified within globular clusters. Optical bursts delayed in time have been observed from three burst sources, MXB 1735 - 44, MXB 1636 - 53, and MXB 1837 + 05 (Ser X-1). The time delay is a few seconds due to travel time distances between the X-ray and optical photons, a few light seconds across an accretion disk, the reprocessing times being negligible.

All the Type I's are located within  $\sim 45^\circ$  of the galactic centre and tend to have soft 'steady' X-ray emission. Variability on the time scale of seconds to days has been observed from some of these sources. As yet only one source, 1658 - 298 has shown characteristic binary system flux variation with a  $1.82 \pm .05$  day period. Figure 1.4.7 shows the resulting folded light curve from Ariel V SSI data (Marshall private communication). No periodic pulsations or eclipses have been detected from the other sources; this does not rule out binary systems with neutron stars as the model, as one, the neutron stars may have no strong magnetic fields and two, certain geometries are possible that give no eclipses (Joss and Rappaport 1979). The thermonuclear flash model (Joss 1978) at present seems the most promising to explain Type I bursts, the bursts being produced by the accumulation of a critical density of accreted matter on a neutron star, the accretion from the primary also producing the steady X-ray emission of the source. Simple models predict that the intervals

TABLE 1.4.2

## PROPERTIES OF BURST TYPES

	<u>Type I</u>	<u>Type II</u>	<u>Peculiar</u>
Rise time	$\leq 1$ sec smooth	$\leq 1$ sec 50 m sec structure	$\leq 1$ sec
Decay time	3 - 30 sec	1 - 30 sec	30 - 60 sec
Tails	$10 - 10^3$ sec	$< 10$ sec	Trapezoidal profile ~ minutes
Time to following burst	few hours	$10 - 10^3$ sec	$10^2 - 10^3$ sec
Spectrum	Blackbody	Blackbody	Blackbody
$T_{\max}$	$3 \times 10^7$ K Cooling	$\sim 2 - 10^7$ K No cooling	?
$L_{\max}$	$\sim 10^{38}$ erg/sec	$\sim 10^{38}$ erg/sec	$\sim 10^{38}$ erg/sec
Energy in burst (Assuming $d=10$ Kpc)	$\sim 10^{39}$ erg	$\sim 10^{38-40}$ erg	$10^{39-40}$ erg
Radius (Assuming $d=10$ Kpc, Blackbody)	$\sim 10$ km constant	$\sim 15$ km decreasing during decay	?
Possible Mechanism	Thermonuclear Flash	Accretion Instabilities	?
Stellar Object	Neutron star or	black hole	$1M_{\odot}$
Single or Binary system	?	Probably binary	

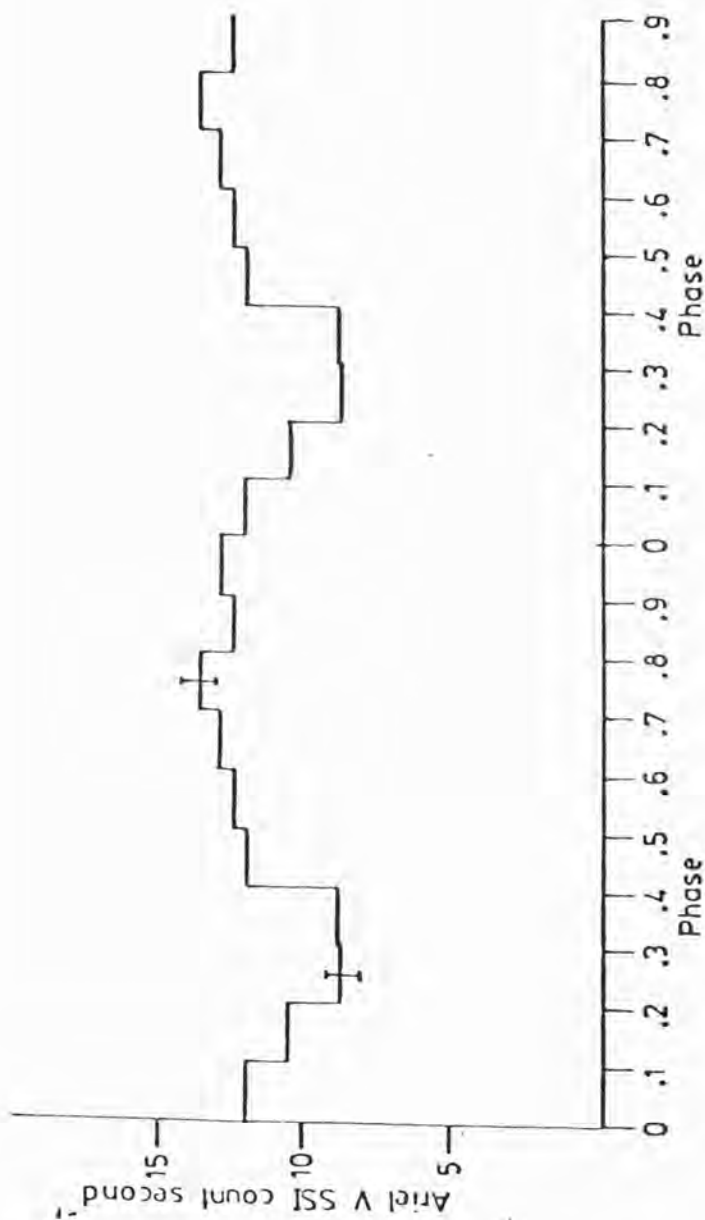


Figure 1.4.7. Folded Ariel V SSI lightcurve of 1658 - 298. The curve is the result of folding all SSI data (the result of one orbit flux measurements) in ten phase bins at the most probable period of 1.82 days as indicated by a  $\chi^2$  test against constant flux. A convincing binary type flux variation is evident. (From Marshall 1981)

between bursts will become shorter as the accretion rate and hence steady emission increases. At present some sources show this correlation, but not all, the model is unable to explain the multiple peaks observed from some sources. Figure 1.4.8 shows typical burst profiles from a number of sources.

#### 1.4.2.1. The Rapid Burster

The rapid burster produces both Type I and II bursts (Hoffman et al., 1978). It is thought that the Type II bursts replace the 'steady' emission in the case of this source. The source was thought to be a recurrent transient type burst source which became active for a few weeks to months approximately every 6 months. However, the source was not observed as expected in 1980. Infra-red, optical and microwave bursts in addition to X-ray bursts have been observed from this source. The source until 1979 had two distinct modes of bursting (Type II bursts), in 1979 a third mode of peculiar bursts was observed by Hakucho, see Table 1.4.2 (Inoue et al., 1980).

In Mode I the total burst energy distribution is doubled peaked with bursts varying over two orders of magnitude in energy, while in Mode II the distribution has single peak with a spread in energy less than a magnitude. The rapid burster on becoming active started in Mode I and changed to Mode II, the change occupying a period of a few hours, then died in the second mode. However the 1979 and 1980 data have upset this previously consistent behaviour.

The exact nature and behaviour of burst sources is by no means clear. Detection with good spatial, temporal, and spectral data for all sources might enable these sources to be understood in detail. Spatial resolution enabling new sources to be located, temporal and spectra data being required for a study of the burst mechanism.

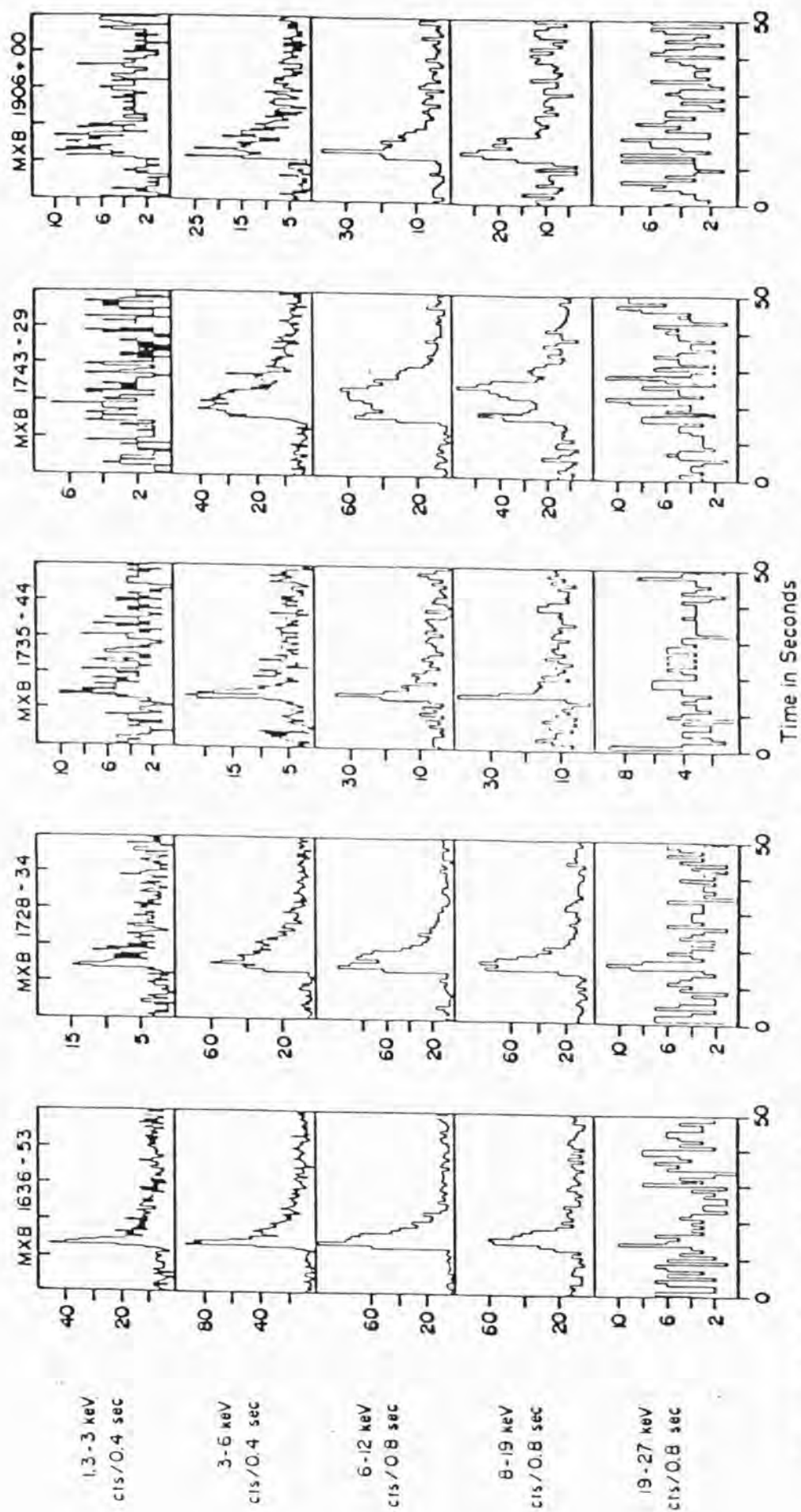


Figure 1.4.8. Typical X-ray burst profiles. Profiles of Type 1 X-ray bursts from five different sources as observed by SAS-3. Note the gradual decay, that is burst tail, persists longer at the lower energies than at the higher energies. This indicates cooling of the burst emission region. Note also complex time structure of bursts from 1743 - 29. (From Lewin and Joss 1980)



## 1.5. Other Sources of Extreme Variability

### 1.5.1. Active Galaxies

Approximately 50 active galaxies have been identified as X-ray sources, excluding the imaging data from Einstein, where a specialised survey has been made. Down to a flux level of  $10^{-3}$  of the Crab  $\sim 40$  active galaxies have been detected. Many show variability on a time scale of weeks to days, this variability pointing to a source at the galactic nucleus of small size.

A detailed review of known variability has been given by Pounds 1980(a). Marshall et al., 1981 have used Ariel V SSI data to investigate the long term and short term variability of active galaxies. Table 1.5.1 adapted from Pounds (1980(a)) summarises all the Ariel V observations of short term variability. These results show that variability on a time scale of  $\sim 0.5 - 5$  days is common in active galaxies.

Active galaxy types which show this form of variability include two quasi-stellar objects, two BL Lac objects and several Seyferts. It is thought that all identified X-ray active galaxies sources would show this form of behaviour if monitoring of a large number occurred. Figure 1.5.1 shows the Ariel V SSI light curve for 3C273; as can be seen a dramatic increase in the 2 - 10 keV flux occurs within  $\sim 0.5$  day. Figure 1.5.2 shows the Ariel V SSI light curve for NGC 7469 showing evidence of  $\sim 2$  day flare.

NGC 4151 shows evidence of repeated flaring on a time scale of days (Elvis 1976, Lawrence 1980) and Tanabbaum et al., 1978 have reported an order of magnitude variation in  $\sim 730$  seconds.

Approximately 50% of the active galaxies examined by Marshall et al., showed evidence of long term variability, this being of time scale months to years. The overall characteristics of variability however are poorly defined due to the poor sensitivity and limited temporal coverage.



TABLE 1.5.1.

SHORT TERM VARIABILITY CHARACTERISTICS OF ACTIVE GALAXIES OBSERVED BY ARIEL V SSI  
Variability

Source Name	Common Name	Flux (SSI counts/s)	2 - 10 keV Luminosity (Erg/s)	Overall Time Scale (days)	Variability Factor (flux)	Energy Content (Erg)
2A0120-353	NGC 526A	1.03	7.4 E43	3	3	3 E49
2A0241+622		0.64	2.7 E44	2	8	-
2A0943-140	NGC 2992	1.52	1.8 E43	3	2	3 E48
2A1102+384	MKN 421	1.04	2.2 E44	3	4	7 E49
				1	2	3 E49
2A1207+397	NGC 4151	3.32	6.2 E42	2-4	2	5 E47
2A1219+305		0.96	-	4	3	-
2A1225+027	3C 273	1.96	1.1 E46	0.5	2	-
2A1332-427	Cen A	8.8	5.2 E41	2	2	1 E47
2A1410-029	NGC 5506	1.55	1.3 E43	3	3	8 E48
2A2259+085	NGC 7469	0.88	5.4 E43	2	6	2 E49

Note: The exponential format of Fortran has been used, namely  $1E1 \equiv 1 \times 10^1$

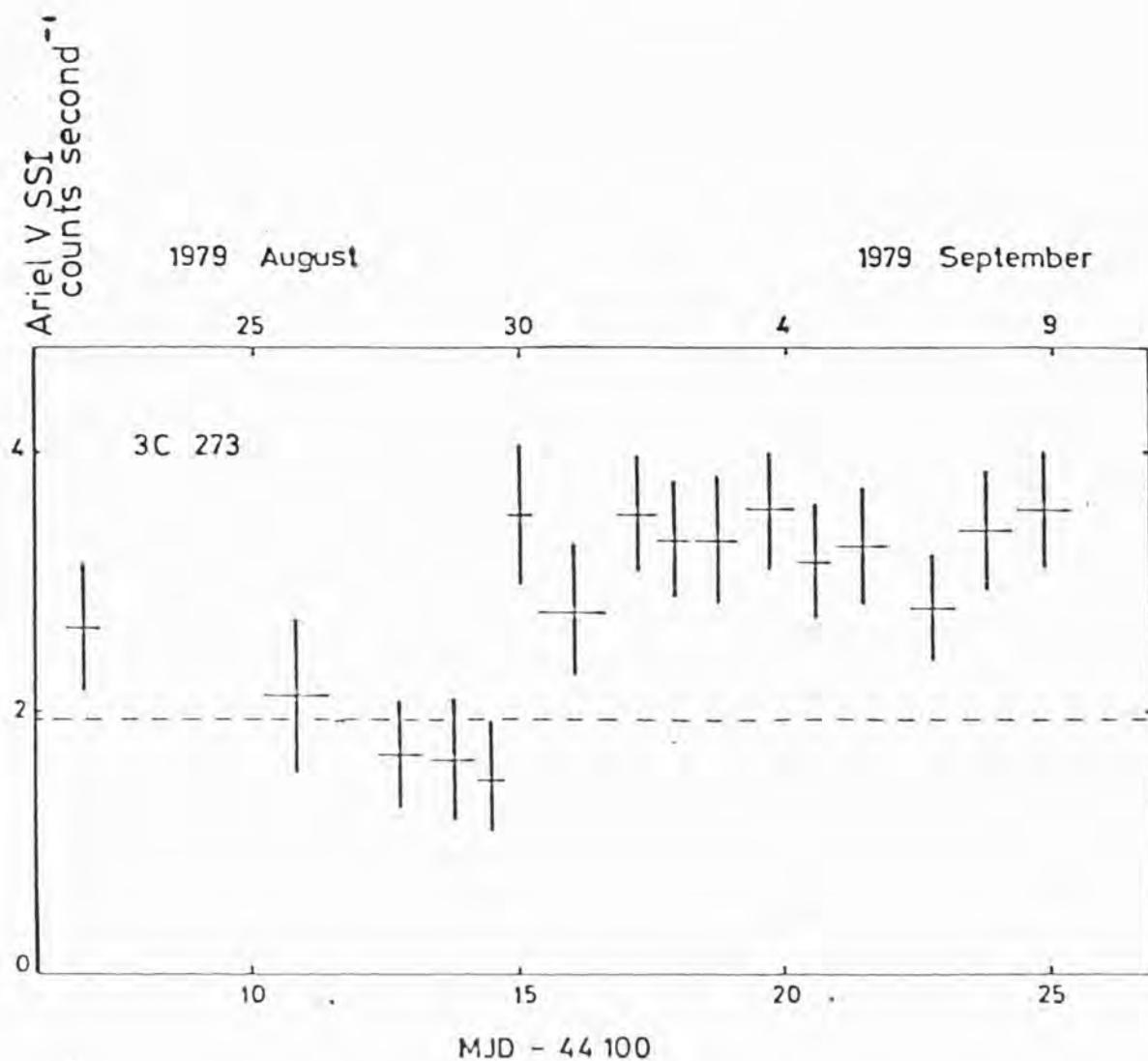


Figure 1.5.1. Ariel V SSI light curve for the quasar stellar object 3C273. A dramatic increase in the 2-10 keV flux within ~0.5 day is evident. The dashed line represents the mean (5 year average) SSI flux for the source. (From Pounds 1980)

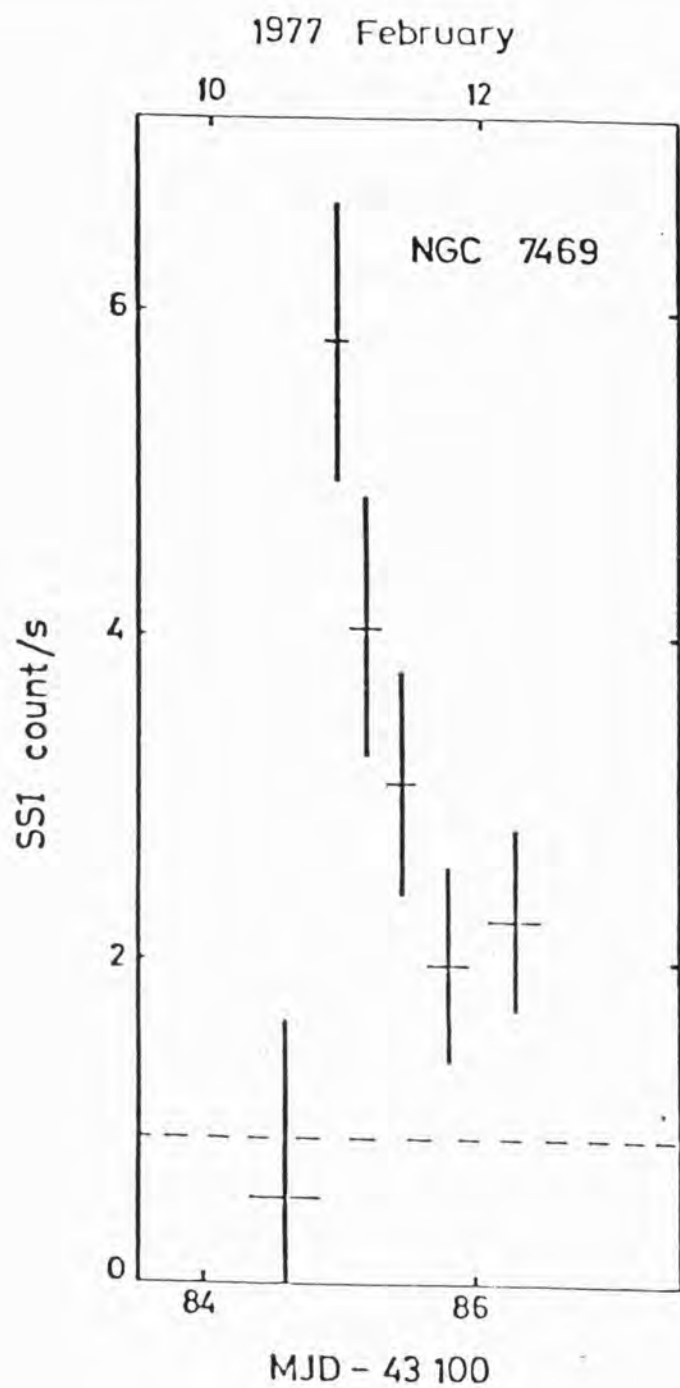


Figure 1.5.2. Observation of NGC 7469 (Seyfert galaxy) showing evidence of an ~2 day flare, Ariel V SS1 observation. (From Pounds 1980)

Variations of a factor  $\sim 2$  to 5 times can occur on time scales of days. Future observations require fuller coverage and spectral information before detailed modelling can occur.

### 1.5.2. Hard X-ray, $\gamma$ -ray Bursts

Gamma ray bursts were first observed by the Vela satellites (Klebesadel et al., 1973). At present approximately 100 bursts have been detected. However, their origin is still a mystery. These bursts have the following characteristics (Klebesadel 1976, Mazets 1979 a,b,c). Total integrated energy runs from  $10^{-4}$  to  $10^{-7}$  erg cm $^{-2}$ , at present the index of the number intensity log-log relationship is thought to be  $-1$ . Total burst durations vary between tenths of a second and 50 seconds, the rise time varying from tens of milliseconds to seconds. Typical duration however is about 5 seconds, although secondary and precursor pulses are often associated with a burst, and complex internal time structure has also been seen. Approximately 80% of the energy in a burst lies above 100 keV. However most photon flux is in fact below 50 keV, the spectra so far measured have been remarkably uniform with a photon number index of  $\sim 1.4$  below 100 keV. The spectra of these bursts differs considerably from that of the X-ray bursters whose intensity falls sharply round 15 keV while the  $\gamma$ -ray burst spectra appear flat in this range, in addition X-ray bursts are  $10^{-2}$  to  $10^{-3}$  smaller in intensity.

At present only one identification of a  $\gamma$ -ray burst source exists, as most positional accuracies are of the order of several to many square degrees, these positions being derived from timing differences between detection of the burst by several satellites. In March 1979 an unusual event was observed by nine different spacecraft (Terrell 1980 and references therein). The position of the event was determined to be coincident with the supernova remnant N49 in the Large Magellanic Cloud. In addition an

8 second periodicity was found in the flux after the intense initial outburst which may indicate the source was a neutron star, possibly an old pulsar. The identification with N49 could however be in some doubt because of the large associated energy of the burst.

Detailed spectral and temporal data on these bursts would shed further light on the burst mechanisms, a wide field X-ray camera being able to provide information from the extension of the burst spectrum to X-ray energies.

#### 1.6. Instrumentation to Study Variability

As can be seen many forms of variability have been detected in X-ray astronomy. Most studies until recently have used proportional counters with mechanical collimators; the collimator giving the counter crude angular resolution. The proportional counter has several advantages, reasonable energy resolution, good quantum efficiency over a designated energy range (dependent on design and gas filling) and large areas  $\sim 1000$ 's  $\text{cm}^2$  can be constructed. The counter can however only be used in two distinct modes, each of which has a disadvantage. First, the counter can be pointed continuously at one source to monitor its variability as long as the satellite or rocket stability or observational program limitations allow it. Second, it can be used in a scanning mode observing a fraction ( $360^\circ$  by a few degrees) of the sky with only a short exposure over an orbit to any one area. In the first mode only a single source or small collection of sources can be studied missing variability over the rest of the sky, and if more than one source is present in the collimator response, the detector is unable to provide positional information on which source, if any, is varying. In the second mode only gross changes of a source can be studied, ignoring any problems of source confusion, hence fine time scale structure is missed, for example, bright short events can be easily

missed, the integrated brightness over a long period being very much lower than the maximum value. However the majority of variability of burst sources, binaries etc., has been studied using these modes.

More recently grazing incidence telescopes have been launched (for example Einstein) or have been proposed. These telescopes are true imaging experiments providing positional information over their field of view, and energy information with a suitable detector, for example imaging proportional counters. This telescope has several advantages over mechanically collimated proportional counters, good angular resolution can be achieved and hence a low background is present, making the telescopes over reasonable time scales, photon counting statistic limited. However the telescope has two disadvantages, first it is impossible to construct a single telescope with a field of view more than a few degrees (although several telescopes may be employed pointing in different directions), and second, the device has low effective areas above 4 keV. Figure 1.6.1 gives the effective area of the Einstein Observatory as a function of energy for one of the two imaging proportional counters on board (Schreier 1978). The high energy cut off is given by the mirror response.

The very nature of the sources that require study, that is primarily burst and transient sources, rapid intensity changes, and rare events over  $4\pi$  steradians, rule out the mechanically collimated proportional counter or grazing incidence telescopes as ideal instruments.

The ideal instrument covers  $4\pi$  steradians continuously. However, this is impossible to achieve with one instrument, so one requires a wide field camera or combination of them, that give a near continuous coverage of as large an area of sky as possible. The instrument must be able to give positional information, such that an angular resolution of the order of arc minutes can be achieved, with some energy information, and with a large effective area in the keV to tens of keV region. Previous work has

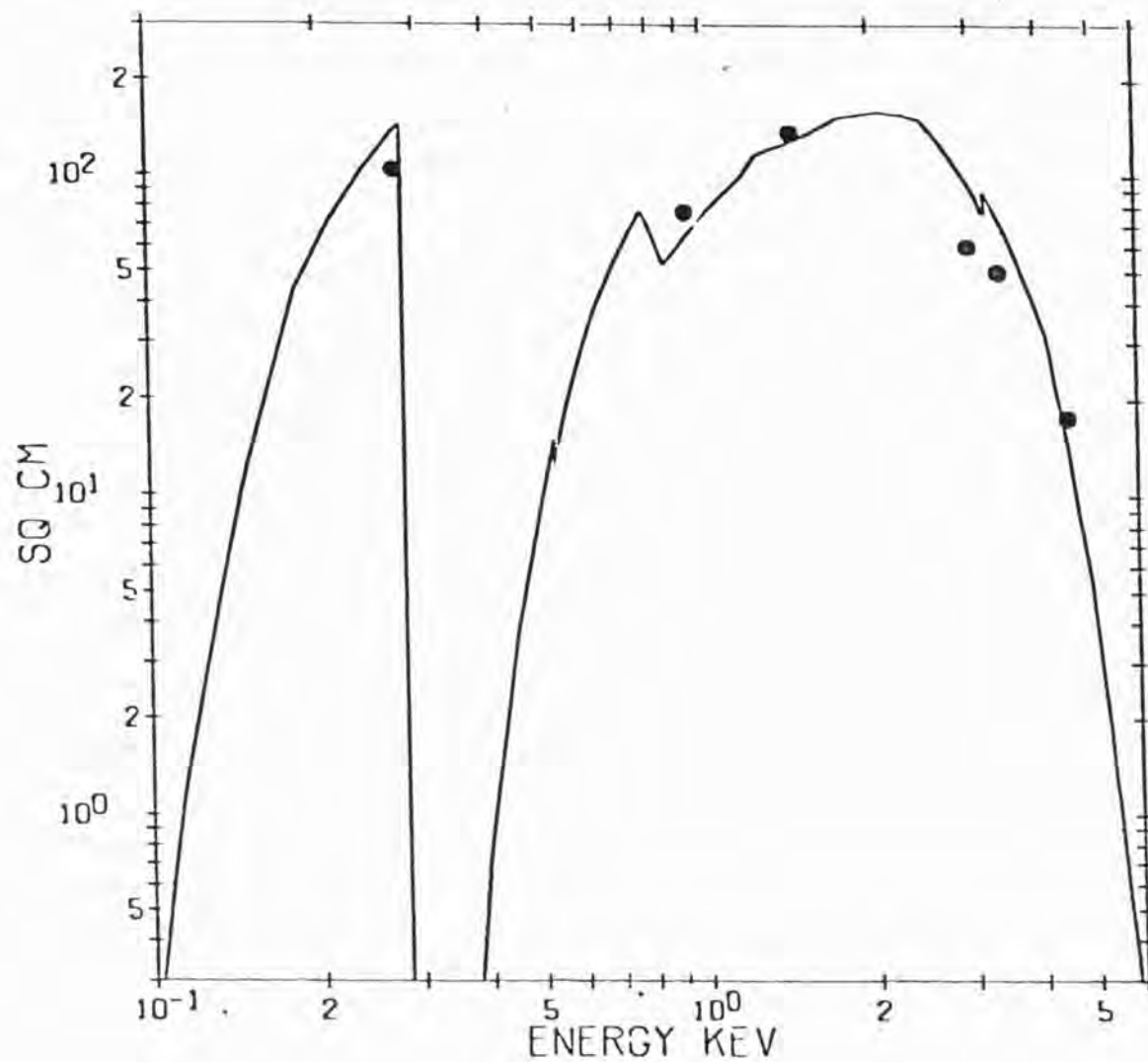


Figure 1.6.1. Effective area as a function of energy for one of the two IPC's on board Einstein. Circles are measured calibration points, theoretical value solid line. High energy cut-off is due to mirror response. low energy due to detector window response.



shown that any sources with an error box of the order of square arc minutes or smaller can normally be easily identified except in the case of the galactic centre region.

The instrument must not however be thought of as an end in itself, it must be able to give sufficient information, so that other instrumentation, the proportional counter, grazing incidence telescopes, etc., can if possible study the source giving more detailed information on any one source. However if no other instrument is available, such as in the case of a short high latitude transient enough information must be able to be obtained, that optical or other identification, timing and spectral data can lead to an understanding of the nature of the source and its emission processes.

An instrument that is at least theoretically capable of giving sufficient performance is the shadow camera, known also as the transform telescope or Dicke camera.

### 1.7. The Shadow or Dicke Camera

Some of the first imaging experiments in X-ray astronomy utilised the pinhole camera concept, enabling a wide field of view to be studied with modest angular resolution, for example the Ariel V All Sky Monitor (ASM) (Holt 1975). Dicke 1978 showed that a mask of many randomly spaced apertures could replace a single pinhole, increasing the sensitive area without loss of angular resolution. A point source in the field of view casts a shadow of the mask. If the resulting pattern is then recorded using an imaging device, the direction can be recovered by finding the necessary sideways movement of the mask to match its shadow. In practice many X-ray sources will be visible in the field of view so a deconvolution analysis must be used, hence the Dicke camera, also known as the shadow camera or transform telescope codes an image of the X-ray sky.

The performance of the camera and theory will be discussed in detail in Chapters 2 and 3.

The shadow camera can be built in two distinct forms, the simple and cyclic versions (see Chapter 2, Section 2.2.2). The simple camera imperfectly codes the sky and so is incapable of imaging extended objects, but can provide the spatial distribution of point sources, while the cyclic version theoretically provides complete coding enabling extended objects, for example, clusters of galaxies to be imaged with good spatial resolution in a narrow field configuration, but has several disadvantages which will be discussed in later chapters.

In concept the shadow camera is quite simple. However, it requires a suitable detector with reasonable energy resolution, and good spatial resolution over a large area, that is an effective area of hundreds of square centimeters.

This thesis relates development work towards a working shadow camera with a wide field of view to monitor the variability of celestial X-ray sources. This experiment, has been proposed for several future missions, as discussed in Chapter 2, and in fact the concept has several possible future developments, for example narrow field imaging.

The work naturally divides itself into three main areas, first, the development of the imaging detector (in fact an imaging proportional counter) second, computer modelling of the device to study its limitations and response, and finally, the practical construction, possible configurations, and optimisation of design. These areas are covered in the following chapters.

## CHAPTER 2

### THE SHADOW CAMERA

#### 2.1. Introduction

This chapter first describes the theory of the shadow camera, its sensitivity and basic design parameters. This is followed by some practical design considerations, and a brief description of several shadow cameras that have been proposed for future X-ray astronomy space missions.

#### 2.2. Principle of the Shadow Camera

The shadow camera is known in the literature under many names, the scatter hole camera, Dicke camera, coded mask camera and transform telescope. The principle of the device was first proposed in a paper by Mertz 1965, then in a slightly different form by Dicke, and Ables in 1968. The camera principle is very simple and is illustrated in Figure 2.2.1. The camera consists of a box with a patterned mask of holes at one end and a position sensitive detector at the other. A distant source shadows the pattern of holes in the mask on to the detector, the centre of the shadow being displaced by  $D \tan \theta$ , where  $\theta$  is the angle of the source from the instrument axis, and  $D$  is the distance between mask and detector. X-rays have such a short wavelength, that diffraction effects are generally negligible. The mask must, of course, be opaque at the required photon energies.

If there are many sources in the field of view a set of overlapping displaced shadows of the mask is recorded, and this resultant pattern can be shown to have the form of a convolution between the source distribution and mask pattern. The recorded pattern, often known in the literature as a hologram, must be decoded to produce a usable image.

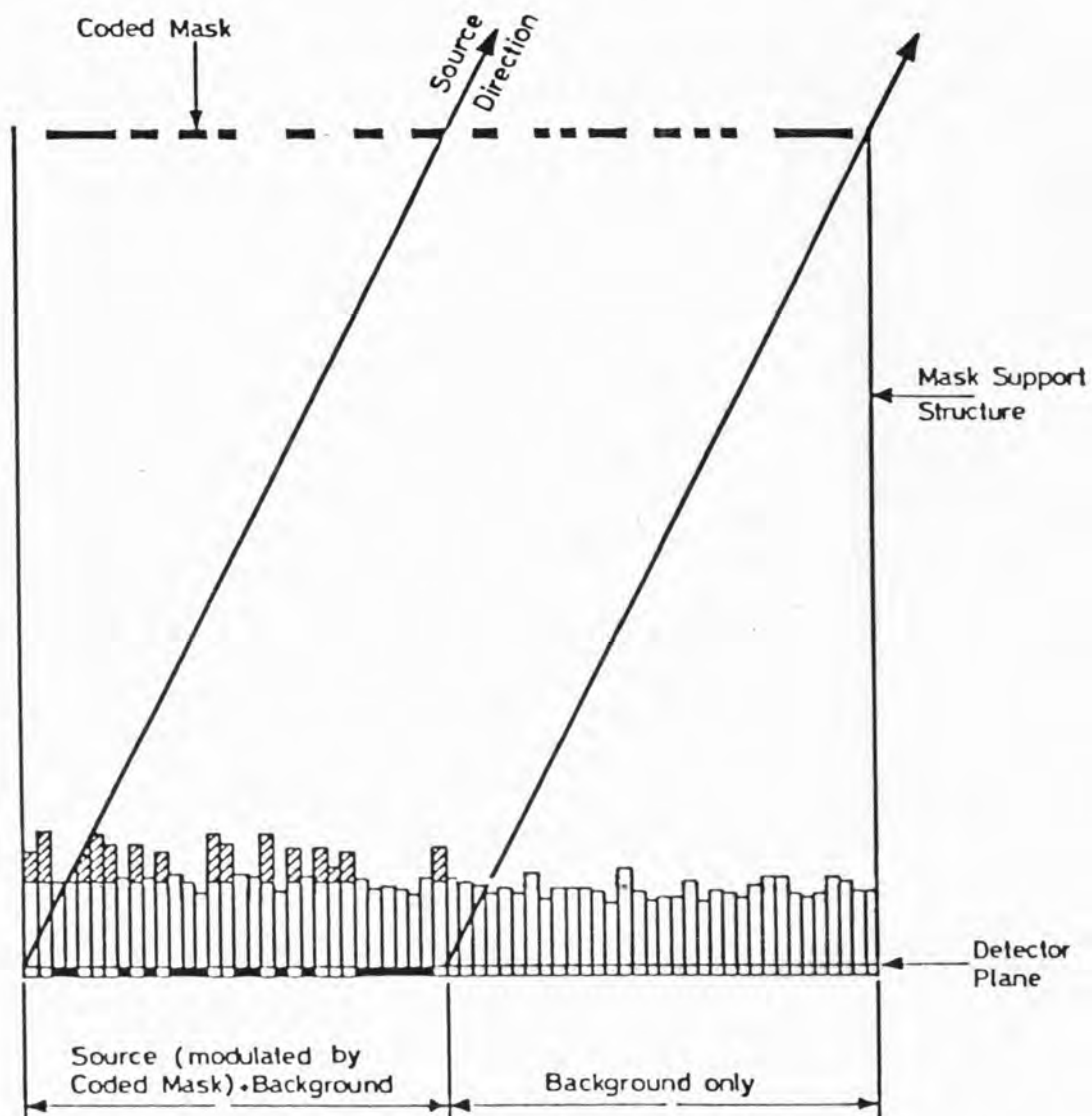


Figure 2.2.1 The principle of operation of the shadow camera. The histogram represents the accumulated counts in one row of pixels in the coded image.

The camera has one obvious advantage over a single pinhole device, in that a far larger detector collecting area is exposed to any one area of sky and hence provided the image can be decoded, the instrument has a large signal to noise advantage over a single pinhole. The shadow camera is a multiplexing device since it records many sky positions in one detector element simultaneously, in contrast to a slit collimated proportional counter which can only be used to view the sky sequentially, and a pinhole camera with one sky element per detector element. The angular resolution of the camera is fixed by the hole dimensions in the mask pattern, and the distance of the mask from the detector, providing the imaging detector has a high enough spatial resolution.

The shadow camera has some inherent complexity in that it requires a position sensitive detector and an efficient decoding system in order that the source distribution can be recovered in analysis.

### 2.2.1. Basic Theory of Image Formation

The following argument is adapted from Willingale 1976, and gives the basic coding and decoding theory of the shadow camera.

Consider Figure 2.2.2 which shows the basic planes in the instrument.

Where  $m(\underline{r}')$  is the mask plane,  
 $m(\underline{r}') = 0$  or  $1$  the transmission function of the mask  
 $s(\underline{r})$  is the flux from area  $d\underline{r}$  at position  $\underline{r}$  in the  
 source plane per unit solid angle, per unit area,  
 per unit time  
 $i(\underline{r}'')$  is the flux passing through the detector plane at  
 position  $\underline{r}''$ , per unit area per unit time

Now  $\underline{r}'' = \underline{r}' + R$   
 $R = D_2 \tan \theta$

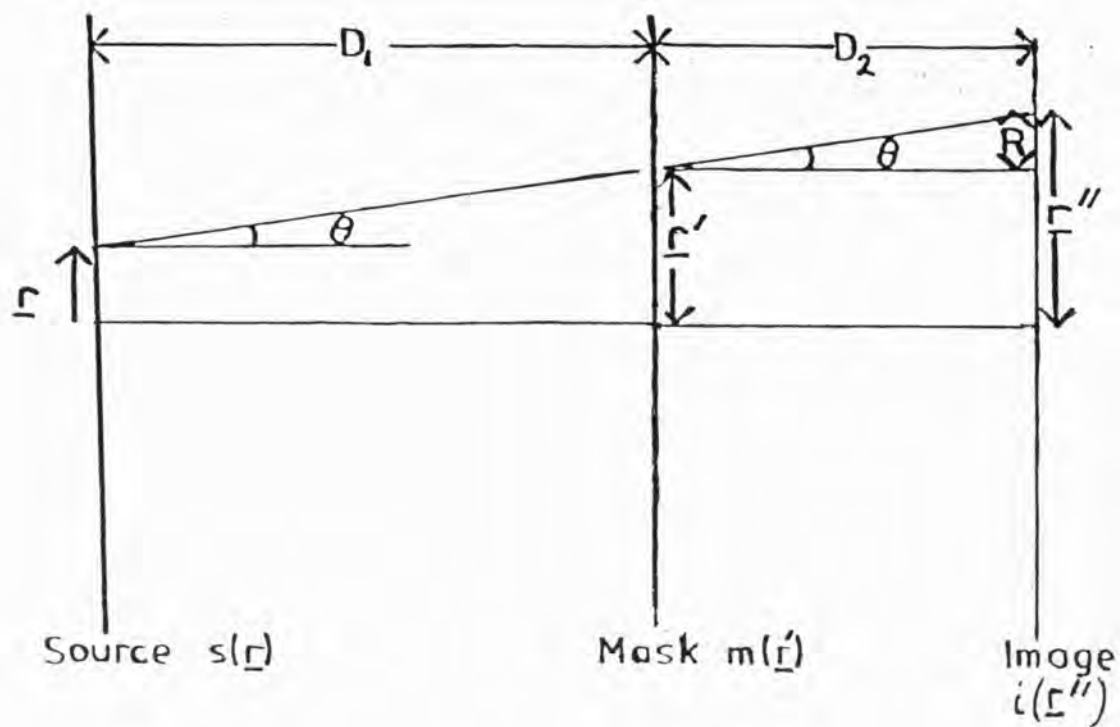


Figure 2.2.2 The three planes involved in image formation in the shadow camera, namely the source distribution  $S(\underline{r})$ , the mask  $M(\underline{r}')$ , and the image plane  $i(\underline{r}'')$ . Each represents the respective intensity or transmission distributions of each plane.

But  $\tan \theta = (\underline{r}' - \underline{r})/D_1$

Therefore  $\underline{r}'' = \underline{r}' + (D_2/D_1) (\underline{r}' - \underline{r})$

Hence  $\underline{r}' = (D_1 \underline{r}'' + D_2 \underline{r}) / (D_1 + D_2)$

The solid angle ( $d\Omega''$ ) subtended by the area  $\underline{dr}''$  is

$$1/(D_1 + D_2)^2$$

Now  $i(\underline{r}'') = 1/4\pi \int m(\underline{r}') s(\underline{r}) d\Omega'' \, dr$

or  $i(\underline{r}'') = 1/4\pi \int m(\underline{r}') s(\underline{r}) \, 1/(D_1 + D_2)^2 \, \underline{dr}$

Substituting from above for  $\underline{r}'$  and writing

$$A = D_1/(D_1 + D_2) \quad B = D_2/(D_1 + D_2)$$

one derives

$$i(\underline{r}'') = 1/4\pi \int 1/(D_1 + D_2)^2 m(A\underline{r}'' + B\underline{r}) s(\underline{r}) dr$$

A and B are only scaling factors so can be absorbed into the functions, hence

$$i(\underline{r}'') = \int s(\underline{r}) m(\underline{r}'' + \underline{r}) dr$$

or  $i(\underline{r}'') = \int s(-\underline{r}) m(\underline{r}'' - \underline{r}) dr \quad (2.2.1)$

Hence the flux distribution recorded by the detector has the form of a convolution between the inverted source distribution and mask pattern.

By the convolution theorem of Fourier analysis

$$I(\underline{w}) = M(\underline{w}) S'(\underline{w}) \quad (2.2.2)$$

where capitals represent the Fourier transforms of the respective planes.

$S'$  represents the inverted source distribution,  $\underline{w}$  is the spatial frequency vector.

Since equation (2.2.2) is a direct product, provided  $M(\underline{w})$  is



never zero, the inverted source distribution can in principle be retrieved. The process of recovering the source distribution is known as deconvolution.

The simplest method of deconvolution involves cross-correlation of the mask pattern with the total recorded distribution from the imaging detector. This is achieved by a step by step movement of the mask in a raster over the image. At each step the correlation of the mask pattern and recorded image is calculated, the number of counts at each step then represents the incident intensity distribution over the field of view, provided the mask is properly designed. Assuming that the mask is 50% transparent then for points in the deconvolved image corresponding to an X-ray source all counts from that source contribute as well as half the total background counts and half the counts from all other sources in the field of view. At positions in the final image not corresponding to a source, half the background and half the counts from all sources in the field of view are recorded, thus a source is seen against a background created not only by the diffuse X-ray emission of the X-ray sky and detector noise, but by all sources in the field of view, including itself.

Cross-correlation has the form

$$i(\underline{r}'') \otimes m(\underline{r}) = s'(\underline{r})$$

where  $\otimes$  represents correlation, notation as above, but by the convolution theorem, in the Fourier transform domain

$$I(\underline{w}) M(\underline{w}) = S'(\underline{w})$$

hence cross-correlation can be performed in the Fourier transform domain. Equation (2.2.2) states however

$$I(\underline{w}) = M(\underline{w}) S'(\underline{w})$$

hence  $S'(\underline{w})$  is also given by

$$S'(\underline{w}) = I(\underline{w}) M(\underline{w})^{-1}$$

a deconvolution in the Fourier transform domain (FTD).

This apparent contradiction states a requirement for the mask pattern namely

$$M(\underline{w}) = M(\underline{w})^{-1}.$$

These two deconvolution methods can be unified by writing

$$S'(\underline{w}) = I(\underline{w}) F(\underline{w}) \quad (2.2.3)$$

where  $F(\underline{w})$  is a spatial frequency filter function dependent on the mask type and decoding method used. Cross-correlation is only a special case of this general deconvolution formula.

More advanced methods and the practical details of deconvolution are dealt with in Chapter 3.

The shadow camera can be thought of as a spatial frequency analyser which, given adequate position resolution in the detector, can measure the amplitude and phase of the sky brightness distribution at all spatial frequencies present in the mask pattern, the unit hole in the mask limiting the angular resolution.

### 2.2.2. Basic Configurations of the Shadow Camera

In the original concept the shadow camera has a mask equal in size to the detector, the mask in Dicke's paper (1968) consisting of randomly arranged holes. This camera is the so-called 'simple camera' in this thesis and Sims et al., (1980), and has two disadvantages. The random nature of the mask pattern leads to 'ghosting' as some form of correlation will exist in other positions than directly over the mask pattern; secondly, for sources not in the centre of the field of view an incomplete mask pattern is projected onto the detector, again leading to incomplete coding, and ghost images. As a source moves off-axis the available detector area falls, being zero at the edge of the field of view, and hence the sensitivity is

not uniform across the field of view (FOV). The camera has a triangular type response similar to that given by a mechanical collimator.

The first problem can be overcome by careful design of the mask pattern, as discussed in 2.6.; the second, off-axis fall off in pattern, can be eliminated, but requires a mask larger than the detector, or a detector larger than the mask.<sup>+</sup> This second type of camera is known as the 'cyclic shadow camera' in this thesis. The two types of camera are illustrated in Figure 2.2.3. The best solution for the cyclic camera is to use a mask containing at least four complete identical patterns, along with a collimator limiting the field of view to that of one complete pattern after projection onto the detector. The alternative of a detector larger than mask is not utilised due to the problems of construction of a large area imaging detector and the inherent higher detector background. (For a two-dimensional system the area of the detector would need to be four times the mask area.)

The restriction of the field of view introduced by the collimator results in the need to halve the detector-to-mask separation in order to achieve the same field of view as the simple system. Hence for a given mask hole size, the angular resolution is degraded by a factor of two. In the case of perfect deconvolution the cyclic camera therefore offers higher sensitivity, but poorer angular resolution.

The collimator of the cyclic camera must be designed such that it will modulate the shadowed pattern at spatial frequencies at which the recorded distribution contains no information in order that no effect on the image coding occurs. This is achieved in narrow field cameras by constructing a slit collimator with pitch equal to the mask hole size, which in addition acts as a detector window support.

Due to the difficulty of quantifying any sensitivity advantage between the two types of system, both were examined by computer simulation (as discussed in Chapter 3).

<sup>+</sup> Procter et al 1979

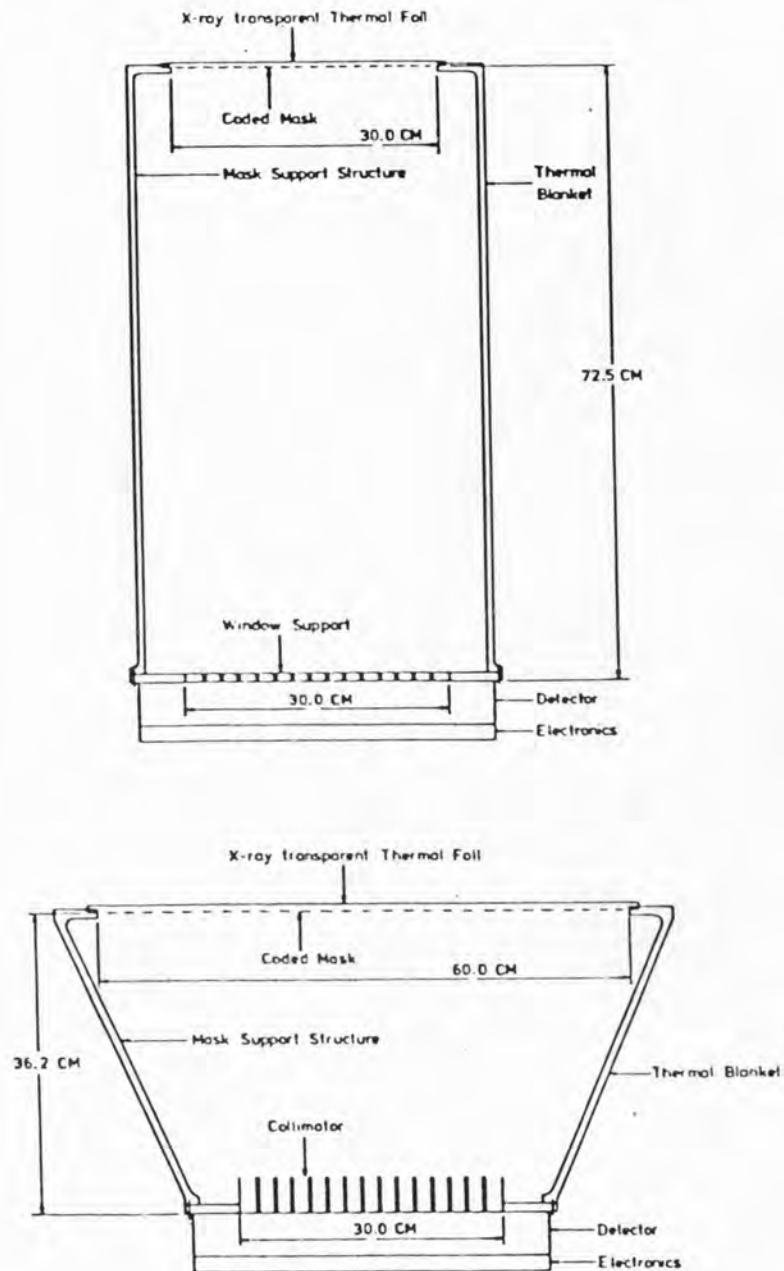


Figure 2.2.3 Schematic cross-sections of the shadow camera in the simple configuration (top) and in cyclic mask configuration. These two configurations have identical FOV's and areas. Cameras with these dimensions were used in the simulations described in chapter 3.

### 2.3. Sensitivity of the Shadow Camera

This section describes the theoretical deduction of the sensitivity of the shadow camera, its conversion to parameters of the design, and finally discusses problems with a pure analytical approach.

Calculation of the sensitivity of the shadow camera is a matter of comparing the background in the deconvolved image with the source peak and has been treated by many workers (e.g., Dicke 1968, Palmieri 1974 and Gunson and Polychronopoulous 1976). The following argument is adapted from the paper of Gunson and Polychronopoulous.

Let  $N_p$  be the total number of photons incident on the mask of the shadow camera in a time  $t$  with a chance of being detected if they penetrate the mask.  $N_p$  includes all sources within the FOV and the contribution due to the diffuse X-ray background.

Let  $N_s$  of these photons be from a point source, and  $B$  be the total number of cosmic ray counts recorded in the same time by the detector. If the transmitting fraction of the mask is  $r$  and the detector efficiency  $\eta$  the total recorded count will be

$$r \eta N_p + B$$

Correlating the counts with the mask pattern will produce an average value of

$$r^2 \eta N_p + r B$$

Fluctuations and peaks will occur due to counting statistics and point sources. At the positions where there is no point source the  $r \eta N_p + B$  counts have a probability of contributing of  $r$  and of  $(1-r)$  of not contributing. The probability distribution due to the total will therefore be binomial with mean as above and variance

$$r(1-r) (r \eta N_p + B)$$

At a source position a peak of height  $r(1-r) n N_s$  above the mean will occur. The significance of the peak is therefore given by

$$n_{\sigma} = \frac{r(1-r) n N_s}{[r(1-r)(r n N_p + B)]^{\frac{1}{2}}} \quad (2.3.1)$$

This is the detection sensitivity for the shadow camera; not the sensitivity of measurement, but a measurement of chance of noise having this size fluctuation.

As the number of total possible source positions is increased by making the number of mask elements larger, the probability of a spurious noise peak increases. If  $P(n_{\sigma})$  is the probability of finding a peak greater than  $n_{\sigma}$  at a given point, then the probability of one not occurring in any of the  $N$  possible positions is

$$[1 - P(n_{\sigma})]^N \approx 1 - NP(n_{\sigma}) \quad \text{if } NP(n_{\sigma}) \ll 1$$

Therefore, for 99% confidence,

$$NP(n_{\sigma}) = 10^{-2}$$

Using the normal approximation to the binomial, when the total count is large, gives the following significance values for 99% confidence

$$N = 512 \quad n_{\sigma} = 4.2$$

$$N = 512^2 \quad n_{\sigma} = 5.5$$

The number of counts required to achieve a given significance is therefore not a strong function of the number of mask elements.

### 2.3.1. Sensitivity in Detector and Source Parameters

$N_s$ ,  $N_p$  and  $B$  can of course be expressed in terms of detector and source parameters. Let



$A$  = detector on-axis area

$T$  = integration time

$\Omega$  = effective solid angle

$S$  = photon flux from the source

$B_d$  = diffuse background flux per unit solid angle

$B_c$  = charged particle count rate per unit area of the detector

$f(\theta, \phi)$  = fraction of detector area seen for source at co-ordinates  $\theta, \phi$ . Where  $(0,0)$  is defined as the detector viewing axis,  $\phi$  being the azimuthal angle around the axis measured from a zero perpendicular to one of the side walls of the detector and  $\theta$  is the zenith angle of this source from the axis.

Hence for a single point source in the FOV

$$N_s = S f(\theta, \phi) A T$$

$$B = B_c A T$$

$$N_p = S f(\theta, \phi) A T + B_d \Omega A T$$

$f(\theta, \phi)$  applies also in the case of the cyclic camera, because although the whole detector area sees a source, the flux is reduced by a factor  $f(\theta, \phi)$  by the collimator.

Substituting in equation (2.3.1)

$$n_\sigma = \frac{r(1-r) \eta S f(\theta, \phi) A T}{[r(1-r)(r \eta (S f(\theta, \phi) A T + B_d \Omega A T) + B_c A T)]^2} \quad (2.3.2)$$

It can be shown (Appendix A) that  $f(\theta, \phi)$  has the form

$$f(\theta, \phi) = \cos \theta [1 - b/a \tan \theta |\cos \phi|] [1 - b/a \tan \theta |\sin \phi|] \quad (2.3.3)$$

where



a = full active width of the detector

b = height from mask to detector

and  $\Omega$  the effective solid angle for the simple camera is given by

$$\Omega = \iint f(\theta, \phi) d\Omega$$

$$\Omega = 4 \left[ (\sqrt{a^2 + b^2}/a) \cdot \tan^{-1}(a/(\sqrt{a^2 + b^2})) - b/a \tan^{-1}a/b \right]$$

$$+ b^2/a^2 \ln((a^2 + b^2)^2/(b^2(2a^2 + b^2))) \quad (2.3.4)$$

### 2.3.2. Comparison with Pinhole Camera

Consider equation (2.3.1) in a case  $r = 0.5$ ,  $\eta = 1$  that is detector inefficiency neglected

$$n_{\sigma} = 1/2 N_s / [1/2 N_p + B]^{1/2}$$

which is simply the ratio of the source count to the square root of the total count.

Now the equivalent expression for a pinhole camera is given by

$$n_{\sigma} = q N_s / [q N_s + q B]^{1/2}$$

where  $q$  is the ratio of the pinhole area to that of the detector, or the ratio of the angular resolution of the image to its field of view.

In order to compare the two instruments and determine the detection sensitivity advantage of the coded mask camera for various conditions, it is necessary to solve the above equations for  $S$ . The ratio of the minimum detectable source intensity of the coded mask camera ( $S_c$ ) to that of the pinhole camera ( $S_p$ ), with an identical detector with the same angular resolution, is given by

$$\frac{S_c}{S_p} = \frac{r n_{\sigma}^2 + [r^2 n_{\sigma}^2 + 4r(1-r)(r N_p + B)t]^{1/2}}{n_{\sigma}^2 + [n_{\sigma}^2 + 4qBt]^{1/2}} \cdot \frac{q}{r(1-r)}$$

where  $N_p$ ,  $B$  are in counts per second and  $t$  is the integration time.

### 2.3.3. Limitations of the Formula

In the case of the simple camera, or a cyclic camera with a non-perfect collimator or window support on the detector, the sensitivity of the shadow camera will not follow the formula developed above, because of side lobes from strong point sources. Ghosting, that is the production of ghost images or side lobes to the main peak, results due to the non-perfect coding of the above systems. These side lobes do not reduce the number of counts in the source peak, but increase the noise fluctuations in the rest of the image. The degree of ghosting is dependent on the mask design, detector effects and the source distribution in the FOV. The effect can be somewhat minimised by choice of the mask pattern, but in the case of cross-correlation is never zero. However it can be reduced further by more advanced methods of deconvolution. Chapter 3 gives a full account of imperfect coding, and of deconvolution methods,

### 2.4. Parameters of the Shadow Camera

The fundamental parameters of a shadow camera design are related to one another by simple expressions; that is the choice of parameters is not free. These relationships have implications on the design of the shadow camera.

The following basic parameters are involved in the design of a shadow camera;

- a full width of the detector
- b mask to detector distance
- $r'$  best possible angular resolution

- N    number of spatial resolution elements across the  
       detector or mask
- $\delta$     spatial resolution of the detector
- $\theta$     half open angle of FOV along and perpendicular to sense  
       axes of the detector

#### 2.4.1. FOV Angular Resolution Relationships

Obviously

$$\tan \theta \approx a/b \quad (2.4.1)$$

If  $r'$  is small, then the best possible angular resolution (ideal detector) is given by

$$r' \text{ (radians)} = \frac{a}{bN} \quad \text{on axis}$$

$$\text{also} \quad N\delta = a$$

$$\text{or} \quad br' = \delta \quad (2.4.2)$$

The actual angular resolution of the device is a convolution of the detector response with the mask element size. However the above expressions relate the parameters approximately. The above relationships hold approximately however  $\delta$  is defined.

It is evident from equation (2.4.2) that if we choose a value of  $r'$  and a value  $\delta$ ,  $b$  is automatically defined. In fact,  $\delta$  is probably itself a function of detector area. The relationship between  $b$  and  $\delta$  for various values of  $r'$  is plotted in Figure 2.4.1.  $\theta$  is now a function of  $a$  and  $\delta$ , for a given  $r'$ . Hence  $r'$  and  $\delta$  partially define the experiment; however,  $\theta$  appears to be a free parameter.

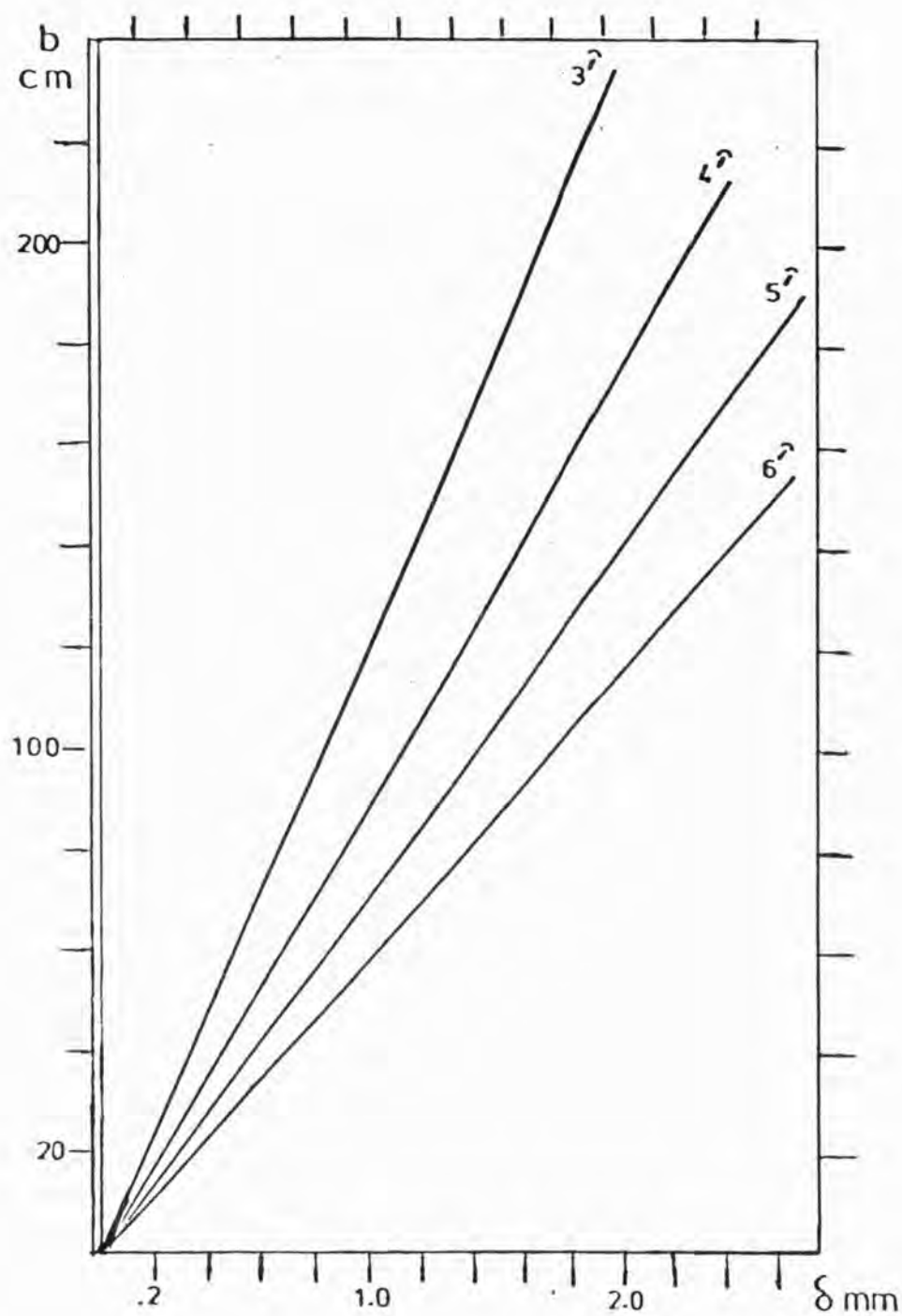


Figure 2.4.1 The relationship between  $b$ , the mask to detector distance  $\delta$ , the spatial resolution of the detector and  $r'$  the best possible angular resolution of the shadow camera as defined by equation 2.4.2.

#### 2.4.2. The Field of View

From the above

$$Nr' \approx \frac{a}{b} = \tan \theta \quad (2.4.3)$$

All efficient decoding systems use a fast data transform for deconvolution, for example the fast Fourier transform. In this case one can state, for optimum use, the additional requirement that

$$N = 2^M$$

If this requirement is stated, then quantised steps in  $\theta$  exist once  $r'$  is defined.

There are various design strategies using the above equations, for example, say  $r'$ ,  $\delta$ ,  $N$  are fixed.

Equation (2.4.3) defines  $\theta$ , equation (2.4.2) defines  $b$ , and then from equation (2.4.1) one can derive  $a$ .

Consider

$$r' = 3 \text{ arc min } = 8.73 \times 10^{-4} \text{ radians}$$

$$N = 1024$$

$$\delta = 0.05 \text{ cm } (0.5 \text{ mm})$$

$$Nr' = 0.894 \Rightarrow \theta = 41.79$$

$$\Rightarrow b = 57.27 \text{ cm}$$

$$\Rightarrow a = 51.2 \text{ cm}$$

However two other parameters are required to aid design, the total solid angle viewed by the camera (coverage), and the effective solid angle (for calculation of sensitivity).

### 2.4.3. Effective Solid Angle and Total Solid Angle

The effective solid angle is given by

$$\Omega = \iint f(\theta, \phi) d\Omega$$

It can be shown (Appendix A) that

$$\Omega = 4[(\sqrt{a^2 + b^2})/a \cdot \tan^{-1}(a/(a^2 + b^2)) - b/a \tan^{-1} a/b] \\ + b^2/a^2 \ln((a^2 + b^2)^2/b^2(2a^2 + b^2))$$

The total solid angle viewed by a simple camera is given by

$$\Omega_{\text{TOTAL}} = 2\pi - 8 \sin^{-1} (b/(\sqrt{2(a^2 + b^2)}))$$

$\Omega$  and  $\Omega_{\text{TOTAL}}$  against the ratio  $a/b$  is plotted in Figure 2.4.2.

The above equations examine the relationships between the parameters of the shadow camera. However, all practical designs are nearly always limited by source sensitivity, and detector considerations. A detector-limited system will be discussed next.

### 2.5. The Shadow Camera: A Detector Limited System?

In principle, any size of shadow camera, field of view, angular resolution, etc., can be built. In a practical case, however, the design is almost always limited by detector considerations. The limitations placed on the design by the detector are the area and position resolution achievable.

The prime candidate at present for the imaging detector is the Imaging Proportional Counter (IPC). First, reasonably large area devices have been built or are under construction; second, the IPC provides crude energy information, enabling some spectral characteristics of a source to be defined, and finally spatial resolution of the order of millimetres to fractions of a millimetre have been achieved in the relevant energy range.

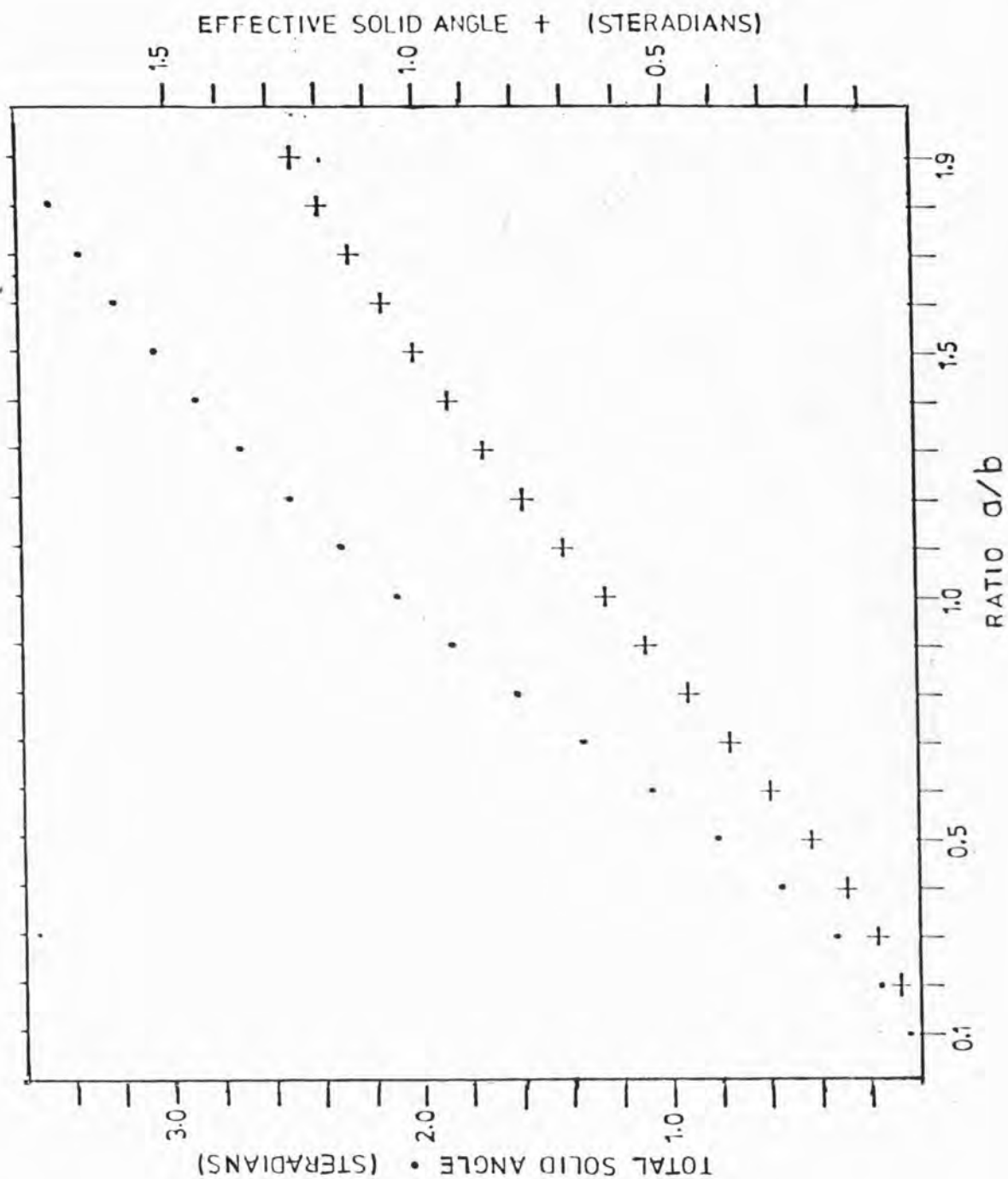


Figure 2.4.2 The total solid angle (., left hand scale), and effective solid angle (+, right hand scale) as a function of the ratio  $a/b$  for the shadow camera.



The basic characteristics, theory of operation and construction of these counters, and other possible imaging detectors will be discussed in Chapter 4.

The true angular resolution of the shadow camera is a convolution of the detector's response function with that of the mask. The parameter  $r'$  in the previous section is really the best possible angular resolution achievable.

The detector should not dominate the system, hence the position resolution (Full Width Half Maximum (FWHM) response) must be comparable to or, ideally, smaller than the mask hole size. This requirement is discussed in detail in Appendix B. The detector area must in addition be sufficiently large (in the order of hundreds of square centimeters) so that the shadow camera sensitivity is adequate to fulfill its purpose as a wide field X-ray sky monitor.

In general, the larger the detector area the worse the spatial resolution achievable. This is perhaps best thought of as a percentage of the width of the detector; for example, 1 mm is 1% of 10 cm, but 0.5% of 20 cm etc. Various methods can be employed to improve the spatial resolution in large area detectors. However, this results in a more complicated system, so one must try and arrive at an optimum design in which cost and complexity can become important factors.

In summary, using the parameter notation of section 2.4 we have

$$N\delta = a$$

and  $\delta = f(a)$

where  $f$  is some function dependent on design, so if one can solve for  $a$  one has an approach to optimisation of the design.

If (a) is decided by science and detector considerations, along with  $N$ , (b) is now a free parameter. However  $r'$  is instantly fixed once  $b$  or  $\theta$  is chosen.

Two other detector characteristics can also limit the performance of the shadow camera.

#### 2.5.1. Detector Construction and Off-axis Response

In the case of a wide field camera, for a source towards the edge of the field of view, the incident X-rays will hit the detector plane at a considerable angle, perhaps of the order of tens of degrees. The detector must therefore have a good off-axis response function so that angular resolution and coding efficiency does not drop at the edge of the field of view.

Finally the detector should be constructed such that it does not interfere with the coding of the shadow camera. Most detectors, however, have an entrance window, which needs to be supported against internal pressure (IPC). This window support must be designed such that the efficiency of coding is impaired as little as possible. This problem becomes of prime importance in large area detectors.

In the case of the cyclic system the field of view collimator can double as a detector window support structure, but only in the case of narrow field imaging, in a wide field version, mechanical stresses make the use of some extra support structure essential.

The detector response, and window support structure problems were investigated by computer simulations, the results of which will be discussed in Chapter 3.

The design as can be seen depends heavily on detector considerations.

#### 2.6. Mask Patterns; Required Characteristics

Many types of mask pattern have been proposed for use in the shadow camera. Mertz (1965) proposed the use of a fresnel zone plate and Dicke (1968) the use of randomly positioned pinholes. However, whatever the

mask pattern, it must have certain basic characteristics in order that the source field can be deconvolved.

As per the notation of section 2.2, let

$M(\underline{w})$  be the Fourier transform of the mask  
transmission function

$S'(\underline{w})$  the Fourier transform of the inverted  
source distribution

$I(\underline{w})$  the Fourier transform of the recorded image

where  $\underline{w}$  is the spatial frequency vector.

Equation (2.2.2) states

$$I(\underline{w}) = M(\underline{w}) S'(\underline{w})$$

Rearranging

$$S'(\underline{w}) = I(\underline{w}) \cdot M(\underline{w})^{-1}$$

This immediately places restrictions on  $M(\underline{w})$  and hence the mask pattern itself. First,  $M(\underline{w}) \neq 0$  or  $S'(\underline{w}) = \infty$ . Second  $M(\underline{w})$  must not be too small, or this leads to amplification of any noise present at corresponding  $\underline{w}$ . The pattern must therefore have a reasonably flat power spectrum. Finally for good counting statistics, the overall transmission of the mask should be as high as possible.

The mask properties required can be further determined by considering the auto-correlation function of the mask, that is the result of cross-correlating the mask with itself. Figure 2.6.1(a) shows the ideal mask, no side lobes being present, while Figure 2.6.1(b) shows schematically the auto-correlation function of most masks for the shadow camera. One has a strong sharp peak at the centre with extended triangular wings.

Various mask patterns have been proposed; fresnel zone plate; random distribution of pinholes; hadamard masks; and masks constructed from cyclic

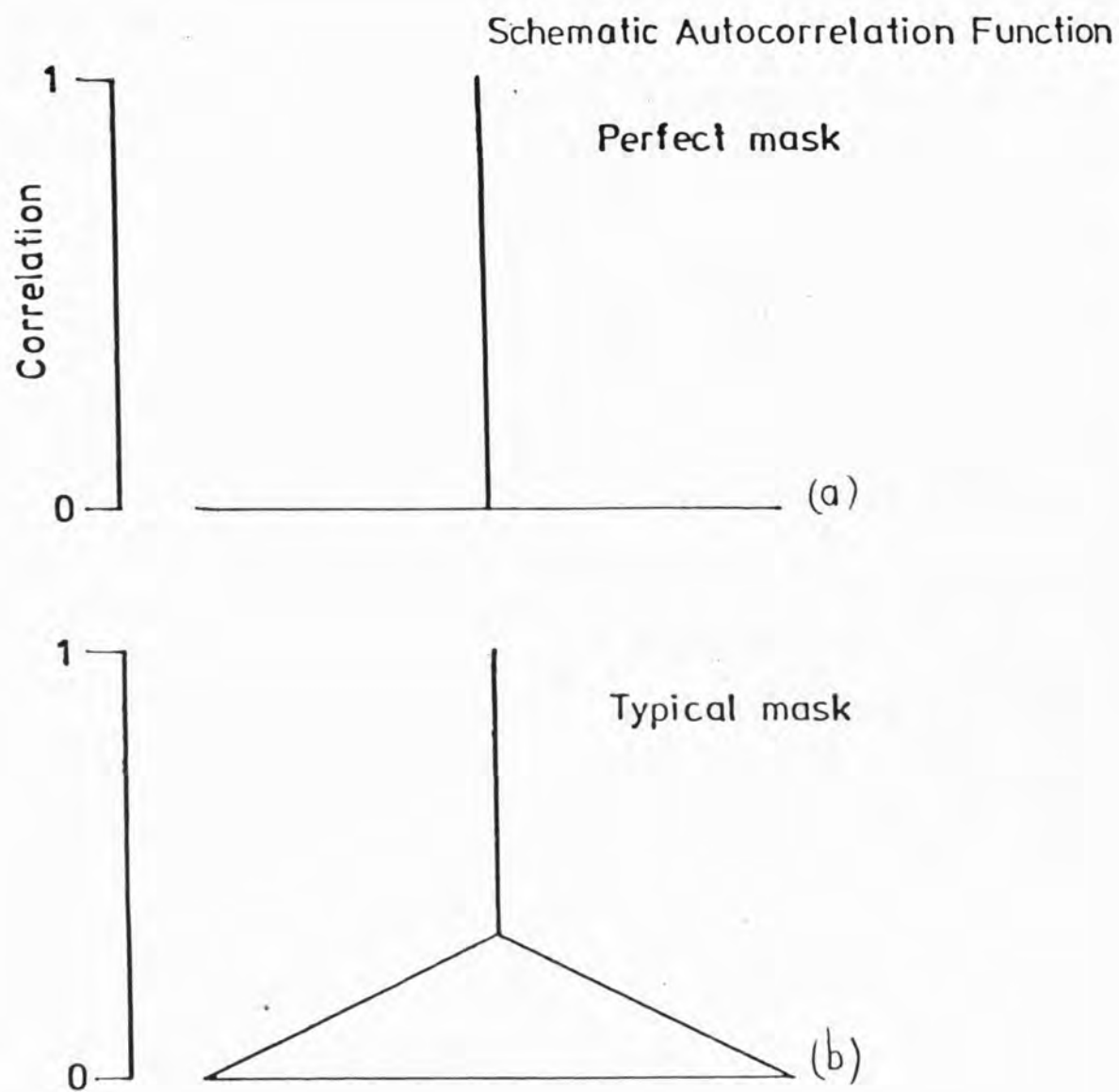


Figure 2.6.1 Schematic auto correlation functions of (a) perfect mask and (b) typical mask for the shadow camera. The total correlation point (correlation 1) occurs when the mask is vertically on top of itself.

difference sets (pseudonoise type sequences). The choice has been tackled by many workers, Willingale 1976, Palmieri 1974, Gunson and Polychronopulous 1976, Miyamoto 1977 amongst others.

In the case of the simple camera the problem of incomplete coding cannot be totally overcome, but can be reduced to a large degree by selection of the mask pattern. The problem of side lobes in the deconvolved image becoming more dominant once a single source is off-axis or a complex source distribution is present. In the case of the cyclic camera, the side lobe problem can be totally eliminated by use of the optimum masks reviewed in the work of Gunson and Polychronopulous 1976 or use of a mask based on hadamard waveforms Miyamoto 1977. These 'perfect' masks with ideal properties are designed to be self-orthogonal under circular cross-correlation, the cyclic camera situation. These patterns are random in the sense that no self-correlation exists under circular shifts, and in isolation small sections appear random, but on a large scale they generally exhibit a definite structure.

The optimum mask for Gunson and Polychronopulous is based on the use of cyclic different sets, these masks being found in the course of the work described in this thesis, as discussed in Chapter 3, to give the best performance of all the types tested.

In the case of the simple camera one has the problem of defining a good mask pattern. A 'theoretical' definition is possible. The best pattern is one that has a delta-like auto-correlation function, with a minimum of side lobes, a flat Fourier transform, and finally acts as a good spatial frequency filter. Translating into practical formulae, let

$M(\underline{w})$  be the discrete Fourier transform of the pattern, and  $M^*(\underline{w})$  its complex conjugate. The best filter is such that the amplitude of  $M(\underline{w})$  is as large as possible for all values of  $\underline{w}$ . Approximately

$$\sum_{\underline{w}} \frac{1}{M(\underline{w}) \cdot M^*(\underline{w})} \quad \text{is a minimum.}$$

The other properties required are a minimum value of the variance of  $MM^*$ ,

$$\sigma_{FT}^2 \rightarrow \text{minimum}$$

and a minimum value of the variance of the auto-correlation function

$$\sigma_{AC}^2 \rightarrow \text{minimum}$$

Hence the best mask can be defined theoretically by

$$\sum \frac{1}{M(\underline{w}) \cdot M^*(\underline{w})} \sigma_{FT}^2 \sigma_{AC}^2 \rightarrow \text{minimum}$$

In the case of most mask patterns there are only a finite number of possibilities and hence it is possible to consider testing all patterns by computer, and to find a best mask.

This approach has not been adopted in the work discussed here, as only the general performance characteristics of the shadow camera have been investigated. Further research is not required as the performance of the shadow camera is dominated by other factors. For the simulation work a set of standard masks were used. The transparency  $r$  of the mask must also be considered before a final pattern is chosen.

## 2.7. A One- or Two-Dimensional System

Two forms of the shadow camera are possible, in addition to simple and cyclic; these are a system which is sensitive in either one- or two-dimensions.

Each system has its own advantages. Firstly, it is practically easier to produce a one-dimensional imaging detector. In addition the mask of a one-dimensional system is easier to support, consisting effectively of a series of slats or slots. The main disadvantage is that two cameras are required to position a source at a given time, or a single camera must move



within the source timescale so that another line of position is determined, the intersection of the two lines of position giving the source position. The use of lines of position can of course lead to source confusion problems with a dense spatial distribution of sources such as the galactic centre. The two-dimensional system obviously overcomes this problem, one stationary camera being able to position all sources within its given field of view. This system of course requires a two-dimensional position sensitive detector, but two-dimensional detectors have been applied in other fields, for example the grazing incidence systems, radio-isotope imaging.

The one-dimensional system actually has a small signal to noise advantage compared with the two-dimensional system. As discussed in section 2.3, in the case  $N = 512$   $n_{\sigma} = 4.2$  for 99% confidence, for  $N = 512^2$   $n_{\sigma} = 5.5$ .

This advantage however is very small and as a two-dimensional system has the greater promise, for example direct imaging of extended sources with the cyclic camera, and avoids the problem of source confusion, all work has concentrated on this type of system.

## 2.8. The Shadow Camera: Sky Background Limited Case

In general for integration times greater than a few seconds, and for fields of view greater than a few degrees, the shadow camera is sky background limited. Only in the case of viewing strong source concentrations for example the galactic centre will the camera be source dominated.

In the case of a sky background limited shadow camera it is possible to deduce theoretically the number of sources visible as a function of field of view for the simple camera.

The diffuse X-ray background has been measured recently by Schwarz 1979. In terms of photon number the best estimate of the spectrum is



$$I(E)dE = 7.7E^{-1.4} dE \text{ photons sec}^{-1} \text{ cm}^{-2} \text{ sterad}^{-1} \text{ keV}^{-1}$$

for  $E = 1$  to  $21$  keV . Integrating over the range  $2 - 20$  keV one finds

$$B_D = 8.8 \text{ p s}^{-1} \text{ cm}^{-2} \text{ sterad}^{-1}$$

where  $B_D$  is the diffuse background as the notation of section 2.3.1.

In general a wide field camera will tend to have an effective solid angle of the order of a few tenths of a steradian, making the sky background the dominant count for long integration times with weak sources  $\sim 10^{-2}$  to  $10^{-3}$  times Crab strength in the field of view, the general case of observations away from the galactic centre region.

Assuming the camera is sky background limited one can simplify the sensitivity equation (2.3.2). Solving for  $S_{\min}$ , the minimum sensitivity one has

$$S_{\min} = \frac{n_{\sigma}}{\sqrt{1-r}} \left[ \frac{B_D \Omega}{\eta A T} \right]^{\frac{1}{2}} \frac{1}{f(\theta, \phi)} \quad (2.8.1)$$

Now if we assume that sources are distributed uniformly over the sky (true for high latitude transients, active galaxies) with each source type having a number against flux relationship of

$$N(>S) = N_0 S^{-\alpha}$$

The angular density of detectable sources is given by

$$dN(>S_{\min}) = \frac{N_0}{4\pi} \left[ \frac{n_{\sigma}}{\sqrt{1-r}} \right]^{-\alpha} \left[ \frac{1}{\eta A T} \right]^{-\alpha/2} [B_D \Omega]^{-\alpha/2} [f(\theta, \phi)]^{\alpha} d\omega$$

assuming no coding errors are present. In the simple camera this is approximately true for a sparse spatial source distribution.

The integral of the above expression gives the total number of sources visible. For a given field of view, camera design all but the last expression are constant, hence

$$N(>S_{\min}) = \frac{N_0}{4\pi} \left[ \frac{n_0}{\sqrt{1-r}} \right]^{-\alpha} \left[ \frac{1}{\eta AT} \right]^{-\alpha/2} [B_D \Omega]^{-\alpha/2} \int f(\theta, \phi)^\alpha d\omega$$

For  $\alpha = 1.0$

$$\int f(\theta, \phi) d\omega = \Omega$$

Hence

$$N(>S_{\min}) \propto \Omega^{\frac{1}{2}}$$

For the case of  $\alpha = 1.5$  it is not possible to simplify the above expression, hence the integral was evaluated numerically, using software available on the University of Leicester's Cyber 73 computer.

The two cases of  $\alpha = 1.0$  and  $\alpha = 1.5$  were evaluated as a function of  $a/b$  which defines the FOV of a given design,  $n_0$ ,  $r$ ,  $\eta$ ,  $A$ ,  $T$ ,  $B_D$  were treated as constants. The result after normalisation in arbitrary units, taking a fixed  $N$  sources greater than some limiting sensitivity for the two distributions is shown in Figure 2.8.1. Nominal values for the constants,  $n_0$ ,  $r$ ,  $\eta$ ,  $A$ ,  $T$  being taken. As can be seen the increase in diffuse X-ray background due to the enlarged field of view is always offset by the greater solid angle observed.

## 2.9. Practical Design Considerations for the Shadow Camera

This section reviews various practical design considerations of the shadow camera. These points can be divided into three main areas, mechanical design, attitude determination, and telemetry rate from the camera.

### 2.9.1. Mechanical Design

The shadow camera as an instrument proposes several mechanical design problems. First there is the problem of mask support. Most mask patterns are not of the self-supporting type, and although it is possible to produce a self-supporting pseudo noise sequence mask, as will be discussed in Chapter 3, it is impossible to produce such a mask using fresnel

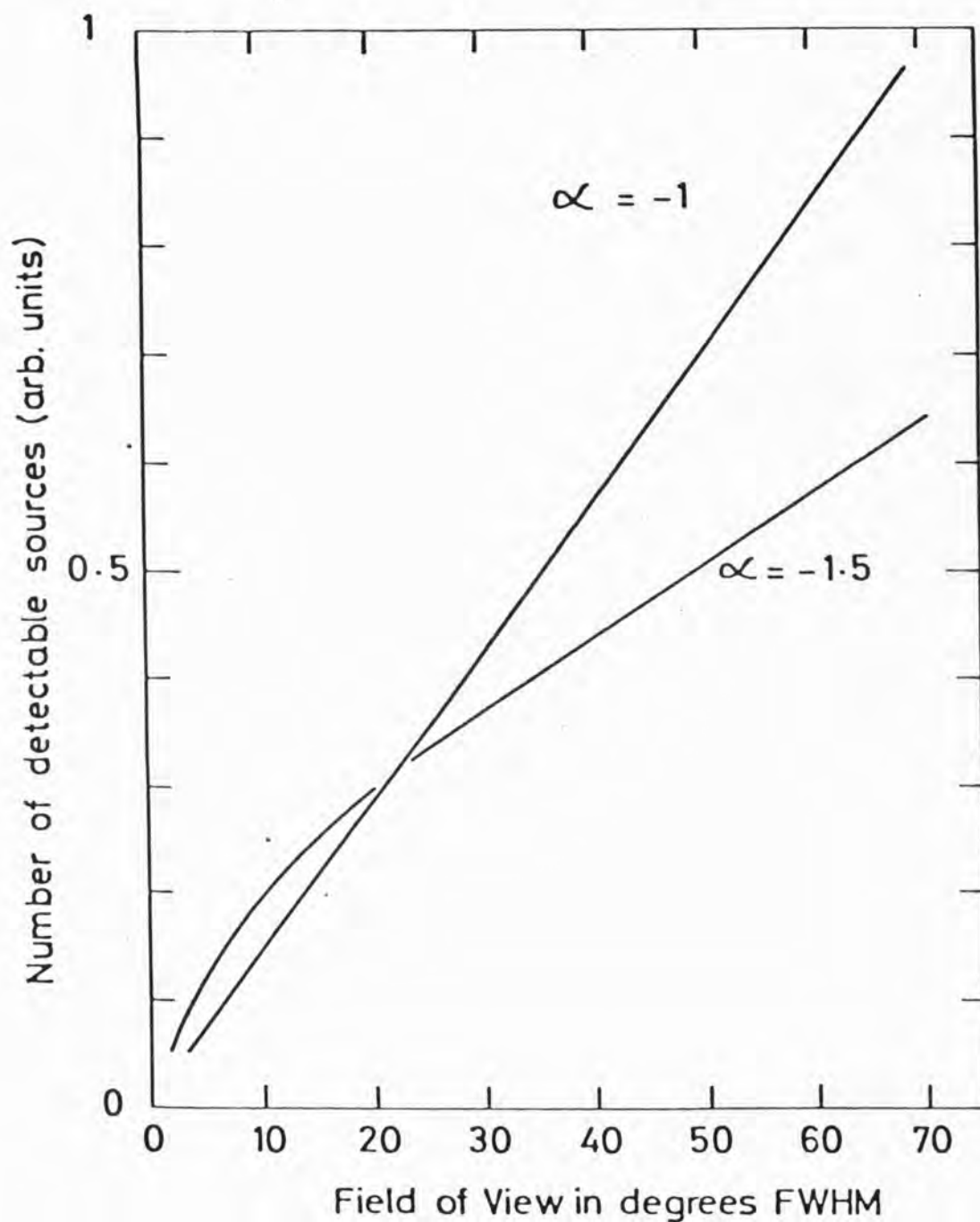


Figure 2.8.1 The number of detectable sources as a function of camera FOV, assuming a uniform source distribution having a number intensity relationship with index equal to  $-1$ , and  $-1.5$ .

patterns. (A self-supporting pattern has each blank or solid element supported at two or more corners.)

Various methods have been proposed to overcome this problem. The first method is to form the mask pattern on top of a fine square grid by electrodeposition. The width of the supporting bars being much smaller than the size of a unit hole. A lower limit to the supporting bars existing by the need for the mask to support its own local weight. In the case of a fresnel pattern or any other of circular symmetry a set of radial supporting spokes could be used. The use of a supporting grid of course reduces the effective transparency of a mask.

Other methods rely on forming the mask pattern on top of some material, normally a thin organic film which is transparent throughout most and preferably all of the shadow camera's range.

The best method may be a combination of each of these ideas, where a thin film enables the supporting bar size to be reduced, and could aid in thermal control of the experiment.

The second major problem is also concerned with the mask, this is the problem of mask distortion and movement.

Mask distortion can be largely avoided by a correct support, Gunson and Polychronopoulos 1976, and Palmieri 1974 have suggested the idea of combining the mask support with the field of view collimator for the cyclic camera. This however may require very fine pitch collimators which are hard to construct, in addition such a collimator may be of more use as an aid to window support on the position sensitive detector.

Mechanical distortion can be eliminated by tensioning the mask into a rigid frame. Separate film layers aiding to prevent any distortion. The correct choice of material for the mask is of course important, nickel being a common choice; the mask can be made opaque by coating a low  $Z$  material with a heavier one such as gold.

A further problem is motion of the mask with respect to the detector position sensing axes. Translation is not really a problem as it only effectively shifts the centre of the field of view. Measurement of translation is possible by the use of fiducial lights (for example, light emitting diodes or solid state lasers as for Transtel, discussed in section 2.11.2.) mounted on the mask or detector, with an appropriate position sensitive detector at the other end. Translation of course involves a loss in coding efficiency of the system.

Rotation of the mask is the major problem, any rotation decreases the effective coding efficiency on deconvolution and results in a loss of sensitivity. Due to the nature of the mask rotation, it affects the outermost elements most, if  $\delta x$  is the hole size and  $D$  the size of the mask, one requires the rotation angle  $r'$  to be (approximately)

$$r' \text{ (radians)} < \frac{2\delta x}{D}$$

in the limit of equality the outermost element has rotated the width of a pixel or mask hole.

The final motion is tilting of the mask with respect to the detector plane. Because of mounting and structural design of the shadow camera and mask this motion will be so small that it is unimportant; the effect is a decrease in hole aperture as viewed from the detector.

Most designs proposed for the shadow camera to date have relied on rigidly mounting the mask above the detector, motion being eliminated by structural design. Nearly all mechanical distortions to a shadow camera in orbit on a spacecraft will be due to temperature differences across the structure, hence thermal control is vital.

Thermal control may take two forms, passive and active control. Passive thermal control is provided by use of thermal blankets (thin films absorbing or reflecting heat) plus heat pipes of one form or another. Active control is provided by electrical heaters, and a cooling or heating



system involving a pumped fluid.

The particular form of thermal control required to avoid mechanical distortion depends on the type of materials used, the distortion allowable, and the thermal conditions the shadow camera will be subjected to.

Two extreme thermal conditions exist in orbit, continuous pointing at or near the sun, and viewing deep space.

In extreme near sun pointing which is not advisable, as the sun is itself an X-ray source, cooling of some form may be necessary; this can be provided by the use of heat pipes and radiators.

In the case of deep space viewing for a prolonged period, heaters are certainly required, with perhaps assistance by heat pipes from hot areas of the pointing platform.

The mechanical design must of course take into account all shocks encountered during the launch and operation of the spacecraft, 'g' forces, thermal, and pressure forces.

#### 2.9.2. Shadow Camera Attitude Determination

The attitude, and any subsequent motion of a shadow camera, once a pointing direction is established must be determined in order that a meaningful deconvolution can be undertaken enabling positions of X-ray sources to be reconstructed. Consider Figure 2.9.1 which shows the shadow camera and three axes around which motion can take place. Any motion can be resolved into motion in roll, pitch and yaw.

The attitude with respect to the sky can be determined by use of a star tracker or star camera as used for most space astronomy measurements.

In order to use the shadow camera to its full advantage the accuracy to which the pointing direction is obtained must exceed the angular resolution of the camera, the exact type of attitude measurement system being dependent on experimental design. Any motion, once a pointing

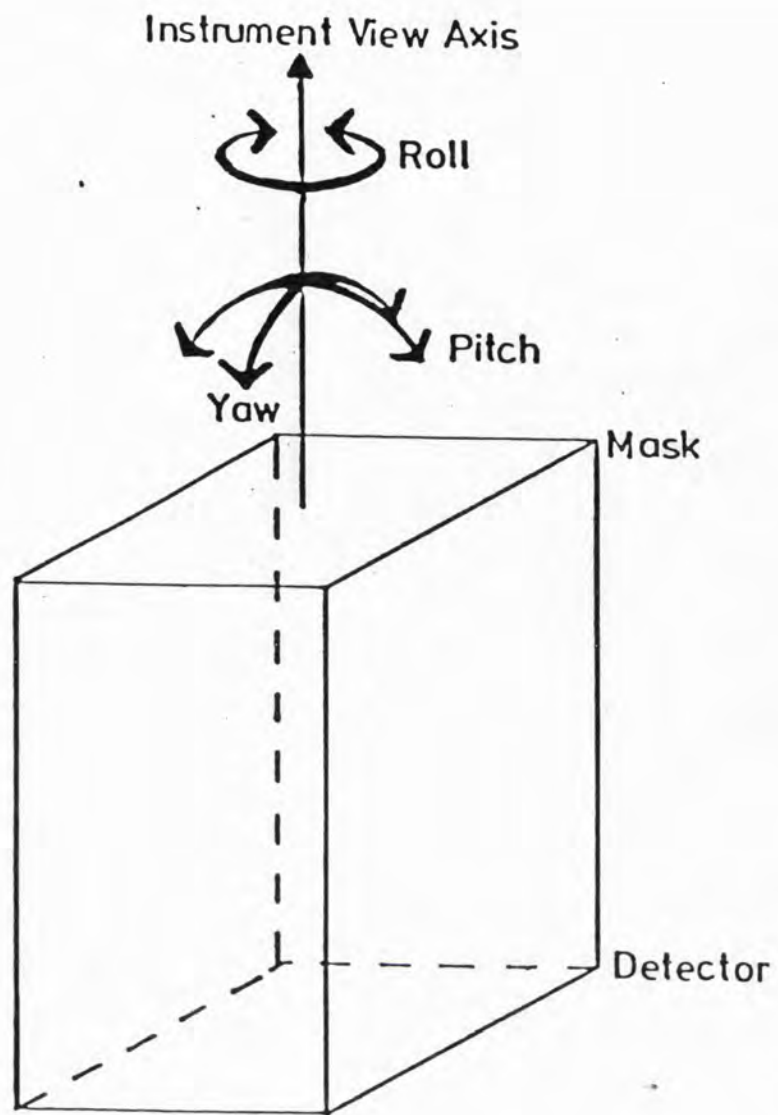


Figure 2.9.1 The basic axes of motion around the shadow camera view axis.



direction has been established can be determined by the tracking system, whose measurement rate must exceed likely drift times of the spacecraft or rocket to which the shadow camera is attached. A gyro pack is an alternative if only relative motions are required. This attitude measurement system must be rigidly attached to the shadow camera(s), as mechanical distortions on a large spacecraft for example the N.A.S.A. Space Shuttle could render the system next to useless if remote from the experiment.

If a set of known celestial X-ray sources with accurate positions are present within the field of view, and can be identified on deconvolution, they can be used as an attitude measurement system-information on relative motion still being required for deconvolution of the data.

If the spacecraft is totally stable no problem exists in correcting data, as only the pointing direction is required to relate the deconvolved X-ray picture to the celestial sphere. Any practical system will most likely have an attitude jitter on it, or will drift slowly in attitude, hence any motion during an integration period for the shadow camera must be corrected for.

Consider first the case of motion in the yaw or pitch axis. In the case of small angular motion, that is the order of a few times sky resolution, the motion is equivalent to a good approximation to a translation of the deconvolved picture, hence data may be easily corrected back to the starting detector co-ordinates before deconvolution. The exact limits of motion and deconvolution of such data are discussed in Chapter 3.

Roll is a distinct problem, in the case of non-circularly symmetric masks, each particular attitude must be deconvolved and added to previous deconvolved images until the motion or observation terminates. This is because on rotation the recorded pattern for a given source distribution after roll correction is totally different in the original detector co-ordinates. Whereas for a circularly symmetric mask the recorded data will itself have circular symmetry and hence roll correction may be done

before deconvolution.

Of course motion will not occur only around the camera view axis, however; any motion can be resolved provided the angular motion is small, into a translation plus roll correction.

In conclusion the shadow camera is not an ideal instrument for an unstable pointing platform, unless considerable computer time is going to be invested in deconvolution of the data. Ideally for attitude motion correction a shadow camera should have a circularly symmetric mask. This however has disadvantages due to an unfavourable point response function (see Chapter 3).

### 2.9.3. Telemetry Requirements

Consider a shadow camera with basic mask pattern of  $m' \times m'$  elements. In order to deconvolve an image one needs the recorded intensity distribution over  $m \times m$  elements on the detector (where  $m \geq m'$ ), hence a detector has  $m$  co-ordinates. Let  $T$  be the integration time of an observation and  $r$  the mean photon arrival rate through the mask averaged over the detector in any one co-ordinate bin. Then approximately  $m^2 Tr$  photons are detected in a single observation. In addition let there be  $n$  energy channels, that is the photon energy is measured and each photon assigned to an energy bin characteristic of the energy, and energy resolution of the detector.

If a co-ordinate and energy bin number is assigned to each photon as it is detected the telemetry bit total will be

$$m^2 Tr \log_2 m^2 n$$

per integration time  $T$ .

As shown in Appendix B a minimum value of  $m = 2m'$  is required. This data of course only has a time resolution of  $T$ .

For large values of  $m'$ ,  $r$ , and  $n$  the bit rate from a shadow

camera can be quite considerable. Various strategies are possible to reduce this possible problem.

If a stable pointing platform is available or onboard attitude correction by computer is invoked  $T$  can be made very long until observation or attitude constraints terminate the data collection. The average bit rate over  $T$  can therefore be reasonably small, assuming  $r$  is a reasonable value.

Alternatives, for example, high time resolution images, involve the use of (multiple) data memories, data from a given observation is then stored until telemetry requirements can be met by the spacecraft data transmission system.

Other data channels in addition to image data can be used. If temporal variation is of importance a total detector count rate channel can be used, the shadow camera acting effectively like a poor resolution, mechanically collimated proportional counter. Another possible interest is a high spectral low time resolution mode (statistics just not allowing good spectral and time resolution). Each of the above modes of course provides information without imaging by looking for absolute changes in count rate against time and energy channel.

The total telemetry rate from a shadow camera must also include attitude measurement data and "housekeeping" data such as detector temperatures, performance figures. This will, however, be generally of a low data rate.

The actual data transmitted from a spacecraft is of course a compromise between available telemetry and science requirements.

A possible way of reducing telemetry rates is alteration of the mask transparency, the data rate being proportional to the transmission fraction of the mask. The questions of optimum mask transparency is not tackled in this work, if sensitivity is a weak function of transmission, and as the data rate is a strong function a reduction in transmission may not compromise

the performance of the instrument,

#### 2.9.4. Other Practical Considerations

As mentioned above, the IPC chosen as the imaging detector for the shadow camera has a thin window which must be supported against the counter's internal pressure. The window support structure must be designed such that it interferes as little as possible with the coding mechanism of the camera.

A large area detector system is almost certain to use a segmented type of readout system in order to achieve the necessary spatial resolution, so gaps of poor or zero resolution may exist across the detector. This problem may be reduced or even removed if the window support is so designed that it overlays these regions.

Finally in the case of an IPC (or most detectors), the spatial resolution of the detector is energy dependent, this fact must be taken into account when the experiment is designed. Hence there will exist a finite range of energy over which a certain angular resolution can be achieved. Outside this range the sky is blurred.

The problem of finite detector response is discussed in Chapter 3 and Appendix B.

#### 2.10. Review of a Shadow Camera Design

One particular practical design will be reviewed in this section, the following section of this chapter will review the basics of some other proposed designs.

In response to the N.A.S.A. announcement of opportunity A0-OSS-2-78 (High Energy Astrophysics) the X-ray Astronomy Group of the University of Leicester, England, and the Center for Space Research of the Massachusetts Institute of Technology, United States of America, proposed a simple shadow

camera to conduct an all sky survey of transient X-ray sources, X-ray bursts and flares on Spacelab Missions 1981-1983.

The proposed instrument (partially designed by the author) consisted of an array of twelve two-dimensional shadow cameras, providing a continuously recorded  $2\pi$  steradians picture of the sky in its basic mode, known as the 'fly's eye' mode. X-ray transients outbursts, plus other variability being extracted by use of time filtering the deconvolved picture. Resolution was designed to be approximately 3 arc minutes, the cameras having a total energy range of 1.5 to 50 keV.

Figure 2.10.1 shows the basic 'fly's eye' mode, the array of cameras mounted on a spacelab pallet.

Each shadow camera has a  $22.5^\circ \times 22.5^\circ$  field of view (FWHM). It was proposed that this array be realigned on command for narrow field observation, eight of the modules moving to align along the -z axis of the Space Shuttle Orbiter. In addition, each module has a deployable  $10^\circ \times 10^\circ$  FWHM collimator to limit the field of view and exclude bright off-axis sources, these collimators being deployed on command from the ground.

Table 2.10.1 gives a basic summary of the instrument parameters. Table 2.10.2 summarises the shadow camera module and detector characteristics. These tables are adapted from the proposal (Leicester, MIT 1978). Figures 2.10.2 and 2.10.3 taken from the proposal show cross sections of the shadow camera module and position sensitive proportional counter respectively.

#### 2.10.1. Mask Construction, Alignment and Resolution

It was proposed to construct the 30 cm x 30 cm mask from BeCu alloy 75  $\mu\text{m}$  thick, etched with the required pattern. The mask was to be plated with 75  $\mu\text{m}$  layer of gold to reduce transmission of high energy X-rays.



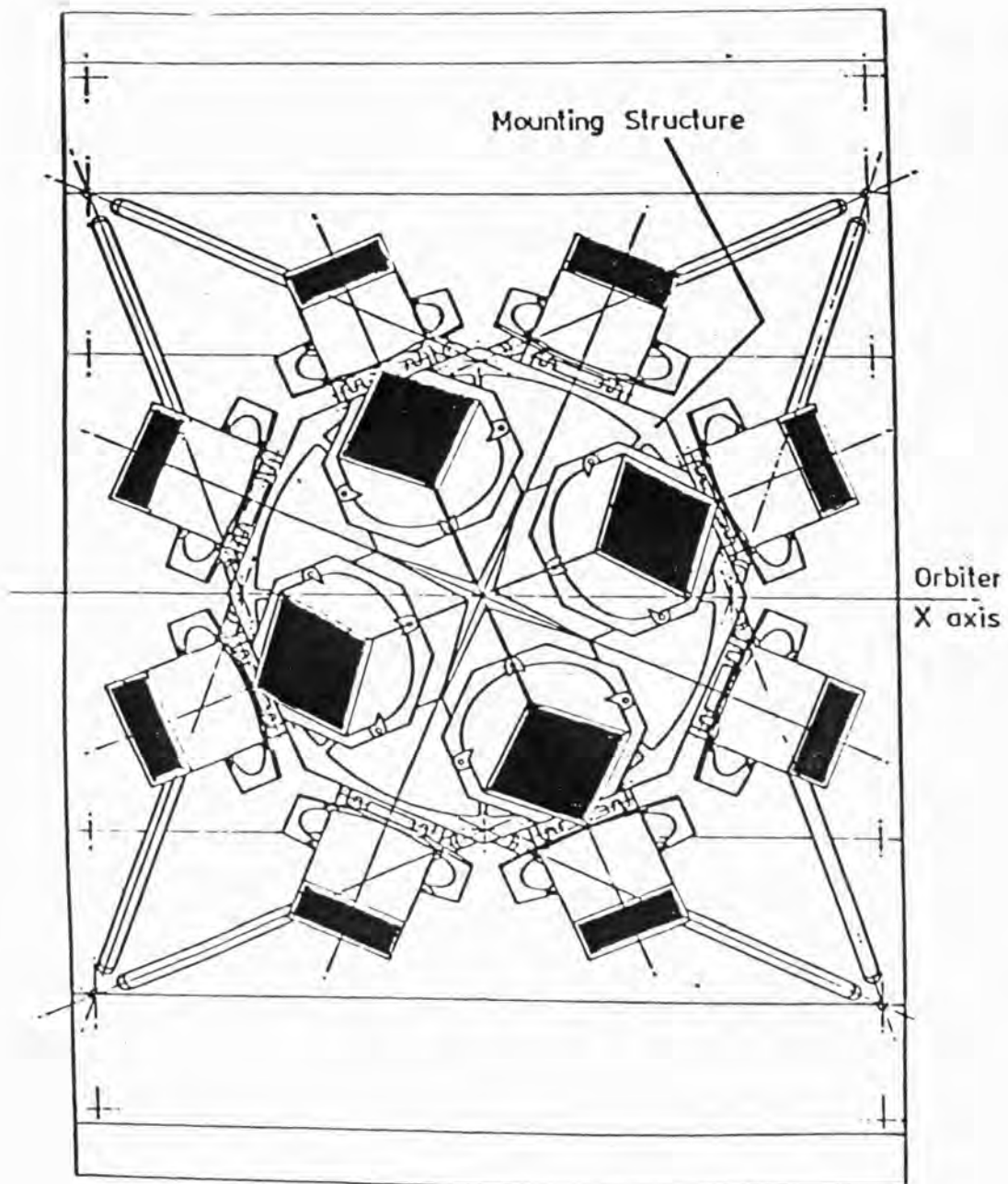


Figure 2.10.1 Plan view of the array of shadow cameras proposed for Spacelab (Leicester, MIT 1978) in 'fly's eye' mode. The 12 cameras cover half the celestial sphere with their combined FOV's.

TABLE 2.10.1.

## INSTRUMENT SUMMARY

Instrumentation	12 shadow camera modules 3 star cameras electronics packages
Volume and mounting	occupies 1 Spacelab pallet
Mass (inc. structure)	859 kg
Power	84 watts (exc. heaters)
Telemetry	410 k bits sec <sup>-1</sup> (maximum)
Configuration	(a) 'fly's eye' mode, with 12 cameras covering $2\pi$ steradians. (b) narrow field mode, with 8 cameras co-aligned and $10^\circ \times 10^\circ$ collimation.
Sensitivity ( $6\sigma$ , on-axis) (in milliCrabs, where 1 mCrab = 1 Uhuru unit)	(a) 200 mCrab, galactic pole } in 480 mCrab, galactic centre } 1 second  17 mCrab, galactic pole } 100 secs 45 mCrab, galactic centre }  2 mCrab, galactic pole } 5000 secs 6 mCrab, galactic centre } (1 orbit) (b) 90 mCrab, galactic centre - 1 sec 8 mCrab, " " - 100 secs 1 mCrab, " " - 5000 secs
Time Resolution	100 millisec (imaging) 10 millisec (timing)
Energy Range	1.5 - 50 keV overall 1.5 - 15 keV for position readout
Angular resolution	3.4 arc min, on-axis degrading to 3.7 and 4.2 arc min for off- axis incidence at $10^\circ$ and $22^\circ$ respectively.
Position Location (typical)	$\frac{\theta^2}{n_\sigma} \sim \frac{11.6 \text{ arc min}^2}{6} \sim 1.9 \text{ arc min}^2$



TABLE 2.10.2.

## SHADOW CAMERA MODULE CHARACTERISTICS

Size	40 cm x 40 cm x 80 cm
Mass	29 kg
Full Field of View (FWHM)	22.5° x 22.5°
Field of View with Deployed Collimators	10° x 10°
Mask Area	30 cm x 30 cm
Mask-Detector Window Separation	72.5 cm
IPC Effective Area	380 cm <sup>2</sup>
Mask Hole Size	0.6 mm

## DETECTOR CHARACTERISTICS

Window Size	30 cm x 30 cm
Window Material	Beryllium
Gas Mixture	Xenon-methane (90:10)
Gas Pressure	2 atmospheres
Energy Resolution	20% FWHM at 5.9 keV
Spatial Resolution	FWHM = 0.6 mm (2 - 8 keV)

	<u>Anode</u>	<u>Cathode</u>	<u>Anti-Co Anode</u>
Wire Pitch (mm)	1.0	1.0	10.0
Wire Diameter (μm)	20	50-125	20
Interelectrode Gaps			
Window to Cathode			15.0 mm
Cathode to Anode			5.0 mm
Guard Cell			15.0 mm

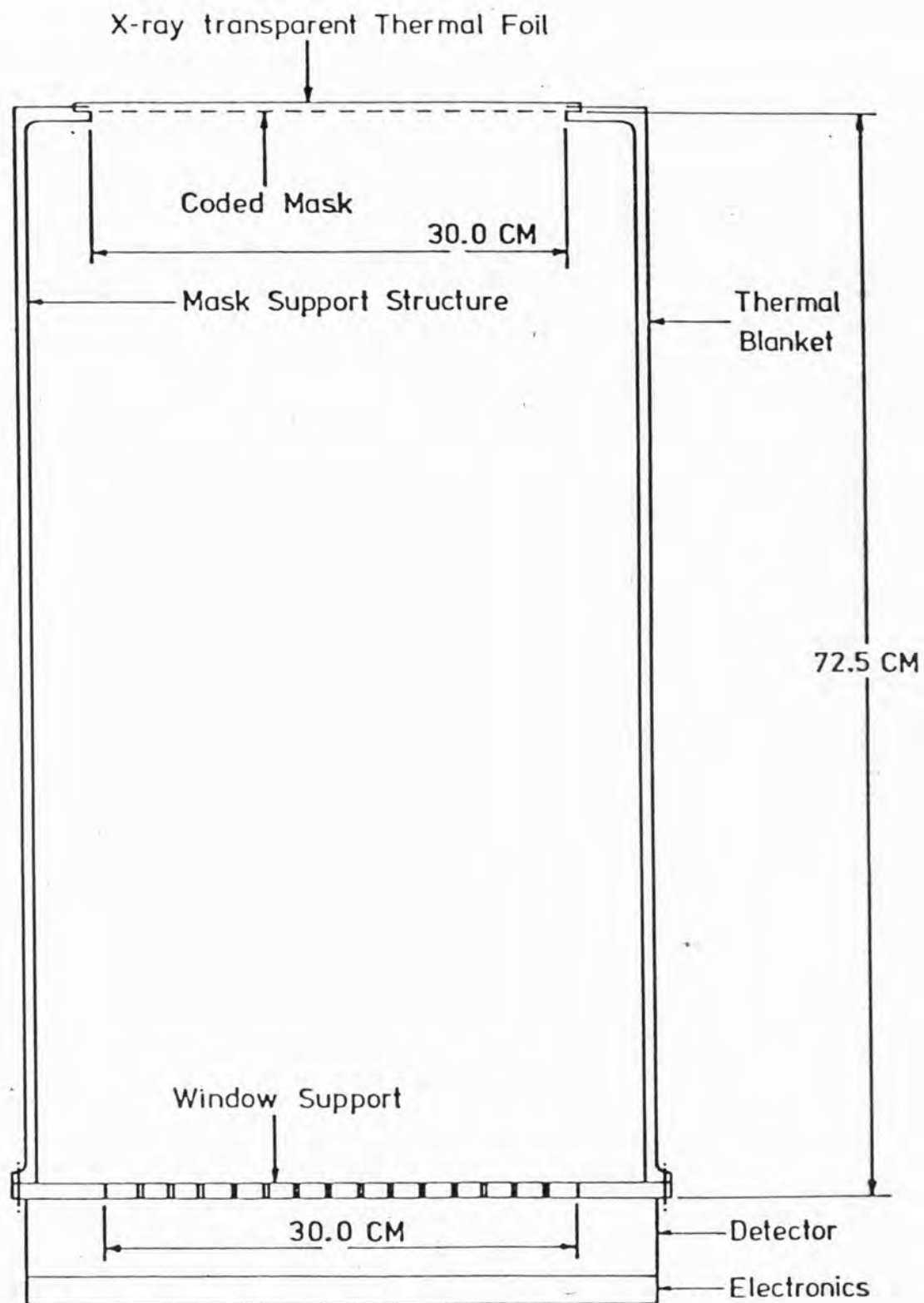


Figure 2.10.2 Schematic cross-section of a shadow camera module.  
(From Leicester, MIT 1978).

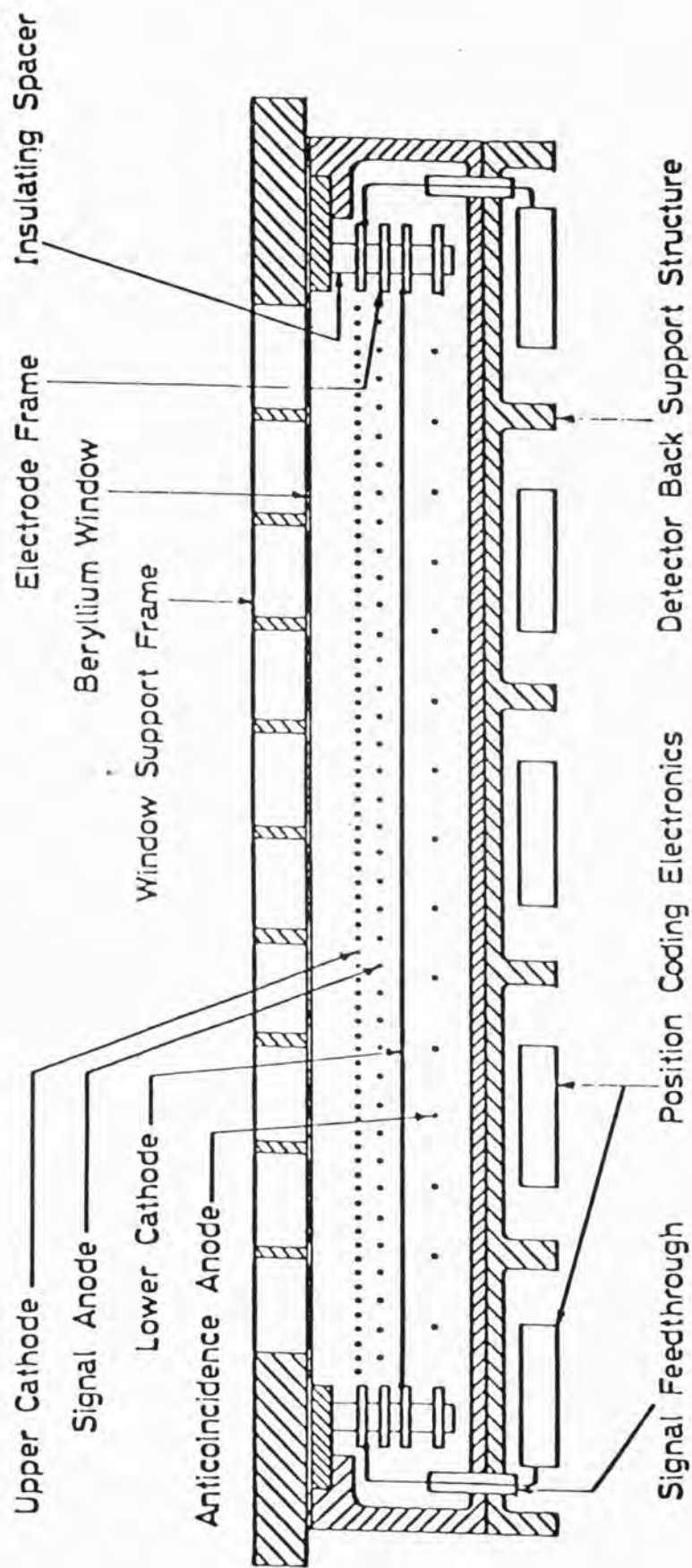


Figure 2.10.3 Schematic cross-section of the position sensitive proportional counter for Spacelab proposed shadow camera design. (From Leicester, MIT 1978).

The problem of mask distortion and alignment is removed by a proposed rigid mounting structure aligning the mask to within  $\pm 0.1$  mm with respect to the detector position sense axes.

The mask to IPC separation is 72.15 cm giving an on-axis resolution element of  $3.4' \times 3.4'$  for the mask with a hole size of 0.6 mm and a matched IPC resolution of 0.6 mm. The corresponding pixel area is  $\sim 11.6$  arc minutes<sup>2</sup>. The angular precision with which a source can be positioned depends on the signal to noise of detection, the area of an error box is therefore

$$\sim \frac{11.6}{n_\sigma} (\text{arc min})^2$$

a minimum  $6\sigma$  was proposed for detection, hence the resultant error boxes would be less than  $2(\text{arc minutes})^2$ .

The mask design was not fixed, however, and was to consist of  $512 \times 512$  elements.

#### 2.10.2. Thermal Control

It was proposed that the thermal control would consist of thermal blankets plus electric heaters; the final design of the control pending a detailed thermal analysis during a design stage.

#### 2.10.3. Attitude Determination

The prime attitude measurement system proposed for this experiment was a set of three CCD star cameras mounted on the instrument support structure. Some initial pointing information being derived from the Orbiter state vector, and the alignment information between cameras and the attitude measurement system being provided by the known X-ray sky.

The expected Orbiter limit cycle of  $\pm 0.1^\circ$  in pointing direction leading to some image blurring, and loss in sensitivity for sources at

the edge of the field of view.

#### 2.10.4. Telemetry Requirement

Due to the mask having 512 by 512 elements, this lead to a 20 bit X-Y position code for every photon detected, along with 2 bits for energy, and a 4 bit module identification code. The total is therefore a 26 bit word for every photon detected.

Each word was to be transferred to a double buffered system; serving to de-randomise the data and transfer it to the telemetry downlink. It was proposed that the data was transmitted in blocks of intervals of a 1/10 second, count rates having an upper limit to stop jamming by an observation of the sun of Sco X-1 .

In addition to this image data, a channel of 16 energy channels time resolution 1/10 second and four energy channels with a time resolution of 10 milliseconds were proposed.

This leads to a telemetry rate of ~ 410 kilobits per second, considering the 'worst' cases of two cameras viewing the galactic centre, one viewing Sco X-1 , and the other nine viewing the diffuse background.

Due to the large telemetry band width of the Space Shuttle Orbiter no real consideration was made in this proposal to reduce telemetry requirements. Table 2.10.3 summarises the calculation of telemetry requirements.

#### 2.10.5. Other Experiment Requirements

The mass budget, experiment power requirements and command requirements for the experiment is summarised in Table 2.10.4. This table and 2.10.3 were adapted from the proposal to NASA.

TABLE 2.10.3  
EXPERIMENT TELEMETRY REQUIREMENTS

Image Data 13000 photons at 26 bits	= 340 kbps
Integration Count Rate Data	
Time: 4 energy channels of 8 bits every 10 milliseconds from 12 modules :	= 38 kbps
Energy: 16 energy channels of 10 bits every 1/10 second from 12 modules:	= 19 kbps
Housekeeping and Aspect Data:	= ~ 1 kbps
Quick look data - total count from each camera every 10 milliseconds to be available continuously on ground:	= <u>10 kbps</u>
Total:	~ 410 kbps

TABLE 2.10.4  
OTHER REQUIREMENTS

Mass Estimate

Individual Modules:

Module support:	8.2 kg
Window support:	4.6
Detector structure:	6.4
Detector wire arrays:	5.0
FOV collimator:	2.0
Electronics:	3.0

Module Total	29.2 kg
--------------	---------

Total Instrument

Modules (12):	350.0 kg
Array structure:	250.0
Drive units:	36.0
Support legs:	80.0

---

716.0 kg

Contingency (20%)	143.0
-------------------	-------

---

Total	859.0 kg
-------	----------

Command Requirements

Discrete Commands:

Power control:	26
Spare:	6
	<hr/> 32

Digital Experiment Commands:

Collimator deployment:	24
Module drive:	24
Heater power:	48
High voltage power supplies:	72
Anti-co logic:	24
IPC control settings:	216
Telemetry, camera control	80
	<hr/> 488



TABLE 2.10.4 (contd.)

Power Requirements

Item:	Power (watts)
Preamplifiers, 12 per detector, 12 detectors	4.8
Measurement chains, ditto	10.8
A/D converters, ditto	3.6
Digital electronics and telemetry format system	7.2
Detector HT supplies	27.6
Telemetry memories	16.0
CCD Star Cameras (3)	6.0
Contingency 10%	8.0
Total	<hr/> 84.0

## Additional items

Collimator drives twice per orbit	14
Detector drives ditto	15
Heaters	300 nominal

#### 2.10.6. Summary of Experiment Design

The overall experiment design is extremely ambitious, many exact details however are not defined. However the design could fit within defined Spacelab limitations. No contradictions, with the practical points developed within the sections 2.2 - 2.9 exist. The major problem area is the FOV limiting  $10^\circ \times 10^\circ$  collimator, due to off-axis shadowing; with this deployed a considerable loss in sensitivity (coding efficiency) would result.

#### 2.11. Other Designs for the Shadow Camera

This section will briefly describe one camera which has been flown and several other proposed designs for the shadow camera. These designs are not reviewed in great detail, but are to show configurations and typical experiment requirements.

Four particular experiments will be described, these are: the Skylark 1501 experiment; TRANSTEL, a large area transform telescope; the Wide Field Cameras for the ESA X-90 (Spectroscopy, Timing, and Transient) mission; and finally ultra-high resolution imaging using the shadow camera. Not all these experiments are of course for wide field monitoring of sources, but illustrate rather the uses of the shadow camera principle.

##### 2.11.1. The Skylark 1501 Experiment

The Skylark rocket 1501 was flown in June 1976. This was the first flight of a coded mask telescope to study celestial X-ray sources. The imaging detector was an imaging proportional counter. Blake et al., 1974, had previously used photographic film to record a coded image of the sun at X-ray wavelengths.

The purpose of the Skylark flight was to image a small region

$4^\circ \times 4^\circ$  at the galactic centre. The experiment is described in two papers, Procter et al., 1978, 1979.

The shadow camera used an argon-methane filled imaging proportional counter along with cyclic pseudo noise mask in order that complete coding and true imaging was achieved.

The mask transmission was nominally 50% , but reduced to an actual 43.7% by a supporting grid. The mask although square did not have square elements, the 1023 element mask was arranged as  $93 \times 11$  elements, as resolution was high in one direction in the detector, much lower in the perpendicular direction. The mask was etched from stainless steel, elements measuring  $1.387 \text{ mm} \times 11.40 \text{ mm}$  .

The detector sensitive area dimensions were  $250 \text{ mm} \times 205.2 \text{ mm}$  giving a geometrical area of  $513 \text{ cm}^2$  . The  $12.5 \text{ }\mu\text{m}$  aluminium coated Melinex window of the detector was supported against the internal 1.1 atmosphere pressure by the FOV collimator. The position resolution of the counter was  $1.25 \text{ mm}$  at  $2 \text{ keV}$  ,  $0.85 \text{ mm}$  at  $6 \text{ keV}$  and  $0.7 \text{ mm}$  at  $8 \text{ keV}$  (FWHM) in one direction by  $11.4 \text{ mm}$  in the other direction, this was dictated by the readout scheme. The overall energy range was  $2.2$  to  $10.2 \text{ keV}$  .

The complete mask ( $258.0 \text{ mm} \times 250.8 \text{ mm}$ ) was  $1.86 \text{ m}$  in front of the detector giving a FWHM point response of  $2.54 \times 20.9$  arc minutes, the full field of view was  $3.96^\circ \times 3.86^\circ$  . The time resolution of the experiment was limited by telemetry to  $0.512$  milliseconds.

Due to a mechanical failure the required FOV collimator (designed not to interfere with the coding) was not flown, but a  $4.5^\circ \times 5.6^\circ$  was flown causing some spurious shadowgram modulation. However pointing drift during the galactic centre observation smoothed out the collimator modulation to below the noise level.

The rocket flight was successful and deconvolution of the data revealed three separate steady sources. One of which was identified with

the near galactic centre recurrent transient A1742 - 294 , the second GX + 0.2, - 0.2 , later identified in Ariel 5 RMC data, the last (95% confidence) was GX 1.1 , - 1.0 . In addition during the flight three weak bursts of X-rays were observed, and their locations found.

#### 2.11.2. TRANSTEL, a Large Area Transform Telescope

In response to the NASA AO-OSS-2-78 a Spacelab experiment called TRANSTEL was proposed by the X-ray astronomy groups at the Naval Research Laboratory, Washington D.C., U.S.A., the Department of Space Research, University of Birmingham, Birmingham, England, and the Los Alamos Scientific Laboratory, New Mexico, U.S.A. TRANSTEL was a large area shadow camera with variable mask to detector distance. This experiment was not accepted for flight at that time, but is reviewed as it points the way to high resolution imaging using the shadow camera.

The experiment is based on the cyclic shadow camera. In the proposal 12 modular detectors each of  $1025 \text{ cm}^2$  of active area would sit below a cyclic mask with many repeated patterns on. Each detector had the required collimator so that it would act as a single cyclic camera. The sum of the resulting deconvolved images was equivalent to a shadow camera with a total active area of  $1.2 \times 10^4 \text{ cm}^2$ .

Figure 2.11.1 taken from the proposal to NASA (Naval Research Laboratory, University of Birmingham and Los Alamos 1978) shows TRANSTEL mounted on a Spacelab pallet.

The mask was to be moved to three separate positions using 3 Astromasts, motor driven support beams, developed for the American Air Force, for use in space. The basic mode was to be with the mask 1.25 metres from the detector, with a detector resolution of 0.5 mm FWHM giving an angular resolution of 3.4 arc minutes, FOV being  $4^\circ \times 4^\circ$  FWHM.

On command the mask could move to the fine mode, 10 metres away.

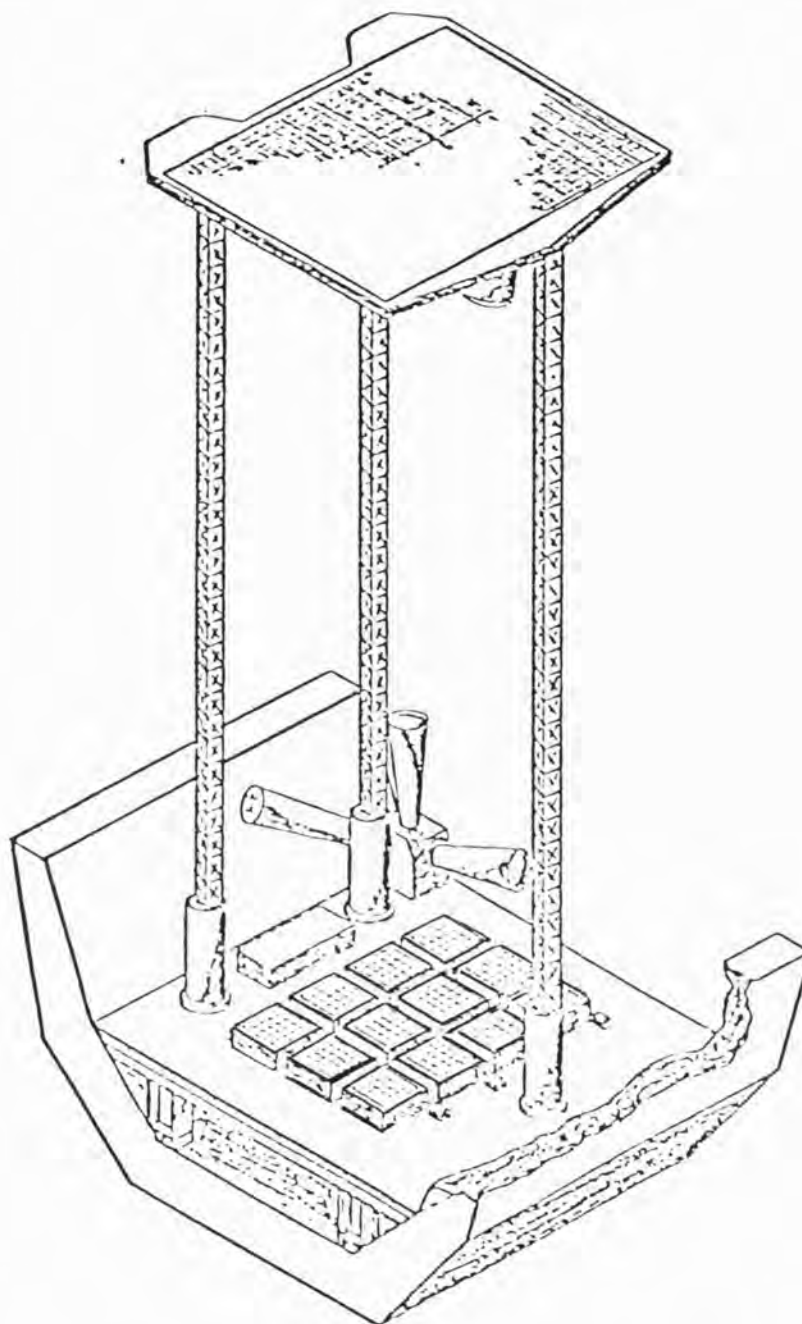


Figure 2.11.1 Artist's impression of TRANSTEL mounted on a Spacelab Pallet. The mask array is suspended above an array of IPC's by three Astromasts. (From Naval Research Laboratory, University of Birmingham and Los Alamos 1978).

At this point secondary detector collimators would be deployed to limit the field of view to one cycle of the mask pattern. The field of view being  $0.85^\circ \times 0.85^\circ$  FWHM with an angular resolution of 25 arc seconds in this mode.

The final position or mode was with the mask moved to a distance 20 m away from the detector giving a resolution of 12.5 arc seconds, the field of view remaining at  $0.85^\circ \times 0.85^\circ$ . At this point however each detector would see 4 complete mask cycles giving four fold ambiguity on deconvolution. As bright point sources only were intended to be observed in this mode this causes no major problem.

The experiment was proposed to conduct a survey of galactic bulge X-ray sources, to act as a narrow field burst monitor, and to map clusters of galaxies in the 2 to 20 keV energy range, when in the coarse resolution mode. The fine resolution modes were proposed for a survey of the galactic centre region, a mapping of the source distribution in M31, and studies of supernova remnants with hard spectra.

The proposed mask was to consist of multiple patterns of a single basic pseudo noise sequence type of  $255 \times 257$  elements, photoetched onto molybdenum sheets with a fine supporting mesh. The mask was to be coated with 10 microns of gold to render it opaque to 20 keV X-rays. Each mask element was a square, side 1.25 mm, making one cycle approximately 32 cm x 32 cm. The cycles being bound together to create one large area mask.

The detector modules are based on a Spacelab 2 experiment to map clusters of galaxies with a coded mask telescope. Each detector was to be an IPC with sensitive area 32 cm x 32 cm, 3 cm deep, filled with Xenon plus a quench gas (mixture not decided) to a pressure of 1.5 atmospheres. An eggcrate type mechanical collimator limited the field of view, and provided detector window support.

Aspect determination using NASA standard star trackers, and mask



TABLE 2.11.1

## TRANSTEL INSTRUMENT CHARACTERISTICS

Mask to detector distance:	Variable 1.25, 10, 20 m
FOV:	4° x 4°, 0.85° x 0.85°, 0.85° x 0.85°
Resolution:	3.4', 25", 12.5"
Energy range:	2 - 20 keV Imaging 1.5 - 50 keV Overall
Mask transmission:	50%
Mask area:	32 cm x 32 cm One cycle 26 m x 2.6 m Overall
Detector area (geometric):	1024 cm <sup>2</sup> Per detector 1.24 x 10 <sup>4</sup> cm <sup>2</sup> Total
Configuration:	One pallet containing 12 detector modules plus mask and support
Mass:	925 kg
Size overall:	3 x 2.9 x 1.5 m in coarse mode
Thermal control:	Thermal blankets plus heaters
Telemetry rate:	.256 M bit sec <sup>-1</sup> Typical 1 M bit sec <sup>-1</sup> Maximum
Power required:	360 W
Sensitivity:	Coarse mode ~ 10 <sup>-5</sup> x Crab in 10 <sup>4</sup> s (point source)



alignment was to be measured using a series of alignment telescopes and fiducial lights, and the use of known X-ray sources. The mask to detector distance being sensed by cables inside the mask support beams.

The instrument characteristics are summarised in Table 2.11.1 adapted from the original proposal.

The concept of TRANSTEL was proposed as a step to a 'next generation' instrument capable of arc second imaging using free flying satellites and the Space Shuttle Orbiter. This idea is reviewed in section 2.11.4.

### 2.11.3. The Wide Field Cameras for the X-80 Mission

Currently a design study is under way for ESA for a spectroscopy timing and transient mission in X-ray astronomy, the X-80 Mission. Amongst the payload is a set of Wide Field Cameras based on the shadow camera principle to act as monitors of variability. Their fields of view are perpendicular to the narrow field instrumentation onboard.

The original design of the cameras was based on the cyclic shadow camera, enabling true imaging to an approximate resolution of 5 arc minutes to be achieved. Table 2.11.2 lists the characteristics of the cameras.

Recently the study team has changed the design to that of a simple camera, the science emphasis switching to that of variability of X-ray sources. As the design study is still underway no further details of this experiment will be given.

Figure 2.11.2 shows an artists impression of the X-80 mission spacecraft the WFC's arrowed. The table and figure being taken from the initial study report (ESA 1980).

TABLE 2.11.2  
CHARACTERISTICS OF WIDE FIELD CAMERAS  
FOR THE X-80 MISSION

FOV	34° x 34° FWZR per camera
Angular Resolution	5 arc min (Original)
Error Box Area	1 (arc min) <sup>2</sup> limited by camera internal alignment
Energy Range	2 - 50 keV Overall 2 - 20 keV Imaging
Mask Area	60 cm x 60 cm (Original now 30 cm x 30 cm)
Detector Area	30 cm x 30 cm
Detector Effective Area	320 cm <sup>2</sup>
Mask Transmission	50%
Mask to Detector Distance	48.6 cm (Original now 98.1 cm)
Configuration	4 Cameras
Mass	166 kg Total
Size	<div style="display: flex; align-items: center;"> <div style="margin-right: 10px;"> Front face 0.7 m x 0.7 m  Rear face 0.4 m x 0.7 m  Depth 0.6 m  Now 0.4 m x 0.4 m x 1.2 m </div> <div style="font-size: 3em; margin-right: 10px;">}</div> <div>per camera</div> </div>
Thermal Control	Thermal blanket plus heaters
Telemetry Requirement	28 bits per photon per camera
Maximum Expected Rate	~ 70 k bit sec <sup>-1</sup>

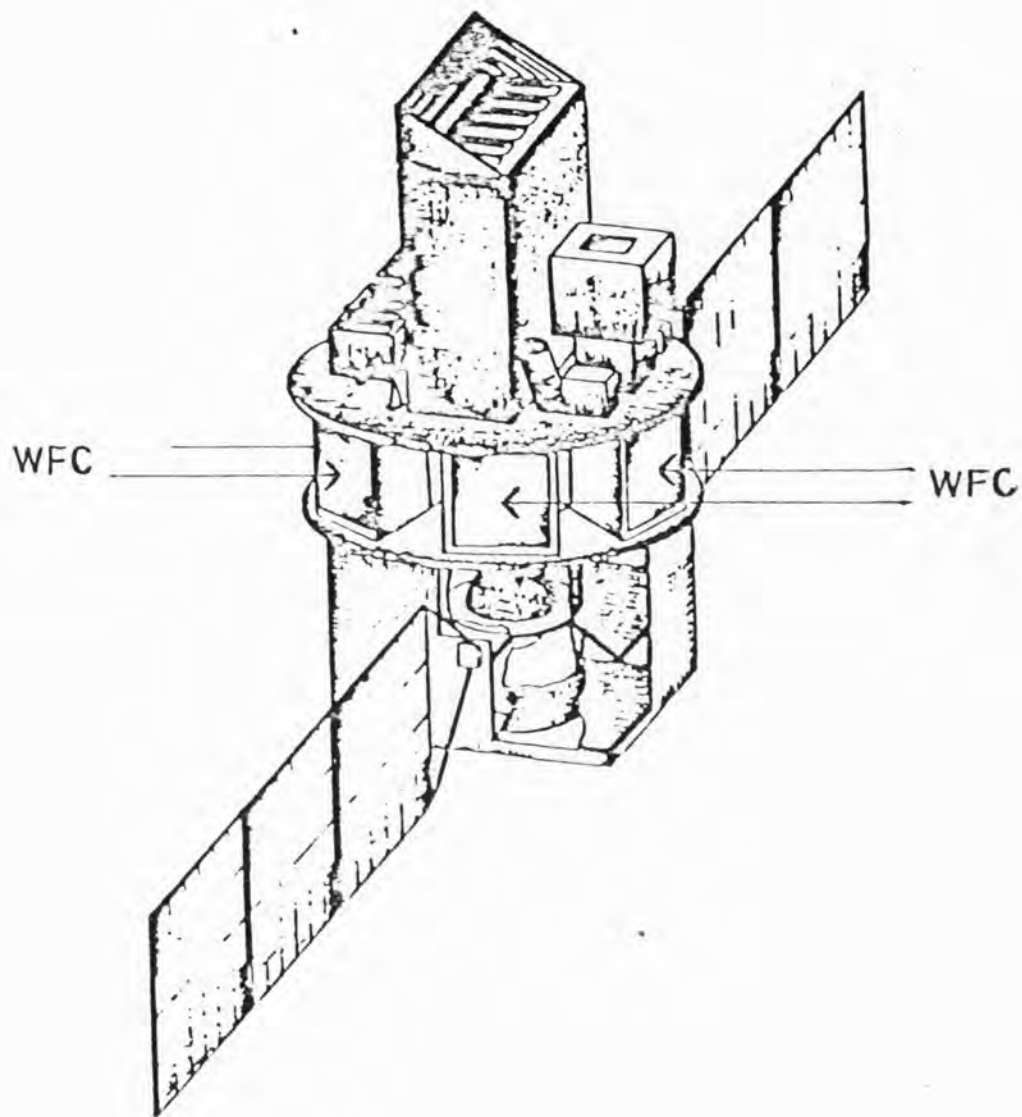


Figure 2.11.2 Artist's impression of the X-80 spacecraft.  
The positions of the four WFC's are arrowed  
(From ESA 1980).

#### 2.11.4. High Resolution Imaging with the Shadow Camera

The shadow camera is in concept capable of very high spatial resolution in the energy range outside which grazing incidence telescopes can operate. The TRANSTEL proposal points the way to how such imaging may be achieved. As true imaging is required (for the study of extended sources) the simple camera which is ideal as a variability monitor cannot be used; some form of the cyclic camera must be used.

As it is not possible to build any arbitrary size imaging detectors, any large area system must use an array of detectors. Hence one is naturally lead to a TRANSTEL idea of a mask pattern repeated many times, FOV collimators on the detector eliminating source ambiguities.

It has been proposed to fly in the late 1980's a large area grazing incidence telescope called AXAF (NASA report 1980). This telescope is capable of resolving to 0.5 arc second. What parameters does this imply for a shadow camera capable of the same performance.

Consider a 'standard' detector with resolution of 0.5 mm at some energy, and a mask with hole size 0.5 mm, what is the required separation of mask and detector for 0.5 arc sec. to be the best possible angular resolution.

From equation 2.4.2.

$$r' \approx \delta/b$$

where  $\delta$  hole size

$b$  mask to detector distance

$r'$  angular resolution (radians)

with  $\delta = 0.5$  mm

$$r' = 0.5 \text{ arc sec} = 2.42 \times 10^{-6} \text{ radians}$$

$$\Rightarrow b = 206.3 \text{ m .}$$

The required mask to detector distance is 206.3 m . This at first seems to be an impossibly large size. However several authors, Hudson and Lin 1978 , Peterson et al., 1976 amongst others, have suggested methods around the problem of practical construction.

Two ideas are at present thought to be capable of overcoming the problem. The first is the use of subsatellites, that is the mask and detector are placed on separate spacecraft, enabling large mask to detector separations to be achieved. It is thought the problem of alignment measurements can be overcome by the use of laser alignment and measurement techniques.

The second is the use of large space structures. Such structures, kilometres in dimension, are planned for solar power satellites or orbiting space stations. Recently an aluminium beam builder has been demonstrated for use on the Space Shuttle in the 1980's. At present no insuperable technical difficulties in large structures are foreseen, hence it may be possible to construct a larger version of TRANSTEL using such a scheme. The alignment and measurement techniques proposed for TRANSTEL being easily applied to a larger version.

One of the main uses of high resolution shadow cameras may be in the study of the sun's chromosphere and corona by use of the hard X-rays emitted in these regions. An upper limit to use of the shadow camera exists, approximately 200 to 300 keV due to the problem of making the mask opaque at the required energies.

## 2.12 Summary

In concept the shadow camera is capable of high resolution imaging, and wide field monitoring of celestial X-ray sources in an energy range inaccessible to grazing incidence telescopes.

This chapter has reviewed the basic theory and design of the shadow camera, pointing out some of the practical design problems. The chapter has concentrated on the simple camera rather than the cyclic as this is thought, and will be shown in the next chapter, to be more suitable as a wide field camera.

The shadow camera in detail is an exceedingly complicated device and it is not possible to use entirely theoretical arguments to evaluate its performance. The camera has been studied using computer simulation. The next chapter will review the subject of simulation and deconvolution of data from the shadow camera, and results from the computer simulation studies.

## CHAPTER 3

## DECONVOLUTION AND SIMULATION OF THE SHADOW CAMERA

3.1. Introduction

This chapter is concerned with deconvolution of data from the shadow camera, giving special emphasis to practical aspects and the application of advanced methods, in particular the Wiener Filter. In order to provide data on deconvolution and performance of the camera, the design detailed in Chapter 2, section 2.10, has been simulated, so far as available computer time and storage allowed. This enables practical problems to be considered and results of importance to the design of the camera to be produced. The limitations of the simulations will be discussed and, finally, further problem areas and practical points of simulation and deconvolution of the shadow camera will be covered. The work on deconvolution and simulation in this chapter has centred on the practical aspects of the shadow camera, since the theory of coding of the shadow camera and image processing has been covered fully by many authors.

3.2. Deconvolution: Advanced Methods3.2.1. Introduction: Basics of Deconvolution

As shown in Chapter 2, section 2.2.1, the data from the shadow camera has the form of a convolution of the inverted source distribution and mask pattern, namely

$$i(\underline{r}'') = \int s(-\underline{r}) m(\underline{r}'' - \underline{r}) d\underline{r} \quad (3.2.1)$$

notation as in Chapter 2. By the convolution theorem of Fourier analysis.

$$I(\underline{w}) = M(\underline{w}) S'(\underline{w})$$



where capitals represent the respective Fourier transforms,  $i$  being the recorded image,  $m$  the mask, and  $s$  the source distribution. Hence one can in principle recover the inverted source distribution.

$$S'(\underline{w}) = I(\underline{w}) M(\underline{w})^{-1} \quad (3.2.2)$$

provided that  $M(\underline{w}) \neq 0$  at any point.

In practice the source distribution can be recovered by filtering in the Fourier domain or cross-correlation in the real domain.

If we express cross-correlation in the Fourier domain we have

$$I(\underline{w}) M(\underline{w}) = S'(\underline{w})$$

The two approaches can therefore be unified in a sense by considering

$$I(\underline{w}) F(\underline{w}) = S'(\underline{w})$$

where  $F(\underline{w})$  is a filter function dependent on the mask used and decoding method. The inversion operation itself can be absorbed into the filter function. An advanced method of deconvolution is the Wiener Filter which improves the signal-to-noise in the deconvolved image (see section 3.2.2.).

These equations specify a requirement for the mask, namely  $M(\underline{w}) = M(\underline{w})^{-1}$  which is true for pseudo noise sequence masks in the cyclic camera case.

Other advanced methods of deconvolution use iterative procedures in which successive approximations to the image are found with an improvement in signal to noise at each step, the image quality being monitored by a given parameter. Two such iterative procedures have been used in the course of this work, the Maximum Entropy Method of image reconstruction, and a method based on a Bayesian deconvolution (Turner, 1978). Both methods give a large improvement in recovery of source distributions

eliminating most of the ghosting problems encountered with the simple camera. However both are very demanding in terms of computer time and storage.

### 3.2.2. The Wiener Filter

The Wiener Filter naturally develops from the inverse filter described above. It is an attempt to solve the problem of fluctuations in  $M(\underline{w})$ , and produces an estimate of the source distribution with the minimum mean square error between the original distribution and filtered image.

In the notation of 3.2.1. the Wiener Filter is given by

$$F(\underline{w}) = \frac{M^*(\underline{w})}{M(\underline{w}) M^*(\underline{w}) + N/S}$$

where  $N/S$  is an estimate of the ratio of noise power spectral density to that of signal.

The basic theory of the Wiener Filter will be described next. (This is adapted from Willingale 1976). As the images etc. are best thought of as matrices the notation will be altered from that used so far. Consider a model of system response

$$\phi_{ij} = \sum \sum k_{ijk\ell} \psi_{k\ell} + n_{ij} \quad (3.2.3)$$

where  $\phi_{ij}$  is the recorded image matrix  
 $k_{ijk\ell}$  is the system response kernel  
 $\psi_{k\ell}$  is the source distribution matrix  
 and  $n_{ij}$  is the noise matrix (statistic noise etc.)

If the same pattern is recorded for all source positions except for a cycle shift, then the response kernel  $k_{ijk\ell}$  is said to be isoplanatic (this is only true for an cyclic camera with perfect mask; this is only an

approximation for the simple camera where loss of information occurs), and one can express equation (3.2.3) as a direct product in the discrete Fourier transform domain (hereafter referred to as the DFT domain),

$$\phi_{ij} = K_{ij} \psi_{ij} + N_{ij} \quad (3.2.4)$$

One requires a filter matrix  $Q_{ij}$  such that in the DFT domain

$$\hat{\psi}_{ij} = Q_{ij} \phi_{ij} \quad (3.2.5)$$

where  $\hat{\psi}_{ij}$  is an optimum estimate of the unknown source distribution matrix.

The Wiener Filter is obtained by minimisation of the mean square error in the DFT domain. The mean square error is given by

$$E\{(\hat{\psi}_{ij} - \psi_{ij})(\hat{\psi}_{ij} - \psi_{ij})^*\} \quad (3.2.6)$$

where  $E\{x\}$  is the expectation value, the expression in the bracket being the square of the difference in the DFT domain. Minimisation of the above results in minimisation of the mean square error in the real domain since apart from a normalisation constant the sum of the squares of the elements in the real domain is equal to the sum of the squares in the Fourier domain. The Fourier Transform is therefore an energy conserving transform.

If one treats the source and noise matrices as stochastic (random) processes, all errors being gaussian in nature and independent with zero mean, then a linear estimator for the filter can be used. Filters tailored to the statistical nature of the image are considerably more complicated. The exact details of statistical interpretation of images and image formation will not be dealt with in this work. These subjects are covered fully in Willingale 1979.

If we substitute equations (3.2.4) and (3.2.5) into (3.2.6) on reduction we have

$$\begin{aligned}
E_r = \sum_{ij} E \{ & |Q_{ij}|^2 (|K_{ij}|^2 |\psi_{ij}|^2 + |N_{ij}|^2 + K_{ij} \psi_{ij} N_{ij}^* + K_{ij}^* \psi_{ij} N_{ij}) \\
& + |\psi_{ij}|^2 - Q_{ij} K_{ij} |\psi_{ij}|^2 - Q_{ij} \psi_{ij}^* N_{ij} \\
& - |\psi_{ij}|^2 Q_{ij}^* K_{ij}^* - \psi_{ij} N_{ij}^* Q_{ij}^* \} \quad (3.2.7)
\end{aligned}$$

This equation can however be simplified by use of the properties of the stochastic processes describing  $\psi_{ij}$  and  $N_{ij}$ . Firstly assume

$$E\{\psi_{ij} N_{ij}^*\} = 0 ;$$

that is, the noise and source are uncorrelated. Secondly

$$E\{N_{ij} N_{ij}^*\} = N \quad (3.2.7(a))$$

one has a white noise process and finally

$$E(\psi_{ij} \hat{\psi}_{ij}) = S_{ij} \quad (3.2.7(b))$$

If this is a white noise process then  $S_{ij} = S$  a constant.

The above two expressions will be explained further.

For the noise, equation (3.2.7(a)) implies that the expectation value of the rms is a constant, independent of position (a linear approximation). Gaussian noise is a good approximation for the shadow camera in a high background case, as the variation between pixels is then not too large.

Equations (3.2.7(b)) implies, for the signal  $S$ , that the expectation value of its fluctuations is also independent of position. One hence models the source as a random process, that is the source distribution is taken as random. This is a good approximation provided the sources are not extended.

Making the above assumptions, equation (3.2.7) reduces to

$$E_r = \sum_{ij} E (Q_{ij} Q_{ij}^* (|K_{ij}|^2 S + N) + S - S(Q_{ij} K_{ij} + Q_{ij}^* K_{ij}^*)) \quad (3.2.8)$$

One requires  $E_r$  to be a minimum, take

$$\frac{\partial E_r}{\partial Q_{ij}^*} \equiv 0$$

$$\frac{\partial E_r}{\partial Q_{ij}} \equiv 0$$

or

$$Q_{ij} (|K_{ij}|^2 S + N) - S K_{ij} = 0$$

$$Q_{ij}^* (|K_{ij}|^2 S + N) - S K_{ij}^* = 0$$

This is of course not strictly correct as the two are not independent. However a full solution gives an identical answer (Willingale 1976 and 1979).

Hence the minimum square error estimating filter is given by

$$Q_{ij} = \frac{S K_{ij}^*}{|K_{ij}|^2 S + N}$$

or

$$K_{ij}^* (|K_{ij}|^2 + N/S)^{-1}$$

or using the notation of Chapter 2, section 2.2.

$$F(\underline{w}) = \frac{M^*(\underline{w})}{M(\underline{w}) M^*(\underline{w}) + N/S} \quad (3.2.9)$$

The Wiener Filter is perhaps best thought of as a weighted cross-correlation where the weighting tries to compensate for the signal to noise in the image. Use of the Wiener Filter gives the minimum mean square error estimate of the source distribution matrix  $\psi_{ij}$ . However one must have an estimate of  $N/S$ .

### 3.2.2.1. Estimate of N/S for the Wiener Filter

The required value is the ratio of Noise Power Spectral Density to that of Source Power Spectral Density. It can be estimated as follows.

Assume the noise in the data is Poissonian (true for shadow camera statistics) then the noise power spectral density is proportional to  $\sum h_i$  where  $h_i$  are the data pixel values.

The signal power spectral density is given by the mean square fluctuations of the data pixels not including the noise fluctuations as we are only concerned with the signal. The signal spectral power density is therefore proportional to

$$\sum h_i^2 - \frac{[\sum h_i]^2}{N} - \sum h_i$$

where  $N$  = number of pixels in the recorded data. The power density is namely the sum of the squares, minus the d.c. offset, minus the noise fluctuations. Since the constant of proportionality is introduced by the Fourier transform in each case, we have

$$S/N = \frac{\sum h_i^2 - \frac{[\sum h_i]^2}{N} - \sum h_i}{\sum h_i}$$

This is, however, the  $S/N$  value in the recorded shadowgram and the required signal to noise ratio is the signal in the source, not the data.

Each signal spatial frequency is modulated; that is it is attenuated by the square of the modulation transfer function of the mask. The average attenuation is given by  $(\sum |\Lambda_w|^2)/N$ , where  $\Lambda_w$  are the eigenvalues of the DFT of the mask pattern. Therefore the required  $S/N$  is given by

$$S/N = \left\{ \frac{\sum h_i^2 - \frac{[\sum h_i]^2}{N} - \sum h_i}{\sum h_i} \right\} \frac{\sum |\Lambda_w|^2}{N} \quad (3.2.10)$$

$N/S$  for the Wiener Filter is then simply the reciprocal of equation (3.2.10).



### 3.2.2.2. Error in Estimate

The average mean square error in the estimate is given by

$$E_{\min} = \sum_{ij} (S - Q_{ij} K_{ij} S_{ij})$$

Substituting for  $Q_{ij}$

$$E_{\min} = \sum_{ij} \frac{N}{|K_{ij}|^2 + N/S} \quad (3.2.10)$$

and the mean square error per pixel in the filtered image is  $E_{\min}/\text{Number of pixels}$ .

### 3.2.3. Bayesian Deconvolution

This method of deconvolution will only be discussed very briefly as a simple approach to iterative procedures, the maximum entropy reconstruction being much more complicated. Little practical work was attempted using this method, and no results will be presented in later selections.

Bayes rule from probability theory states

$$P(A/B) = \frac{P(B/A) P(A)}{\int P(B/A) P(A) dA} \quad (3.2.11)$$

In the shadow camera we have  $B$  as the detected count and  $A$  as the unknown source, if we consider them in terms of probabilities.

Consider a one-dimensional shadow camera for simplicity.

Let  $N(i)$  be the counts recorded in the  $i^{\text{th}}$  detector bin.

$R(i,x)$  the response function of the instrument (mask transmission)

and  $I(x)$  the intensity emitted from a point source position

$x$  in the shadow camera FOV.



No information is available about  $I(x)$  apart from that contained in  $N(i)$  ; therefore let us approximate  $I(x)$  and iterate converging hopefully towards the actual distribution.

Converting the above parameters into probability terms we have

$$P(B/A) = R(i,x) / \sum_i R(i,x)$$

$$P(A) = I(x) / \int_x I(x) dx$$

$$P(B) = N(i) / \sum_i N(i)$$

Now  $P(A) = P(A/B) P(B)$

where  $P(A/B)$  is given by equation (3.2.11). Unfortunately  $P(A)$  is unknown, so start with an estimate for  $P(A)$ , namely  $P_k(A)$ , then

$$P_{k+1}(A) = \int_B P(A/B) P(B) = \int_B P(B/A) P_k(A) P(B)$$

or in terms of actual measurements, the integrations become summations, namely

$$P_{k+1}(x) = \frac{\sum_i \frac{R(i,x)}{\sum_i R(i,x)} P_k(x) \frac{N(i)}{\sum_i N(i)}}{\sum_x \frac{R(i,x)}{\sum_i R(i,x)} P_k(x) dx} \quad (3.2.12)$$

One of course has to assume an initial  $P_k(x)$ , a flat distribution was found to work in practice. The above is not a solution to Bayes rule, but an iterative procedure. The bottom term of the expression is an estimate of the recorded data, say  $\hat{D}_i$ , produced by folding the estimate of the source field  $P_k(x)$  through the instrument response. If we let  $N(i)/\sum N(i) = D_i$  (recorded data), and  $R(i,x)/\sum R(i,x) = M_{x-i}$  then equation (3.2.12) can be rewritten. The new estimate of the source field is hence given by

$$P_{k+1}(x) = P_k(x) \sum_i \frac{D_i}{\bar{D}_i} M_{x-i}$$

This has the form of a weighted cross-correlation, the formula giving actual counts detected, as the instrument response is folded in. If  $D_i < \hat{D}_i$  an average for a given  $x$   $P_k(x)$  is then reduced for a given position, and vice versa, the iteration proceeding to  $D_i/\hat{D}_i = 1$ . The result of  $D_i/\hat{D}_i$  is weighted by the response function at that point to allow for off-axis effects. The response function in this case is the fraction of mask pattern holes visible at a given sky position from a given detector bin.

The method of course has problems; possibly no unique solution, unknown behaviour in the case of multiple sources, and finally it requires a reliable test for convergence. It is detailed here as a simple iterative procedure.

Primitive simulation work showed that the method could reproduce simple source distributions (2 to 5 sources) for a one-dimensional position sensitive shadow camera. However the method has not been investigated in any detail.

#### 3.2.4. Maximum Entropy Method of Deconvolution

The maximum entropy method of deconvolution was developed at Leicester by R. Willingale, based on the work of Kikuchi and Soffer 1977, and Gull and Daniell 1978. The principles of the technique are discussed in Appendix C. Practical implementation of the technique is covered in Willingale 1979 and 1981.

The method produces a solution for the source distribution which can occur in the largest number of ways and is consistent with the data, that is the configurational entropy is maximised. The maximum entropy solution forces the object field to fit the data using the known response function of the mask, it automatically takes into account the off-axis

fall off effect in the simple camera and hence eliminates the problem of ghosting.

Only a few results using this technique, the most advanced method of deconvolution, will be presented. As with all iterative procedures, the complex response function of the shadow camera must be stored, and at least one convolution occurs for each iteration. The method is therefore expensive in computer time and storage. Hence the improvement in signal to noise that results from its use has to be balanced against the demands on the data analysis computer system.

### 3.3. Computer Simulation: Method

The shadow camera, as described in the last chapter and the first section of this chapter, is a very complicated device although the concept is relatively simple. The details of the response and sensitivity are difficult to calculate analytically. A real understanding of the principles and problems particularly in the case of the simple camera can only come from computer simulation. The approach of this work has been to produce a generalised simulation program which is not specific to the design or type of shadow camera.

The data resulting from a shadow camera is essentially a convolution of the mask pattern and source distribution (ignoring any disturbing effects such as detector window support structure and motion). The source distribution, mask pattern and recorded data are essentially of a discrete nature, particularly the mask, since only zero or total transmission can occur through any one element. The data is therefore best dealt with in terms of matrices, the row and column number describing the position, and the value or amplitude of the pixel describing the intensity or transformation information.

Software has been developed at Leicester for handling and processing

of large matrices up to  $1024 \times 1024$  elements (Willingale 1979), specialist routines for the shadow camera being added to the original library of routines. In order to limit the memory requirements for such processing, the rows and columns of each matrix were processed sequentially using disc files on the University's Cyber 73 to hold the matrix data, rather than loading the entire matrices into the computer central memory. Operations were therefore limited by the time taken to access the matrix data using unformatted READ and WRITE statements. This was however found to be a very weak restriction compared to the calculation time required for most matrix operations.

### 3.3.1. Computer Limitations

The dominant factor in the computer simulation of the shadow camera was found to be the time taken for convolution of two matrices. Figure 3.3.1 shows the processing time in seconds required for the 2-D FFT and convolution on the CDC Cyber 73 computer as a function of dimension of the matrix.

The computer system is run in a time sharing mode. Computer time considerations rapidly lead to the conclusion that the size limit for the matrices for the simulation work was a maximum of  $128 \times 128$  elements, if a turn-round time for each simulation was to be under 24 hours. The above size limit was therefore adopted for all simulation work.

The X-ray Astronomy Group at Leicester has recently acquired a PDP 11/34 complete with array processor which would make much larger simulations a practical proposition. However the basic properties of the shadow camera can be investigated with the smaller size. The new system was not available during the course of this work.

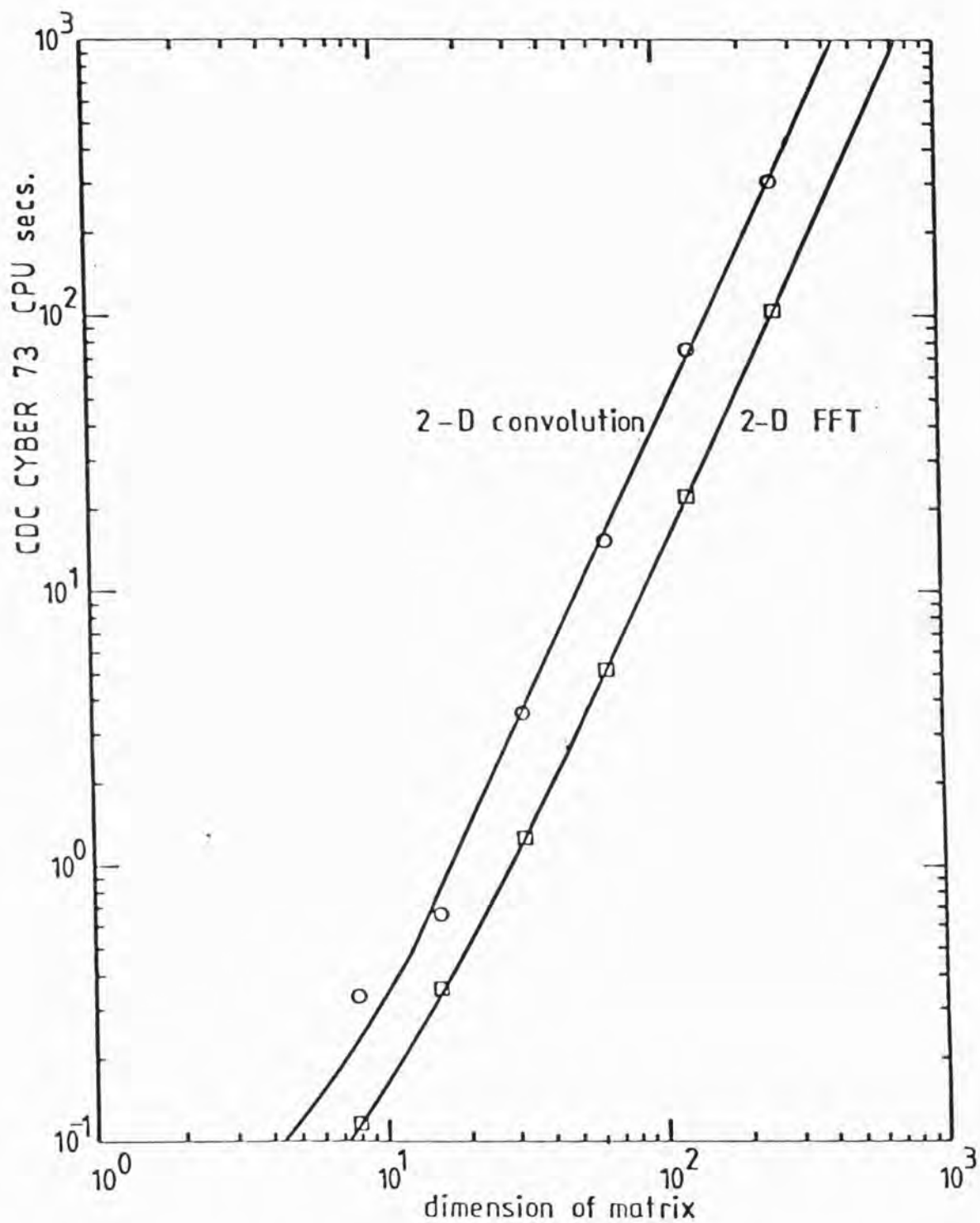


Figure 3.3.1 Computer processing time for 2D FFT and convolution as a function of matrix size using CDC Cyber 73 computer.



In order to further limit the computer simulation the following was done. For a  $128 \times 128$  element source matrix, the mask is of size  $64 \times 64$  elements; for correct sampling of a true shadowed image one really should sample in a  $128 \times 128$  element array, the Nyquist criterion of sampling theory demanding two detector elements per mask element. In this case however the detector array could be taken as  $64 \times 64$  elements. This under sampling does not in fact matter because of the special way the data is created, and considerably simplifies the simulation work as only two basic matrix sizes are involved.

### 3.3.2. Sampling Limitation

The Nyquist criterion does not apply in the simulation case, due to the digital nature of the simulations. In the real situation the sky is of an analogue nature, whereas the mask and detector are essentially digital in nature.

In the simulations no sources are present in 'positions' between mask samples, the simulations using samples the same size as the mask holes. A real source will produce an actual response shape requiring two samples per mask element in order for the deconvolution to produce the correct result.

The placing of the sources at discrete positions does not affect the calculated sensitivity. A demonstration of the under sampling limitation is given in section 3.5.3.

### 3.3.3. Background

The data recorded by the imaging detector consists of a convolution between the mask pattern and source field (the correct area of the resultant matrix having to be sampled to allow for the off-axis fall-off effect

of the simple camera) plus a convolution between the mask pattern and the diffuse X-ray background distribution, together with an overall cosmic ray background count. Each component of the data in addition has photon statistics attached to it.

The following approximations were made to simplify the simulation method. Firstly, the diffuse background was assumed to be entirely extragalactic in nature and uniform in spatial distribution to the sensitivity of the shadow camera. This is of course only true at high galactic latitudes. Secondly, the mask was taken to be reasonably uniform in transmission on a large scale (true for a random pattern), so that each detector pixel would receive approximately the same background count, namely the expected total background count divided by the number of pixels. The total background count ( $T_B$ ) is given by

$$T_B = B_D \Omega A T.t$$

notation as Chapter 2, section 2.3.1, where  $t$  is the overall mask transmission.

Hence the simulation of diffuse background can be made by adding a constant value to each detector pixel (apart from photon statistics). The cosmic ray background is similarly a constant value.

#### 3.3.4. Statistics

To further speed the simulation the photon statistics can be added as the last step. A routine NOISE was written to simulate counting statistics using a random number generator, taking each pixel value as a mean and producing a sample of the statistical distribution about that value.



### 3.3.5. Sources

As a Fourier transform is energy conserving for the simulations the source distributions were normalised to actual counts after convolution, by calculation of the number of counts a standard source would give.

In reality each source has an individual spectrum, and hence the image produced is both energy and source dependent. For this work a fixed energy range of 2 to 20 keV was assumed. In addition each source was taken to have a Crab like spectrum, and energy dependent detector properties ignored. An overall detector effective area was taken for the above energy range. These assumptions/approximations greatly simplify the simulation but do not affect the general properties of the shadow camera which are derived.

### 3.3.6. Program Input Parameters

Making the above approximations the following basic input parameters are required for a simulation, assuming a perfect camera with no disturbing effects present:

- (i) mask pattern
- (ii) source distribution
- (iii) effective area of the detector
- (iv) integration time of observation
- (v) width of the counter, and height from counter to mask in  
order to calculate the effective solid angle
- (vi) diffuse background rate photons/sec/cm<sup>2</sup>/steradian
- (vii) cosmic ray background photons/sec/cm<sup>2</sup>
- (viii) normalised source strength photons/sec/cm<sup>2</sup>.

### 3.3.7. The Mask Pattern

For the simulation work various mask patterns were used: a random pattern; a Fresnelzone plate of 8 rings (which is optimum for a  $64 \times 64$  element system, Willingale 1976); an ideal mask based on a  $63 \times 65$  element pseudo noise sequence (from Procter et al., 1979); a self-supporting pseudo noise sequence (Giles 1980); a Walsh mask; and finally a circularly symmetric pseudo noise sequence mask producing a circular pattern from a one-dimensional sequence. Routines were written to generate all these patterns by choice of one input parameter. Some of the mask patterns are shown later in this chapter.

In order to simulate the cyclic camera; each mask pattern could be 'aliased' to produce a four fold pattern of  $128 \times 128$  elements to produce no off-axis fall-off, and perfect coding in the case of the ideal masks. For the simple camera a  $64 \times 64$  element pattern only was used.

### 3.3.8. Source Distribution

Source distributions for the simulations were produced using existing X-ray source catalogues (Ariel V, 4th Uhuru). Three sky fields were used; the Galactic centre, the Scorpius region (Sco X-1 not in the FOV) and the Coma region, each giving different observing conditions for the shadow camera. These conditions were, respectively, source dominated, partially source dominated, and diffuse background dominated.

The source distribution was input as a set of matrix co-ordinates plus intensities, enabling changes in source co-ordinates and intensities to be made by editing of a data file. The intensities were input in units of  $10^{-3}$  of the Crab Nebula flux (2 to 20 keV, photons/sec/cm<sup>2</sup>), i.e., one milliCrab.

The source co-ordinates were found by measurement of computer plots

of the source distributions, the distributions being plotted with an equal angle projection onto a flat area, given a R.A., Dec of the centre and FWHM of the FOV. Square FOV's only were available. This software was provided by M.J. Ricketts of the X-ray Astronomy Group, the program being based on one used for analysis of the Ariel V SSI data.

For the Scorpius and Coma regions all known sources were input; for the galactic centre only sources greater than 10 milliCrabs were included to save measurement time from the plots.

### 3.3.9. The Overall Program

The overall flow diagram of the basic simulation program is shown in Figure 3.3.2. This shows how the program elements detailed above fit together into the main program. This flow diagram is, of course, for the case of no disturbing effects; that is, a perfect shadow camera as defined in this work.

The Fourier transform used for the program was the fast Fourier transform algorithm of Cooley and Tukey 1965. This reduces the number of operations required for a 2D transform from  $N^4$ , for a slow transform, to  $4N^2 \ln N$ , where  $N$  is the number of rows across the matrix.

To further speed-up operation of the program, the most frequently used mask patterns were stored as disc files.

The resultant simulation data from the program were also stored on disc file. The deconvolution program was entirely separate, operating on these files at a later time. The resultant data set was an array of size 64 x 64 elements for the simple camera, and 63 x 65 elements for the cyclic case, to ensure perfect coding.

Throughout most of the simulation program the matrix size used was 128 x 128 elements, any smaller matrices such as the mask pattern being padded out with zeros to the required size.

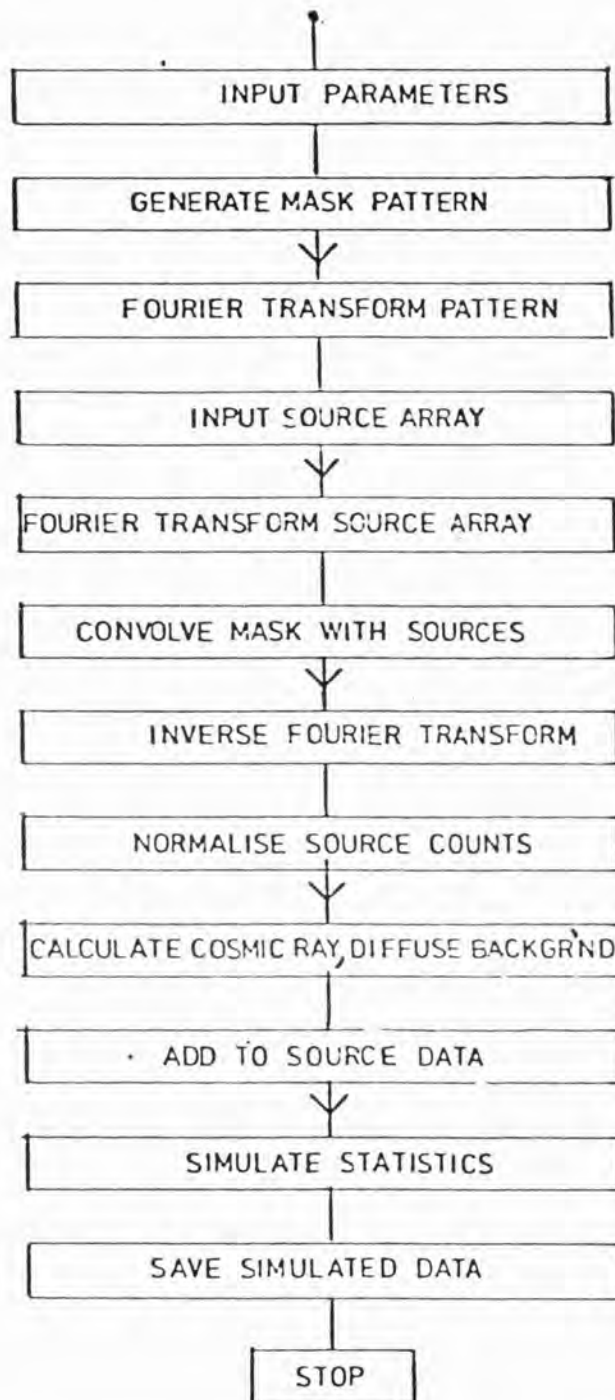


Figure 3.3.2 Flow diagram for the simulation program showing main program elements.

In a true shadow camera, on deconvolution an inverted image results (see Chapter 2, section 2.2); for the simulations no inversion was made, making no correction necessary on deconvolution of the data.

#### 3.3.10. Disturbing Effects

In a real shadow camera various practical effects can disturb the coding principle, and lead to a degradation in the performance of the camera. The four major effects are:

- (i) loss of information due to loss of photons in a detector window support;
- (ii) motion of the shadow camera with respect to the sky;
- (iii) finite detector response, that is non-perfect performance of the detector;
- (iv) energy dependent detector response.

Only the first three were investigated; the last effect will be discussed briefly later in this chapter.

In order to study the three effects additional approximations had to be made, and additional software written. A completely integrated simulation program was available only towards the end of the work described in this chapter.

#### 3.3.11. Disturbing Effects: Detector Window Support

The only major approximations made throughout the simulation work concerned the effect of a detector window support on the performance of a shadow camera.

A detector window support is required for an IPC. Unless the support has the form of a FOV collimator (for the cyclic camera), the effect

of the support will depend on the source distribution. A collimator for a wide field cyclic camera cannot be constructed to limit the FOV and support the detector window at the same time. So even in the case of the cyclic camera some additional form of window support will be required.

Such a support will cast a shadow, the direction and length being different for every given source position in the FOV. Hence a true simulation would calculate each shadow, the data within the shadow and under the support structure (from the source) being lost, and not recorded by the detector. The effect of the support is therefore loss of data.

A quick calculation using the data from Figure 3.3.1 shows that 20 source positions would occupy in convolutions alone ~400 CPU seconds, much more than the time available under the computer system limitations. The following approximation was therefore made giving a 'worst' case effect. The shadow length was made to be the same for each source, and made to occur on all sides of the detector window support structure. The shadow length was taken to be  $\frac{2}{3}$  of its maximum, this corresponding to a source halfway to the edge of the FOV in a planar case. Hence a 'worst' case exists for all sources which would produce a smaller shadow (a 'good' case for all other sources).

The window support loses data in two forms: the area directly under the support receives no data apart from cosmic ray background, and data is lost by shadowing. Using the above approximation the effect can be simulated by multiplying the perfect camera detector recorded distribution (sources only not cosmic ray background) by a transmission function, dependent on the particular design of window support and shadowing conditions.

Mechanical design work on the detector window support has lead to two basic shapes for the support. (This work will be briefly discussed in Chapter 4).



The first structure consists of a set of circular open holes packed in an hexagonal pattern in a plate. Thin supporting bars exist between most of the circular areas and a large area of support occurs at the junction of three. This support has a very good overall transmission. The second structure consists of a set of bars arranged in a square grid.

Two subroutines were written to produce the transmission function of the above supports from a particular set of parameters. For the circular support the parameters are:

R hole radius in cm  
 S hole spacing in cm between centres  
 L full width of detector in cm  
 WT vertical height of window support above detector window.

For the bar support, the following parameters are required:

L as above  
 WT as above  
 S spacing in cm between bars  
 TL thickness of each bar in cm  
 RTHETA rotation angle of bar axes with respect to nominal detector sensing axes.

The transmission function of a support is of course analogue in nature, whereas the program is entirely digital. Hence a further approximation was made at this point. Transmissions of only 1 or 0 were considered, the value of a transmission matrix pixel being 0 or 1 depending on whether the centre of the pixel was either under or not under the window support structure, or in, or not in its shadow.

The shadowing was further approximated by increasing TL or decreasing R by the shadow length, effectively placing the shadow on all

sides of the support, producing the 'worst' case as above.

Several versions of the two structures were investigated in the work, the results of which are presented in section 3.6.1 of this chapter.

### 3.3.12. Disturbing Effects: Camera Motion

As discussed in Chapter 2, section 2.9.2, motion of the shadow camera can occur in three axes, hence investigation of such motions of the camera performance and sensitivity is of importance.

In order to make the simulation of spacecraft motion practicable, the following assumption was made; the motion could consist of pitch and yaw about the centre of the FOV axis, but with zero roll. Roll was not simulated, because of the problem of deconvolution in this case; roll correction can only be achieved by deconvolution of the image for each roll orientation (section 2.9.2), unless the mask is circularly symmetric.

If the pitch and yaw angles are small such that no pixel smearing occurs at the edge of the FOV, motion enables better sampling of the coded image, with a window support, than would be possible with a stationary shadow camera. This is only true if all the photon events are converted back to the original co-ordinate scheme of a stationary shadow camera viewing the FOV that is the starting co-ordinate frame of the observation. Motion then consists simply of a blurring of the window support structure, i.e. a convolution between the window support transmission function and a matrix describing the pointing directions of the camera as a function of time during the observation.

In order to compare zero motion and simulations with camera movement, the motion matrix was normalised so that its area was 1; that is the total observation time was the same. Any movement can be taken into account using this method provided the above approximations are made.

Simulation with camera movement always involved the case of a

shadow camera with window support as this is the real situation encountered in operation of a camera.

Two forms of camera movement were explicitly written into the simulation program, the first was jitter of a gaussian nature, the rms of the jitter being specified in detector pixels, the second was linear motion or slews. The motion matrix for the linear movement consisting of a set of pointing directions specified by pixel positions (pixel 1,1 of the matrix being the initial pointing direction). The relevant observation times at each position were given by the pixel height. For gaussian jitter the matrix consists of a discrete gaussian, the gaussian being approximated to relevant pixel positions and discrete values.

Motion was therefore simulated in the following manner. Firstly the data was created as if for a perfect camera viewing the given FOV. Then the relevant window support and motion matrices were created and convolved to produce the effective transmission function. Multiplication of the perfect data by the effective window transmission function producing the required data, the final step being addition of the statistics.

In order to compare the motion and detector window response simulations with those of the perfect camera, the effective area in the non-perfect simulations was increased to allow for the transmission fraction of the support, so that approximately the same count was recorded as in the perfect camera case.

### 3.3.13. Disturbing Effects: Finite Detector Response

The final disturbing effect taken into account was that of finite detector response. This was only implemented in the case of zero window support to demonstrate the effect on coding alone, not to show the total performance capabilities of a real camera.

The perfect camera simulations assume a detector which does not

blur the image. Any real detector has a finite response function, describing its imaging capabilities as a function of position and angle of incident of the X-rays. The finite response function arises from a combination of detector readout mechanism and detector physics. For this work a gaussian response was assumed, which is a very good approximation in the case of an IPC (see Chapters 4,5 and 6). In addition, zero angular dependence was assumed to further simplify the matter.

In reality, of course, an IPC has an energy; and angular-dependent response, particularly in the case of higher energy photons, where penetration effects in the detector lead to an off-axis dependence, and hence blurring, with energy. This effect was not simulated.

For the case of a uniform detector point response, the recorded data consists solely of the perfect camera data, blurred by the response function, that is a convolution of the data and response function. Hence for this type of simulation the perfect data was convolved with a discrete gaussian representing the finite response, the rms of the gaussian being defined in terms of detector pixels.

#### 3.3.14. Other Points

In the case of finite detector response or with a window support, zero motion, the data set required for the deconvolution is  $64 \times 64$  elements as for a perfect camera. However for the case of motion, areas outside the original co-ordinate scheme are sampled; hence in this case an array of  $128 \times 128$  elements was saved for deconvolution. The stored data, as for all simulations, consisted of a header describing the simulation and matrix size followed by an unformatted list of the matrix elements.

### 3.3.15. A Full Simulation

Due to the computer systems limitations and a lack of time a full simulation of the shadow camera was not possible during this work. However by a series of approximations as detailed above various aspects of the camera were investigated.

A full simulation program would consist of the following. First, the diffuse background contribution to the data consists of a convolution between a constant intensity source field and the mask on a pixel by pixel basis in order that the window support, shadowing, motion and point response effects can be allowed for. Next, the cosmic ray background, consisting of a uniform background spread over the whole detector area must be added. Then, for each source position, a convolution between source and the mask, allowing for window support, motion, and finite response, must take place. Finally statistics must be added.

In addition the simulation should ideally be energy dependent. Hence the simulation must occur for a number of different energy channels, the effective area, response function etc., being altered together. The final data set consists, as in a real shadow camera, of a set of energy, count, tagged photon co-ordinates.

A full simulation, by its nature, is very expensive on both computer time and storage. Fortunately it is not required for investigation of the general properties of the shadow camera, although such a simulation is highly desirable for detailed design work on a particular camera.

### 3.4. Simulation Deconvolution, Display and Analysis

The above section details the simulation procedure adopted for this work. This section will describe the deconvolution of data from the shadow camera, its display, and subsequent analysis.



As mentioned in section 3.2 deconvolution is carried out in the Fourier transform domain in the non-iterative methods for reasons of speed. The practical implementation of the maximum entropy method is discussed in Willingale 1979 and 1981. The basic method of deconvolution uses a filter function as shown in section 3.2. Deconvolution, as simulation, was implemented using the specialist library of subroutines created at Leicester for image processing.

#### 3.4.1. Overall Program Structure

Figure 3.4.1. outlines the basic method of deconvolution and hence the overall program structure. The method applies to a perfect camera, no matter how the data is simulated.

Two deconvolution programs were used, the main program giving cross-correlation or Wiener Filter deconvolution (by choice of an input parameter). A second program was written by Willingale (1979) for maximum entropy method of deconvolution.

#### 3.4.2. Perfect Camera Deconvolution

For the perfect camera, that is, with no disturbing effects as defined here, the mask pattern is the only required parameter for deconvolution.

The diffuse background adds a constant level, introducing a problem in image analysis. This constant level results in a 'triangular' (pyramid) response superimposed on the source distribution on deconvolution. This background level contains no information and was removed by reducing the data to fluctuations around zero before deconvolution. This was accomplished by calculating the average count per pixel and subtracting this value from every data pixel. This removes the background shape but does not



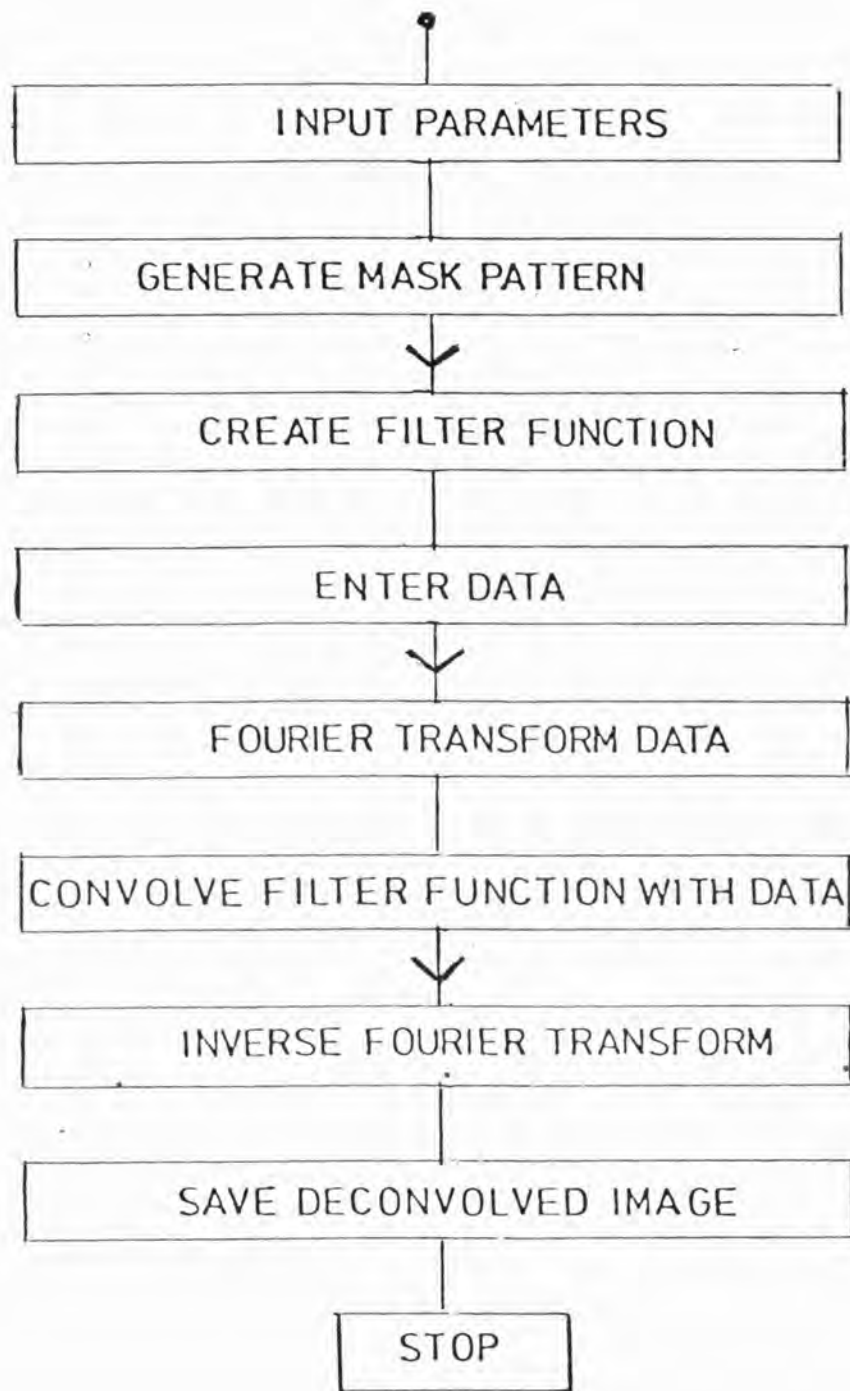


Figure 3.4.1 Flow diagram for the deconvolution program showing main program elements.

remove the fluctuations due to it.

For the Wiener Filter the filter function was constructed using the mask Fourier transform and an estimate of noise to signal in the data by a specialised routine (WFILT). The Wiener Filter was not applied to the cyclic camera because of its 'perfect' coding.

For the cyclic camera simulations the data was aliased into a 128 x 128 element array, producing a four-fold redundant data set. Deconvolution then proceeded with a single mask pattern, enabling the 'perfect' coding to be retained. The final image also had four fold redundancy; hence only a quarter was saved, simulating automatically the poorer angular response of the cyclic system.

To speed up the deconvolution program as in the simulation program, pregenerated mask patterns from computer disc files were used. Ideally one would like to store the DFT of each pattern; however, computer storage limitations prevented this approach from being adopted.

In order for the deconvolution to produce the correct image, one requires to place the data set in an identical position in a 128 x 128 element array as for its removal in the simulation program.

The implementation of deconvolution for the perfect camera is therefore quite straightforward.

### 3.4.3. Deconvolution with Disturbing Effects: (a) Window Support

This section describes the deconvolution of data from the simulation program, when shadowing and loss of information due to the detector window support (zero motion) was simulated. In this case the data produced by the simulation program consists of areas of near zero count (just cosmic ray background) underneath and in the shadow of the support, and areas of counts containing the recorded coded image. One obviously cannot replace the missing data, so the method adopted was to reduce the recorded coded

image to fluctuations around zero.

In the case of the simulations the exact shadow and hence transmission function are easily calculated from the window support parameters. The data was then reduced to fluctuations around zero by the following method.

Firstly the data was multiplied by the transmission function of the support to remove the unwanted cosmic ray counts. The mean count level was then calculated by summing the resultant matrix and dividing by the total transmission of the detector window support.

The mean count was then subtracted from the matrix reducing the data areas to fluctuations around zero, but leaving a large negative offset in the shadowed areas. This was finally removed by multiplying the matrix again by the window support transmission function. The result being fluctuations around zero for the recorded data, and zero where no data was present.

In a real camera, of course, the shadowing of a detector window support will result in a gradual roll-off in accumulated counts towards the actual edge of the support bars or circles as the shadow length is source position dependent. Hence in deconvolution a roll-off function would have to be used, the solid angle viewable from any detector pixel, divided by the total solid angle of the FOV, to weight each pixel correctly.

The deconvolution can then proceed as for the perfect camera. However, because of the loss of information coding errors will occur for the cyclic camera, and will be much worse for the perfect simple camera.

#### 3.4.4. Deconvolution with Disturbing Effects: (b) Motion

For the case of the presence of a detector window support, plus shadow camera motion in the yaw and pitch axes round the view axis, a rather different procedure for deconvolution of the simulations was

followed, the transmission function having a non-integer value at many positions.

The cosmic ray background was first removed by calculating the expected count per pixel and subtracting this from each pixel. From the known motion and the window support parameters, the effective transmission function was calculated by convolution of the motion matrix and window support. The aim, as above, was to reduce all the data to fluctuations around zero.

This was achieved by normalising the area under the effective transmission function to the total count left in the data after cosmic ray background removal and subtracting one matrix from the other. Deconvolution then proceeded as in the perfect camera.

In a practical camera the motion matrix would have to be convolved with the window support roll-off function (transmission function) described above.

In order for the extra information gained outside the initial detector co-ordinate frame to be used the data used in the program consisted of a 128 x 128 element matrix.

#### 3.4.5. Deconvolution with Disturbing Effects:(c) Finite Detector Response

For the simulations with finite detector response two forms of deconvolution were attempted. Firstly the simulated data was deconvolved as with the perfect camera. Secondly, as an attempt to improve the appearance of the image, the data was deconvolved using the mask convolved with the detector response function.

#### 3.4.6. Deconvolution with Disturbing Effects: The Wiener Filter

The above descriptions of deconvolution of a shadow camera with

some disturbing effects apply only to the case of cross-correlation for both simple and cyclic simulations.

Wiener Filter deconvolution was only performed for the simulations of the perfect camera, and simulations with the presence of a detector support structure. It was found necessary in the latter case to increase the estimate used for noise to signal ratio in the data. This was accomplished by multiplying the theoretical value by the reciprocal of the window support transmission. This decision was taken in order to attempt to allow for the decrease in detector pixels, exposed to the sky, in this case the Wiener Filter, then produced near identical results to the perfect camera, whereas without the term the filter's performance was degraded to worse than the result of cross-correlation. Results to prove the case will be presented in section 3.6 of this chapter.

#### 3.4.7. Deconvolution: Analysis and Display of the Image

To analyse the resultant images from the deconvolution program, an analysis program was written, which analysed each image in two separate sections. Firstly, the image pixel height distribution was determined by using a crude pulse height analysis routine. The program required as input parameters both a sample size and minimum rms fluctuation criterion for detection of a source. The sample size was chosen such that a 'tidy' sorted distribution resulted, the correct sample size was found by experience. For many of the deconvolved images a variety of sample sizes were used. It was found that the results were a very poor function, in fact almost independent, of the sample size chosen.

The upper tail of the pixel height distribution, hopefully mainly sources, was then determined by finding the first positive bin in the sorted distribution containing zero pixels.

A global mean and rms was then calculated for all pixels excluding those in the upper tail. From the global rms the pixels were then sorted



and 'sources' greater than the given rms fluctuation criterion listed. The pixel co-ordinates of each source were recorded into a data array.

The second part of the analysis program investigated the image for local variation of mean and rms values. Each deconvolved image was divided into 64 (8 x 8) equal areas, a local mean and rms was then calculated for each area ignoring the obvious sources found in the first analysis. The number of sources greater than the source criterion (on the local value of rms) were then listed. The rms ( $\sigma$ ) and mean as a function of position were then listed in table form. Finally a plot was produced showing the obvious sources from the global analysis, by plotting their respective number of  $\sigma$  at the relevant point in the image.

For detailed display of an image a plot was produced on a graph plotter peripheral, using the plotting library GHOST on the University computer. The output consists of a plot line by line across the rows of pixels, each pixel value joined by a straight line. Each line of the image is displaced vertically on the resultant plot. The software for this display was written by Willingale (1979).

### 3.5. Simulation Results I: The Perfect Camera

In order to ascertain the value of the simulations, in addition to those presented in this section and the next, simulations were carried out with the addition of random sources, changes of source fluxes, different statistical samples of the same observations, and slightly different camera pointing directions. This work, of which one illustration will be presented later, demonstrated that the results presented are not biased by any of these effects, and hence may be regarded as representative of the average simulated performance of the shadow camera.

This section describes some of the results obtained with simulation of the perfect shadow camera. That is, as defined here, a shadow camera, cyclic or simple, with no disturbing effects, such as detector



window support, camera motion, or finite detector response included in the simulation. As mentioned above most work was done using three real areas of X-ray sky, the Galactic centre, the Scorpius region (field of view not including Sco X-1) and the Coma region giving the three main types of the fields of view of a practical shadow camera.

### 3.5.1. Comparison of Deconvolution Methods

The results of the sky areas include deconvolution using all three main methods, viz cross-correlation, Wiener Filter, and Maximum Entropy Method (MEM).

First the results of simulations on the Galactic centre and Coma region will be discussed. These regions represent the two viewing extremes in the practical use of the shadow camera. For the Galactic centre region, a near totally source-dominated field of view, an integration time of 100 seconds was chosen, a typical flight observation time. For the Coma region, a near totally background dominated field of view, an integration time of 5000 seconds was chosen. Both observation times were chosen to be of the right order of magnitude for study of temporal variation in each field of view, ~100 seconds giving temporal information on intensities of relatively weak sources in the Galactic centre and ~5000 seconds providing sufficient sensitivity in the Coma region for study of the brightness of active galaxies, NGC 4151 being in the chosen FOV.

The shadow camera parameters used in the simulations were as the instrument proposed for Spacelab, Chapter 2, section 2.10. Table 3.5.1 summarises the shadow camera characteristics.

The mask patterns chosen were an 'ideal' mask based on a 63 x 65 pseudo-noise sequence, and the Fresnel zone plate of 8 rings, as discussed above.

The simulations performed are detailed in Table 3.5.2.

TABLE 3.5.1  
SHADOW CAMERA CHARACTERISTICS

(a) Simple mask camera

Field of view (FW Zero Response)	45° x 45°
Mask Area	30 cm x 30 cm
Mask-Detector Separation	75.5 cm
Number of Mask Elements	512 x 512
Angular Resolution (set by mask)	2.8 arc min.

(b) Cyclic mask camera

Field of view of collimator (FW Zero Response)	45° x 45°
Mask Area	60 cm x 60 cm
Mask-Detector Separation	36.2 cm
Number of Mask Elements	4 identical patterns each 511x 513
Angular Resolution (set by mask)	5.6 arc min.

(c) Detector (common to both (a) and (b))

Window Size	30 cm x 30 cm
Window Material	Beryllium (125 micron)
Gas	Xenon at 2 atm. pressure
Spatial Resolution	0.6 mm FWHM
Effective Area	380 cm <sup>2</sup>

Note: Mask Size Simulated 64 x 64 elements

TABLE 3.5.2  
COMPARISON OF DECONVOLUTION METHODS, SIMPLE AND CYCLIC CAMERAS

Simula- tion number	Instrument type	Source field	Integration time secs	Detector particle back- ground count	Sky back- ground count	Deconvolution method	Theoretical rms on axis in cross- correlation	rms of pixels excluding obvious sources	Significance of largest false peak, or $\geq 5$ rms peaks	No. of sources $\geq 5$ rms	No. of sources > largest false peak	Significance of a typical source ( $N$ rms)
(1)	(2)	(3)	(4)	(5)	(6)	(7)	(8)	(9)	(10)	(11)	(12)	(13)
1	Fresnel mask with 8 rings	Galactic centre Centre RA 270.00 DEC -30.00 All sources $\geq 10$ mCrab (2-18 keV)	100	380	19000	Cross-correlation Wiener filter MEM ( $\chi^2 = 4.19$ )	393	660	4.62 3.82 33.0 13.3 12.4	8 9 14	8 12 10	6.17 6.32 252.4
2	Simple PN mask	Galactic centre	100	380	25550	cross-correlation Wiener filter MEM ( $\chi^2 = 3.44$ )	435	638 544 3.13	4.09 4.71 18.3 8.52	10 11 14	11 11 12	9.46 8.36 306.0
3	Cyclic PN mask	Galactic centre	100	380	25550	cross-correlation	435	406	6.00 3.86	12	14	10.95
4	Simple PN mask	Coma region Centre RA 190.0 DEC +40.0 All sources	5000	19000	1277500	cross-correlation Wiener filter MEM ( $\chi^2 = 1.16$ )	1163	643 452 71.7	5.00 5.14 3.28	2 2 2	2 2 2	30.7 28.0 7.26
5	Cyclic PN mask	Coma region	5000	19000	1277500	cross-correlation	1163	1117	3.32	2	2	17.7
6	Simple PN mask	Coma region without counting statistics	5000	19000	1277500	cross-correlation	1163	295	5.59	3	3	65.4

Columns 1 - 7 describe the simulation and deconvolution method. Column 8 shows the theoretical standard deviation of the count in a pixel, the sensitivity formula of Chapter 2 being used. Column 9 shows the standard deviation calculated from the simulation using the pulse height analysis (PHA) program (global estimate only). For the MEM the same calculation has been used, although fluctuations from pixel to pixel are not Gaussian and are heavily correlated so that the rms value does not have the normal interpretation. Column 10 gives the significance of the largest false peak, assuming a Gaussian distribution, as the number of standard deviations. In the case of the MEM, where the 'rms' is small the significance of all peaks greater than 5 times the rms value is given, while column 12 gives the number of real sources with peaks greater than the largest false peak. Column 13 gives the significance of the same typical source as determined by the three methods of deconvolution. Figures 3.5.1, 3.5.2, 3.5.3, 3.5.4, 3.5.5 are pictorial representations of the deconvolved images described in the table.

Figures 3.5.6 and 3.5.7 show slightly different pointing directions for the Galactic centre (PN mask) showing the results presented are typical.

The Fresnel zone plate serves as an example of a pattern with imperfect response function, while the pseudo-noise (PN) sequence mask has perfect response in the cyclic case. Coding errors will of course occur for the simple mask.

Comparing columns 8 and 9 shows that the predictions of the sensitivity formula of Chapter 2 are correct for the cyclic PN mask while the coding error in the simple camera (PN mask) causes ghosts giving a larger than theoretical rms and a lower global sensitivity in the source-dominated Galactic centre region.

The simulations of the diffuse background-dominated Coma region (Figure 3.5.5) highlight an effect, previously neglected in the literature, which can make the simple mask more sensitive than the cyclic mask camera,

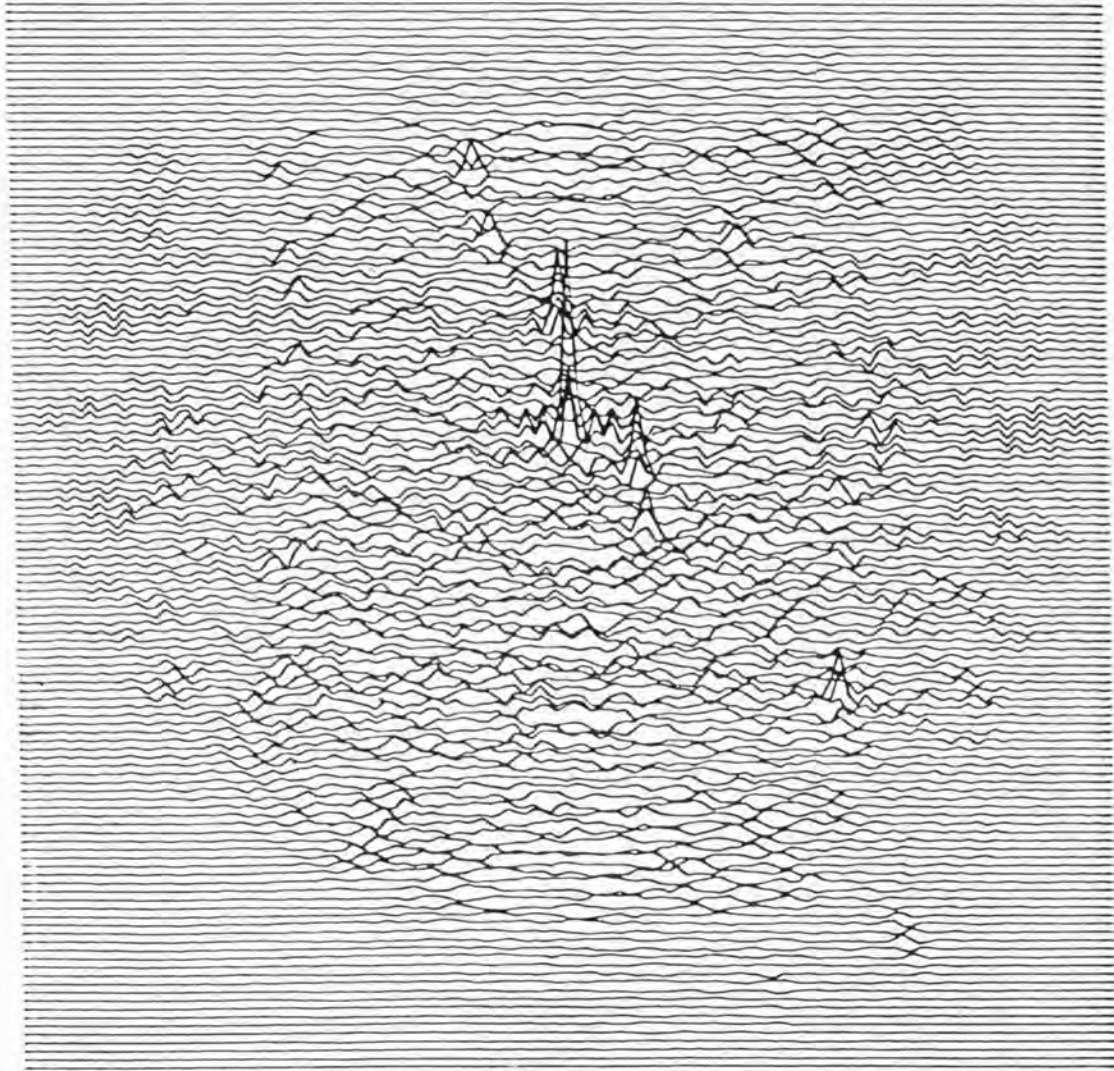


Figure 3.5.1 A simulated 100-second observation of the Galactic Centre obtained with a Fresnel mask pattern (simulation 1 table 3.5.2) deconvolved using cross-correlation (perfect simple camera).



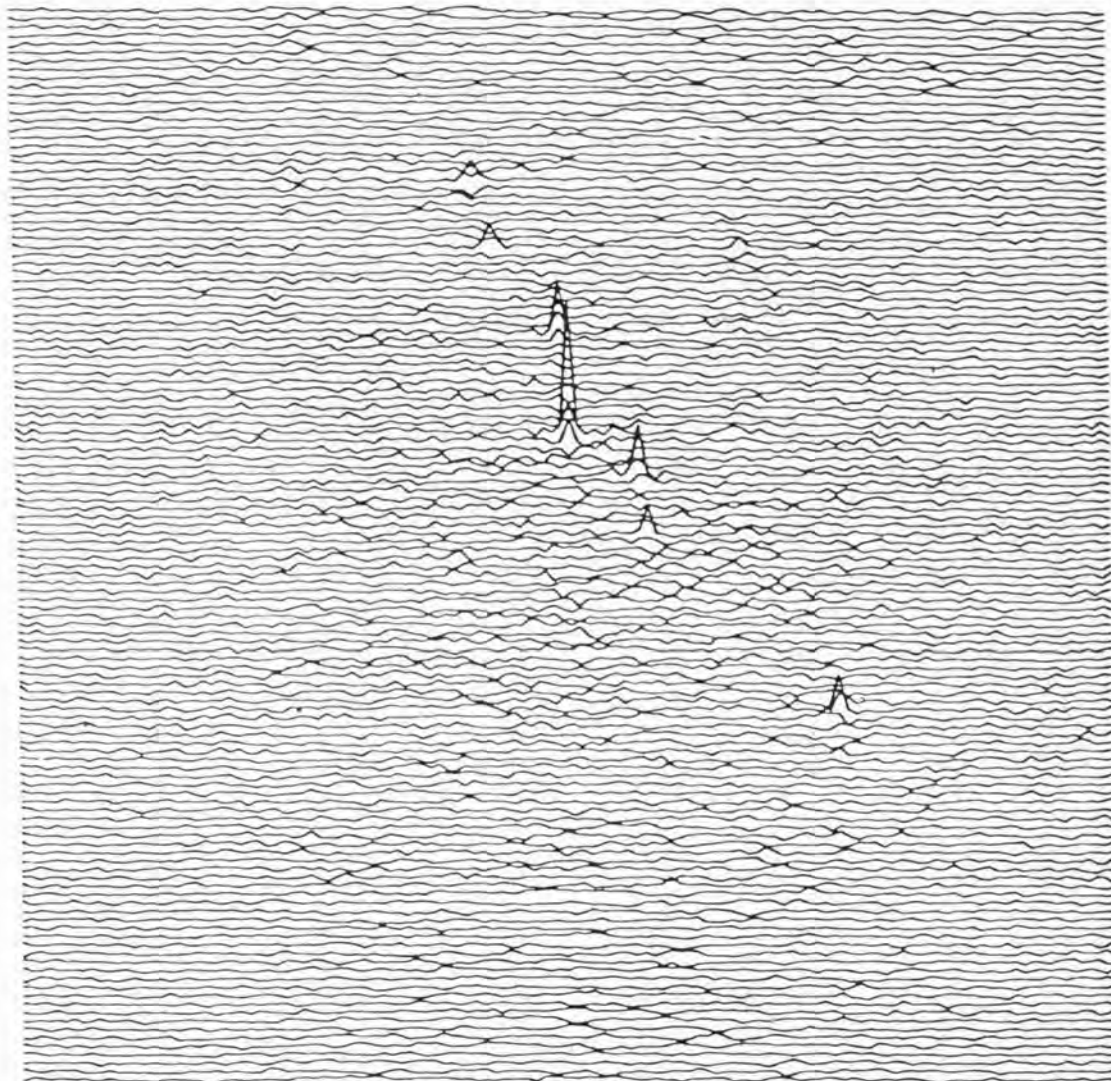


Figure 3.5.2 Simulation 1 deconvolved using the Wiener Filter, showing improved signal to noise, compared to Figure 3.5.1.



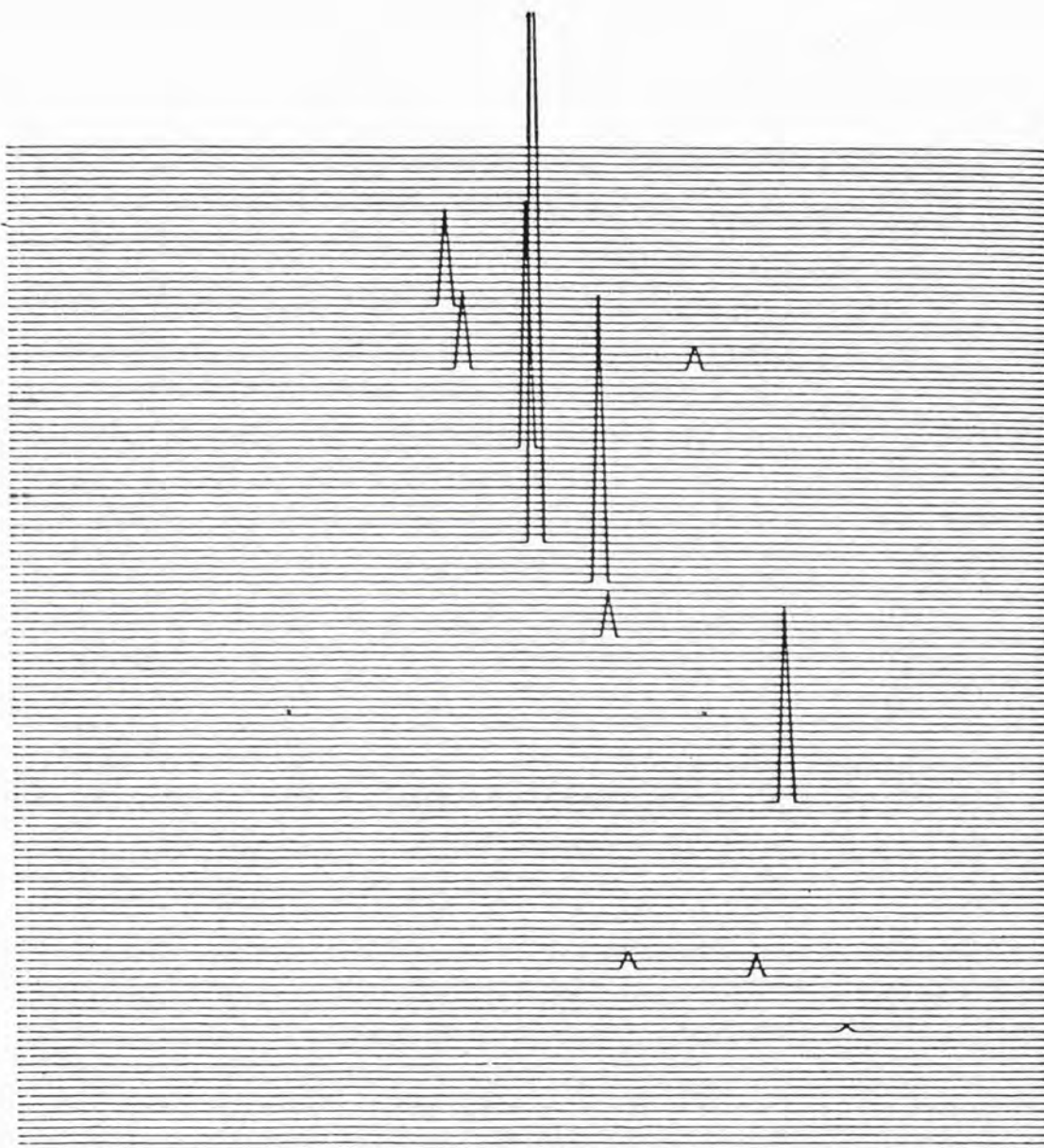


Figure 3.5.3 A simulated 100-second observation of the Galactic Centre obtained with a PN mask (simulation 2) deconvolved using MEM (perfect simple camera). Some significant real peaks are too small to be seen on this scale.

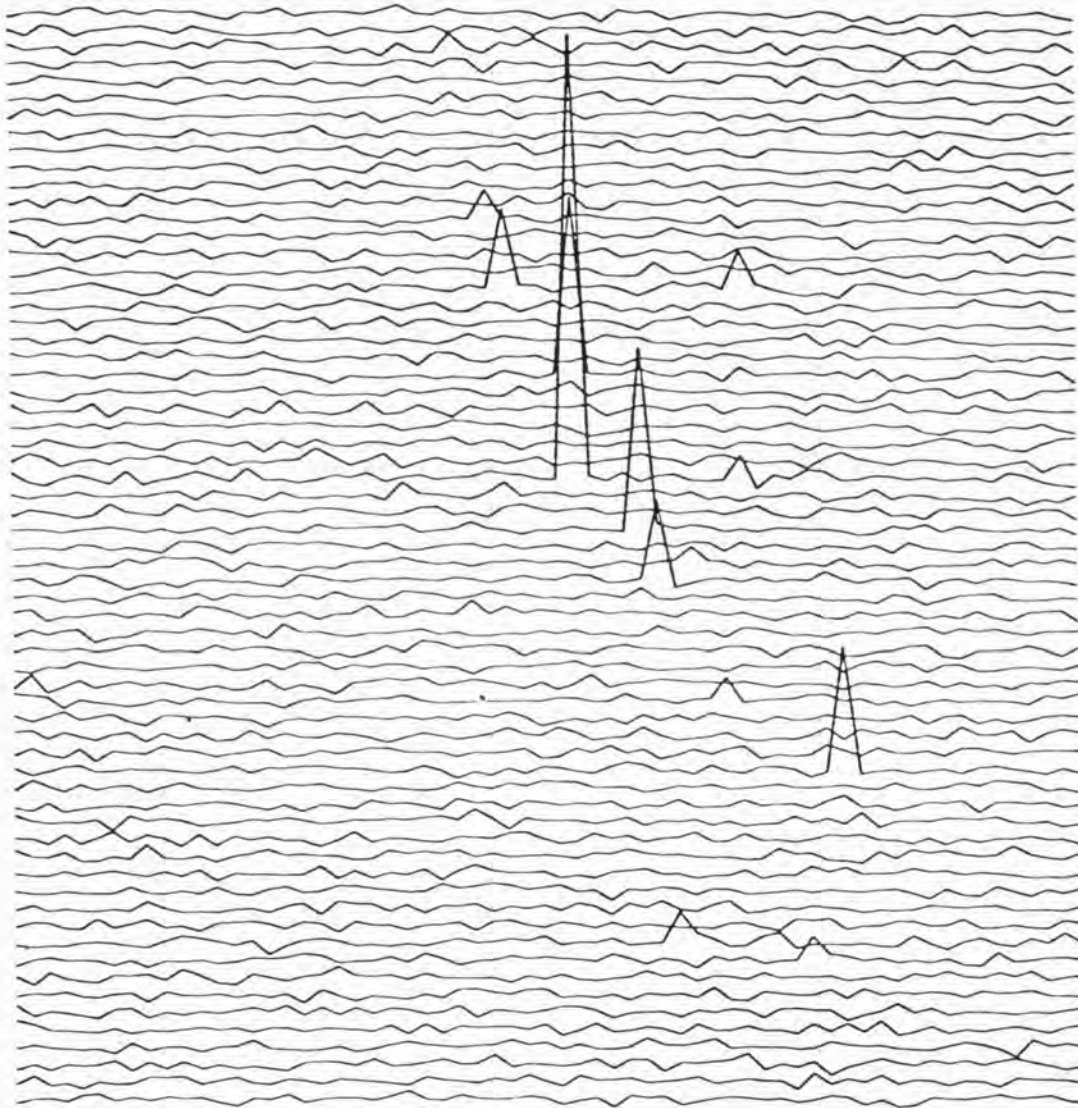


Figure 3.5.4 A simulated 100-second observation of the Galactic Centre obtained with a cyclic PN mask (perfect camera, simulation 3) deconvolved by cross-correlation. The sensitivity is somewhat greater than that of simple PN mask, but the angular resolution is degraded.

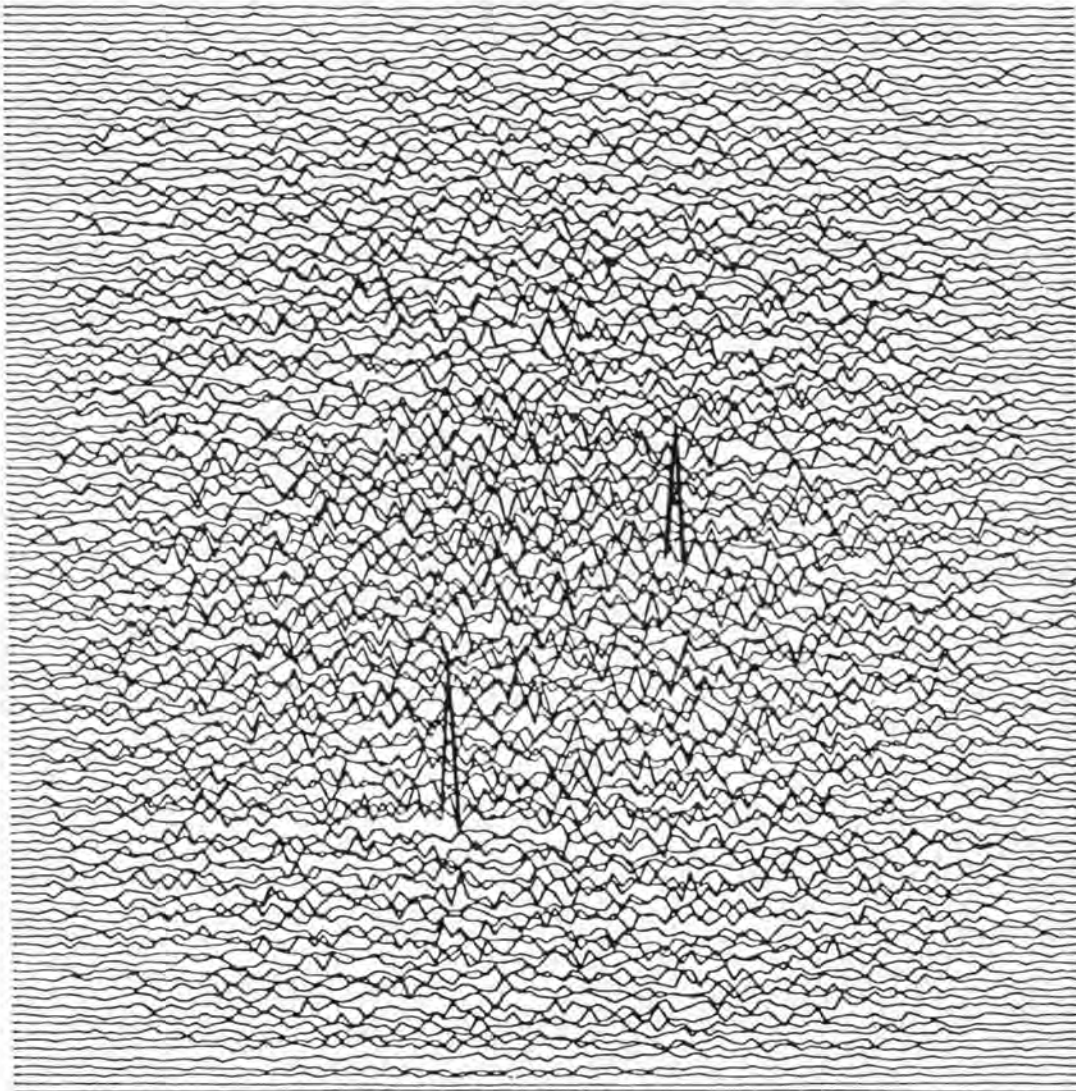


Figure 3.5.5 A simulated 5000-second observation of the Coma region (simulation 4) deconvolved by cross-correlation (perfect simple camera). This figure shows the reduced background fluctuations near the edge of the field of view.

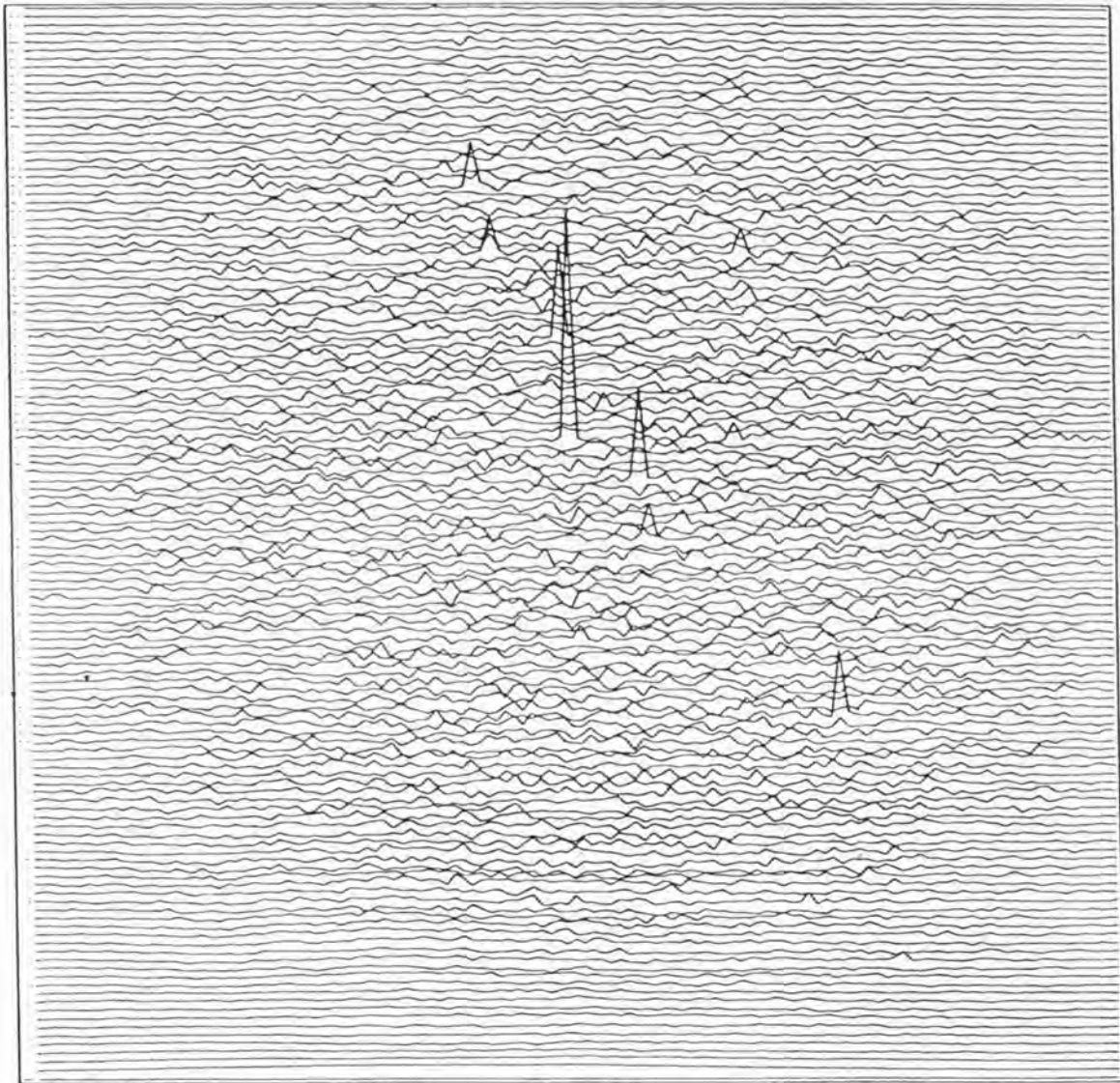


Figure 3.5.6 A simulated 100-second observation of the Galactic Centre (perfect simple camera) with PN mask with slightly different pointing direction compared to simulation 2.



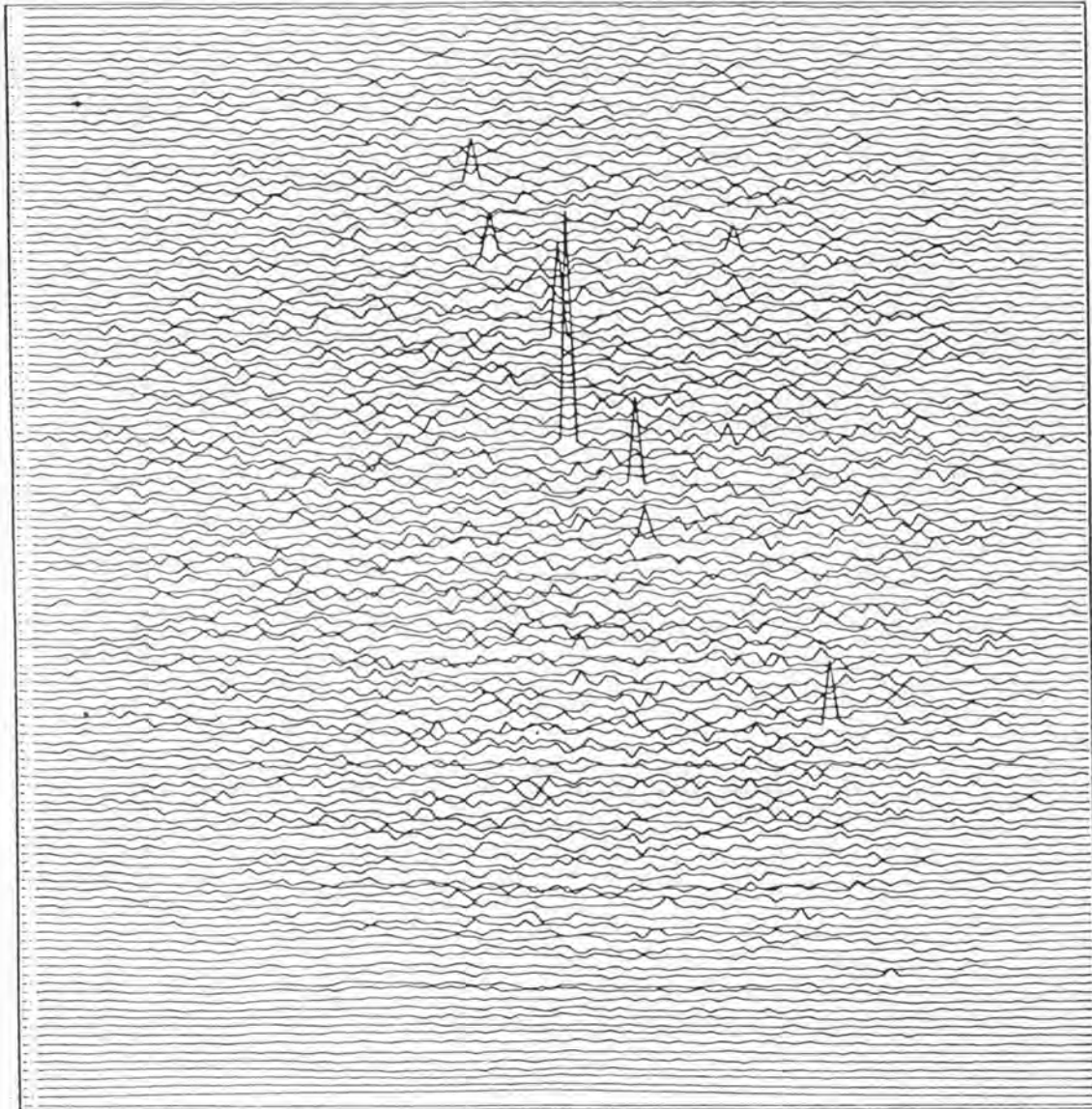


Figure 3.5.7 A simulated 100-second observation of the Galactic Centre (perfect simple camera) with PN mask with slightly different pointing direction compared to simulation 2 and Figure 3.5.6 showing results are typical and not biased by camera pointing direction (amongst other effects, see section 3.5).

more than cancelling the effect of the coding error. The total recorded count from a source is the same for both simple and cyclic masks, since the effect of the additional collimator in the cyclic mask camera is identical to that produced by the mask alone in the simple mask camera. However this signal is spread over the whole image in the cyclic mask camera, while, in the case of the simple mask, the signal from an off-axis source is only spread over a fraction of the image. On deconvolution the total background appears at every point in the decoded image for the cyclic mask, while a reduced fraction of the background appears for off-axis points in the simple mask case, falling to zero at the edge of the FOV. Specifically the rms fluctuations across the image are constant for the cyclic case, but vary and fall to zero at the edge of the field of view for the simple camera.

A detailed analysis of this effect including investigation of the variation in rms is presented in section 3.5.4 of this chapter. This improvement in signal to noise for off-axis sources is substantial as shown in simulations 4 and 5.

Each simulated observation (simple camera) was deconvolved using the three methods. The capability of the Wiener Filter and MEM of reducing effects of an imperfect mask pattern is clearly shown in simulation 1 and figures 3.5.1, 3.5.2 and 3.5.3 where the signal-to-noise is substantially improved over that found with cross-correlation. The small improvement in recovering the coding error is shown by comparing 2 and 3. The use of the Wiener Filter is clearly indicated for imperfect masks, and since it uses no more time than cross-correlation (using the FFT algorithm) its use to recover some of the coding error may be appropriate for perfect masks used in the simple configuration. For a perfect mask used in the cyclic configuration there is clearly no advantage over cross-correlation.

Columns 11 and 12 of Table 3.5.2 clearly demonstrate that the MEM is superior in all cases in that it recovers more sources from the



data. This is particularly evident in the Galactic centre simulations with the simple mask where it largely removes the effect of the coding error. The anomalously large rms for the Coma region (MEM) is due to the large variation in background over the FOV, rather than fluctuations. Willingale 1979 takes this effect into account, reducing the rms to 30.

The basic improvement in coding even in the simple case between the Fresnel zone plate and the PN mask can be seen even in cross-correlation by comparing columns 9, 10, 11 and 12.

### 3.5.2. The Self-Supporting Mask

The self-supporting mask performance is compared in this section, with the PN mask used throughout most of the work, a direct comparison being made for all simulated regions of the X-ray sky. The results of the simulations are summarised in Table 3.5.3.

Only the simple camera was simulated as the self-supporting mask (Giles 1980) is a 'perfect' mask hence will perform as well as the PN mask in the cyclic case. As can be seen in Table 3.5.3 the self-supporting mask performs very adequately in the case of a background limited situation, Coma, but produces a significantly larger rms in the case of Sco and the Galactic centre where source confusion ('coding' problems) plays a bigger and bigger role. The Wiener Filter can however reduce the global rms to a near identical value to the ordinary PN mask. The significance of typical sources is also down in each case compared to the original PN mask.

This is entirely due to the nature of the self-supporting mask. The self-supporting mask tried consisted of triangular patterned holes, (see Figure 3.5.14). In the cyclic case this of course does not matter. However, in the simple case for off-axis sources there is a ghosting problem due to the very similar shapes existing across the mask, as cross-

TABLE 3.5.3.

## COMPARISON OF PN MASK AND SELF-SUPPORTING PN MASK

Simulation	Integration Time	Type	Deconvolution Method	Theoretical RMS on axis	RMS of pixels excluding obvious sources	Significance of largest false peak	No. of sources > 5 rms	No. of sources > largest false peak	Significance typical source
Galactic Centre	100 seconds	Ordinary	Cross-correlation	435	638	4.09	10	11	9.46
		PN Mask	Wiener Filter		544	4.71	11	11	8.36
		Self-supporting	Cross-correlation	437	787	4.42	8	9	5.19
			Wiener Filter		515	4.35	10	12	6.18
Scorpius Region	200 seconds	Ordinary	Cross-correlation	324	394	5.20	7	7	13.93
		PN Mask	Wiener Filter		371	5.15	6	6	10.65
		Self-supporting	Cross-correlation	319	563	5.48	6	5	7.85
			Wiener Filter		345	4.86	6	6	9.92
Coma Region	5000 seconds	Ordinary	Cross-correlation	1163	643	5.00	2	2	30.7
		PN Mask	Wiener Filter		452	5.14	2	2	28.0
		Self-supporting	Cross-correlation	1163	643	5.48	2	2	27.95
			Wiener Filter		437	5.60	2	2	27.30

correlation is basically a pattern matching process.

When the Wiener Filter is used, the mask shows comparable performance with the ordinary PN mask, and has the fundamental practical advantage of being mechanically self-supporting unlike the ordinary PN mask.

### 3.5.3. Demonstration of Undersampling

In order to demonstrate the undersampling limitation of the simulations, some source splitting was done for the Scorpius region; that is the placing of sources between sky pixels and splitting the flux. Two sources were split into various combinations and fluxes. The results from these simulations are summarised in Table 3.5.4.

As can be seen in the table the effect of splitting the sources has a small effect on the global rms value, as the overall coding error for the simple camera is dependent on the exact source distribution. The Wiener Filter as in all previous simulations recovers a large part of the coding error. As can be seen the expected ratio of the split is retained through the simulation. However the total S/N of the split source on addition (where  $\Sigma S/N = \sqrt{\Sigma \sigma^2}$ ) is approximately a factor of 2 down on the unsplit source. Consider the two-way split; respective  $\sigma$ 's for the two points are 7.02 and 7.43 in the case of cross-correlation. Hence, total S/N in terms of  $\sigma$  for the split source is 10.22, compared to 13.93 unsplit.

As mentioned in section 3.3.2 the detector array is in fact undersampled for the case of analogue source positions, that is sources effectively between sky pixels. So when we split a source, as in the above simulations we actually see 4 times the background count we should see, as we undersample by a factor of 2 in each direction. Hence the total S/N of the combined pixels is down by a factor of 2 on what it should be. What we are doing in terms of a real camera is effectively

DEMONSTRATION OF UNDERSAMPLING: SOURCE SPLITTING

[illegible]

placing sources next door to one another.

For a properly sampled detector one does not lose this S/N factor; however the source location is given by the sharing of counts between adjacent deconvolved pixels as in the above simulations. This set of results is included to show one of the limitations of the simulations adopted. The simulation is however accurate for the discrete source position case, which is used throughout the rest of the work.

#### 3.5.4. Off-axis Variation in Image RMS

As discussed in section 3.5.1, after the presentation of Table 3.5.1 the rms ( $\sigma$ ) in the case of the simple camera appears to vary across the deconvolved image, but not in the case of the cyclic system. This off-axis  $\sigma$  variation was examined by use of the subdivided PHA built into the deconvolved image analysis program. The results of this analysis in the case of the perfect camera are presented in this section.

Firstly simulations of each region of the sky were produced for the normal PN mask (simple camera case) and subjected to the block by block analysis. Each block in this case being 16 x 16 pixels in the deconvolved image. From the resultant matrix of rms ( $\sigma$ ) fluctuations versus block position, the average  $\sigma$  value along the four diagonals was calculated to average out any local effects due to coding errors in the simple camera configuration. It must be noted that the variation is across pixel diagonals and not along or across the pixel co-ordinates, that is the fundamental 'step' length is different and hence the variation is different compared to that along or across the pixels.

The resultant  $\sigma$  variation is plotted as a function of distance from the centre of the deconvolved image (along the diagonal) for cross-correlation deconvolution (for the three sky regions) in Figure 3.5.8.

As can be seen the local  $\sigma$  varies considerably over the image

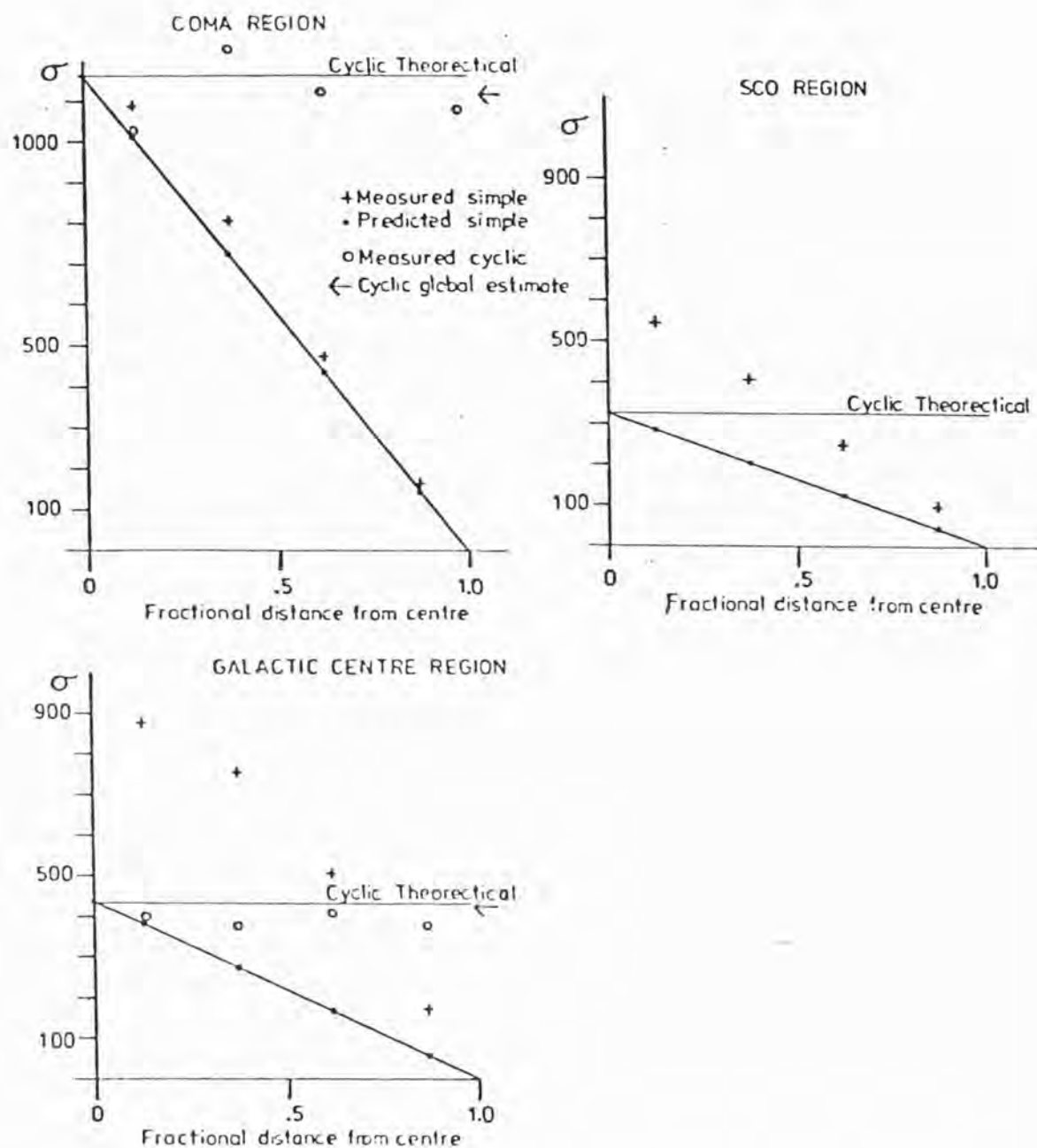


Figure 3.5.8  $\sigma$  as a function of fractional distance along diagonal for each region of the X-ray sky, simulated (perfect camera cross-correlation deconvolution). Cyclic camera results are presented for Coma and Galactic Centre regions. Predicted and theoretical performance are shown for both simple and cyclic systems.



and even in the Galactic centre falls to zero at the edge of the FOV.

For comparison the theoretical performance of a cyclic camera is shown in each case the expected  $\sigma$  variation being constant. As confirmation of this, results of cyclic camera simulations using the PN mask for the Coma region and Galactic centre are also shown in Figure 3.5.8. In the cyclic camera case the blocks analysed consist of  $8 \times 8$  pixels due to the poorer angular resolution. As can be seen the cyclic camera does produce a flat  $\sigma$  distribution unlike the simple case.

As mentioned previously the simple camera  $\sigma$  variation is due to the off-axis fall-off in background (that is total count as far as the deconvolved image is concerned). Hence assuming this, the resultant predicted  $\sigma$  variation for the simple camera is shown as well in Figure 3.5.8.

The displacement of the measured  $\sigma$  vs predicted  $\sigma$  must be due to coding errors in the simple camera, the resulting displacement being largest in the Galactic centre, a source, hence coding error, dominated region, and being least in the Coma region, a background dominated region. It is interesting to note that the local  $\sigma$  for the simple camera is, in all sky regions, at some point considerably lower than the theoretical (and practical) cyclic case. Hence an approximate sensitivity advantage of the simple camera versus the cyclic camera can be calculated for each simulated region of X-ray sky.

Figure 3.5.9 shows the advantage in terms of  $\sigma$  over the cyclic theoretical case, as a function of fractional distance along the diagonal from the centre of the FOV for all three regions.

The overall sensitivity advantage is given by

$$\frac{\int_0^1 A f d d f d}{\int_0^1 f d d f d} \quad (3.5.1)$$

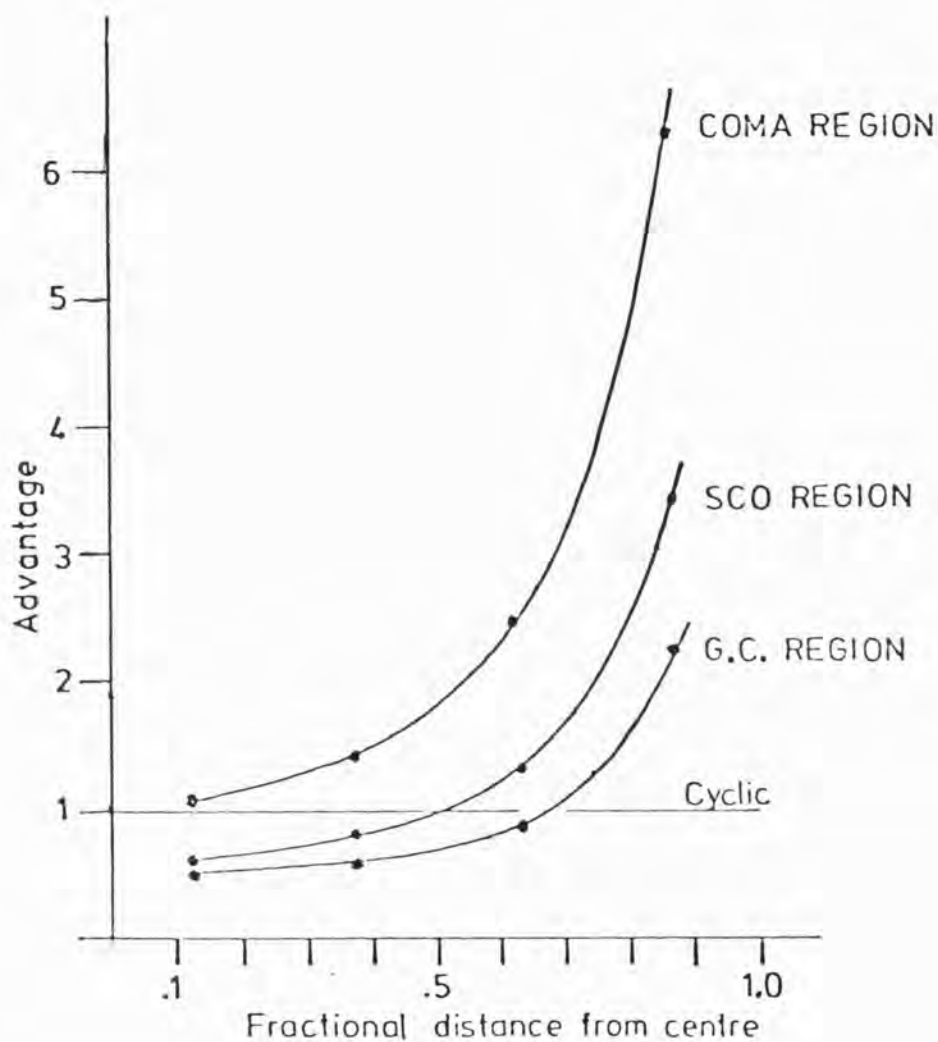


Figure 3.5.9 Sensitivity advantage of simple (perfect) camera over theoretical performance of cyclic camera as a function of fractional distance along the diagonal from the centre of the FOV for all three regions of simulated X-ray sky.

where  $A$  is the advantage (that is simple  $\sigma$  divided by theoretical cyclic) and  $fd$  is the fractional distance from the centre. The advantage must be weighted as a function of  $fd$  due to the "area" viewed as a function of fractional distance.

This of course assumes circular symmetry by making  $A$  only a function of  $fd$  (the diagonal distance). This approximation is made for both the simple and cyclic cases.

Hence integrating equation 3.5.1 graphically, one obtains the following.

The sensitivity advantage to a random event of the simple camera over the cyclic camera is:

1.56 for the Galactic centre region

2.13 for the Scorpius region

4.52 for the Coma region.

The calculated source to background ratios, from the expected total background, and total count of the simulation are as follows:

Galactic centre 6.4

Scorpius region .5

Coma region .035

Hence even in the Galactic centre region the simple camera is more sensitive on an average basis to a random event. This is because, although the actual  $\sigma$  does not drop below the theoretical cyclic case until approximately  $\frac{2}{3}$  of the distance from the centre, the large solid angle viewed at this distance more than makes up for this.

In the background dominated Coma region the advantage for the perfect simple camera is greater than a factor of 4 .

In order to demonstrate this advantage the following test was made. A source which would be  $6\sigma$  on-axis for the theoretical case was placed

towards the edge of the FOV (pixel co-ordinates 10,64) for all regions of the X-ray sky, appropriate scaling being made for source strengths to allow for the collimation effect of the mask and detector.

Figures 3.5.10 and 3.5.11 show the Coma region deconvolved by the cross-correlation method with and without the extra source.

The global estimate for the rms excluding obvious sources was

Coma without extra source	643.25
with extra source	652.69 .

The extra source appearing globally at  $10.01\sigma$  on deconvolution, showing already the improved sensitivity. In terms of the  $16 \times 16$  pixel block analysis the source was in fact  $13.89\sigma$  above local background. Whereas for the theoretical cyclic case it would only have been  $\sim 6\sigma$ ; hence the sensitivity advantage is real for the Coma region.

In the Scorpius region the source was not visible in the global analysis; however it was at  $5.43\sigma$  in the block analysis, showing comparable sensitivity with the cyclic case.

In the Galactic centre region it was found that the source was only visible  $\sim 5\sigma$  in certain positions around the edge of the FOV. Coding errors resulting in large local fluctuations enabling a source to fall into a 'hole' in the deconvolved image.

One can of course ask "What happens in the case of the Wiener Filter?" . Figure 3.5.12 shows the local variation in  $\sigma$  compared with the theoretical cyclic case for all three regions of sky with the Wiener Filter as the deconvolution method for the simple camera.

The sensitivity advantage on integration becomes;

Galactic centre	1.152
Scorpius region	1.397
Coma region	4.003 .

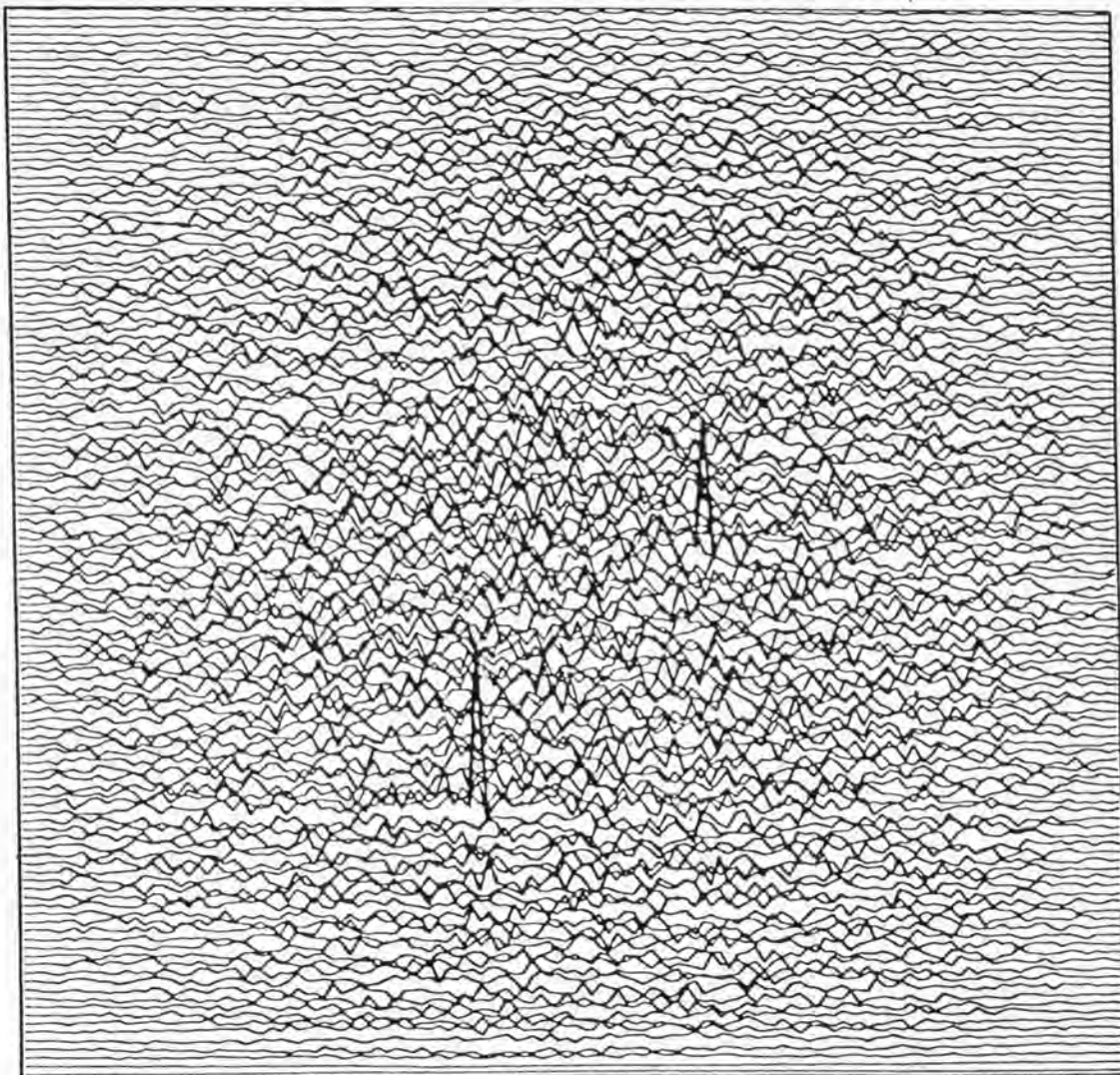


Figure 3.5.10 Simulated 5000-second observation of Coma region with simple PN mask (perfect camera, cross-correlation deconvolution).



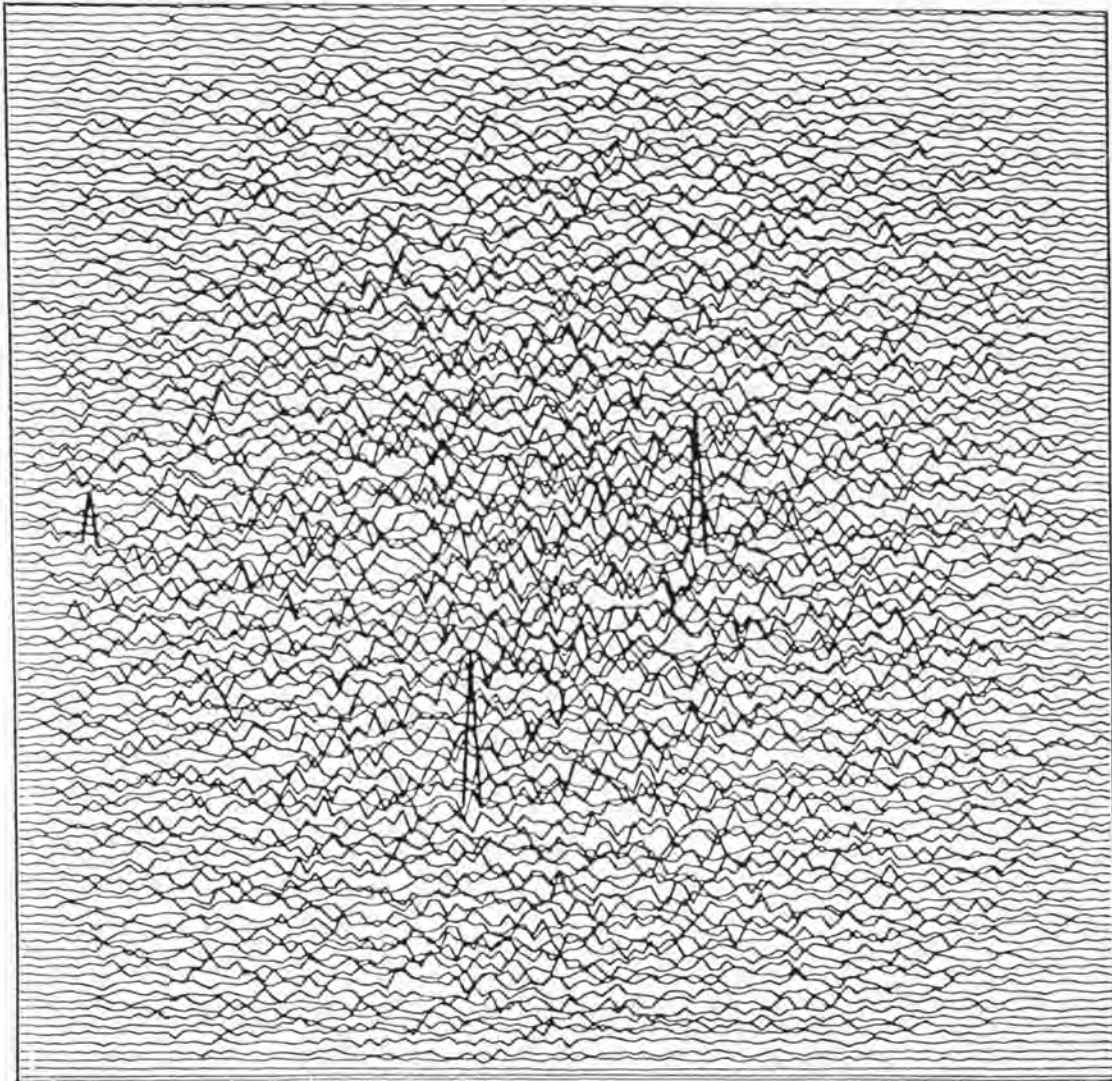


Figure 3.5.11 Simulated 5000-second observation of Coma region with simple PN mask and extra source towards edge of FOV (perfect camera, cross-correlation deconvolution).



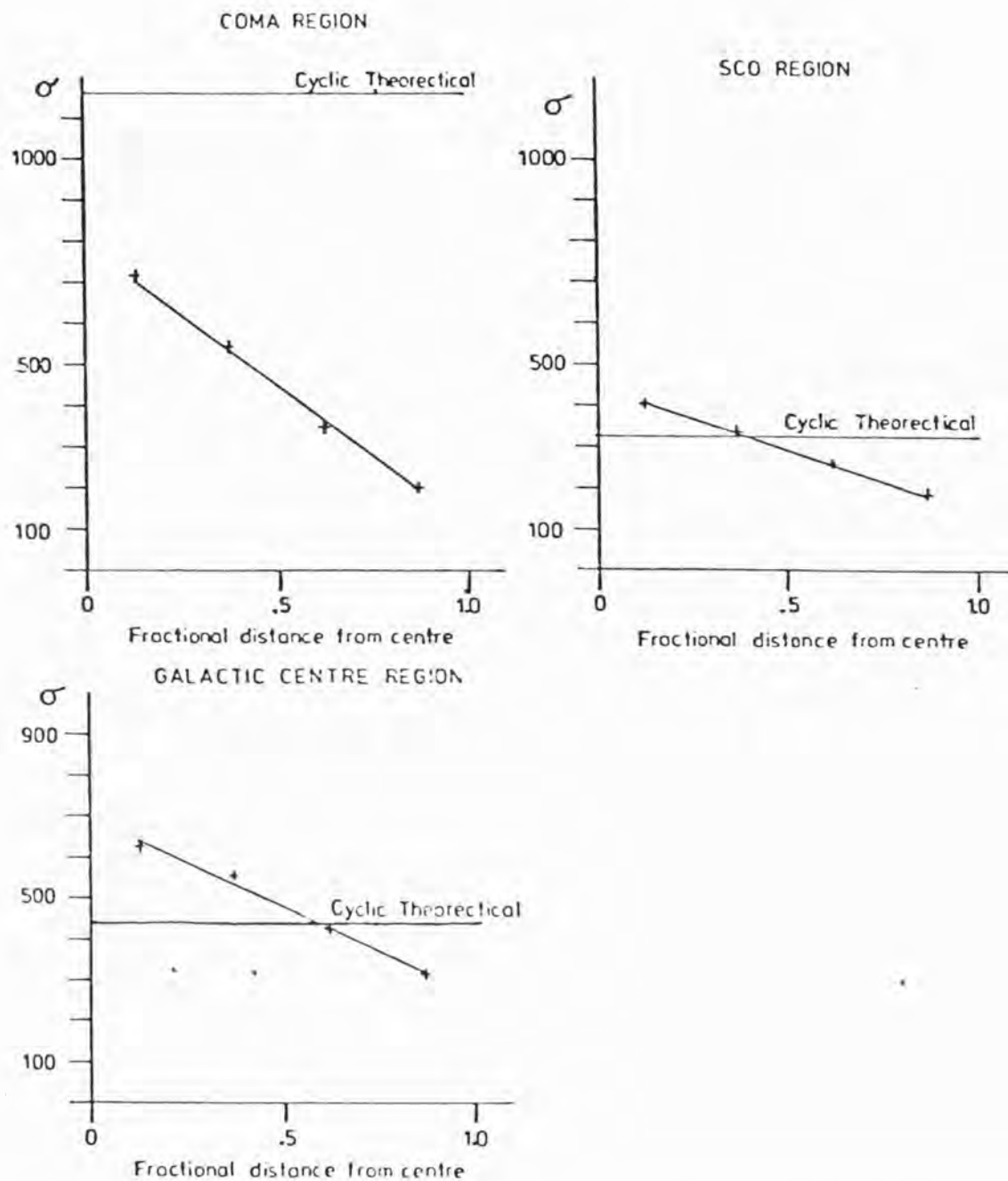


Figure 3.5.12  $\sigma$  as a function of fractional distance along the diagonal for each region of the X-ray sky simulated, for the case of Wiener Filter deconvolution, predicted theoretical cyclic camera is also shown.

This is because although the Wiener Filter reduces the global rms, it also flattens out (or tries to) the variation in  $\sigma$  across the image, as can be seen in Figure 3.5.12.

Table 3.5.5 shows the local  $\sigma$  as a function of block analysis for the Coma region for both the cyclic and simple camera configuration as a final confirmation of the variation of  $\sigma$  across the image. This is for the case of cross-correlation deconvolution,

As is evident from the table, the cyclic camera exhibits a flat  $\sigma$  distribution while the simple camera shows the fall-off effect of approximately triangular response shape like a collimator. Variation about this basic shape being due to the coding errors and statistics in the system.

As will be shown in the next section the off-axis  $\sigma$  variation still exists even in the presence of disturbing effects.

### 3.5.5. Effect of Different Mask Patterns

Although the simulation program was capable of producing many types of mask pattern, only three were used for the majority of the work. These masks were the PN mask, self-supporting PN mask, and Fresnel zone plate mask. These patterns are shown in Figures 3.5.13, 3.5.14 and 3.5.15.

Initial trials showed that the PN mask performed best on all three sky fields and so was used for the majority of the investigation. The self-supporting mask was investigated because of its mechanical properties, and the Fresnel zone plate taken as an 'imperfect' mask pattern with poor autocorrelation function. (In addition the Fresnel zone plate is circularly symmetric, a distinct advantage where roll correction of data is required.)

Detailed investigation of mask pattern performance is not covered in this work and is not necessary as the performance of the shadow camera is dominated by other effects, as discussed in the following section.

TABLE 3.5.5

BLOCK BY BLOCK ANALYSIS OF DECONVOLVED IMAGES FOR COMA REGION FOR CYCLIC  
AND SIMPLE CAMERA TO SHOW VARIATION IN  $\sigma$

RMS as a function of block number

Simple

171	293	433	460	448	411	305	159
298	531	641	734	799	644	526	253
368	608	845	991	977	864	639	338
400	765	936	1084	1039	918	688	381
400	694	935	1154	1077	861	706	414
331	564	737	867	826	788	591	281
234	401	563	652	677	586	430	286
161	239	296	387	408	325	288	156

Cyclic

991	1063	1005	1035	1149	1145	1081	1113
1124	1116	1188	1202	1333	1032	1135	1133
1189	993	1344	1108	1197	1102	1012	1195
1145	876	1120	1067	1041	1030	1151	1083
1048	1142	1247	1046	953	1161	970	1018
1017	1033	1247	1087	1254	1224	1027	1043
1145	1139	1076	1045	1083	1060	1103	1295
1117	1003	1060	940	1108	1204	1123	1088

Figure 3.5.13 PN mask used during simulation work. (From Procter et al., 1979) Black squares represent transmission, holes in mask, white squares zero transmission, blanks in mask. (As for Figures 3.5.14 and 3.5.15)



Figure 3.5.14 Self-supporting mask used during simulation work. (From Giles 1980).



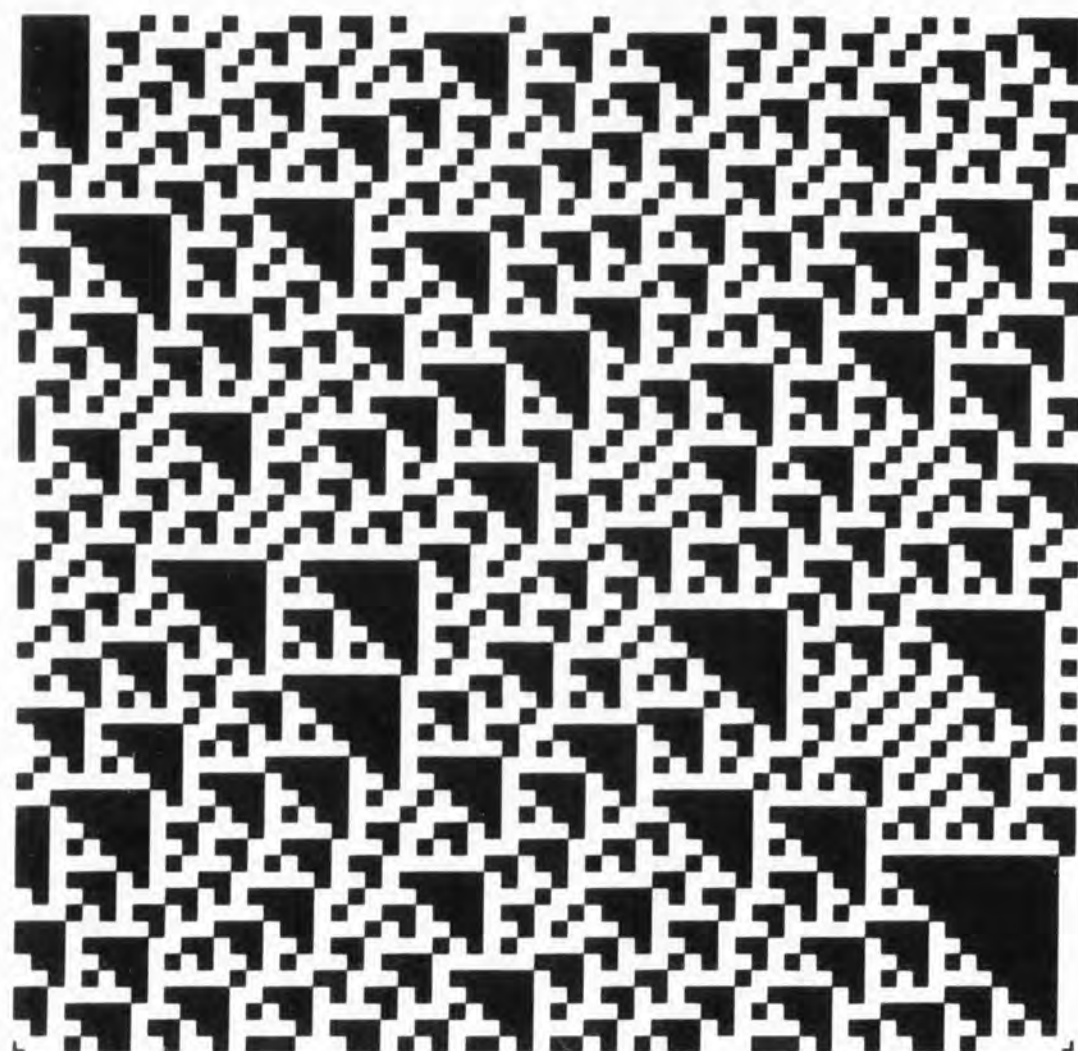


Figure 3.5.15 Fresnel zone plate mask of 8 rings used during simulation work.



### 3.6. Simulation Results II: Disturbing Effects

This section reports the results of simulations of a non-perfect shadow camera in both cyclic and simple forms. Three disturbing effects were considered; firstly the case of loss of information due to the detector window support and its shadowing effect; secondly the effect on shadow camera motion with respect to the FOV in addition to the detector window support effect; and finally the effect of finite detector response on a perfect camera, that is one with no window support or motion.

#### 3.6.1. Results of Detector Window Support Simulations

In order to understand fully the simulations made, the rationale behind the window support types chosen will be described. In the presence of a window support the total count will obviously drop because of the loss of counts under the support and its shadow so in order to compare directly the perfect and non-perfect camera simulations, the effective area used in the simulation program was increased.

An identical set of cameras as specified in Table 3.5.1 were simulated. For the experiment described in Chapter 2, section 2.10, only one type of window support was actually designed in detail (mechanically), that is the circular support.

Actual flight design parameters are as follows:

Circular holes hexagonally packed

Circle diameter = 1.9 cm

Circle to circle centre = 2.1 cm

Thickness of plate = 1.0 cm

Overall size of detector = 30 cm x 30 cm .

This support was called the flight circular support.

The bar type of support was not designed in detail, but the following parameters have approximately the correct dimensions to meet the engineering design requirement for the experiment:

Centre of bar to centre of bar	=	1.9 cm
Thickness of individual bar	=	.5 cm
Thickness of plate	=	1.0 cm

Both types of window support structure were simulated. Two alignments of the flight bar support with respect to the detector sensing axes were considered, namely 0 and 45°.

In addition to the flight design support two other types were simulated, as the flight support does not simulate one of the real effects of a support, when used in the simulation program. The actual flight detector has 512 x 512 elements, each element corresponding to approximately 0.6 mm, whereas the simulated detector has only 64 x 64 elements. In the real flight camera the circular support structure therefore has approximately 32 elements across each hole and therefore blocks out relatively low spatial frequencies. In order to simulate this effect on the 64 x 64 element simulations the flight design support structures were scaled to give approximately the same number of elements across a hole.

The support structure was scaled to give 2 circular holes or 2 ribs across the detector. The height that is plate thickness was also scaled so that identical shadowing to the flight supports occurred.

It was found that because of the discrete nature of the transmission function of the shadowed support for the bar pattern, a scaling factor of only 0.333 rather than 0.666 for the shadow length calculation was required to give the same approximate total count and correct physical amount of shadowing.

In order to investigate the size and sampling effect of the detector window support, all 6 types of support, both flight and corrected support

were simulated. Table 3.6.1 summarises the window support parameters in terms of program parameters (see section 3.3.11).

Figure 3.6.1 shows the on-axis (that is zero shadow) transmission functions, zero (white) or 1 (black) produced by the relevant program sub-routines for the four basic support structures, RTHETA being zero for the bar support. The circular structure is very clear for the corrected support, whereas for the flight support only a crude approximation to the shape is visible due to the discrete nature of the simulation (see section 3.3.11).

Figure 3.6.2 shows the result of cross-correlation with uncorrected data for the Galactic centre region with the corrected circular support. As can be seen, zero correction results in a pattern (dependent on window support shape) being superimposed on the deconvolved image.

As discussed in section 3.4.3 it is impossible to replace the data lost by the effect of the detector window support, but one can approximate it by a constant value, namely zero, reducing the recorded data to fluctuations around zero.

To investigate the deconvolution method a window support simulation was first done for each sky region (simple camera), and deconvolved by four methods. The support used was of the corrected circular variety.

The four methods of deconvolution used were:

- (i) Cross-correlation ; data only corrected for unshadowed  
support structure
- (ii) Cross-correlation ; full data correction window support  
plus shadow
- (iii) Wiener Filter ; full data correction, original  
estimate N/S
- (iv) Wiener Filter ; full data correction, improved  
estimate N/S .



TABLE 3.6.1  
SIMULATED WINDOW SUPPORT PARAMETERS

Corrected Support

<u>Circular</u>		<u>Bar</u>	
R	= 6.8 cm	R	= - cm
S	= 15.0	S	= 15.2
L	= 30.0	L	= 30.0
TL	= 4.0	TL	= 4.0
WT	= 7.2	WT	= 8.0
		RTHETA	= 0.0 or 45.0°

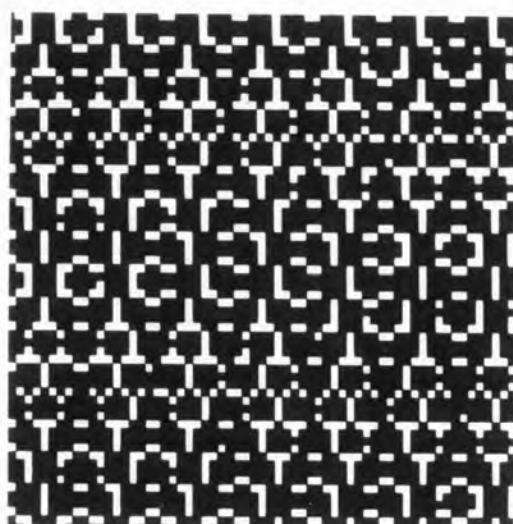
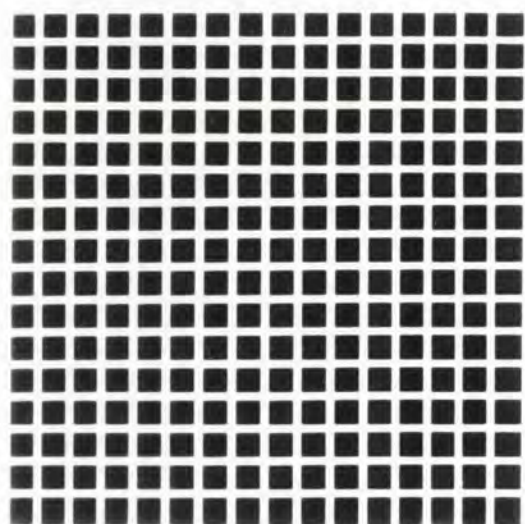
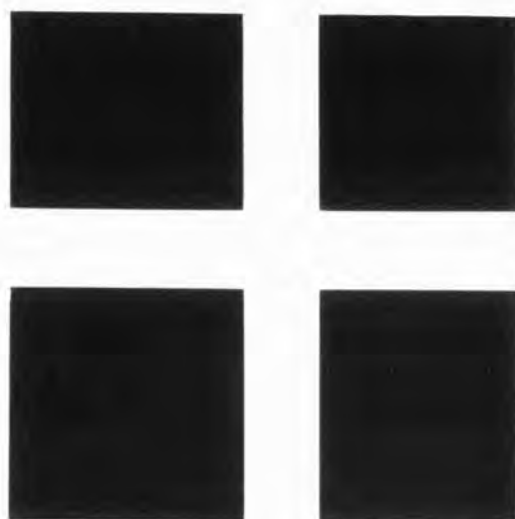
Flight Support

<u>Circular</u>		<u>Bar</u>	
R	= 0.95 cm	R	= - cm
S	= 2.1	S	= 1.9
L	= 30.0	L	= 30.0
TL	= 0.5	TL	= 0.5
WT	= 1.0	WT	= 1.0
		RTHETA	= 0.0 or 45.0°

Figure 3.6.1 On axis (zero shadow) transmission functions for four basic window supports simulated, (a) corrected circular, (b) corrected bar, (c) flight circular, and (d) flight bar window support.

(a) (b)

(d) (c)



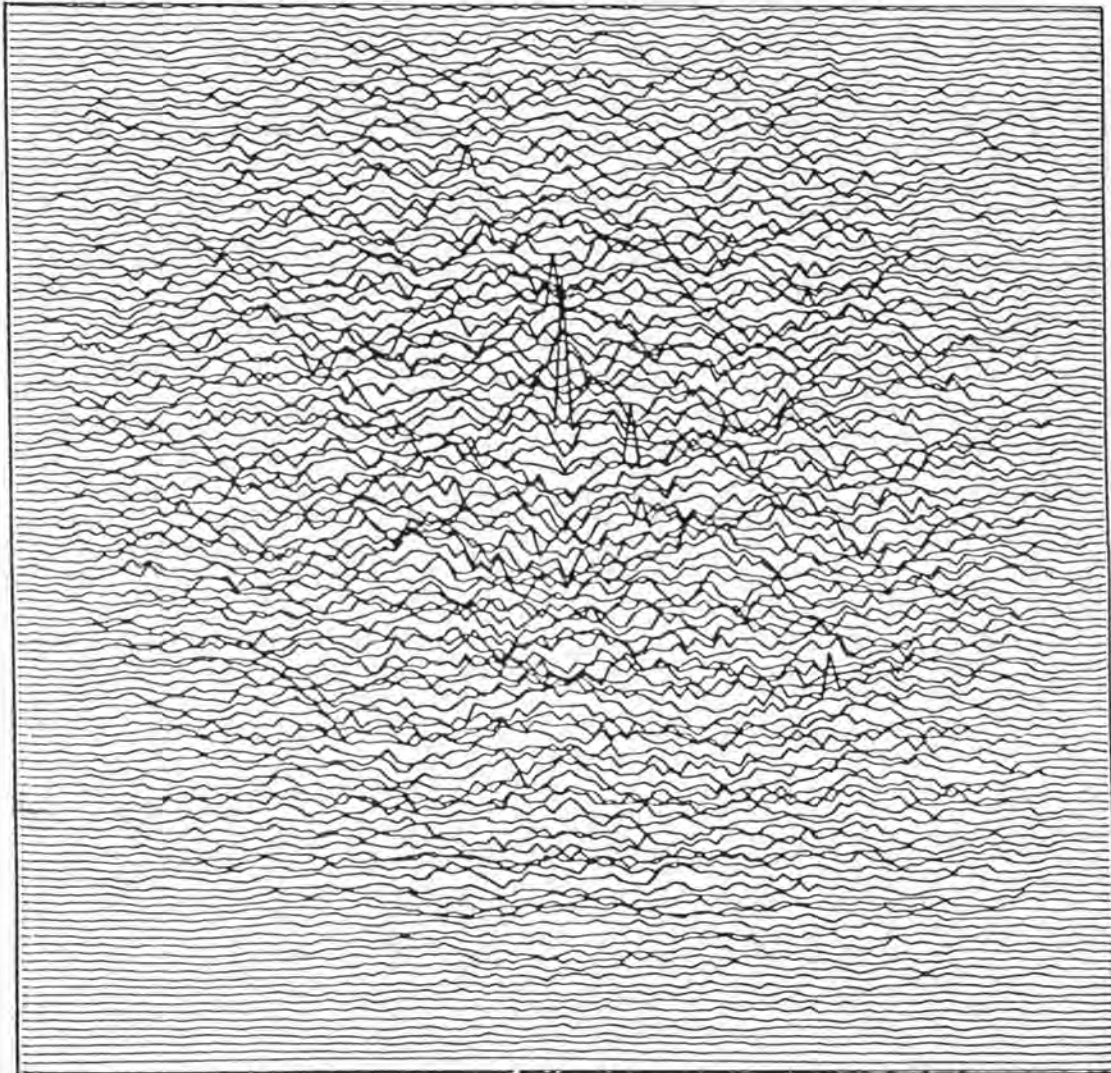


Figure 3.6.2. Simulated 100-second observation of Galactic Centre (simple camera) with corrected circular window support. Deconvolution method used is cross-correlation with no correction made to data to allow for window support.

The results of these simulations are summarised in Tables 3.6.2, 3.6.3 and 3.6.4.

Table 3.6.2 summarises the results for the Galactic centre, a source dominated region where side lobes are largest, and hence a window support should have the biggest effect. Figure 3.6.3 shows the resultant image of the Galactic centre after deconvolution by cross-correlation, method (ii) above, with full data correction. Figure 3.6.4 shows the Galactic centre deconvolved with the improved Wiener filter, method (iv) above.

For cross-correlation:

perfect simple camera (no support) global rms = 1.45 x theoretical  
 with support no shadow rms = 3.37 x theoretical  
 with support allowing for shadow global rms = 2.15 x theoretical

As expected cross-correlation with full data correction, that is the shadow being corrected for properly, produces the minimum global rms with comparison to theory, as we are reducing the data correctly to fluctuations around zero. The perfect simple camera is of course worse than theory because of coding errors introduced by the off-axis fall-off in recorded pattern.

For the Wiener Filter:

perfect simple camera rms = 1.23 x theoretical  
 with window support original estimate N/S rms = 2.24 x theoretical  
 with window support improved estimate N/S rms = 1.75 x theoretical

It was found that in all areas, the Wiener Filter as it stood (original estimate N/S) performed worse than cross-correlation. However the filter with full data correction and the improved estimate again

TABLE 3.6.2.

Simulation	Integration Time	Type	Deconvolu- tion Method	RMS of Theoretical pixels excluding obvious sources	X	Theoretical sources > 5 $\sigma$	No. of largest false peaks > 4 $\sigma$	No. of sources > largest false peak	Typical source peak
Galactic centre	100 secs	Perfect	Cross- correlation	441	638	1.45	10	2	34.49
			Wiener Filter	544	544	1.23	11	3	34.40
		Correc- ted circular	Cross- correlation without shadow	356	1199	3.37	6	17	12.95
			Cross- correlation allowing for shadow		764	2.15	8	4	19.85
		Window support	Wiener Filter original estimate N/S	799	799	2.24	7	3	17.08
			Wiener Filter improved estimate	623	623	1.75	7	4	18.81



TABLE 3.6.3.

Simulation	Integration Time	Type	Deconvolu- tion Method	RMS of Theoretical pixels excluding obvious sources	X	Theoretical sources > 5 $\sigma$	Largest false peak > 4 $\sigma$	No. of false peaks > 4 $\sigma$	No. of sources > largest false peak	Typical source
Scorpius region	200 secs	Perfect	Cross- correlation	324	395	1.22	5.19	11	7	44.34
			Wiener Filter		372	1.15	5.14	6	6	36.76
		Correc- ted Circular	Cross- correlation without shadow	266	552	2.08	5.81	21	3	22.88
			Cross- correlation allowing for shadow		467	1.76	5.76	14	5	27.18
		Window support	Wiener Filter original estimate N/S		485	1.82	5.87	8	3	22.25
			Wiener Filter improved estimate		361	1.36	6.11	9	3	24.24

TABLE 3.6.4.

Simulation	Integration Time	Type	Deconvolu- tion Method	RMS of Theoretical pixels RMS excluding on axis obvious sources	X Theoretical	No. of sources > 5 $\sigma$	Largest false peak > 4 $\sigma$	No. of false peaks > 4 $\sigma$	No. of sources > largest false peak	Typical source false peak
Coma region	5000 secs.	Perfect	Cross- correlation	1163	0.55	2	5.01	20	2	30.67
			Wiener Filter	452	0.39	2	51.4	12	2	27.97
		Correc- ted Circular	Cross- correlation without shadow	744	0.77	2	6.68	25	2	15.25
			Cross- correlation allowing for shadow	571	0.60	2	6.43	20	2	21.78
			Wiener Filter original estimate N/S	404	0.42	2	5.57	10	2	19.67
			Wiener Filter improved estimate	Identical	to	above	as	S/n	too	low

Note: The Wiener Filter routine of Willingale (1979) imposed a limit on N/S to prevent amplification of noise unnecessarily, hence the Wiener Filter results are identical.

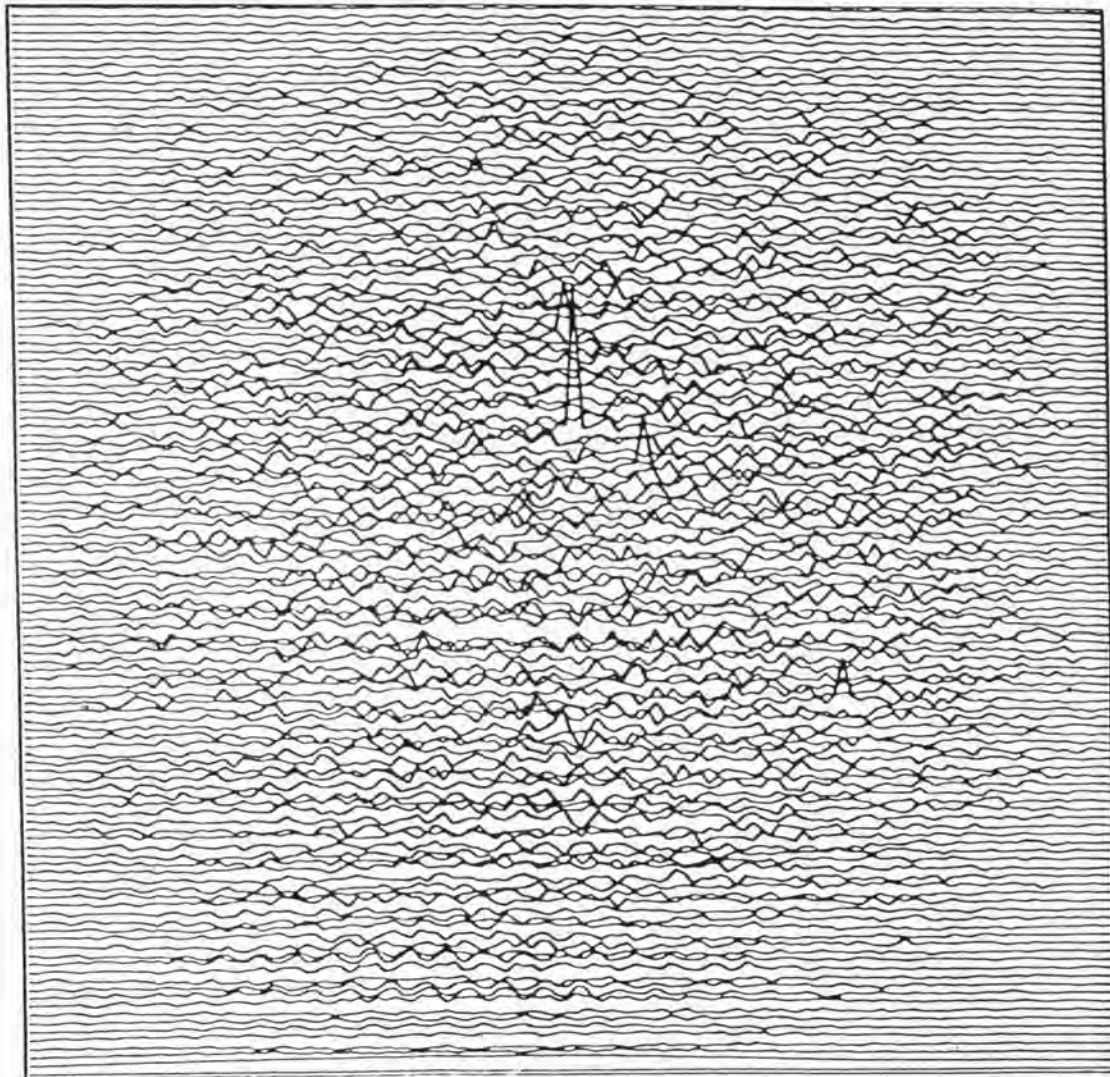


Figure 3.6.3 Simulated 100-second observation of Galactic Centre (simple camera) with corrected circular window support. Deconvolution method used is cross-correlation with full correction to data to allow for window support, showing improvement in resulting image compared to Figure 3.6.2.

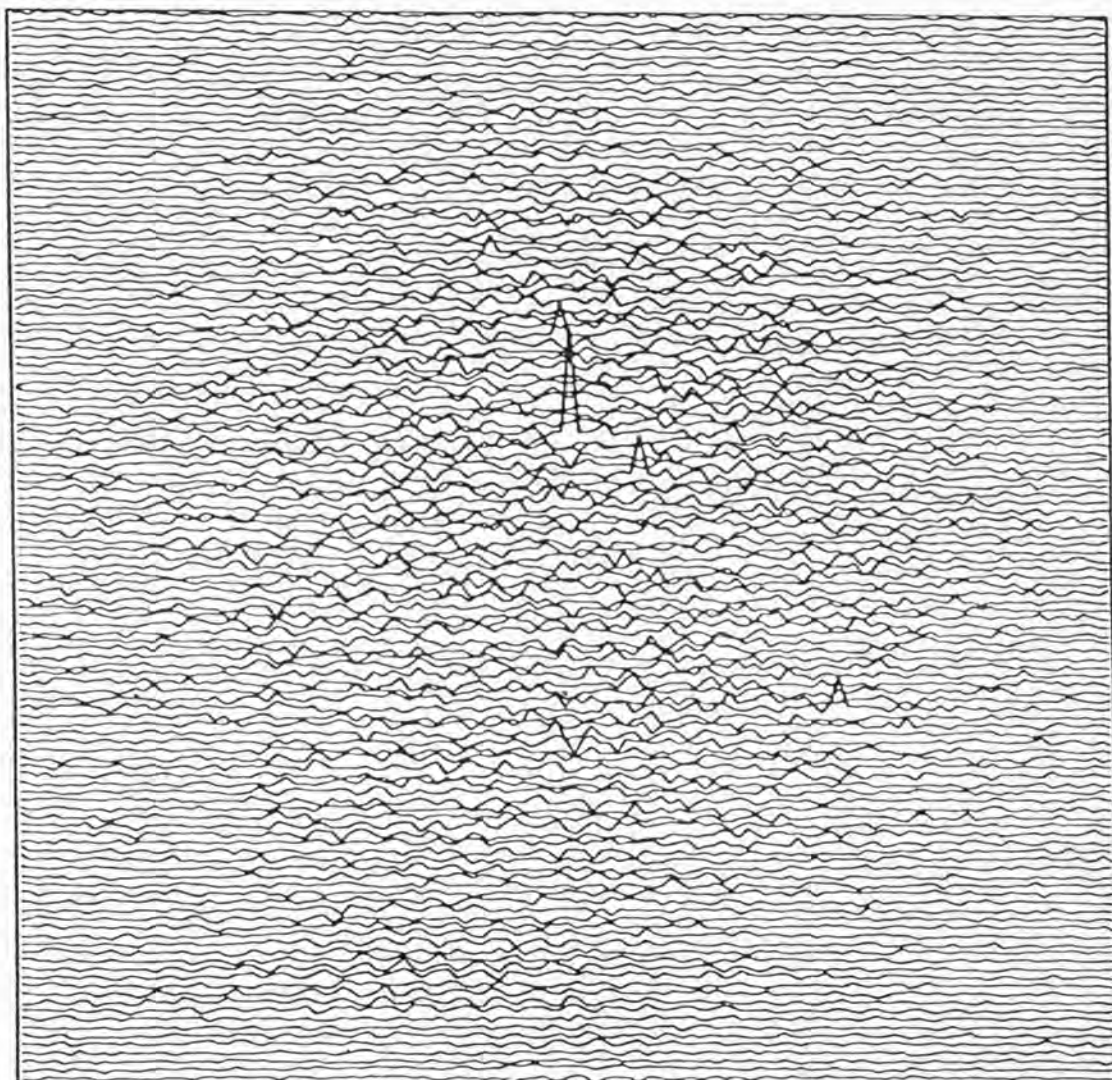


Figure 3.6.4 Simulated 100-second observation of Galactic Centre (simple camera) with corrected circular window support. Deconvolution method is improved Wiener Filter with full data correction to allow for window support, showing improvement over cross-correlation deconvolution of Figure 3.6.3.



performed better than cross-correlation, as did the original filter in the case of the perfect simple camera.

Although deconvolving the data correctly does reduce the global rms, it is never as good as the perfect simple camera case, as expected due to the loss of coding with the window support.

These conclusions are equally valid for the Scorpius and Coma region results. In the Coma region a comparable performance with the perfect simple camera case is achieved. Note the rms is below the theoretical due to the off-axis variation in  $\sigma$  effect.

The results of the comparison of the window support types will now be presented. The results of the simulations for each region are summarised in Tables 3.6.5, 3.6.6 and 3.6.7.

As can be seen from the tables little difference exists in performance between any of the support structures. All regions, apart from Coma, and all supports are worse than theory as expected from the resultant loss of information with the shadowed support structure. No clear choice of type of support or its effect can therefore be made from the data. Hence as little in performance exists, and the circular type of support is better mechanically (this is discussed in Chapter 4), this was adopted as the standard support type for all other detector window support simulations.

The initial studies presented above of the effect of window support structure utilise the simple configuration of shadow camera. To compare the cyclic camera performance with that of the simple camera, it was simulated with identical window supports. (The FOV collimator does not drastically change the overall support structure in a real camera.)

The cyclic camera was simulated for the Coma and Galactic centre regions, with the two spatial frequencies of circular support, cross-correlation being used as the method of deconvolution. Table 3.6.8 summarises the results of these simulations.

TABLE 3.6.5

## RESULTS OF DETECTOR WINDOW SUPPORT SIMULATIONS: SIMPLE CAMERA

Simulation region	Integration Time	Type	RMS of		Theoretical sources $> 5\sigma$	X <sub>r</sub>	No. of false peaks $> 4\sigma$	No. of sources $> 4\sigma$	No. of sources $> 4\sigma$	Typical source false peak
			Deconvolu- tion Method	Theoretical RMS on axis						
Coma region PN Mask	5000 secs.	Correc- ted Circular	Cross correlation Wiener Filter	957	570	0.60	2	6.43	20	21.78
		Correc- ted Bar	Cross- correlation Wiener Filter	1064	643	0.61	3	6.02	26	32.12
		Correc- ted Bar 45°	Cross- correlation Wiener Filter	864	530	0.61	2	5.65	34	24.45
		Flight Circular	Cross- correlation Wiener Filter	930	549	0.59	2	5.50	23	19.48
		Flight Bar	Cross- correlation Wiener Filter	948	559	0.59	2	5.91	23	20.58
		Flight Bar 45°	Cross- correlation Wiener Filter	906	536	0.59	2	6.60	16	19.79
		Flight Bar 45°	Cross- correlation Wiener Filter	906	536	0.59	2	6.60	16	19.79
		Flight Bar 45°	Cross- correlation Wiener Filter	906	536	0.59	2	6.60	16	19.79

Note: Wiener Filter with Improved N/S estimate.



TABLE 3.6.6

## RESULTS OF DETECTOR WINDOW SUPPORT SIMULATIONS: SIMPLE CAMERA

Simulation	Integration Time	Type	Deconvolu- tion Method	RMS of		Theoretical sources > 5 $\sigma$	No. of false peaks > 4 $\sigma$	No. of sources > largest false peak	Typical source false peak
				RMS on axis	excluding obvious sources				
Galactic centre PN Mask	100 secs.	Correc- ted Circular	Cross- correlation Wiener Filter	356	764	2.15	8	4.61	19.85
					623	1.75	7	4.54	18.81
		Correc- ted Bar	Cross- correlation Wiener Filter	381	819	2.15	8	4.59	18.14
					728	1.91	8	4.82	16.67
		Correc- ted Bar 45°	Cross- correlation Wiener Filter	317	699	2.21	7	5.13	15.84
					558	1.76	7	5.81	15.30
		Flight Circular	Cross- correlation Wiener Filter	347	749	2.16	7	5.57	16.47
					608	1.75	5	5.76	15.81
		Flight Bar	Cross- correlation Wiener Filter	363	782	2.16	8	5.60	18.30
					618	1.70	7	4.96	17.95
		Flight Bar 45°	Cross- correlation Wiener Filter	342	751	2.20	8	5.00	17.25
					592	1.73	6	5.20	16.71

TABLE 3.6.7

## RESULTS OF DETECTOR WINDOW SUPPORT SIMULATIONS: SIMPLE CAMERA

Simulation	Integration Time	Type	Deconvolu- tion Method	RMS of		X	No. of sources > $5\sigma$	No. of false peaks > $4\sigma$	No. of sources > largest false peak	Typical source peak
				Theoretical pixels on axis	RMS excluding obvious sources					
Scorpius region PN Mask	200 secs.	Correc- ted Circular	Cross- correlation Wiener Filter	266	467	1.75	5	5.76	14	27.18
					361	1.36	4	6.11	9	24.24
		Correc- ted Bar	Cross- correlation Wiener Filter	294	529	1.80	6	5.34	25	26.80
					470	1.60	4	5.46	13	22.78
		Correc- ted Bar 45°	Cross- correlation Wiener Filter	241	430	1.78	5	5.33	13	24.53
					312	1.29	3	5.09	18	22.97
		Flight Circular	Cross- correlation Wiener Filter	259	471	1.82	5	5.48	17	23.57
					360	1.39	4	6.26	20	20.82
		Flight Bar	Cross- correlation Wiener Filter	264	482	1.83	4	5.80	18	26.53
					358	1.36	3	5.51	20	24.75
		Flight Bar 45°	Cross- correlation Wiener Filter	250	478	1.91	4	5.88	35	22.48
					363	1.45	3	5.22	18	20.49

TABLE 3.6.8

## RESULTS OF WINDOW SUPPORT SIMULATIONS: CYCLIC CAMERA

Simulation	Integration Time	Type	Deconvolu- tion Method	RMS of Theoretical pixels RMS excluding on axis obvious sources	X Theoretical sources	No. of largest false peak $> 5 \sigma$	No. of false peaks $> 4 \sigma$	No. of sources > largest false peak source		
Galactic centre	100 secs.	Flight Circular	cross - correlation	335	866	2.59	6	0	7	16.33
		Correc- ted Circular		347	878	2.53	5	0	8	14.51
Coma region	5000 secs.	Flight Circular		918	904	.98	2	0	2	12.92
		Correc- ted Circular		946	951	1.01	2	0	2	15.12

As expected the cyclic camera performs as badly, if not worse, than the simple system due to destruction of the perfect coding of the cyclic camera due to the window support. Little difference exists between the two frequencies simulated.

For the Galactic centre the cyclic camera has a global rms  $\sim 2.59$  or  $2.53 \times$  theoretical, whereas the simple camera values are  $\sim 2.16$  and  $2.15$  for identical support structure and shadowing. For Coma the cyclic case  $\sim .98$  or  $1.01 \times$  theoretical, whereas the simple case is  $\sim .60$  or  $.59 \times$  the theoretical. Comparable performance with the perfect cameras was achieved due to the few sources present and great redundancy in the mask pattern.

On average i.e. the global rms, the cyclic camera actually performs worse than the simple camera, for both simulated regions of X-ray sky.

### 3.6.2. Off-axis Variation in Image RMS with Window Support

In the perfect camera, see section 3.5.4, the simple camera was shown to have a sensitivity advantage over the cyclic camera due to its variation in rms or  $\sigma$  over the deconvolved image. Figure 3.6.5 shows the local average  $\sigma$  value as a function of distance from the centre of the FOV, along the diagonals, for both cyclic and simple systems. The Coma and Galactic centre regions were only simulated and analysed for the corrected circular support for both types of camera.

As can be seen the simple camera has retained its off-axis  $\sigma$  variation, whereas the cyclic camera appears to show no such variation. (Detailed examination of the variation in  $\sigma$  across the whole deconvolved image in the case of the cyclic system and the Galactic centre shows the distribution is flat.) Hence again, for a random event the simple system will have a sensitivity advantage over the cyclic system. As here, unlike the perfect camera, the cyclic system does not obey the theory (in the

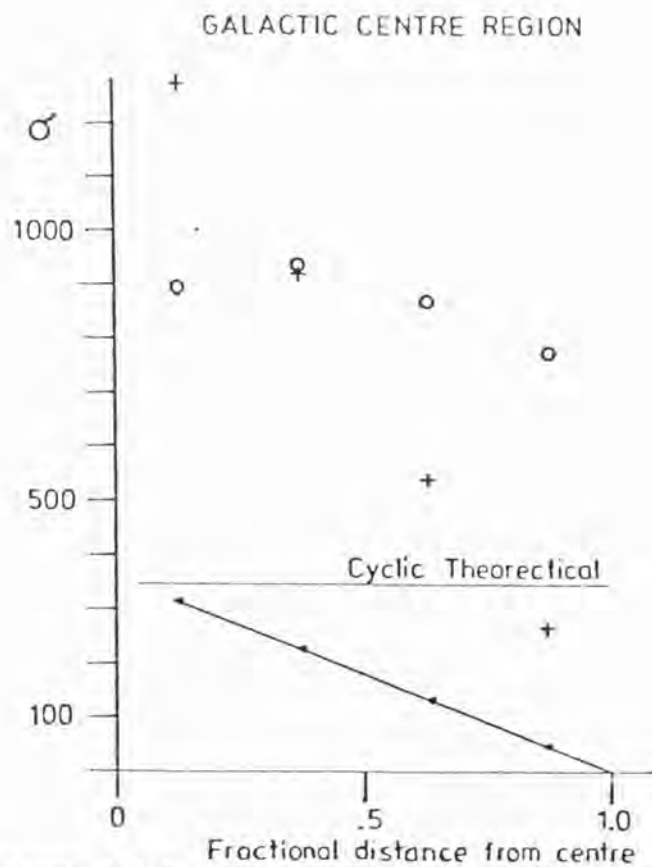
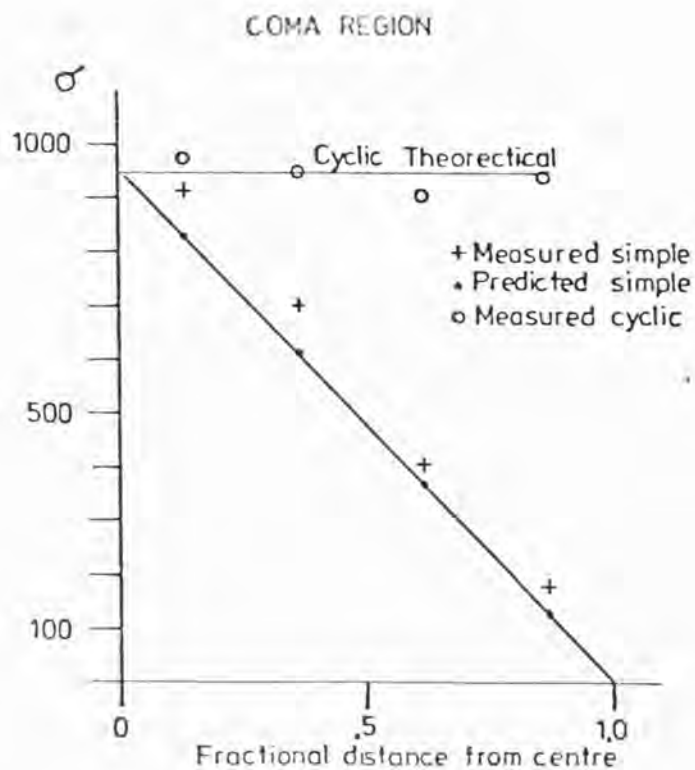


Figure 3.6.5  $\sigma$  as a function of distance along diagonal for both cyclic and simple cameras for Coma and Galactic Centre regions with corrected circular window support. Theoretical cyclic, and predicted simple variation in  $\sigma$  are also shown.

Galactic centre region) one has to calculate the sensitivity advantage by comparing the two simulations.

Performing the same integration as section 3.5.4 gives the following figures;

in the Galactic centre

sensitivity advantage = 2.15

Coma = 3.572

under identical simulation conditions.

Figures 3.6.6 and 3.6.7 show the simple and cyclic cameras deconvolved images, with window support, for the Coma region, the off-axis variation in sigma being clearly visible in the simple camera case.

### 3.6.3. Results with Shadow Camera Motion Included

It will now be demonstrated that provided the image from the simple camera can be corrected for camera motion, motion improves the sensitivity by giving better coding. As mentioned above, section 3.3.12, roll about the instrument view axis was not simulated due to the problem of deconvolution in this case.

A variety of motion was simulated, Gaussian jitter, a linear drift, and a number of spot pointing positions with instantaneous slews between them. These simulations assume of course no rotation and correction of the photon detected co-ordinates back to the original pointing positions.

(see section 3.3.12)

There is a definite maximum motion in either the pitch or yaw axes (for the camera view axis), see Figure 2.9.1, which can occur before translation correction of the image is no longer valid. The motion in each axis of course is a rotation, see Figure 3.6.8. The limitation on the motion



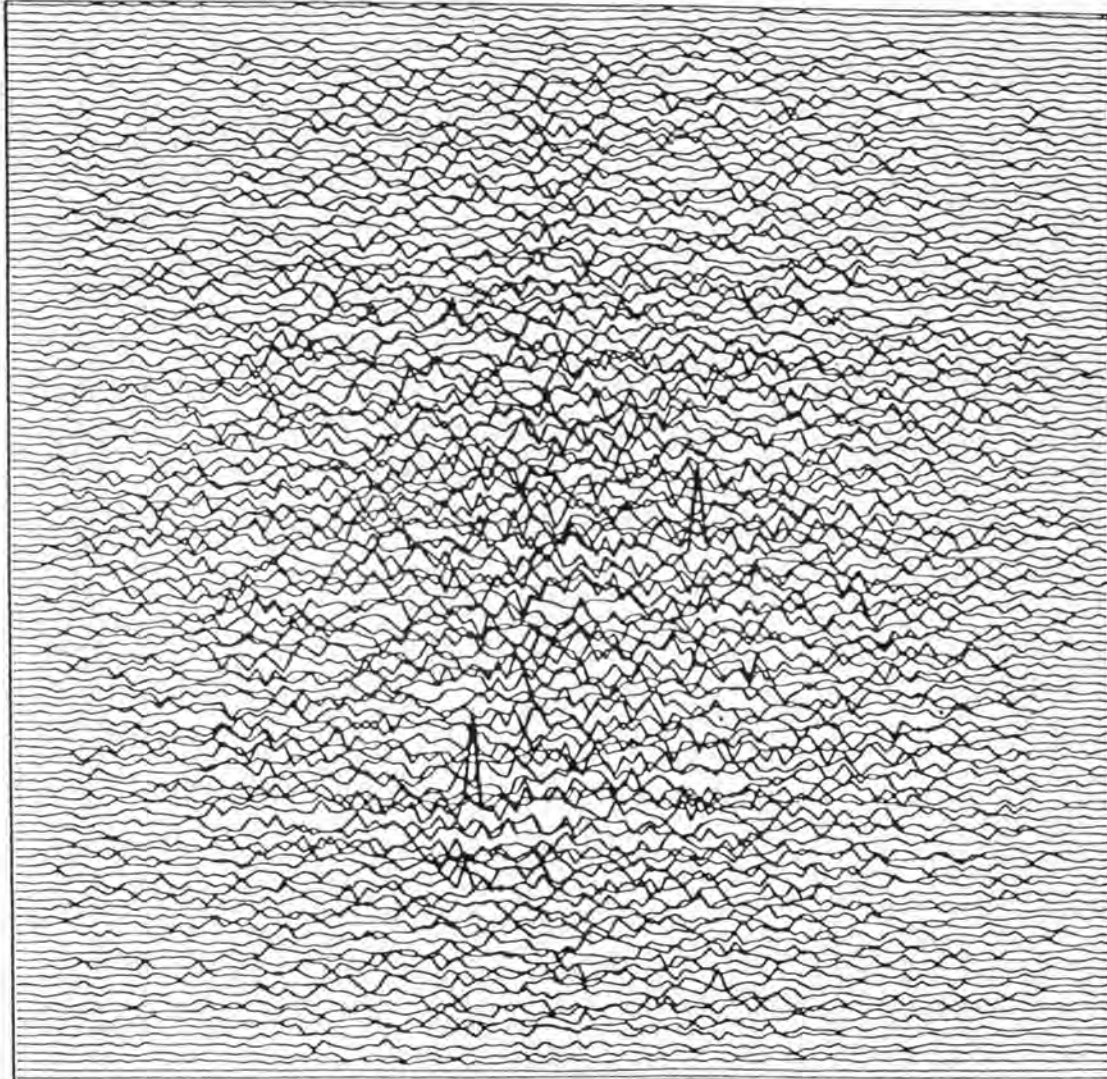


Figure 3.6.6 Simulated 5000-second observation of Coma region, simple camera, with corrected circular window support (cross-correlation deconvolution). Note: off-axis variation in  $\sigma$  is clearly visible.

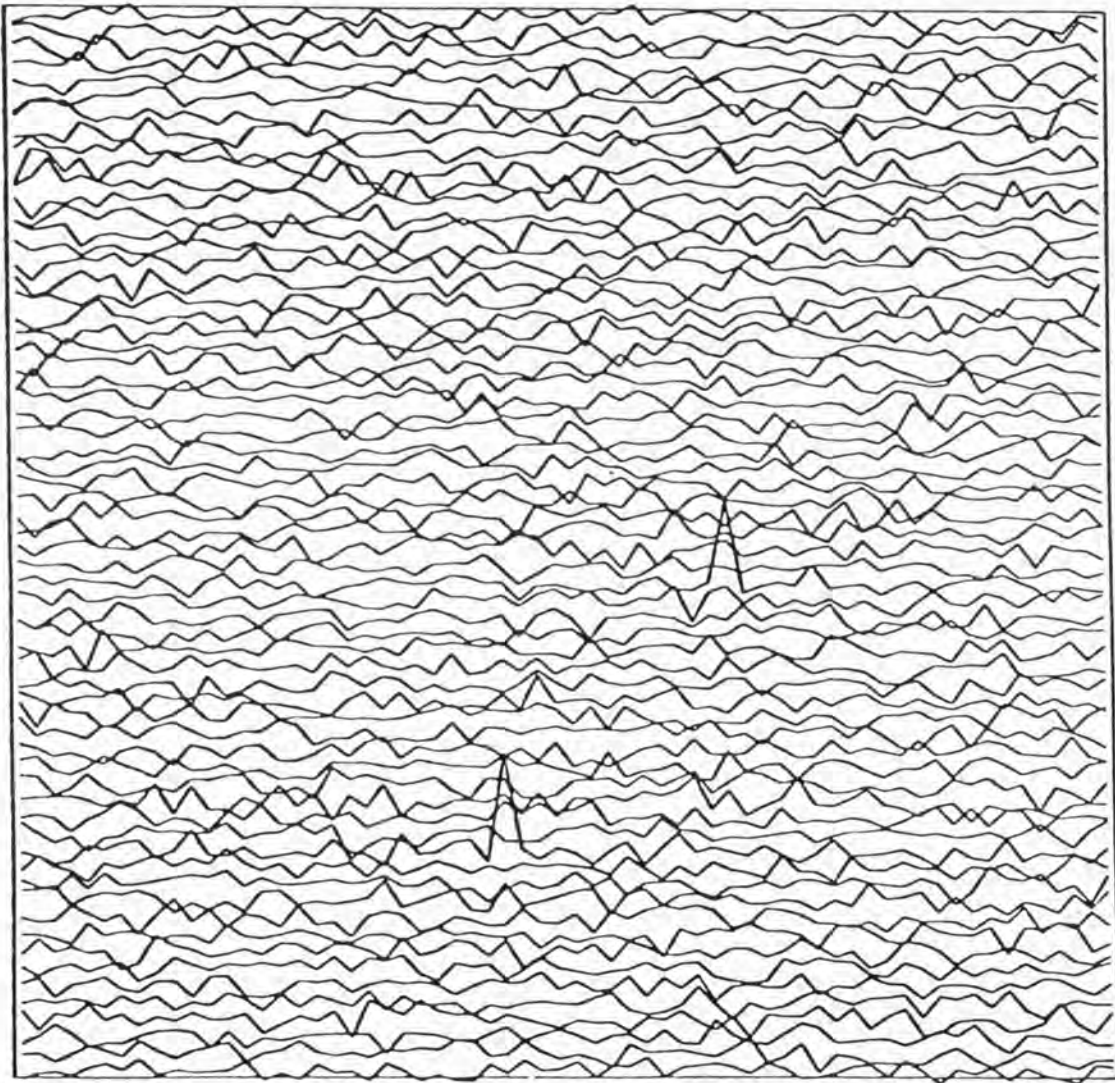


Figure 3.6.7 Simulated 5000-second observation of Coma region,  
cyclic camera, with corrected circular window support  
(cross-correlation deconvolution).

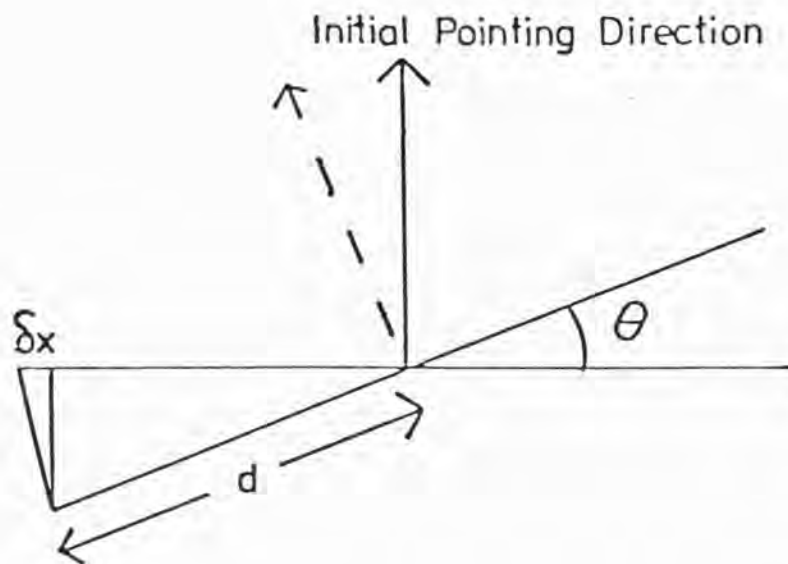


Figure 3.6.8 The above figure shows parameters for maximum motion of the shadow camera for translation correction of the data in pitch or yaw axes.  $d$  is the half width of the detector. Let the smearing of the image be limited to one pixel. For motion greater than this a form of spherical aberration of the image results, because the centre of the mask shadow is displaced by  $D \tan \theta$ . Hence as the camera rotates in pitch or yaw, one can only correct the photon co-ordinates by an average  $\theta$ , as one does not know the angle a particular photon arrived from. Any source off axis in the original FOV will not have the true correction and hence will be blurred.

must be when  $\delta x$  is the size of a detector pixel.

If  $\theta$  is the maximum rotation angle then

$$\delta x = d \sin^2 \theta$$

Now  $\delta x = 2d/M$

where  $M$  is the number of elements across the detector.

Hence  $\theta = \sin^{-1} \sqrt{\frac{2}{M}}$

$$M = 64 \quad \theta = 10.18^\circ$$

$$M = 512 \quad \theta = 3.58^\circ$$

Hence considerable motion can take place before translational correction of the photon co-ordinates is no longer valid.

Table 3.6.9 summarises the results of the motion simulations. Cross-correlation was the only method of deconvolution used.

As can be seen from the table motion improves the global rms due to the improved sampling of the coded image.

Zero motion has an global rms  $\sim 2.15 \times$  theoretical

Gaussian jitter, motion rms = 3 pixels, has an rms  $\sim 1.62 \times$   
theoretical

Gaussian jitter, motion rms = 2 pixels, has an rms  $\sim 1.96 \times$   
theoretical

The larger the motion the bigger the improvement.

Linear drift has an global rms  $\sim 1.99 \times$  theoretical

Three spot pointing directions have an rms  $\sim 1.73 - 1.93 \times$   
theoretical

Two spot point directions has an rms  $\sim 1.96$

There is a definite improvement no matter what the motion, despite the fact that the overall integration times (and hence total count

TABLE 3.6.9

## RESULTS OF SIMULATIONS WITH MOTION: SIMPLE CAMERA

Simulation	Integration Time	Type	Deconvolution Method	RMS of		Theoretical sources	X	No. of sources $> 5\sigma$	Largest false peak $> 4\sigma$	No. of false peaks $> 4\sigma$	No. of sources $> 4\sigma$	Typical source peak
				RMS on axis	excluding obvious sources							
Galactic centre	100 secs.	Zero		356	764	2.15	8	4.93	5	8	20.04	
		Gaussian										
		Jitter rms = 3 pixels		352	569	1.62	9	4.57	6	9	24.98	
		"										
		rms = 1		354	695	1.96	8	4.63	6	8	21.67	
		Linear										
		Drift 4 pixels total		350	698	1.99	7	4.35	9	9	20.72	
		Two spot points 4 pixels apart		351	689	1.96	8	4.23	7	8	20.90	
		Three spot points		353	607	1.72	9	4.85	8	9	23.42	
		Three spot points (diffnt)		351	677	1.93	8	5.05	6	8	19.80	

cross - correlation

\* Rms in Type column refers to rms of Gaussian jitter in sky pixels.

approximately) are the same as the zero motion case.

In most cases this results in a S/N improvement for a given source. However as can be seen in the last case in the table a decrease in S/N can result, dependent on the interaction of coding, source distribution, support structure, and motion convolution.

#### 3.6.4. Results with Finite Detector Response

The final disturbing effect to be considered was that of finite detector response or resolution. This was treated as a single effect in order to find its magnitude, by convolving the perfect simulation with the finite simulated detector response. The Galactic centre region only was used for the simulation. The results of the simulations are summarised in Table 3.6.10.

As can be seen there is a distinct loss in S/N as the rms response increases from zero to 2 detector pixels. As can be seen in Figures 3.6.9, 3.6.10 and 3.6.11 the source in normal deconvolution is just blurred slowly out; at an rms of 2.0 only one source can be recognised. The effect appears to have a knee beyond rms = 0.5 pixels, this being expected by theoretical considerations, see Appendix B.

Deconvolution with a blurred mask does not improve the S/N for a source distribution but rather visually 'filters' or improves the picture of the deconvolved image.

#### 3.7. Summary

This chapter has described the deconvolution and simulation of data from a shadow camera. A simple computer model was adopted due to computer limitations, and a variety of topics investigated.



TABLE 3.6.10

## RESULTS OF FINITE DETECTOR RESPONSE SIMULATIONS: SIMPLE CAMERA

Simulation	Integration Time	Type	Deconvolu- tion Method	RMS of		X Theoretical sources	No. of sources > 5 $\sigma$	Largest false peak > 4 $\sigma$	No. of false peaks > 4 $\sigma$	No. of sources > largest false peak	Typical source peak
				RMS on axis	excluding obvious sources						
Galactic centre	100 secs.	Perfect	Cross- correlation	441	638	1.45	10	4.09	2	11	34.49
PN mask		rms = 0.5 Detector pixels	With mask	441	507	1.14	8	4.23	3	9	25.76
			With blurred mask		402	.91	7	< 4 $\sigma$	0	7	21.75
		rms = 1.0 Detector pixels	With mask	440	407	.92	4	< 4 $\sigma$	0	5	8.68
			With blurred mask		264	.60	3	4.43	1	3	7.73
		rms = 2.0 Detector pixels	With mask	439	374	.85	1	4.12	2	2	5.53
			With blurred mask		208	.47	0	4.09	5	0	no sources visible

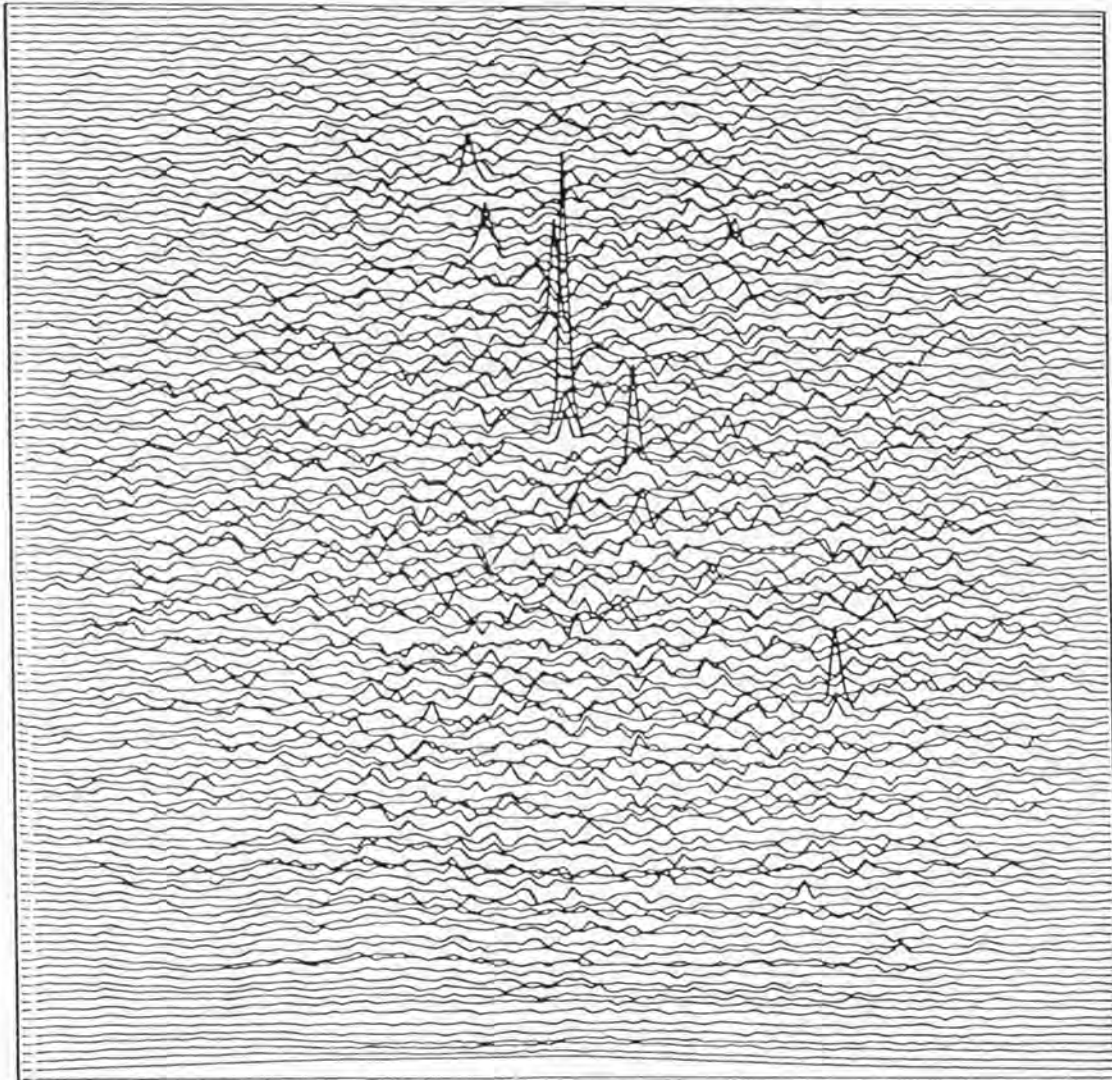


Figure 3.6.9 Simulated 100-second observation of Galactic Centre (simple camera) with finite detector response, rms = 0.5 pixels, included (cross-correlation deconvolution).

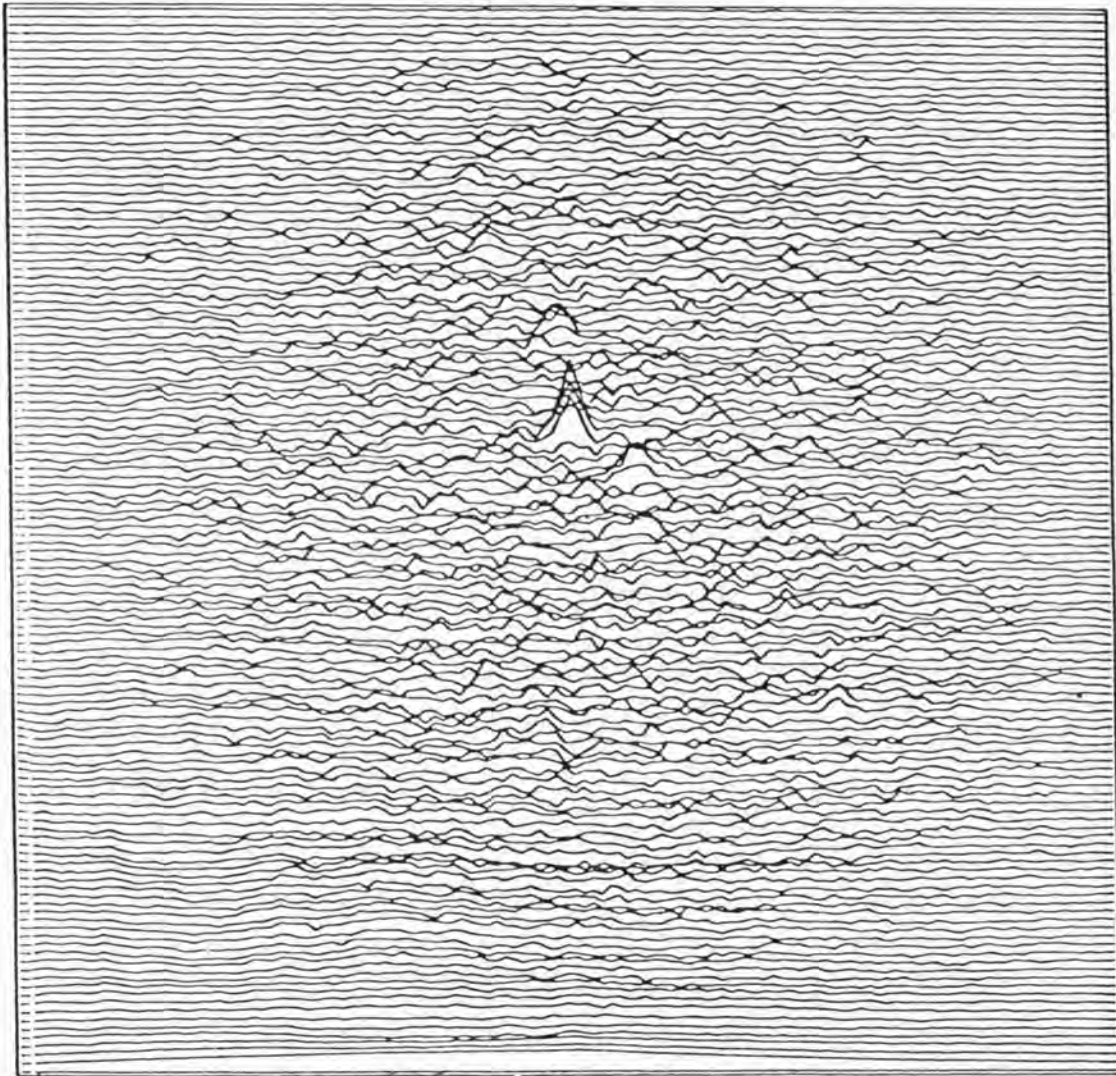


Figure 3.6.10 Simulated 100-second observation of Galactic Centre (simple camera) with finite detector response, rms = 1.0 pixels, included (cross-correlation deconvolution). Note: distinct blurring and loss in signal to noise is visible compared to Figure 3.6.9 and 3.5.6.

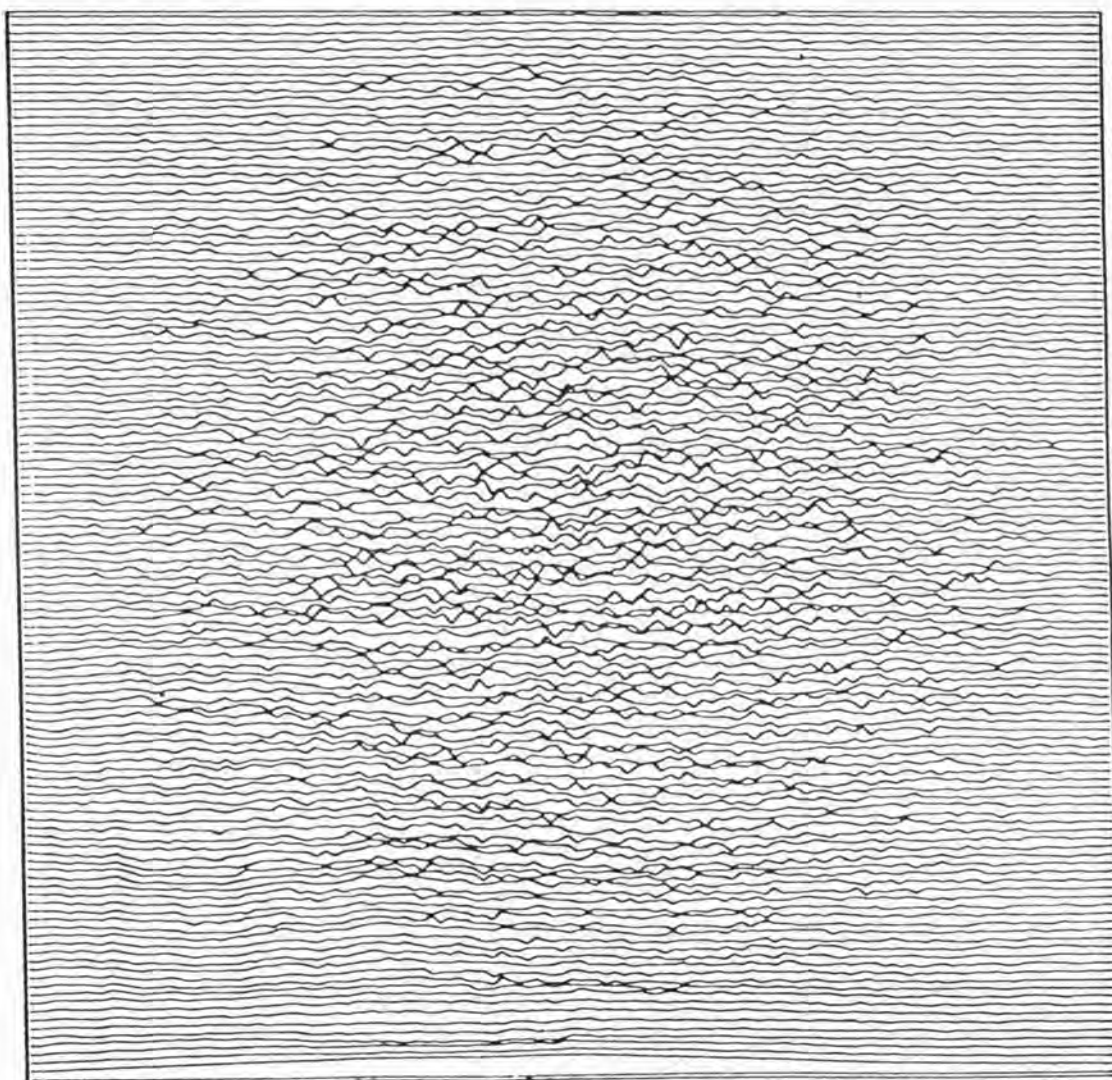


Figure 3.6.11 Simulated 100-second observation of Galactic Centre (simple camera) with finite detector response, rms = 2.0 pixels, included (cross-correlation deconvolution). Note: no sources are visible. 2 real sources are present on PHA of image.

A full computer model of the shadow camera is possible and should be undertaken in order to check scaling and the results presented in this work, as many reasonable approximations were introduced for simulation purposes. Work along these lines is being undertaken at the University of Utrecht, Holland, by Dr. A.C. Brickman and J. Heise. Their work so far bears out all conclusions which can be reached using the model in this work (private communication).

The work described here has shown that the advanced methods of deconvolution, Wiener Filter, Maximum Entropy Method can compensate for the coding error introduced by the simple camera, compared to the cyclic under all simulation conditions.

The simple camera is in fact more sensitive on average than the cyclic camera to a random event such as a burst, even in the Galactic centre. In a diffuse background-dominated region, the simple camera is always more sensitive due to an off-axis variation in  $\sigma$  in the deconvolved image. This effect is solely due to the deconvolution method for the data, and the redundancy which exists for recognising the mask pattern. This is only true when a few sources are present. A large number of strong sources results in a source distribution, dependent off-axis variation in  $\sigma$  on top of the background variation. The simple camera has additional advantages of a better angular response for a given FOV and mask element number, and the fact that no FOV limiting collimator is required.

Various disturbing effects were introduced to the perfect camera, the effect of detector window support structure, motion, and finite detector response.

A worst case situation was taken for the window support with all sources giving equal shadow length either side of the support itself. Little difference existed between the performance of any of the chosen support (and shadow) structures. Mechanical constraints (see Chapter 4)



however suggest a circular support structure. In the case of source-dominated regions the performance of the simple camera is degraded by a large amount (cross-correlation deconvolution), but no modulation across the image occurs if the correct deconvolution is done on the data. The Wiener Filter can again improve the global rms, to values approaching the cross-correlation values for the perfect system.

The off-axis variation in image  $\sigma$  is still present with the window support. The cyclic camera with identical support structure has a worse performance than the simple camera in both Galactic centre and Coma regions, showing no variation in  $\sigma$  across the deconvolved image. The simple camera retains (and in fact improves) its sensitivity advantage over the cyclic camera.

As expected motion of a small amount can partially remove the effects of the window support in the simple camera (cross-correlation) by more complete sampling of the mask shadowgram and reduce the rms of the deconvolved image. This can lead to an increase in signal to noise ratio for sources, but not for all sources in every case.

As expected the finite response (rms) of the detector must be smaller than approximately half the mask hole size or a distinct loss in signal to noise for sources in the image results.

The effect of a varying off-axis response due to gas penetration, and an energy dependent model have not been considered.

In conclusion the simple camera has a much better performance for wide field monitoring than the cyclic case, motion of the camera actually improving its capability.

One problem has come to light, and this is the definition of sensitivity, and absolute calibration of a shadow camera. In addition to detecting any changes in a source distribution one requires to quantify these.

For all non-perfect versions of the shadow camera how does one define sensitivity, and source detection? An arbitrary definition of



$\geq 60$  global or local for a source can be made. Simulations show that almost no false sources of this size exist. Calibration of source strength is a major problem, due to the interactions of the source distribution and camera effects, even for the cyclic camera (with window support). The reconstructed count depending entirely on these interactions. J. Heise of Utrecht is currently investigating these problems for the X-80 mission study.

Several practical deconvolution problems also exist for the shadow camera. Firstly software is needed to handle the data from the shadow camera, enabling the correct deconvolution, allowing for all effects to be done efficiently. Secondly, the necessary hardware and storage facilities to deal with the large volume of data, are required, together with a fast efficient computer to process the data.

Despite these problems, the shadow camera is a most efficient device capable of wide field monitoring of the X-ray sky, enabling many timescales of variability to be studied.

## CHAPTER 4

### THE IMAGING PROPORTIONAL COUNTER

#### 4.1. Introduction

Although many X-ray imaging devices are now available, micro-channel plate cameras, CCD's, and gas scintillation imaging counters, only one type, the Imaging Proportional Counter (IPC) has been built with relatively large areas and shown good reliability and stability in its performance characteristics. Hence the IPC at present appears to be the best imaging detector for the shadow camera.

This chapter will briefly review the principles and construction of an IPC, and discuss some of the design requirements for a prototype shadow camera. The topics of counter efficiency, electrostatics and gas mixture will be covered. The theory of the two methods of position sensing used in this work will be reviewed in detail. Finally other possible future detectors for the shadow camera will be discussed.

#### 4.2. Advantages and Disadvantages of the IPC

The proportional counter has been one of the traditional instruments of X-ray astronomy for the medium energy range ( $\sim 1$  to 20 keV). Recently, however, developments in theory and technology have made it possible to determine position as well as photon energy. The proportional counter has several important theoretical and practical advantages for imaging work:

- (a) The IPC has a large gas gain, giving a large output charge  $\sim 10^6$  electrons per photon detected, that is, it can have a very good signal to noise ratio for the position encoding method.

- (b) The IPC is very adaptable in its shape and size; large areas of the order of hundreds of square centimetres have been built.
- (c) A good detection efficiency, almost 100%, over a chosen energy range can be achieved.
- (d) A proportional counter has moderate energy resolution; hence a source spectrum can be determined.
- (e) A good detection area to weight and depth ratio can be achieved.
- (f) A working life of greater than  $10^8$  integrated counts, and a good rate capability of  $\sim 10^3$  to  $10^4$  counts per second over 1 mm of anode length is possible.
- (g) The operation is essentially low noise, apart from ambient background radiation. The reasonably low capacitance of the device contributes to a low noise position encoding scheme by reducing the noise contribution of preamplifiers and electronics.
- (h) The power consumption of a proportional counter is essentially negligible, in that room temperature operation occurs, and low power electronics are used.

The device of course has several disadvantages:

- (a) A finite absorption depth for X-rays exists in the gas. This, with other gas effects, for example diffusion of secondary electrons produced after the primary ionisation, can produce positional uncertainty and image blurring. These effects can however be reduced by choice of the detector gas filling.

- (b) The output charge is proportional to the incident energy.

Hence a counter operating over an energy range of an order of magnitude (say 1 to 10 keV) will give 1/10 of the charge, at the low end of energy range, that it does at the upper end. Hence the positional resolution, which is essentially governed by signal to noise in any readout system, will also vary by a factor of 10, assuming no other effect comes into play. (Such an effect was encountered during the work, and will be discussed in Chapter 6.) The counter design must therefore take into account the variation of position resolution with energy and must be optimised for the required energy range.

- (c) Most designs involve grid type electrodes, and therefore require a much higher voltage than for a single wire counter for a given gain. A trade off must occur between position and energy resolution, and a lower gain and a more stable device, as a counter will only be semiproportional at high gains, and may be liable to breakdown problems.

The imaging proportional counter has now been flown in a variety of forms and designs on several X-ray astronomy satellites or rocket payloads. The first practical use being on board Ariel V, the all sky monitor using a one-dimensional position sensitive IPC (Holt 1976). Other payloads have used the IPC as an imaging detector; Skylark 1501 (see Chapter 2), the first flight of a shadow camera (Procter et al 1978, 1979); MIT/Leicester University rocket flights of a grazing incidence telescope imaging supernova remnants (Rappaport et al 1979, Levine et al., 1979); and HEAO-B the Einstein Observatory (Humphrey et al., 1978).

The IPC has seen considerable development work since its first flight. However most work has concentrated on IPC's for grazing incidence telescopes. The work presented in this thesis will discuss an IPC

suitable for the shadow camera.

#### 4.3. Basic Principles of the IPC

Although the basic theory of proportional counters has been covered by many authors (Snell 1962 amongst others), the principles of an IPC for X-ray astronomy have not been adequately reviewed. This section will discuss the basic technology and principles of the IPC.

Consider Figure 4.3.1 a schematic cross-section through a typical imaging proportional counter. The counter can essentially be split into two separate volumes, the drift region, and active region. The drift region consists of a layer of gas with uniform electric field existing between the window and top cathode. This region can serve two purposes; first it acts as a 'stopping' or conversion region for the X-rays. That is, most counters are designed such that nearly all (required) X-ray absorption occurs in this region, eliminating any effects due to X-ray absorption above and below the anode. Secondly, the region may serve to spread the electron cloud which results after the primary ionisation, enabling quantisation effects in position sensing across the anode to be eliminated by avalanches occurring on more than one anode wire. The centroid of the electron cloud retains the original position at which the photon was absorbed, because of the electric field configuration (non-diverging).

The active region consists of the anode plus any position sensing electrodes, and any field grids that may be present in a particular design.

In principle, the detector therefore works as follows; an X-ray photon enters through a nearly (X-ray) transparent window and is absorbed; in the drift region, producing a primary ion pair. The electron of the pair absorbs most of the X-ray energy. This initial pair then creates approximately  $n$  ion pairs where

$$n = h\nu/W$$

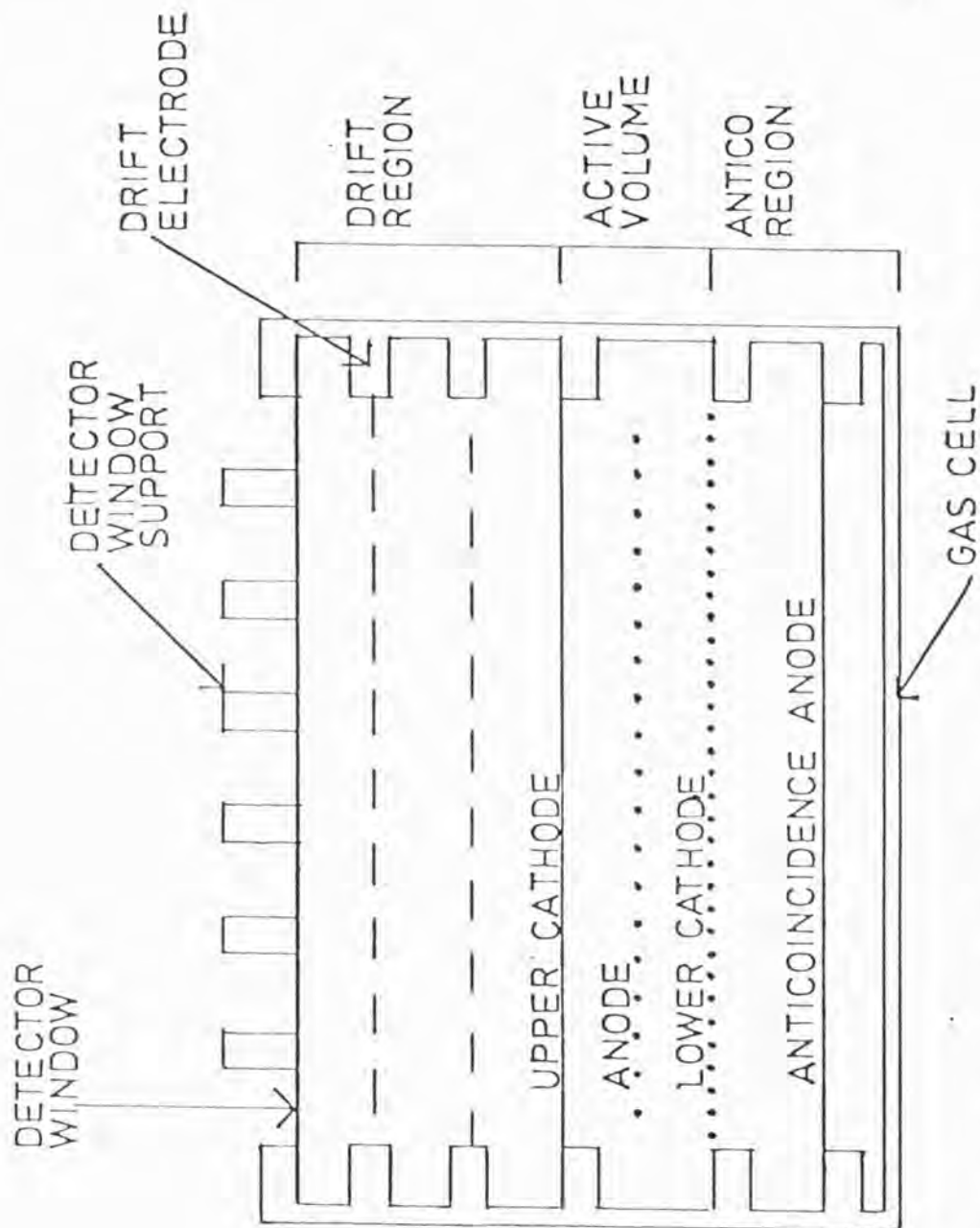


Figure 4.3.1 Schematic cross-section of a typical IPC showing component parts.  
 (An anticoincidence anode is included in most designs for cosmic ray background rejection).



where  $h\nu$  is the energy of the photon

$W$  is the ionisation energy of the counter gas.

(Note that the detailed physics of the interaction process for an initial prototype of an IPC for the shadow camera will be dealt with in Chapter 6.) This electron cloud then drifts slowly down the counter towards the anode, diffusing outwards as it moves. The electrons, on entering the intense field region around the anode wires, avalanche, producing a pulse on the anode, the peak height being proportional to the X-ray photon energy (assuming the counter is operated in the proportional mode).

In addition because of the movement of positive ions and electrons an induced charge will occur on each of the cathodes. The position of the photon is usually determined from this induced charge, by having each cathode consisting of a set of wires forming a plane, perpendicular to the other, so that each by some position sensing method may provide one co-ordinate.

The position sensing methods used can be divided into two types; those that shape or delay the induced charge distribution, and those that measure amplitudes alone. The purpose of each method is to locate the centroid of charge distribution.

The 'shaping' methods have taken two distinct forms; one involves using an electrode of high resistance and observing the risetime or amplitude of the pulses at each end of the electrode. The second uses a delay line measuring time differences at each end.

The 'amplitude' methods all involve measuring amplitudes of the induced charge distribution on single wires, or planes of wires joined in a particular pattern. The simplest system involves two cathodes each split in half, hence giving two co-ordinates; the most advanced (complicated) involves a separate readout for every wire in the detector, and use of a computer to determine photon position.

A review of position readout schemes is given in section 4.5 of this chapter.

The 'shaping' methods have until the present been used in all flown IPC designs, because of the early practical development of the method. The resistive line method is complicated by the inter-grid capacitance between the anode and cathode (or any field grid) making the behaviour of the system hard to predict theoretically. However the recent work by Fraser 1980 on resistive-capacitive encoding has eliminated many of the theoretical problems, enabling 'optimum' readout systems to be designed.

The 'amplitude' methods at present have had little detailed development work and use, but show promise for future instrumentation.

#### 4.4. Gas Choice for the IPC

Because of the energy range of the shadow camera a long X-ray absorption depth in the IPC gas will produce blurring of the resulting image. Hence the prime requirement for the gas is good X-ray absorption.

X-rays entering a proportional counter are absorbed by the photoelectric effect. A noble gas is used because of the low ionisation potential and hence high initial ionisation, and high obtainable gas gain. For good performance of a counter one requires a low  $Z$  window, and a high  $Z$  gas.

The counter gas efficiency is best characterised by the photoelectric absorption length, also known as the  $1/e$  depth; defined as the length of gas required to reduce the initial number of photons to  $1/e$  ( $\sim 0.368$ ) of their original number. Figure 4.4.1 plots the absorption length as a function of energy for the noble gases (Argon, Krypton, Xenon).

One can see that Xenon has the best overall performance. Krypton is not suitable due to contamination by the radioactive isotope  $Kr^{85}$  since the atomic bomb atmospheric testing occurred. In the shadow camera one has the problem of photons at large angles of incidence to the normal. In order to avoid problems (blurring of images) due to the finite absorption

# ABSORPTION DEPTH (1/E) (MICRONS)

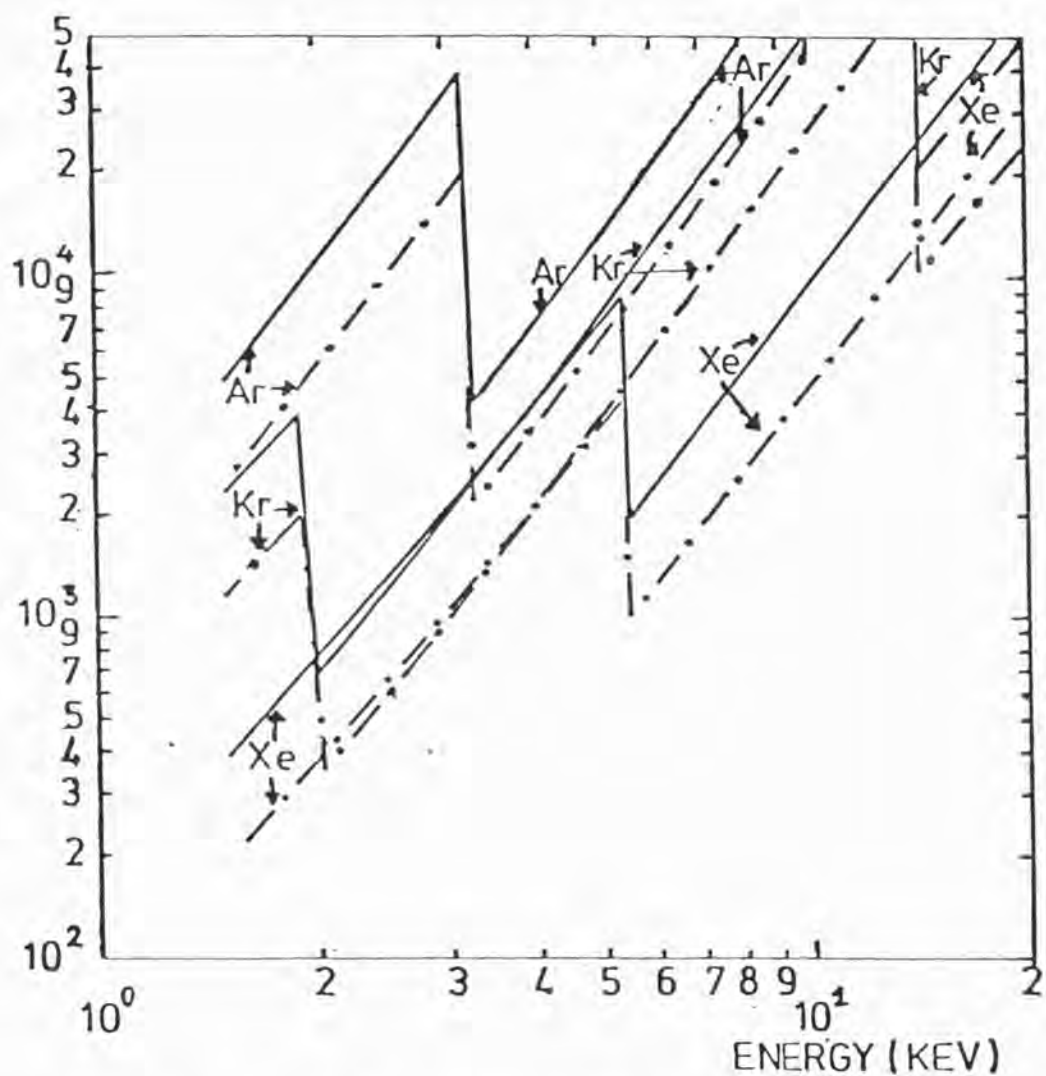


Figure 4.4.1 The 1/e absorption depth as a function of energy for Argon (Ar), Krypton (Kr), and Xenon (Xe). 1 atmosphere pressure solid line, 2 atmospheres dotted line.

depth, the counter gas has to be highly efficient; the efficiency of absorption can be further improved by pressurising the counter gas to higher than atmospheric pressure (the dotted lines on Figure 4.4.1).

Most proposed designs of shadow camera as reviewed in Chapter 2 have chosen Xenon as the counter gas. This work will describe a prototype IPC and results obtained using Xenon, to assess the performance characteristics of this gas. The rest of this section devotes itself to the choice of window material, quench gas and characteristics for a Xenon IPC counter gas mixture.

#### 4.4.1. Choice of Window Material

For the soft X-ray region ~0.1 to 1.5 keV, organic windows and Argon gas mixtures have been used (see for example Humphrey et al., 1978). One can in principle use an organic window with Xenon, extending a counter's lower energy limit, but severe practical problems have been found with this approach, as Xenon counters have been found to require very high levels of gas purity. In addition such a system, due to the high diffusion leak rate through such a window, requires a gas flow system. Most designs of IPC for the shadow camera have adopted Beryllium as the window material, due to its low density and photoelectric cross-section. In addition Beryllium can be produced in vacuum tight sheets enabling a sealed counter to be produced.

The detection efficiency of a counter may be calculated from the following formula:

$$\eta(E) = e^{-\mu_w(E)t_w/\cos(i)} \cdot (1 - e^{-\mu_g(E)t_g/\cos(i)}) \quad (4.4.1)$$

where  $\eta(E)$  is the detection efficiency

$\mu_w(E)$  the linear absorption coefficient of the window

$\mu_g(E)$	the linear absorption coefficient of the counter gas
$t_w$	the thickness of the window film
$t_g$	the thickness of counter gas
$i$	the angle of incidence of the photon.

$\eta$ ,  $\mu_w$ ,  $\mu_g$  are all functions of the energy ( $E$ ) of the incident X-ray photon.

Figure 4.4.2 shows the overall efficiency of a 2 cm deep Xenon filled counter for various thicknesses of Beryllium window and atmospheric pressure, as a function of incident photon energy. The required thickness of window material is of course a compromise between practical design requirements, as discussed in section 4.6, and energy range requirements.

#### 4.4.2. Choice of Quench Gas

In a proportional counter or IPC a quench gas must be present for stable operation. The quench traditionally is believed to absorb ultraviolet photons produced by excited atomic or metastable states in the avalanche process; these photons unless absorbed can cause secondary avalanching and non-proportional operation of the counter (Snell 1962). In addition the quench speeds up electron drift, and reduces the problem of electron capture. The addition of the quench gas, usually a polyatomic molecule, enables a counter to work at a high stable gain, unlike a pure noble gas filled counter. One requires to keep the percentage of quench as low as possible in order not to reduce the efficiency of the counter due to the lower density resulting from the addition of the quench, and low photoelectric cross-section of the quench constituents.

A variety of gases can be used as a quench, the 'traditional' gases being methane and carbon dioxide, although nitrogen and isobutane have been used.

The exact type of quench gas to be added depends partially on the

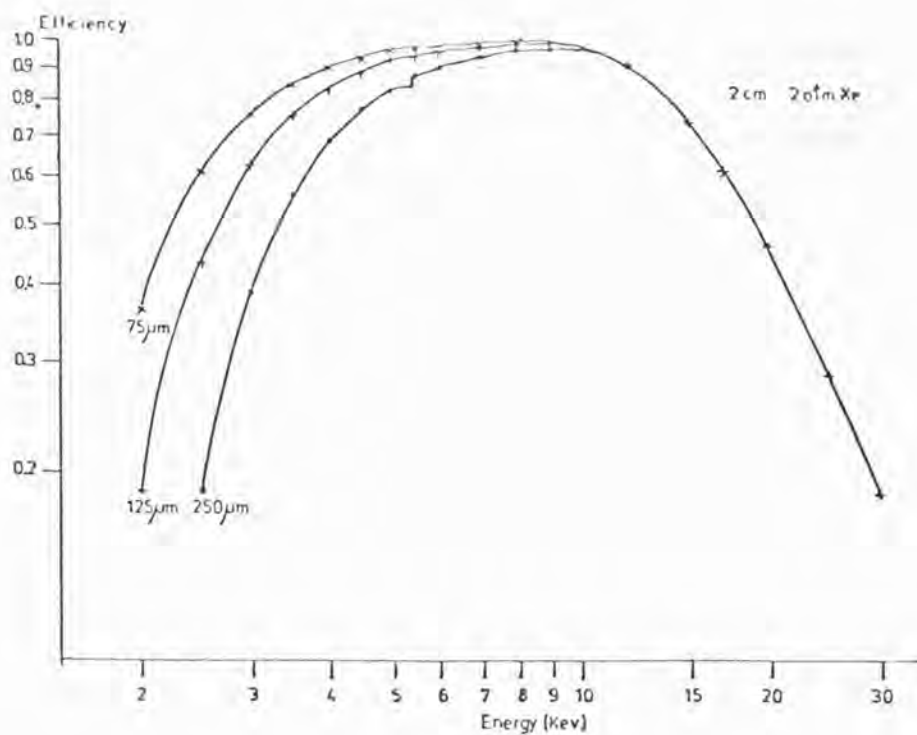
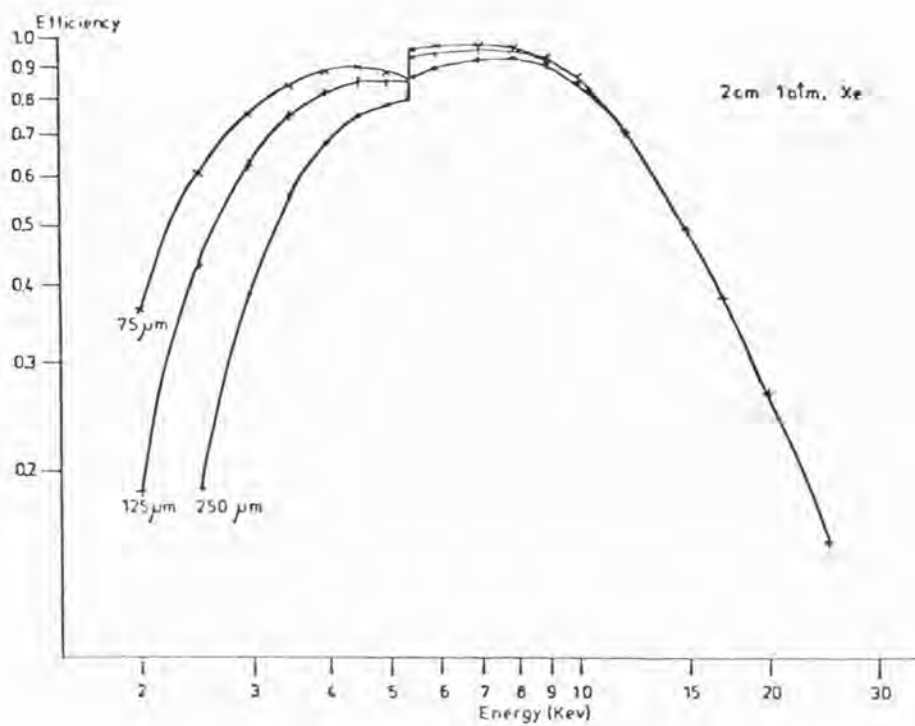


Figure 4.4.2 Efficiency as a function of energy for a 2 cm deep counter filled with Xenon at 1, and 2 atmospheres pressure, for various thicknesses of Beryllium window.



secondary light emission characteristics of the noble gas. Breskin et al., 1979 summarises the light emission for the noble gases and gives the photoionisation potential of various quench gases. The quench gases discussed are carbon dioxide, methane, ethane, ethanol, acetone, benzene and triethylamine. In order for the quench to work at all its photoionisation threshold energy must be higher than the highest energy emitted by the noble gas to prevent photon mediated avalanches. From the data in Breskin et al., 1979, all gases but triethylamine are suitable as quenches for Xenon, whereas only the first three are suitable as an Argon quench on this criterion. This however takes no account of the actual absorption spectra of the gases. The ultra-violet absorption properties of methane will be discussed in Chapter 6 in the light of the results from a prototype IPC.

In addition the quench also prevents positive ions releasing electrons from the wall of the chamber (producing secondary avalanches) (Schnell 1962).

In summary, the quench has three effects; increase of the drift velocity of electrons; positive ion quenching; and absorption of ultra-violet light emission from the avalanche. The choice is therefore dependent on these properties. Methane has been the traditional choice for most designs of IPC. Most proposed designs of shadow camera IPC, see Chapter 2, assume the use of this gas. Work on Xenon, for example Gorenstein et al., 1979, has shown the necessity of pure gas mixtures with low levels of contaminants. Xenon/methane mixtures having a larger drift velocity than Xenon/carbon dioxide mixtures (Christophorou et al., 1980) are therefore less susceptible to poisoning by electronegative contaminants. Methane was hence adopted as the quench gas for the work described in this thesis.

#### 4.4.3. Energy Resolution

The energy resolution of a single wire counter is found to be proportional to  $E^{-\frac{1}{2}}$ , where  $E$  is the incident X-ray photon energy (see for example Charles and Cooke 1968). The IPC can be assumed to be the equivalent of a number of single wire counters joined together. The theoretical energy resolution  $R$  (FWHM) is then identical to that of a single wire counter, and is given approximately by

$$R = 2.355 (1 + F)^{\frac{1}{2}} W^{\frac{1}{2}} E^{-\frac{1}{2}} \quad (4.4.2)$$

where  $W$  is the energy required to produce an ion pair and  $F$  is the Fano Factor of the gas mix (Fano 1947); assuming that the photon energy is completely deposited in the counter gas, that is fluorescent yield is ignored.

As mentioned by Charles and Cooke 1968, Sipila 1976(a) and (b) and others, in fact

$$R = 2.355 (b + F)^{\frac{1}{2}} W^{\frac{1}{2}} E^{-\frac{1}{2}}$$

where  $0 \leq b \leq 1$  so that equation (4.4.2) must be regarded as an upper limit.

Table 4.4.1 gives the relevant gas parameters for the noble gases plus common quench gases used in proportional counters. This table is adapted from Sipila 1976(a).

Hence, using the table, the theoretical resolution as a function of energy, assuming  $b = 1$ , will be

$$\begin{aligned} R &= .416 E^{-\frac{1}{2}} && \text{for Argon} \\ R &= .373 E^{-\frac{1}{2}} && \text{for Xenon} \end{aligned}$$

where  $E$  is in keV, and  $R$  is resolution FWHM. Hence Xenon, under the assumption  $b = 1$  is theoretically capable of greater energy resolution than Argon.

TABLE 4.4.1

ENERGY RESOLUTION: GAS PARAMETERS

<u>Gas</u>	W eV <u>Experimental</u>	F <u>Theoretical</u>	F <u>Experimental</u>
He	42.8	.17	
Ne	36.2	.17	
Ar	26.2	.17	.19
Kr	24.3		
Xe	21.5		.17
CH <sub>4</sub>	27.3	.26	
CO <sub>2</sub>	32.8	.32	
N <sub>2</sub>	34.3	.28	

In practice, the pulse height distribution may contain more than one peak. The second peak is called an escape peak, and occurs when the original photoelectric absorption results in an atom de-exciting by emitting an X-ray or Auger electron which can physically escape from the counter. The detailed interaction process in Xenon will be discussed in Chapter 6. The escape peak if present must be taken into account when interpreting energy information from the counter.

#### 4.4.4. Counter Gain

A detailed review of gas amplification is given by Charpak 1970. Various formula have been derived, over the years, to predict (theoretically and empirically) the gas gain from the counter design parameters and a knowledge of gas constants; Rose and Korff (Korff 1955); Diethorn 1956; Williams and Sara 1962; Zastawny 1966; Charles 1972 and Planinic 1976, amongst others. The counter gain is dictated by the electric field configuration inside the counter. The topic of electrostatics in an IPC has been covered by many researchers, Charpak 1970, Tomitani 1972 amongst others.

The Diethorn equation has been tested by Charles 1972, Hendricks 1972 and Wolff 1974 and the gas parameters derived. This equation is accurate enough for present purposes. The Diethorn equation is

$$\ln A = \frac{V}{\ln b/a} \cdot \frac{\ln 2}{\Delta V} \cdot \ln \left[ \frac{V}{K p a \ln b/a} \right] \quad (4.4.3)$$

where  $A$  is the amplification factor

$\Delta V, K$  are gas dependent constants

$b, a$  are the cathode and anode radii respectively

$p$  is the gas pressure.

The equation as stated above only applies to a single wire counter.

However, Tomitani 1972 has derived an effective  $b$  for various cathode to

anode separations ( $L$ ) and anode wire spacing  $s$ , making the formula applicable to multiwire proportional counters within certain design limits. Figure 4.4.3 shows  $\log 2b/L$  versus  $L/s$ , where  $b$  is the effective radius required for the Diethorn equation for an IPC, derived from Tomitani 1972.

Equation 4.4.3 requires a value for  $\Delta V$  and  $K$  for each type of gas mix. Wolff 1974 has measured these parameters for a variety of gas mixtures, principally Argon mixes, whilst Hendricks 1972 has published values for Xe/CH<sub>4</sub> and Xe/CO<sub>2</sub> mixtures, respective percentages being 90/10 and 95/5. Table 4.4.2 summarises the relevant results. As can be seen Xenon mixtures have a higher  $\Delta V$ , but lower  $K$  value. Substituting in equation (4.4.3) for a given  $V$ ,  $b$ ,  $a$ ,  $p$  one finds for 90/10 Xe/CH<sub>4</sub> a lower gain than 90/10 AR/CH<sub>4</sub>. This is a clear disadvantage of Xenon as a counter gas.

#### 4.4.5. Summary

Because of the energy range of the shadow camera and operating principle a long absorption length can lead to severe problems. Xenon is the clear choice for the IPC counter gas due to its high photoelectric absorption cross-section. In addition Xenon is theoretically capable of giving a better energy resolution. However problems with the use of Xenon do exist due to the slow drift velocity and lower gain for a given geometry.

Little previous work on Xenon IPC's has been done; a review will be presented in Chapter 7, presenting the need for development work, particularly in the context of an IPC for the shadow camera. Chapters 5 and 6 describe a prototype of the IPC and results from the detector. The rest of this chapter will concern position readout and design considerations of an IPC.

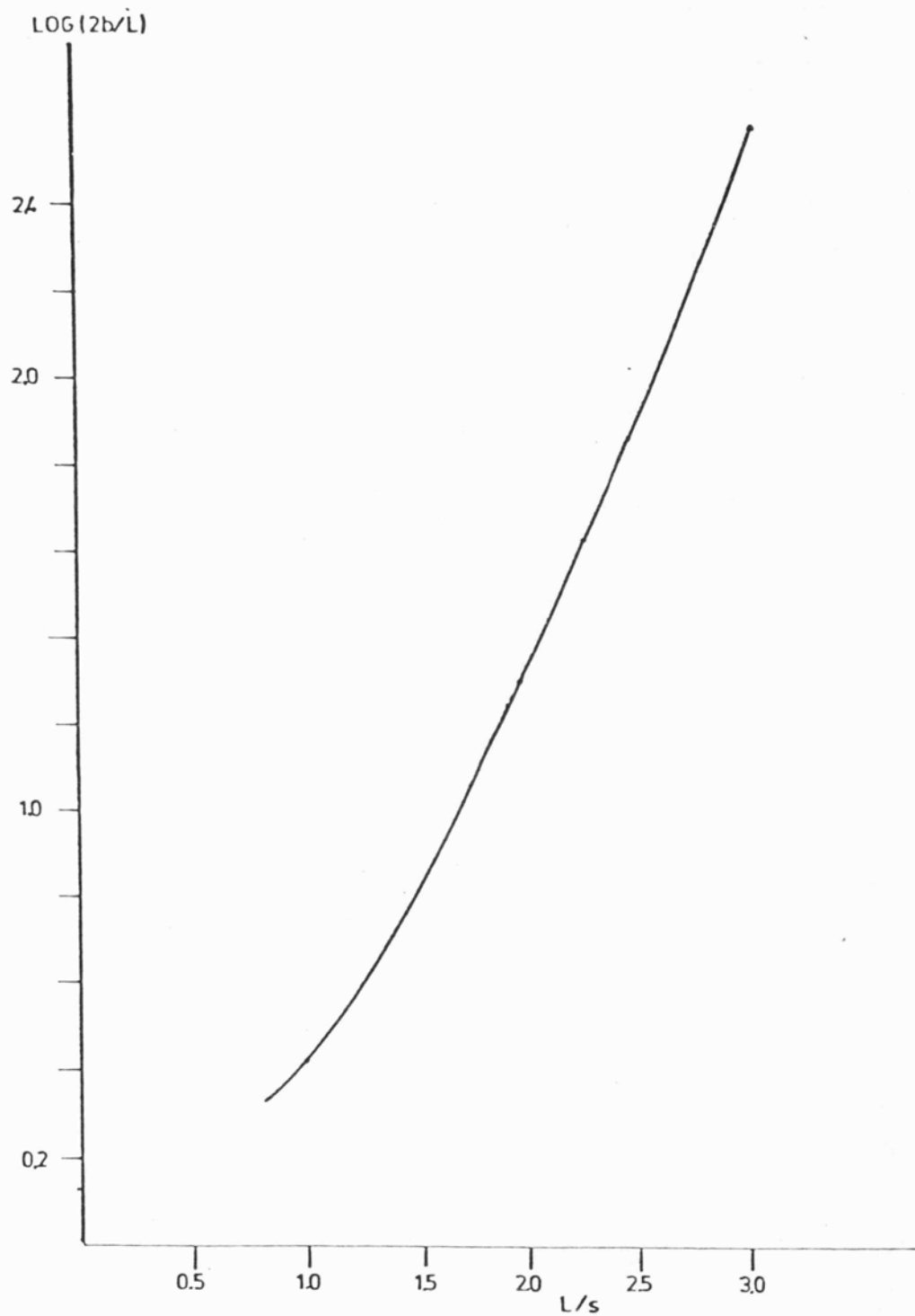


Figure 4.4.3 Relationship between cathode to anode separation ( $L$ ), anode wire spacing ( $s$ ) and  $b$  effective cathode radius, for application of Diethorn equation to multiwire proportional counters.



TABLE 4.4.2

## DIETHORN EQUATION PARAMETERS

<u>Gas Mixture</u>		<u><math>K \times 10^{-4}</math> (V/cm atm)</u>	<u><math>\Delta V</math> (eV) (<math>\pm</math> approx. errors)</u>
P10	90% Ar 10% CH <sub>4</sub>	$4.8 \pm 0.3$	$23.6 \pm 5.4$
P 5	95% Ar 5% CH <sub>4</sub>	$4.5 \pm 0.4$	$21.8 \pm 4.4$
	100% CH <sub>4</sub>	$6.9 \pm 0.5$	$36.5 \pm 5$
	90% Xe 10% CH <sub>4</sub>	3.62	33.9
	95% Xe 5% CO <sub>2</sub>	3.66	31.4

#### 4.5. Position Sensing in an IPC

Two methods of position encoding have been investigated in the course of this work, one a 'shaping' method using a resistive-capacitive line, and the second an 'amplitude' method, the graded density cathode. The history of position sensing will be first briefly reviewed before the theory of the two methods are considered in detail. Position sensing is of course possible both along and across a multiwire anode; sensing across it presents some additional problems, hence the following discussion of methods will devote most space to the encoding methods themselves. The problem of across-wire position determination is discussed last,

##### 4.5.1. Position Encoding Methods

Historically for IPC's, the 'shaping' methods were the first to be used. Risetime and timing methods can give a digital output position directly via clock pulses through a gate, and hence were developed first, as ADC's were originally costly and had heavy power requirements.

##### 4.5.1.1. Resistive-Capacitive Lines

Borkowski and Kopp 1968 described position encoding in a variety of detectors using high resistance collectors. This work was based heavily on position encoding in semiconductor detectors by Owen and Awcock 1968, Kalbitzer and Meltzer 1967, and others,

The collector in the case of the proportional counter built by Borkowski and Kopp 1968 was the anode wire. Position was determined by measuring the risetime of the anode pulse via the resistive line. The risetime is independent of charge and dependent on position in such a system. In order to measure the risetime a start signal is necessary; this was provided in the original paper by a sense wire placed close to the

resistive anode.

The technique was further developed by Borkowski and Kopp (1972) themselves as well as other authors, for example Christie et al., 1976.

In its final form the technique consists of measuring the output pulse waveform from each end of a resistive line (continuous wire, wires joined with discrete components, lumped components or continuous film). The difference in risetime or pulse height ratio (following filtering) at each end is found to be proportional to the position at which charge injection occurred.

The topic of RC position encoding is covered in full detail by Fraser 1980. The method can be used on the anode itself, the whole anode forming a resistive line or sheet, or using the induced charge distribution on the cathodes. The second type has tended to become the standard procedure, where the anode only is used to provide energy information.

Sanford et al., 1979, have used an extension of the RC technique by making the anode a resistive sheet and measuring co-ordinates by use of four pick-up points. The ratio of the pulse heights determines the position.

#### 4.5.1.2. Delay Line Readout

The other 'shaping' method used extensively is the delay line readout pioneered by the work of Grove et al., 1970, Parker et al., 1971, Kaplan et al., 1973, and Radeka 1974.

The basic system uses cathodes and induced charge distributions for position sensing. The cathode wires are isolated by resistors from a fixed potential to allow a voltage signal to occur on them. This is communicated to a delay line by capacitive or direct coupling.

Position sensing is achieved by timing, the anode signal or one end of the cathode providing a start pulse, and the arrival of the cathode pulse at one end of the line providing the stop pulse. The time difference is

then uniquely related to the position of the induced charge distribution.

Both RC and delay line methods of course do not see a spatial delta function of charge but see a charge distribution and therefore measure the centroid of that distribution.

Figure 4.5.1 shows the basic configuration of a delay line readout scheme. The delay line readout has been used extensively in biomedical imaging (for example Kaufman et al., 1972), and particle physics (for example, Breskin and Zwang 1978). The problem is to construct an accurately uniform electromagnetic delay line. The system however has a distinct advantage over any 'amplitude' methods in that a large range of pulse heights does not matter, as only timing is required, in principle giving the system a large dynamic energy range.

#### 4.5.1.3. The Amplitude Methods

The amplitude methods of counter readout have been pioneered by the CERN group (see Charpak and Sauli 1979 for a review). The true 'amplitude' methods involve no signal shaping at all. However the RC line, ratio of pulse heights could itself be thought of as an 'amplitude' method. In its most complex form, the 'amplitude' method consists of attaching each cathode and anode wire or group of wires to a separate amplifier and measurement chain. The centroid of the charge distribution is then calculated directly using a computer (Breskin et al., 1977). Figure 4.5.2 shows the basic configuration of this readout scheme. This system has produced position resolutions  $\sim 60 \mu\text{m}$  FWHM along the anode wires.

Other amplitude methods Gatti et al., 1979, Mathieson et al., 1980, Reid et al., 1979, have used cathode wires joined in chosen groups, the ratio of pulse heights giving the centroid. These methods require less electronics and less sophisticated signal processing, and hence are more applicable to X-ray astronomy instrumentation, because of spacecraft payload limitations.

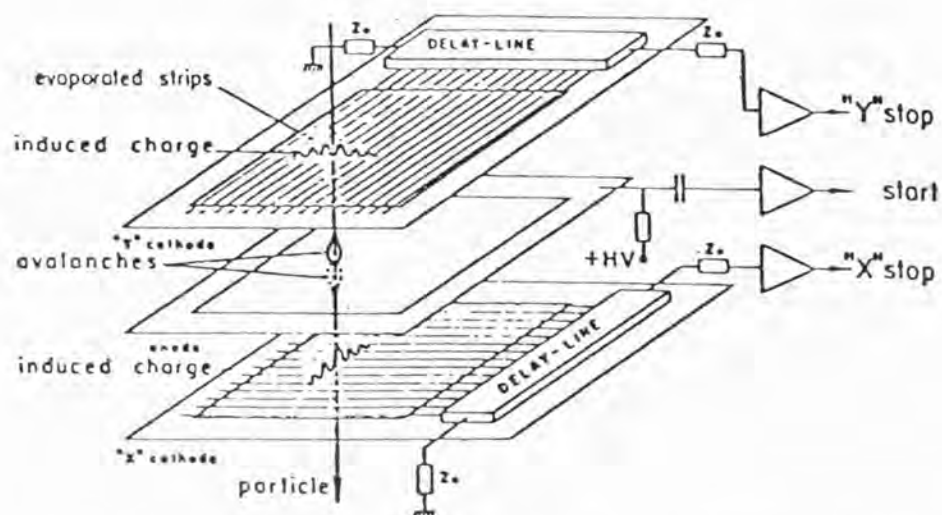


Figure 4.5.1 Principle of delay readout from IPC. (From Breskin and Zwang 1978).

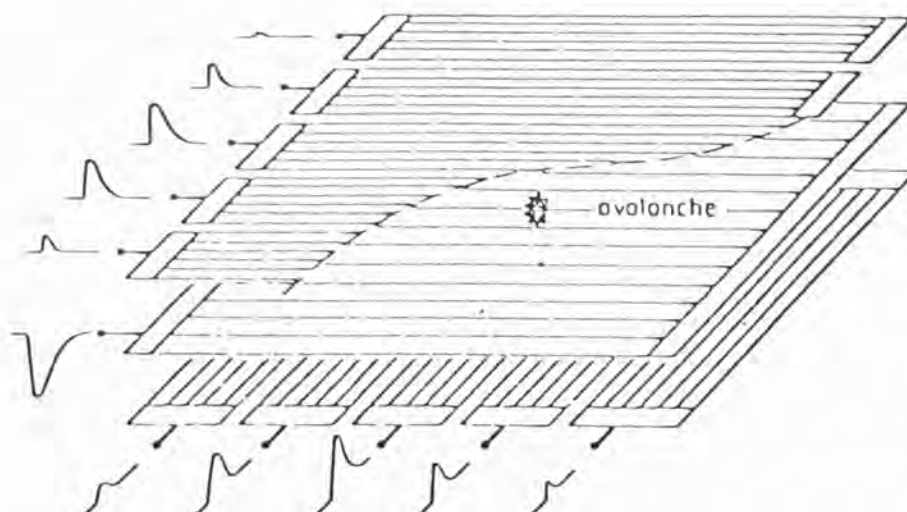


Figure 4.5.2 Principle of one 'amplitude' method; avalanche centre of gravity readout method. The avalanches surrounding a wire induce a positive pulse on the cathode strips. The pulse height of the induced pulse is measured and stored for each cathode strip, and the centre of gravity of pulse height distribution is computed giving the position of the avalanche. The two cathode planes are equipped with strips parallel and orthogonal to anode wires giving the two co-ordinates. (From Breskin et al 1977).



The 'amplitude' method is often called the cathode induced charge centroid or centre of gravity readout scheme in the literature.

During this work two methods of position encoding for an IPC have been investigated, the RC line and the graded density cathode. The first is a 'shaping' method, the second an 'amplitude' method.

#### 4.5.1.4. Across Anode Position Sensing

Whatever readout method is used however, one has the problem of across anode wire position sensing. This is a major problem in the development of a true two-dimensional detector. Along the wire, avalanches can form at any point, whereas in the perpendicular direction, avalanches can only form on a wire, leading, without an interpolation effect, to quantisation in spatial location of the anode wire pitch. Two methods are available to overcome this deficiency. The simplest method is to make an avalanche occur on more than one wire, by spreading the initial electron cloud sufficiently in a drift region, and choosing the anode wire spacing such that avalanches occur on two or more wires. This can give a direct interpolation effect leading to a continuous spatial resolution across the anode wires.

The second scheme is to use the effect of angular localisation of the anode avalanche. For a considerable time it was thought that an avalanche would naturally develop uniformly all the way round a wire. However this is not always the case; the avalanche can show quite strong angular localisation (see for example Fischer et al., 1978(a)(b), Harris and Mathieson 1978). This effect has been used by Charpak and his group (see review of Charpak and Sauli 1979) to provide spatial resolution across the wires, by using amplifiers attached to every wire. The induced charges on neighbouring wires enable the angle at which an avalanche occurs to be read (wire shielding effect), providing spatial information across



the wires. Accuracies of about  $5^\circ$  for 2 mm wire spacings have been achieved, leading to spatial resolutions  $\sim 150 \mu\text{m}$  ( $\sigma$ ) across the wires.

Another approach to the problem is to effect position sensing both along and across the wires simultaneously. This has been achieved by placing the anode at  $45^\circ$  to the two cathode sense directions. Quantisation effects then occur to a lesser extent in both directions (for example Bateman et al., 1976).

The prototype described in this work utilises a small drift region in order to investigate anode wire localisation problems in Xenon-methane gas mixtures.

#### 4.5.2. RC Position Encoding

Fraser 1980 reviews in detail the theory and previous work on RC position encoding for position sensitive X-ray astronomy detectors. This section will only describe the elements of the theory and computer models of Fraser 1980 and the implications for practical design.

In a real detector the resistive part of the position encoding scheme is provided by the position sensing electrode, and the capacitance arises from the detector geometry and construction. The following equation, a form of the Diffusion equation, gives the voltage at time  $(t)$  co-ordinate  $x$  in a RC line;

$$\frac{\partial V}{\partial t}(x,t) = \frac{L^2}{RC} \frac{\partial^2 (V(x,t))}{\partial x^2}$$

This equation is known as the Telegraphy equation. Fraser 1980 has solved this equation and derived the fundamental parameters for the model system shown in Figure 4.5.3. One requires the voltage  $V_o(t)$  at the output of a filter network. The system consists of a resistive line of length  $L$ , with total resistance  $R$  and distributed total capacitance to earth  $C$ , terminated at each end by a capacitance  $C_d$ . Each end of the line



is then connected to a charge sensitive preamplifier with feedback capacitor  $C_o$ , finally linked to a filter with  $|H(j,\omega)|^2$  as the filter function.

In order to create a universal model system, a parameter form for the primary system variables has been developed. The working variables are:

$$\begin{aligned} X' &= X/L \\ CDC &= Cd/C \\ T &= Ta/(RC/\pi^2) \end{aligned}$$

where  $Ta$  is the filter integrating time constant, and the system is symmetric about  $X/L = 0.5$ . The most commonly used filter is a three-element passive filter, doubly differentiating and singly integrating, producing a bipolar output. This filter was considered (with filter time constants,  $S_1, S_2, Ta$ ) in detail.

In the model system a delta function of voltage was injected, that is a step function of charge ( $q_o$ ). The output  $V_o(t)$  can be manipulated to extract four parameters, approximately linear with injection co-ordinates  $X$  and dumped charge  $q_o$ . The general shape of the output waveforms from a RC line is shown schematically in Figure 4.5.4. The four parameters are:

$$\begin{aligned} \text{Timing} & \left\{ \begin{array}{l} \text{(i) Zero cross time } t_X \\ \text{(ii) Difference zero cross time } T_X = t_X - t_{1-X} \end{array} \right. \\ \text{Ratio} & \left\{ \begin{array}{l} \text{(iii) Amplitude ratio} \\ \qquad q_X = V_{1-X}/(V_X + V_{1-X}) \\ \text{(iv) Difference ratio} \\ \qquad Q_X = (V_{1-X} - V_X)/(V_{1-X} + V_X) \end{array} \right. \end{aligned}$$

Practically,  $t_X$  is highly nonlinear, so methods (ii) and (iii) have been adopted for most work.

A computer program was developed to generate, knowing the system parameters, the parameters  $T_X$ ,  $q_X$  and  $Q_X$ . From these parameters the

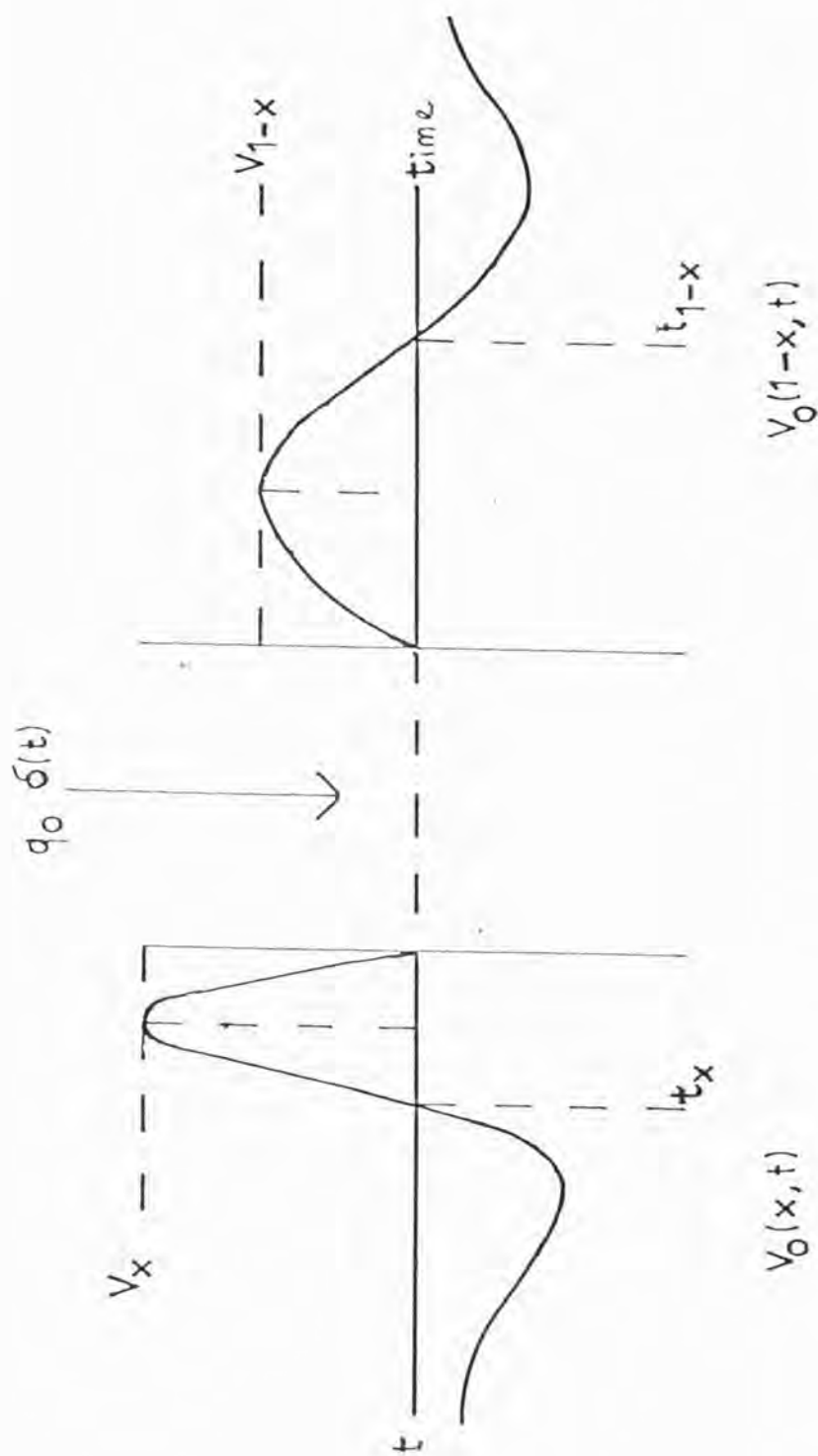


Figure 4.5.4 Schematic output waveforms, after filtering, from model RC system depicted in Figure 4.5.3. (Voltage as a function of time).  $V$  and  $t$  represent pulse heights and zero cross time respectively for each waveform from each end of model system.

sensitivity (function derivatives with respect to position), rms non-linearity (rms deviation from straight line fit to sensitivity), and resolution as function of position can be derived, enabling a RC system to be evaluated.

From this model an optimum theoretical RC readout scheme can be chosen. First, however, two further parameters must be defined. It can be shown (Fraser 1980) that the fractional resolution of a line is given by

$$\Delta x = \frac{1}{q_0} D(x,T) \sqrt{C k T_e \mu(T,CDC)^2 + q_a^2} \quad 4.5.1.$$

where  $C$  is the line capacitance

$T_e$  is the absolute temperature

$k$  is Boltzmann's constant

$q_a$  is the rms noise charge due to the preamplifier  
loaded with  $C$

$q_0$  is the charge dumped on the line

$D(x,T)$  is a dimensionless function of  $T$  and  $x$

$\mu(T,CDC)$  is a dimensionless function of  $T$  and  $CDC$ .

The position resolution as shown in the above equation arises from two distinct terms; firstly it is limited by the thermal noise from the RC line and secondly by noise from the preamplifier. In the case of line noise dominating the above reduces to

$$\Delta x = \frac{1}{q_0} \mu D (k T_e C)^{\frac{1}{2}}$$

For a fixed counter electrode capacitance  $C$  and operating temperature  $T_e$ , the product  $\mu D$  defines the resolution. The approach that has been adopted (Fraser 1980) is to optimise for the middle 85% of the line length, using mean values of  $\mu(T,CDC)$  and  $D(x,T)$ , called  $\mu$  and  $D_m$  respectively, the optimum line having smallest resolution compatible with a low rms non-linearity.

#### 4.5.2.1. Zero Cross Timing Optimum

The minimum value of  $\mu D_m$  for zero cross difference timing is found to occur at  $T = 1.68$ ,  $CDC = 0.2$  with a value of 1.61 with a rms non-linearity value  $\sim 1\%$ . The resolution however has a shallow minimum. It is compatible with non-linearities of  $1\%$ , and is approachable to within  $1\%$  of  $0.3\%$  theoretically in the region

$$1.4 \leq T_{OPT} \leq 2.0$$

$$CDC_{OPT} \approx T/5.5$$

where  $T_{OPT}$  and  $CDC_{OPT}$  represent the optimum theoretical values of  $T$  and  $CDC$ . The minimum value of  $\mu D$  at the line centre occurs at open circuit

$$CDC \leq 0.1 \quad \text{and} \quad T \approx 0.6.$$

The optimum zero cross line then theoretically can be shown to give a limiting performance averaged over the central 85% of the line of

$$(\Delta x)_m = 1.024 C^{\frac{1}{2}} q_o^{-1} \mu\text{m/cm of line length}$$

where  $C$  is in picofarads

and  $q_o$  is in picocoulombs

assuming  $T_e = 293 \text{ K}$  or  $20^\circ\text{C}$ .

#### 4.5.2.2. Ratio Optimum

In terms of resolution, the two ratio methods can be shown to be equivalent. The minimum of  $\mu D_m$  is again shallow; the minimum value is found to be 0.895 at  $T = 1.2$ ,  $CDC = \infty$ , that is, short circuit (Fraser 1980). The minimum value of  $\mu D$  (0.772) at line centre occurs at short circuit,  $T = 0.8$ .

The optimum ratio line gives a limiting performance (central 85%) of

$$(\Delta x)_m = 0.569 C^{\frac{1}{2}} q_o^{-1} \mu\text{m/cm of line length.}$$



#### 4.5.2.3. Other Theoretical Considerations

If one compares the performance of the position encoding methods, Fraser 1980 has shown that the amplitude method of encoding is theoretically superior to the zero cross timing difference method by a factor of 1.8 in terms of resolution. In addition the ratio encoding method is exactly linear in the limit  $T \rightarrow \infty$   $CDC \rightarrow \infty$ . This optimisation only applies to the standard bipolar filter (doubly differentiating and singly integrating).

#### 4.5.2.4. Practical Points

The above gives the theoretical optimum values for  $T$  and  $CDC$  which can be converted into detector parameters using

$$CDC = Cd/C$$

$$T = Ta/(RC/\pi^2)$$

enabling an optimum readout system to be designed for a given detector.

In a real system  $q_a$  is never small so a true line noise dominated system never exists. However, the ideal practical approach is to adopt the above values for  $Cd$ ,  $Ta$  and  $R$  for a given design and attempt to reduce the amplifier noise contribution, although an optimisation procedure is given in Fraser 1980 for a known  $q_a$ .

Unfortunately the work of Fraser was not completed before construction of the prototype IPC and hence a trial and error process was adopted for the line parameters. The above theory will be compared with results from the prototype detector in Chapters 5 and 6.

#### 4.5.3. The Graded Density Cathode

The 'amplitude' method used in this work is the graded density cathode of Mathieson et al., 1980. This method only uses two signal

channels, and hence was investigated due to its low noise, and simplicity compared with other methods (a large advantage in the case of X-ray astronomy experiments with limited spacecraft resources). The method obtains position information by noting the fraction of charge induced on two specially tailored components of a divided cathode. The principle of operation is very similar to the wedge-shaped 'backgammon' cathode by Allemand and Thomas 1976, but has two distinct advantages: firstly, the cathode is simple to construct, and secondly, it is also transparent to X-rays and electron clouds. The basic theory of position encoding only will be presented here (adapted from Mathieson et al., 1980); the noise theory and hence predicted resolution and further developments of the graded density cathode will be covered in Chapter 6, in the light of the prototype detector results.

The graded density cathode consists of a planar set of uniformly pitched wire of constant diameter. The wires are divided and joined into two groups A and B, such that the linear density (that is number per unity length across the cathode) varies in a specific manner. Consider the case of the linear density of group B,  $\rho_B$ , such that it increases approximately linearly with position  $x$  across the cathode, while group A density,  $\rho_A$ , decreases. Let

$$\rho_B \approx N \left\{ \frac{1}{2} + a \left( x - \frac{1}{2} \right) \right\}$$

$$\rho_A \approx N \left\{ \frac{1}{2} - a \left( x - \frac{1}{2} \right) \right\}$$

where  $N$  is the total number of wires and  $x$  is the distance normalised to the total width. The principle is indicated in Figure 4.5.5, taken from the paper by Mathieson et al., 1980.

Provided each group is connected to a virtual earth (a charge sensitive preamplifier in practice), as the pitch of the wires remains constant, then the cathode is identical both electrostatically and geometrically to an ordinary cathode.

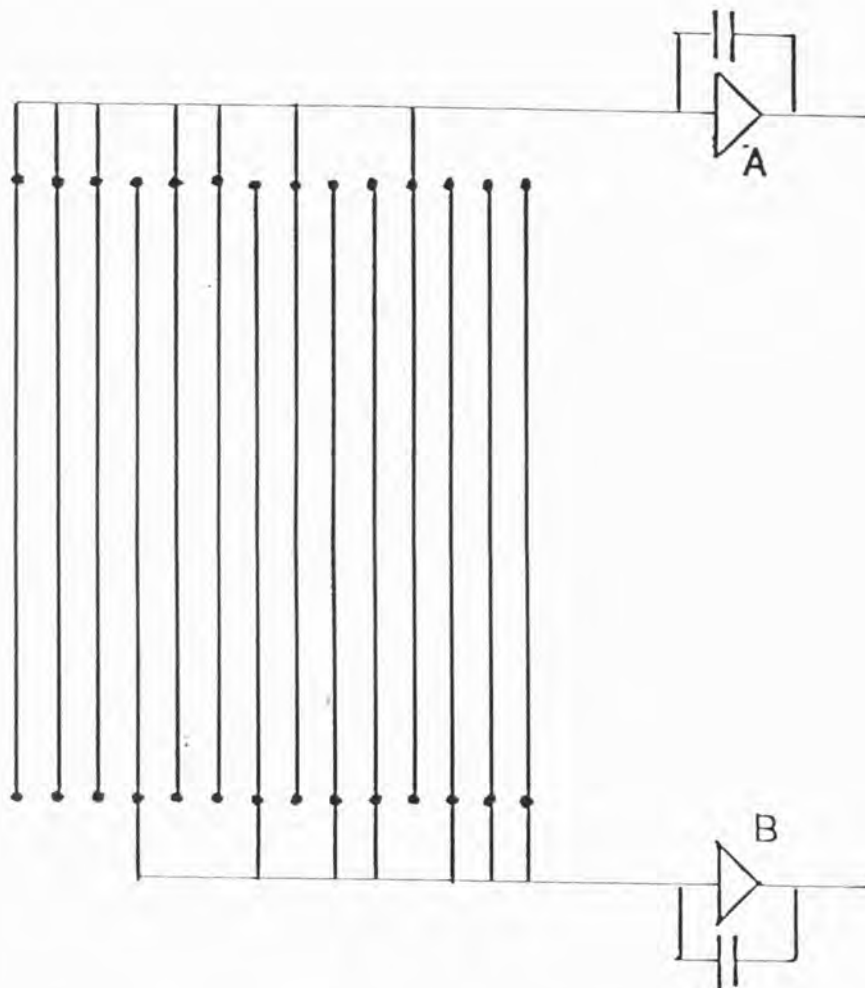


Figure 4.5.5 Principle of graded density cathode. Diagram illustrates schematically connections of cathode. (From Mathieson et al 1980).

Consider the case of an avalanche occurring, with the centroid of the induced charge distribution at position  $x$ . Provided that the charge distribution size is small compared to the total cathode width, and the cathode wire pitch is small compared to the distribution size, the size of the charge induced on each wire group will be proportional to the local linear density of each group. Mathieson 1979 amongst others, has shown that the rms of the induced charge distribution is  $\sim 0.8$  times the anode to cathode separation. Hence if the induced charges have values  $q_A$  and  $q_B$  then

$$Q = \frac{q_A}{q_A + q_B} \approx \frac{\rho_B}{\rho_A + \rho_B} \approx ax + \frac{1}{2} (1 - a)$$

Hence the quantity  $Q$  is an approximately linear function of position of the induced charge centroid. It is independent of the charge dumped, and can therefore be used as a position signal.

For the work described here the wire connections of the graded density cathodes utilised were made (to the closest approximation allowed by the constant pitch requirement) such that, ( $a = 1$ )

$$\rho_A = N (1 - x)$$

$$\rho_B = Nx$$

If one considers linearity alone, the ideal graded density cathode would of course have an infinite number of wires at an infinitesimally small pitch, giving exactly linear grading of density for each wire group. Because of the actual finite pitch some non-linearity results. This non-linearity has only been briefly investigated (experimentally) in this work, but is covered in the work of Mathieson et al., 1980.

#### 4.5.4. Summary

Many methods of position encoding along with relevant theory have been developed. In this work only two methods have been investigated, the RC line and graded density cathode. Each method theoretically can produce the required resolution for the shadow camera IPC and both are relatively simple. The practical implementation of both methods for the prototype IPC discussed in this work will be covered in Chapter 5. The rest of this chapter will devote space to practical design considerations for an IPC.

#### 4.6. IPC Mechanical Design Considerations

Five main design considerations exist for an IPC; these are:

- (i) sealing and construction of the gas cell
- (ii) detector window support
- (iii) grid construction and wire tension
- (iv) high voltage breakdown
- (v) selection of materials

Each topic will be reviewed in this section and the practical implementation for the prototype IPC will be discussed in Chapter 5.

##### 4.6.1. IPC Gas Cell Construction

IPC's have been built in two forms; flow type counters, and sealed counters. In the first the gas cell is not particularly gas tight, and usually has a thin organic window to allow entrance of low energy X-rays (see for example Humphrey et al., 1978). Gas losses through the window and walls are then made up by a flow type gas system (either a continuous flow or make-up type system). This technique has been used with

medium energy detectors as well, even with thick metallic windows, in which gas tight cells have been difficult to construct.

The approach adopted for an IPC for the shadow camera (see design reviews Chapter 2) has been mainly to consider only sealed counters owing to a number of reasons. First, the required energy range 2 to 20 keV allows the use of a vacuum tight window material, that is Beryllium. Second, the flight version of an IPC may have to give good performance for a long period, the order of years on a satellite. Hence a sealed system if it can achieve the required lifetime is a much better system, as mass must not be put aside for gas supplies and a flow system. Thirdly the shadow camera requires, for good efficiency, Xenon; this gas is particularly costly, hence the sealed approach allows lighter funding requirements.

A variety of counter sealing techniques are available. Standard construction of a gas cell consists of leak tight welded joints, if any; the only sealing required normally is the sealing of a window assembly onto the main detector body. Three basic techniques of sealing have been used:

- (i) epoxy joint
- (ii) use of a crushable seal
- (iii) knife edge to metal seal.

The first consists of literally glueing the window onto the body assembly. This technique was used for the Ariel 6 Leicester experiment detectors (Whitford et al., 1981). Leak rates smaller than  $10^{-8}$  torr litres per second can be achieved using this technique.

The second technique gives an easily demountable seal. 'O' rings are not suitable due to their large diffusion leak rate, and hence quick poisoning of a detector. Indium (J. Turner et al., 1962) is one of the best suitable materials. When compressed between two flanges (machined to an accuracy  $\sim 25 \mu\text{m}$ ) it enables sealing with leak rates  $\leq 10^{-9}$  torr litres per second to be achieved. Indium does have disadvantages in having a



low melting point (156.4°C) and lack of elasticity requiring very rigid flanges; this limits the bakeout temperature of a sealed system (if bakeout is required).

The third type of seal involves the use of metal gaskets and knife edge seals as mentioned by Tobin 1963 amongst others. This type of seal is known in high vacuum technology as a 'Conflat' type seal. In this technique two knife edges are driven into a metal gasket, normally copper, producing a seal. Tobin used this technique to seal a window to a flange by dulling slightly the knife edge, and driving the knife edges together, the window material being then trapped between one edge and the gasket. The principle of the technique is illustrated schematically in Figure 4.6.1. The copper flowing produces a seal before the window material shears. Although this type of technique has been used with Beryllium the technique is considerably safer with stainless steel windows, as Beryllium is particularly fragile and can be highly toxic. This type of seal is capable of very high bakeout temperatures (see for example Tobin 1963).

Three sealing techniques are therefore available for the shadow camera; because of weight and complexity considerations nearly all flight designs have relied on the use of the epoxy joint. For the prototype work discussed in this thesis the metal gasket type of seal has been used, because of its reliability and demountable property.

#### 4.6.2. Detector Window Support

The detector window must be supported in some manner against the high internal pressure of the IPC. The prime requirement for the shadow camera IPC window support is high transparency for both on and off-axis X-rays in order to interfere as little as possible with the coding principle of the camera. In addition the support should be cheap to produce and have a low mass.

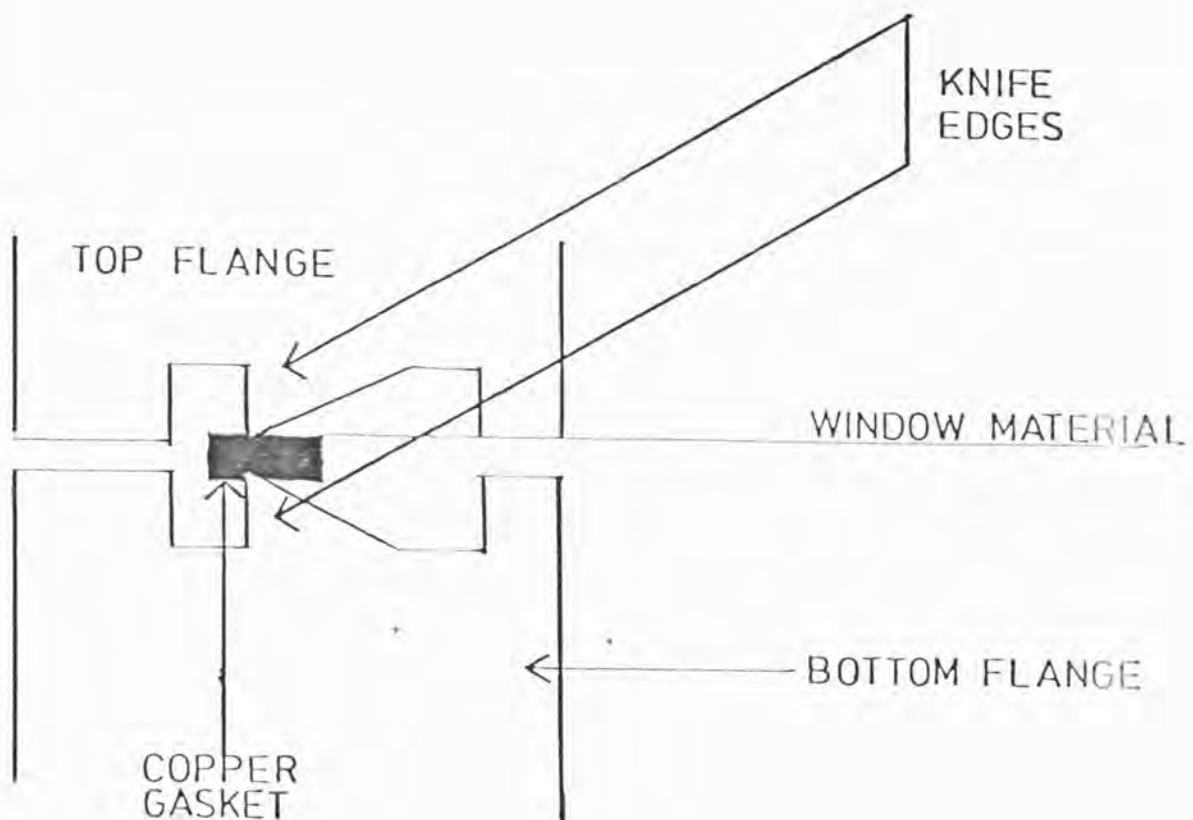


Figure 4.6.1 Principle of the knife seal technique. The window material is trapped between one knife edge and a copper gasket.

The conventional approach to considering a window support is to assume that the outside edges of the window material are clamped and not allowed to move. Roark and Young 1975 (p.406) gives a solution for the case of a circular plate supported at the edge with a large deflection. Assuming an ultimate tensile strength of 110,000 pounds per square inch from data obtained from the Leicester Ariel 6 experiment (J. Spragg 1979, private communication) then the largest diameter of 125  $\mu\text{m}$  Beryllium which can be unsupported except at the edges is  $\sim 0.8$  inches, assuming a worst case condition of 100 psi gas pressure for design and safety purposes (as per Ariel 6 experiment). Such a window has a maximum stress of 113,405 psi under such conditions.

As mentioned in Chapter 3 a design study was initiated for the experiment reviewed in section 2.10 of Chapter 2. Two basic support structures were considered; a set of supporting bars, and a set of circular open areas. The circular window support for this design of shadow camera IPC was evaluated in detail. Table 4.6.1 gives the proposed design parameters.

The circular type is considered as the main choice, as circular holes are mechanically easier to produce (and hence, cheaper). The bar type is considerably more difficult to produce and leads to very heavy stresses in each corner of a square pattern, hence necessitating the rounding of each corner to relieve the stresses. The bar type of support was not evaluated in the design study for the experiment discussed in section 2.10, Chapter 2. However, typical parameters to meet the engineering requirements were assumed for the simulation work of Chapter 3.

#### 4.6.3. Grid Construction and Wire Tension

Another problem in the construction of an IPC, involves the construction of the wire grids and the tension required for the wires. Many

TABLE 4.6.1  
CIRCULAR WINDOW SUPPORT PARAMETERS

Design:	Plate with hexagonally packed open circular areas
Plate Thickness:	1.0 cm
Hole Diameter:	1.9 cm
Centre to Centre Hole Spacing:	2.1 cm
On-axis Transmission:	75%
Window Material:	125 $\mu$ m Beryllium
Total Size:	30 cm x 30 cm

techniques have been invoked in the papers on IPC's for winding of the wire grids, all involving using a winding rig of some kind. The practical problem of constructing high precision, closely pitched grids of small diameter wires, with arbitrary wire connections, has been solved by J. Spragg 1980 (private communication) at Leicester. The technique consists of winding the grid wire continuously onto a helically cut former using a lathe. The wire connections to grid end frames are then made by conducting epoxy or soldering. The wires are then cut, and end frames removed and tensioned onto the final electrode frame. This technique was utilised for the prototype as described in Chapter 5.

As discussed by Trippe 1969 a minimum wire tension is required to avoid the problem of electrostatic repulsion between the anode wires at the high operating potential of an IPC. For small chambers this is not a fundamental problem and can be easily achieved by pretensioning the grid after winding. However the problem can become important for large chambers  $\sim 1\text{ m} \times 1\text{ m}$ .

The main tensioning problem that can occur in the design of an IPC exists due to detector cleaning procedures; the case of a vacuum bakeout to ensure low contamination levels for a sealed counter. Care must be taken to ensure that tension will be maintained during bakeout and problems with unmatched thermal expansion coefficients, between the frames and wires, must be avoided. This problem occurred frequently during the prototype IPC research programme discussed in this thesis.

#### 4.6.4. High Voltage Breakdown

Careful mechanical design is also required for the design of the grid frames, and electrical feedthrough assemblies, in order that electrical breakdown, particularly tracking, cannot occur. (When a sufficiently high potential exists across a surface, a current may flow temporarily,

producing local breakdown or tracking) This breakdown can appear like an anode pulse; hence points and small gas gaps should be avoided, and insulators (ceramic) of sufficient length must be used.

A particular problem may occur across small gas gaps, with a large dielectric constant material on one side. The gas gap has a low permittivity compared to the material which can result in a large electric field, if a potential difference exists, across the gap. Breare et al., 1972, give a formula to calculate the electric field across such a gap. Such a high field can lead to problems in corona and breakdown. Hence use of high dielectric constant materials and small gaps must be avoided under high voltage/field operating conditions.

#### 4.6.5. Types of Material

The types of material used in an IPC depends very much on the proposed design and use of the IPC.

If mass is a problem Beryllium can be used to construct the detector body as in the medium energy EXOSAT experiment (Pounds 1981). For a light flow system even aluminium can be used, although this has a low work function, perhaps giving problems with electrons released by ultra-violet photons produced during the avalanche process. In general detector bodies have been constructed of steel, mostly in the form of thin sheet vacuum tight stainless steel, for example the Leicester Ariel 6 detectors (Whitford et al., 1981). For high purity systems, stainless steel is ideal. In such a system the use of epoxy, fibreglass and glass itself should be kept to the minimum to avoid outgassing and cleaning problems. That is, in general the standards of high vacuum practice should be followed (see for example van Atta 1965). This level of purity however is not necessary in a high rate flow system, as the gas is constantly replaced, and poisoning by electro-negative contaminants is not a problem. An in-between situation can exist,



a low flow rate system, where gas is bled in only to make up large pressure losses.

In order to avoid breakdown problems all grease, dust etc., must be removed from the internal volume of the detector. All assembly work should therefore take place in a clean dust free environment such as a clean room, or laminar flow cabinet.

High purity, that is low outgassing rates can be obtained by vacuum baking components individually, and assembling the detector in a dry inert gas atmosphere, or under vacuum, and/or by vacuum baking the assembled detector until a low base pressure is obtained. Hence any such design must allow for large temperature increases, with little or no distortion. As mentioned previously this can be a severe problem with the grids themselves. However problems could occur with the whole design, due to mismatch of thermal expansion coefficients and use of thin materials. (For example, in the Leicester experiment for Ariel 6 the stainless steel used for the body was chosen such that no thermal problems with the epoxied Beryllium window existed.)

The choice of materials will be outlined for the prototype IPC in Chapter 5.

#### 4.7. Readout Electronics: Design Considerations

One has a minimum number of three signals to process from an IPC, for a one-dimensional position sensitive detector, or five for a two-dimensional position sensitive detector, the anode signal plus cathode outputs. This section will review some of the practical design considerations for the readout electronics for an IPC. Generalities only will be covered; most principles apply to both a flight electronic design and laboratory prototype. However the complex design of flight electronics is outside the scope of this work, so that the principles tend to concentrate on the laboratory prototype electronics.

The position sensing methods employed in this work are use of the RC line and graded density cathode. In the first method either zero cross times or ratio of pulse heights  $A/(A+B)$  after filtering is required, in the second method the ratio only.

The first step in processing any signal is, however, amplification and filtering. The output from anode or cathode consists of a small (of the order of a pico-coulomb or less) charge development, as a function of time. In order to measure this, the first step is preamplification. A charge sensitive preamplifier has become the standard preamplifier for a variety of reasons; firstly, to a first approximation its output signal is independent of load capacitance unlike a voltage sensitive preamplifier; and secondly historically a low noise charge sensitive preamplifier was easier to build. Over the years a variety of designs have been produced, and in the course of this work three designs were considered. The three preamplifier designs employed were one developed at M.I.T. U.S.A., another by Pye Ltd. of Cambridge, England, and finally a fully commercial design by Canberra Ltd., U.S.A. Some of the design characteristics are presented in Chapter 5.

A good discussion of preamplifier noise is given in the paper by Smith and Cline 1966. Figure 4.7.1 shows the general characteristic noise function of a preamplifier versus an amplifier filter time constant. The noise can be effectively split into two components, noise generated by the F.E.T., and thermal noise from the gate resistor. The F.E.T. produces most noise at short filter time constants, noise from the resistor becoming dominant at long time constants (Smith and Cline 1966).

The preamplifier design must therefore be chosen to give the lowest non-loaded noise at the typical time constants to be employed. In addition during operation the preamplifier will be loaded with a large capacitance (that is capacitance of the electrode to ground typically - tens of picofarads), hence a low noise with large load capacitance is required,

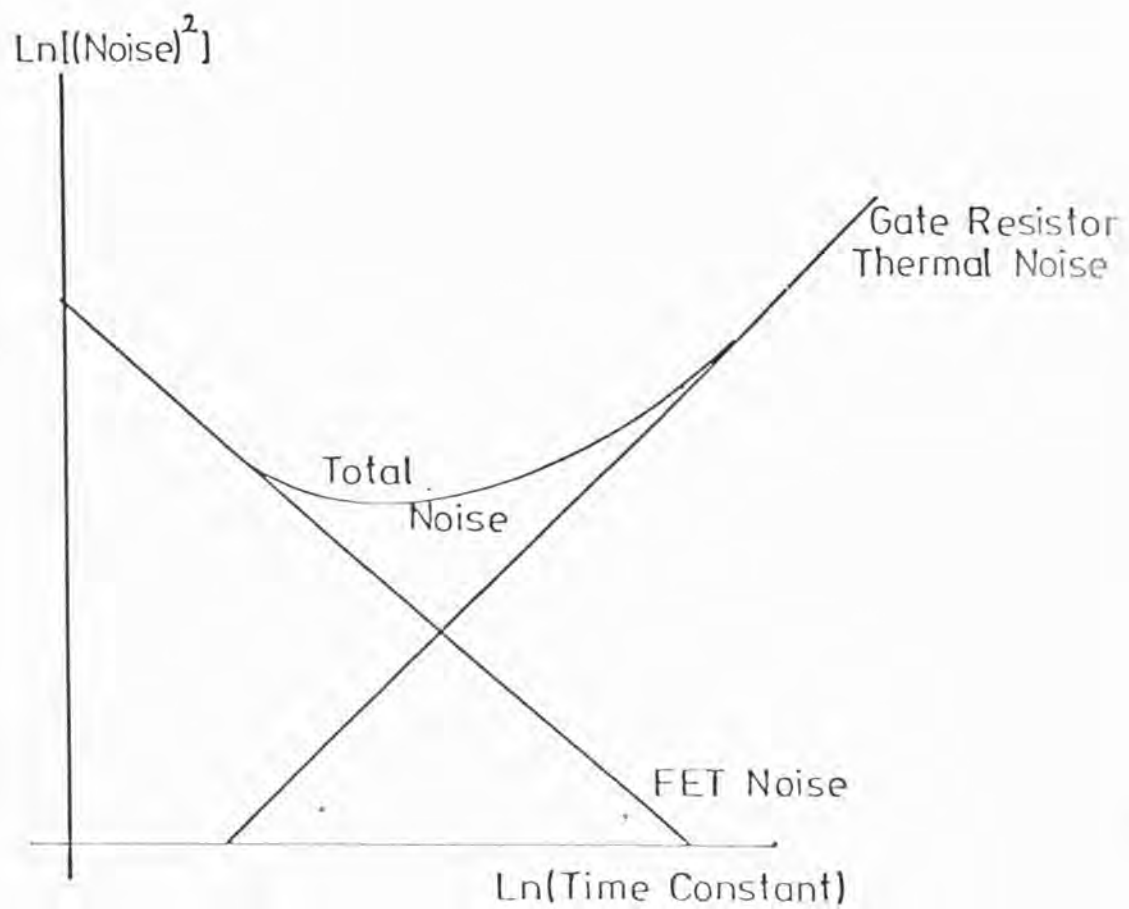


Figure 4.7.1 General characteristic noise function of a preamplifier versus amplifier filter time constant.  
(Adapted from Smith and Cline 1966).

The value of noise per loaded unit capacitance must therefore be in addition small, at the time constants required.

After preamplification, the resulting signal requires further amplification and filtering in order to shape the pulse and raise its level to a sufficiently large value for standard signal processing electronics to be employed. The most standard filter amplifiers in use involve single or double differentiating and single or multiple integrating, the input signal producing a bipolar or unipolar output pulse. During the work undertaken in this thesis, both types of amplifiers were employed.

The anode signal even after shaping contains energy information in that the pulse height is proportional to the incident photon energy. However, the signal is also required to trigger position coding electronics; hence two output paths may be required for this signal. The cathode signals after shaping contain position information via either their pulse height in both RC and graded density methods, or their zero-cross time in the RC line method. In the first case

$$x \propto \frac{A}{A + B}$$

where  $A$  and  $B$  are the two peak pulse heights, in the second

$$x \propto t_{1-X} - t_X$$

where  $t_{1-X}$  and  $t_X$  are the zero-cross times of the bipolar signal, from each end of the line (employing the formalism of section 4.5.2.). One therefore requires, for each position sensitive direction, one of the two processing schemes shown in Figures 4.7.2 and 4.7.3. The preamplifier and filter are by necessity analogue devices. However, the rest of the processing scheme can be implemented using digital (after analogue to digital conversion) or analogue electronics. During the whole of this work all circuits utilised analogue electronics. A flight electronic design would use digital electronics to improve accuracy and dynamic range.

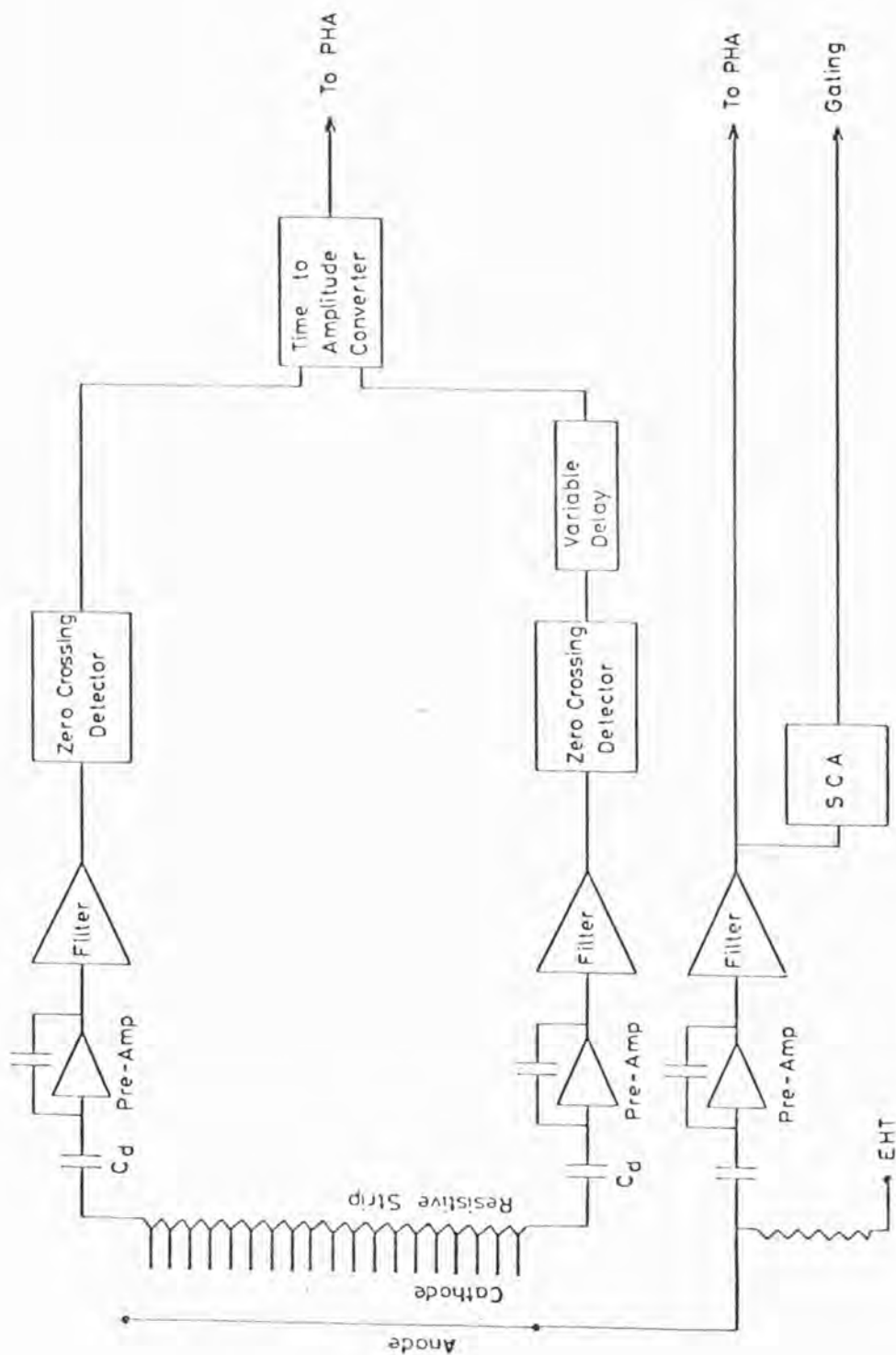


Figure 4.7.2 Position processing electronics required for zero cross (timing difference) position encoding from a RC line.

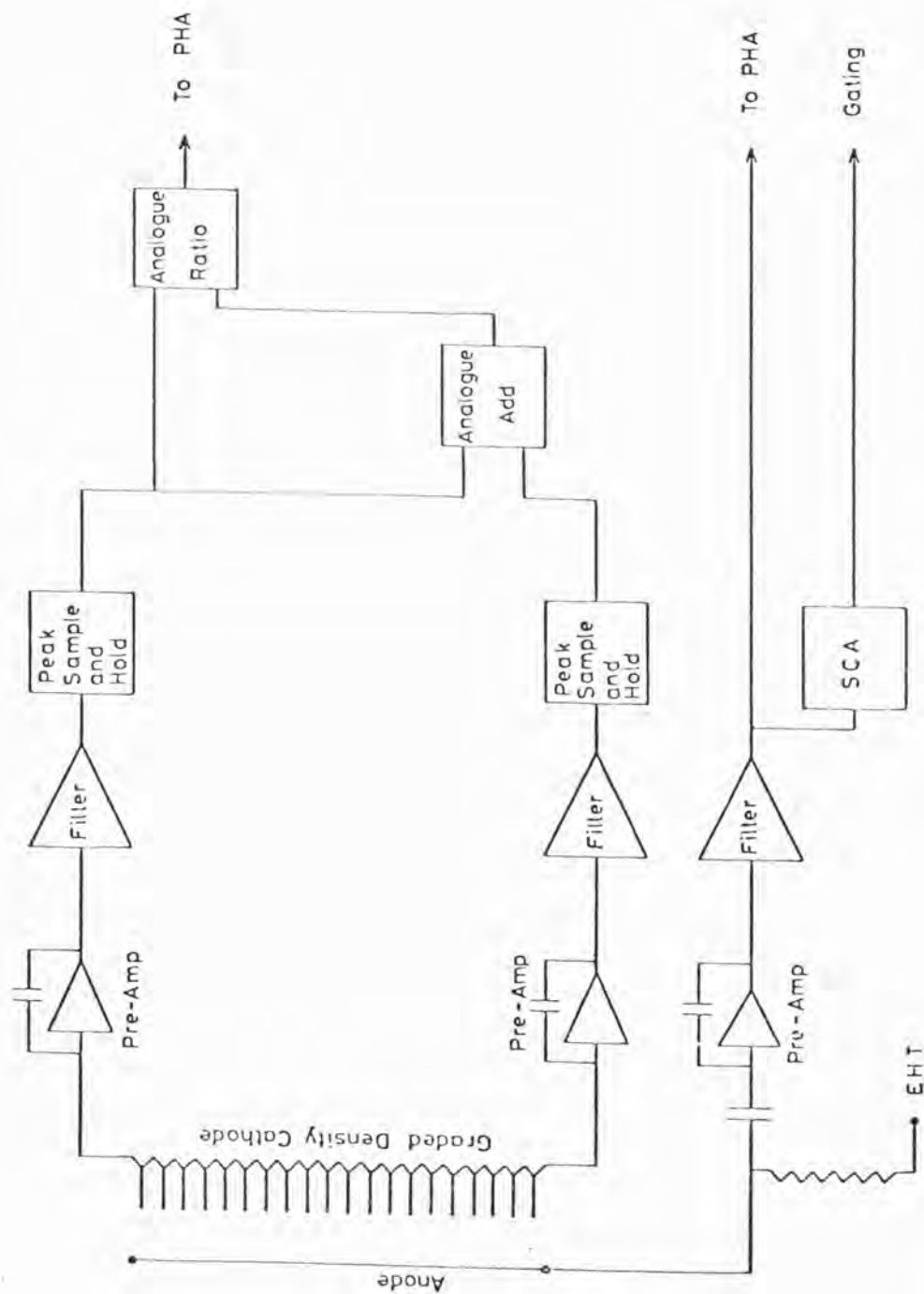


Figure 4.7.3 Position processing electronics required for ratio position encoding from graded density cathode or RC line.



Each type of electronics has its own advantages and disadvantages. Digital processing enables a large dynamic range to be handled, whereas most analogue circuits have a quite limited signal range. Analogue circuits are usually cheap compared to the cost of ADCs, can be implemented quickly, and have no interface problems to standard signal display and analysis equipment. Good linearity is a prime requisite on any design, as non-linearity will tend to amplify any non-linearity intrinsic to the position encoding method itself.

Processing schemes can be built almost entirely from commercially available units (NIM or CAMAC); however, for the work described here most of processing electronics after amplification and before display were produced by the Electronics Workshop of the Leicester X-ray Astronomy Group.

In a flight type detector the final output signal, whose amplitude is proportional to position, would be digitised along with energy information and fed to the spacecraft telemetry interface. For the laboratory a large amount of display equipment is available; these can be divided into two types, an X-Y display, and a one-dimensional cut type.

In the X-Y display, each detected photon produces two signals  $X$  and  $Y$  each proportional to its position in each co-ordinate, which is placed in some kind of store, producing an intensity map. In the one-dimensional cut display, an intensity versus position plot is produced as a one-dimensional cut through the image. The Pulse Height Analyser (PHA) is a readily available device of this type.

This section has attempted to review detector electronics in terms of general concepts, and some of the practical considerations in design of an IPC data processing scheme. The exact scheme utilised in this work for the prototype IPC will be described in detail in the following chapter.

#### 4.8. Future/Other Detectors for the Shadow Camera

Of all the imaging X-ray detectors available at present the IPC appears to be the most suitable for application to the shadow camera. (The microchannel plate type of detector is too inefficient and CCDs are not available in large enough areas.) Recent developments in imaging detectors, however, suggest two other detectors which may be suitable for application to the shadow camera with future development; the Multistep Avalanche Chamber; and Imaging Gas Scintillation Proportional Counter.

##### 4.8.1. The Multistep Avalanche Chamber

Recently work has been reported, particularly by the CERN group, under the leadership of Charpak on a device known as the Multistep Avalanche Chamber. This device uses a photon-mediated avalanche as the amplification process, instead of an electron-mediated one, as in the standard proportional counter.

All noble gases have characteristic emission spectra in the vacuum ultra-violet. Electrons accelerated in an electric field can excite this emission, leading to production of ultra-violet photons; in a normal counter a quench is added to absorb these photons as mentioned in section 4.4.2. The Multistep Avalanche Chamber seeks to enhance the process. Breskin et al., 1979 published one of the first papers, describing this type of chamber with basic theory, and giving results obtained; Charpak and Sauli publishing the first in 1978.

The chamber divides the multiplication process into a number of steps. The first step consists of a preamplification and transfer section, known as a PAT section in the literature. Consider Figure 4.8.1 which shows a schematic of a PAT element, adapted from the paper by Breskin et al., 1979. The PAT section is identical in fact with a parallel plate avalanche counter, with some field lines escaping to the lower region. Hence,

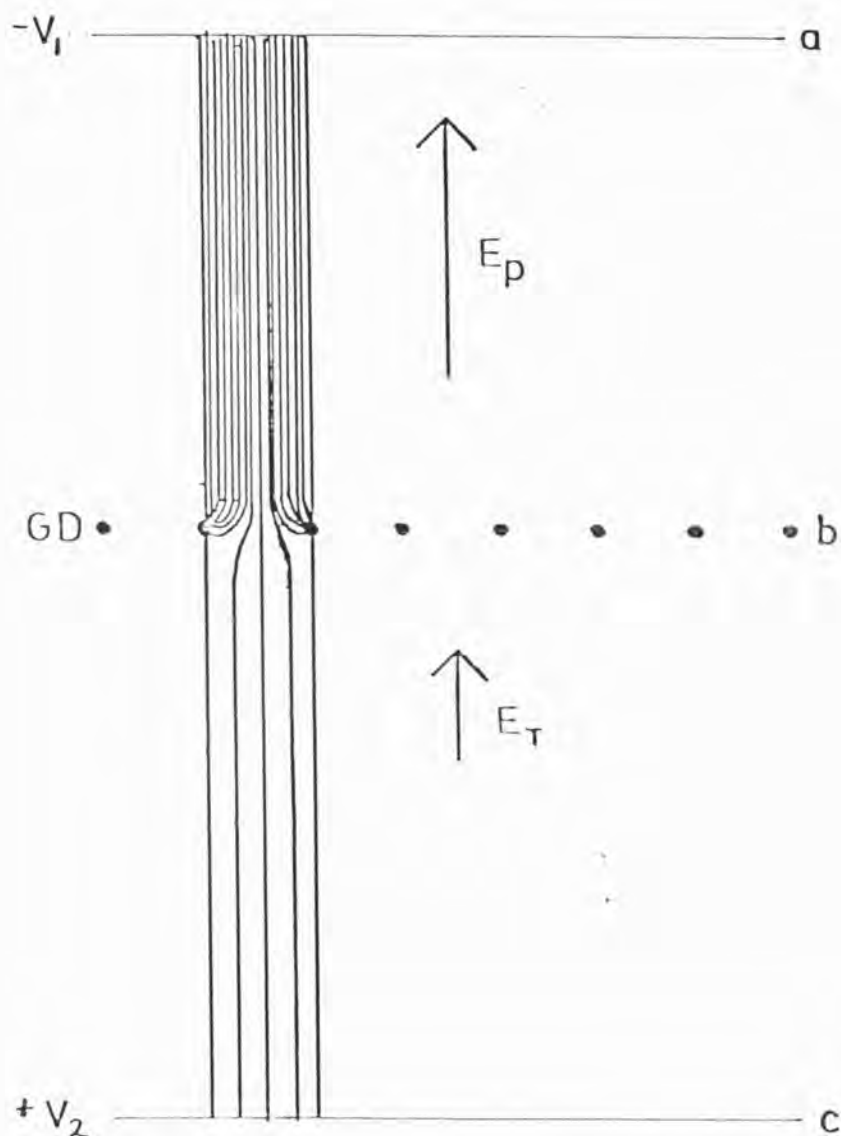


Figure 4.8.1 Schematic PAT element. A high electric field  $E_p$  is followed by a lower field  $E_T$ ; the electrodes, a, b, c can either be wire grids or crossed wire mesh. Avalanche multiplication takes place in high field  $E_p$ , and a fraction of the electrons is transferred into low field ( $E_T$ ) region. (From Breskin et al 1979).

assuming that avalanche multiplication could occur in the upper region, the charge transferred to the lower region would simply be from those avalanches which develop along the field lines that penetrate through the grid into that region.

The multiplication process in the PAT element is achieved by ultra-violet photons. The photon-mediated avalanche occurs due to the presence of an additive gas which has a low enough ionisation potential to be ionised by the noble gas ultra-violet emission. Triethylamine is suitable for Xenon; acetone, ethanol, and benzene are suitable for Argon. (Breskin et al., 1979)

Figure 4.8.2 shows a suitable design for an imaging X-ray detector proposed by Breskin et al., 1979. A PAT element is followed by a multi-wire proportional counter (MWPC). The addition of a drift and conversion space is necessary in order that a known charge is injected into the PAT element. If the drift and conversion space is omitted all energy information is lost in the PAT element, as each photon absorbed in the PAT element will undergo a different amplification, depending on the depth of absorption. The final signal is dependent on the length of avalanche produced.

The PAT element provides initial amplification, while the multi-wire proportional counter provides a second stage of amplification and imaging capability.

A counter such as that mentioned by Breskin et al., 1979, can operate stably at gas gains  $\sim 10^6$  (whereas proportional counters usually only operate  $\sim 10^4$ ), so providing a large signal-to-noise advantage. In addition the PAT element can largely eliminate sensing problems across the anode wires due to the large mean free path,  $\sim 200 \mu\text{m}$ , of the photons in the PAT element, which leads to a very large electron cloud size entering the MWPC. Avalanches then occur on a large number of anode wires, giving good interpolation across the wires. Finally, the system can provide an inbuilt delay by the drift space between the PAT element and MWPC. This could be

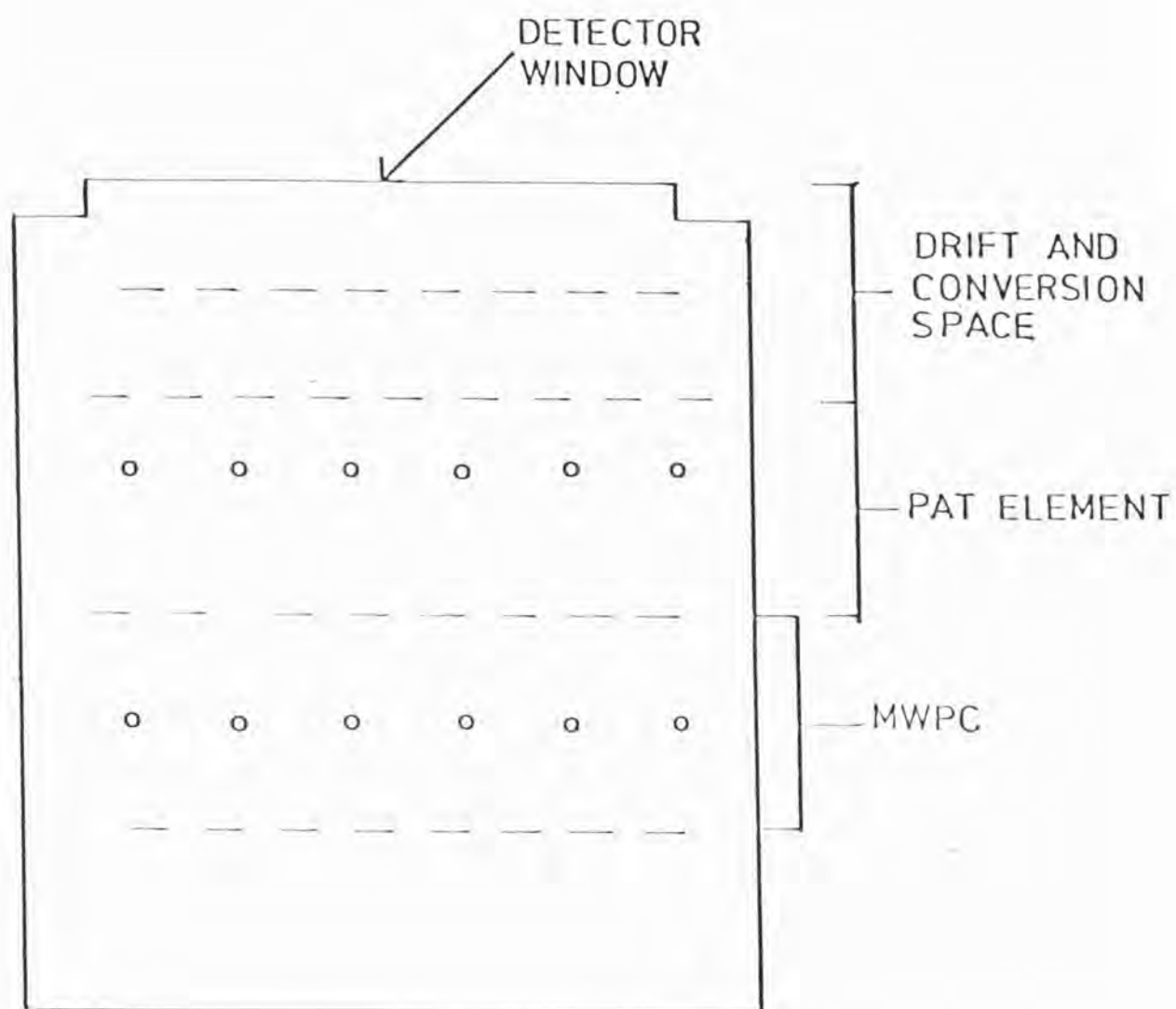


Figure 4.8.2 Schematic cross-section of a Multistep Avalanche. Chamber suitable for X-ray imaging. (From Breskin et al 1979).

sufficient to avoid secondary avalanche problems, developing from photons hitting the entrance window, leading to a degradation in position resolution. (This subject will be discussed in Chapter 6.) The multistep avalanche chamber is therefore a possible future detector for the shadow camera.

#### 4.8.2. The Imaging Gas Scintillation Proportional Counter

Recently much work has been presented on the Imaging Gas Scintillation Proportional Counter, Davelaar et al., 1980, Ku and Hailey 1981, Anderson 1980, 1981, amongst others. This work is a natural development of the original work, on non-imaging gas scintillation proportional counters (GSPC), for use in X-ray astronomy, by Andresen et al., 1976.

The basic principle of the GSPC is as follows. The initial electrons produced by the photon absorption of an X-ray are drifted into a very high electric field region. For non-imaging GSPC's (see Peacock et al., 1979(a)) a spherically symmetric electric field is used to increase effective areas and improve performance, by electron focusing. For imaging GSPCs (for example Davelaar et al., 1980), a linear field region (parallel plate type) is required to avoid image distortion. In the high electric field region the electrons acquire sufficient energy to excite noble gas atoms (usually Xenon) into producing ultra-violet emission ( $\sim 1500 - 2000 \text{ \AA}$ ). The subsequent burst of UV photons is then detected. The traditional detector is a photomultiplier tube, the integrated output pulse having an amplitude proportional to the energy of the initial X-rays, making the detector proportional.

The energy resolution of the device is of course given by the variance of the number of electrons produced initially, and the variance on the number of UV photons detected by the photomultiplier tube. The limiting resolution is of course given just by the variance on the number of electrons,



$$R = 2.355 F^{\frac{1}{2}} W^{\frac{1}{2}} E^{-\frac{1}{2}}$$

using the notation of section 4.4.3.  $R$  is the theoretical energy resolution FWHM,  $W$  is the mean energy required to create an ion pair and  $F$  is the Fano Factor for the gas. By contrast, for a proportional counter  $R$  is given (approximately) by

$$R = 2.355 (1 + F)^{\frac{1}{2}} W^{\frac{1}{2}} E^{-\frac{1}{2}}$$

Since  $F < 1$  the GSPC is theoretically capable of a much better energy resolution than a proportional counter. An energy resolution of 7.5% for  $\text{Fe}^{55}$  radiation has been obtained (Peacock et al., 1979 (b)) compared to ~14.5% for a proportional counter (Charles and Cooke 1968).

Non-imaging GSPC's have used just one photomultiplier (PM) tube; imaging has been achieved by use of a multiple number of PM tubes (Davelaar et al., 1980 amongst others), the principle of the Anger camera (Anger 1958). Figure 4.8.3 shows schematically the standard imaging GSPC configuration. Each event presents a differing amount of light, dependent on its position, to each PM tube, due to the variation in solid angle. By appropriate ratios between photomultiplier output signals an unambiguous position can be achieved. The energy information is produced by summing the output signals. This type of detector has produced resolutions (FWHM) ~2.5 mm with an energy resolution ~10% at 6 keV (Davelaar et al., 1980).

Recent work, Anderson 1980, 1981, Ku and Hailey 1981, has suggested another approach. This new type of device is known under several names. However the 'Scinprop' name of Anderson 1981 will be adopted here. The Scinprop consists of coupling a gas scintillation cell to an IPC. The IPC is used with a gas mixture with an additive, TMAE (Anderson 1980), which has a low enough ionisation potential to be ionised by Xenon light emission, enabling the IPC to directly detect the burst of UV photons from the gas scintillation cell. Figure 4.8.4 shows schematically the Scinprop. The idea was originally proposed by Policarpo 1978.

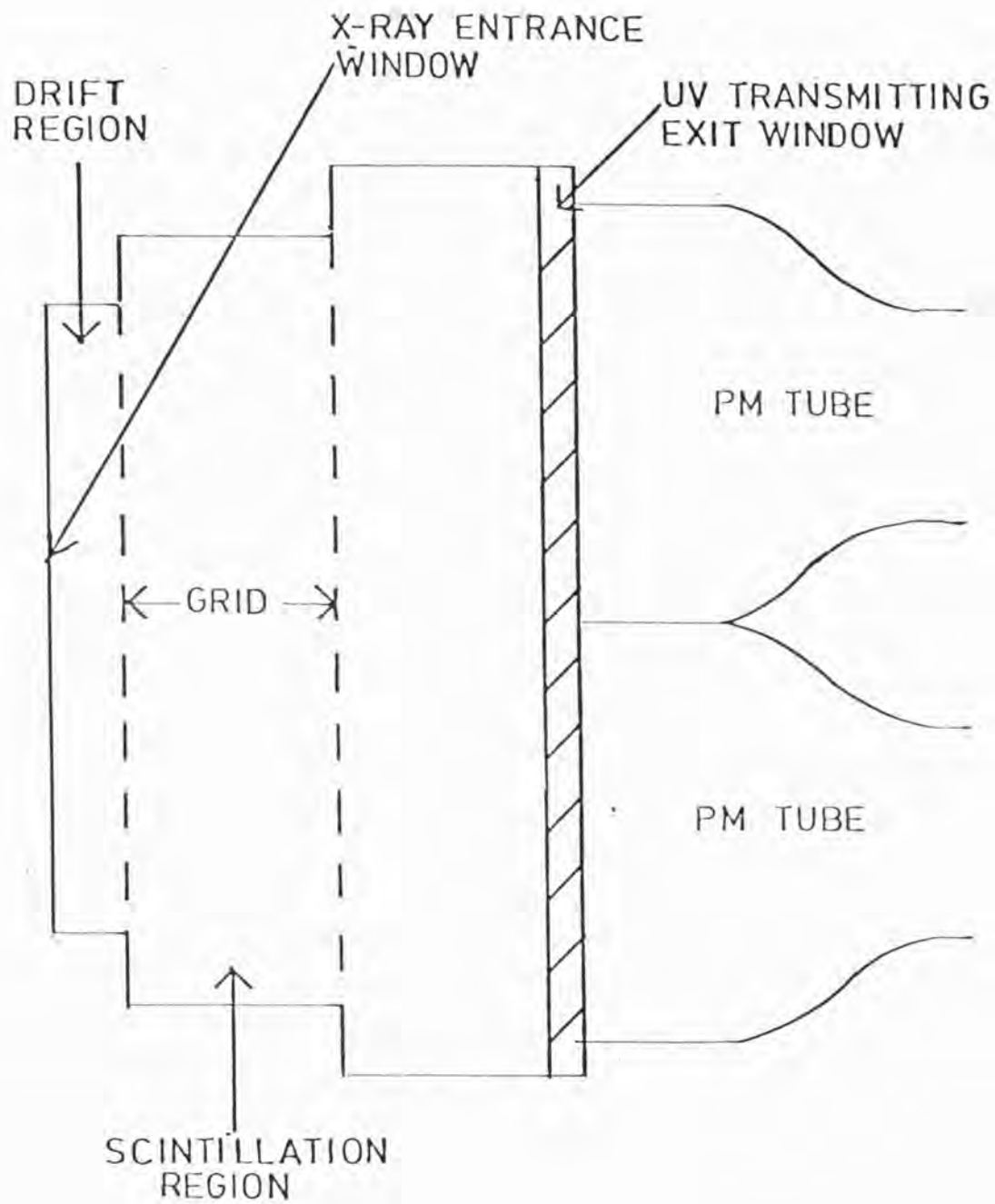


Figure 4.8.3 Schematic cross-section through a parallel electric field imaging gas scintillation proportional counter. Note: UV transmitting window between photomultiplier (PM) tubes and scintillation cell. (Adapted from Davelaar et al 1980).

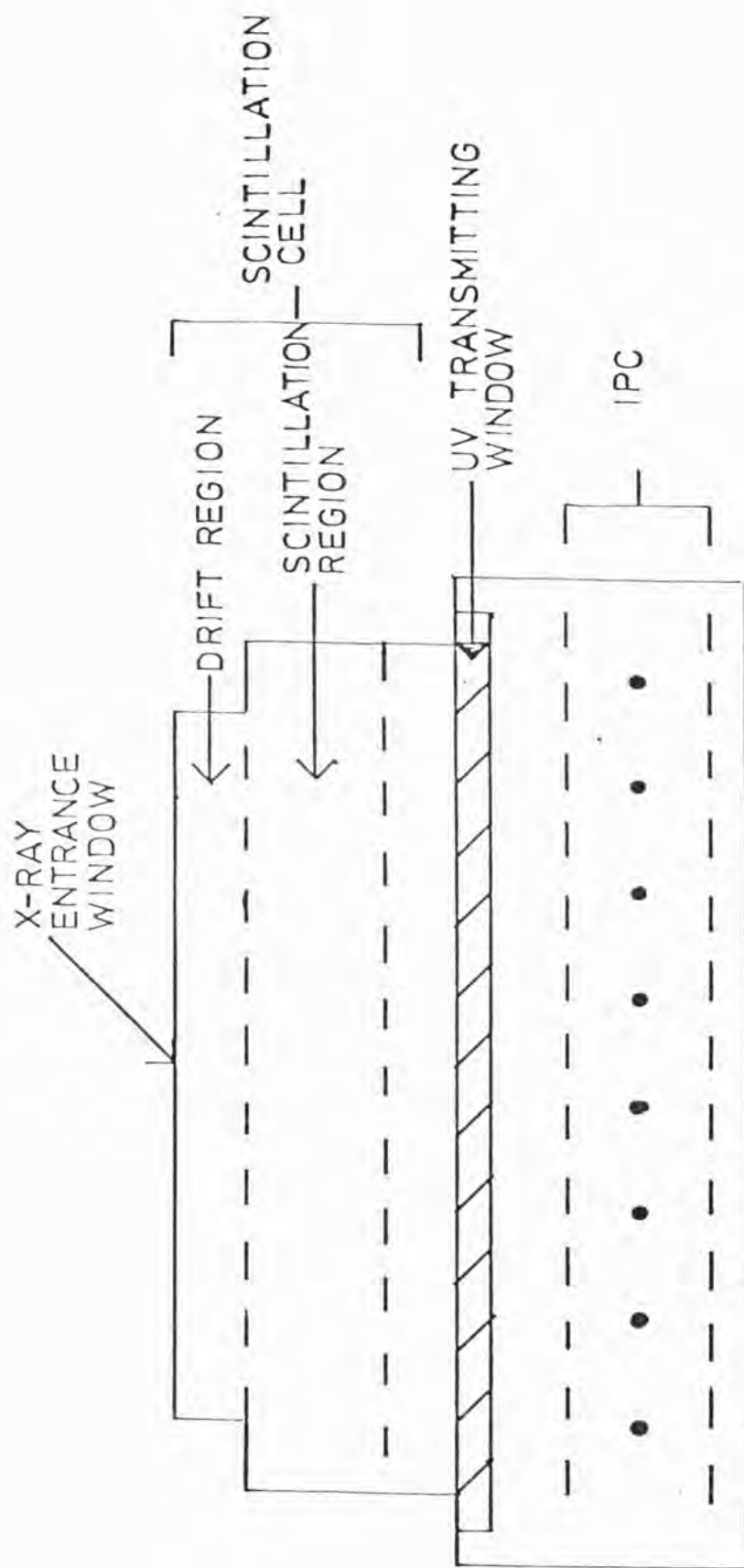


Figure 4.8.4 Schematic cross-section of a Scinprop. (Adapted from Ku and Hailey 1981).

Ku and Hailey 1981 have already demonstrated a measured performance of 9% (FWHM) energy resolution and a spatial resolution of 0.9 mm (FWHM) at 6 keV . Theoretical arguments presented by the above, and Anderson 1981 indicate that the Scinprop may exceed the performance of the multiple PM tube approach.

Although neither of the forms of Gas Imaging Scintillation Proportional Counter presented here can match the position resolution performance of the IPC at present, both are probable future detectors for the shadow camera.

## CHAPTER 5

## A PROTOTYPE IPC FOR THE SHADOW CAMERA

5.1. Introduction

This chapter will describe the mechanical and electrical construction of a prototype IPC suitable for development to the shadow camera. Little detailed work has been performed on Xenon filled IPCs suitable for X-ray astronomy, making the necessity for a prototype.

The detector described is not suitable for direct application to a shadow camera, as its size is only 9 cm x 9 cm, but will be shown to demonstrate submillimeter spatial resolution of the order required, and help to define the gas limits of a Xenon filled IPC. In order to minimise gas penetration effects the counter described uses Xenon at 2 atmospheres pressure plus quench gas.

The choice of a 9 cm x 9 cm detector was governed by the availability of hardware from a research programme in Argon/Methane IPCs conducted at Leicester, for the energy range 0.1 to 1.5 keV, in support of an earlier rocket-borne experiment to image supernova remnants (Rappaport et al., 1979, Levine et al., 1979). This size was also convenient in that a standard mechanical vacuum seal could be used for detector construction. Finally for cost, safety and reliability the prototype IPC had a stainless steel window, limiting testing to the use of  $\text{Fe}^{55}$  (5.9 keV) and more energetic X-ray sources.

Although the main purpose of the work described here is the wide field camera, the prototype IPC has another possible application, namely to grazing incidence telescopes. As mentioned previously in the late 1980s NASA plans to launch AXAF, a large area grazing incidence telescope intended to give sub-arc second resolution. This telescope will have a large effective area up to ~8 keV and, again, a Xenon-filled IPC, which

limits photon gas penetration effects and retains good spatial resolution in this higher energy range is very desirable. A comparison of the prototype detector performance with previous work will be given in Chapter 7.

First, in this chapter, the mechanical construction of the prototype will be described. Secondly, the detector filling procedure, followed by a brief description of the electronics used in the work will be given. This is followed by a description of the IPCs that have been constructed and of their measured parameters. Finally, results from the initial prototype, a one-dimensional position-sensitive detector, will be presented.

## 5.2. Mechanical Construction

The mechanical design for the prototype IPC emphasised the following aspects; reliability, cleanliness and safety. Stainless steel was adopted both as the main body material and for the window. The 'conflat' type of vacuum seal was used, enabling a reliable seal to be achieved. The sealed approach to the IPC was adopted on two criteria; first, the high cost of Xenon, and secondly, the greater simplicity of mechanical design of a sealed counter for the shadow camera.

### 5.2.1. IPC Body Assembly

Figure 5.2.1 shows a schematic cross-section of the development IPC. As can be seen from the diagram, the detector has 5 parts; the base plate; main cylindrical body; top plate; window and window support; and internal grid electrodes plus supports.

The base plate contains electrical feedthroughs for the anode and cathode signals and the voltage supply lines, as well as one half of a knife-edge seal. The cylindrical body has two half-seals and the upper plate a single knife-edge. Sealing was achieved using a standard 10 in. flange copper gasket under compression from 24 bolts connecting the base



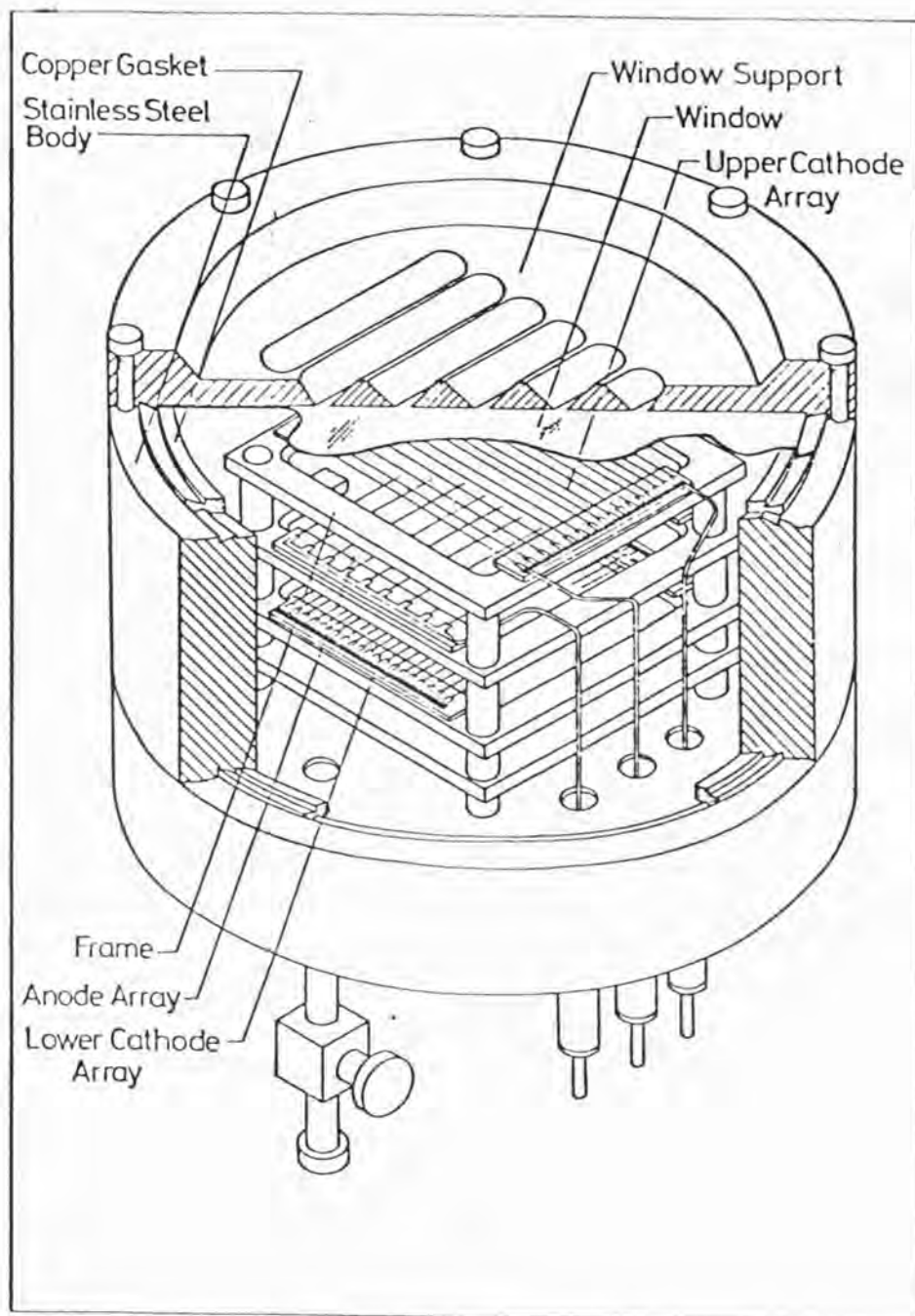


Figure 5.2.1 Schematic cross-section of prototype IPC. Window support depicted is for the one-dimensional position sensitive IPC constructed during this work.

plate to the body, and a further 24 the body to the top plate. The window support is removable to allow easy change or rotation. The body, base and top plate are constructed of stainless steel. Table 5.2.1 lists the main mechanical design parameters of the detector.

The base plate contains six high voltage feedthroughs, one for the anode, four for the cathode outputs, and one for an anti-coincidence anode, if required, two gas supply lines to allow the possibility of a gas flow system, and a 16-way low voltage feedthrough. All these were welded into appropriate size apertures in the base plate. The multiway feedthrough was included in the design to allow for individual cathode wire readout, if required. The gas supply lines were terminated with a male Cajon fitting, allowing compatibility with the gas filling rig, and high vacuum Nupro stainless valves.

Internally four vertical stainless steel pillars were screwed into the base plate, terminating 0.5 mm below the window. These pillars are spaced on a 10.8 cm side square, allowing any grid assembly within the detector depth limitation to be constructed. The grid assembly consisted of grids spaced with stainless steel spacers, complete with a base plate and any underlying spacers. The assembly was held down with M5 skinned nuts and wavey washers.

The body spacers were constructed by the mechanical workshop in the Physics Department at the University. All tolerances, spacing, flatness etc., of the components were set at  $\pm 100 \mu\text{m}$  (peak-to-peak variation). The high voltage feedthroughs were purchased from Vacuum Generators and the low voltage feedthroughs from Moores (Evic) Glassworks Ltd. The specification of each is detailed in Table 5.2.2.

TABLE 5.2.1  
MECHANICAL DESIGN PARAMETERS

Overall diameter:	25 cm
Overall depth :	16.3 cm (top plate to ceramic feed-through)
Internal diameter:	20.1 cm
Internal depth:	6 cm
Body material:	stainless steel
Sealing:	Knife edge into copper gasket. Standard OFHC Copper 10 in. diameter VG Type Cu 200
Window material:	Stainless steel sheet 25 $\mu$ m thick
Electrodes:	Active area nominal 9 cm x 9 cm Three , two cathodes , one anode Variable spacing, variable wire pitch Frame material G10
Electrical feedthroughs:	6 high voltage feedthroughs Nominal operating range 0 to 6 kV 1 low voltage feedthrough Nominal operating range 0 to 1 kV
Gas lines:	2 stainless steel tube $\frac{3}{8}$ " outside diameter. Terminated with Cajon vacuum coupling.

TABLE 5.2.2.  
ELECTRICAL FEEDTHROUGH SPECIFICATION

High Voltage (Type EFT 1AN)

Diameter:	1.2 cm
Overall length:	6.7 cm
Outside thread:	M5
Ceramic length:	2.0 cm
Spark breakdown voltage:	15 kV
Feedthrough achieved by welding 8.5 cm threaded rod to base	

Low Voltage

Diameter:	5.1 cm
Overall length	5.5 cm
16 Nilo-K pins .05 in. diameter spaced on 31.5 mm pitch circle diameter.	
Nominal operating voltage 0 to 1000 V .	

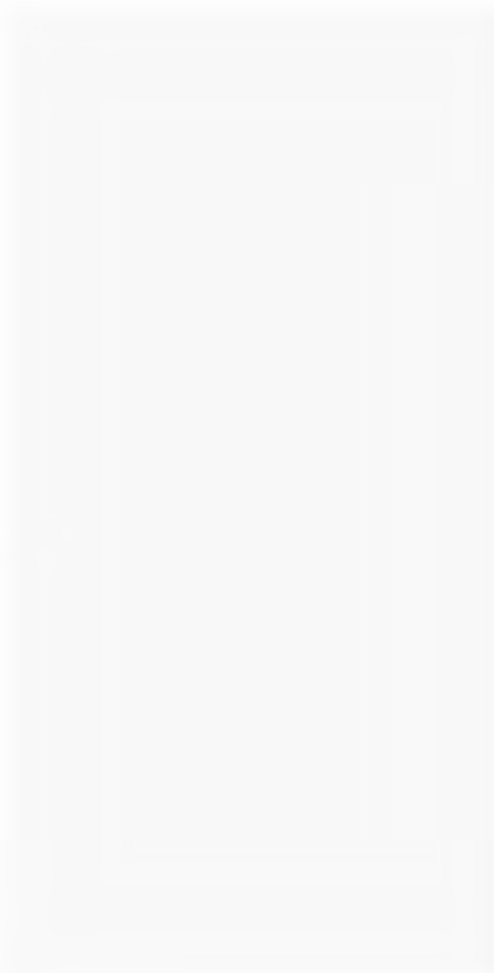
### 5.2.2. Electrode Construction

The electrode assembly in the prototype IPC consisted only of three electrodes, the anode, plus two cathodes. All electrode frames were constructed of G10 fibreglass board, 4 mm thick, the wires being mounted on top by a variety of methods. An anti-coincidence anode was omitted, enabling a reasonably symmetric field arrangement inside the counter.

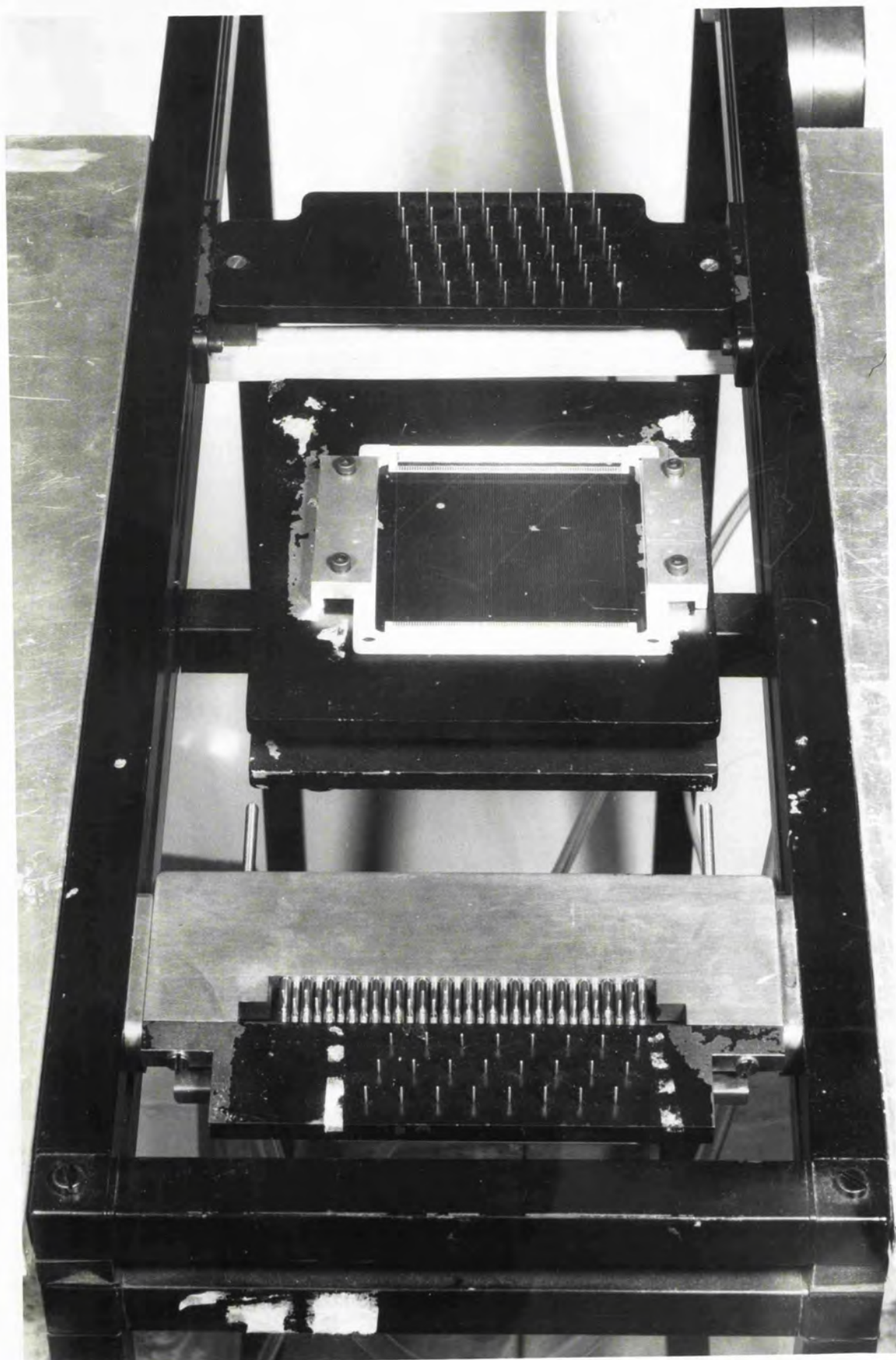
Two grid-winding techniques were used in the course of this work. Initially a hand winding technique was used, this was improved to the lathe winding approach as specified in Chapter 4. The anodes were formed throughout the work using plain ceramic cards, the wires being epoxied down onto metal strips; the graded density cathodes were produced similarly, but with metal strips on G10 fibreglass board. The RC cathodes, by necessity, were constructed rather differently. These were produced using ceramic cards (from EMI Ltd.) forming part of the end pieces of a G10 frame. The cathode wires were soldered directly onto the cards which had contact fingers along their length, the fingers being joined by a resistive ink strip. The cards on receipt from EMI were mounted on an electrode frame with another ceramic card with unjoined contact fingers at the other end.

As mentioned above two grid-winding techniques were used in the course of the work. In addition two methods of wire attachment were used, in the case of the RC cathodes, soldering, and for the anodes and graded density cathodes, conductive and non-conductive epoxy was used. The winding technique applied to the RC cathodes stemmed directly from previous work, the Argon/Methane IPC research programme. This technique used a winding frame, as illustrated in Figure 5.2.2. The wires were wound by hand round the end pins from a small bobbin. Wire spacings in whole millimetres up to the frame size could be achieved. Wire tensioning was achieved by use of pneumatic pistons pushing one set of end pins away from

Figure 5.2.2 Initial grid winding frame. Note: end pins, and at bottom pneumatic pistons for wire tensioning. A RC cathode is included (centre) to show size of the winding frame.







the centre. Each wire was then soldered into position on each metallic finger using a solder paste, excess paste after soldering being removed by washing the grid in iso-propyl-alcohol (i.p.a.) using a fine brush. After a check of connections the wires were then cut and the frame removed. Special care was required to ensure that no wire stubs protruded upwards or downwards in order to avoid potential breakdown problems.

This technique, although adequate for the Argon/Methane work, was found to have several problems on application to the Xenon-filled prototype IPC. In this case the grids have to undergo thermal cycling during detector bakeout prior to filling with gas. Initial anode grids were wound using the above technique. However, problems in grid distortion were found due to expansion of the electrode assembly under bakeout. As in addition considerable man hours were invested in producing one grid, a different winding procedure was developed by J. Spragg of the X-ray Astronomy Group.

The new grid winding rig is shown in Figure 5.2.3. In this technique the grids are produced by winding the wire continuously onto a helical former on the lathe. A variety of formers were produced enabling grids of 2 mm, 1 mm or 0.5 mm pitch to be wound, inserts in the former holding the end pieces for a particular electrode frame. Wires are attached to the end pieces using two layers of epoxy, a non-conducting layer to hold the wires firmly to the end pieces, and a conducting silver epoxy layer to join the wires to the metal strips bonded onto the end pieces. The graded density wire connections were produced by breaking given wires using a punch driven through the non-conducting epoxy layer. The wires are then cut directly between the end pieces.

The resulting electrode was then removed and the epoxy cured at 100°C for an hour. The electrode is then tensioned into position on the G10 frame using four grub screws. The final step is glueing the array into place.

Figure 5.2.3 New grid winding rig. Note: helical former (1 mm pitch) mounted on lathe. Wire is fed via small wheel above former. The lathe is driven by hand towards left hand side of photograph.



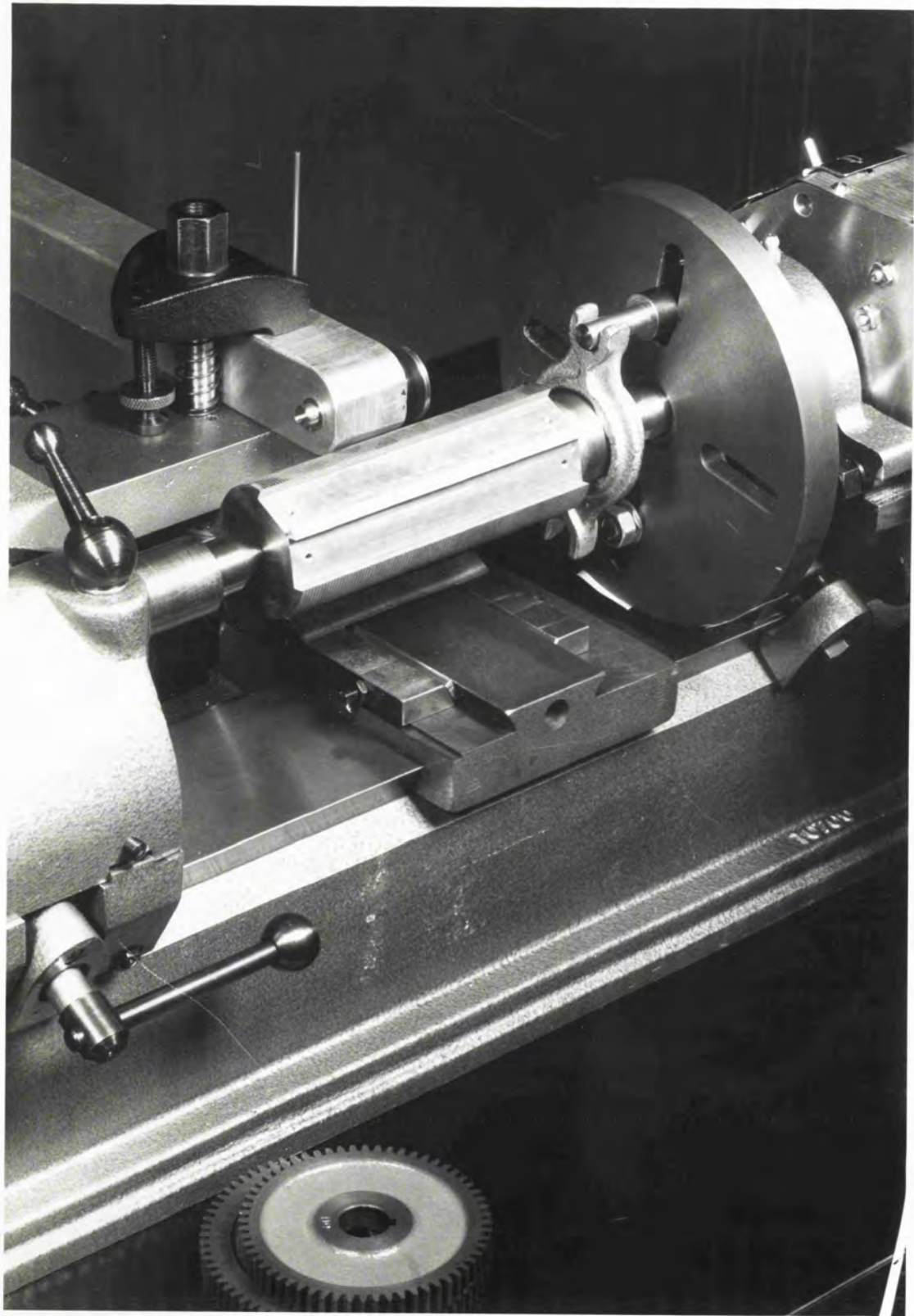




Figure 5.2.4 shows the three types of electrode used in this work produced by the above techniques; an RC cathode; a graded density cathode; and an anode. The RC cathode had a wire spacing of 1 mm, whereas, because of linearity considerations (Mathieson et al., 1980), the graded density cathode was constructed with an 0.5 mm wire pitch. Table 5.2.3 gives the relevant wire connections used for the graded density cathode described in this work (Gilvin 1980, private communication).

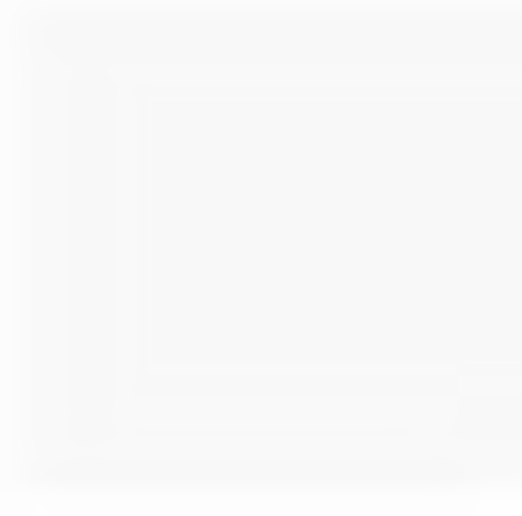
For the cathode arrays, wires of constant diameter were used in every position while for the anode, thick field wires were used in order to avoid counter breakdown problems due to high gain on the end wires. The gain variation results because of the electrostatic configuration of such an unprotected counter, a high field existing on the end wires. The field was decreased in practice by use of large diameter wires, the end three having diameters of 50, 125, and 250  $\mu\text{m}$  respectively on each side. These wires were added by hand, after the initial winding procedure for the anode.

### 5.2.3. IPC Assembly Procedure

Before assembly of the development IPC all parts were cleaned. All assembly work was carried out in a 'class 10000' clean room in order to keep counter internal contamination to a minimum. The IPC assembly procedure was divided into three separate sections; cleaning; upper body assembly, and lower body and electrode assembly.

The first task in assembly was the cleaning of all detector components. First all ceramic feedthroughs were bead blasted with  $\sim 5 \mu\text{m}$  diameter aluminium oxide powder to remove surface contamination in order to avoid tracking problems. The base plate was then ultrasonically cleaned in i.p.a. to remove excess powder. All metal parts including the base plate were ultrasonically cleaned, first in inhibisol for  $\sim 20$  minutes

Figure 5.2.4 Three types of electrode used in this work; top 2mm pitch, anode; centre 1mm pitch, RC cathode, and bottom 0.5mm pitch, graded density cathode. Note: punch marks through non-conducting epoxy on graded density cathode.





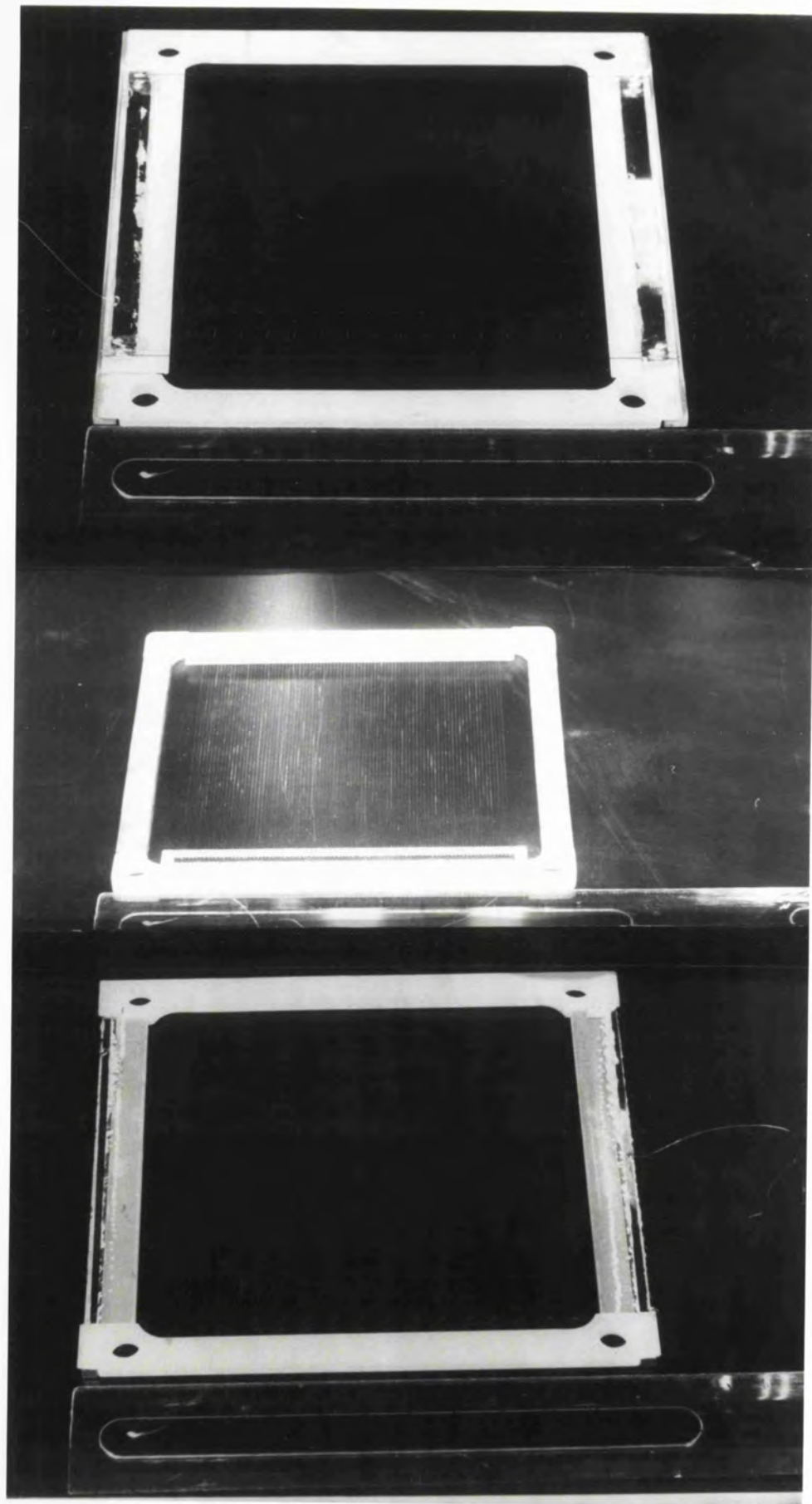


TABLE 5.2.3

## SUMMARY OF WIRE CONNECTIONS FOR GRADED DENSITY CATHODE

The graded density cathode is split, in its basic form into two electrodes, A and B, the following table lists the wire connections to the two groups by wire number from one end.

<u>Wire Number</u>	<u>Group</u>	<u>Wire Number</u>	<u>Group</u>
1 to 19 inclusive	A	96	B
20	B	97	A
21 to 27	A	98	B
28	B	99	A
29 to 33	A	100	B
34	B	101	A
35 to 38	A	102	B
39	B	103	A
40 to 43	A	104,105	B
44	B	106	A
45 to 47	A	107	B
48	B	108	A
49 to 51	A	109	B
52	B	110	A
53 to 55	A	111,112	B
56	B	113	A
57,58	A	114	B
59	B	115	A
60,61	A	116,117	B
62	B	118	A
63,64	A	119	B
65	B	120	A
66,67	A	121,122	B
68	B	123	A
69,70	A	124,125	B
71	B	126	A
72	A	127,128	B
73	B	129	A
74,75	A	130,131	B
76	B	132	A
77	A	133,134	B
78	B	135	A
79,80	A	136 to 138	B
81	B	139	A
82	A	140 to 142	B
83	B	143	A
84	A	144 to 146	B
85	B	147	A
86,87	A	148 to 151	B
88	B	152	A
89	A	153 to 156	B
90	B	157	A
91	A	158 to 162	B
92	B	163	A
93	A	164 to 170	B
94	B	171	A
95	A	172 to 190	B

to remove any grease, followed by ~ 5 minutes in acetone to remove any remaining inhibisol, the final ultrasonic clean using i.p.a. (~ 5 minutes) to remove any moisture. For all subsequent assembly work and handling (after the initial inhibisol wash) gloves were used. The electrodes, anode and cathodes were gently washed with i.p.a. and a fine brush to remove any dust or contamination. Dust was removed in order to prevent problems with counter breakdown with the anode at operating voltage. Dust removal was in fact repeated throughout the assembly procedure by use of an inert gas spray.

The second stage was assembly of the upper body. First a window was cut from 25  $\mu\text{m}$  stainless steel foil using a copper gasket as a template. The window was then placed between the centre cylindrical body section, a new gasket and upper flange, and the bolts tightened by hand until the assembly was complete. The bolts were then tightened equally until a seal was formed (see Figure 4.6.1.). The lower section was assembled from the bottom up, in the order base plate, spacers, electrodes. Connections were made to the relevant feedthroughs with nickel wire.

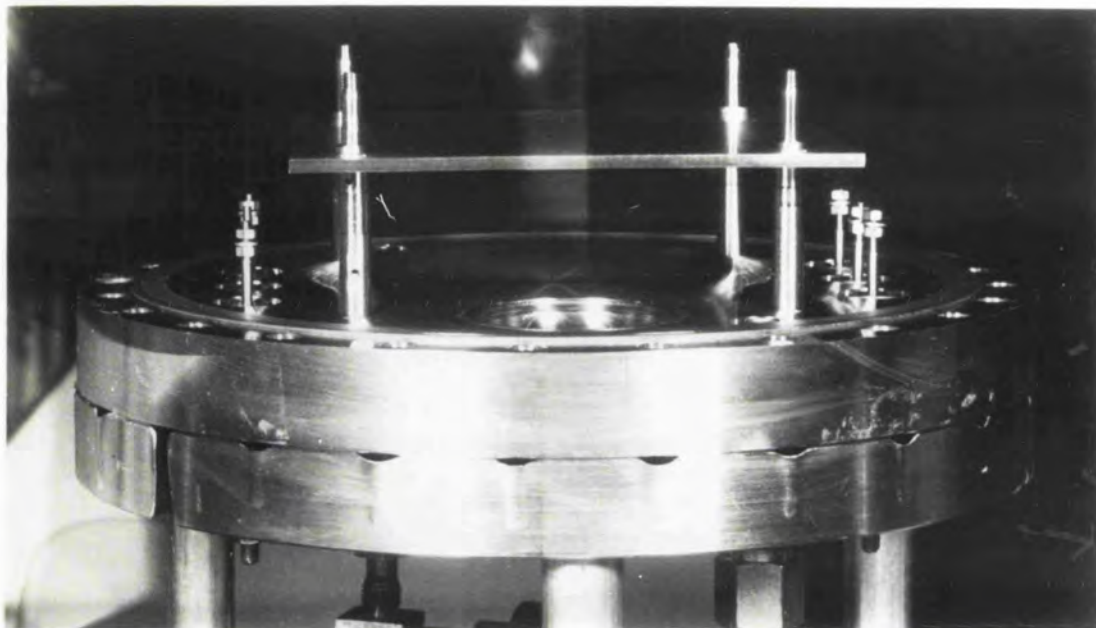
Figure 5.2.5 shows an assembled electrode array (graded density cathodes), and the base plate plus spacers before electrode assembly.

#### 5.2.4. Test and Inspection Procedure

During assembly all parts were visually inspected for faults; the grid electrodes were examined with a travelling microscope for loose wires, faulty connections, and tested using a digital multimeter before assembly.

After assembly two tests were made on the detector. First a breakdown test on the assembled grid array was conducted to ascertain whether the electrode array would survive the operating voltage conditions inside the detector. For this test the cathodes and body were earthed, and the anode connected to a preamplifier and measurement chain, and a variable H.T. supply. The measurement apparatus is shown schematically in Figure

Figure 5.2.5 Top: detector base plate with spacers before positioning and attachment of electrode assembly. Bottom: Full assembled electrode array, graded density cathodes plus anode (2mm pitch) Note: flying leads to feedthroughs (3 either side of array).





5.2.6. The measurement electronics is required to detect any electrical breakdown or 'tracking' occurring in the counter. The prototype IPC was intended to be operated with X-rays at a charge level of greater than 0.1 picoCoulombs (pC), therefore the following test criterion was adopted. For successful operation, less than one breakdown pulse  $\geq 0.1$  pC must occur per second, as the cosmic ray counting rate is of this order. The measurement electronics was therefore set to count all pulses greater than 0.1 pC. The number of counts per minute was recorded as a function of applied voltage, up to the maximum operating voltage. An average value was used for each voltage by measuring the number of counts over a five minute time period. Only electrode arrays which passed this procedure were allowed to undergo the final assembly test; a detector leak test. If for any reason counter breakdown occurred the detector was dismantled and the arrays inspected for faults. The leak test will be described in the next section, 5.3. Some practical problems were encountered using the above procedure. It was found to be necessary to 'burn in' the measurement system without the detector present. This was accomplished by wiping the test leads before starting and performing a breakdown test to the maximum required voltage on the system alone. Only when the apparatus passed this test was the detector connected and the breakdown test started. Some tracking problems were found to occur during testing due to moisture on the ceramic feedthroughs and test leads. This was removed by wiping the external surfaces with i.p.a. and drying the apparatus by passing a current of hot air over it.

During assembly a test was conducted on the upper body section to check for leaks through the detector window. This was accomplished by attaching a test plate to the upper flange, and placing the whole assembly onto a leak tester, the volume between window and test plate was then pumped by the leak tester. The apparatus used was a Centronic Leak Tester incorporated in the assembly clean room. Leak testing was achieved



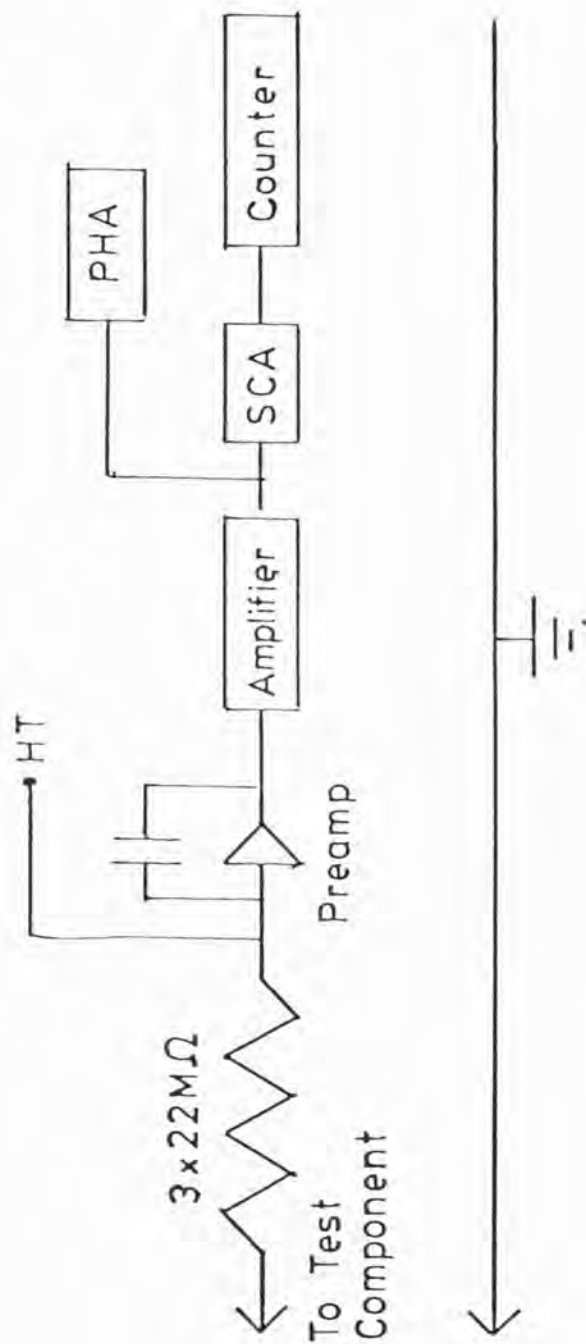


Figure 5.2.6 Breakdown test: electronic measurement chain. Resistors are present to act as current limiters. The Counter was gated via a single channel analyser (SCA), and PHA was present to record resulting pulse height distribution.

using a helium spray. The allowable leak criterion for the development IPC was taken from the UK6 and EXOSAT detector programmes. Successful performance of sealed detectors was found to require leak rates of less than  $\sim 2 \times 10^{-9}$  torr litres second<sup>-1</sup> (J. Spragg, M.J.L. Turner 1977, private communication).

### 5.3. Detector Filling

#### 5.3.1. Detector Leak Test

Prior to filling the detector a leak test was made on the fully assembled detector. This test was made in order to ascertain the leak rate into and out of the detector body, hence the internal volume of the detector was connected to the leak tester. However because of the one-way nature of the window support, namely against internal gas pressure, an auxilliary vacuum rotary pump was required to evacuate the volume between the test plate and window to prevent the window imploding into the counter during the test.

The following test procedure was adopted. First, the Centronic was started up and calibrated using a standard leak. Second, the auxilliary pump was started and a partial vacuum  $< 10^{-1}$  torr established above the window. At this point the internal volume of the detector was pumped down, the window pressure increasing temporarily as the window was pulled down releasing trapped air.

The flanges were then tested by injecting helium at a slow rate into the volume between flanges, the gas being trapped in place for the test using sellotape. The gas was injected for a period of  $\sim 20$  minutes to establish any leak rate. The top joint and lower joint were tested separately. If either joint failed the test, the flange bolts were retightened and the test repeated. Repeated failures required the use of a new copper gasket and counter disassembly.

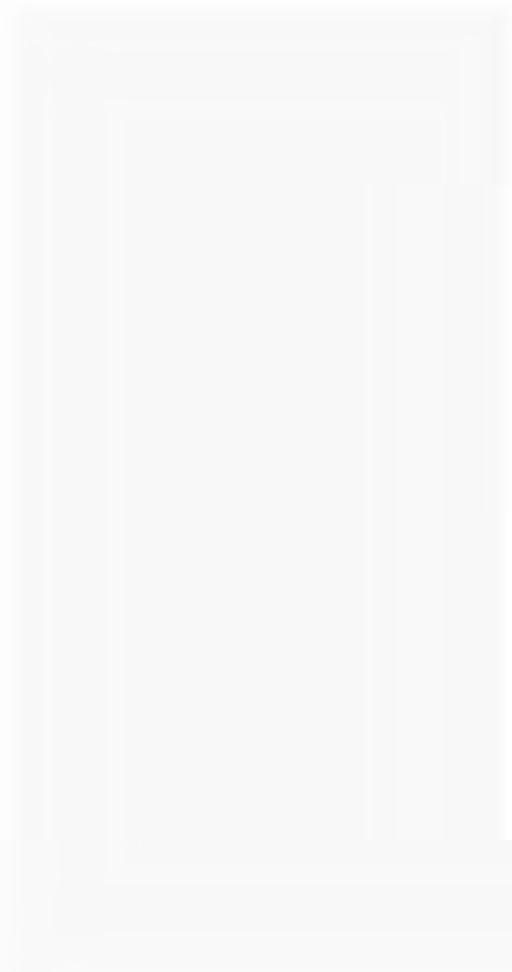
If both joints passed the test the helium was then sprayed on all feedthroughs and gas valve joints to check for leaks. After passing the leak test the internal volume was let up to atmospheric pressure and the auxilliary window pump was shut down. The concept of knife edge window sealing was tested using a set of test flanges before construction of the prototype IPC was started.

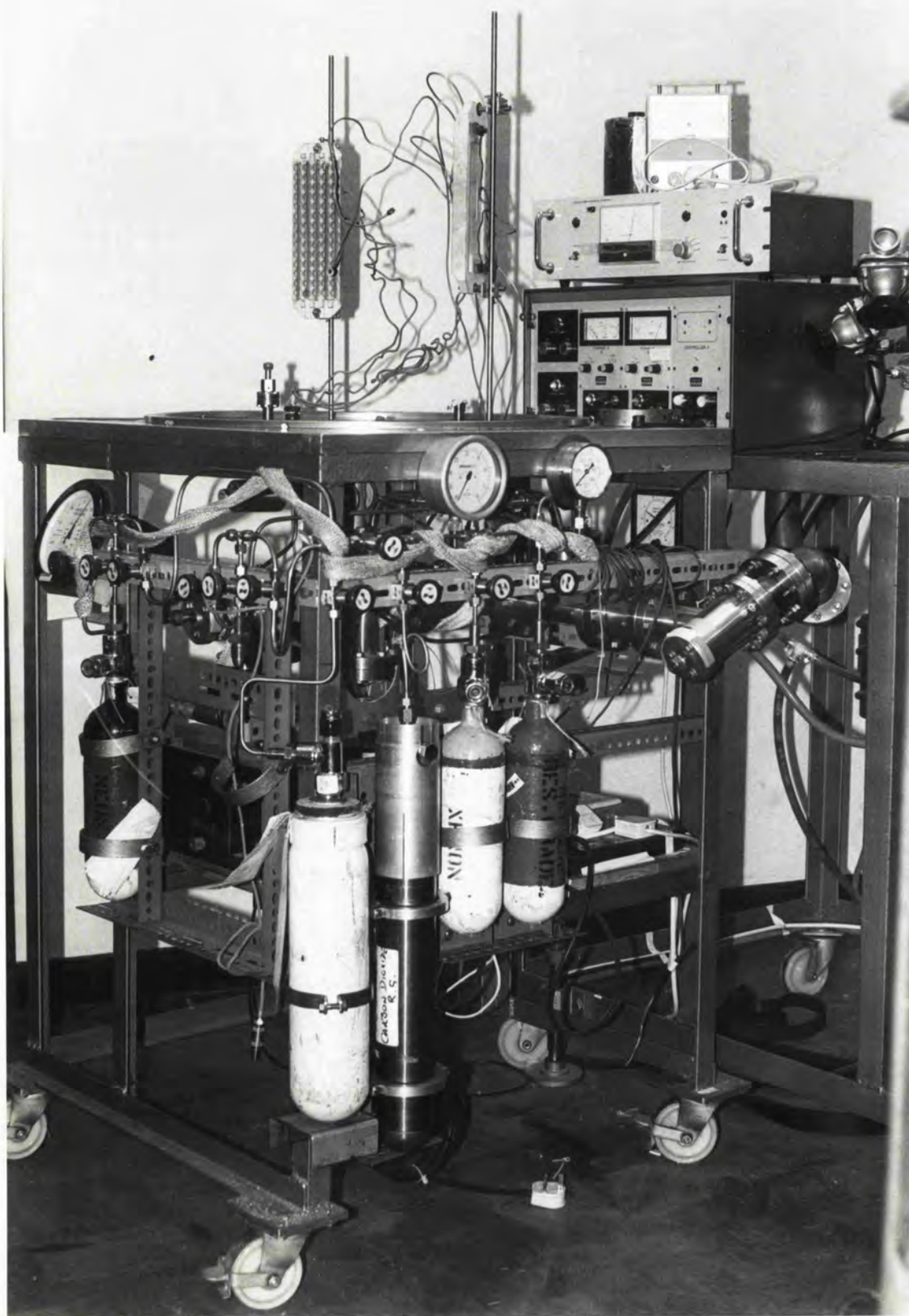
### 5.3.2. Filling Procedure

The primary method of ensuring low contaminant levels in the prototype IPC was the counter bakeout occurring during detector filling. The counter filling and bakeout was accomplished using a gas filling rig, constructed at Leicester, for the EXOSAT medium energy large area proportional counter development programme. The filling rig is shown in Figure 5.3.1; as can be seen, it consists of a number of pumping systems interlinked to a detector filling valve and bell jar (not shown in figure) complete with a gas bottle filling system.

The filling counter bakeout procedure for the detector was as follows. First, the relevant gas bottles were attached to the rig (if necessary), and the filling piping system pumped down, using rotary, then diffusion, and finally ion pumping until a base pressure at room temperature of  $<10^{-8}$  torr was achieved. The detector, on a stand, was then clamped via a Cajon coupling to the main pump and filling pipe network. The bell jar 'O' ring seal was then cleaned and greased using vacuum grease. Two thermocouples were attached to the detector body for bakeout control and temperature measurement. One thermocouple led to a temperature monitor, the second to a control thermostat for the main heaters. The filling rig has three sets of electrical heaters; first, a set of two tape type heaters for bakeout of the filling pipe network; second, a gauge heater for the filling pressure gauge; and finally two high power 'bar'

Figure 5.3.1 Detector filling rig. Note: gas bottles, main pumping controls at right and detector filling valve and heaters at top.







type heaters to bakeout the detector inside the bell jar. The thermostat controls this last set of two heaters.

The heaters were then positioned approximately 10 cm away on either side of the detector; the actual angular separation was of the order of  $120^\circ$  apart from the centre of the detector because of the design of the filling rig. A thermal shield to try and establish temperature homogeneity, consisting of a sheet of aluminium, was then wrapped in a circle round the heaters and detector.

The bell jar was then lowered and pumped down using rotary and diffusion pump until a pressure of  $\sim 10^{-4}$  torr was achieved. This pressure with the leak rate through the bell jar seal enabled the bell jar to remain at vacuum  $<$  few torr for greater than 12 hours if mains power failed, stopping window implosion. For this initial stage the detector remained at atmospheric pressure, valved-off from the rest of the system. Having achieved a low pressure in the bell jar, the bell jar was then valved-off, and the internal volume of the detector pumped down using rotary, diffusion, and finally ion pumps. The bell jar was then pumped using the diffusion pump, to ensure window safety, once the detector was on the ion pump. At this point the piping and gauge heaters were turned on and the piping allowed to outgas. The main detector heaters were then turned on, and the thermostat set only for  $40^\circ\text{C}$  to enable the high initial outgassing rate to be coped with by the ion pump. After the detector temperature and ion pump pressure had stabilised at this temperature, the thermostat was increased to  $65^\circ\text{C}$  maximum bakeout temperature. This temperature was selected as the maximum in order to avoid problems with the thermal expansion mismatch existing between grid components producing distortion. This limit was selected on advice from J. Spragg.

The detector temperature, internal pressure and bell jar pressure were then monitored every few hours, until the base pressure decreased to  $\sim 5$  to  $7 \times 10^{-8}$  torr. At this point all heaters were switched off,



and the system left to cool. Typical room temperature detector base pressures of 0.7 to  $4 \times 10^{-8}$  torr were then achieved on cooling.

The detector was then filled with the correct gas mixture, using the following procedure. The gases used were of research grade but not further purified. The ion pump was closed off from the piping network, and the detector filled to the correct pressure of methane, the quench gas, and then valved off. The piping was then evacuated and filled with Xenon to several hundred torr above the methane gas pressure, the detector valve opened and the detector filled to the correct pressure with Xenon.

Note: 1520 torr was taken as the total fill pressure at room temperature, namely 20°C. The detector was then valved off from the piping, and the piping pumped down, using the rotary, diffusion and finally ion pumps. The bell jar was then slowly let back up to air, and removed. The thermal shield was removed and the integral detector valve closed by hand. The detector was then removed from the rig for evaluation. The filling rig and detector filling procedure were designed to emphasise both safety and reliability for the detector assembly.

#### 5.4. Prototype IPC Electronics

Before the counter evaluation method is described, this section will describe the electronics used for the prototype IPC. The properties and test procedure for the electronics will be presented. For most work described here a minimum measurement system was used. This consisted of a single position measurement chain plus preamplifiers for the cathode and anode output plus relevant power supplies. For some work a second measurement chain was used enabling two-dimensional images to be produced. As mentioned above the electronics used consisted of both commercially available units and parts designed and constructed by the Electronics Workshop of the X-ray Astronomy Group.

First, in this section the position measurement chain will be described, followed by a brief description of the preamplifiers and their properties used for the work described in this thesis.

#### 5.4.1. Position Measurement

The first major item in the chain, apart from preamplifiers, is the filter amplifier. The purpose of the amplifier is to amplify the signal sufficiently for standard signal processing electronics (0 - 10 V) to be used. In the course of the work two types of amplifier were used, one produced inhouse by the Electronics Workshop, the second being a Nuclear Enterprise Type NE4658 amplifier. Each type provided both uni-polar and bipolar outputs with a variety of time constants from 0.2 to 10  $\mu$ sec depending on the amplifier type.

The preamplifiers and amplifiers are the only common components to both types of measurement chain. For the RC line zero cross-over timing was used initially as the position encoding scheme. The measurement chain as described in Chapter 4 consisted of a cross-over detector, variable delay, and time-to-amplitude converter. The cross-over detector and time-to-amplitude converter were produced by the Electronics Workshop. The cross-over detector was constructed with a dynamic range in filter time constant of 0.2 to 10  $\mu$ sec, the delay (built into the time-to-amplitude converter (T.A.C.)) was adjustable to within this range, to allow for the risetime of signals down the RC line. The final T.A.C. output had a signal height of 0 to 10 V with a risetime of greater than 250 nano seconds in order for the signal to be compatible with most makes of pulse height analyser (P.H.A.).

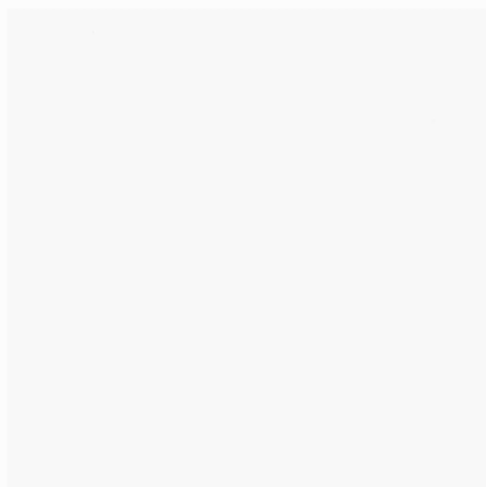
In the ratio method one requires division of the output signals A and B from the amplifiers in the ratio  $A/(A + B)$  or  $(A - B)/(A + B)$ . In order to do this division by analogue means, a fast risetime and fall-time signal is not suitable, hence the first step in the measurement chain

after the filter amplifier is a peak and hold stretcher. A set of six stretchers were built inhouse, each capable of dealing with signals (0 to 10 V) with a positive leading risetime of greater than  $0.1 \mu\text{sec}$ . Each stretcher was inhibited and reset using a single channel analyser gated anode signal from a master clock unit, which also triggered the analogue divider. The output from the stretcher unit was passed to a dual sum and invert module (Ortec Type 433A) to sum the signals, and invert them for the divider circuit, as the inhouse built unit required negative input signals. In this work only the position encoding method of  $A/(A + B)$  was used, a second dual sum and invert would be required for the case of  $(A - B)/(A + B)$ . The analogue divider was constructed to produce the output  $10 z/x$  from two stretched input signals  $x$  and  $z$ . The resultant pulsed output was designed, as per the T.A.C. output, to be compatible with most makes of P.H.A. (Ortec Type 6240 used in this work).

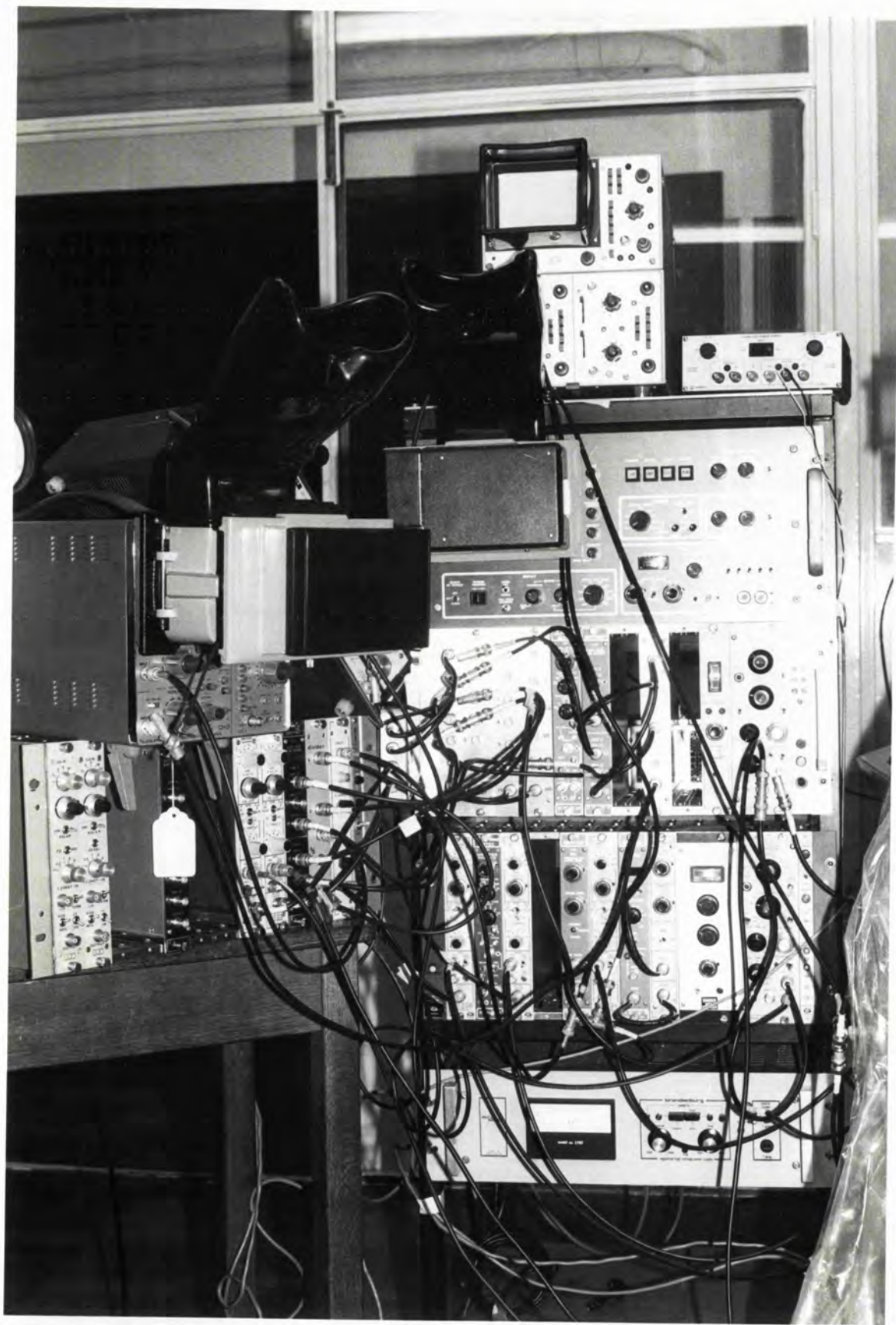
The whole ratio chain, as previously mentioned, was driven by a master clock unit. This was triggered via a single channel analyser (Ortec Type 550) from the anode shaping amplifier. The single channel analyser was adjusted so that only signals within a preset total charge level triggered the measurement chain enabling a large percentage of cosmic ray events to be rejected. The various drive signals were carefully adjusted to prevent problems with pulse pile up occurring.

Before use and periodically during use each set of measurement electronics was carefully checked and all signals adjusted to within required limits. Figure 5.4.1 shows the measurement chain electronics mounted in standard 19 in. N.I.M. racks providing power for the measurement system. This is the ratio position measurement system. For true imaging a second set of electronics, integral in the above racks, was used to provide the second position co-ordinate. The two position signals were used to drive an X-Y oscilloscope, a trigger pulse for the scope being provided from a

Figure 5.4.1 Position measurement chain electronics mounted in standard 19" NIM racks. Full 2-D imaging (ratio method) is shown. X-Y scope is positioned at left, top C.R.O. (above PHA) was used for calibration and electronic checkout procedures.







purpose built unit driven from the anode amplifier output. Images were recorded on Polaroid Film with a Shackman Oscilloscope Camera. The anode voltage for the detector was provided by an 0 to 5 kV power supply (Nuclear Enterprise Type 4660) via the anode preamplifier. The cathodes were supplied with a positive potential, to provide a drift field, via separate lines from a common 0 to 3 kV power supply (Ortec Type 456). All power supply lines had an RC filter to remove any high frequency noise components, and a current-limiting resistor before reaching the relevant electrode.

#### 5.4.2. Preamplifiers: Properties; Calibration; Use

During the course of the work a variety of preamplifier designs were used. The initial design was provided by M.I.T. This type was found to have an unsatisfactory noise performance for use with the position encoding methods, hence was only used throughout the work for the anode preamplifier where noise is relatively unimportant. For the majority of the work two other designs were used, one from Pye Ltd. of Cambridge, England, and the second a commercially available preamplifier, the Canberra Type 2001A supplied by Canberra Industries Inc. These two designs were chosen for their low noise performance with a large load capacitance. Figure 5.4.2 compares the rms noise from each design for an amplifier shaping time constant of 1  $\mu$ sec (double differentiation single integration). Load capacitance from a detector was found to be at least 40 pF. In order to reduce noise to a minimum, all leads from the preamplifiers to the detector were kept as short as possible to reduce the load capacitance.

Before use all the preamplifiers were calibrated in order that the feedback and test capacitor values were known. Output charges from the detector were measured using the pulse matching method (Mathieson and Charles 1969, Hendricks 1973) of applying a known voltage step to the



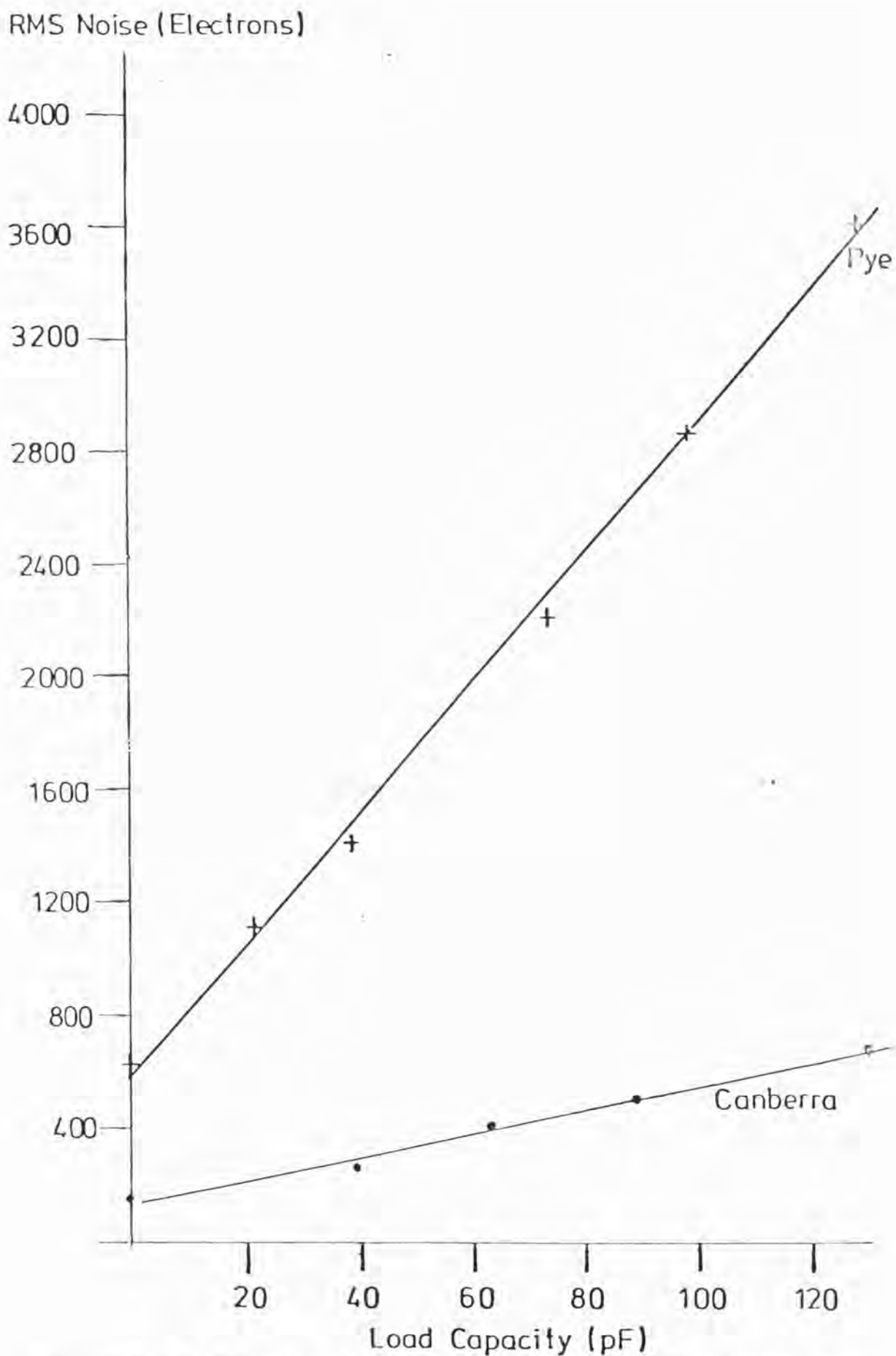


Figure 5.4.2 RMS noise in electrons as a function of load capacitance for Pye and Canberra preamplifiers. Measurements are for two typical preamplifiers.

preamplifier test capacitance and comparing the output. In practice the output charges were usually measured after shaping and amplification, a fast risetime pulse  $.05 \mu\text{sec}$  being used for calibration. Test pulses for both preamplifier and other calibration purposes were provided by a pair of B.N.C. BH-1 tail pulse generators.

Some precautions were taken in use of the Canberra preamplifiers to avoid destroying the front end P.E.T. in each, as the design incorporates no protection diodes against H.T. voltage spikes. The anode voltage was always increased slowly up to operating voltage, and the Canberra preamplifiers not attached until an anode pulse height spectrum was taken and checked that no breakdown was occurring. If any was observed the anode H.T. supply was reduced to 0V until the problem was cured. If no breakdown was observed the Canberra preamplifiers were attached to the relevant leads, and the drift field supply adjusted to the correct voltage. On completion of a set of measurements the power supplies were slowly reduced to 0V and then turned off. The Canberra preamplifiers were only removed after 5 minutes had passed to allow decay of the power supply voltages to zero.

#### 5.4.3. Other Practical Points

In the initial part of the work described some problems were encountered with noise through the mains power supply and pick-up from a local radiotransmitter. Some of this noise was found to be caused by earth loops present between various parts of the apparatus. Hence all the apparatus was powered from a single mains socket using a set of mains extension boards. All preamplifiers and H.T. power supplies were grounded to the detector, and the counter was placed on a large 2m x 1m aluminium sheet. All preamplifiers were enclosed in earthed metal boxes to prevent pick-up problems. Some problem was encountered with noise via the mains

supply and this was removed by use of a mains filter.

In order to ascertain the resolution due to counter effects alone it is necessary to measure the contribution due to the position encoding method and measurement electronics. This was accomplished in the following manner. The preamplifiers were connected to the detector to provide the correct capacitance loading, and noise contribution from the position encoding method. A voltage signal of the correct counter rise-time was then input to both cathode preamplifier test capacitors simultaneously and the resulting electronic resolution (FWHM) in P.H.A. channels ascertained for that input charge. By varying the input charge which can be directly related to equivalent anode charge an electronic resolution versus gain graph was produced showing the relevant contribution to resolution. The resolution was related to real measurements by the correct linearity scale ascertained from measurements from the counter with X-rays.

Finally, throughout the work the preamplifiers were recalibrated and other electronics checked on many occasions to ensure correct operation. Any apparatus which no longer met specification was replaced or repaired immediately.

#### 5.5. IPC Configurations: Parameters; Evaluation Method

This section will describe the exact IPC configurations constructed during the course of this work, and the measured parameters, (mechanical and electrical) for the detectors alone. Finally, the test apparatus and counter evaluation method will be described.

### 5.5.1. IPC Configurations

Only two types of anode design were investigated in this work; an 8 mm spaced array for a one-dimensional position sensitive detector; and a 2 mm spaced anode for a two-dimensional position sensitive detector. As mentioned above two types of position encoding method and hence cathode were used, the RC line, and graded density type. Table 5.5.1 lists the configurations built and tested during this work. The table lists all nominal and measured construction parameters.

The initial detector constructed was a one-dimensional position sensitive detector (Table 5.5.1(a)). This choice was made on two grounds; first, a 'new' gas mixture was being tried, hence a simple system was required for investigation of its properties; second, this actual IPC configuration of an 8 mm spaced anode was proposed for a one-dimensional position sensitive shadow camera in 1976 (MIT/Leicester 1976). The value of resistance for the position sensing top cathode was chosen on availability from the Argon/Methane IPC development work towards the rocket flight of Rappaport et al., 1979.

Throughout the work a drift region of 5.5 mm was used, this being the smallest available within the development IPC design. This was chosen so that the counter's overall thickness was as small as possible and the results were dominated by the gas physics. Thus the smallest possible diffusion of an initial electron cloud would enable the modulation and resolution of the counter to be as near intrinsic to the gas mixture as possible. Electron diffusion blurs out any across-anode wire modulation and reduces the achievable resolution along the wire (as discussed in Chapter 6).

For the two-dimensional position sensitive detector work, an anode spacing of 2 mm and an anode cathode spacing of 5 mm was chosen on

TABLE 5.5.1

## IPC CONFIGURATIONS

(a) One-Dimensional Position Sensitive Detector

Anode to cathode spacing:	9 cm
Anode to wire spacing	8 mm (nominal)
Anode wire diameter	15 $\mu\text{m}$ (nominal)
Anode wire	Gold plated tungsten
Cathode wire spacing	1 mm (nominal)
Cathode wire diameter	125 $\mu\text{m}$ (nominal)
Cathode wire	Copper-Beryllium (98-2) alloy
Anode and cathode wire attachment method	Solder
Upper cathode to window distance	5 mm (nominal)
Lower cathode to base plate	5.5 mm (nominal)
Readout RC line	Nominal 25 k $\Omega$
In direction along anode wires only	
Actual resistance	23.1 k $\Omega$
Cathode capacitance to earth	39 $\pm$ 1 pF
Other cathode direct short	
Detector window support :	Parallel to anode wires
	Strips 3 mm wide x 6.5 cm long
Detector window material:	1 thou. (25 $\mu\text{m}$ ) stainless steel

(b) Two-Dimensional Position Sensitive DetectorMechanical

Anode to cathode spacing	5 mm
Anode wire spacing	2 mm
Anode wire diameter	15 $\mu\text{m}$
Anode wire	Tungsten
Upper cathode to window distance	5.5 mm
Lower cathode to base plate distance	5.5 mm
Window support:	Hexagonally packed circles
	diameter 1.2 cm
	centre to centre spacing 1.6 cm
Window material:	1 thou. (25 $\mu\text{m}$ ) stainless steel

TABLE 5.5.1 (contd.)

(b) contd.

CathodesRC line

Cathode wire spacing	1 mm
Cathode wire diameter	125 $\mu$ m
Cathode wire	Copper Beryllium (98-2) alloy
Wire attachment method	Solder
RC line	Nominal 100 k $\Omega$
Top cathode (perpendicular to anode wires)	
Actual resistance	101.1 k $\Omega$
Capacitance to earth	38.4 $\pm$ 1 pF
Lower cathode (parallel to anode wires)	
Actual resistance	98.9 k $\Omega$
Capacitance to earth	40.8 $\pm$ 1 pF

Graded Density Cathode

Cathode wire spacing	0.5 mm
Cathode wire diameter	20 $\mu$ m
Cathode wire	Gold plated Tungsten
Wire attachment method	Epoxy
Capacitance to earth	
Upper cathode (perpendicular to anode wires)	
	96.4 pF
Lower cathode (parallel to anode wires)	
	102.7 pF

Note: Cathode values averaged over two halves of each electrode for one counter. The total resistances were measured using a Wayne Kerr Component Meter Type B424, and the capacitances, with a Marconi Universal Bridge Type TF2700 with all other counter electrodes earthed.



three criteria; firstly, the Argon/Methane work (G.C. Smith 1977, private communication) showed that a 2 mm anode spacing could produce sufficient resolution and linearity across the anode; secondly, this configuration enabled an operating voltage of ~3 to 4 kV for the anode to be used, limiting power supply requirements and breakdown problems; and finally such a wide-spaced anode would enable investigation of across-anode wire modulation in Xenon gas mixtures to be made.

The choice of 25  $\mu\text{m}$  stainless steel for the window material was made (as discussed in Chapter 4) on cost, availability and safety criteria. The window support structures were designed by J. Spragg for this material. Stainless steel was also a requisite for the counter sealing approach adopted. The transparency of the window can be calculated from mass absorption coefficients (McMaster et al., 1969) to be 17% for  $\text{Fe}^{55}$  (5.9 keV) radiation, adequate for prototype evaluation.

The three configurations built, one-dimensional detector, two-dimensional RC, and two-dimensional graded density, were initially filled to 1520 torr (20°C) with Xenon/Methane 90/10 by pressure. The purpose of these builds were to primarily investigate the detector position read-out methods with this particular gas mixture, and to obtain data on the gas mixture's limitations to resolution and across-wire modulation. Having established these parameters a graded density configuration was then filled with 75/25 and 50/50 mixtures of Xenon/Methane and evaluated in order to determine the effect of quench gas on these parameters.

Not all counter configurations constructed were successful initially, because of counter breakdown problems, and grid failure under bake-out. The significant results from the successful counters are presented in section 5.6 of this chapter and Chapter 6.

### 5.5.2. Counter Evaluation Apparatus and Method

Before some of the practical points of taking data from the IPC are discussed, some of the counter test apparatus will be described. The radiation source used throughout most of the work was the electron capture source  $\text{Fe}^{55}$  (5.9 keV). This was used for a variety of reasons; first, it is a monochromatic source of X-rays; second, it is able to penetrate the detector window; and finally, it also corresponds closely to the top of the energy efficiency curve for the proposed shadow camera IPC, section 2.10, Chapter 2. The source used was a 7 milliCurie source of dimensions 3 mm by 8 mm, enclosed in a stainless steel holder. Some counter measurements were also taken using a  $\text{Cd}^{109}$  (22 keV) source to determine the effects of higher energy photons. Both sources were used in conjunction with a helium tube and slit assembly, to provide collimation for measurements on the counter. For the one-dimensional position sensitive detector work a 60 cm helium container was assembled from plastic tubing. The source was then mounted on the top of the tube, and a narrow slit on the bottom. Measurements were taken using a scale in millimetres stuck to the detector window support. For the two-dimensional work a sealed 50 cm helium tube was constructed from stainless steel tube with 125  $\mu\text{m}$  Beryllium windows at each end. This sealed tube was refilled with helium before each new counter configuration or gas mixture was tested. On the bottom of the tube a slit assembly of variable width was attached. This assembly was capable of rotation through  $90^\circ$ .

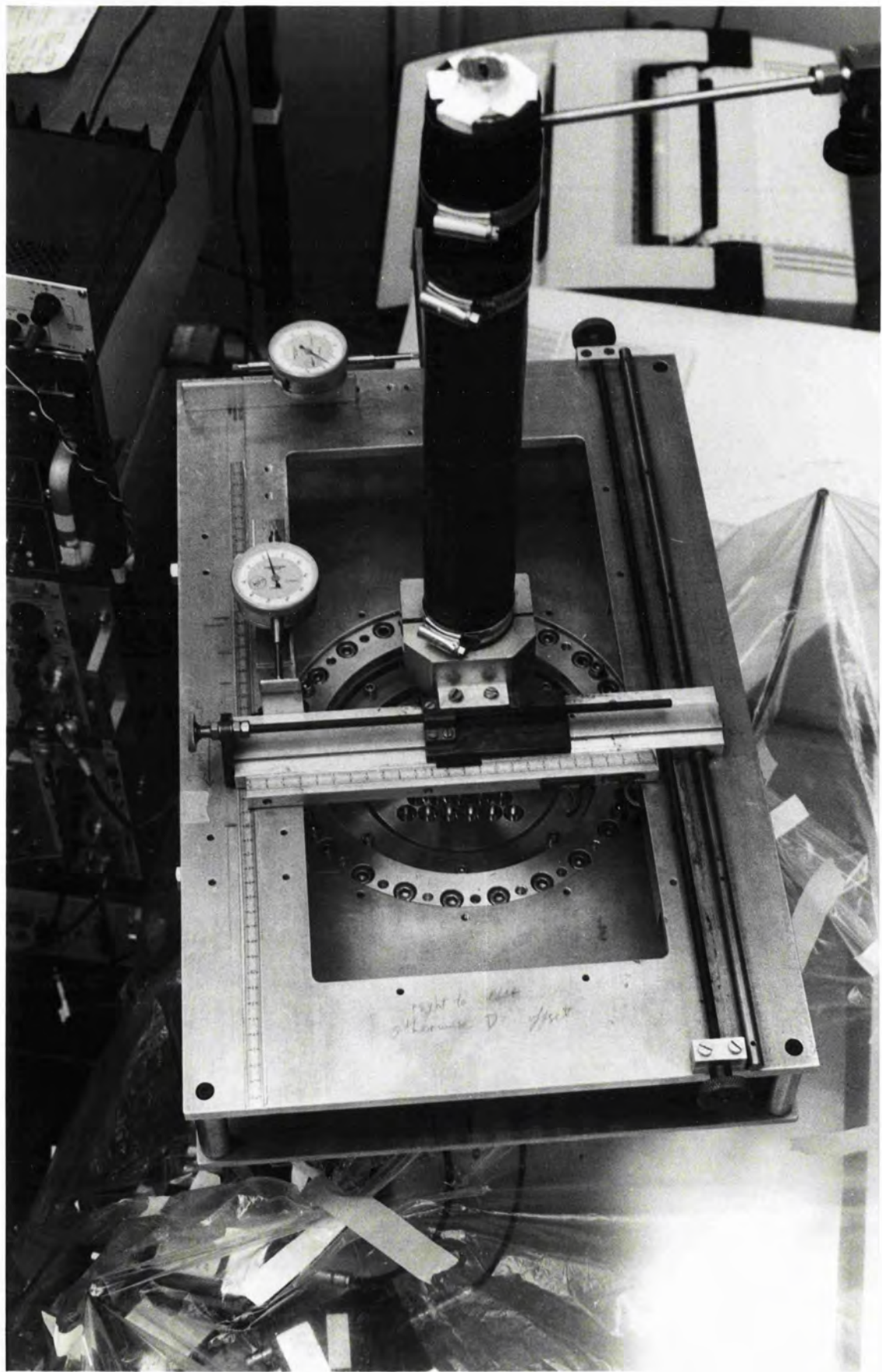
The helium tube was used in conjunction with an X-Y table aligned by fiducial marks on the detector to the along- and across- the-anode sensing axes. The slit assembly was aligned to the X-Y table by using a flat test bed and measurement tools. The fiducial marks on the detector corresponded to a set of scribed lines internal to the detector to which the anode wires were aligned. The X-Y table was mounted by four points

to the top flange of the detector, enabling approximately the whole open area of the detector window to be traversed by the helium tube. Absolute motion of the tube and slit assembly were measured using two scales in millimetres mounted on the table. Relative motion from a preset starting co-ordinate was measured using two dial gauges reading in  $10\text{ }\mu\text{m}$  intervals mounted against pusher plates on each detector axis. With the dial gauges in place an area of  $\sim 3\text{ cm} \times 3\text{ cm}$  could be traversed. The absolute scales were found to be readable to a random error of  $\pm 100\text{ }\mu\text{m}$ . Figure 5.5.1 shows the X-Y table with dial gauges and helium tube mounted on the detector.

The ratio position measurement electronics during testing was found to have a limiting operating condition of a maximum  $4\text{ V}$  input to the adder for good linearity. This resulted in a rather elaborate detector evaluation method. Before any measurements of position resolution were taken the counter output charge was measured and the gains of the cathode amplifiers adjusted such that the output voltages from the two stretchers were equal and had a value of  $\sim 1.5\text{ V}$ , the midpoint of the linearity range for the stretchers and adder combined. The cross-over position measurement electronics had no such problems and the amplifier gains were nominally adjusted such that a  $5\text{ V}$  output signal, half maximum was used. A variety of parameters were measured from the prototype IPC. The key parameters are of course position resolution, linearity, and energy resolution. The optimisation and measurement of energy resolution in the counter were largely ignored, the majority of the work concentrating on evaluating position resolution and linearity. This was accomplished largely by the use of small local scans at various regions across the detector area measuring position resolution and output position as a function of real position, and a counter parameter, for example anode voltage. In addition, spot point measurements of resolution were made. The results

Figure 5.5.1 X-Y tables with dial gauges and helium tube mounted on top of the detector. Note: circular window support of detector and plastic tent (for humidity control) enclosing preamplifiers (at bottom) for high voltage ( $> 4$  kV) operation .





of these measurements and others will be presented in the next section of this chapter and Chapter 6 for the various configurations of prototype IPC constructed.

## 5.6. Results from the One-Dimensional Position Sensitive Detector

The one-dimensional position sensitive detector configuration was constructed primarily to obtain data on the resolution achievable in Xenon. At the time an accurate X-Y table was not available, hence the measurements tend to be of a spot point nature, little emphasis being placed on linearity measurements. The configuration parameters are summarised in Table 5.5.1 of the previous section. The detector was filled on 2/11/78 with Xenon/Methane in the ratio 90/10. The detector continued operating until the 2/2/79 when breakdown problems due to deposition on the anode wire prevented further work.

### 5.6.1. Energy Resolution

As a test of gas purity the energy resolution was measured every day at a spot point to determine any degradation and hence poisoning. These measurements were taken at an anode voltage of 2.2 kV with a drift field voltage of  $+50$  V supplied to the cathodes. On filling, the energy resolution (FWHM) for  $\text{Fe}^{55}$  was found to be  $\sim 29\%$ . This decreased to 21% after 5 hours and two days later to 16%. This improvement in resolution is presumably due to long time constant exchange processes within the body of the detector, either gas mixing or gas wall interactions. Figure 5.6.1 shows the energy resolution achieved with the counter three days after filling by which time the energy resolution had stabilised. This energy resolution is for a measured charge of 1.0 pC (at the pre-amplifier input). The plot shows the resolution with both  $\text{Fe}^{55}$  and  $\text{Cd}^{109}$ , the anode voltage being adjusted such that an identical charge level was



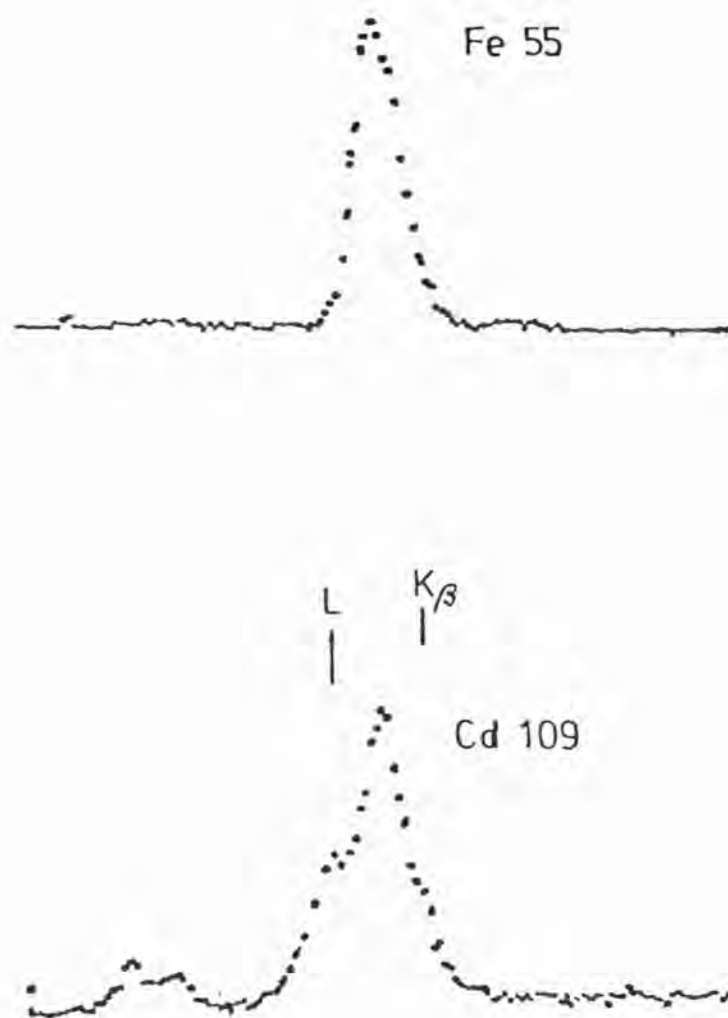


Figure 5.6.1 PHA distributions showing energy resolution for 1-D position sensitive prototype for a measured charge of 1.0 p.c for Fe<sup>55</sup> and Cd<sup>109</sup>; K $\beta$  peak and L escape peak are marked.

measured for both sources. The  $\beta$  peak, and L edge Xenon escape peak, are clearly visible for the  $\text{Cd}^{109}$ .

Spatially localised counter breakdown preceded by a deterioration in energy resolution was found to occur at spot points on the anode wires where a large number of measurements (hence counts and dumped charge) had occurred. This localised breakdown was traced on disassembly to deposition on the anode wires. The effect was however very localised hence other areas of the same wire were unaffected enabling measurements to be obtained at other spots. Figure 5.6.2 shows a scanning electron microscope photograph of the deposition on the anode wire after total counter breakdown had occurred. The effect is obviously less extreme under the above conditions.

Counter energy resolution was found to deteriorate above anode operating voltages of 2.6 kV, and was  $> 70\%$  FWHM with  $\text{Cd}^{109}$  at an operating voltage of 2.8 kV. (The drift supply was set at  $+50$  V). This change was accompanied by a marked change in the anode pulse profile.

#### 5.6.2. Anode Pulse Profile

The anode pulse profile from the output of the anode preamplifier was investigated as a function of anode voltage and drift voltage. Figure 5.6.3 shows the anode pulse profile from the preamplifier compared to the pulse profile from the cathode with no line terminating capacitor for  $\text{Fe}^{55}$  in the centre of the counter. The 90% risetime of anode signal is 1.5  $\mu\text{sec}$ , which is comparable with the risetime from the RC line. These profiles were obtained with an anode voltage of 2.75 kV and a drift voltage of  $+50$  V. Positive ion collection time by the cathodes was found to occur after approximately 2 msec at an anode voltage of 2.4 kV, decreasing to 1.5 msec for a voltage of 2.9 kV.

A distinct kink in the anode pulse profile started to become visible at an operating voltage of 2.9 kV corresponding to a dumped charge of

Figure 5.6.2 Scanning electron micrograph showing deposition on anode wire after total counter breakdown. Insert shows an unaffected wire.



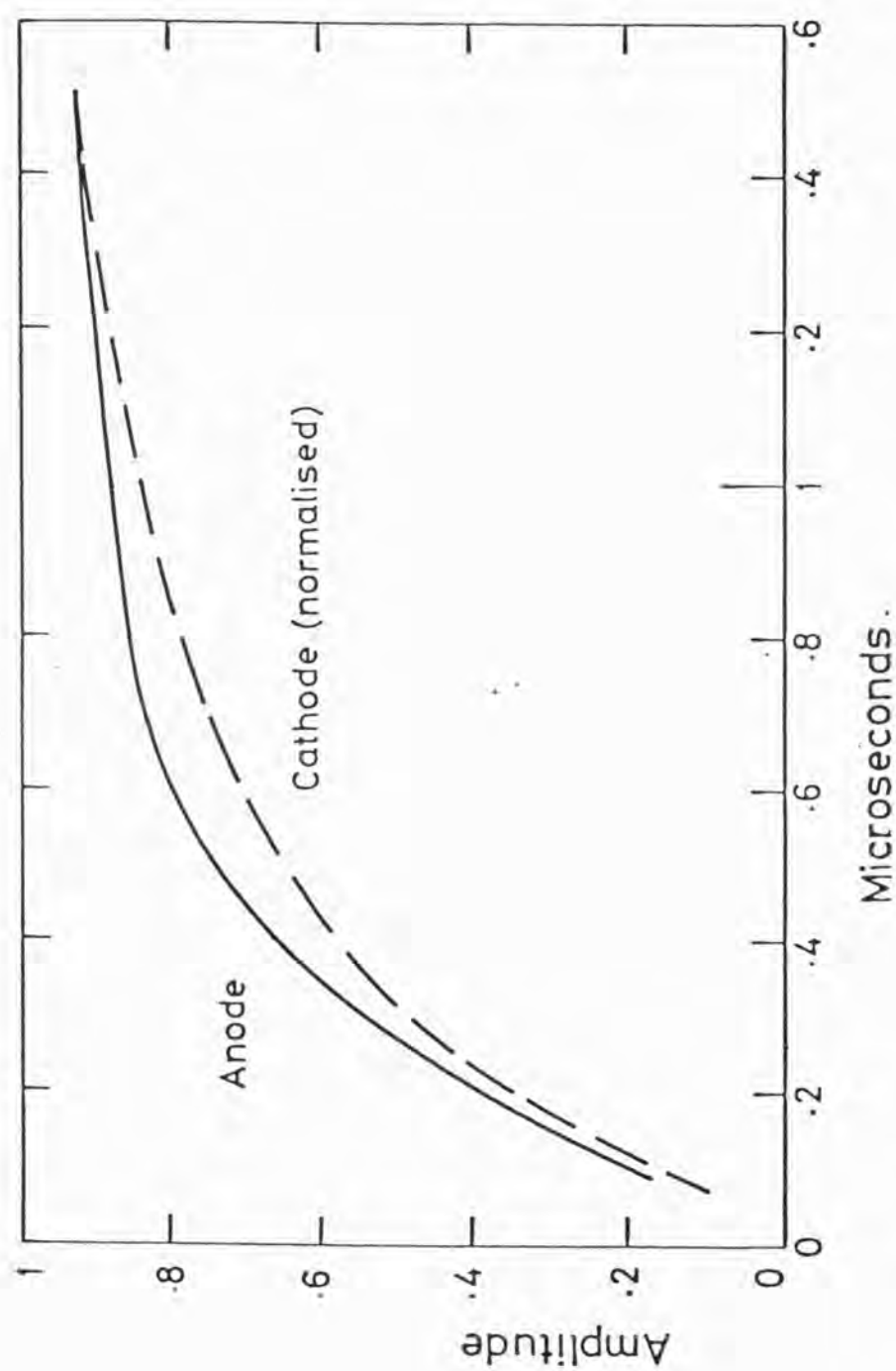


Figure 5.6.3 Anode and cathode (Cd not present) pulse profile from preamplifiers for  $\text{Fe}^{55}$  source in the centre of the counter. Anode voltage was + 2.75 kV, drift voltage + 50 V.

approximately 1.6 pC with  $\text{Fe}^{55}$ . Figure 5.6.4 shows the resulting pulse profile. The time of the kink after the start of the anode pulse was found to vary with drift field, the time difference becoming shorter as the drift field was increased, the anode voltage being increased to maintain an identical counter gas gain. Figure 5.6.5 shows the approximate time of the start of the kink in the anode pulse profile, as a function of drift field. The counter gain was balanced as for an anode voltage of 2.9 kV, drift field  $+50 \text{ V}$ . This kink was most likely due to secondary avalanches resulting from electrons released from the counter window, by ultraviolet photons released in the avalanche process. This effect is invoked in Chapter 6 to explain the resolution obtained with the two-dimensional position sensitive IPC. It will be shown that this effect can dominate the position resolution achievable with a Xenon/Methane filled detector. Secondary avalanching is most likely to explain the above results due to the decrease in time after the start of the pulse for the kink as a function of drift voltage. This decrease represents the reduction in transit time for photoelectrons from the window due to the higher drift field. These data are the only independent positive physical evidence of secondary avalanching found in this work.

### 5.6.3. Position Resolution

For this detector configuration the RC method of position encoding was used. Both possible methods of zero cross-timing and pulse height ratio were used. The preamplifiers used for the work described in this section were copies of the Ortec Type 109PC design, having an inbuilt isolation capacitor of 200 pF nominal, for use as a line terminating capacitor (Cd). For the initial part of the work an additional Cd of 3 pF was used; this was later changed to 16 pF. The initial value was taken before the completion of the relevant calculations of Fraser (1980).

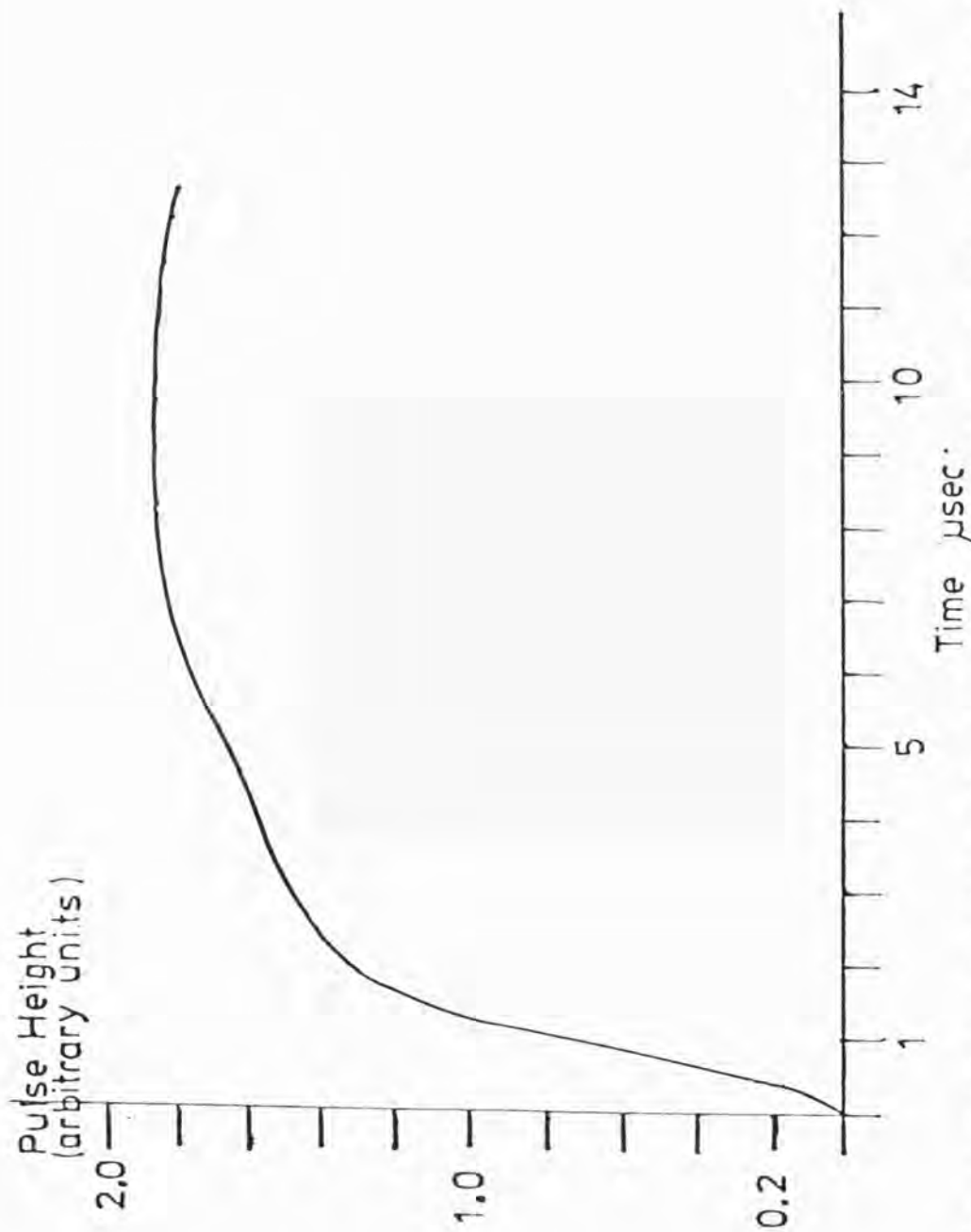


Figure 5.6.4 Anode pulse profile from preamplifier for anode voltage of + 2.9 kV, drift voltage + 50 V. Note: a distinct kink is visible in the profile, starting  $\sim 4\mu\text{sec}$  after main pulse. This profile and previous profiles (Figure 5.6.3) are obtained from Polaroid photographs and hence are average typical profiles.



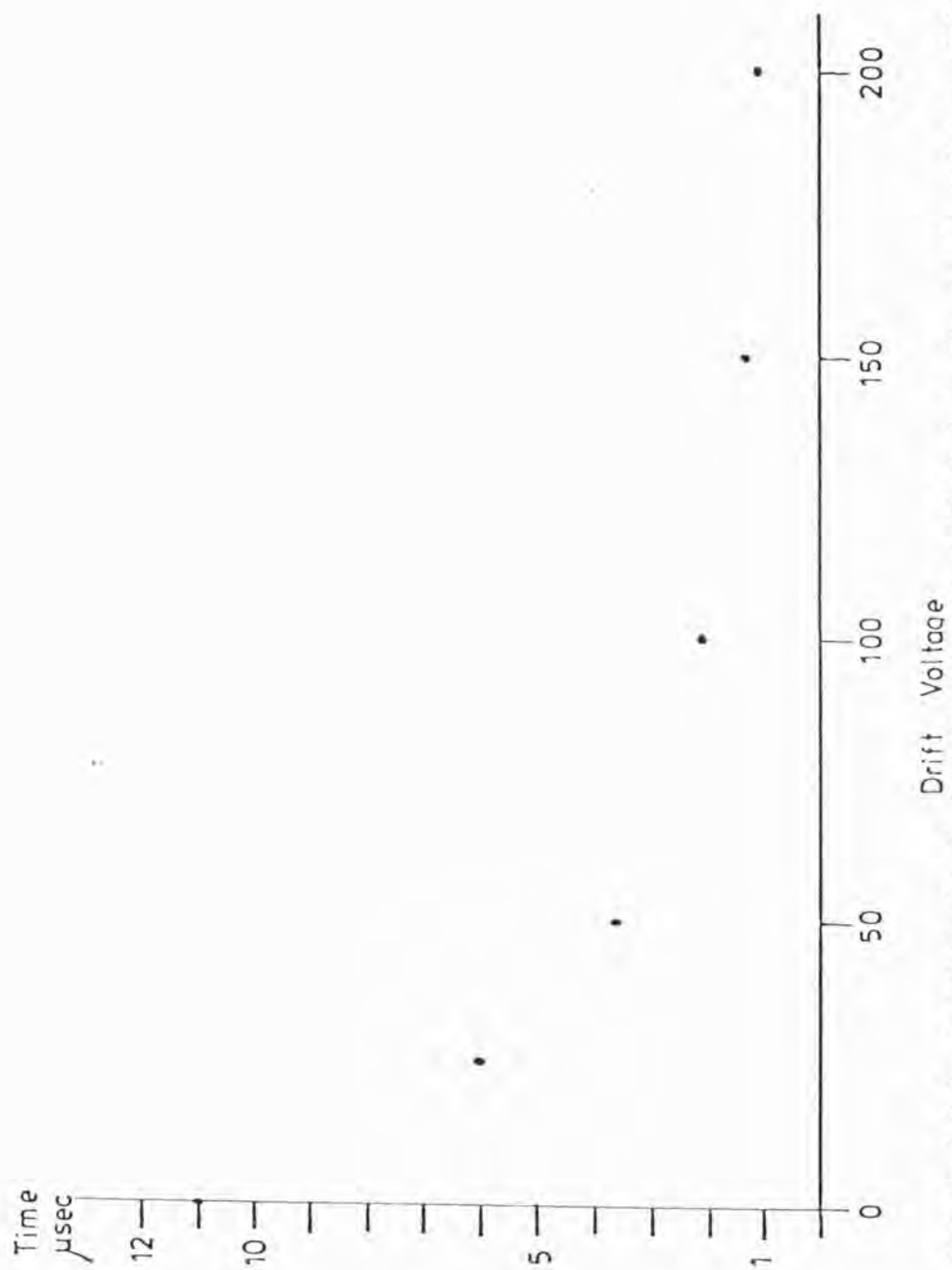


Figure 5.6.5 Approximate ( $\pm \frac{1}{2}\mu\text{sec}$ ) start time of kink in the anode pulse profile (from preamplifier) as a function of drift field.

For the ratio method the external Cd's were removed and the preamplifiers used at short circuit; Cd was therefore 200 pF, the isolating capacitor value.

Figure 5.6.5 shows the position resolution achieved for each read-out configuration tested as a function of anode collected charge. At this point a comment on the IPC results presented in this work must be made. The results were found to be reproducible exactly without measurable true statistical error, the random error in reading the PHA being found to be the dominant error. Hence the errors shown in any figures hereafter are the maximum random error in the result. The resolutions presented are the result of measuring the resolution at three spot points a fixed distance apart (2 mm) and calculating the average resolution from the average sensitivity (PHA channels per millimetre). Figure 5.6.7 shows the resolution as a function of cathode-amplifier shaping time constant, showing that the best combinations were as presented in Figure 5.6.6. The resolution versus time constant ratio was found to be independent of counter gain. Little variation was found of position resolution with drift voltage over the range 0 to  $+400$  V for a given gas gain, all measurements agreeing within the system random errors.

In Figure 5.6.6 the resolution data obtained from the counter is compared with the electronic noise limitation from the position encoding method. This was calculated from the theoretical work of Fraser (1980) and a knowledge of the preamplifier noise characteristics using equation (4.5.1). The programme input parameters and relevant theory are summarised in Table 5.6.1. As can be seen the data are in close agreement with the theoretically predicted spatial resolution especially at low charge levels. The ratio method at a time constant of 0.5  $\mu$ sec provided the best measured resolution. The best achieved position resolution is about 30% worse than predicted by the theory. This is most likely due to some unknown additional noise source, or the limitation of the model in

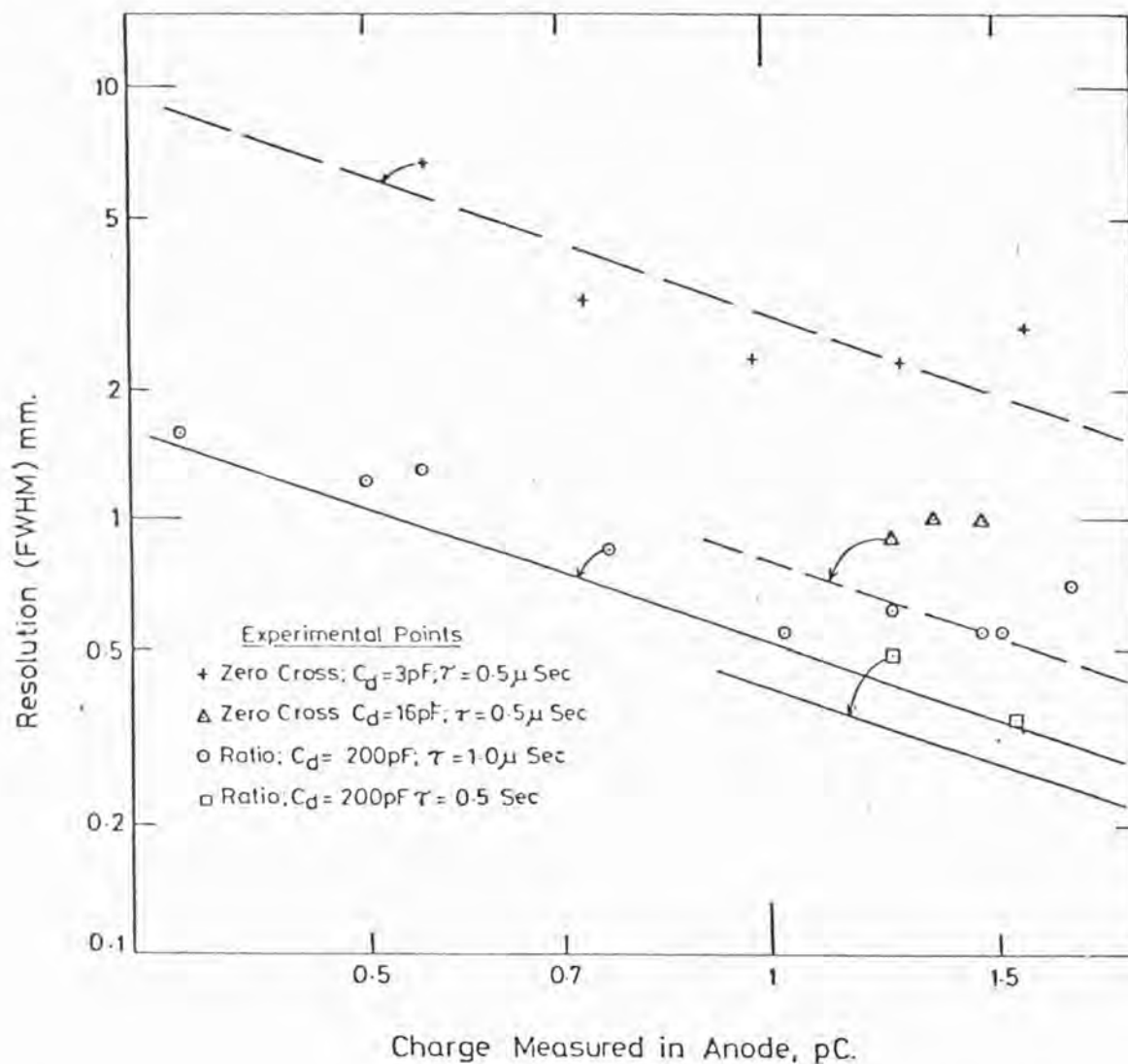


Figure 5.6.6 Position resolution (FWHM, mm) as a function of anode collected charge for the zero cross and ratio methods for various cathode time constraints ( $\tau$ ). Solid lines are theoretical predicted performance, arrows link relevant data points to theoretical predictions.

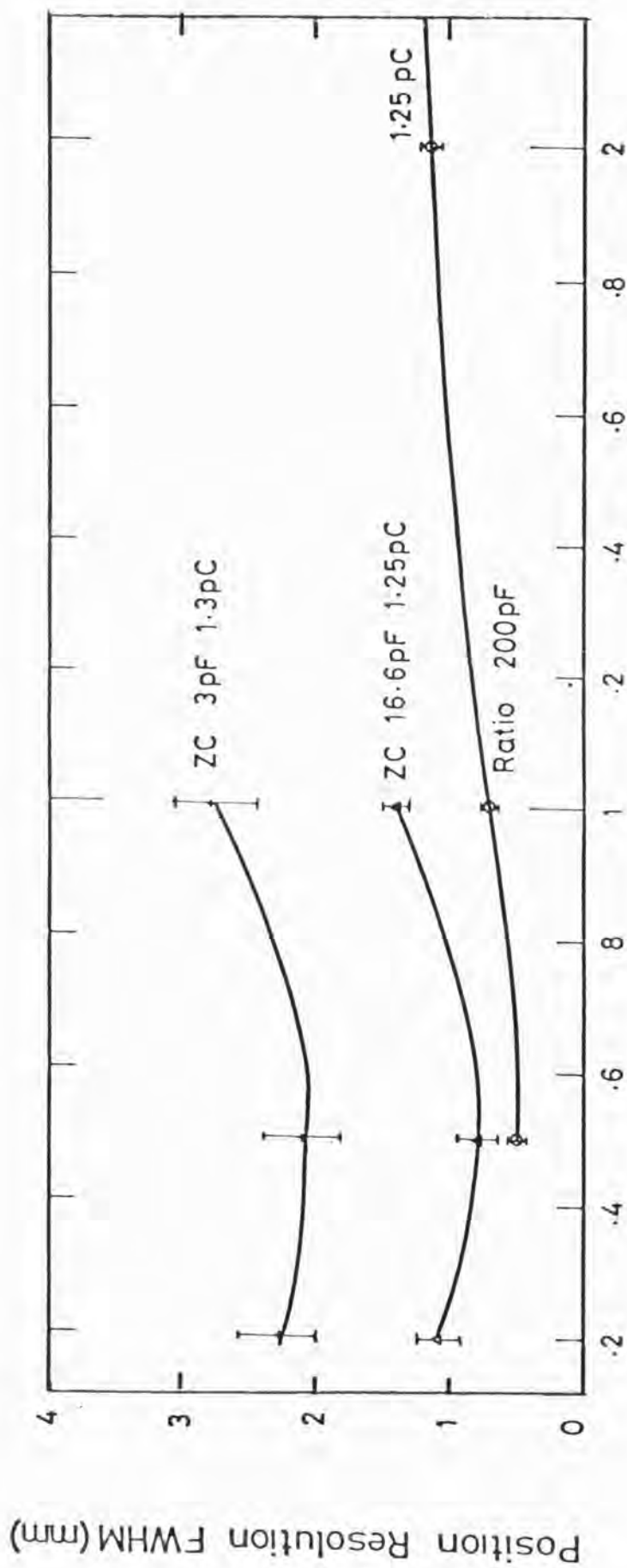


Figure 5.6.7 Position resolution (FWHM, mm) as a function of cathode-amplifier time constant for zero cross (ZC) and ratio methods of position encoding for near identical charge levels. Error bars are (maximum) random error in determining position resolution.

TABLE 5.6.1

## RC LINE PARAMETERS

## FOR THEORETICAL CALCULATION OF PERFORMANCE

Total resistance (R) of line	23.1 k $\Omega$
capacitance (C) to earth	39 pF
Nominal Cd    3 pF                      Actual	2.96 pF
Cd    16.6 pF	15.33 pF
Cd $\infty$	200 pF

(Sum of isolating capacitor + Cd)

Amplifier preamplifier noise loaded with 39 pF to simulate detector

Time Constant	Noise ( $q_a$ ) RMS electrons
0.2 $\mu$ sec	4300
0.5 $\mu$ sec	2380
1.0 $\mu$ sec	2042

Predicted Resolution as fraction of line length is given by

$$\Delta x = 2.355 \frac{D_m e}{q_o} - \sqrt{q_n^2 + q_a^2}$$

$$\text{where } q_n = \frac{C^{\frac{1}{2}} (k T_e)^{\frac{1}{2}}}{e} \mu$$

notation as section 4.5

$\mu$  and  $D_m$  are dimensionless line constants given by programme of Fraser 1980.

$q_a$ , C as given above.

$T_e = 293$  K (20°C)

$q_o$  is dumped charge on line

Assumed 50% of anode for calculation purposes.

using a heaviside step input of charge, whereas as shown above the charge risetime of the anode (and hence induced charge distribution on the cathode) is comparable with the risetime of a pulse from the far end of the line. The zero cross method has a distinctly poorer resolution performance than the ratio method.

Clearly from the data the position resolution is limited at high gains by some physical effect. For the given collimation the equivalent slit width is  $227 \mu\text{m}$   $1 \text{ cm}$  below the slit, hence particularly with the zero cross timing data, this cannot be the limiting factor. The limitation in position resolution is thought to be due to secondary avalanches, evidence for which is given above. This factor was encountered in the two-dimensional position sensitive detector work and will be discussed in detail in the following chapter, Chapter 6. It is interesting to note that with the ratio at a time constant of  $0.5 \mu\text{sec}$ , the measured resolution appears to decrease with increasing gain. This is due to the fast shaping constant not seeing the secondary avalanches due to their long transit time. This effect is again encountered (and discussed) in the results presented in Chapter 6.

#### 5.6.4. Summary

The one-dimensional detector showed that a sealed Xenon filled IPC could be built with good performance figures and reasonable lifetime. The effect of secondary avalanching was encountered pointing towards a limiting factor in achievable position resolution. The results were however sufficiently encouraging to continue with the development programme and build a two-dimensional position sensitive detector.



## CHAPTER 6

## RESULTS OF A TWO-DIMENSIONAL IMAGING PROPORTIONAL COUNTER

6.1. Introduction

This chapter will present the results achieved with the two-dimensional prototype IPC described in the last chapter. As mentioned previously two types of position encoding method, the resistive-capacitive line, hereafter referred to as the RC line, and the graded density cathode were investigated during the course of this work. The graded density cathode, as will be shown in this chapter, can give much better performance in terms of position resolution. This readout scheme was then adopted and three gas mixtures 90/10, 75/25, and 50/50 Xenon/Methane at a fill pressure of 2 atmospheres were evaluated, in order to ascertain the effect of the quench gas on imaging in Xenon/Methane gas mixtures. Because of the results obtained from the prototype the chapter sections split into two main topics. First, a distinct across anode wire modulation in both output position and anode gain as a function of real position was found for all gases and position encoding methods. The second topic concerns the position resolution achieved in the direction along that which is parallel to the anode wires.

First, in this chapter some of the basic counter parameters (detector filling parameters, counter gain; and counter energy resolution) will be described. The second section will discuss the position resolution results achieved along the anode wires. This is followed by a discussion of the across wire modulation effects, and possible theoretical explanations. The penultimate section of this chapter will deal with the limits to position resolution in the IPC, in particular the gas physics of the detector, and the explanation of the prototype's position resolution results. Finally the concluding section reviews current problems with

the detector, future possible improvements, and the imaging capability of an IPC. Throughout the chapter some comparisons to other work will be made. However comparison with results from other Xenon filled IPC's will be covered in Chapter 7, the conclusion of the work.

## 6.2. Basic Counter Parameters

### 6.2.1. Detector Filling Parameters

Only four detector fillings were made for the results presented in this chapter. The detector was assembled only three times, the 50/50 results were obtained from a refill of the detector assembly initially filled with the 75/25 mixture. Table 6.2.1 summarises the detector filling parameters for each detector configuration tested and presented in this chapter. The data is presented to show the accuracy and bakeout pressures achieved during the detector filling procedure.

### 6.2.2. Operating Voltage: Counter Gain

Due to the variety of gas mixtures, different operating conditions existed for each detector configuration. These are summarised in Table 6.2.2. During the work on 75/25 and 50/50 some difficulty was encountered due to tracking across the anode feedthrough in high humidity conditions. This problem was solved by sealing the feedthroughs and preamplifiers into a plastic tent, dry air from a dehumidifier constantly blowing across them.

Before any position resolution measurements were taken from a detector, in order to set up the signal processing electronics, the collected charge level was measured as a function of amplifier time constant. The charge level was measured using the pulse matching method as described in Chapter 5. Figures 6.2.1, 6.2.2, and 6.2.3 show the

TABLE 6.2.1

## DETECTOR FILLING PARAMETERS

<u>Configuration</u>	<u>Gas Mix Xenon/Methane</u>	<u>Bakeout Base Pressure (Temperature)</u>	<u>Fill Pressures (20°C)</u>		
			<u>Xenon</u>	<u>Methane</u>	<u>Total Pressure</u>
RC	90/10	$10^{-8}$ torr (30°C)	1375 torr	150 torr	1525 torr
Graded Density	90/10	$7 \times 10^{-9}$ torr (34°C)	1377	152	1529
	75/25	$6 \times 10^{-9}$ torr (30°C)	1147	382	1530
	50/50	$6 \times 10^{-8}$ torr (20°C)	766	760	1526
(Refill of 75/25)					

TABLE 6.2.2

## COUNTER OPERATING CONDITIONS

Configuration	Gas Mix	Operating Voltage Range	Corresponding Charge Level (measured with anode amplifier shaping time constant of 1.6 $\mu$ sec)	Drift Voltage Range Investigated	X-Ray Sources Used
RC	90/10	+3300 to +3700 V	-.12 to .72 pC	-50* to +300 V	Fe <sup>55</sup> , Cd <sup>109</sup>
Graded Density	90/10	+3300 to +3625 V	-.19 to .74 pC	"	Fe <sup>55</sup>
	75/25	+3600 to +3950 V	-.14 to .52 pC	"	"
	50/50	+3950 to +4350 V	-.165 to .59 pC	"	"

\* Note: Negative drift voltages can be used due to field leakage from anode through cathode grids

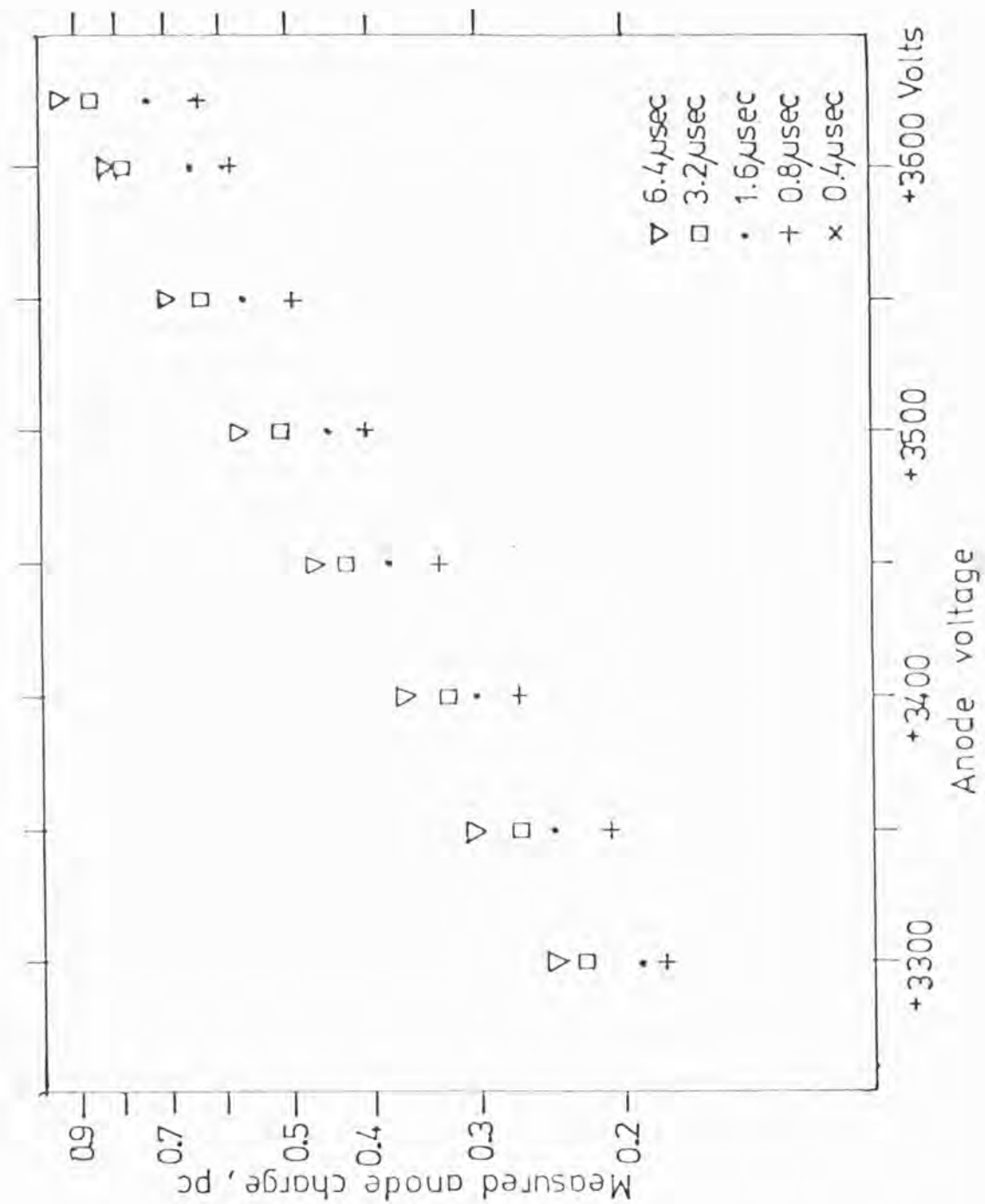


Figure 6.2.1. Measured anode charge as a function of anode voltage and amplifier time constant, along the anode, for the 90/10 gas mix. (Spot point measurement, graded density cathode counter).  $\text{Fe}^{55}$  source

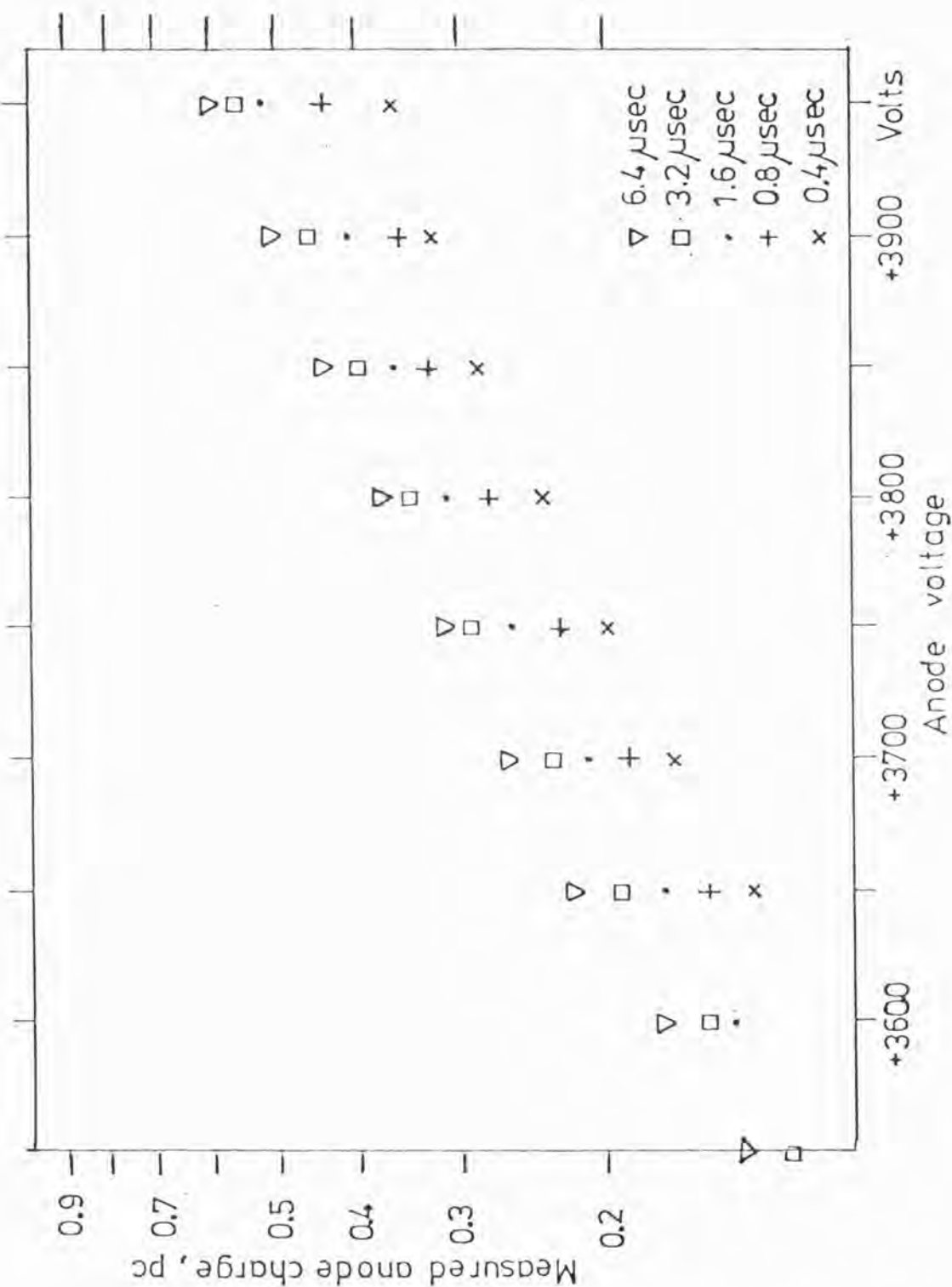


Figure 6.2.2. Measured anode charge as a function of anode voltage and amplifier time constant, along the anode, for the 75/25 gas mix. (Spot point measurement, graded density cathode counter).  $\text{Fe}^{55}$  source.



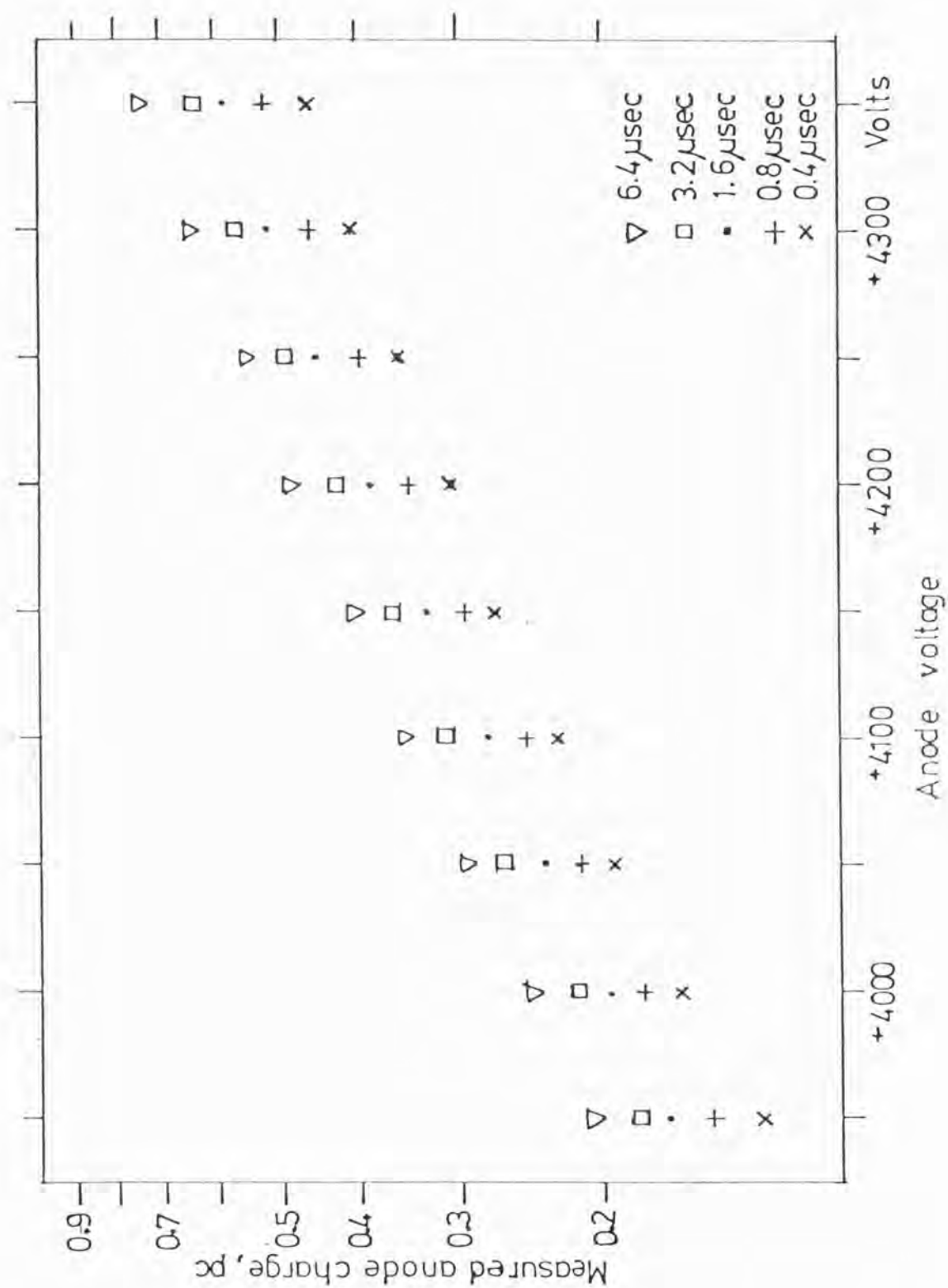


Figure 6.2.3. Measured anode charge as a function of anode voltage and amplifier time constant, along the anode, for the 50/50 gas mix. (Spot point measurement, graded density cathode counter).  $\text{Fe}^{55}$  source.

resulting measured charge levels as a function of anode amplifier shaping time constant and anode voltage for each gas mix with the graded density cathode. This was for a slit aligned, major axis, across the wire, i.e. a measurement along the anode wires as defined here. The anode gain measurements were found to be repeatable in time for all detectors; and almost no variation ( $< 2\%$ ) occurred along the scanable length of the wires. The maximum random error in measuring the gain from the PHA display is  $\pm .007$  pC.

Across the anode wires a distinct modulation at the wire pitch was found in both measured anode gain and detector output position. In this case the output charge was measured at highest and lowest gain positions across the wire pitch. No basic change in the modulation form occurred as a function of anode voltage. Due to operational problems and time considerations not all time constants were measured for all voltages. Figures 6.2.4, 6.2.5, 6.2.6. show the resulting charge for the three gas mixtures for a high gain and low gain position, later utilised for position resolution measurements.

The data can be replotted as charge versus amplifier time constant versus voltage. This reveals some information on the characteristic shape of the anode pulse. The charge values were normalised at the lowest time constant ( $0.4 \mu\text{sec}$ ) to the lowest gain for which a full data set was available. All gas mixes measured, both along and across the anode wires, as per Figure 6.2.7, therefore showed a change in pulse profile as the gain is increased. This change in all cases is outside the measurement error, and is systematic for all time constants and gains. The change is also different for the high and low gain points across the anode. However, as the change in actual anode pulse profile is difficult to quantify because of the amplifier shaping, the data will not be presented fully. Figure 6.2.7 shows the normalised charge values as a function of time constant and anode voltage for 75/25 along the anode.

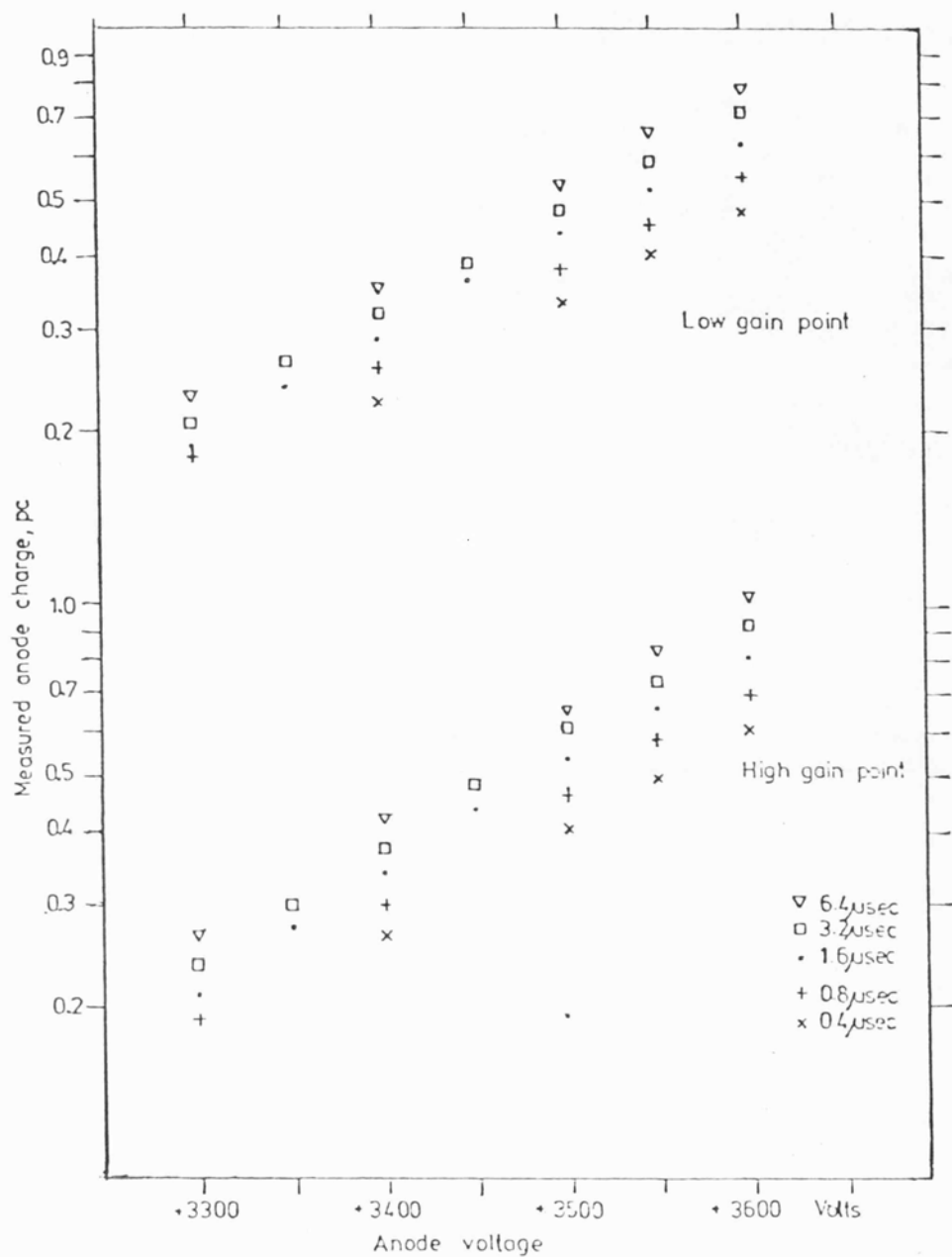


Figure 6.2.4. Measured anode charge as a function of anode voltage and amplifier time constant, across the anode wires, for high and low gain points, for the 90/10 gas mix. (Spot position measurements, graded density cathode counter)  $\text{Fe}^{55}$  source.

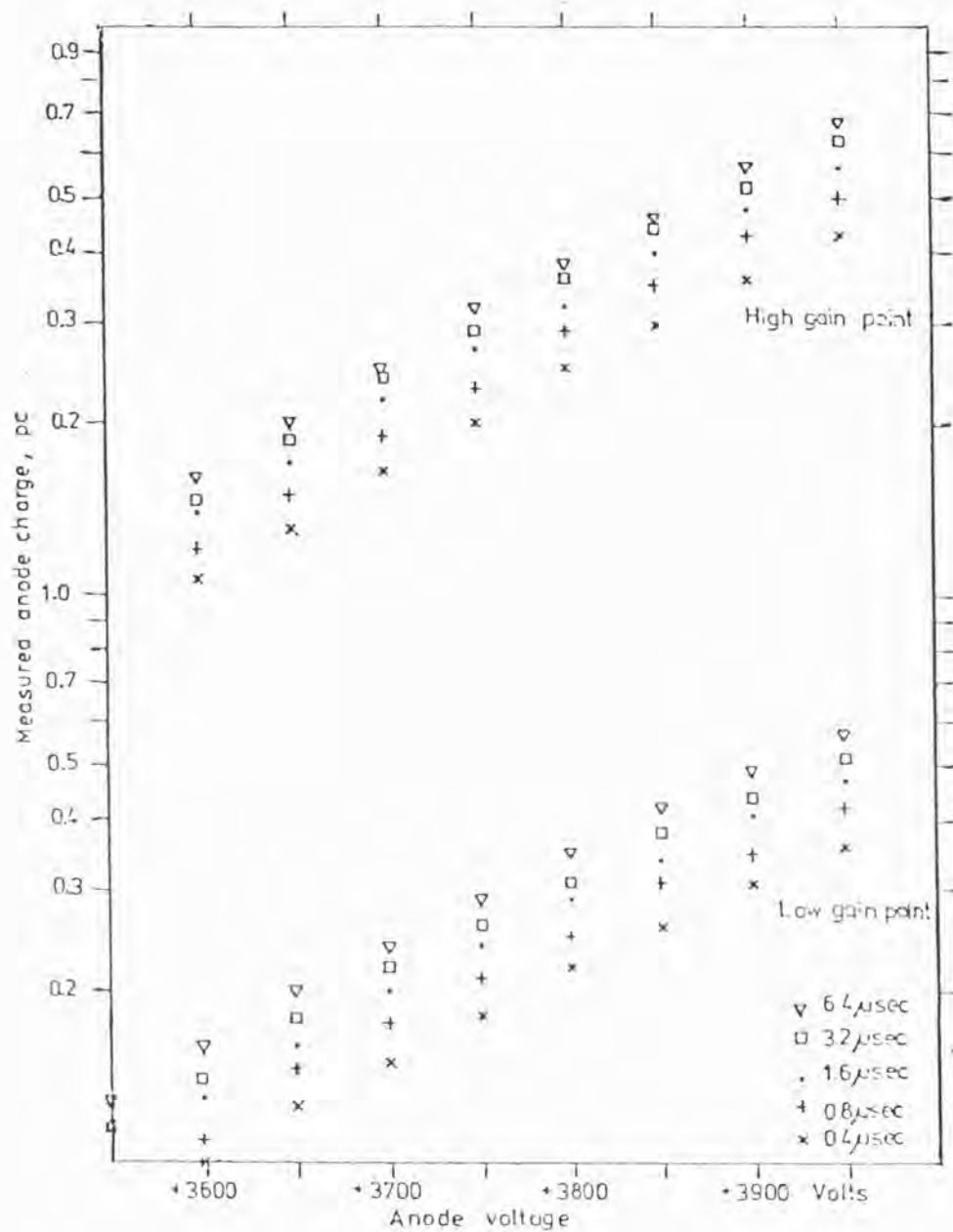


Figure 6.2.5. Measured anode charge as a function of anode voltage and amplifier time constant, across the anode wires, for high and low gain points, for the 75/25 gas mix. (Spot position measurements, graded density cathode counter)  $\text{Fe}^{55}$  source.

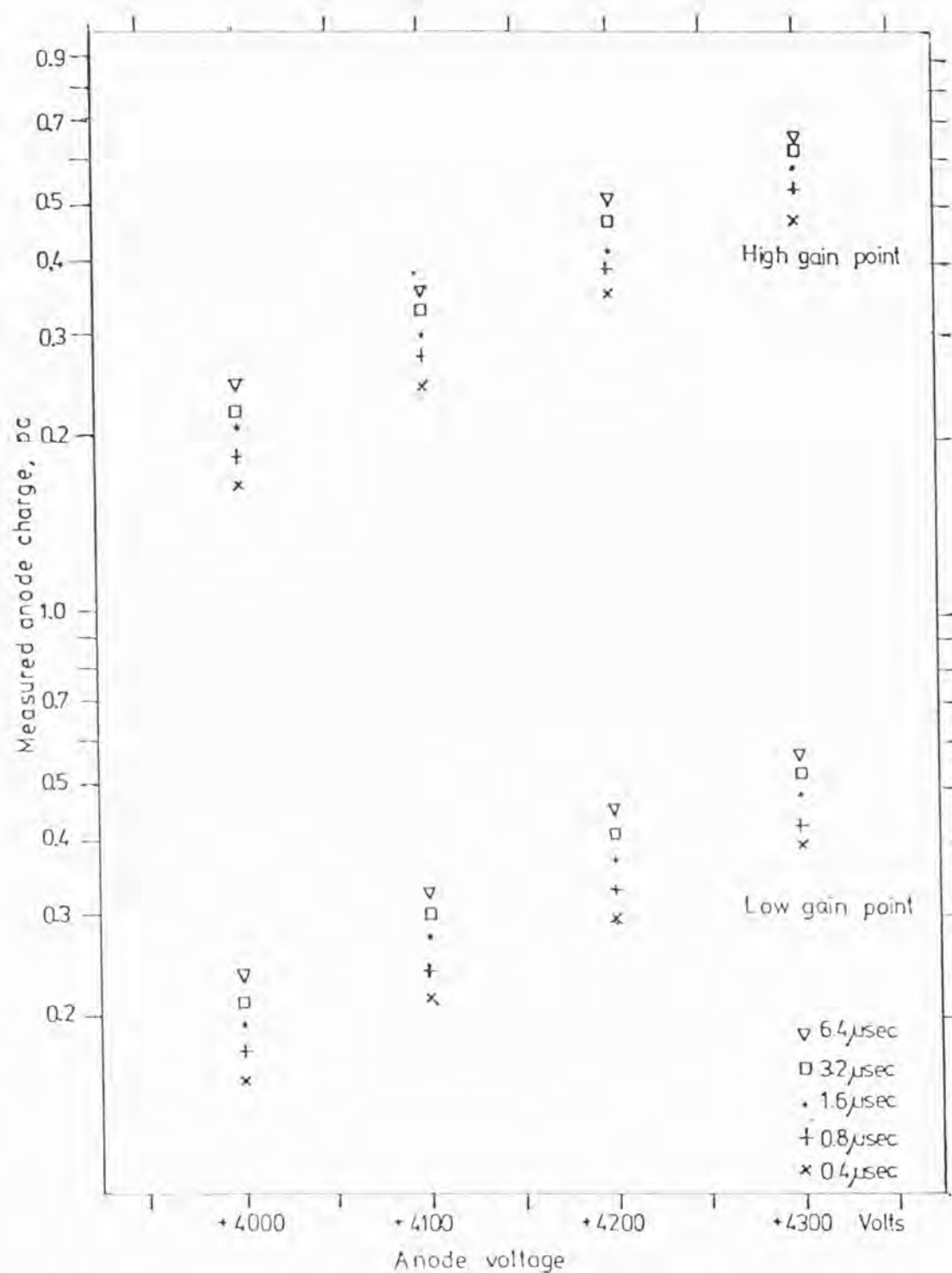


Figure 6.2.6. Measured anode charge as a function of anode voltage, and amplifier time constant, across the anode wires, for high and low gain points for the 50/50 gas mix. (Spot position measurements, graded density cathode counter)  $\text{Fe}^{55}$  source.

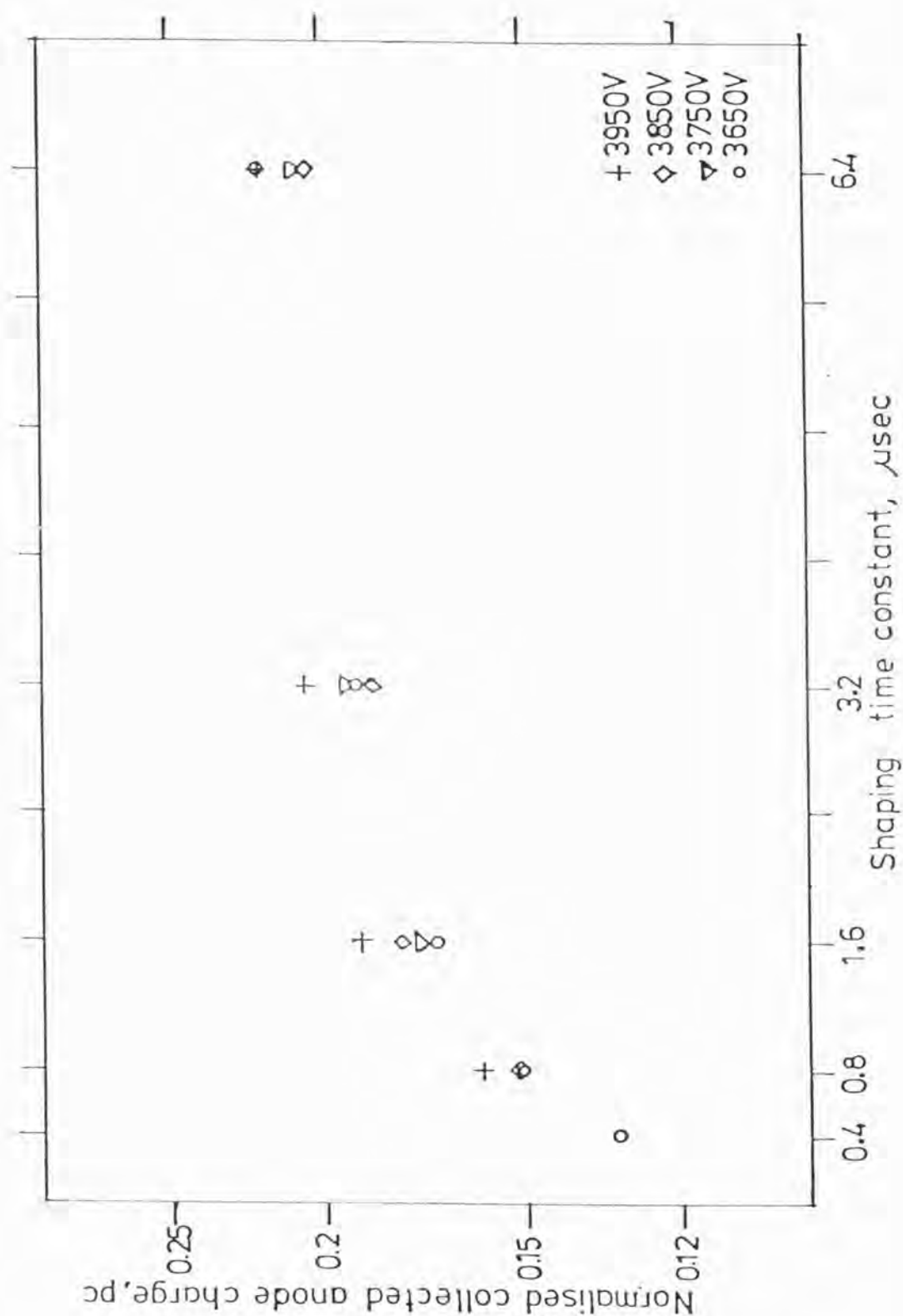


Figure 6.2.7. Data for 75/25 gas mix, ( $\text{Fe}^{55}$ ) along anode, plotted as a charge versus time constant for various anode voltages. Charges are normalised at 0.4  $\mu\text{sec}$  to anode voltage of 3650 V in order to show change in profile as a function of gain. (Graded density counter,  $\text{Fe}^{55}$  source)



### 6.2.3. Energy Resolution

Finally in this section, the energy resolution data obtained from the detector will be detailed. Energy resolution of the development IPC was not measured or investigated in any great detail due to the priority placed on position resolution measurements. Table 6.2.3 lists the overall energy resolutions achieved with various X-ray astronomy experiments for  $\text{Fe}^{55}$ .

The energy resolution of the prototype detector was found to vary with both anode voltage and anode amplifier time constant. Figure 6.2.8 shows the measured energy resolution for each gas mixture as a function of anode voltage for amplifier time constants of 0.4 and 6.4  $\mu\text{sec}$ . Distinct trends in the behaviour of energy resolution were observed, the exact variation with voltage was found to be slightly different for each time constant. The most noticeable trend, for all time constants, is a degradation in energy resolution towards high voltages and hence counter gain. In addition the resolution degrades with increasing percentage of methane.

Across the anode a distinct modulation in energy resolution, a total variation of ~3 to 5% , was evident in all gas mixtures with a 1 mm modulation. The worse resolution points were found to be coincident in position with the high and low anode gain positions. The best resolution in general was comparable with that measured along the anode. As seen along the anode, at all time constants the energy resolution was seen to degrade at high counter gain.

In summary the energy resolution of the counter was found to be gas, gain, amplifier time constant, and position, dependent. A detailed investigation was not made.

The best overall performance was obtained with the 90/10 gas mixture and is comparable to that achieved with other counters (see Table

TABLE 6.2.3

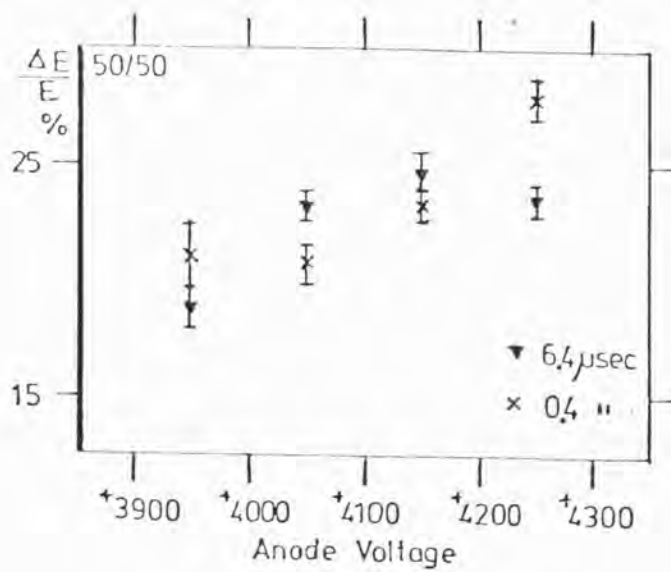
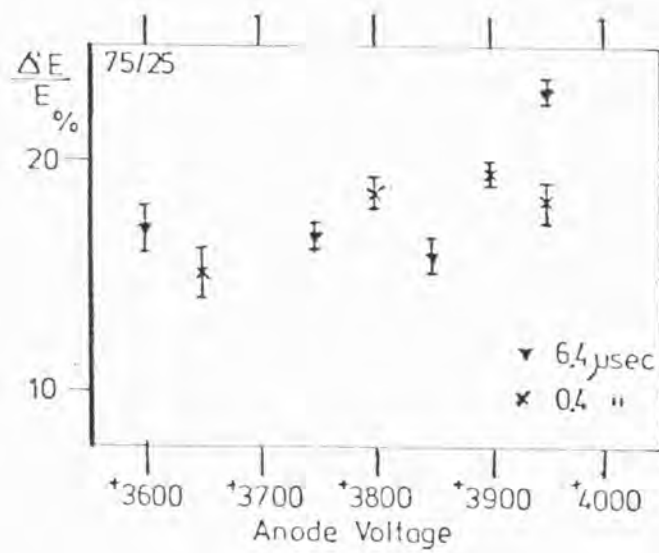
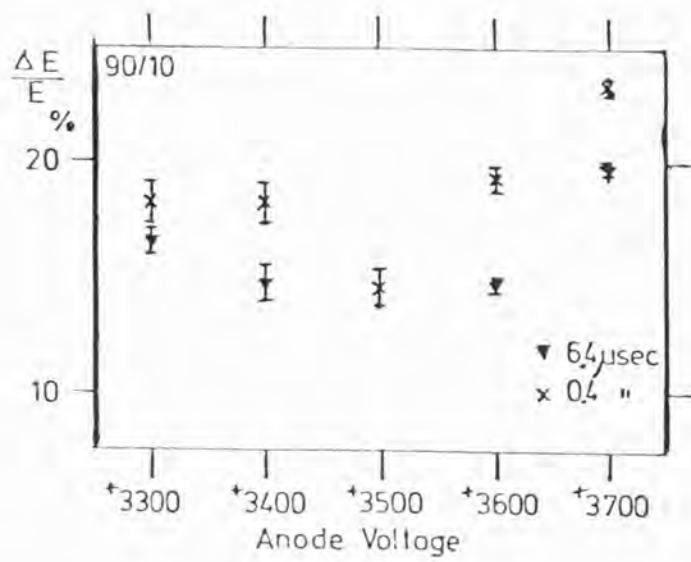
## MEASURED ENERGY RESOLUTIONS

<u>Experiment</u>	<u>Gas Filling</u>	<u>Pressure (Atmospheres)</u>	<u>Energy Resolution (<math>\Delta E/E</math> FWHM %)</u>
Ariel V SSI	76% Ar 16% Xe 8% CO <sub>2</sub>	1.18 atm.	- 40%
Ariel 6 Leicester experiment	95% Xe 5% CO <sub>2</sub>	1.45 atm.	- 19%
IPC Gas camera *	90% Ar 10% CH <sub>4</sub>	1 atm.	- 17%
Exosat Medium Energy experi- ment, low energy section	97% Ar 3% CO <sub>2</sub>	2 atm.	- 14%

\* Leicester Argon/Methane IPC programme.

[Data for table from M.J.Ricketts, P.J.Gilvin, M.J.L.Turner 1981  
(private communication)]

Figure 6.2.8. Measured energy resolution, ( $\text{Fe}^{55}$ ) for prototype IPC (graded density cathodes), for each gas mix, as a function of anode voltage, amplifier time constants of 0.4 and 6.4  $\mu\text{sec}$ . (Direction along anode) Errors bars are maximum random errors in determining resolution from PHA.



6.2.3). However all gas mixtures showed an adequate performance for an IPC for the shadow camera.

### 6.3. Position Resolution versus Position Encoding Method: Along Anode

This section will present the position resolution measurements achieved in the direction along the anode for the two position encoding methods; the RC line; and graded density cathode. No gas dependent modulation in position resolution or output position was found to occur along the anode. The factors that dominate in this direction are non-linearity of the position encoding method, and non-position dependent gas effects. The resolution performance for all counters constructed in this work will be detailed, and a comparison made with the theoretical predicted performance. The position resolution in all detectors was found to vary strongly, with cathode amplifier time constant and anode gain, and had a weak dependence on drift field.

Resolution along the anode was determined using the following method. An area close to counter centre (mechanical and electronic) was chosen. A linearity scan of  $\sim 5$  mm, along the anode was performed to obtain the local sensitivity that is position output scale, PHA channels per mm, for each counter operating condition. The resolution was then measured at two points 1 mm apart, and an average value produced. Random spot checks were made at other positions in the area and along the anode to check that the resulting resolution has two errors. The first is the random error in measuring the FWHM, and the second is the error, resulting from calculating the sensitivity by least squares fitting of a straight line to the data. The random error is the maximum error in estimating the FWHM and hence will be quoted separately. The error in sensitivity is the standard error and will be quoted immediately after each position resolution figure. The FWHM of each resolution measurement is

not a whole number of channels, hence an estimate of the FWHM was made, and the position resolution remeasured at a higher PHA gain as a check. The FWHM was then scaled back down to the original gain. On any gain the random error in estimating the FWHM was taken as a  $\pm 1/4$  of a channel.

As an additional check on resolution measurements an average resolution from many points along the wire was calculated to check a particular variation with given counter variable. In all cases the spot values were found to follow the average measurements.

### 6.3.1. The RC Counter

#### 6.3.1.1. Results

The results presented from the RC counter were taken only with the Pye type of preamplifier. For the RC counter no variation (within experimental errors) was found of resolution with gain versus time constant, that is the ratio between time constant values did not change significantly with the counter gain. Table 6.3.1 gives the spot resolution measurements for an anode voltage of 3550 V, and a drift voltage of +50 V, the best operating counter condition. A best individual spot resolution was found to occur for the cathode amplifier time constant of 1.6  $\mu$ sec.

Figure 6.3.1. shows the measured resolution for this time constant versus collected anode charge, measured with an anode amplifier shaping constant of 1.6  $\mu$ sec, for  $\text{Fe}^{55}$  radiation. The measured electronic noise calculated from the average sensitivity is also plotted on the figure. As can be seen the resolution at low charges closely follows the electronic noise, but turns off the noise line at approximately 0.4 pC and then degrades at high charge (gain) values. The resolution improving from  $1.78 \pm .11$  mm ( $\pm .07$  mm random) at a charge level of .151 pC (anode voltage 3350 V) to  $.890 \pm .06$  mm ( $\pm .07$  mm random) for .367 pC (3550 V), degrading to  $1.037 \pm .07$  mm ( $\pm .07$  mm random) at .66 pC (3700 V). These



TABLE 6.3.1

POSITION RESOLUTION VERSUS TIME CONSTANT (90/10 RC)

<u>Cathode Amplifier Time Constant</u>	<u>Resolution FWHM</u>	<u>Random Error</u>
0.4 $\mu$ sec	1.03 $\pm$ .07 mm	$\pm$ .07 mm
0.8 $\mu$ sec	.88 $\pm$ .06	$\pm$ .07
1.6 $\mu$ sec	.89 $\pm$ .06	$\pm$ .07
3.2 $\mu$ sec	1.19 $\pm$ .07	$\pm$ .07

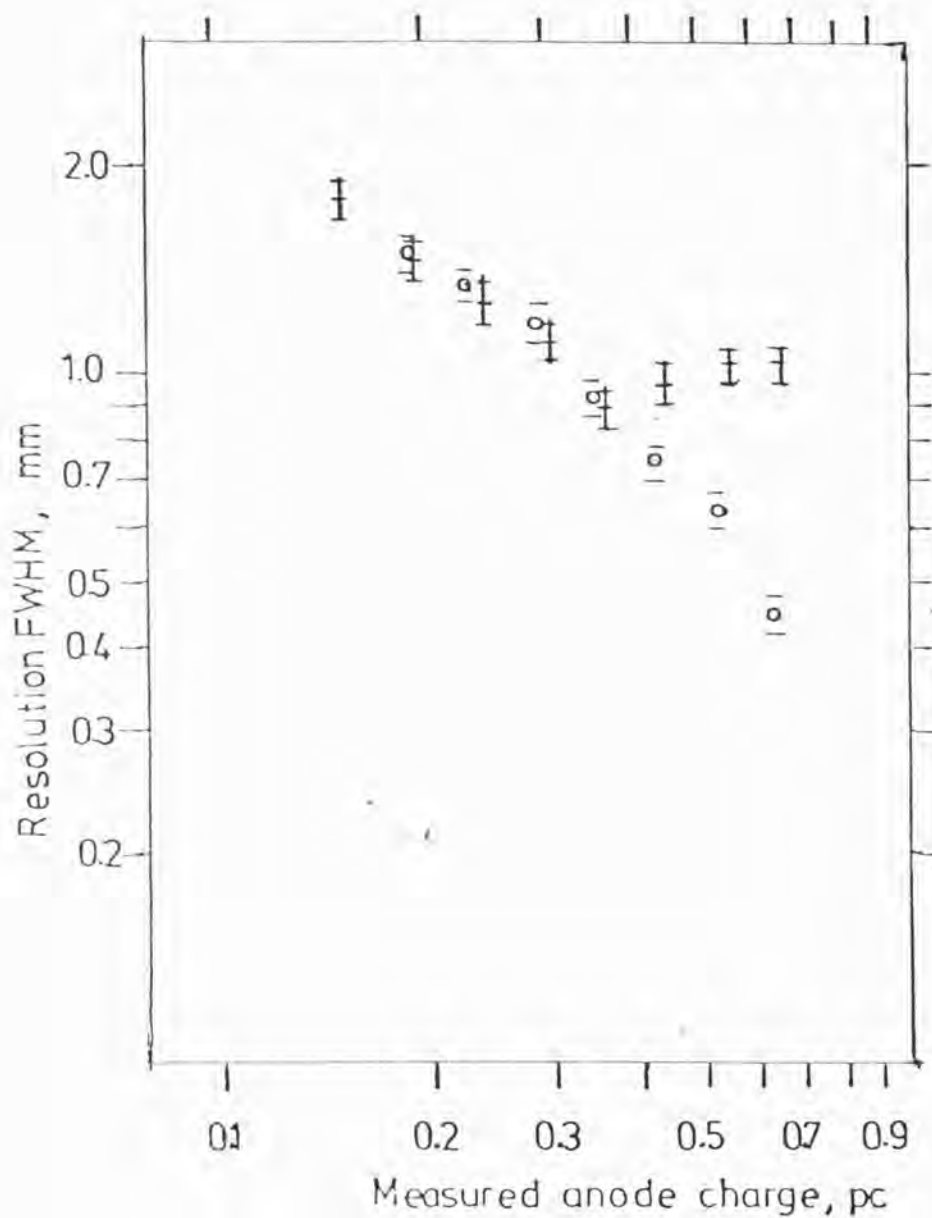


Figure 6.3.1. Position resolution (+) (FWHM) as a function of measured anode charge (amplifier time constant 1.6  $\mu$ sec), for cathode amplifier time constant of 1.6  $\mu$ sec. 90/10 RC Counter,  $\text{Fe}^{55}$  source. Measured electronic noise (o) is also shown. Errors bars are maximum random errors, resulting from measurements from PHA.

measurements are again a two spot average. All these measurements were taken with a 320  $\mu\text{m}$  width slit.

Figure 6.3.2 shows resolution versus anode collected charge for identical conditions as above, for  $\text{Cd}^{109}$  radiation, a different characteristic shape is evident, degradation at high gains is much less. In all counters and position encoding schemes tried the degradation at high gains always occurred. It is suggested, see section 6.5, that this is due to secondary avalanching. With the  $\text{Cd}^{109}$  source, X-ray absorption occurs throughout the active volume of the counter whereas  $\text{Fe}^{55}$  is absorbed only in the drift region. The best resolution achieved  $.89 \pm .06 \text{ mm}$  is identical with that achieved with  $\text{Fe}^{55}$ .

The electrical co-ordinates of these spot measurements were .50 along the length of the RC line. This was found by comparing the output co-ordinate with that of the electrical centre measured during the electronic noise measurements. The characteristic resolution versus gain shape was found to occur for all cathode shaping time constants.

The resolution averaged over the 5 mm linearity scan (electrical co-ordinates .442 to .503) for the same conditions as Table 6.3.1 showed identical behaviour with amplifier time constant, Table 6.3.2 gives the 5 mm averaged resolutions. No change in linearity was found for a given scan length as the counter gain was changed.

Figure 6.3.3 shows the measured variation (two point average) in resolution as a function of drift voltage. The counter gain being balanced as for the initial conditions of anode voltage  $+3550 \text{ V}$ , drift voltage  $+50 \text{ V}$ . The following trend is visible, a worsening of resolution from a drift voltage of  $+50$  to  $-50 \text{ V}$ , and a possible slight worsening to  $+300 \text{ V}$ . The degradation at low fields is most probably due to the large electron cloud size resulting from increased diffusion, see section 6.5.3, and the degradation at high drift fields due to an increase in the amount of secondary avalanching seen at that amplifier shaping

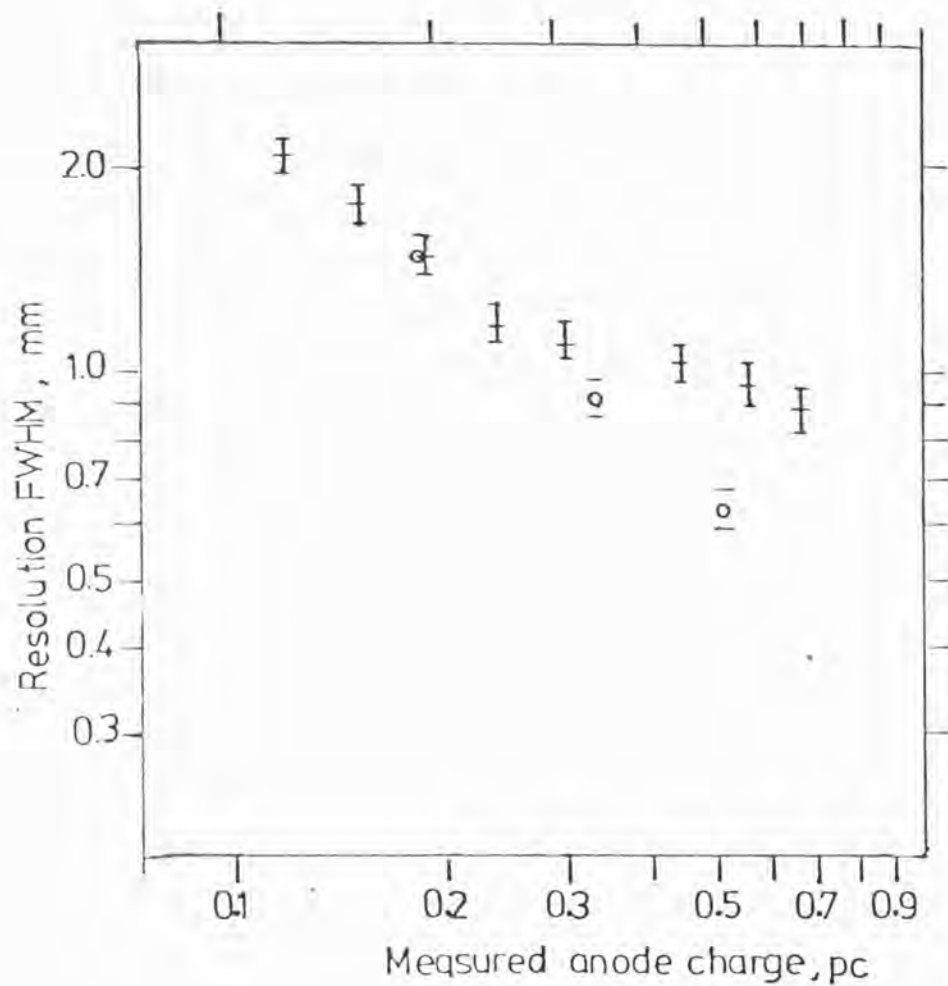


Figure 6.3.2. Position resolution (+) as a function of measured anode charge, identical time constants as Figure 6.3.1, for  $\text{Cd}^{109}$ . Measured electronic noise (o), as per Figure 6.3.1, is also shown. 90/10 RC Counter.

TABLE 6.3.2  
5mm AVERAGED RESOLUTIONS

<u>Cathode Amplifier Time Constant</u>	<u>Resolution FWHM</u>	<u>Random Error</u>
0.4 $\mu$ sec	1.11 $\pm$ .10 mm	$\pm$ .07 mm
0.8 $\mu$ sec	1.01 $\pm$ .09	$\pm$ .07
1.6 $\mu$ sec	1.07 $\pm$ .09	$\pm$ .07
3.2 $\mu$ sec	1.21 $\pm$ .11	$\pm$ .08

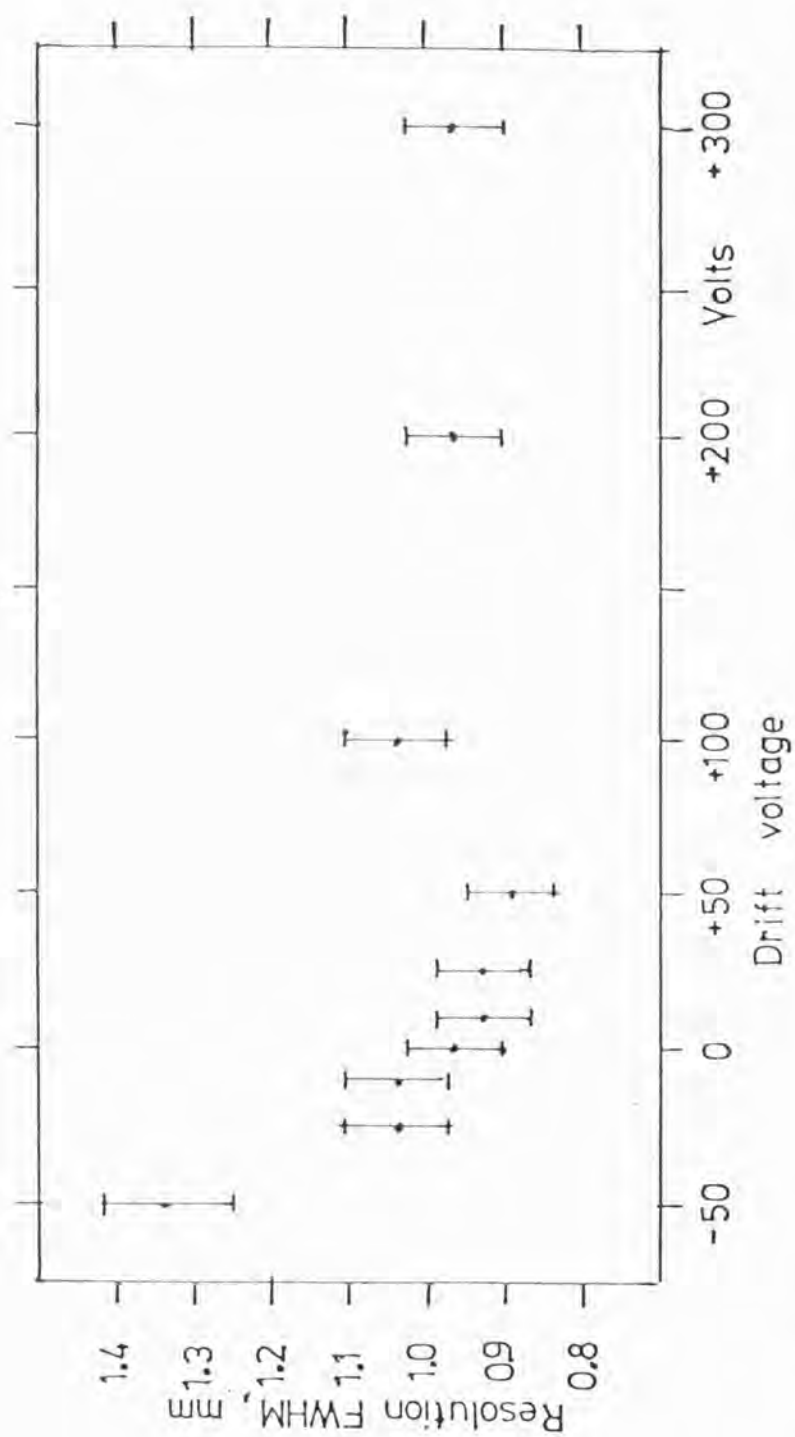


Figure 6.3.3. Position resolution (FWHM) as a function of applied drift voltage. Counter gain balanced as for anode voltage of +3550 V, drift voltage +50 V,  $\text{Fe}^{55}$ , 90/10 RC Counter.



constant, see section 6.5.5.

#### 6.3.1.2. Comparison with RC Line Theory

The work of Fraser 1980 (see Chapter 4) enables a theoretical prediction of resolution with an RC line to be made. The total resistance and capacitance to earth of each RC cathode was measured. The mean resistance ( $R$ ) was found to be  $100 \text{ k}\Omega$ , and capacitance to earth  $\sim 39 \text{ pF}$ , Table 6.3.3 lists the values of the line parameters as calculated by Fraser 1981 (private communication) for the shaping characteristics of the Nuclear Enterprises amplifiers used. (Notation as Chapter 4). In order to calculate the predicted performance the amplifier noise contribution was measured. Table 6.3.4 lists the measured noise for the Pye type preamplifier loaded with a pure capacitive load of  $39 \text{ pF}$ , for various shaping constants of the amplifier. An input pulse risetime of  $.05 \text{ }\mu\text{sec}$  was used to give the nearest achievable to a delta function input of charge with respect to time. Listed errors are the random measurement error.

As stated in Chapter 4, with amplifier noise, the predicted resolution as a function of line length is given by

$$\Delta x_{\text{FWHM}} = 2.355 \frac{D_m e}{q_o} \sqrt{q_n^2 + q_a^2}$$

The length of the RC line is  $9 \text{ cm}$ , and at most a charge  $\sim 0.5 \text{ pC}$  is developed on the anode, hence giving a dumped charge of  $\sim .25 \text{ pC}$  on each cathode line. Table 6.3.5 gives  $\sqrt{q_n^2 + q_a^2}$ ,  $D_m \Delta x$  for  $q_o = 1.0 \text{ pC}$  charge, and  $\Delta x$  in  $\text{mm}$  for the line for an anode charge of  $0.5 \text{ pC}$ , assuming 50/50 charge split between cathodes.

Using the X-ray fitted linearity the measured electronic noise was  $.63 \pm .04 \text{ mm}$  ( $\pm .07$  random) for an equivalent anode charge of  $.525 \text{ pC}$  for cathode time constant of  $1.6 \text{ }\mu\text{sec}$ . Scaling as  $1/q_o$  the

TABLE 6.3.3.  
LINE PARAMETERS FOR RC CATHODE

$$R = 100 \text{ k}\Omega \quad C = 39 \text{ pF}$$

Amplifier Time Constant	$\mu$	$D_m$	$\mu D_m$	$q_n(\text{rms})$
0.4 $\mu\text{sec}$	.974	.957	.932	2418 electrons
0.8	1.189	.859	1.031	2952
1.6	1.572	1.008	1.585	3902
3.2	2.177	.996	2.169	5404
6.4	3.061	.993	3.040	7599

TABLE 6.3.4  
MEASURED PREAMPLIFIER AMPLIFIER NOISE  
FOR 39 pF CAPACITIVE LOAD

Amplifier Time Constant	Noise $q_a$ rms
0.4 $\mu\text{sec}$	$1819 \pm 129$ electrons
0.8	$1438 \pm 102$
1.6	$1504 \pm 107$
3.2	$1685 \pm 120$
6.4	$2011 \pm 143$

TABLE 6.3.5  
PREDICTED PERFORMANCE OF LINE

Amplifier Time Constant	$\sqrt{q_a^2 + q_n^2}$ RMS	$D_m$	$\Delta x$ for $q_o = 1.0 \text{ pC}$	$\Delta x$ mm Anode charge .5 pC
0.4 $\mu\text{sec}$	3026 electrons	.957	$1.091 \times 10^{-3}$	$.393 \pm .028$
0.8	4182	1.008	$1.588 \times 10^{-3}$	$.572 \pm .041$
3.2	5661	.996	$2.125 \times 10^{-3}$	$.765 \pm .054$
6.4	7861	.993	$2.941 \times 10^{-3}$	$.1059 \pm .075$

measured noise is therefore  $\sim .66$  mm , whereas the predicted resolution is  $.57 \pm .04$  mm . A good agreement of the theory with the measured noise therefore exists at 1.6 sec. 'What is the predicted X-ray resolution allowing for beam width, assuming  $320 \mu\text{m}$  width beam?'

Anode charge level = .37 pC

Predicted electronic resolution =  $.773 \pm .055$  mm

(Assuming 50/50 charge split)

Electronic plus slit =  $.836 \pm .059$  mm

(Quadratic addition)

Measured resolution =  $.89 \pm .06$  mm for .367 pC .

The predicted resolution therefore agrees very well with that measured for the detector, the difference corresponding to the gas physics limits to resolution. This agreement is somewhat closer than that for the one-dimensional detector, although in that case the amplifier noise errors were poorly defined. The RC position encoding scheme was abandoned because of its poor resolution achievable at low gains compared to the graded density cathode, and a large degree of modulation across the wires (see section 6.4.1.).

#### 6.3.2. Graded Density Cathode

The graded density cathode, hereafter referred to as the GD cathode, was originally tried in 90/10 with the Pye preamplifiers, before the Canberra preamplifiers became available. These results will be briefly presented.

### 6.3.2.1. Results with Pye Preamplifiers

Table 6.3.6 lists the resolution versus time constant values achieved with the GD cathode with the Pye preamplifiers; for an anode voltage of  $+3550$  V, and a drift voltage of  $+50$  V, corresponding to a charge level of  $.56$  pC. These measurements are the average for a  $5$  mm scan, the error quoted for the resolution is a statistical combination of the sensitivity error, and standard error for the data points. The slit width used was  $200$   $\mu$ m. As can be seen the best resolution occurred at a time constant of  $1.6$   $\mu$ sec, the worst at  $0.4$   $\mu$ sec. This behaviour was found to be independent of gain. The resolution achieved is better than the RC, however not substantially.

The best two spot average resolution value was obtained at an anode voltage of  $+3550$  V, drift voltage  $+50$  V, anode and cathode shaping time constant  $1.6$   $\mu$ sec, and was  $.626 \pm .007$  mm ( $\pm .065$  random error). During an overall GD linearity scan along the anode,  $-2.62$  to  $+2.58$  cm either side of the centre, the average resolution for the above conditions was found to be  $.748 \pm 0.22$  mm ( $\pm .066$  mm random error). Measurements were taken every  $5$  mm along the scan.

Figure 6.3.4 shows the measured resolution, electronic plus two spot point average; as a function of gain for a cathode shaping time constant of  $1.6$   $\mu$ sec. The ( $5$  mm) average values obtained during some of the sensitivity measurements are also plotted on the graph, illustrating the validity of using spot measurements. These measurements were taken at a point  $\sim .51$  electrically from one end of the cathode.

As in the RC work, the measured X-ray resolution follows the electronic noise then departs and flattens out as the resolution degrades. The resolution was  $1.253 \pm .017$  mm at  $.145$  pC,  $.626 \pm .007$  mm at  $.545$  pC, and  $.692 \pm .009$  mm at  $.75$  pC. The charge levels were measured with an anode shaping constant of  $1.6$   $\mu$ sec, all measurements having a maximum random error of  $\pm .065$  mm.

TABLE 6.3.6

RESOLUTION VERSUS TIME CONSTANT 90/10 GD

PYE PREAMPLIFIERS ANODE  $+3550$  V DRIFT  $+50$  V

<u>Cathode Amplifier Time Constant</u>	<u>Resolution FWHM</u>	<u>Random Error</u>
0.4 $\mu$ sec	$1.02 \pm .04$ m	$\pm .091$
0.8	$.76 \pm .03$	$\pm .075$
1.6	$.67 \pm .03$	$\pm .066$
3.2	$.83 \pm .04$	$\pm .065$
6.4	$.82 \pm .03$	$\pm .065$

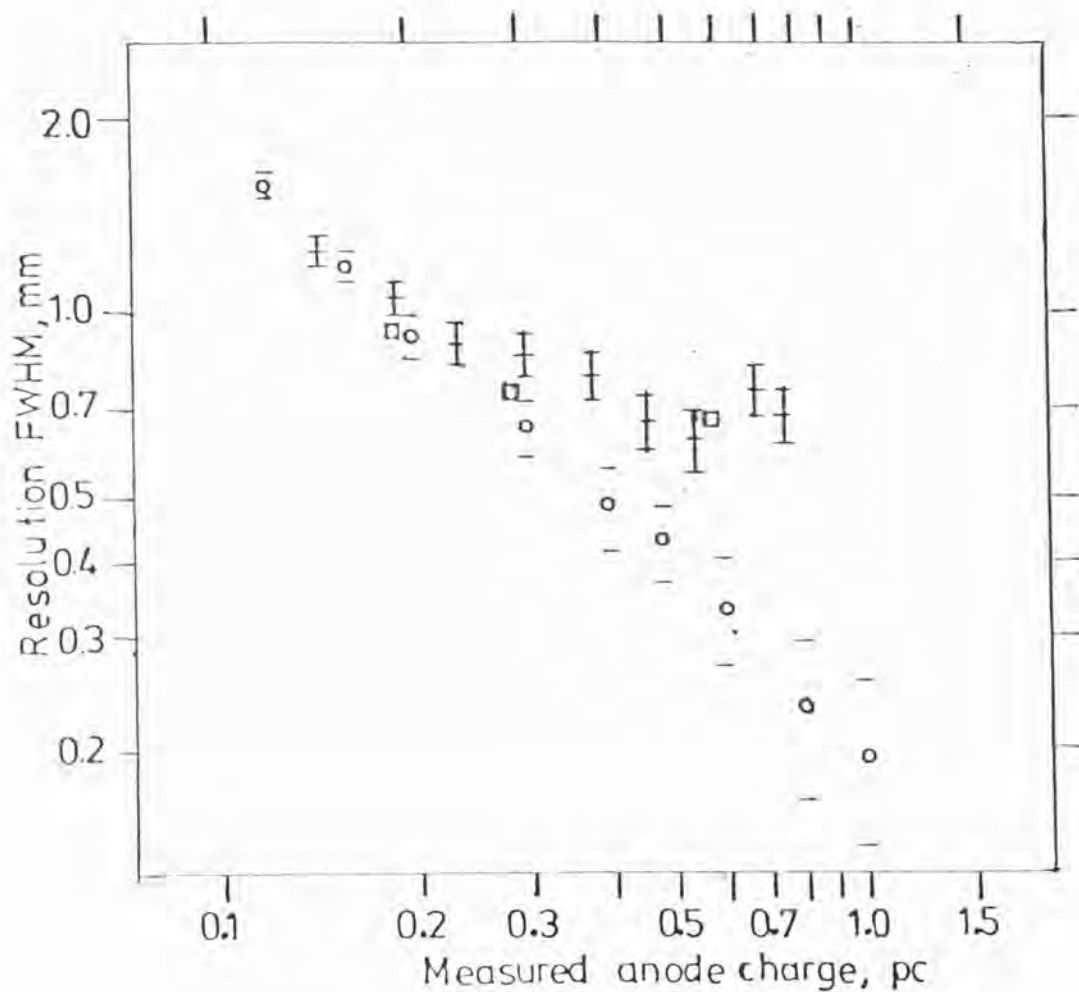


Figure 6.3.4. Position resolution (+) (FWHM) as a function of measured anode charge (amplifier time constant 1.6  $\mu$ sec), for cathode amplifier time constant of 1.6  $\mu$ sec,  $\text{Fe}^{55}$  source, 90/10 graded density counter, Pye preamplifiers. Measured electronic noise (o) from counter, and average 5 mm resolution values (◻) are also shown. Errors bars are random errors in determining resolution.



Position resolution as a function of drift voltage was found to be essentially flat, a slight worsening occurring towards high drift fields. Due to counter breakdown problems, these measurements occurred in a different area from the above resolution measurements. The gain was balanced as for an anode voltage of  $+3550\text{ V}$  and a drift voltage of  $+50\text{ V}$ . The anode and cathode time constants used were both  $1.6\text{ }\mu\text{sec}$ . The two spot average resolution was found to be,  $.692 \pm .095\text{ mm}$  at  $-50\text{ V}$  drift,  $.725 \pm .010\text{ mm}$  at  $+50\text{ V}$ , and  $.791 \pm .011$  at  $+200\text{ V}$ . Random error for all measurements was  $\pm .066\text{ mm}$ .

#### 6.3.2.2. Results with Canberra Preamplifiers

With the GD cathode using the low noise Canberra preamplifiers, gas effects were found to start to dominate the resolution, in that the resolution versus gain graphs were found to have a different characteristic shape dependent on cathode amplifier time constant. All such results show a worsening in resolution at high charge levels. However the exact shape and difference from expected system resolution (electronic plus slit width) differs for each amplifier time constant. Hence the best achieved resolution for each time constant with counter operating conditions will be presented for each gas mix (both two point and  $5\text{ mm}$  scan average resolution values).

Table 6.3.7 gives the resolution versus time constant, with operating conditions achieved with 90/10 2 atm. Drift voltage was  $+50\text{ V}$ . This charge level unless stated hereafter is measured with an anode shaping constant value of  $1.6\text{ }\mu\text{sec}$ .  $0.4\text{ }\mu\text{sec}$  was found to give the best resolution, although the measured electronic noise is worst at this time constant for the GD cathode.

Figure 6.3.5 shows the resolution versus gain curves (two spot average) for each time constant. The measured electronic noise with random error is

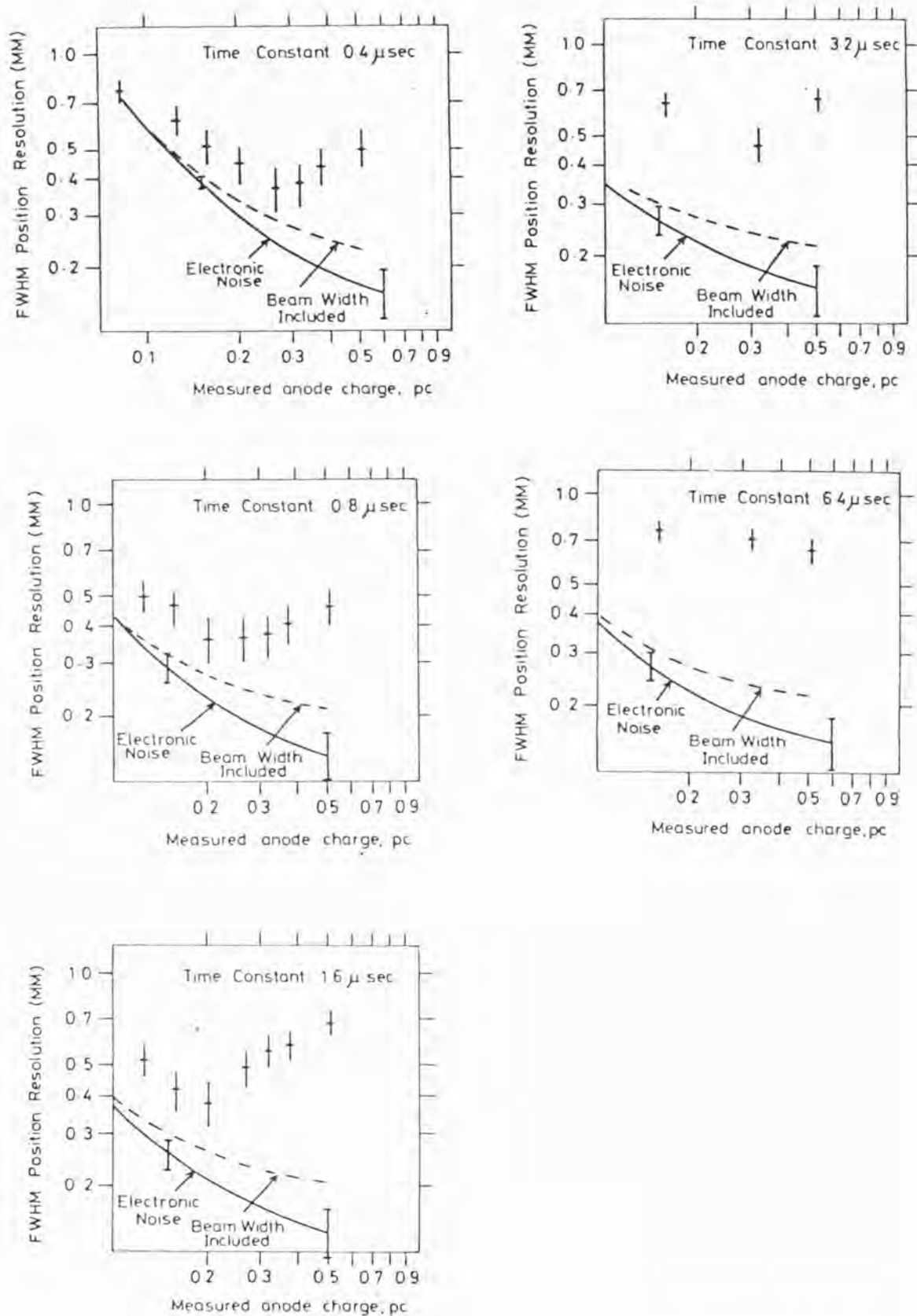


Figure 6.3.5. FWHM position resolution as a function of measured anode charge (anode amplifier time constant 1.6  $\mu$ sec) for each cathode time constant. Random error bars for position resolution, and two error bars for electronic noise are shown. Total contribution (---) from electronic noise and finite beam width is also shown for each time constant. Two spot average measurements 90/10 GD Counter.

shown by the solid curve, which is the best hand drawn curve through the electronic noise measurements. The beam width of  $200\text{ }\mu\text{m}$  is also included by quadratic addition to the electronic noise. This width limits the measured resolution. However the best value of  $.357\text{ mm}$  is too high to be attributal to this. The electronic noise decreases as the time constant increase; this was to be expected from the noise characteristics of the preamplifiers, which govern the signal to noise of the system. The flattening of the electronic noise curve is due to the limitations of the analogue ratio unit, the unit providing a constant noise source for each time constant. The degradation in position resolution for high charge levels is evident at all time constants. However it is much worse for longer time constants, the best resolution was achieved at the shortest time constant, where the electronic noise contribution is greatest.

The electronic noise with the GD cathode is dominated by the preamplifiers as the load is a pure capacitive load, whereas with the RC cathode the thermal noise from the RC strip contributes to a very large extent. The resolution versus gain graphs will be discussed in detail in section 6.5 which deals with the gas limitations on position resolution in Xenon/Methane detectors.

For 90/10 GD, a definite degradation occurred towards high drift fields at all time constants. This is thought to be due to an increased contribution from secondary avalanches because of the high drift field and hence shorter time taken for a photoelectron to reach the anode. For a cathode time constant of  $0.8\text{ }\mu\text{sec}$ , balancing the anode gain as for an anode voltage of  $+3500\text{ V}$  drift voltage  $+50\text{ V}$ , a resolution of  $.427 \pm .006\text{ mm}$  (two point average) was measured for  $+50\text{ V}$  drift, the resolution degrading to  $.611 \pm .009\text{ mm}$  at  $+200\text{ V}$  drift. This was a charge level  $\sim .45\text{ pC}$ , maximum random error was  $\pm .061\text{ mm}$ .

For 75/25 and 50/50 the tabulated best resolution versus time constant values only will be presented, as the gain curves are discussed, for all

TABLE 6.3.7

BEST RESOLUTION VALUES 90/10

Time Constant	Two point Average Resolution (FWHM)	Average Resolution (FWHM) 5 mm scan	Maximum Random Error	Anode Voltage	Charge Load (Amplifier Time Constant 1.6 $\mu$ sec)
0.4 $\mu$ sec	.357 $\pm$ .009mm	.393 $\pm$ .025mm	$\pm$ .059 mm	+ 3450 V	.38 pC
0.8 $\mu$ sec	.366 $\pm$ .005	.477 $\pm$ .015	$\pm$ .061	+ 3350	.245
1.6 $\mu$ sec	.373 $\pm$ .005	.522 $\pm$ .026	$\pm$ .061	+ 3350	.245

Electrical co-ordinates as per RC counter results

TABLE 6.3.8

BEST RESOLUTION VALUES 75/25

Time Constant	Two Point Average Resolution (FWHM)	Average Resolution (FWHM) 5 mm scan	Maximum Random Error	Anode Voltage	Charge Load (Amplifier Time Constant 1.6 $\mu$ sec)
0.4 $\mu$ sec	.299 $\pm$ .005mm	.334 $\pm$ .915mm	$\pm$ .029 mm	+ 3850 V	.36 pC
0.8 $\mu$ sec	.344 $\pm$ .007	.346 $\pm$ .016	$\pm$ .030	+ 3850	.36
1.6 $\mu$ sec	.362 $\pm$ .006	.379 $\pm$ .017	$\pm$ .029	+ 3850	.36

Electrical co-ordinates ~ .5

TABLE 6.3.9

BEST RESOLUTION VALUES 50/50

Time Constant	Two Point Average Resolution (FWHM)	Average Resolution (FWHM) 5 mm scan	Maximum Random Error	Anode Voltage	Charge Load (Amplifier Time Constant 1.6 $\mu$ sec)
0.4 $\mu$ sec	.334 $\pm$ .006mm	.381 $\pm$ .018mm	$\pm$ .030 mm	+ 4100 V	.278 pC
0.8 $\mu$ sec	.285 $\pm$ .006	.332 $\pm$ .017	$\pm$ .030	+ 4200	.385
1.6 $\mu$ sec	.315 $\pm$ .011	.356 $\pm$ .019	$\pm$ .029	+ 4000	.195

gas mixtures in section 6.5. Tables 6.3.8 and 6.3.9 give the best resolution and operating conditions for each gas mix. The drift voltage used was  $+50$  V for these results. For all gas mixes the resolution at the time constant of 3.2 and 6.4  $\mu\text{sec}$  is considerably worse, and hence is not included in the above tables.

All gas mixtures showed a degradation in position resolution at high drift fields and smaller (negative drift voltages) fields.

As can be seen from the tables a gradual improvement in very best resolution occurs as the percentage of methane is increased. The best time constant changing from 0.4  $\mu\text{sec}$  for 90/10 and 75/25 to 0.8  $\mu\text{sec}$  for 50/50. It is interesting to note that the charge level (operating condition) is approximately the same for all the best resolution values - .36 - .39 pC .

The non-linearity of the GD cathode along the anode was briefly investigated during the course of the work. It was found that the sensitivity for all time constants for all counters and gas mixes for a given position were consistent within the errors. No significant change in rms deviation from a straight line fit on a local scale occurred for a given time constant with gain. Also no significant change in rms non-linearity along the scanable length of the anode wires occurred between counters, or as a function of gain.

For 75/25 a detailed 5 cm scan along the anode was made, position resolution was measured every 3 mm giving 18 data points in all. The counter operating conditions were anode voltage  $+3850$  V , drift voltage  $+50$  V , both anode and cathode amplifier time constants 1.6  $\mu\text{sec}$ . The average resolution was  $.405 \pm .021$  mm , and rms deviation from a straight line was  $.260 \pm .002$  mm (maximum random error  $\pm .030$  mm), Hence for the scan length, electrical co-ordinates .22 to .75 , an rms non-linearity of 0.52% was measured.

### 6.3.2.3. Comparison with Theory

As for the RC system, a theoretical prediction of the performance of the GD cathode can be made. From the theory a check can be made between the measured electronic noise and predicted performance, taking into account the ratio system noise.

The output position for the two measured charges  $q_A, q_B$  is given by

$$Q = \frac{q_B}{q_A + q_B} \quad (= x)$$

Hence

$$dQ = \frac{q_A dq_B - q_B dq_A}{(q_A + q_B)^2}$$

The uncertainty in position is given by  $(\overline{dQ^2})^{\frac{1}{2}}$

$$\overline{dQ^2} = \frac{q_A^2 \overline{dq_B^2} + q_B^2 \overline{dq_A^2} - 2 q_A q_B \overline{dq_A dq_B}}{(q_A + q_B)^4}$$

It can be shown that

$$\overline{dQ^2} = \frac{q_A^2 + q_B^2}{(q_A + q_B)^2} \cdot \left\{ 1 - 2 \frac{q_A + q_B}{(q_A^2 + q_B^2)} r_{AB} \right\} \frac{dq^2}{(q_A + q_B)^2}$$

where  $\overline{dq_A^2} = \overline{dq_B^2} = dq^2$ , that is the noise contribution for

A and B are identical and

$$r_{AB} = \frac{\overline{dq_A dq_B}}{dq^2}$$

which represents the correlation in noise between either end of the cathode.

Substituting for Q

$$\overline{dQ^2} = [(1 - Q)^2 + Q^2] \left\{ 1 - 2 \frac{(1 - Q)Q r_{AB}}{(1 - Q)^2 + Q^2} \right\} \frac{dq^2}{q_o^2}$$

where  $q_o = q_A + q_B$  total dumped charge.



The above can be reduced to

$$\overline{dQ^2} = \{1 - 2(1 + r_{AB}) \cdot Q(1 - Q)\} \left(\frac{dq}{q_0}\right)^2$$

Gilvin et al 1981b (private communication) have shown that  $r_{AB} = -1$ , that is anti-correlation exists between the noise from either end, hence

$$\overline{dQ^2} = \left(\frac{dq}{q_0}\right)^2 \quad \text{or} \quad (\overline{dQ^2})^{\frac{1}{2}} = \frac{dq}{q_0}.$$

This gives the fractional rms resolution for the GD cathode, in fact with  $r_{AB} = -1$  it is just noise to signal. In the case of the GD cathode the preamplifier and amplifier noise is the main dominant factor in the electronic noise. The analogue ratio unit in addition provides a noise source which is time constant dependent (see Table 6.3.10); This dependence on time constant presumably arises from the analogue stretchers, these are the last item in the processing electronics which deal with shaped signals.

Using the average sensitivity from the linearity scans, Table 6.3.10 lists the ratio unit system noise in  $\mu m$ , for each time constant, estimated from the electronic noise measurements. The error is the estimated standard error in deriving these numbers.

The total predicted resolution is therefore

$$\overline{\delta x^2} = \overline{dQ^2} + \delta d^2$$

where  $\delta d$  is the system noise.

In order to calculate the predicted performance  $dq$  must be known. The rms noise of the preamplifier loaded with a pure capacitative load equivalent to the detector (100 pF) was measured and a mean value of  $dq$  with associated standard error derived. Table 6.3.11 details the calculation of theoretical performance for an anode charge of .196 pC

TABLE 6.3.10

## ANALOGUE RATIO NOISE LIMIT TO RESOLUTION

<u>Amplifier Time Constant</u>	<u>System Noise Limit, FWHM</u>
0.4 $\mu$ sec	$118 \pm 15 \mu\text{m}$
0.8	$110 \pm 14$
1.6	$101 \pm 15$
3.2	$91 \pm 15$
6.4	$73 \pm 15$

TABLE 6.3.11

## CALCULATION OF PREDICTED PERFORMANCE GD

<u>Amplifier Time Constant</u>	<u>dq</u>	<u>Predicted Electronic Resolution Performance <math>q_0 = 1.0 \text{ pC}</math></u>	
		$\Delta x = \frac{dq}{q_0}$	$\Delta x \text{ FWHM}$ for 95 mm cathode
0.4 $\mu$ sec	$626 \pm 52 \text{ electrons}$	$1.0 \times 10^{-4}$	$22.4 \mu\text{m}$
0.8	$540 \pm 43$	$8.64 \times 10^{-5}$	19.4
1.6	$438 \pm 44$	$7.01 \times 10^{-5}$	15.7
3.2	$450 \pm 43$	$7.2 \times 10^{-5}$	16.1
6.4	$526 \pm 48$	$8.42 \times 10^{-5}$	18.9

<u>Amplifier Time Constant</u>	<u>Analogue Ratio Limit</u>	<u>Anode Charge Predicted Resolution (FWHM)</u>	<u>,196 pC Measured</u>
0.4 $\mu$ sec	$118 \pm 15 \mu\text{m}$	$258 \pm 40 \mu\text{m}$	$313 \pm 33 \mu\text{m}$
0.8 $\mu$ sec	$110 \pm 14$	$228 \pm 34$	$265 \pm 33$
1.6 $\mu$ sec	$101 \pm 15$	$191 \pm 35$	$206 \pm 33$
3.2 $\mu$ sec	$91 \pm 15$	$189 \pm 36$	$219 \pm 33$
6.4 $\mu$ sec	$73 \pm 15$	$207 \pm 47$	$216 \pm 33$

assuming a 50/50 cathode charge split. The predicted resolution is compared with that measured during electronic noise measurements with identical risetime pulse and calculated using the average sensitivity derived from overall (5 cm) linearity scans.

As can be seen the measured electronic resolution corresponds closely to that predicted by a knowledge of the system parameters. Only  $0.4 \mu\text{sec}$  is substantially lower than measured. The difference is most probably due to the finite resistance existing at r.f. frequencies along the substrate of each cathode providing an additional, thermal noise source.

In Table 6.3.11 the resolution for the GD cathode is given for a dumped charge of  $1.0 \text{ pC}$  indicating the resolving power of the readout. Unfortunately gas physics and system noise stop counter resolution of this value from ever being achieved.

#### 6.4. Across the Anode Wire Modulation Effects

All two dimensional position sensing prototype IPCs showed a modulation in both measured counter gain and output position for sensing across the anode wires. This modulation occurred at  $2 \text{ mm}$  pitch, the anode wire spacing.

The modulation in output wire spacing is due to incomplete interpolation across the wires, resulting in what is known as the 'binning' effect. In a completely 'binned' condition the output signal consists of a step-like function plotted against real position, the centre of each step occurring above a wire. This results from an avalanche occurring only on a single wire. This was never observed in any of the counters investigated hence some form of interpolation was always present. The worst case of across the anode wire modulation occurred with the RC readout scheme, the modulation in part being due to the nature of the readout. The results of the RC counter will be dealt with first.

#### 6.4.1. 90/10 RC Across Wire Modulation

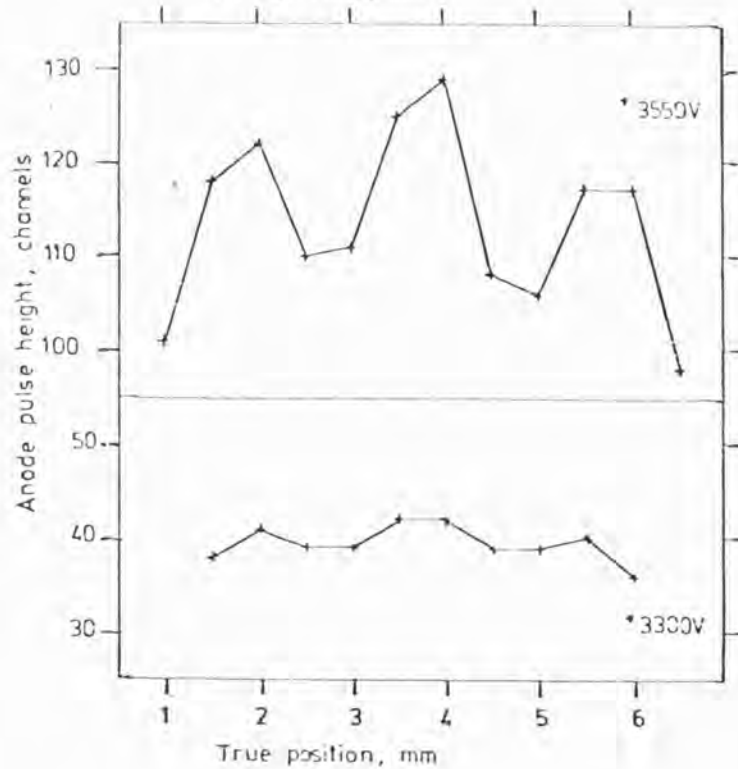
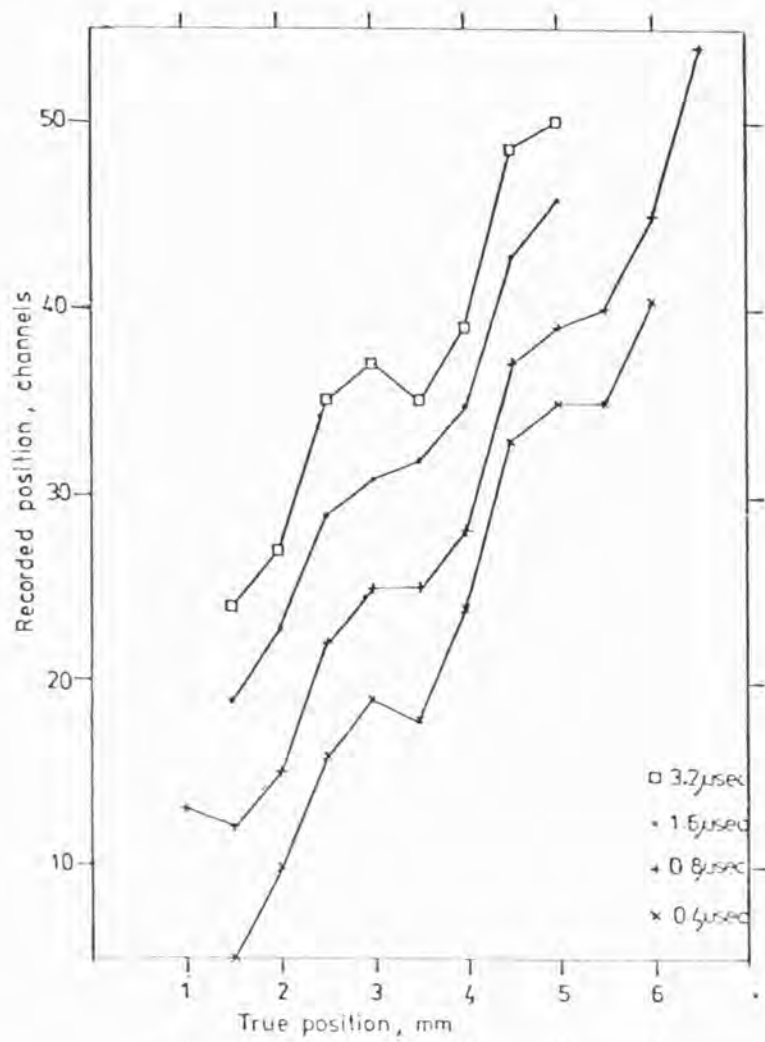
A distinct modulation of anode gain versus position was found in across anode scans, the modulation was of a 2 mm pitch. However for a given point, the anode gain was a smooth function of applied voltage. The amount of modulation increased as the anode voltage increased, the peak to peak modulation in percent being 20.6% of the mean anode gain at an anode voltage of  $+3550$  V, but only 10.1% at  $+3300$  V  $+50$  V drift. There was also no change in basic shape in modulation over the voltage range  $+3300$  to  $+3700$  V (charge level  $\sim .12 - .72$  pC for  $1.6 \mu\text{sec}$  anode amplifier time constant). That is the high gain value always remained high. Fixed in phase to the gain modulation, an accompanying modulation in output position versus real position existed. This was the case in all counters. In the RC case the modulation was found to depend on three things, distance from the electrical centre, anode gain, and cathode amplifier time constant. Under certain conditions a 'turnback' in output position was observed, that is the output position slope changed sign; in addition to these points flat regions occurred, as expected by the binning argument.

The modulation was investigated in detail for several regions of the counter after initial discovery. This was achieved by scans for each counter variable, the position resolution, output position, and anode gain were recorded at least every .5 mm over a 6 mm scan region.

##### 6.4.1.1. Variation with Cathode Amplifier Time Constant

Figure 6.4.1 shows a local scan at electrical co-ordinates .302 to .347 (derived from noise measurements) for a typical counter gain, anode voltage  $+3550$  V,  $+50$  V drift. The modulation is illustrated as a function of cathode amplifier time constant. The anode gain modulation for the same region for two anode voltages is shown below. All readings

Figure 6.4.1. Across wire linearity scan showing output position (in channels from arbitrary start position) versus real position (top) for various cathode amplifier time constants (various time constant results displaced vertically) (Anode voltage +3550 V +50 V drift). Real position is shown as a distance in mm from the start position. The anode gain modulation for two anode voltages, for identical detector co-ordinates is shown at bottom. 90/10 RC Counter, Fe<sup>55</sup> source.





if necessary, to ensure accuracy, were taken at a higher PHA gain setting and scaled to a common value.

Table 6.4.1 lists the rms and mean absolute deviation (m.a.d.) in terms of millimetres from a least squares fit of a straight line for the region, as a function of time constant. The turnback effect is evident at both 0.4 and 3.2  $\mu\text{sec}$ . The non-linearity, both visually and in terms of deviation is least at 0.8 and 1.6  $\mu\text{sec}$ , greatest at 3.2  $\mu\text{sec}$ , 0.4  $\mu\text{sec}$  is not quite as bad. The turnback occurs approximately at the high gain position.

Figure 6.4.2 shows the position modulation as a function of time constant, 0.4, 0.8 and 1.6  $\mu\text{sec}$  for identical co-ordinates for an angle voltage of  $+3300\text{ V}$ , the lowest gain operating condition of the counter. Table 6.4.2 lists the respective rms and m.a.d. values. At this counter gain no turnback is visible, and in all cases the modulation is much less. These results illustrate the interdependence problem of counter effects.

#### 6.4.1.2. Variation with Counter Position

It was found early in the work the degree of modulation in output position, in particular 'turnback' was a strong function of position on the counter. Figure 6.4.3 shows a long scan, made under typical counter conditions. Only data from part of the scan is plotted in order to illustrate the modulation. The anode voltage used was  $+3600\text{ V}$ , drift  $+50\text{ V}$ , both anode and cathode amplifier time constants were set at 1.6  $\mu\text{sec}$ . The electrical centre of the counter as found by electronic noise measurements is also shown on the graph. The electrical co-ordinates of the whole scan were .28 to .657 of the line length. The 2 mm modulation is evident across the whole scan. However the modulation gets worse away from the centre, and a different characteristic shape to the modulation occurred each side of the electrical centre. This differ-

TABLE 6.4.1

RMS AND MAD FROM A STRAIGHT LINE FIT

AS A FUNCTION OF TIME CONSTANT 90/10 RC ANODE VOLTAGE +3550 V

Amplifier Time Constant

0.4 $\mu$ sec	rms = .149 $\pm$ .013 mm m.a.d. = .205 $\pm$ .018
0.8 $\mu$ sec	rms = .126 $\pm$ .011 mm m.a.d. = .212 $\pm$ .019
1.6 $\mu$ sec	rms = .124 $\pm$ .010 mm m.a.d. = .182 $\pm$ .014
3.2 $\mu$ sec	rms = .165 $\pm$ .020 mm m.a.d. = .295 $\pm$ .035

TABLE 6.4.2

RMS AND MAD FROM A STRAIGHT LINE FIT

AS A FUNCTION OF TIME CONSTANT 90/10 RC ANODE VOLTAGE +3300 V

Amplifier Time Constant

0.4 $\mu$ sec	rms = .095 $\pm$ .004 mm m.a.d. = .135 $\pm$ .005
0.8 $\mu$ sec	rms = .104 $\pm$ .004 mm m.a.d. = .138 $\pm$ .006
1.6 $\mu$ sec	rms = .083 $\pm$ .004 mm m.a.d. = .153 $\pm$ .007

Note: All errors quoted for rms and m.a.d. values are errors in calculation of sensitivity.

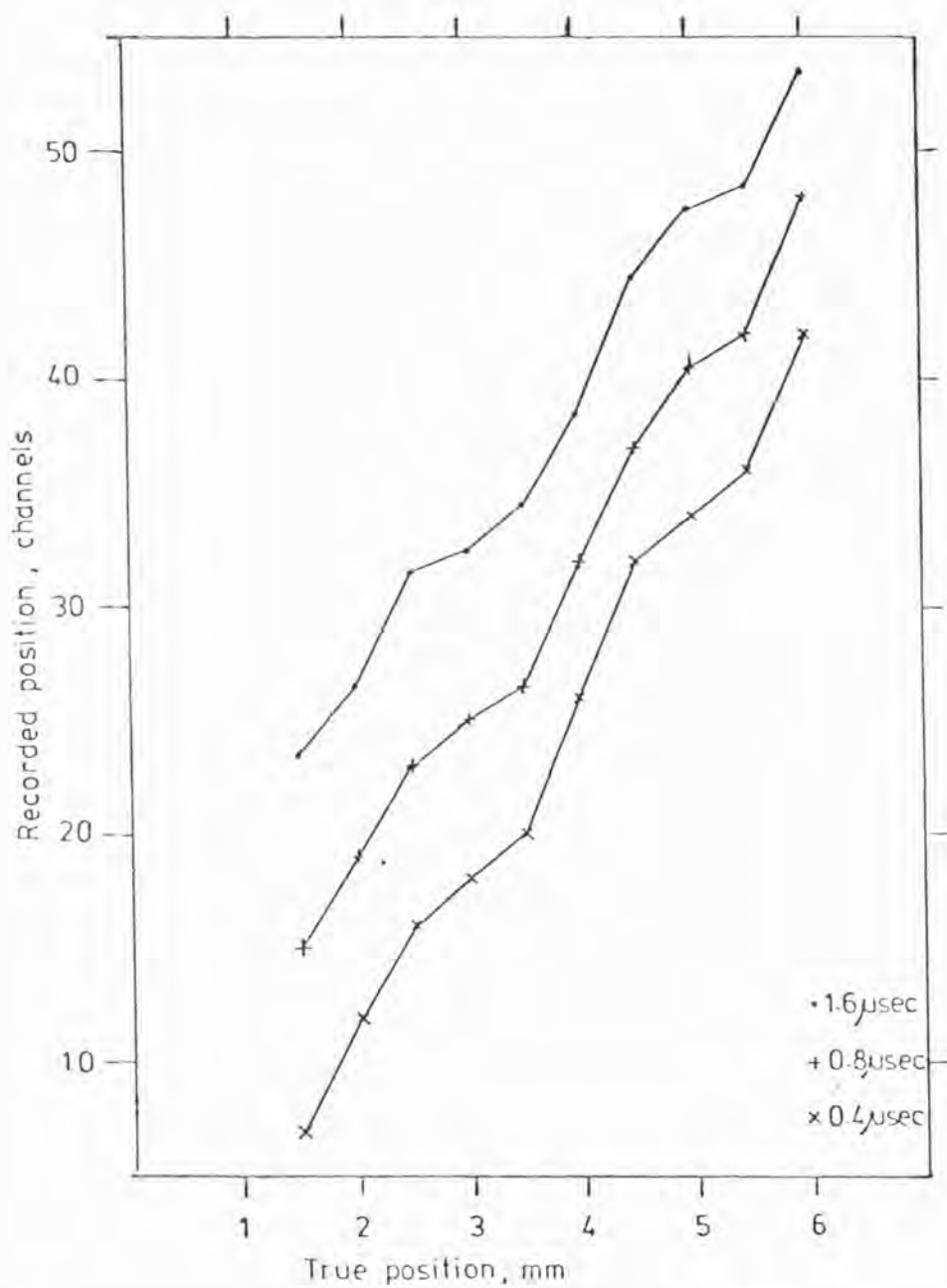


Figure 6.4.2. Across wire linearity scan showing output position versus real position, identical co-ordinates to Figure 6.4.1, as a function of cathode amplifier time constant. Anode voltage +3300 V , drift voltage +50 V , 90/10 RC Counter,  $\text{Fe}^{55}$  source.

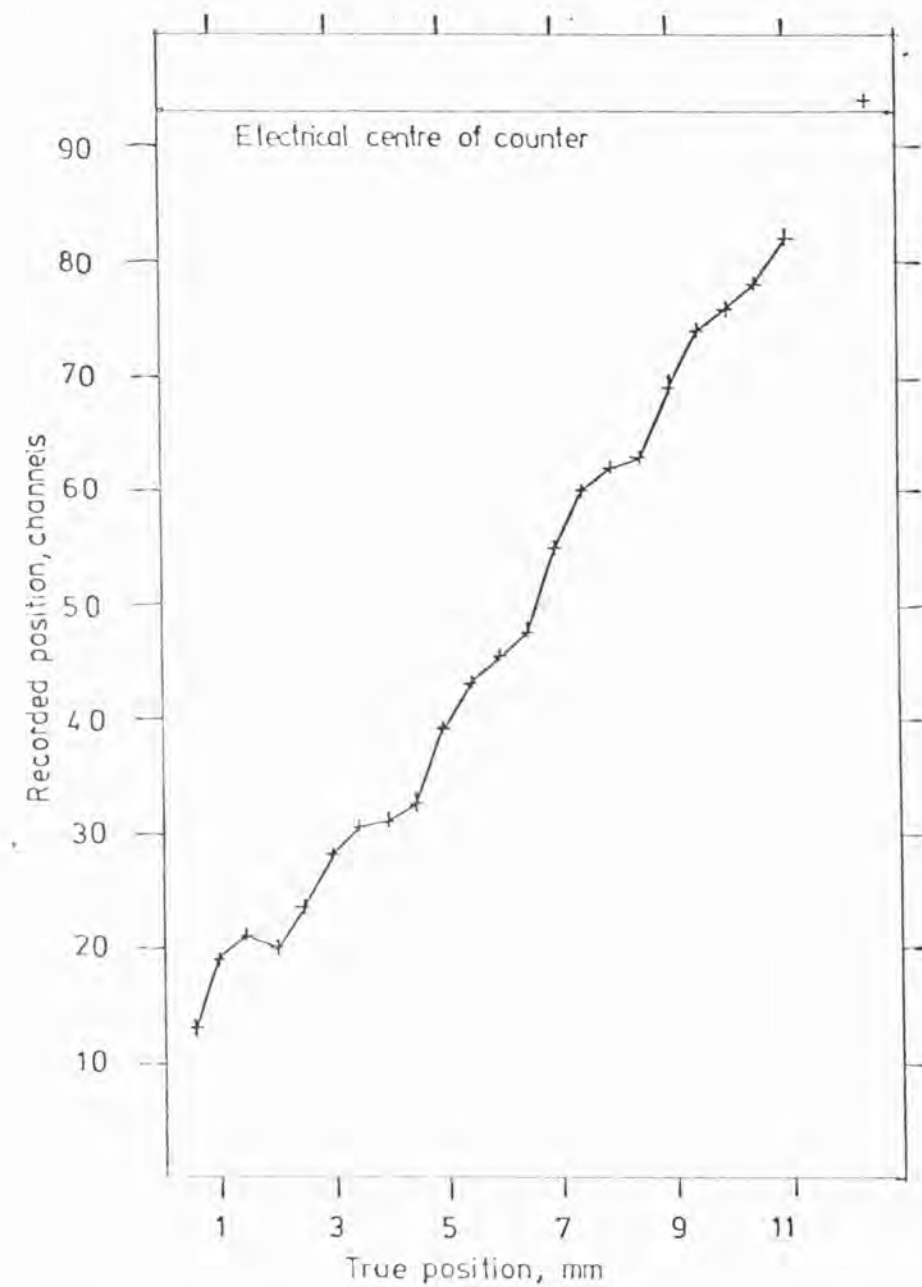


Figure 6.4.3. Across wire linearity scan showing output position versus real position. Anode voltage +3600 V , +50 V drift, amplifier time constants 1.6  $\mu$ sec. Note how the modulation in output position increases away from electrical centre of the counter. 90/10 RC Counter, Fe<sup>55</sup> source.

ence in shape is only evident at large distances away from the electrical centre. The difference consists of a dip in the modulation shape occurring, whereas a peak occurs on the other side of the electrical centre, if one measures co-ordinates in terms of anode wire spacing from the centre. That is the peak position in the modulation shape changes with respect to the anode gain modulation. The modulation shape was found to reverse around the electrical centre with a change of ratio from  $A/(A+B)$  to  $B/(A+B)$ .

#### 6.4.1.3. Variation with Gain

The modulation as a function of gain was investigated in detail for a couple of spot counter areas only. Figure 6.4.4 shows the output position as a function of real position and anode voltage for one region of the counter. Table 6.4.3 gives the respective rms, m.a.d. values. These measurements were taken with a  $200\ \mu\text{m}$  slit, a drift voltage of  $+50\ \text{V}$  and both anode and cathode shaping constants were  $1.6\ \mu\text{sec}$ .

As can be seen from the figure and table the modulation worsens as the anode voltage, and hence counter gain increases. The 'turnback' is not evident at low gains, but a distinct flattening in output position occurs, the 'turnback' gradually appearing and increasing as the anode voltage increased.

A small region of the counter was investigated using a  $100\ \mu\text{m}$  slit in order to accurately determine the shape of the modulation. Figure 6.4.5 shows the result of these measurements. The electrical co-ordinates for the data of Figure 6.4.4 were .297 to .347 and for Figure 6.4.5, .594 to .627, in this case the ratio  $B/(A+B)$  rather than  $A/(A+B)$  was used. Motion away from the original measurement area was necessary due to breakdown in the counter. The error in locating the position peak was  $\pm .05$  channels maximum (random).

As can be seen in Figure 6.4.5 the overall linearity, as given by

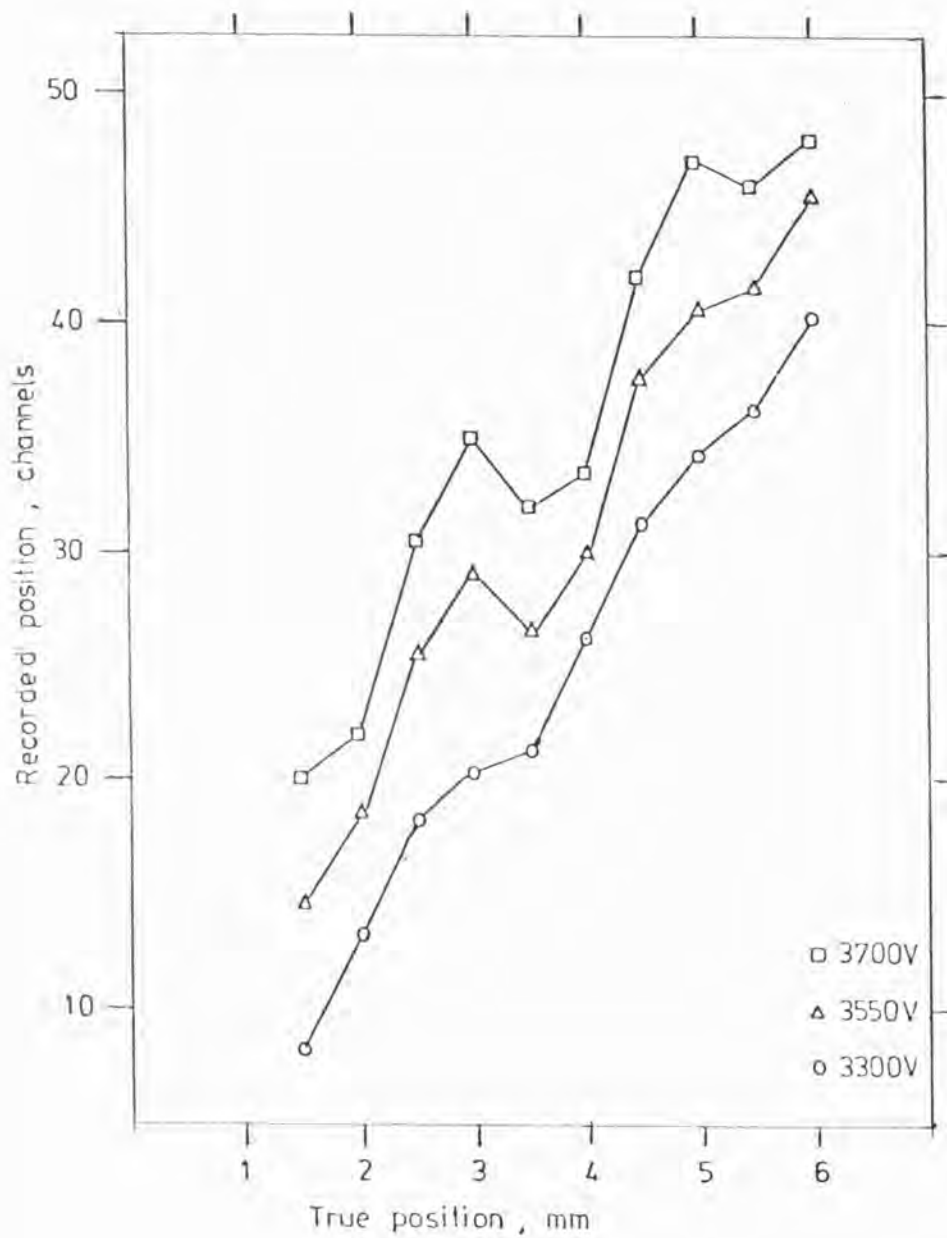


Figure 6.4.4. Across wire linearity scan showing output position versus real position, as a function of anode voltage (+50 V drift) for a cathode amplifier time constant of 1.6  $\mu$ sec, 90/10 RC Counter, Fe<sup>55</sup> source.



TABLE 6.4.3

RMS M.A.D. VALUES : MODULATION AS A FUNCTION  
OF ANODE VOLTAGE 90/10 RC

Anode Voltage

+ 3300 V	rms = .092 ± .003 mm m.a.d. = .121 ± .004
+ 3550	rms = .144 ± .011 mm m.a.d. = .266 ± .02
+ 3700	rms = .182 ± .020 mm m.a.d. = .399 ± .043

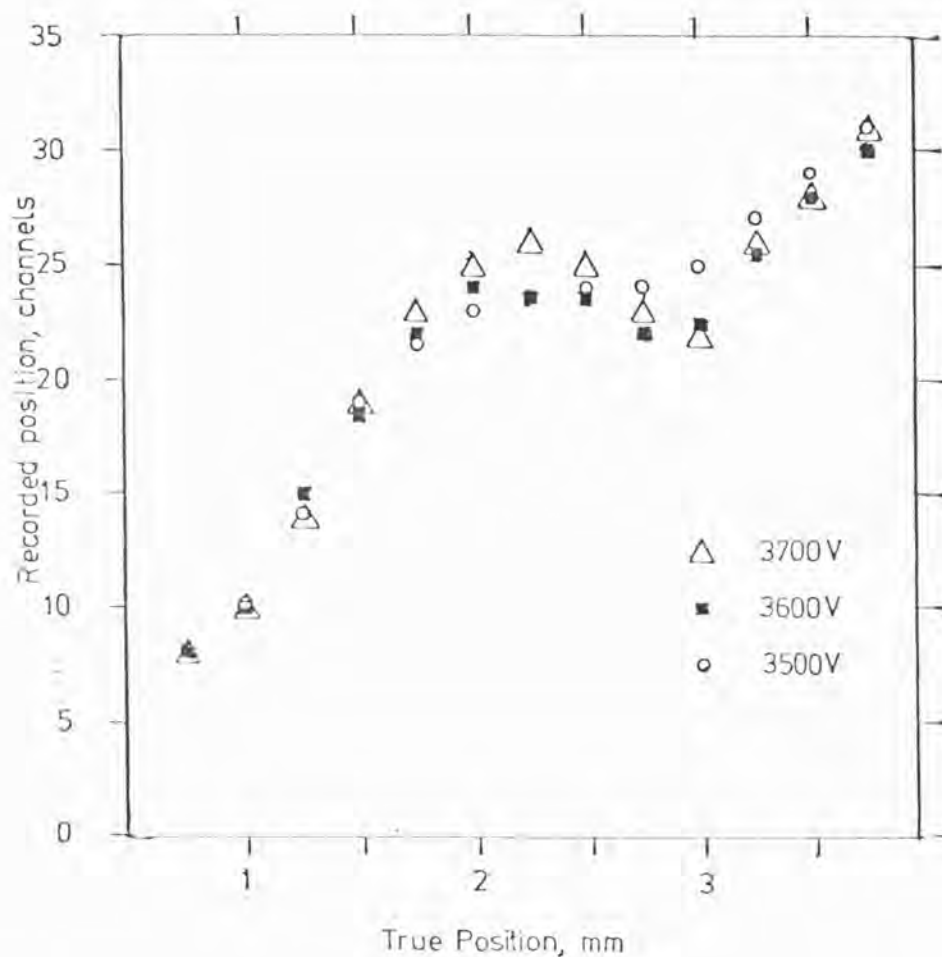


Figure 6.4.5. Across wire linearity; output position versus real position, as a function of anode voltage (0.25 mm steps) for a cathode amplifier time constant of 1.6  $\mu$ sec. 90/10 RC Counter,  $\text{Fe}^{55}$  source. Note here various results have not been displaced vertically as in all other diagrams.

the slope of the least squares fit, does not change with gain. However the modulation gradually worsened as the gain increased.

#### 6.4.1.4. Variation with Drift Voltage

Some investigation into variation of modulation with drift voltage was made. This was achieved by scans for various drift fields, the anode voltage being altered to balance the gain such that an identical measured charge (at  $1.6 \mu\text{sec}$ ) was obtained. The modulation was found to be evident at all drift voltages in the range  $-40 \text{ V}$  to  $+50 \text{ V}$  for a given time constant, the overall sensitivities were all consistent within the measurement errors. Some gradual change with time constant was found. One interesting result was obtained at  $-40 \text{ V}$  where the variation with time constant was checked. Unlike at positive drift volts, here the modulation was found to be greater at  $1.6 \mu\text{sec}$  than  $0.8 \mu\text{sec}$  amplifier time constant. Figure 6.4.6 shows the results of a scan at identical co-ordinates to Figure 6.4.1. This difference could be due to the different leakage fields, from the anode to cathode into the drift field, resulting from the changed anode voltage.

#### 6.4.1.5. Position Resolution Across the Anode

Figure 6.4.7 shows the position resolution, FWHM, in terms of output channels as measured for a high and low gain position in the detector for an anode and cathode shaping time constant of  $1.6 \mu\text{sec}$ . The FWHM is different for each position. However the local sensitivity is very different for each point. The low gain corresponds to a high sensitivity that is large number of channels per  $\text{mm}$ , the high gain position to a low sensitivity. Hence the real position resolution as a function of gain varies with position. The effect of the modulation is most evident with a picture showing the cross-section through a group of slits

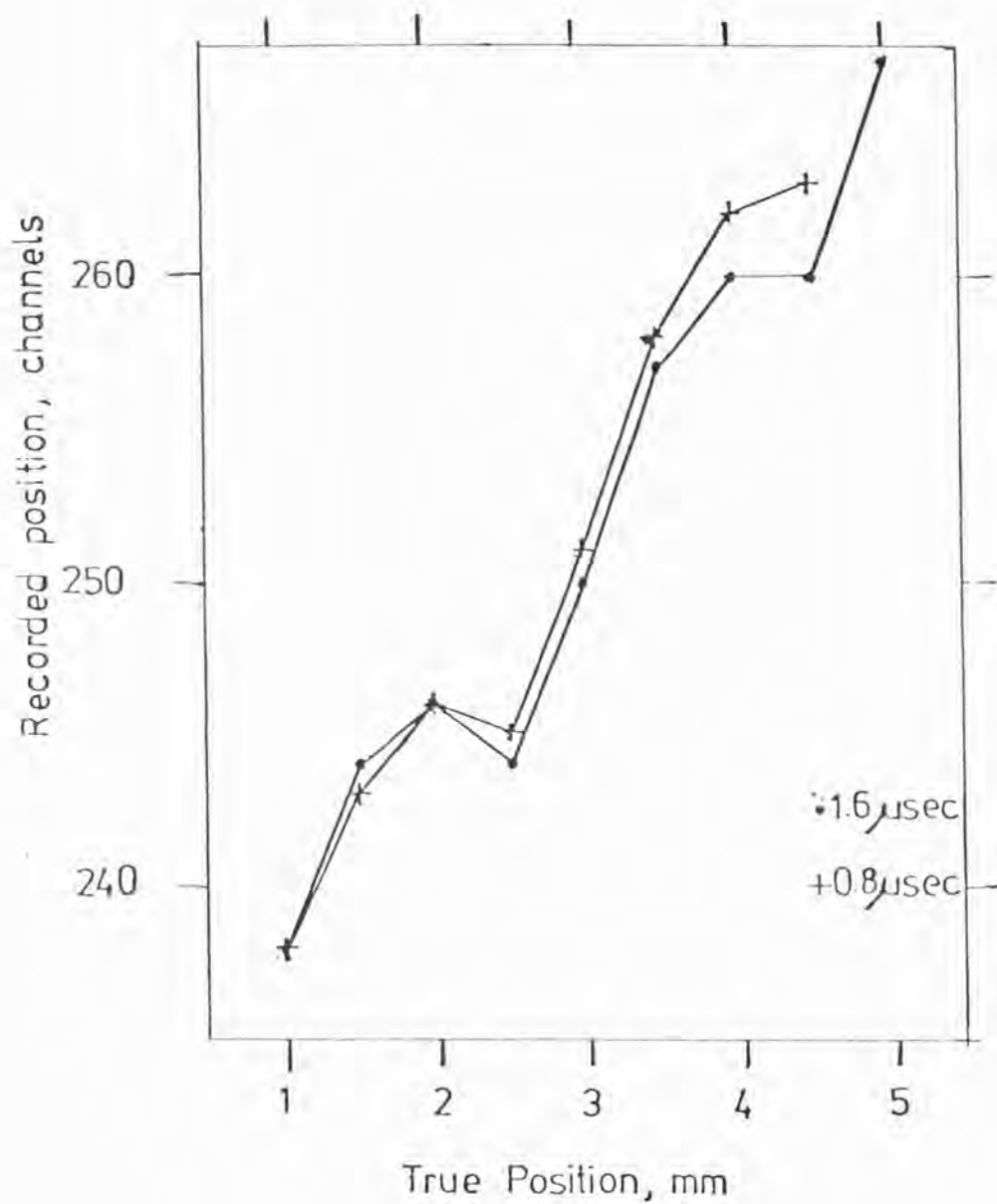


Figure 6.4.6. Across wire linearity; output position versus real position, for two cathode amplifier time constants (0.8, 1.6  $\mu$ sec, drift voltage -40 V ). Anode voltage balanced to give equivalent gain to anode +3550 V, drift +50 V. Scan co-ordinates identical to Figure 6.4.1. 90/10 RC Counter,  $\text{Fe}^{55}$  source.

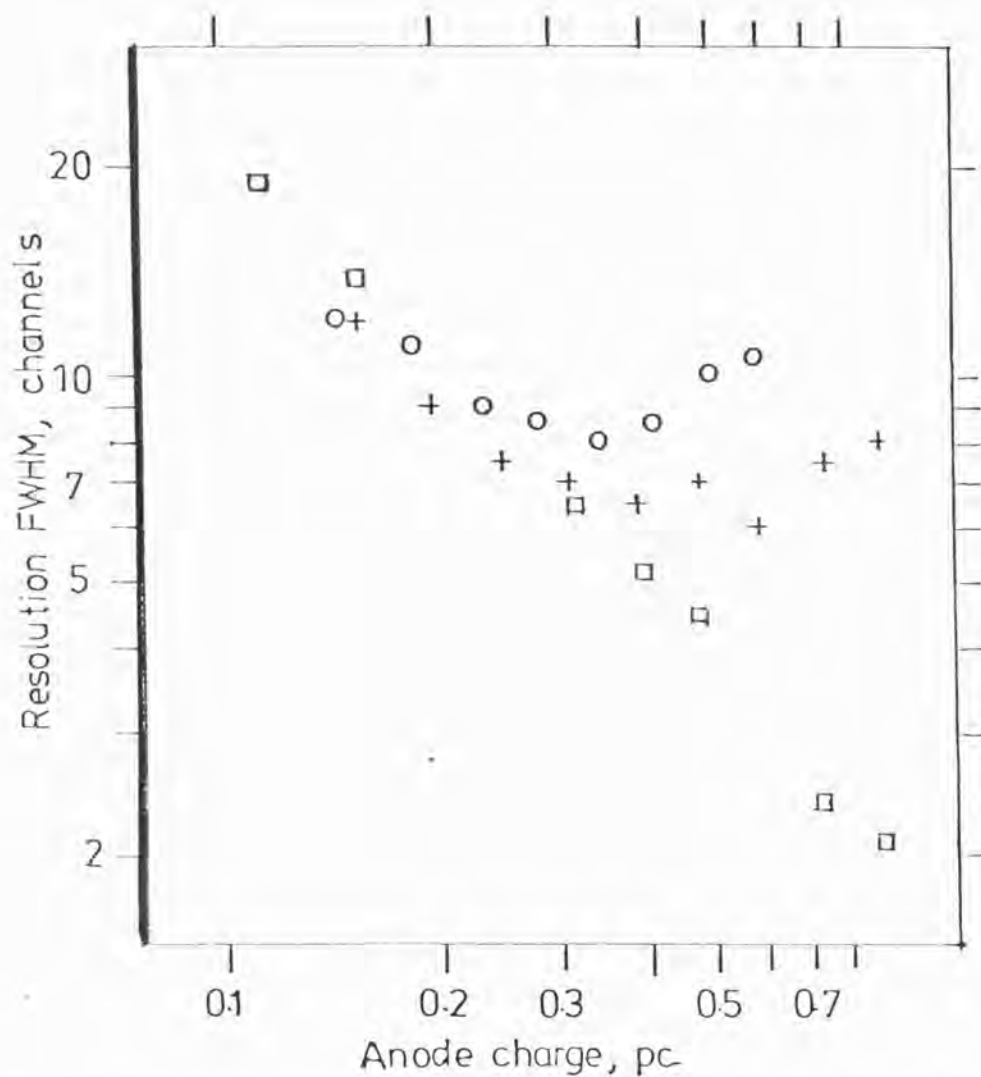


Figure 6.4.7. Position resolution (FWHM) in PHA channels as a function of measured anode charge (amplifier time constants 1.6  $\mu$ sec), for one high (+) and low (o) gain position across the anode wires. Electronic noise ( $\square$ ) is also shown. Note random error is not shown in this case. 90/10 RC Counter,  $\text{Fe}^{55}$  source.

aligned across the wires, as will be shown in the case of the graded density.

Consider the following data taken from Figure 6.4.7.:

Anode voltage  $+3550$  V

Drift voltage  $+50$  V

Amplifier Time Constant  $1.6$  sec, both anode and cathode;  
for nearly identical charge levels (Q);

Low gain position  $Q \sim .42$  pC; Position FWHM =  $8\frac{1}{2}$  channels

High gain position  $Q \sim .39$  pC Position FWHM =  $6\frac{1}{2}$  channels.

Local sensitivity from scans over relevant co-ordinates are:

Low gain  $\sim 6$  channels per  $0.5$  mm

High Gain  $\sim 2$  channels per  $0.5$  mm

Hence approximate position resolutions are:

Low Gain  $\sim .7$  mm FWHM

High Gain  $\sim 1.6$  mm FWHM

As expected from the modulation graph at certain points due to the lowering of sensitivity it is impossible to tell between two points  $\sim 1$  mm apart.

In terms of average resolution the behaviour with amplifier time constant was found to be identical with that observed along the anode. The best spot resolution were compatible with those along. Resolution versus drift field was found to be flat within the errors for the range  $-40$  to  $+300$  V for all operating conditions.



#### 6.4.1.6. Comparison with Other Work and Theory

The fundamental modulation across the wires is of course because of binning, but the position modulation as a function of counter co-ordinate and in particular the turnback cannot be explained by this. At low charge levels, Gilvin et al., 1980, have seen similar modulation which in their case could be explained by angular localisation of the avalanche around the anode. The experimental results showed a good agreement with the theoretical model. With angular localisation the waveform of the induced cathode charge and hence of the RC line output has been shown to depend upon the local position of the origin of the initial electrons. Borkowski and Kopp 1977 used this effect, which can be large, to differentiate between events absorbed above and below the anode plane.

The IPC of Gilvin et al., 1980, utilised the method of zero cross timing for position location. However as the zero cross time is related to the pulse height by shaping the effect is also evident when the ratio method is used.

In the zero cross method the position is given by

$$t_{1-X} + d - t_X$$

where  $t_{1-X}$  is the stop signal from one end of the RC line,  $t_X$  is the start signal from the other end, and  $d$  is the processing electronics delay. The delay must be at least half the signal travel time down the line for the system to work.

Figure 6.4.8 shows schematically the variation in zero cross time on the cathode between wires for the schematic line below, as measured by Gilvin et al., 1980. This data was obtained using a shorted cathode (without RC line).

Consider first region (i). Here the start signal comes before the stop, so that the size of the position signal falls as one moves from over a wire to between the wires. This interwire modulation is super-

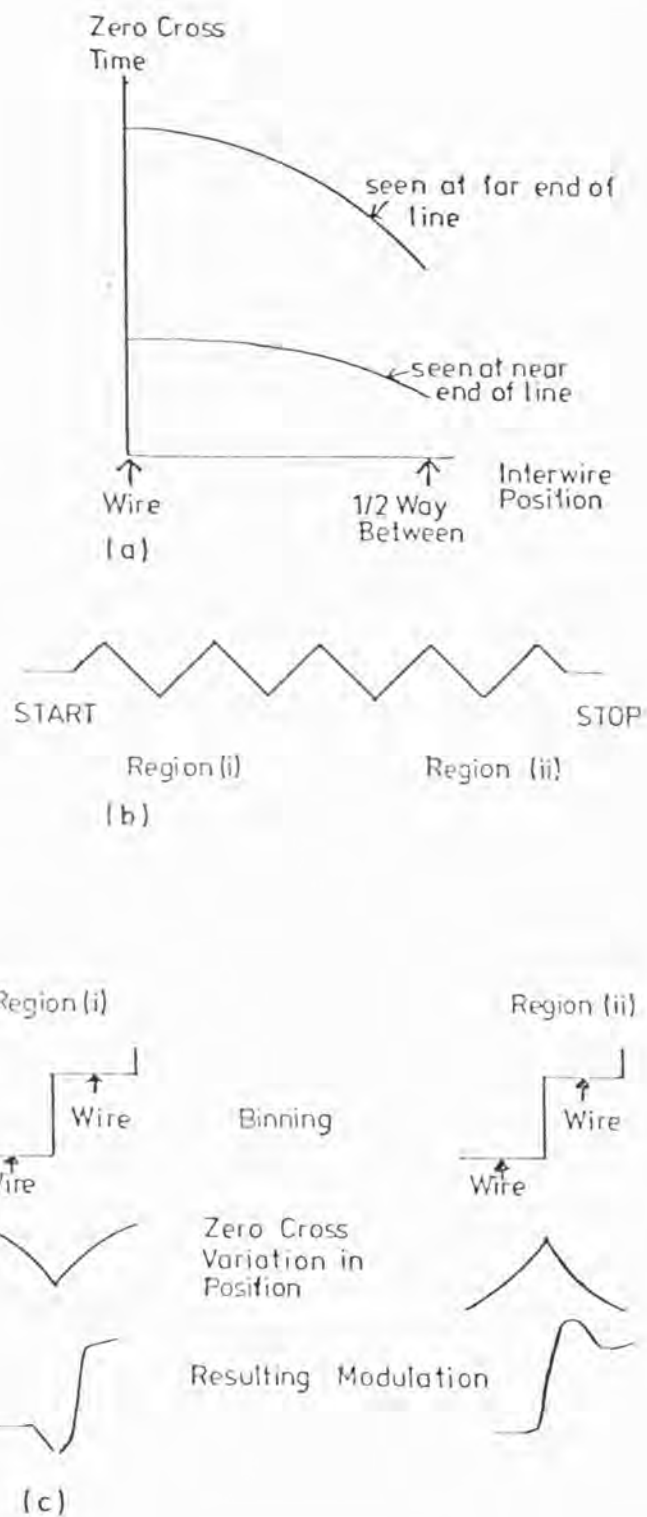


Figure 6.4.8. (a) Schematic variation in zero cross time as a function of inter-anode-wire position as viewed from each end of RC line.  
 (b) Schematic RC line.  
 (c) Binning effect; resulting variation in output position, for zero cross-time variation, across anode wires; and final resulting modulation in output position for both effects combined, for each region of (b).

imposed on the overall time difference along the wire. As the time difference between start and stop signal increases, the modulation effect increases. Hence the modulation increases away from the electrical centre.

In region (ii) the stop signal arrives at its end of the line before the start, so that the size of the difference stop minus start falls, but as this difference, as far as position output is concerned, is a negative quantity, the position signal increases as we go from over to between the anode wires. This difference is also imposed on the binning effect hence Figure 6.4.8 shows the resulting output position modulation for each region.

This qualitative argument shows how position modulation for a RC readout can arise. Mathieson 1980 (private communication) has attempted to model the 90/10 RC counter. The results indicate that angular localisation of the avalanche with a risetime dependence with position could produce modulation. However the resulting modulation should decrease as the anode voltage increases, unlike the experimental results. This is because as the voltage increases the angular localisation decreases. A second distinct mechanism can also rise with angular localisation, that is a variation with gas gain with position due to the non-radial field distribution around the anode wires, this effect is voltage dependent. (Mathieson and Harris 1978]. Modelling of this effect has not yet been considered by Mathieson. At present no model predicts the measured across wire modulation.

The RC readout scheme was abandoned for two reasons, the poor resolution and position dependent modulation, compared to the graded density cathode.

#### 6.4.2. Across Wire Modulation: Graded Density Cathode

With the graded density cathode a 2mm pitch modulation in output position was evident. However no 'turnback' or counter position dependence was observed, a distinct difference in modulation was found with each gas mixture. The results obtained with the Canberra preamplifiers only will be presented.

##### 6.4.2.1. 90/10 Across Wire Modulation

As in the case of the 90/10 RC the modulation was investigated by local linearity scans. Table 6.4.4 gives the rms and m.a.d. values from a straight line fit to the data, for electrical co-ordinates .66 to .62, as a function of time constant and anode voltage. These results were typical of the across wire modulation encountered with the 90/10 GD. The drift voltage was  $+50$  V for all measurements. Figure 6.4.9 shows the across wire modulation, output position versus real position for an anode voltage of  $+3550$  V, as a function of cathode amplifier time constant.

As can be seen in Table 6.4.4 and Figure 6.4.9, at all counter voltages (gains) measured,  $0.4 \mu\text{sec}$  exhibits the worse modulation. For voltages  $+3400$  to  $+3550$   $1.6 \mu\text{sec}$  gives the least modulation. However at low gains  $0.8 \mu\text{sec}$  was found to have a much better linearity. Note: Both rms and m.a.d. values indicate to some degree the linearity. However the general trends are not always followed by both. The m.a.d. values were found to closely follow the visual impression given by examination of the linearity graphs.

No improvement in linearity was found for a shaping time constant of  $3.2 \mu\text{sec}$  which was only measured in detail at an anode voltage of  $+3550$  V, where the rms value was  $.092 \pm .003$  mm and m.a.d.  $.146 \pm .005$  mm. As can be seen from the table some dependence on anode voltage exists for the modulation. However this is a weak function.

TABLE 6.4.4

## ACROSS WIRE MODULATION LOCAL LINEARITY SCAN

90/10 GD, RMS, M.A.D. VALUES FROM A STRAIGHT LINE

Cathode Amplifier Time Constant	Anode Voltage			
	<u>+3300 V</u>	<u>+3400 V</u>	<u>+3450 V</u>	<u>+3550 V</u>
0.4 $\mu$ sec	rms = $.095 \pm .005$ mm m.a.d. = $.173 \pm .010$	$.068 \pm .004$ mm $.174 \pm .010$	$.058 \pm .003$ mm $.147 \pm .007$	$.119 \pm .007$ mm $.173 \pm .011$
0.8 $\mu$ sec	rms = $.056 \pm .002$ mm m.a.d. = $.123 \pm .005$	$.087 \pm .005$ mm $.156 \pm .008$	$.062 \pm .002$ mm $.119 \pm .005$	$.058 \pm .003$ mm $.138 \pm .006$
1.6 $\mu$ sec	rms = $.073 \pm .005$ mm m.a.d. = $.147 \pm .007$	$.084 \pm .004$ mm $.114 \pm .005$	$.054 \pm .002$ mm $.086 \pm .003$	$.058 \pm .002$ mm $.072 \pm .002$

TABLE 6.4.5.

## ACROSS WIRE MODULATION LOCAL LINEARITY SCAN

75/25 GD, RMS, M.A.D. VALUES FROM A STRAIGHT LINE

Cathode Amplifier Time Constant	Anode Voltage		
	<u>+3650 V</u>	<u>+3850 V</u>	<u>+3950 V</u>
0.4 $\mu$ sec	rms = $.087 \pm .004$ mm m.a.d. = $.205 \pm .010$	$.094 \pm .004$ mm $.195 \pm .009$	$.106 \pm .004$ mm $.169 \pm .007$
0.8 $\mu$ sec	rms = $.090 \pm .004$ mm m.a.d. = $.175 \pm .007$	$.076 \pm .003$ mm $.186 \pm .008$	$.076 \pm .003$ mm $.169 \pm .007$
1.6 $\mu$ sec	rms = $.073 \pm .003$ mm m.a.d. = $.149 \pm .005$	$.073 \pm .003$ mm $.161 \pm .006$	$.073 \pm .003$ mm $.165 \pm .006$
3.2 $\mu$ sec	rms = $.054 \pm .001$ mm m.a.d. = $.106 \pm .005$	$.059 \pm .002$ mm $.116 \pm .003$	$.063 \pm .002$ mm $.122 \pm .004$
6.4 $\mu$ sec	rms = $.046 \pm .001$ mm m.a.d. = $.097 \pm .002$	$.067 \pm .002$ mm $.095 \pm .002$	$.064 \pm .002$ mm $.095 \pm .002$

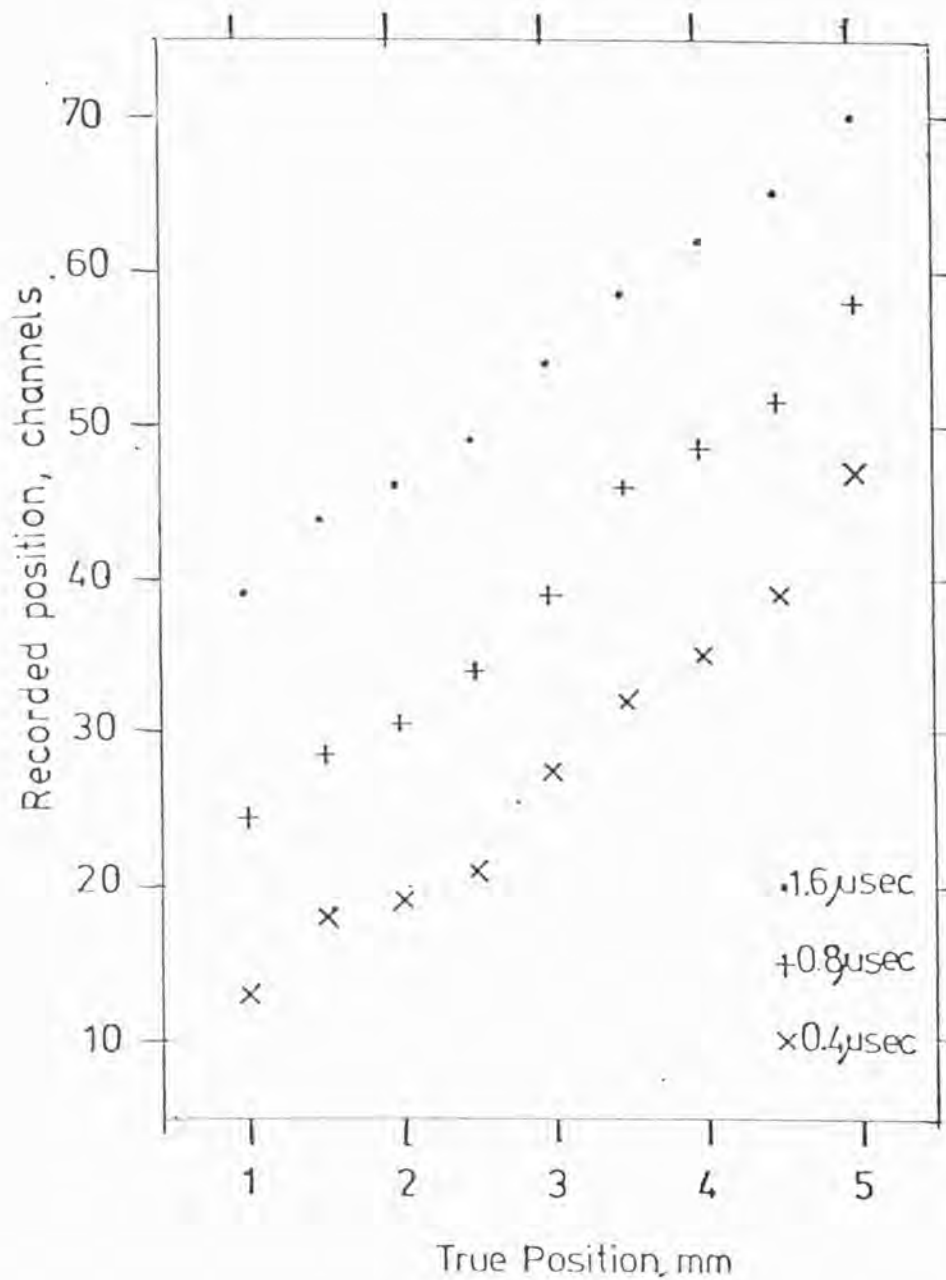


Figure 6.4.9. Across wire linearity scan; output position versus real position, as a function of cathode time constant, 90/10, graded density cathode. Results are displaced vertically to show difference in across wire modulation for each time constant. Anode voltage +3550 V, drift +50 V, Fe<sup>55</sup> source.



#### 6.4.2.2. 75/25 Across Wire Modulation

Table 6.4.5 gives the rms and m.a.d. values from a straight line fit to the data, for 75/25 obtained by scanning the electrical co-ordinates .48 to .53 , a typical area of the counter, as a function of time constant and anode voltage. The drift voltage was  $+50$  V for all measurements. Figure 6.4.10 shows the modulation as a function of time constant for the anode voltage  $+3950$  V .

As can be seen from the table a gradual improvement in linearity occurs as the time constant is increased from  $0.4$   $\mu$ sec to  $6.4$   $\mu$ sec at all gains. There is also some dependence on amount as a function of counter gain (for a given time constant).

#### 6.4.2.3. 50/50 Across Wire Modulation

Table 6.4.6 gives the rms and m.a.d. values from a straight line fit to the data obtained for 50/50 (identical co-ordinates as 75/25) as a function of anode voltage and cathode time constant for the local linearity scans. Figure 6.4.11 shows the modulation as a function of time constant for an anode voltage of  $+4300$  V . Again like 75/25 there is a gradual improvement in across wire linearity as the cathode time constant is increased from  $0.4$  to  $6.4$   $\mu$ sec. Again a weak dependence on counter gain was found.

#### 6.4.2.4. Across Wire Modulation: Variation with Drift

All three gas mixtures showed a small variation in across wire modulation as a function of drift voltage. The anode voltage was always altered to maintain the same charge level measured with an anode amplifier time constant of  $1.6$   $\mu$ sec. A gradual improvement, visually, and in rms and m.a.d. occurring as the voltage was decreased from  $+200$  to  $-50$  V .

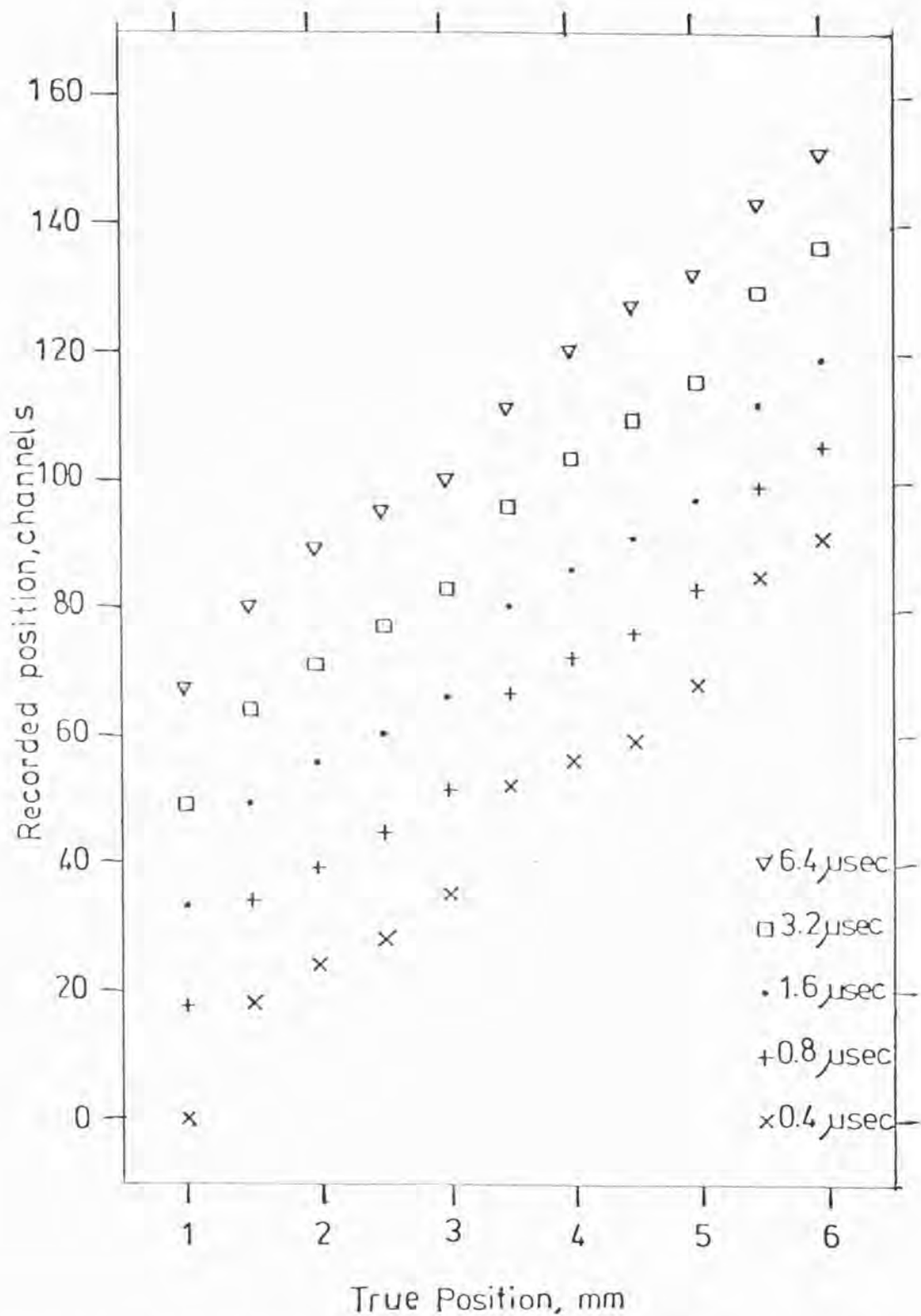


Figure 6.4.10. Across wire linearity scan; output position versus real position, as a function of cathode time constant, 75/25, graded density cathode. Anode voltage +3950 V, drift voltage +50 V,  $\text{Fe}^{55}$  source.

TABLE 6.4.6

ACROSS WIRE MODULATION LOCAL LINEARITY SCAN

50/50 GD, RMS, M.A.D. VALUES FROM A STRAIGHT LINE

<u>Cathode Amplifier Time Constant</u>		<u>Anode Voltage</u>		
		<u>+4000 V</u>	<u>+4200 V</u>	<u>+4300 V</u>
0.4 $\mu$ sec	rms	= .143 $\pm$ .007 mm	.133 $\pm$ .006 mm	.124 $\pm$ .005 mm
	m.a.d.	.173 $\pm$ .008	.162 $\pm$ .007	.171 $\pm$ .008
0.8 $\mu$ sec	rms	= .117 $\pm$ .004 mm	.086 $\pm$ .004 mm	.079 $\pm$ .004 mm
	m.a.d.	= .129 $\pm$ .005	.191 $\pm$ .008	.211 $\pm$ .010
1.6 $\mu$ sec	rms	= .074 $\pm$ .003 mm	.075 $\pm$ .003 mm	.077 $\pm$ .003 mm
	m.a.d.	= .151 $\pm$ .005	.171 $\pm$ .007	.171 $\pm$ .007
3.2 $\mu$ sec	rms	= .064 $\pm$ .002 mm	.069 $\pm$ .002 mm	.066 $\pm$ .002 mm
	m.a.d.	= .139 $\pm$ .004	.122 $\pm$ .004	.122 $\pm$ .004
6.4 $\mu$ sec	rms	= .048 $\pm$ .001 mm	.072 $\pm$ .002 mm	.065 $\pm$ .002 mm
	m.a.d.	= .081 $\pm$ .002	.107 $\pm$ .003	.106 $\pm$ .003

TABLE 6.4.7

LOCAL LINEARITY RMS AND M.A.D. VALUES

AS A FUNCTION OF DRIFT VOLTAGE 75/25, TIME CONSTANT 1.6  $\mu$ sec

<u>Drift Voltage</u>		
+200 V	rms	= .081 $\pm$ .003 mm
	m.a.d.	= .183 $\pm$ .008
+50 V	rms	= .107 $\pm$ .003 mm
	m.a.d.	= .175 $\pm$ .007
-50 V	rms	= .066 $\pm$ .002 mm
	m.a.d.	= .163 $\pm$ .006

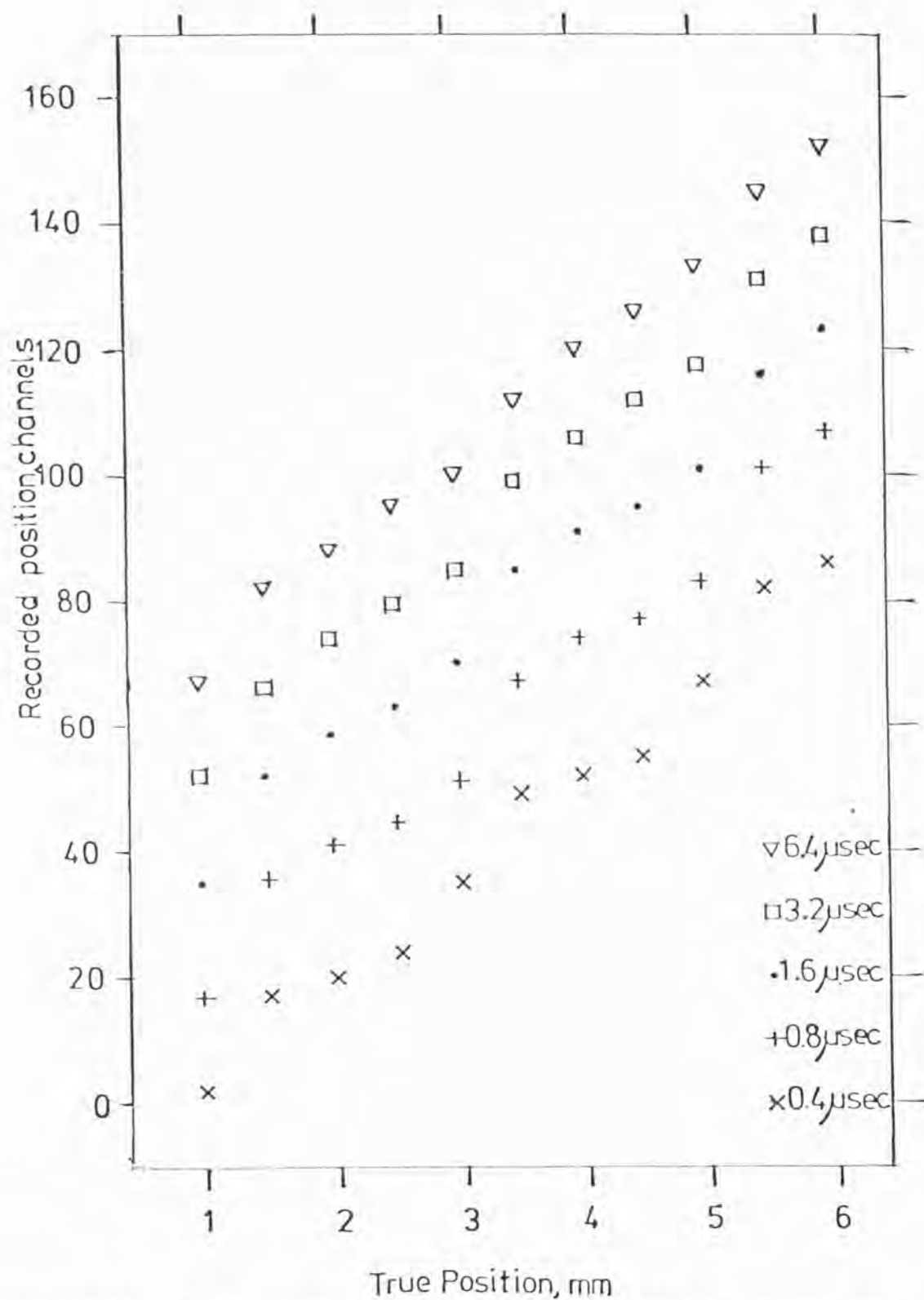


Figure 6.4.11. Across wire linearity scan; output position versus real position, as a function of cathode time constant, 50/50, graded density cathode. Anode voltage +4300 V, drift +50 V,  $\text{Fe}^{55}$  source,

Table 6.4.7 gives the rms and m.a.d. values for 75/25 as a function of drift voltage. The equivalent anode voltage was  $+3900$  V for  $+50$  V drift field. The cathode time constant used was  $1.6$   $\mu$ sec for all measurements presented in the table.

#### 6.4.2.5. Anode Gain Modulation

Like the RC counter the output position modulation was accompanied by an anode gain modulation at  $2$  mm pitch. The % peak-to-peak modulation for a given gain was found to be approximately the same for each gas mix within the measurement errors; for example  $\sim 17\%$  at a charge level of  $\sim .30$  pC. In addition all mixes show an increase in modulation as a function of gain.

For the 50/50 gas mix the gain modulation as a function of anode time constant and gain was investigated. Figure 6.4.12 shows the measured anode charge, as a function of position for a small local scan, and as a function of anode amplifier time constant, for an anode voltage of  $+4200$  V,  $+50$  V drift. A distinct difference is apparent between  $0.4$  and  $6.4$   $\mu$ sec. The  $0.4$   $\mu$ sec scan shows only a single rise per  $2$  mm of scan length. However  $3.2$  and  $6.4$   $\mu$ sec show a second rise in gain, beyond the experimental error. This effect was apparent at all gains, the % rise for the second increase scaling with the modulation.

The 90/10 anode gain modulation results will be presented to give an idea of the percentage modulation. At an anode voltage of  $+3300$  V the % peak-to-peak modulation over a  $5$  mm local linearity scan area (as per modulation graph) was  $12\%$ , the equivalent charge level being  $.18$  pC for an anode time constant of  $1.6$   $\mu$ sec; at  $+3400$  V,  $.38$  pC,  $17\%$ ; and at  $+3550$  V,  $.57$  pC,  $22\%$ . A  $200$   $\mu$ m slit was used for all these measurements.

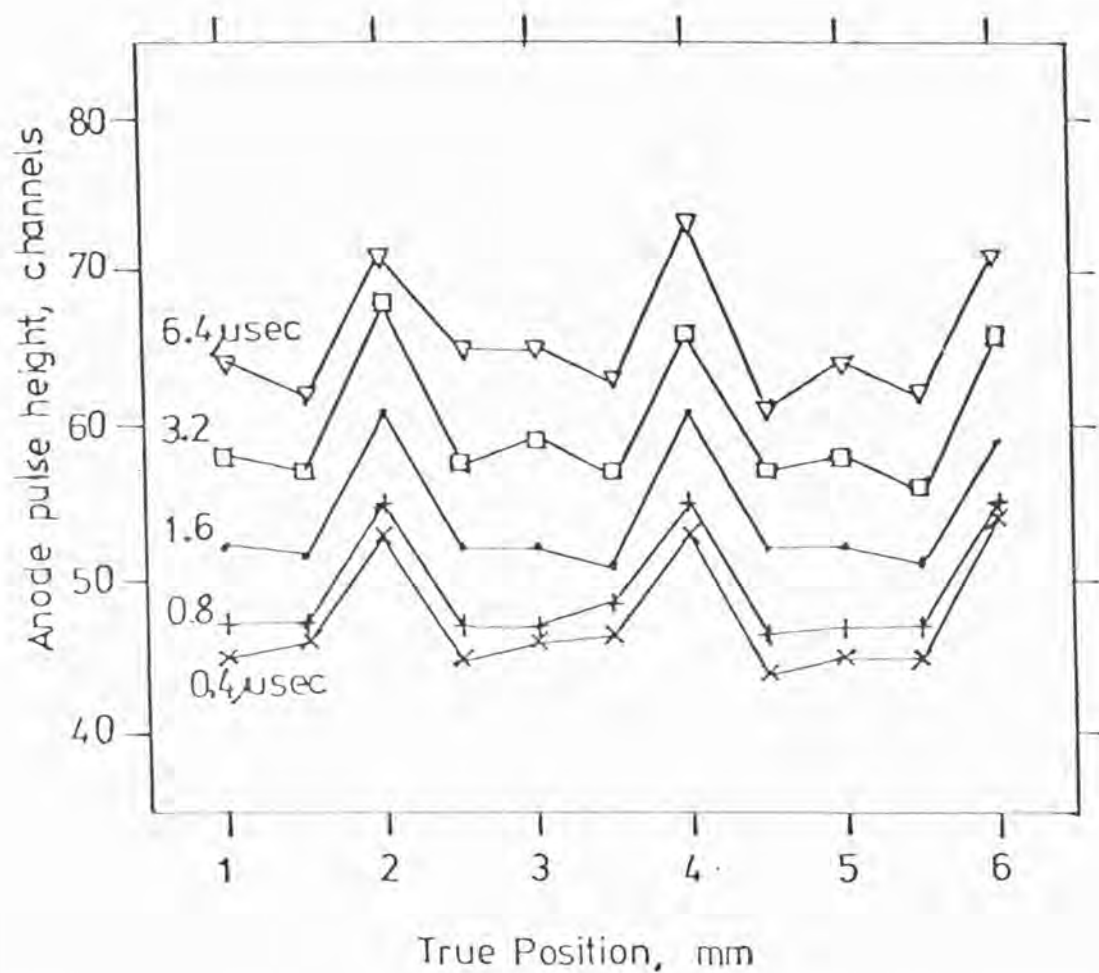


Figure 6.4.12. Measured anode charge (in PHA channels), as a function of amplifier time constant and position across anode (small local scan), for 50/50, graded density cathode. Anode voltage +4200 V, drift +50 V,  $\text{Fe}^{55}$  source.  $0.5 \text{ pC} \equiv 69 \text{ PHA channels}$ .



#### 6.4.2.6. Location of the Anode Wires

In the graded density counters, the high gain points for all gas mixes occur at a steep part of the position output versus real position scans. On the binning argument this steep section should occur between the wires. The work of Mathieson and others predict highest gain over the wires. However Gilvin et al., 1979, have experimentally investigated anode gain modulation Argon/Methane gas mixtures. At low charge levels  $< 0.5$  pC high gain positions coincided with the wire positions as expected. High gain results over the wire due to angular localisation and non-uniform field distribution around the wire. However at around  $0.5$  pC high gain points were found to also occur between the wires, and at very high gains  $> 1.6$  pC only high gains between the wires were observed. The simplest explanation of this behaviour is that around midway between the wires, the primary electron cloud drifting towards the anode, divides between the wires, and under non-proportional conditions ( $\geq 1$  pC) the gain at each wire is greater than the gain for the charge on a single wire. This data however was obtained using a very long shaping constant  $10 \mu\text{sec}$ , whereas a large modulation is evident at all time constants for our counters. In the Argon/Methane results the modulation was only  $\sim 1.9\%$  under  $10 \mu\text{sec}$  with 90/10 gas mix and  $\sim 4.4\%$  for 100% methane. These figures reflect the different amounts of angular localisation and lateral diffusion for the gases.

The data obtained from the Xenon/Methane counters present distinct problems, in that the modulation is extremely large in comparison, occurs at all time constants, and the characteristic shape was found not to change over the range  $\sim .08$  to  $.8$  pC. Operation at high gains was not possible due to counter breakdown problems.

An experimental method was used to determine the wire positions with respect to the gain modulation. As mentioned in Chapter 5 the

detector has a series of alignment marks on its base plate and outside for the alignment of the X-Y table with the detector. During assembly of the 75/25 (50/50) detector an anode wire was placed (1 mm) either side of the centre alignment line, hence the following procedure was adopted to experimentally determine which gain position corresponds to a wire.

A high gain point was determined by measurements with X-rays, and the X-Y table clamped firmly in this position then removed. A small piece of X-ray film in a black plastic envelope was then taped into position on top of the counter window support. The film was marked along each alignment line using a needle and steel ruler. The X-Y table was then replaced, and realigned with alignment marks. The total error in removal and replacement was found in previous tests, by repeatability of output position for X-ray measurements, to be smaller than  $\sim 60 \mu\text{m}$ .

The film was then exposed with a  $\text{Cd}^{109}$  source through the helium collimator tube.  $\text{Cd}^{109}$  was used to give a large charge dump in the emulsion. After initial trials a 15 hour exposure produced a resulting negative with sufficient exposure for the slit position to be measured. The film (Ilford Red Seal 25FW) was developed in Kodak Universal Developer (1+7) for 4 minutes and fixed in Amfix (1+4) for 4 minutes and washed for 20 minutes. The negative was measured using a travelling microscope. The distance of the centre of the slit to the counter datum line was found to be  $1.96 \pm .04 \text{ mm}$  (standard error). As the detector was constructed with a wire either side of the centre line, the wire positions occur at an odd number of millimetres away from the line, in between wires at an even number. Hence the high gain position was found to correspond to between the wires, as expected by the binning argument.

Before possible explanations of the across wire modulation behaviour are presented, a comparison of modulation and position resolution across the anode, between the gas mixtures will be made.

#### 6.4.2.7. Across Wire Modulation: Comparison Between Gas Mixtures

Table 6.4.9 gives the mean rms and m.a.d. values for the three gas mixtures investigated as a function of time constant averaged over gain. These results are taken from the local linearity scans presented above. The values were averaged over gain due to the weak dependence of the modulation on gain.

Note: These results are typical of the counter for all three mixes, other spot areas were checked for modulation and comparable values and identical changes with time constant (and gain) were found.

The three mixtures each have different characteristics. However all show an improvement in local across wire linearity as the shaping time constant is increased. However numerically and visually, for a given time constant (0.4 to 3.2  $\mu\text{sec}$ ) as the percentage of methane quench gas increases the modulation gets worse. For 90/10 a scan at 3.2  $\mu\text{sec}$  showed the modulation to get worse. However 75/25 and 50/50 show a slow improvement up to 6.4  $\mu\text{sec}$  where the across wire modulation is comparable.

Figure 6.4.13 superimposes across wire linearity scans for 0.4 and 1.6  $\mu\text{sec}$  for the three gas mixtures obtained at approximately equal anode gain,  $\sim .38 \text{ pC}$ , to illustrate the effect of additional quench gas. The respective anode voltages were  $+3400 \text{ V}$  90/10,  $+3850 \text{ V}$  75/25, and  $+4200 \text{ V}$  50/50. Drift volts were  $+50 \text{ V}$  for all.

Figure 6.4.14 shows the differential non-linearity derived from the output positions for the two time constants illustrated in Figure 6.4.13. As can be seen the non-linearity increases with increasing quench. Figure 6.4.15 shows the differential non-linearity for 75/25 for an anode voltage of  $+3850 \text{ V}$  showing the gradual improvement with cathode time constant.

TABLE 6.4.9

COMPARISON OF ACROSS WIRE MODULATION: RMS AND M.A.D. VALUES AVERAGED OVER GAIN AS A FUNCTION OF TIME CONSTANT AND GAS MIX FOR LOCAL LINEARITY SCANS

Cathode Amplifier Time Constant	Gas Mix		
	90/10	75/25	50/50
0.4 $\mu$ sec	rms = $.074 \pm .006$ mm m.a.d.= $.165 \pm .015$	$.096 \pm .008$ mm $.190 \pm .015$	$.133 \pm .011$ mm $.169 \pm .014$
0.8 $\mu$ sec	rms = $.068 \pm .004$ m.a.d.= $.133 \pm .007$	$.081 \pm .006$ $.177 \pm .014$	$.094 \pm .006$ $.177 \pm .010$
1.6 $\mu$ sec	rms = $.070 \pm .004$ m.a.d.= $.116 \pm .007$	$.073 \pm .005$ $.158 \pm .011$	$.075 \pm .005$ $.164 \pm .012$
3.2 $\mu$ sec	rms = $.092 \pm .003^*$ m.a.d.= $.146 \pm .005$	$.059 \pm .003$ $.115 \pm .006$	$.066 \pm .003$ $.128 \pm .006$
6.4 $\mu$ sec	rms = m.a.d.=	$.059 \pm .002$ $.096 \pm .003$	$.062 \pm .007$ $.098 \pm .004$

\* Single scan value

All errors, standard errors, random error of measurement from PHA not included.

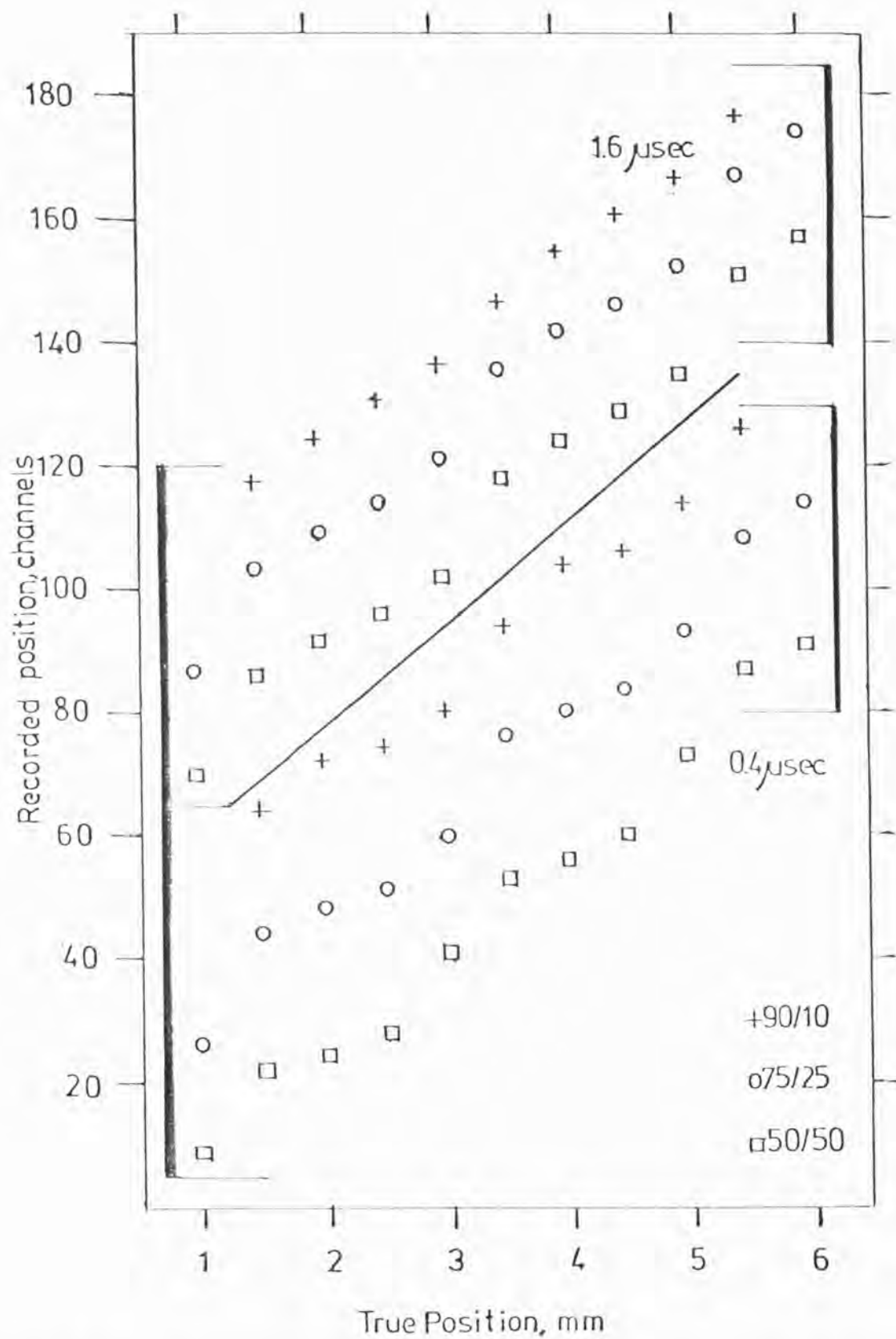


Figure 6.4.13. Comparison of across-anode-wire modulation. Output position versus real position for each gas mix, for two cathode time constants 0.4 and 1.6  $\mu\text{sec}$ . Note increasing modulation with increasing quench percentage. All measurements obtained at approximately equal anode gain ( $\sim .38$  pC).

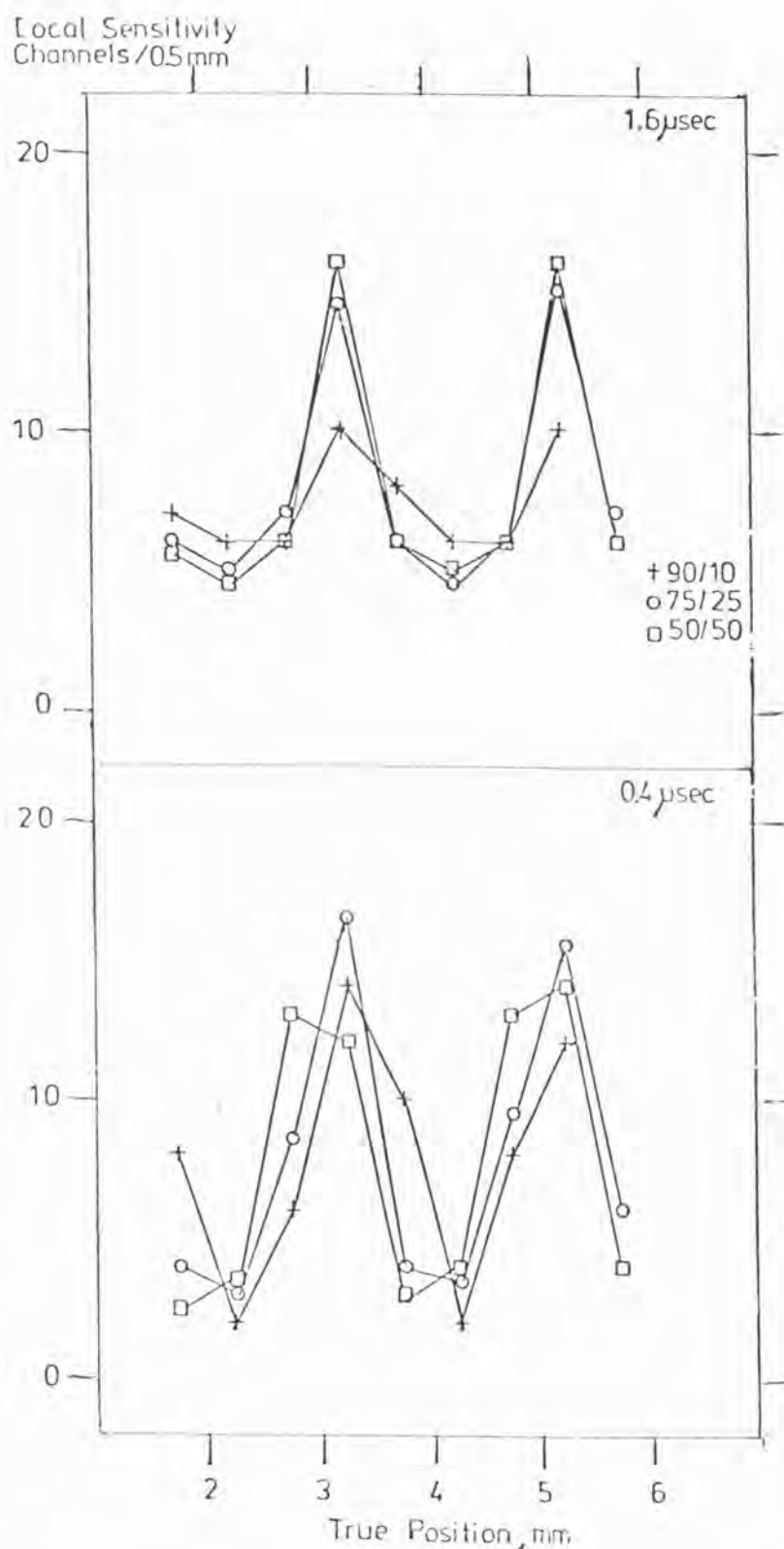


Figure 6.4.14. Differential non-linearity derived from Figure 6.4.13. That is local sensitivity (channels/0.5 mm) as a function of real position (calculated by slope between adjacent points, and plotted at mid-point in real position). Note: how modulation for all gas mixes has 2 mm pitch and is comparable at 0.4  $\mu$ sec. At 1.6  $\mu$ sec modulation is very much less for 90/10.



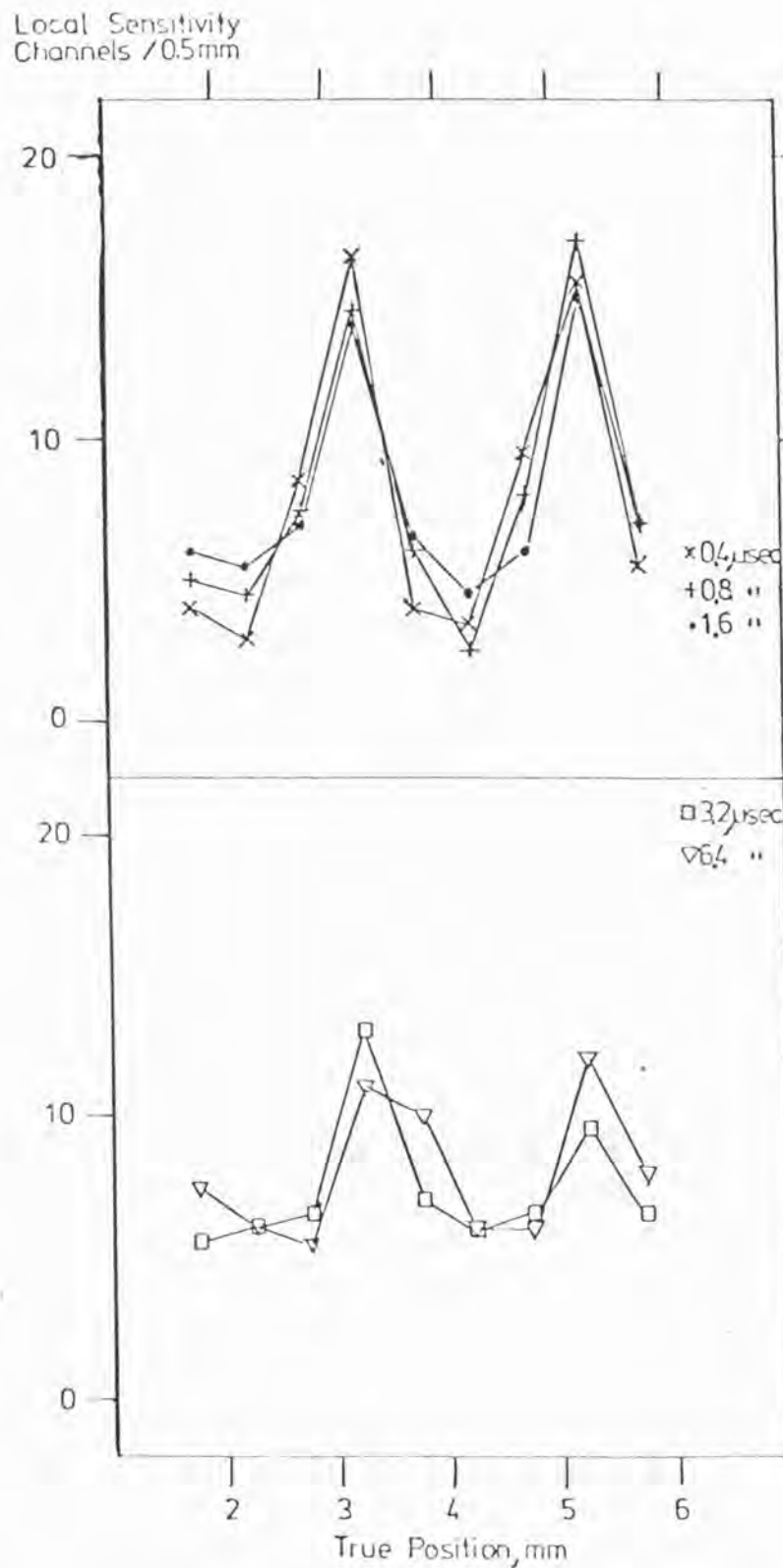


Figure 6.4.15. Differential non-linearity (as calculated per Figure 6.4.14); for 75/25 as a function of cathode amplifier time constant. Identical scan co-ordinates as Figure 6.4.10, anode voltage +3850 V, drift +50 V,  $\text{Fe}^{55}$  source. Note 'steady' decrease in modulation as time constant increases.

#### 6.4.2.8. Position Resolution Across the Anode: Graded Density

Because of the across wire modulation the actual position resolution of the counter is a function of interwire position. The resolution is dependent on the local sensitivity, in some places the resolution will be sub-millimeter; high sensitivity; in others, of the order of a millimeter or more; low sensitivity. Hence for a given time constant, say  $0.4 \mu\text{sec}$  on low sensitivity regions over a wire, the capability of 50/50 is much worse than 90/10 due to its higher modulation.

It was found that for all gas mixtures the high and low gain points had different resolutions and different characteristic shapes for the resolution versus gain graph. However all such graphs showed the characteristic flattening off and degradation of position resolution at high gain.

The across wire resolution measurements will be presented in two forms; first, the resolution in terms of measured (FWHM) in PHA channels; second, the resolution calculated using approximate high and low gain sensitivities, calculated by the local slope between the two points either side of the required spot. The modulation function in reality is continuous not discrete as in the measurements. Hand drawn curves through the data points show that the sensitivity values obtained by the above approximation are very close to the true values. The measured modulation is of course not the true modulation due to the smoothing effect of the finite slit width but a convolution of true across wire modulation and the slit intensity distribution.

Figures 6.4.16, 6.4.17, 6.4.18, show the position resolution as a function of gain and time constant for each gas mix, for both high and low gain positions across the wire. The local sensitivity scales are marked for each time constant and gas mixture enabling the actual position resolution to be derived. A maximum random error of  $\pm 1.0$  channels exists for all local slopes. As can be seen the characteristic shape varies

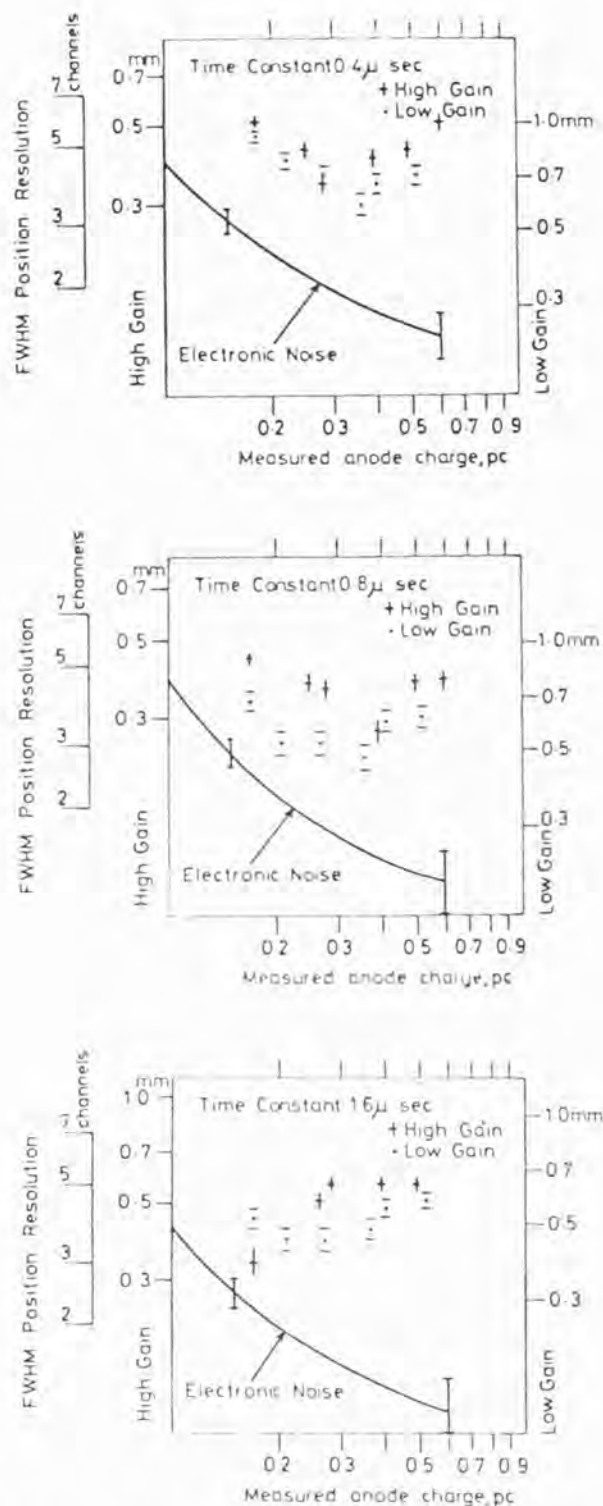


Figure 6.4.16. Across wire position resolution (FWHM) as a function of measured anode charge (amplifier time constant 1.6  $\mu$ sec), and cathode amplifier time constant, for both a high and a low gain point across the wires. 90/10, graded density cathode,  $\text{Fe}^{55}$  source.

Position resolution in channels, and also using approximate local sensitivities (gain averaged) for each position is shown, along with electronic noise (best hand drawn curve through data) and random errors in determining data.

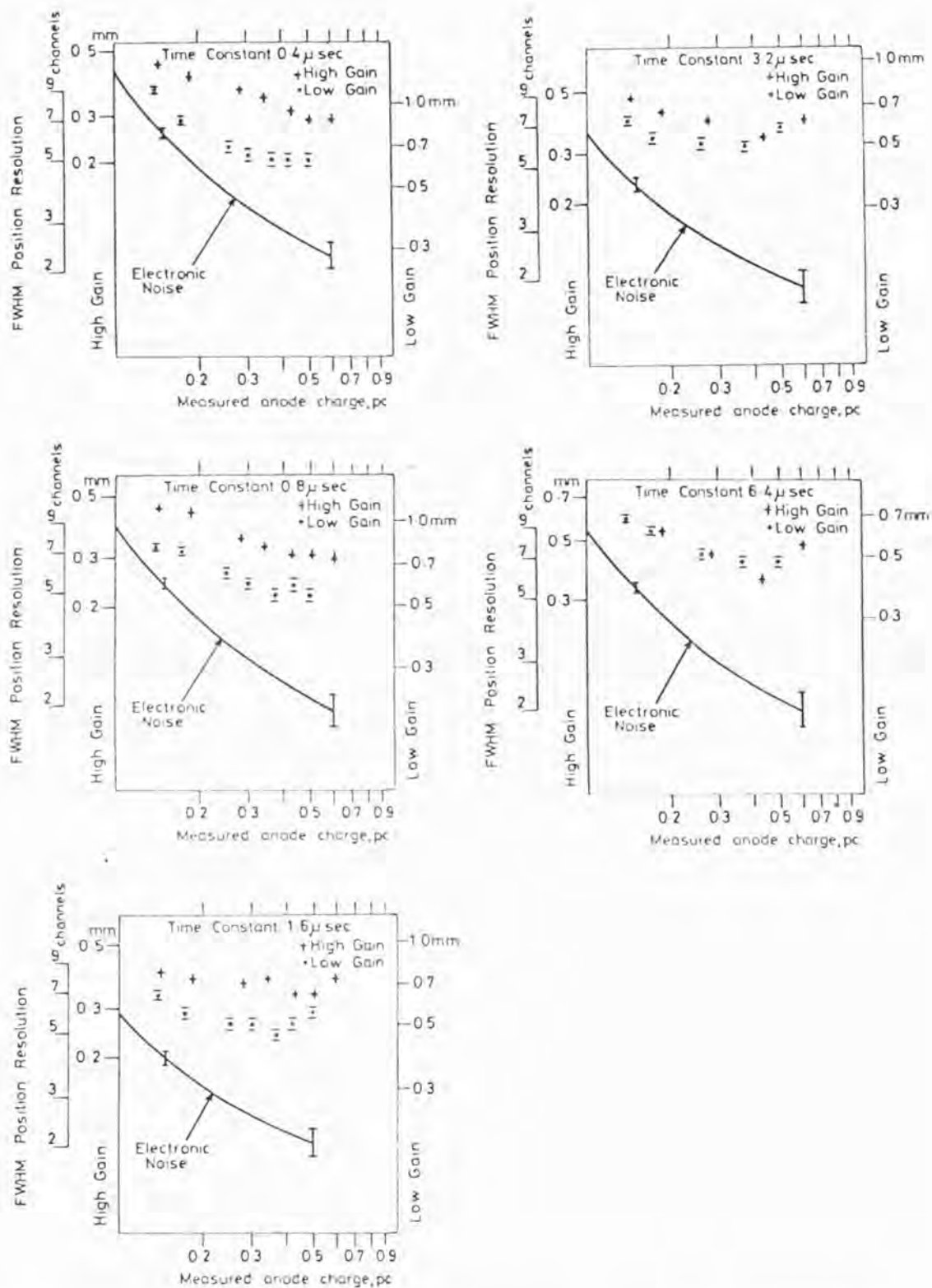


Figure 6.4.17. Across wire position resolution (FWHM) as a function of measured anode charge (amplifier time constant 1.6  $\mu\text{sec}$ ), and cathode amplifier time constant for both a high and low gain point across the wires. 75/25, graded density cathode,  $\text{Fe}^{55}$  source.

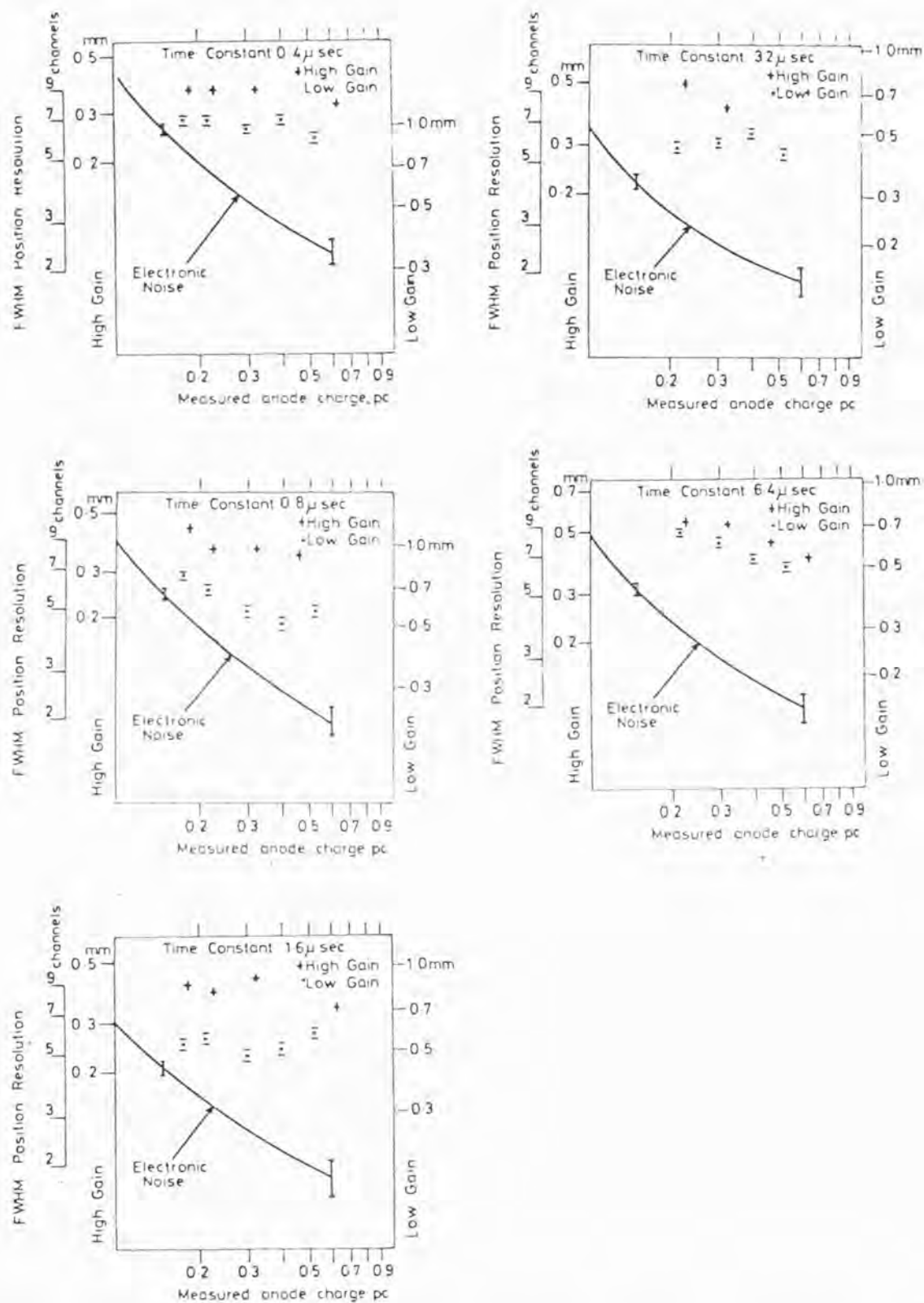


Figure 6.4.18. Across wire position resolution (FWHM) as a function of measured anode charge (amplifier time constant 1.6  $\mu\text{sec}$ ), and cathode amplifier time constant for both a high and a low gain point across the wires. 50/50 graded density cathode,  $\text{Fe}^{55}$  source.

considerably, depending on time constant, gas mixture, and gain position.

As expected from the modulation data, the real position resolution at the low gain point (low sensitivity region) gradually improves and approaches the resolution of the high gain point, as the time constant increases, and across wire linearity improves. It is interesting to note that for most time constants, gas mixes, and both positions the resolution is  $\leq .5$  mm, better than the shadow camera requirements.

The decrease in modulation is best illustrated by Table 6.4.10 which gives the average local sensitivities obtained from the local linearity scans presented above. The sensitivities are derived by averaging the approximate slopes for two low gain, and two high gain points. As can be seen a considerable change in slope occurs as the time constant increases.

Table 6.4.11 lists the best measured resolutions across the wires for each time constant and gas mix along with anode voltage. Drift voltage was  $\sim 50$  V for all measurements. Note: the optimum operating condition for the low gain point is not always identical to that of the high gain point, hence some compromise must be made in choosing a best counter operating condition. In addition the best counter operating condition for resolution along the anode may also be different from either of the above.

#### 6.4.2.9. Effect of Across Wire Modulation

The effect of the across wire modulation on a real image is a 'bunching' together of photon recorded positions resulting in a series of density stripes at each wire position for an initial uniform distribution, and hence a distorted image across the anode.

This effect is best illustrated by Figures 6.4.19 and 6.4.20. Figure 6.4.19 shows the resultant two dimensional image of four slits 1 mm apart aligned along the anode. Figure 6.4.20 shows the count distribution



TABLE 6.4.10  
LOCAL AVERAGE SENSITIVITIES  
VERSUS TIME CONSTANT VERSUS GAS MIX

<u>Gas Mix</u>	<u>Cathode Amplifier Time Constant</u>	<u>High Gain Position Sensitivity Channels per mm</u>	<u>Low Gain Position Sensitivity Channels per mm</u>
90/10	0.4 $\mu$ sec	11.63	6
	0.8	11.75	5.75
	1.6	8.88	7.75
75/25*	0.4 $\mu$ sec	24.5	8
	0.8	22.67	9.167
	1.6	20.83	10.83
	3.2	19.0	12.167
	6.4	16.83	14.5
50/50*	0.4 $\mu$ sec	25	6.67
	0.8	23.33	8.67
	1.6	22	10.33
	3.2	19.67	12.83
	6.4	17.67	13.0

\* Note: higher P.H.A. gain used.

TABLE 6.4.11

BEST RESOLUTION ACROSS ANODE USING LOCAL SENSITIVITIES

AS A FUNCTION OF TIME CONSTANT AND GAS MIX

90/10

<u>Cathode Time Constant</u>	<u>High Gain Position Resolution (FWHM)</u>	<u>Anode Voltage</u>	<u>Low Gain Position Resolution (FWHM)</u>	<u>Anode Voltage</u>
0.4 $\mu$ sec	.363 $\pm$ .023 mm	<sup>+</sup> 3450 V	.636 $\pm$ .045 mm	<sup>+</sup> 3400 V
0.8	.271 $\pm$ .042	<sup>+</sup> 3450 V	.500 $\pm$ .045	<sup>+</sup> 3450 V
1.6	.333 $\pm$ .028	<sup>+</sup> 3300 V	.500 $\pm$ .036	<sup>+</sup> 3400 V

75/25

0.4 $\mu$ sec	.318 $\pm$ .010 mm	<sup>+</sup> 3950 V	.714 $\pm$ .035 mm	<sup>+</sup> 3850 V
0.8	.307 $\pm$ .011	<sup>+</sup> 3950 V	.433 $\pm$ .025	<sup>+</sup> 3850 V
1.6	.333 $\pm$ .019	<sup>+</sup> 3850 V	.454 $\pm$ .023	<sup>+</sup> 3850 V
3.2	.342 $\pm$ .013	<sup>+</sup> 3850 V	.500 $\pm$ .021	<sup>+</sup> 3850 V
6.4	.314 $\pm$ .014	<sup>+</sup> 3750 V	.444 $\pm$ .019	<sup>+</sup> 3850 V

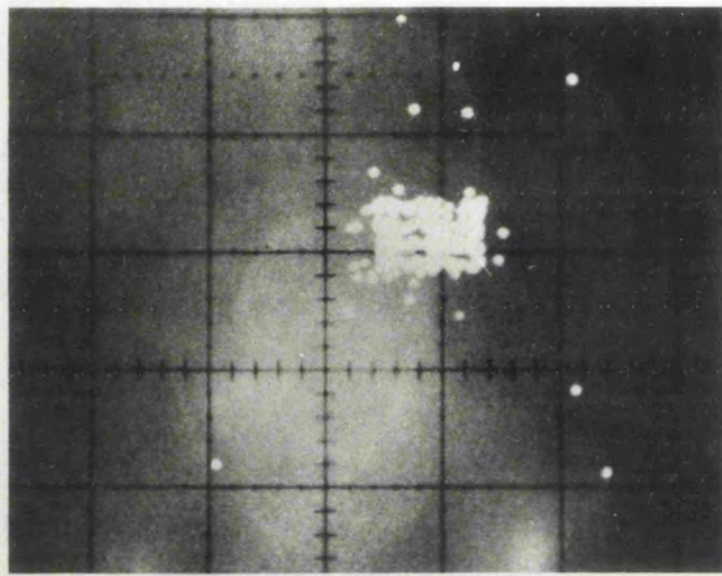
50/50

0.4 $\mu$ sec	.320 $\pm$ .010 mm	<sup>+</sup> 4300 V	1.0 $\pm$ 0.42 mm	<sup>+</sup> 4300 V
0.8	.333 $\pm$ .010	<sup>+</sup> 4200 V	.500 $\pm$ .028	<sup>+</sup> 4200 V
1.6	.341 $\pm$ .011	<sup>+</sup> 4300 V	.500 $\pm$ .025	<sup>+</sup> 4100 V
3.2	.412 $\pm$ .015	<sup>+</sup> 4300 V	.500 $\pm$ .019	<sup>+</sup> 4300 V

Errors quoted are random error in measurement of FWHM, do not include random error on local sensitivities.

Figure 6.4.19. (Top) Two-dimensional image of four slits aligned across the anode wires. Note some binning (across page) is evident. 50/50, graded density cathode, cathode time constant 0.8  $\mu$ sec, anode voltage +4200 V, drift +50 V.

Figure 6.4.20. (Bottom) One-dimensional cut through image in Figure 6.4.19 in direction across wires. Note bunching (binning) of recorded photon positions over anode wires.



from the previous figure in the direction across the anode. As can be seen from both figures the binning or bunching over the wire positions is quite marked. These results were taken with the 50/50 mix, a cathode time constant of  $0.8 \mu\text{sec}$ , anode time constant of  $6.4 \mu\text{sec}$ , an anode voltage of  $+4200 \text{ V}$ , drift voltage  $+50 \text{ V}$ . Note although binning is clearly evident some interpolation between wires does exist as counts are present above background between the wire positions in Figure 6.4.20.

#### 6.4.3. Explanation of Across Wire Modulation: Graded Density

The modulation is due to incomplete interpolation across the wires, binning occurring to some extent. The observed binning is obviously not complete under even the most extreme modulation conditions, some form of interpolation exists. The problem is to explain the improvement in across wire linearity as the cathode amplifier time constant is increased.

Theoretically according to Mathieson 1981 (private communication) angular localisation can provide some interpolation at long time constants providing the positive ions have moved a substantial distance away from the anode wires. However in Xenon the positive ion mobility is probably so low that the positive ions will not have moved sufficiently even under the time constant  $6.4 \mu\text{sec}$  for this effect to be apparent.

A possible solution lies in the slow drift velocities of Xenon gas mixtures. Consider Figure 6.4.21 which shows schematically the field distribution within the counter. The two positions to consider are A and B ; A represents an initial electron cloud incident midway between two anode wires and B a cloud incident partway towards a wire. Consider an exceptionally slow drift velocity. At A the two edges of the electron cloud will take equal time to reach the wires, and hence the outward edges of the cloud of moving positive ions after the avalanche will also take equal time to move away from each wire. With both wires undergoing

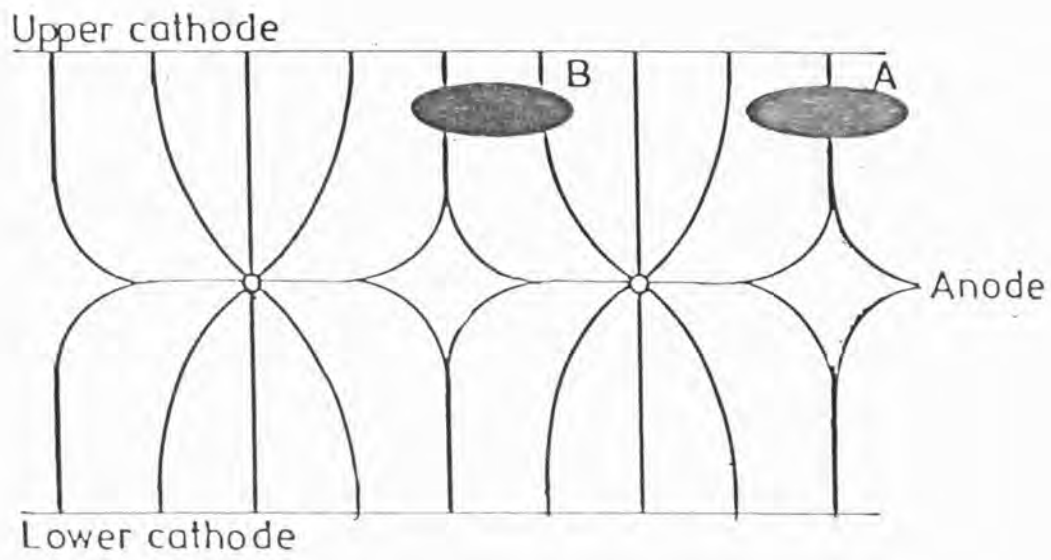


Figure 6.4.21. Schematic of electric field configuration in IPC, with two (schematic) electron clouds at positions A and B.



avalanche simultaneously, across wire interpolation will exist. For position B a time difference will exist between the arrival of one edge of the cloud on one wire, compared to the other edge on the other wire. Hence instead of equal weighting of avalanches occurring on each wire, as at A, the weighting at each anode wire will vary with time. Long shaping time constants will then give greater weighting to the second wire (the wire where part of the cloud arrives last) and hence interpolation will exist and improve. On this argument the longer the time constant the better the across wire linearity is observed. The problem is are the time differences and charge cloud sizes big enough for Xenon/Methane.

In order to calculate times and cloud sizes, the mean drift distance in the gas must be known. This can be derived from the mean absorption depth of photons in the gas. This can be calculated from a knowledge of counter parameters and  $1/e$  absorption depth of the gas (as defined in section 4.4, Chapter 4). Consider Figure 6.4.22; let the incident X-ray flux be  $I_0$ , the overall depth of the counter  $d_m$ . The anode frame is at a depth  $d$  in the counter. The intensity of X-rays at depth  $z$  for linear attenuation coefficient  $\mu_\ell$  is

$$I = I_0 e^{-\mu_\ell z}$$

The number absorbed between  $z$  and  $z + dz$  is given by

$$dI = -\mu_\ell I_0 e^{-\mu_\ell z} dz$$

the negative sign indicating  $I$  decreases as  $z$  increases.

In a counter electrons can drift towards the anode from either  $z = 0$  or  $z = d_m$  directions slightly complicating the situation.

The mean absorption depth ( $\bar{z}_A$ ) is given by

$$\bar{z}_A = \frac{\int_0^{d_m} \mu_\ell I_0 e^{-\mu_\ell z} z dz}{\int_0^{d_m} \mu_\ell I_0 e^{-\mu_\ell z} dz}$$

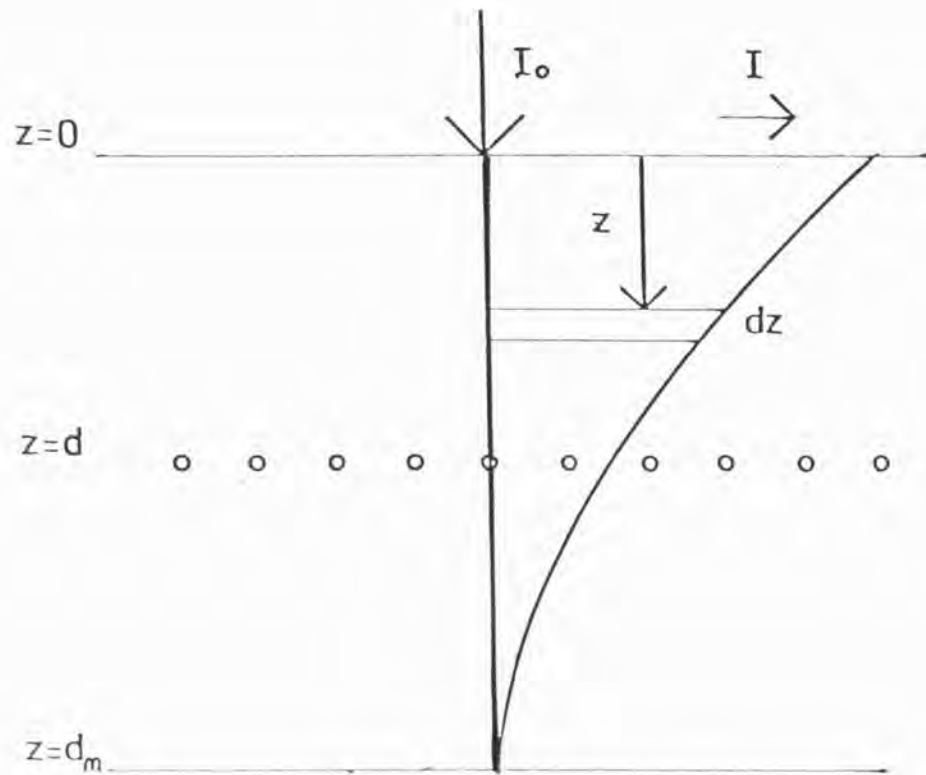


Figure 6.4.22. Schematic of counter showing variation of incident flux ( $I_0$ ) with depth  $z$  in counter. Anode plane is at depth  $z = d$  in counter.

and the mean drift distance  $(\bar{z}_D)$  is

$$\bar{z}_D = \frac{\int_0^d \mu_\ell I_0 e^{-\mu_\ell z} (d-z) dz + \int_d^m \mu_\ell I_0 e^{-\mu_\ell z} (z-d) dz}{\int_0^m \mu_\ell I_0 e^{-\mu_\ell z} dz}$$

Integration gives

$$\bar{z}_D = \frac{\frac{1}{\mu_\ell} [\mu_\ell d - 1 + 2 e^{-\mu_\ell d} - e^{-\mu_\ell d_m} \{\mu_\ell d_m - \mu_\ell d + 1\}]}{[1 - e^{-\mu_\ell d_m}]}$$

$$\bar{z}_A = \frac{\frac{I}{\mu_\ell} - d_m e^{-\mu_\ell d_m} - \frac{e^{-\mu_\ell d_m}}{\mu_\ell}}{[1 - e^{-\mu_\ell d_m}]}$$

The physics of electron diffusion in gases have been covered by many authors, for example Palladino and Sadoulet 1975. Diffusion of the initial electron cloud occurs due to random thermal motion of the electrons in the gas. An initial point source of electrons will undergo diffusion, and form a spherical cloud whose centre will move with the drift velocity parallel to the electric field. The cloud of course is only spherical if lateral and longitudinal (with respect to the electric field) diffusion is the same.

Making this assumption, the width of the cloud can be shown to be a function of time (t) and diffusion coefficient (D) of the gas. The electron density ( $\eta$ ) falls off radially according to the Einstein equation

$$\eta(r,t) = \frac{\eta_0}{(4\pi Dt)^{3/2}} \exp \left\{ -\frac{r^2}{4Dt} \right\}$$

where  $\eta_0$  is the initial number.

The characteristic radius (rms) is

$$\sigma = (2Dt)^{\frac{1}{2}}$$

If  $\bar{z}$  is the mean drift length

$\omega$  is the drift velocity

$$\text{Then } t = \bar{z}/\omega \quad (6.4.1)$$

The mobility  $\mu$  of the gas is defined by  $\mu = \omega/E$  where  $E$  is the electric field (for low fields).

Hence substituting

$$\sigma^2 = 2 \bar{z} (D/\mu) 1/E \quad (6.4.2)$$

$D/\mu$  has been calculated by Mathieson 1981 (private communication) for the gas mixtures investigated as a function of  $E$ .

In order to calculate drift times and cloud sizes a value of  $E$  is required. The counter drift region is 5.5 mm deep and nominally operated with a potential difference across it. However there is some field leakage through the cathode grid from the anode cathode field presenting a problem in finding  $E$  for the drift field. Negative drift voltage operation of the counter enables the value to be measured. It was found under typical operating conditions that no significant decrease in count rate occurred until a drift voltage of -60 V was reached. At -75V a major decrease in count rate (~50%) had occurred, taking this as a good approximation to field leakage then we have ~125 V over 5.5 mm or  $230 \text{ V cm}^{-1}$  and  $E/p \sim .15 \text{ V cm}^{-1} \text{ torr}$ .

In the IPC  $d = 1.05 \text{ cm}$  and  $d_m = 2.1 \text{ cm}$ , Table 6.4.12 gives  $\bar{z}_D$ ,  $\bar{z}_A$  for each gas mix for linear attenuation coefficient values  $\mu_\ell$  for 5.9 keV calculated from McMaster et al., 1969. As the field internal to the cathodes is higher than that in the drift region, and hence smaller  $D/\mu$ , we will calculate drift times and electron cloud sizes for the distance window to upper cathode where we have a measured value for  $E$ , namely we will take

$$\bar{z} = \bar{z}_D - .5 \text{ cm}$$

TABLE 6.4.12

CALCULATION OF MEAN ABSORPTION DISTANCE  $\bar{z}_A$   
AND MEAN DRIFT DISTANCE  $\bar{z}_D$  FOR PROTOTYPE IPC FOR EACH GAS MIX

<u>Gas Mix</u>	<u><math>\mu_\ell</math></u>	<u><math>\bar{z}_D</math></u>	<u><math>\bar{z}_A</math></u>
90/10	7.429 cm <sup>-1</sup>	.915 cm	.135 cm
75/25	6.192	.889	.162
50/50	4.134	.814	.242

TABLE 6.4.13

PROPERTIES OF ELECTRON DRIFT IN COUNTER:  
CLOUD SIZE AT UPPER CATHODE

<u>Gas Mix</u>	<u><math>\bar{D}/\mu</math></u>	<u><math>\bar{z}</math></u>	<u><math>\sigma</math></u>
90/10	.05 eV	.415 cm	134 $\mu\text{m}$
75/25	.046	.388	125
50/50	.038	.314	102

TABLE 6.4.14

PROPERTIES OF ELECTRON DRIFT IN COUNTER:  
DRIFT TIMES TO UPPER CATHODE

<u>Gas Mix</u>	<u><math>\omega_{\text{Theory}}</math></u>	<u><math>\omega_{\text{Experimental}}</math></u>	<u><math>\bar{z}</math></u>	<u><math>t_{\text{Theory}}</math></u>	<u><math>t_{\text{Experimental}}</math></u>
90/10	.27 cm/ $\mu\text{sec}$	.39 cm/ $\mu\text{sec}$	.415 cm	1.54 $\mu\text{sec}$	1.06 $\mu\text{sec}$
75/25	.29		.388	1.35	
50/50	.38		.314	.83	

in the notation of Equation (6.4.2). Table 6.4.13 gives  $\bar{z}$ ,  $D/\mu$  and  $\sigma$  calculated using Equation (6.4.2) for each gas mix. Mathieson 1981 (private communication) in addition to calculating  $D/\mu$  has calculated  $\omega$  for each mix enabling mean drift times to the upper cathode to be assessed. Christophorou et al., 1980 have measured  $\omega$  experimentally for 90/10 Xenon/Methane. Table 6.4.14 gives  $\omega$  theoretically (and experimentally) along with the mean drift times ( $t$ ) of an electron cloud to the upper cathode for each gas mixture.

In order for the timing difference explanation of across wire modulation to be right one requires the electron cloud ( $\sim 3\sigma$ ) to be a fair fraction ( $\sim .4 - .5$  mm) of a millimeter in size, and the drift times in the counter to be of the order of  $\mu$ sec (the amplifier time constants). As can be seen from the tables the values are just of the right order. Mathieson is attempting to model the situation in detail in order to explain the counter results. This work has also shown that the longitudinal diffusion may be much greater than the lateral by a factor  $\sim 2X$ , so in fact a sausage shaped electron cloud arises leading to along anode risetime, and risetime dominated effects. The faster drift velocity from increasing percentage of quench gas may explain the increase in modulation observed with increasing quench.

This explanation of across wire modulation can be tested in a counter experimentally by use of a split anode. The split anode would consist of two sections, alternate wires being joined together to form effectively two separate anodes. The weighting of the avalanche on each wire could then be investigated as a function of time and interwire position.



### 6.5. The Limits of Position Resolution

Ultimately the position resolution achievable in a gas mix depends on the gas physics of that mixture and not on the readout method of the detector. With the GD cathode due to its good electronic (readout) noise we start to see the gas physics effects. In fact these define the resolution measured.

The limits of position resolution will be discussed in the light of the results from measurements in the direction along the anode where no modulation is present. The principal characteristic of all resolution versus gain curves is a flattening off in resolution and in some cases a worsening at high charge levels. Figures 6.5.1, 6.5.2 and 6.5.3 show the resolution versus gain curves for each cathode time constant along the anode for each gas mixture. The contribution from electronics, and the additional amount from the finite slit width is marked on each curve. The position resolution scale is a mean of the sensitivities versus gain for each time constant obtained during the linearity scans. It can be seen from the figures that intrinsic gas resolution, that is measured minus electronic plus slit, depends both on time constant and gas mix.

Various effects contribute to the gas limit of position resolution, namely:

- (i) Electron Diffusion
- (ii) Photoelectron Range
- (iii) K,L,M etc. Shell Interactions
- (iv) Secondary Avalanches

In order to explain the counter results we require an effect which is a strong function of gain. Photoelectron range and shell interactions are only properties of the gas and hence no dependence on counter gain can exist for these. Electron cloud size is a function of anode voltage, in the drift region, because of leakage field through the wires. However

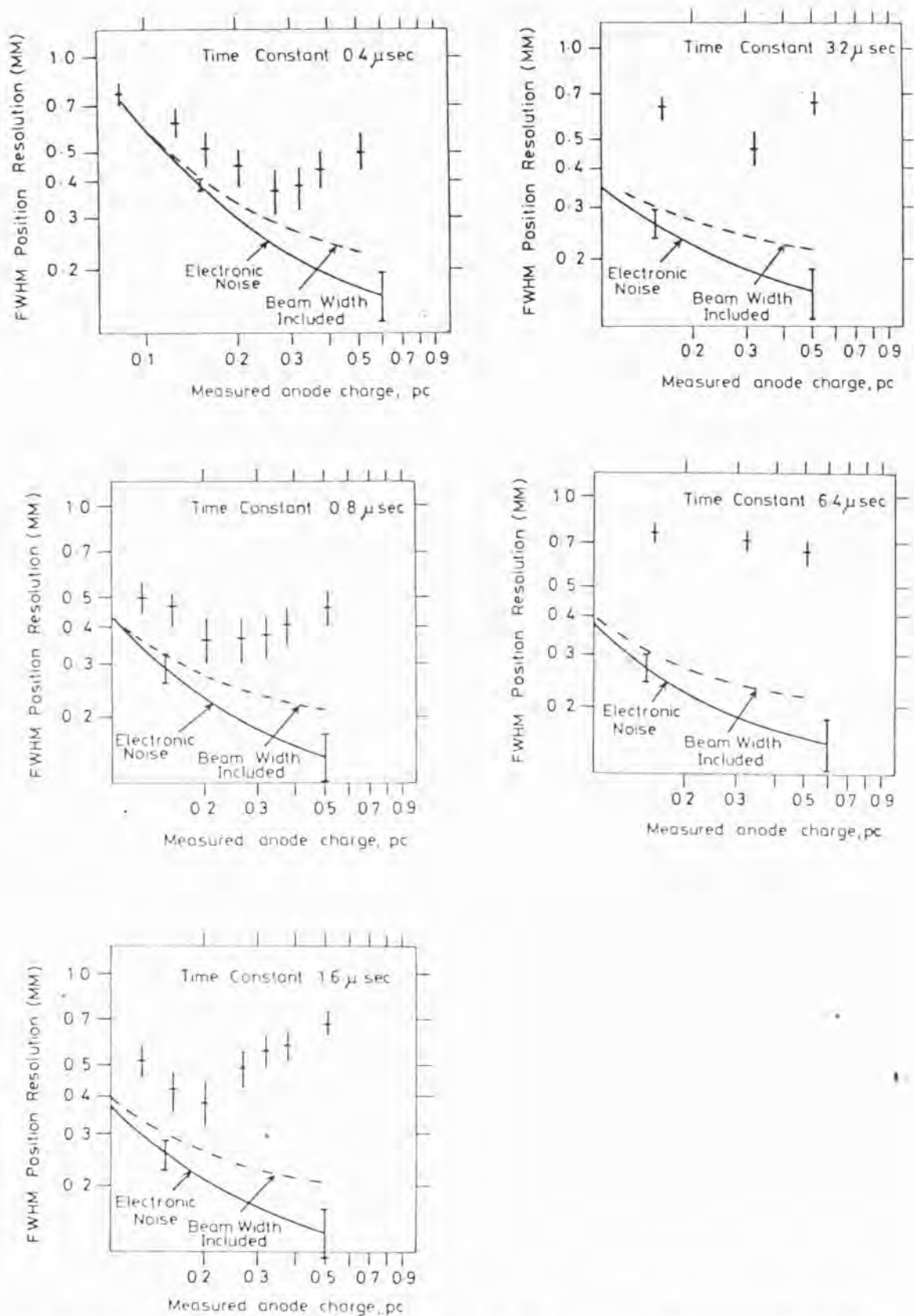


Figure 6.5.1. FWHM position resolution as a function of measured anode charge (anode amplifier time constant 1.6  $\mu$ sec) for each cathode time constant. Random error bars for position resolution and two error bars for electronic noise are shown. Two spot average measurements, 90/10 graded density counter.

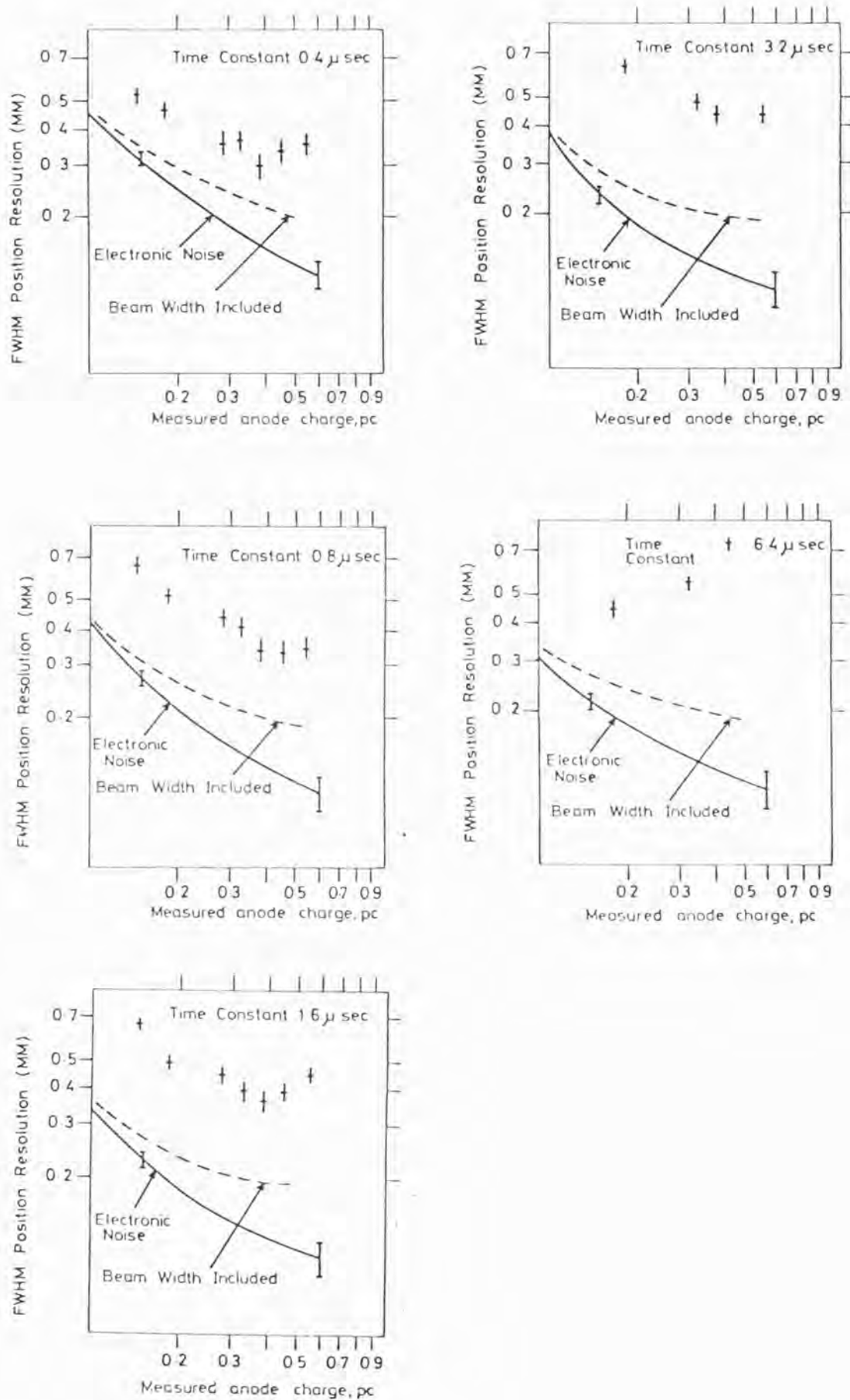


Figure 6.5.2. FWHM position resolution as a function of measured anode charge (anode amplifier time constant  $1.6 \mu\text{sec}$ ) for each cathode time constant. 75/25 graded density counter.

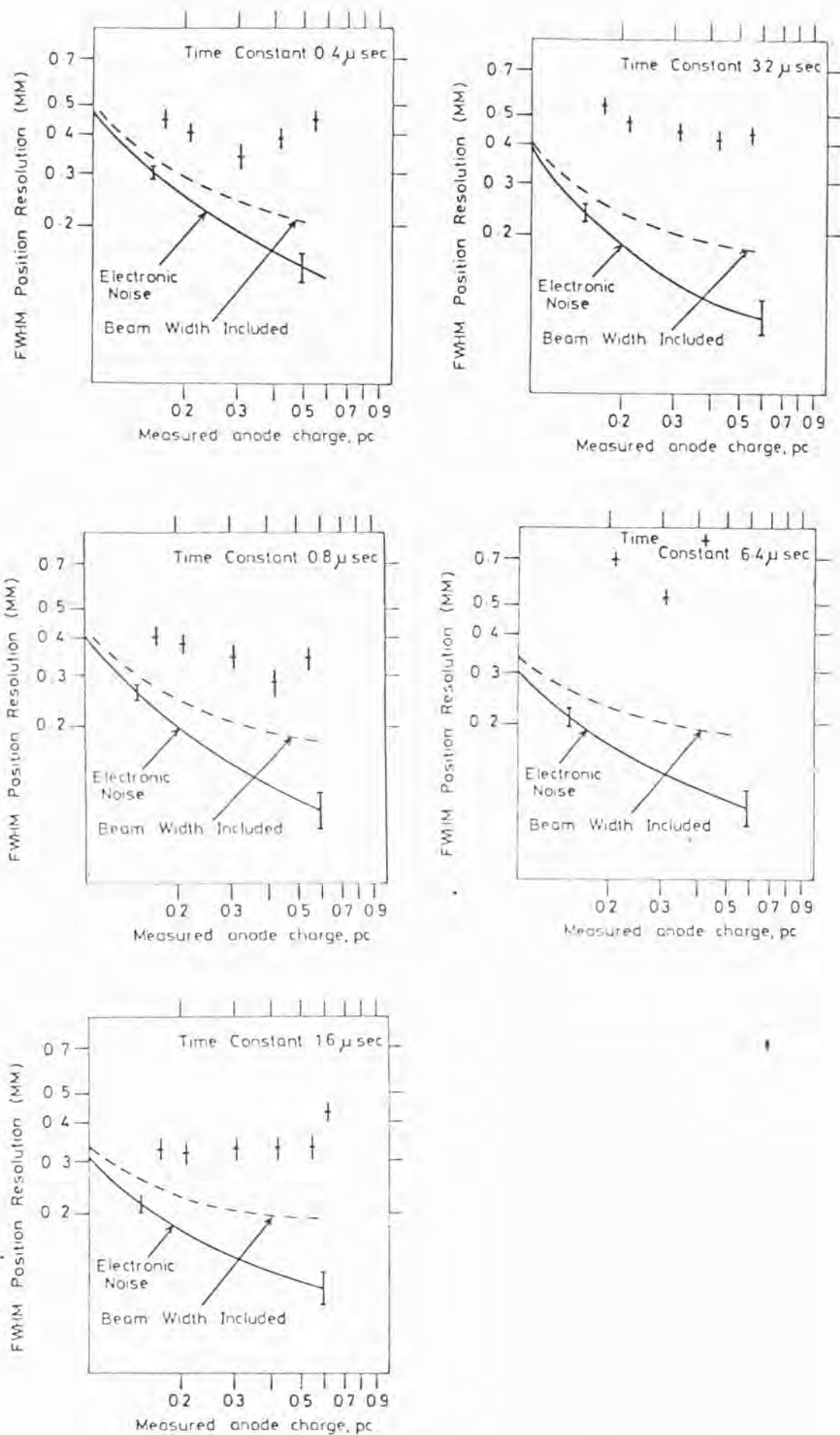


Figure 6.5.3. FWHM position resolution as a function of measured anode charge (anode amplifier time constant 1.6 μsec) for each cathode time constant. 50/50 graded density counter.

the field below the wires changes only relatively slowly as a function of gain (Charpak 1970).

Secondary avalanching (as briefly discussed in Chapter 5) resulting from electrons released from any metal surface by the ultra-violet photons from the main avalanche could have a definite effect on position resolution. The effect is a strong function of counter gain, leading to a degradation in position resolution at high gains.

Each possible effect will be dealt with in turn. However firstly the X-ray interaction sequence in the gas must be discussed.

#### 6.5.1. X-ray Interaction with the Gas in the IPC

The interaction of a 5.9 keV ( $\text{Fe}^{55}$ ) photon with the gas will only be considered, as all measurements were taken with X-rays of this energy. Zombeck 1980 and others give the following shell energies for Xenon;

$I_K$  , K shell energy 34.56 keV

$I_L$  , L shell energy 5.45 keV

$I_M$  , M shell energy 1.14 keV

When the X-ray, energy  $h\nu$ , enters the gas, pure Xenon assumed here a photoelectron of energy

$$h\nu - I_L = .45 \text{ keV}$$

is produced as the X-ray energy is not sufficiently high for K shell interactions, the L shell energy is the next lowest. M shell interactions are of less importance as the cross-section is  $\sim 5\times$  smaller than L, an L interaction is hence most probable. The fluorescent yield  $\omega_L$  is only  $\sim .14$ . So only in 14% of the interaction cases will an M electron jump to the L shell emitting a photon energy  $E_{h\nu}$

$$E_{h\nu} = I_L - I_M = 4.31 \text{ keV} = \Delta E$$

In the other 86% of interactions an Auger electron is emitted with a kinetic energy of

$$\begin{aligned}\Delta E &\sim I_M \\ &= I_L - 2 I_M \\ &= 3.17 \text{ keV}\end{aligned}$$

M and N shell interactions will also occur producing lower energy products.

Eventually all products reduce to ion pairs, where the number is given by approximately

$$n = \frac{h\nu}{E}$$

where E is the ionisation energy of the gas mix (21.5 eV pure Xenon). Hence for  $\text{Fe}^{55}$

$$n = 274 \text{ ion pairs.}$$

Quench gas interactions are not of importance due to the difference in cross-section, the cross-section for Xenon at 6 keV is  $6.695 \times 10^2 \text{ cm}^2/\text{gm}$  whereas for carbon (dominant factor for methane) it is  $1.047 \times 10^1 \text{ cm}^2/\text{gm}$  (McMaster et al., 1969).

Hence after an initial interaction from a  $\text{Fe}^{55}$  photon one has the following primary products:

.45 keV photoelectron.

4.31 keV photon 14% interactions

3.17 keV Auger electron 86%

Plus M and N shell etc. products.

#### 6.5.2. Gas Limits to Resolution: Photoelectron Range

Katz and Penfold 1952 give the following formula for the practical range (R), in a pure element



$$R(\text{cm}) = 0.211 \frac{Z}{\rho}^{0.26} E_p^{(1.265 - 0.0954 \ln E_p)}$$

where  $Z$  is the charge number

$\rho$  is the gas density

$E_p$  is the initial kinetic energy of the electron in MeV.

In the IPC the dominant photoelectron range is that of the Auger electron, hence only that contribution to position resolution will be considered. Applying the above formula we obtain the following practical ranges for pure Xenon and others mixes at 2 atmospheres pressure for the Auger electron:

$R = 14.7 \text{ } \mu\text{m}$	Xenon	2 atm.
$= 16.3$	90/10	"
$= 18.9$	75/25	"
$= 26.3$	50/50	"

This figure is only the practical range that is mean radial distance an electron travels. We will assume that the Auger electrons emerge isotropically. If one takes the simple model of ionisation distributed uniformly along this length then one has a resulting distribution projected onto the image plane of the form shown in Figure 6.5.4(a). In practice of course electrons will lose energy at a given distance, the range falling rapidly as the kinetic energy decreases. The actual projected distribution of dumped charge in reality will be like Figure 6.5.4(b). The peak occurs at ~60% of the range, as calculated by Bateman et al., 1976.

We will take a tophat function of full width  $2R$  as a reasonable approximation in order to calculate the contribution to position resolution  $\sigma_{PE}$ .

The contribution to position resolution is given by the rms of the image plane distribution of charge.

## Dumped charge distribution

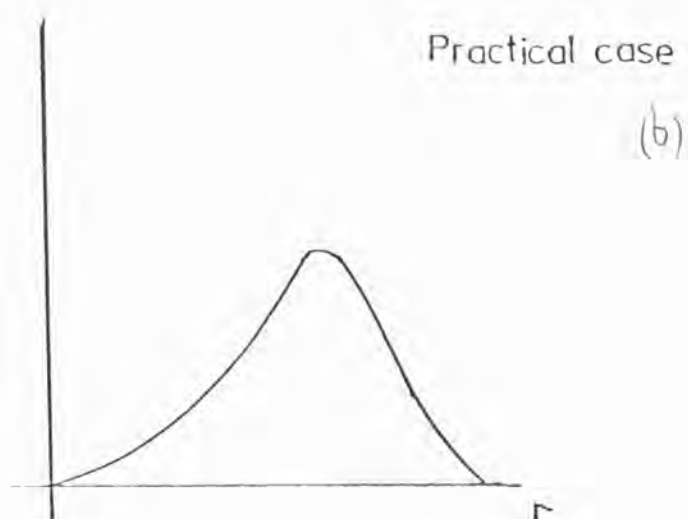
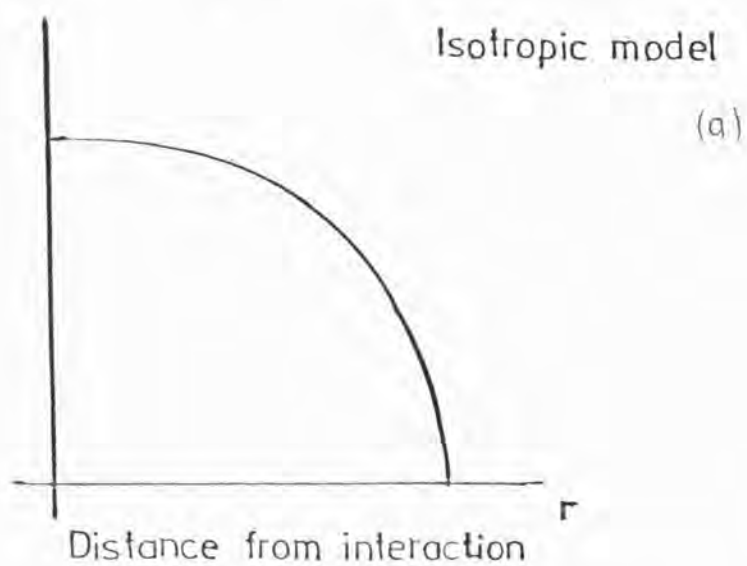


Figure 6.5.4. Schematic showing projected charge distribution on image plane resulting from photoelectrons; top, isotropic model, and bottom practical case.

$$\sigma_{PE} = \frac{2R}{2\sqrt{3}} \quad (\text{rms of tophat function})$$

Hence  $\sigma_{PE} = 8.5 \mu\text{m}$  Xenon 2 atm.

9.4      90/10    "

10.9      75/25    "

15.2      50/50    "

Gilvin et al., 1981, however use another prediction of  $\sigma_{PE}$  derived from the work of Williams 1931 and Tabata et al., 1972:

$$\sigma_{PE} = a(E_p)^n / \rho$$

where  $\sigma_{PE}$  is rms contribution to position resolution in  $\mu\text{m}$

$E_p$  is photoelectron energy in keV

$\rho$  is density in g/l

The work of the above give the constants

$a = 30$  (1 - 5 keV) , 17 (5 - 20 keV)

$n = 1.30$  " , 1.64 "

Hence using this, one obtains

$\sigma_{PE} = 11.5 \mu\text{m}$  Xenon 2 atm.

= 12.6      90/10

= 14.7      75/25

= 21.9      50/50

These second values as the larger will be used from here on as the contribution to resolution from the photoelectron range, for a worst case situation.

### 6.5.3. Gas Limits to Resolution: Electron Cloud Diffusion

It can be shown, Mathieson 1981 (private communication), Gilvin et al., 1981, that the uncertainty in position capability ( $\sigma_y$ ) due to electron diffusion of the initial charge is given by

$$\sigma_y^2 = \frac{1}{N_0} \left\{ 1 + \left( \frac{\sigma_M}{M} \right)^2 \right\} \sigma_d^2$$

where  $M$  is the mean gas gain (assumed to be independent of position) with standard deviation  $\sigma_M$ ,  $N_0$  is the initial number of electrons, and  $\sigma_d$  is the rms (characteristic radius) of the electron cloud after diffusion (see section 6.4.3). The term  $\sigma_M/M$  arises due to the fluctuations in the gas gain  $M$  in the calculations of the centroid.

$$\left[ \begin{array}{l} \text{Pulse Height } P = NM \\ \sigma_P^2 = N \sigma_M^2 + (M \sigma_N)^2 \\ \left( \frac{\sigma_P}{P} \right)^2 = \frac{1}{N} \left( \frac{\sigma_M}{M} \right)^2 + \left( \frac{\sigma_N}{N} \right)^2 \end{array} \right]$$

A worst case assumption is that  $\sigma_M/M = 1$  (see section 4.4.3, Chapter 4) in which case

$$\sigma_y^2 = \frac{1}{N} 2 \sigma_d^2$$

From section 6.4.3

$$\sigma_d^2 = 2 \bar{z} (D/\mu)/E$$

Let us consider the contribution to resolution for the 90/10 gas mix. We have a measured value for  $E$  for the drift region so that  $\sigma_y^2$  can be easily calculated for the drift region. In principle  $\sigma_y^2$  can be calculated for the total drift to the anode. However the main diffusion will occur in the drift region. With the field change occurring on entry into the inter cathode volume the drift velocity will considerably increase and  $D/\mu$  will decrease. For the drift region we will take  $\bar{z}$ ,

not as calculated in section 6.4.3 but as .55 cm to obtain a worst case. Hence for 90/10

$$\bar{z} = .55 \text{ cm}$$

$$D/\mu = .05 \text{ eV}$$

$$E = 230 \text{ V cm}^{-1}$$

$$N_o = 274$$

Hence  $\sigma_y = 13.2 \text{ } \mu\text{m}$

#### 6.5.4. Gas Limits to Resolution: Shell Interactions

The dominant contribution from atomic shell interactions to position resolution is of course the Auger electron. However in 14% of all  $\text{Fe}^{55}$  interactions a photon of energy 4.31 keV is created,

Table 6.5.1 gives the  $1/e$  absorption range of 4.3 keV photons in pure Xenon and each gas mix considered. By comparison with the mean initial absorption depth (see Table 6.4.12) it can be seen that a small fraction can escape from the counter through the window leading to an escape peak. However most are stopped internally. Bateman et al., 1976, have shown that shell interactions form a halo round the main position resolution peak for a given energy. In our L-shell fluorescence we have a 4.31 keV photon absorbed at  $x$  ( $\sim 1/e$  absorption distance away from original interaction point), and a distance ( $\sim 1 \text{ mm}$ ) away a .45 photoelectron plus other products. The weighting of the avalanche will obviously be towards  $x$ , so a halo will be formed by  $\sim 14\%$  of the  $\text{Fe}^{55}$  interactions, leading to wings on the resolution peak distribution. This does not greatly influence the gas contribution to resolution and hence will be ignored in any following argument. A full modelling of the counter situation should of course take this into account.

TABLE 6.5.1

1/e ABSORPTION RANGE 4.3 keV PHOTONS

	<u>Gas Mix</u>	<u>1/e Absorption Range</u>
2 atm.	Xenon	2.52 mm
"	90/10	2.80 mm
"	75/25	3.35 mm
"	50/50	4.99 mm

Note: Ranges are very large as 4.3 keV is below L edge



### 6.5.5. Gas Limits to Resolution: Secondary Avalanching

The effect of secondary avalanches will be to degrade the position resolution of a counter at all gains, the effect increasing with gain as more ultra-violet light is produced in the growing avalanche. Secondary avalanching can only be included by the position sensing electronics if the time taken for the released photoelectron and resulting electron cloud to arrive at the anode from the release point (counter window) is short enough to be seen within the shaping constant used. Drift data, see section 6.4.3, and results from Chapter 5 indicate  $\sim 2 \mu\text{sec}$  for 90/10 and the other gas mixtures, hence the drift time is of the right order. Each secondary avalanche will bias an initial avalanche position creating a new apparent position for each event. The secondary avalanches will of course have some spatial distribution and hence will degrade a spot resolution measurement, as each secondary avalanche will bias each avalanche differently. This qualitative argument appears to be able to explain the resolution degradation at high gains. However can secondary avalanching explain the results quantitatively?

#### 6.5.5.1. A Primitive Model

Let us assume a linear position coding system, e.g. the graded density cathode, with A and B the signals derived from each end of such a one-dimensional position sensitive system:

$$A = S (1 - x)$$

$$B = Sx$$

where S is the size of the dumped charge

x is the fractional distance from end A .

Hence 
$$\frac{B}{A+B} = \frac{Sx}{Sx + S(1-x)} = x$$

Consider two avalanches  $S$  and  $S'$  occurring essentially at the same time, we then measure

$$B = Sx + S'x' \quad \text{and} \quad A = S(1-x) + S'(1-x')$$

where  $x$  and  $x'$  are respective positions of avalanches. Ratio  $B/A+B$  gives a position

$$\frac{Sx + S'x'}{S + S'}$$

thus a new apparent position is seen with a deviation from the true position of

$$\frac{S'(x' - x)}{S + S'} = \frac{S'}{S} (x' - x)$$

if  $S \gg S'$ .

Secondary avalanches seen in IPC's are generally small. However  $x - x'$  can be large in the counter hence each bias will be significant. So as stated above, successive events will bias differently and hence the position resolution will be broadened. The observed position for each event is given by  $P$

$$P = \frac{Sx + S'x'}{S + S'}$$

For large numbers of events,  $x'$  and  $x$  will be distributed about a mean value, let  $\sigma$  and  $\sigma'$  be the rms values of the distributions  $S$  and  $S'$  in  $x$  and  $x'$ . The rms of  $P$  is therefore given by

$$\sigma_P^2 = \frac{\sigma^2 S^2 + \sigma'^2 S'^2}{(S + S')^2}$$

assuming zero correlation between  $\sigma$  and  $\sigma'$ ,

$$\left[ \begin{array}{l}
 p = \frac{Sx + S'x'}{S + S'} = \frac{1}{S + S'} (Sx + S'x') \\
 \text{Ratio } \Delta p = \left( \frac{\partial p}{\partial x} \right) \Delta x + \left( \frac{\partial p}{\partial x'} \right) \Delta x' \\
 = \frac{1}{S + S'} [S \Delta x + S' \Delta x'] \\
 \overline{\Delta p^2} = \frac{1}{(S + S')^2} [S^2 \overline{\Delta x^2} + 2S S' \overline{\Delta x \Delta x'} + S'^2 \overline{\Delta x'^2}] \\
 \overline{\Delta p^2} = \sigma_p^2 \quad \overline{\Delta x^2} = \sigma^2 \quad \overline{\Delta x'^2} = \sigma'^2
 \end{array} \right]$$

Now  $\sigma$  is the rms contribution from all gas effects, that is diffusion, photoelectron range, shell interactions,  $\sigma'$  is the rms of the secondary avalanche distribution.

Define  $\gamma$  to be equal to the number of secondary photoelectrons produced per electron in the main avalanche which produce secondary avalanches which are observed.

Let  $\xi$  be the number of primary electrons from a given event, and  $G$  be the gas gain of the counter. We will assume  $G$  to be independent of  $x$ .

Then  $\gamma \xi G$  is the number of observed secondary avalanches.

Therefore  $S = \xi G$

$$S' = \gamma \xi G^2$$

Substituting in  $\sigma_p^2$

$$\sigma_p^2 = \frac{\sigma^2 + \sigma'^2 \gamma^2 G^2}{1 + 2\gamma G + \gamma^2 G^2}$$

Making the assumption all distributions are the same and Gaussian, the predicted resolution  $\Delta p$  for the counter is given by

$$(\Delta p)_{\text{FWHM}} = 2.355 \left[ \frac{\sigma^2 + \sigma'^2 \gamma^2 G^2}{1 + 2\gamma G + \gamma^2 G^2} + \left( \frac{\Delta}{2\sqrt{3}} \right)^2 + \sigma_n^2 \right]^{\frac{1}{2}} \quad (6.5.1)$$

where  $\Delta$  is the finite width beam entering the counter

$\sigma_n$  is the rms resolution of the electronics

### 6.5.5.2 Total Gas Contribution $\sigma$

$\sigma$  can be easily estimated using the results of sections 6.5.2, 6.5.3. Ignoring the L shell fluorescence we have two contributions, the photoelectron range ( $\sigma_{PE}$ ) and diffusion ( $\sigma_y$ ). The total gas contribution is therefore

$$\sigma^2 = \sigma_{PE}^2 + \sigma_y^2$$

For 90/10 mix

$$\sigma_{PE} = 12.6 \text{ } \mu\text{m}$$

$$\sigma_y = 13.2 \text{ } \mu\text{m}$$

hence total gas contribution is  $\sigma = 18 \text{ } \mu\text{m}$

### 6.5.5.3 Distribution of Secondary Avalanches $\sigma'$

The secondary avalanches must arise from photoelectrons released by UV photons hitting metal surfaces inside the counter. The on axis optical transparency of the cathodes ~96%, hence the most likely source in the counter is the window and base plate. The distribution in secondaries as a reasonable assumption must closely resemble the UV light distribution across the window.

The initial avalanche can be thought of as a point source of light. The rms of the light distribution can therefore be calculated using Lambert's Cosine Law, which gives the illumination (E) across a plane. Consider Figure 6.5.5, the plane is at distance  $r$  from a point source of line,  $d$  is distance from vertical to point of measurement. Then

$$E = \frac{I \cos \theta}{r^2 + d^2}$$

where  $I$  is the luminous intensity (Longhurst 1973).

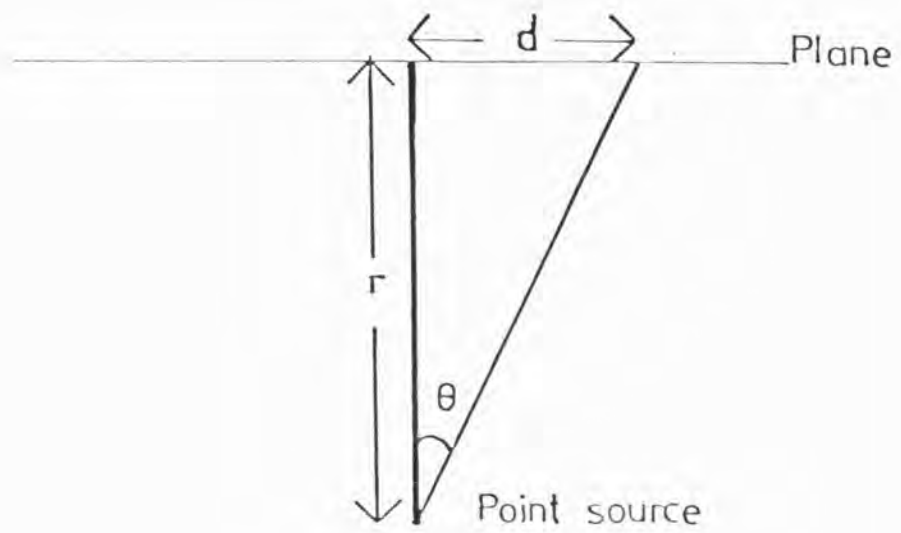


Figure 6.5.5. Notation for Lambert's Cosine Law. Plane at distance  $r$  from point source of light.

$$\cos \theta = \frac{r}{\sqrt{r^2 + d^2}}$$

Hence 
$$E = \frac{I_r}{(r^2 + d^2)^{3/2}}$$

This of course is a two-dimensional distribution,  $d$  must be resolved into along and across the anode wires ( $a, b$ );

$$d^2 = a^2 + b^2$$

$$E(a, b) = I_r / (r^2 + a^2 + b^2)^{3/2}$$

We require the integrated distribution in one direction say  $a$ . If we make the assumption of a true one-dimensional system,  $b$  infinite in extent, the resulting distribution can be calculated analytically. This of course is an approximation,  $b$  should be limited in extent.

$$E(a) = I_r \int_{-\infty}^{+\infty} \frac{db}{(r^2 + a^2 + b^2)^{3/2}}$$

Using Bronshtein and Semedyayev 1973 it can be shown that

$$E(a) = \frac{2 I_r}{(r^2 + a^2)}$$

We require the rms ' for this distribution

$$\sigma'^2 = \frac{\int E(a) a^2 da - [\int E(a) a da]^2}{\int E(a) da}$$

The cathode is limited in extent not infinite (also required for integration), let  $a_1$  and  $a_2$  be the starting and stop co-ordinates for the cathode with respect to the avalanche position, as only secondaries occurring directly above the active area can enter the counter. It can be shown using Spiegel 1968 that



$$\sigma'^2 = \frac{\left[ a - r \tan^{-1} \frac{a}{r} \right]_{a_1}^{a_2} - \left( \left[ \frac{1}{2} \ln(r^2 + a^2) \right]_{a_1}^{a_2} \right)^2}{\left[ \frac{1}{r} \tan^{-1} \frac{a}{r} \right]_{a_1}^{a_2}}$$

Take an avalanche occurring in the centre of the counter in which case  $a_2 = +4.75$  cm,  $a_1 = -4.75$  (full width GD cathode = 9.5 cm),  $r = 1.05$  cm (anode to window distance).

Substituting

$$\sigma' = 1.608 \text{ cm}$$

As expected  $\sigma'$  is comparatively large.

#### 6.5.5.4 Predicted Resolution

The predicted resolution is given by Equation (6.5.1). A program was written to calculate the predicted resolution using measured electronic noise values, sensitivity, and calculated gas parameters,  $\gamma$  being the only variable. The charge (Q) measured from a counter is of course the total of initial avalanches plus secondaries i.e.

$$Q = \xi G + \gamma \xi G^2$$

where Q is in electrons

$$G = -\frac{1}{2\gamma} \pm \sqrt{\frac{1}{4\gamma^2} + \frac{Q}{\gamma\xi}}$$

G must be found as our electronic noise measurements are for a total charge Q. Hence the following procedure was adopted for the program. An input value of electronic noise was taken, G calculated, then the gas contribution, the contribution from the slit added, and finally the predicted resolution was calculated and printed.

Table 6.5.2 lists the input parameters adopted for this program. Figure 6.5.6 shows the predicted resolution for two values of  $\gamma$ . As can be seen the resulting curve is very similar to that observed, hence

TABLE 6.5.2

## PREDICTED RESOLUTION PROGRAM: INPUT PARAMETERS

Electronic Noise    as per 1.6  $\mu$ sec    90/10

<u>Charge</u>	<u>FWHM Electronic Noise</u>	
.098 pC	3	channels
.147	2	
.196	1.75	
.294	1.625	
.392	1.25	
.49	1.125	
.59	1	
.69	1	

Sensitivity = 8.45 channels/mm

Equivalent slit width = .22 mm

Initial number of electrons produced by X-ray = 274

Rms contribution from gas = .018 mm

Rms contribution from secondaries = 16.08 mm

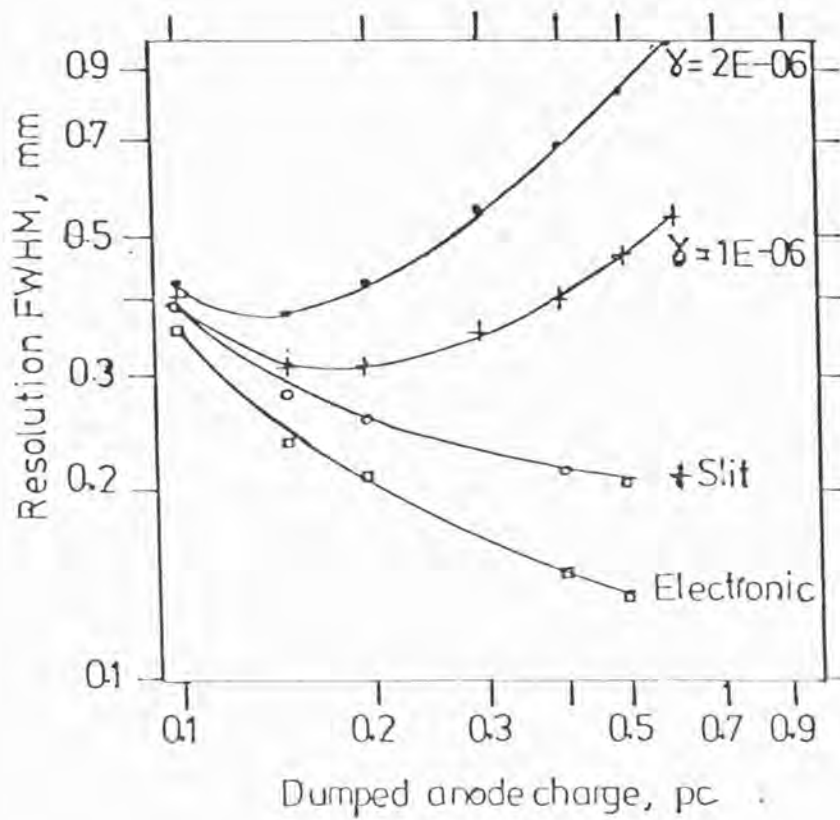


Figure 6.5.6. Predicted position resolution (FWHM) for counter as a function of dumped charge using secondary avalanche model. Results for two values of  $\gamma$  are shown. Note E format of Fortran used,  $1E1 \equiv 10^1$ .

secondary avalanching appears to explain the form of degradation in resolution at high dumped charges. The value which fits the data is  $\gamma \sim 10^{-6}$ .

#### 6.5.5.5 Discussion

The model is of course very primitive.  $\gamma$  in fact embodies many parameters, counter geometry, photoelectron production efficiency, UV production etc. Carver and Mitchell 1967 investigated the statistics of electron multiplication in single wire proportional counters. In order to explain their experimental results on electron pulse distribution, a parameter  $\mu$  was used, where  $\mu$  was the mean number of successors initiated by a single avalanche. This parameter was found to increase rapidly with increasing counter voltage reflecting the increasing size of the avalanche with  $V$ . So they then define a parameter  $\gamma$  denoting the mean number of successors initiated by a single electron in the avalanche.  $\gamma$  was found to be independent of  $V$  with values from  $0.2 - 7.0 \times 10^{-6}$  for the gas mixtures investigated. The counter geometry construction is very similar in one dimension to the prototype IPC. For argon/methane 90.5/9.5 mix a value of  $1.2 \pm 0.9 \times 10^{-6}$  was obtained. Our value of  $\gamma$  is similar  $\sim 10^{-6}$ .

Full quantitative data requires a full modelling of the detector, this could be attempted along the lines of the numerical model of Bateman et al., 1976. In the case of the IPC for the shadow camera only X-rays lower in energy than the K shell need be considered. The following additions to the model are required; diffusion of the initial electron cloud; secondary avalanching effects; and most importantly the time distribution of avalanches versus position and their interaction with the read-out scheme.

The difference in resolution versus gain versus time constant for

the various gas mixtures (Figures 6.5.1, 6.5.2, 6.5.3) is most probably due to the time distribution of the secondary avalanches and increasing amount of methane. As expected from the secondary avalanche argument as the time constant is decreased the contribution will fall (as observed) as insufficient time has elapsed for secondary avalanches to have a major effect.

No direct evidence for secondary avalanches exists from the two-dimensional position sensitive detector apart from the above analysis. The photoelectric after pulses are  $\sim 10^{-2}$  of the main pulse ( $\sim 10^4$  gain). An attempt to see after pulses using a fast shaping amplifier was unsuccessful because of the low count rate and poor spatial resolution achievable on a CRO. However secondary pulses were observed with the one-dimensional detector, see Chapter 5. Some evidence could exist with the change in pulse profile measured with gain, see Figure 6.2.7.

After pulses have been reported by Campion 1968 and others in Argon/Methane. Gilvin et al., 1981, report the observation of secondaries in the anode signal above 1 pC, and in fact cause a marked deterioration in energy resolution. Figure 6.5.7 taken from the paper by Gilvin et al., 1981, gives the measured position resolution of their IPC as a function of anode charge. The degradation at high gains is evident, also the greatly diminished effect in P50 due to the higher UV absorption with methane in this counter.

The question arises of the role of methane in the prototype.

#### 6.5.5.6 Methane and Secondary Avalanching

Traditionally quench gases are supposed to absorb UV photons and thereby quench the discharge. The ionisation potential of methane is certainly higher than the energy of light emission in Xenon (see Chapter 4). However the work of Wilkinson and Johnston 1950 shows that methane has no

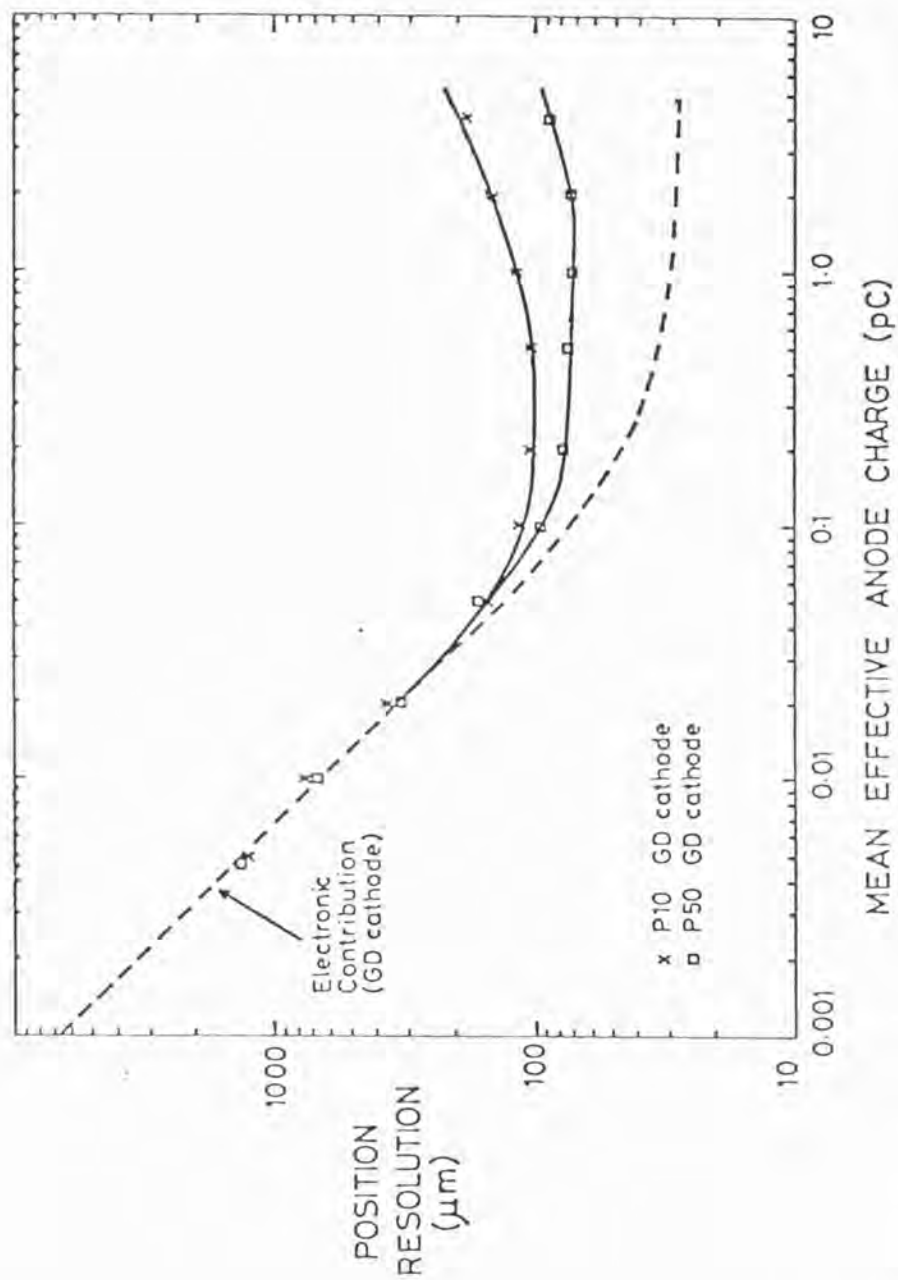


Figure 6.5.7. Experimental resolution (r.m.s.) along anode wire direction plotted against mean effective anode charge for P10 (A/10%  $\text{CH}_4$ ) and P50 (A/50%  $\text{CH}_4$ ). Anode wire spacing 14 mm. (From Gilvin et al., 1981)



absorption bands in the UV and only absorbs above about 8 eV (continuous absorption occurring below 1455 Å). The UV emission of Xenon however only extends to 8 eV (Breskin et al., 1979). In fact the absorption spectrum of methane does not overlap at all with the measured Xenon light emission spectrum. Hence photons with energies greater than the work function of the window ( $> 5$  eV) can travel long distances within the gas mix and reach the window and release photoelectrons to cause secondary avalanches.

It therefore appears that the value of methane as a quench gas for Xenon is based on its superb ability to give high electron mobility in gas mixtures and on its positive ion quench effects. The cathode wires themselves also have a low enough work function (4.5 eV) for secondary avalanches to be initiated from them. However as the on axis optical transparency is ~96% the contribution from cathode compared to window and base plate is very small.

The problem of secondary avalanching in Argon/Methane mix is not so critical as the Argon emission spectrum has considerable overlap with the absorption spectrum. From the work it appears that the methane limits the position resolution in Xenon/Methane mixtures. The present results however show that an IPC with spatial resolution better than 350  $\mu\text{m}$  FWHM can be built using Xenon/Methane.

#### 6.5.5.7 Other Gases for the IPC

The limiting resolution achieved in the IPC points to use of quench gases with better UV absorption. Little data on absorption appears in the literature on counters. Wilkinson and Johnston also measured absorption from 1667 to 1441 Å, and absorption bands at 1690, 1673, 1662 Å. The maximum of the continuum is at 1495 Å. Hence some overlap exists with the Xenon light emission spectrum. Counters filled with Xenon/CO<sub>2</sub>

also show little degradation due to deposition of Polymers on the wire. However  $\text{CO}_2$  mixes have a much lower electron mobility than methane mixes, so are more sensitive to impurities. In addition the lower drift velocity could also pose across wire linearity problems due to the time difference effect if this is the correct explanation of the modulation. Xenon/ $\text{CO}_2$  as a gas mix for the shadow camera IPC is currently being investigated, Thomas 1981 (private communication).

What other possibilities are there? Christophorou et al., 1980, have recently investigated Xenon/ $\text{CF}_4$  mixes for gas filled detectors. At high E/P values these mixes can have a substantially higher drift velocities compared to the standard mixes of 90/10 Xenon/ $\text{CH}_4$  and 90/10 Xenon/ $\text{CO}_2$ . No data on the UV absorption coefficient for  $\text{CF}_4$  appears to be available.  $\text{CF}_4$  is however more tightly bound than methane and will probably have an even poorer absorption spectrum with a cut-off at higher energies than methane (S. Gurman 1981, private communication). Ethane has also been suggested as a suitable quench, due to its lower binding than methane. It is intended that  $\text{CF}_4$  as a quench gas will be investigated in the near future, Thomas 1981 (private communication).

If the UV absorption in the quench is accompanied with emission of electrons rather than re-radiation at other energies, the problem of secondary avalanching can never be overcome. With this problem the best one can do is to modify the distribution of secondaries.

#### 6.6. Conclusion

Sub 500  $\mu\text{m}$  position resolution is achievable in Xenon/Methane gas mixtures in an IPC. The energy resolution and (gas limited) position resolution achieved with  $\text{Fe}^{55}$  is compatible with that required by the shadow camera.

The two prime problems with the detector as it stands are the

across wire modulation, and the limiting of the IPC to low gain levels. A real counter has to have a large dynamic range  $\sim 2 - 8$  keV for imaging. As the energy falls the amount of charge dumped in the counter also falls proportionally, and hence spatial resolution will fall, ignoring shell effects, if the counter is optimised, say, for 6 keV. Using the results of the 90/10 Xe/CH<sub>4</sub>, a resolution  $\sim 600$   $\mu$ m for 2 keV is achievable if the resolution just scales with charge.

What improvements can be made? One way of improving the dynamic range is to improve the electronic noise, the main contribution to resolution at low charge levels. Recently Gilvin et al., 1981, have used a subdivided GD cathode to further improve the electronic noise over the performance achieved in this work. This resulted in reducing the load capacitance on their preamplifiers from 79 pF to 29 pF, and a substantial reduction of 2.5X for the electronic noise at 0.1 pC. The graded density cathode is subdivided into two sections, the readout pulses A and B are taken from each end of the cathode. The theory of subdivision will be briefly described.

Consider a wire cathode total width  $L$  subdivided into  $N$  equal sections with wires of constant pitch  $s$ . The wires of each section are then connected into the two linearly graded groups A and B as in the normal GD cathode. In the condition  $s \ll L/N$  each section will act as a conventional cathode. Now the B type wires of each section are connected to the A type wires of the next section, this results in  $N + 1$  nodes. Let a charge  $q_D$  with centroid  $x$  be induced on the cathode, the centroid of the node charges gives  $x$

$$x = L \frac{\sum_{m=0}^N m q_m}{\sum_{m=0}^N q_m}$$

where  $q_m$  is the charge appearing at the  $m^{\text{th}}$  node due to the linear behaviour of each GD section. As there is a finite capacitance between A and B components of a GD section, when several sections are

connected in series, these capacitances act as a capacitance divider. Charges appear at the extreme nodes and therefore a two channel readout as before can be used. The advantage of subdividing a cathode is the reduction in capacitative loading  $C_L$  for the two signal preamplifiers. The GD cathode was therefore subdivided into two ( $N = 2$ ) and the subsequent reduction in electronic noise used by Gilvin et al., 1981.

A disadvantage does however exist with a subdivided cathode, and this is a systematic non-linearity resulting from the intercomponent capacitance. However the non-linearity can be predicted and largely removed by appropriate non-linear grading.

Practically a limitation on the noise performance of the GD cathode was the finite resistance at r.f. frequencies along the substrate at each cathode. To overcome this a cathode was physically split into two sections. The end sections were placed on a separate frame to the connected midsection, hence greatly increasing the finite resistances between wires of different groups due to the large distances involved, and hence reducing the resistive noise. This type of cathode is known as the low loss GD cathode. Unfortunately the mechanical problem of making the wires lie in the same plane has not yet been solved, leading to some unpredictable non-linearity across the cathode.

Construction of the divided cathode on one frame leads however to an improvement though not as large as the use of the low loss GD cathode. Table 6.6.1 lists the achieved electronic resolution, noise in electrons, and load capacitance achieved with the various forms of GD cathode to date (Gilvin 1981 private communication).

Hence the low noise performance of the detector could be improved by use of the subdivided GD cathode. A Xenon filled detector with a two section single frame GD cathode is presently under construction at Leicester. At the charge levels used for  $\text{Fe}^{55}$  ~0.2 to 0.3 pC an improvement ~1.5 - 2 times will occur in the spatial resolution, sub 500  $\mu\text{m}$

TABLE 6.6.1  
MEASURED PERFORMANCE OF GD CATHODE

<u>Type</u>	<u>Electronic Resolution RMS at 0.1 pC Anode Charge</u>	<u>Noise RMS</u>	<u>Load Capacitance</u>
1 section	~ 235 $\mu\text{m}$	~ 460 electrons	~ 82 pF
Subdivided 2 section	~ 110	~ 360	~ 30
Low Loss	~ 74	~ 260	~ 28

Data from Gilvin 1981 private communication



resolution occurring even at 0.1 pC (cathode time constant 0.4  $\mu$ sec).

One possible way to remove the across wire non-linearity is to increase the depth of the drift region, allowing the electron cloud to diffuse sufficiently that the cloud covers at least two anode wires at all times, interpolation across the wires existing continuously. Gilvin et al., 1981, have experimentally shown that a definite improvement in linearity results with the use of a drift region, see Figure 6.6.1. The change appears small, but the local sensitivity as a function of interwire position has changed significantly. This data was taken with a near identical IPC in Argon/Methane, with 2 mm spaced anode, 0.5 mm spaced GD cathode, and an anode to cathode spacing of 6 mm. Use of a large electron cloud size, however, leads to a deterioration in position resolution due to the increased contribution to the gas resolution by diffusion.

An alternative is use of a 1 mm spaced anode, with perhaps a slightly increased drift region, giving across wire interpolation. However this has the resulting problems of higher operational voltage.

A large drift region should be correctly defined by the use of electrodes joined by resistors between the top cathode and window to give the required linear field. In the current counter as all detailed performance were near counter centre, and the close proximity of the cathode to window, the extra electrodes were not used. Investigation of drift region effects will be studied in the current development program for an IPC for the shadow camera at Leicester (Thomas 1981, private communication).

The across wire non-linearity can be minimised in the current counter by use of the correct cathode time constant, and the effect on imaging is not too severe as will be shown in the concluding Chapter 7 for use in a prototype shadow camera.



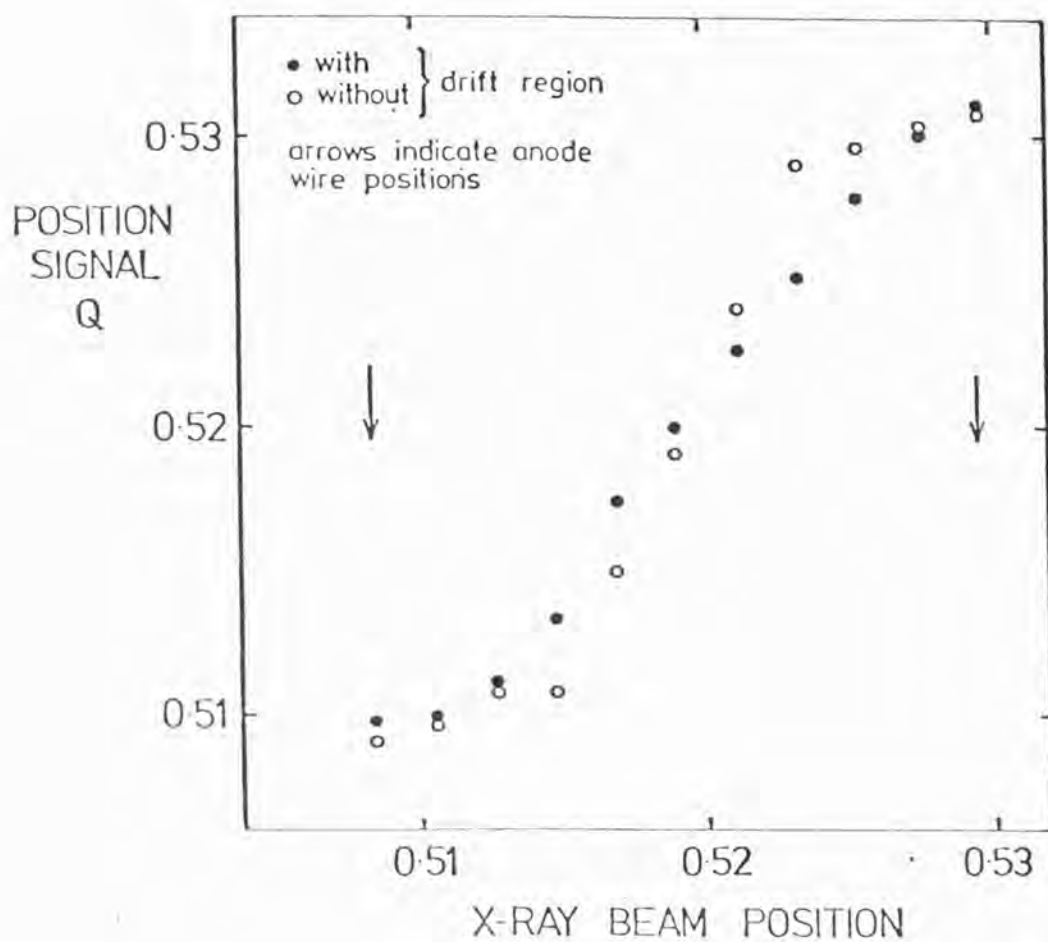


Figure 6.6.1. Position modulation due to 2 mm anode wire spacing, with and without drift region (11 mm deep, field 200 V/cm). Chamber gas used was P50. The abscissa is expressed as a fraction of total cathode width, (From Gilvin et al., 1981)

## CHAPTER 7

## CONCLUSION/FUTURE WORK

7.1. Introduction

The work described in this thesis has covered two main areas, the performance of the shadow camera, and the limits of performance of a Xenon/Methane-filled IPC. Hence this concluding chapter will be divided into three main sections; first the performance of the shadow camera in its wide field monitoring role will be discussed, followed by a comparison with previous work of the resolution achieved here in Xenon/Methane. Finally some comments on future work will be made.

7.2. The Shadow Camera

The basic theory of the shadow camera, as discussed in Chapter 2, is well advanced and a design can be optimised using the known and required parameters of the shadow camera.

The computer simulations have shown that the shadow camera can work under a variety of conditions and is capable of acting as a sensitive and efficient wide field monitor. The simple form of the camera has been shown to fulfill this role very well and some of the fundamental limits in its use have been established (see Summary, section 3.7 and other parts of Chapter 3). A question that up to now has not been tackled in great detail is 'whether the simple shadow camera is the most suitable instrument for wide field monitoring of the X-ray sky?' Table 7.2.1 compares the general characteristics of various X-ray instrumentation for wide field monitoring of the sky. As briefly discussed in Chapter 1 the collimated counter is generally unsuitable for wide field monitoring due to problems resulting from multiple sources in the FOV (a source confusion problem). The scanning modulation collimator (SMC) and rotation modulation collimator (RMC) can

TABLE 7.2.1

## GENERAL CHARACTERISTICS AS X-RAY ASTRONOMY INSTRUMENTATION FOR WIDE FIELD MONITORING

<u>Instrument</u>	<u>FOV</u>	<u>Angular Resolution</u>	<u>Positioning Capability</u>	<u>Typical Time Resolution</u>	<u>Spacecraft Attitude Requirements</u>	<u>Other Points</u>
Collimated Counter						
(a) Pointed	$\leq 1^\circ$ FWHM	$\leq 1^\circ$	$\leq 1^\circ$	Telemetry Limited	Pointed Spacecraft	Non-imaging, problems with multiple sources
(b) Scanning	$\sim 1^\circ \times$ many degrees	$\leq 1^\circ$	few arc mins.	Spin period of Satellite	Spinning or Scanning Satellite	Source confusion can be a problem
Scanning Modulation Collimator	$\sim$ few to ten degrees	$\sim$ few arc mins.	$\sim$ few arc secs.	Limited by time to detect and position source	Multiple positions requiring additional information to locate a source	Confused by sources that vary during a spin period and multiple sources
Rotation Modulation Collimator	$\sim$ tens of degrees	$\sim$ few arc mins.	$\sim$ few to few tens of arc secs.	Limited by spin period	Rotating Spacecraft	Source confusion due to incomplete sampling
Grazing Incidence Telescope	$\sim 5^\circ$	$\sim$ arc min. $\sim$ arc min. Dependent on FOV approximately $10^3$ elements across FOV		Telemetry Limited		True imaging, low effective areas $> 4$ keV
Shadow Camera	tens of degrees	$\sim$ few arc mins.	$\sim$ few arc mins.	Telemetry Limited	Three axis stabilised rotation of FOV a problem	True imaging, large effective area
Pinhole Camera	"	"	"	"	No problem with rotation of FOV	"

provide a large FOV, with good angular resolution and accurate positioning capability. However both instruments make greater demands on the spacecraft attitude, and suffer with problems of source confusion. In particular the RMC and SMC are confused by sources that vary during the spin or scan period (the SMC to a lesser extent than the RMC). Hence both are not suitable for monitoring rapidly varying sources or very dense source concentrations.

These problems are absent, or much reduced, with a true imaging experiment; the grazing incidence telescope; the shadow camera and the pinhole camera. The grazing incidence telescope suffers from a very limited FOV and has low effective areas above 4 keV (see Chapter 1). The choice for a wide field monitor, therefore, reduces to the shadow camera, investigated here, and pinhole camera. Both have theoretically comparable performance in FOV, angular resolution and positioning capability, while the rotation of the FOV can be a problem with the shadow camera. The choice essentially must rest on sensitivity versus complexity and in section 2.3.2 a formula is developed that expresses the sensitivity advantage for the shadow camera for the same detector and identical angular resolution (as a pinhole camera).

The expression is

$$\frac{S_c}{S_p} = \frac{r n_o^2 + [r^2 n_o^2 + 4r(1-r)(r N_p + B)t]^{\frac{1}{2}}}{n_o^2 + [n_o^2 + 4qBt]^{\frac{1}{2}}} \cdot \frac{q}{r(1-r)} \quad (7.2.1)$$

where  $S_c$  is the minimum detectable source intensity of the shadow camera

$S_p$  is the minimum detectable source intensity of the pinhole camera

$r$  is the mask transmission

$q$  is the ratio of pinhole area to that of detector area

$N_p$  is the total number of photons incident on the front of the camera from all sources in the FOV and diffuse background (counts/sec)

$n_{\sigma}$  is minimum detectable source requirement, in terms of number of sigma  
 $B$  is the total number of cosmic ray photons (counts/sec.)  
 $t$  is the integration time

For  $r = 0.5, rN_p \ll B$  and  $t$  relatively long (so that  $n_{\sigma}$  can be neglected), equation (7.2.1) reduces to

$$\left( \frac{q}{r(1-r)} \right)^{\frac{1}{2}}$$

which is the case of narrow field imaging quoted by Procter et al., 1979. In general, for rather small values of  $q$  (i.e. a large ratio of FOV to angular resolution),  $qB$  is small and the pinhole camera is photon limited over a wide range of  $t$ . Also  $n_{\sigma}$  may not be neglected, i.e. the fluctuations in source counts dominate over fluctuations in the background. The shadow camera is nearly always diffuse background dominated, for  $t >$  a few seconds, however.

Figure 7.2.1 illustrates the expression (equation (7.2.1)) evaluated for the instrument described in Chapter 3, section 3.5.1, Table 3.5.1, for three regions of sky; the Coma region where  $N_p$  is dominated by the diffuse background; the galactic centre where  $N_p$  is dominated by sources, and as an extreme case the region near Sco X-1 where  $N_p$  has the largest possible value. It can be seen that, in this case, even for integration times in excess of  $10^5$  seconds, the shadow camera is more sensitive than the pinhole camera, at high galactic latitudes theoretically.

The formula for sensitivity of the shadow camera, developed in Chapter 2, actually breaks down in the case of the camera becoming photon limited, i.e. when source fluctuations become important. However, this case is never met for the FOV used above and integration times greater than a few seconds.

This sensitivity advantage is borne out by the computer simulation results, for example, in the case of the Coma region, with an integration time of 5000 seconds, simulated for the simple camera, the total recorded

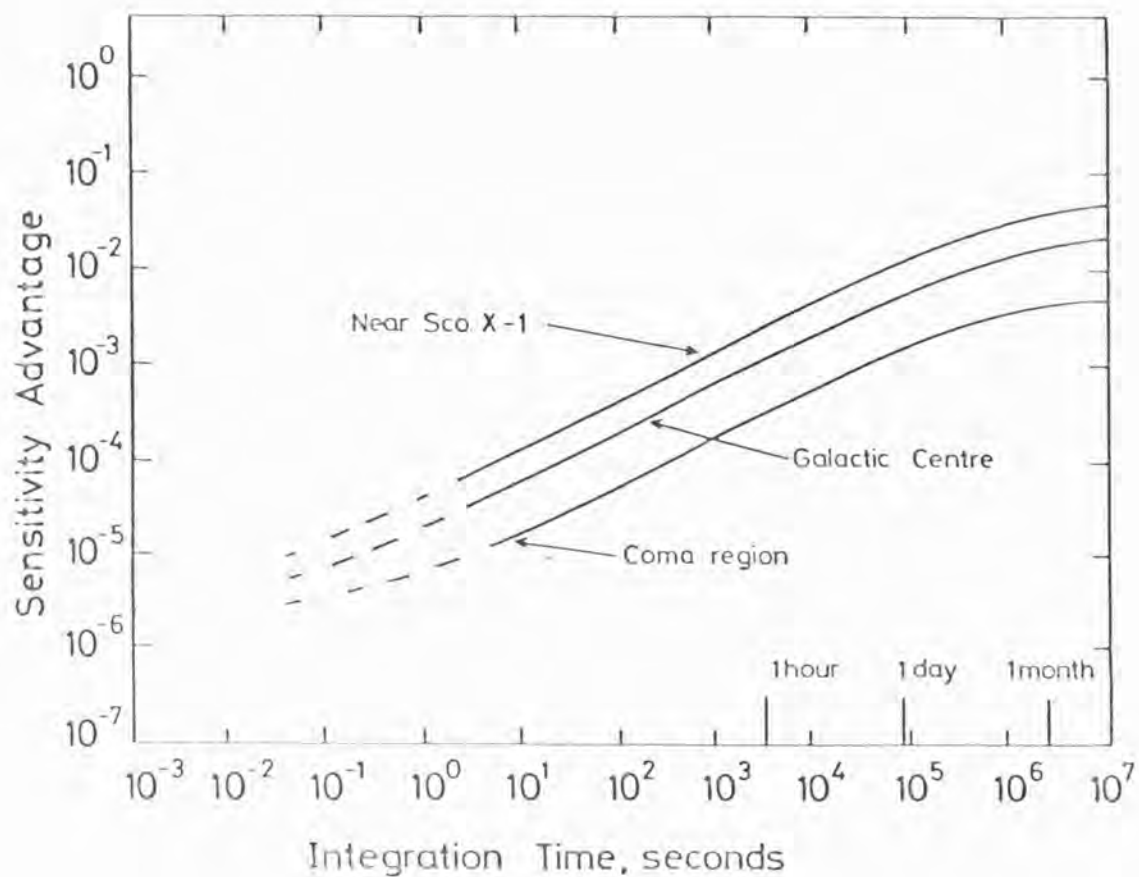


Figure 7.2.1. The sensitivity advantage of the shadow camera over an equivalent pinhole camera as a function of integration time for three regions of the celestial sphere. The advantage is expressed as the ratio of the minimum source intensity, detectable at 6 sigma, for the shadow camera, to that for a pinhole camera having the same detector area and angular resolution.



count was 1352569 . Consider the source at image pixel co-ordinates 80,63 , with a total recorded count of 16413 . The source thus appears at  $25.5\sigma$  on a 'global' comparison. This compares with a simple theoretical expectation (equation 2.3.2) of  $\sim 14\sigma$  , the off-axis fall-off effect reducing the global rms. Approximately 1536 holes in the mask are shadowed onto the detector for a source in this position. Hence a pinhole camera would receive  $\sim 16413/1536$  or  $\sim 11$  counts from the source, corresponding to an intrinsic significance of  $\sim 3\sigma$  for the pinhole camera.

Thus, when the photon limitation of the pinhole camera is taken into account, the shadow camera, for large FOV's with good angular resolution and sensitivity, is a much more suitable device in background dominated conditions.

In extreme source dominated conditions the simulations show a source dominated variation in rms superimposed across the image, and this could make the shadow camera less suitable due to the problems of 'ghosting' and definition of sensitivity.

Another disadvantage of the pinhole camera arises from a practical design consideration. For a large area imaging detector (IPC, Multistep Avalanche Chamber, or Imaging Gas Scintillation Proportional Counter) a detector window support is required. With a pinhole camera with good angular resolution dead areas therefore exist where a source cannot be seen because the resulting counts are blocked by the window support structure. For the shadow camera, in contrast, there is always a chance of detecting a source (within FOV) as a fraction of the pattern will always be recorded. This of course only applies to a stationary camera; with a rocking and/or rotating pinhole camera this problem does not occur,

In summary, the shadow camera is believed to be the most efficient device for wide field monitoring of the X-ray sky.

### 7.3. The IPC for the Shadow Camera

The natural choice for the gas for the IPC of the shadow camera is Xenon. This work has demonstrated that good (sub - 500  $\mu\text{m}$ ) resolution can be obtained with mixtures of Xenon/Methane. Table 7.3.1 lists other reported spatial resolution values achieved with Xenon/Methane.

A distinct problem arises in comparing resolutions between counters due to differing sizes and different energy X-ray sources. The approach adopted here is to consider resolution in terms of fractional resolution (of the detector size).

The best resolution (two point average) achieved in this work was .285 mm in the gas mixture 50% Xe 50%  $\text{CH}_4$ . This is a fractional resolution  $\sim 3 \times 10^{-3}$  of the detector width. Allowing for the finite slit width used, the resolution (FWHM) intrinsic to the detector is .2 mm or  $\sim 2.1 \times 10^{-3}$  of the detector size. Hence the present results, on the above criterion, represent the best resolution yet obtained in Xenon/Methane. In fact, the work presented here has revealed a practical limit in the resolution obtainable in Xenon/Methane due to the effect of secondary avalanching. The solution to this problem may lie in the use of a different quench gas, e.g. carbon dioxide. The effect is not of such importance in Argon/Methane gas mixtures, since there the methane will absorb most of the UV photons which cause secondary avalanching. This effect may well explain other workers results for Xenon/Methane, (for example Sanford et al., 1979), where poor resolution values were obtained.

Table 7.3.2 lists some of the reported spatial resolutions achieved with Argon/Methane mixes. In general these results do not show degradation in spatial resolution with increasing gain up to much higher counter gains than used here in Xenon/Methane (Figure 6.5.7). As can be seen from Table 7.3.2 the present work has achieved comparable resolution

TABLE 7.3.1

## MEASURED RESOLUTIONS FOR XENON/METHANE

Worker(s)	Gas Mixture	Pressure	Best Spatial Resolution FWHM	Resolution (FWHM) fraction of detector size	Radiation Source	Other Points (Detector Size)
Allemand and Thomas 1976	90% Xe 10% CH <sub>4</sub>	1 atm.	.186 mm	$3.1 \times 10^{-3}$	8 keV	One dimensional 6 cm long detector
Gorenstein et al., 1979	95% Xe 5% CH <sub>4</sub>	2 atm.	-.99 mm	$-9 \times 10^{-3}$	Cd <sup>109</sup> (22 keV)	10 cm x 10 cm detector
Borkowski and Kopp 1972	90% Xe 10% CH <sub>4</sub>	2 atm.	~1 mm	$\sim 5 \times 10^{-3}$	Cd <sup>109</sup> (22 keV)	20 cm x 20 cm detector
Anisimov et al., 1981	77% Xe 20% CH <sub>4</sub> 3% C <sub>2</sub> H <sub>5</sub> OH	1 atm.?	1 mm	$2.8 \times 10^{-3}$	8 keV	35.4 cm x 35.4 cm
Bolon et al., 1978	90% Xe 10% CH <sub>4</sub>	1 atm.	1.3 mm	$1.3 \times 10^{-2}$	28 keV	Electronic limited to 1.3 mm 10 cm width
Sanford et al., 1979	90% Xe 10% CH <sub>4</sub>	1 atm.	2.15 mm	$3.2 \times 10^{-2}$	1.5 keV	6.8 cm diameter Resistive Sheet Readout
Lazewatsky and Lanza 1980	?Xe ?CH <sub>4</sub>	1 atm.	2.85 mm	$9.5 \times 10^{-3}$	27 keV	10 cm x 30 cm detector
Present Work	90% Xe 10% CH <sub>4</sub>	2 atm.	.357 mm	$3.8 \times 10^{-3}$	Fe <sup>55</sup> (5.9 keV)	9.5 cm x 9.5 cm detector
	75% Xe 25% CH <sub>4</sub>	"	.299 mm	$3.1 \times 10^{-3}$	"	Graded-Density
	50% Xe 50% CH <sub>4</sub>	"	.285 mm	$3 \times 10^{-3}$	"	Cathode

Note ? = not stated

TABLE 7.3.2

## MEASURED RESOLUTIONS FOR ARGON/METHANE

Worker(s)	Gas Mixture	Pressure	Best Spatial Resolution FWHM	Resolution as fraction of detector size	Radiation Source	Other Points (Detector Size)
Borkowski and Kopp 1975	90% Ar 10% CH <sub>4</sub>	1 atm.	~.100 mm	$\sim 4 \times 10^{-3}$	1.5 - 6.5 keV	RC Readout 2.5cm length
Gilvin et al., 1981	90% Ar 10% CH <sub>4</sub>	"	~.230 mm	$\sim 2.4 \times 10^{-3}$	1.5 keV	Subdivided GD cathode.
	50% Ar 50% CH <sub>4</sub>	"	~.170 mm	$\sim 1.8 \times 10^{-3}$	"	Identical detector size to prototype 9.5 cm x 9.5 cm
Sanford et al., 1979	90% Ar 10% CH <sub>4</sub>	"	.37 mm	$5.4 \times 10^{-3}$	"	6.8 cm diameter
	80% Ar 20% CH <sub>4</sub>	"	~.2 mm			
	70% Ar 30% CH <sub>4</sub>	"	~.2 mm	$\sim 2.1 \times 10^{-3}$	"	Resistive sheet readout
Gatti et al., 1979	90% Ar 10% CH <sub>4</sub>	"	~.3 mm	$\sim 1.5 \times 10^{-3}$	Fe <sup>55</sup>	20 cm width Interwoven grid readout



in Xenon/Methane to some of the best values reported for Argon/Methane. In fact the fundamental gas limits, ignoring secondary avalanching, as discussed by Gilvin et al., 1981, for Argon/Methane are comparable to those for Xenon/Methane gas mixtures. The improved performance with Argon/Methane, compared with Xenon/Methane mixtures, is due to two factors, these being improved electronic noise (certainly in the case of Gilvin et al., 1981) and secondary avalanches.

This work has revealed that considerable across-anode wire modulation exists for the prototype IPC, but this can be minimised by use of the appropriate cathode amplifier time constant.

The problems of secondary avalanching limiting the position resolution in the IPC, and across-wire modulation, as discussed in Chapter 6, may be reduced by use of the subdivided GD cathode (giving low electronic noise), and the use of a deeper counter drift region. The prototype detector, as it now exists, is capable of producing recognisable images. Figure 7.3.1 shows an X-ray image of part of a test shadow camera mask (0.5 mm square holes 32 x 32 elements) obtained with the 50/50 gas mixture. This was obtained by fixing the mask pattern to the top of the detector window support and illuminating the mask via the helium tube with the  $\text{Fe}^{55}$  source. This image was obtained with an anode voltage of +4200 V and a drift voltage +50 V. The cathode time constants were 0.8  $\mu\text{sec}$  in the direction along the anode, and 6.4  $\mu\text{sec}$  in the direction across the anode (to minimise across-wire modulation). Although the binning effect across the wires is evident, the mask pattern is recognisable (lines indicate key features on figure).

#### 7.4. Future Work

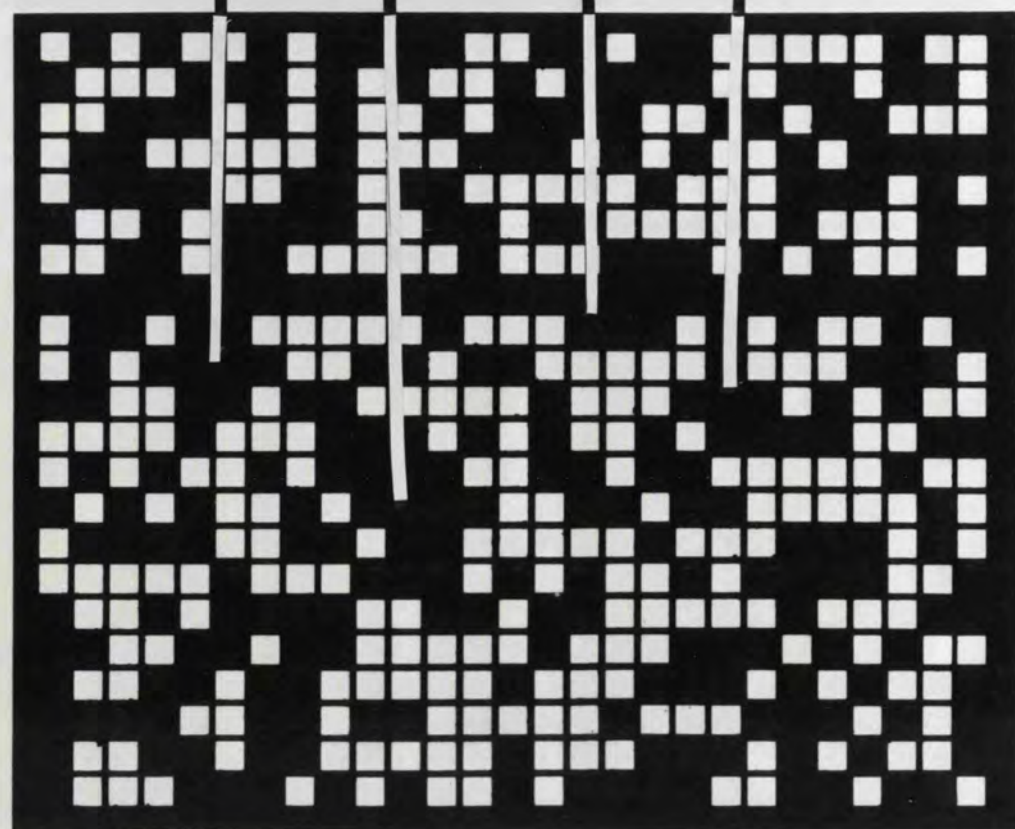
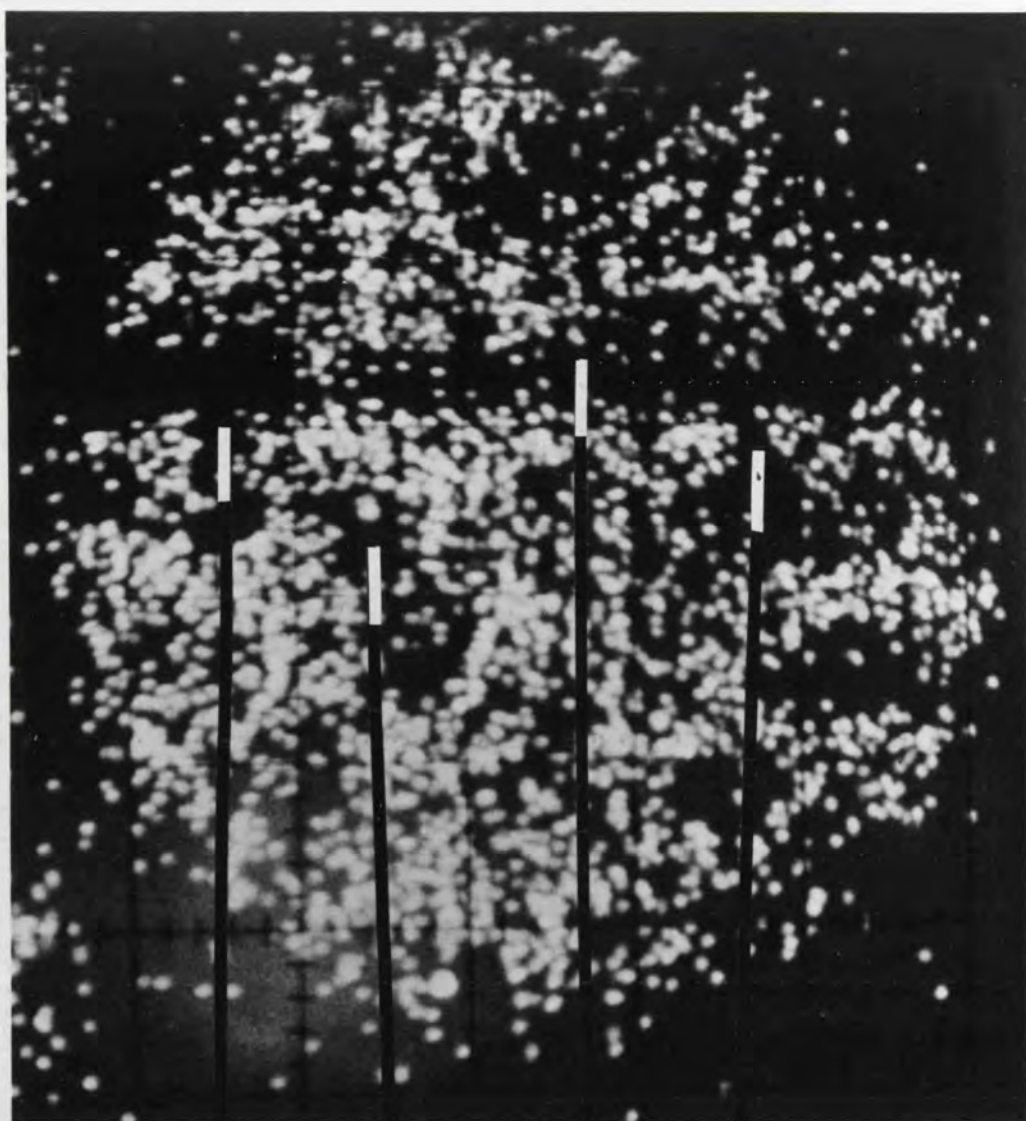
Future work on the shadow camera can be divided into two parts. The first and most important section is the construction and testing of a

Figure 7.3.1. Top: X-ray image obtained with prototype IPC, 50/50 gas mix of section of coded mask at bottom. Note: circular window support (blocking photons) is visible.

This image was obtained at an anode voltage of +4200 V , drift +50 V . Cathode time constant in direction along wires (across image) was 0.8  $\mu$ sec, and in direction across wires (vertically) was 6.4  $\mu$ sec to ensure best resolution and linearity characteristics. Note binning was visible in vertical direction.

Bottom: relevant section of coded mask (supplied by Dr. A.C. Brinkman of Utrecht, Holland) corresponding to X-ray image.





large area IPC ( ~30 cm x 30 cm) for direct application to the shadow camera. The problems of increased electronic noise can almost certainly be removed by use of a many-segmented GD cathode. The choice of IPC gas mixture is not so easy. The effect of other quench gases than methane on the position resolution and across-wire modulation must be found. The performance of Xenon/Methane is adequate in that sub-500  $\mu\text{m}$  position resolution can be achieved here. However, secondary avalanching would limit the available dynamic energy range of such a detector. Hence another gas mixture is desirable.

The second section is a full computer simulation program of a shadow camera in order that a given design can be optimised, and in order that scaling of the results (established here) can be checked for a large number of mask elements. An area of research not covered in this work is that of low transmission masks and the effect on sensitivity. This area could be investigated via computer simulations.

## APPENDIX A

$f(\theta, \phi)$  AND THE CALCULATION OF  
EFFECTIVE AND TOTAL SOLID ANGLE

A.1. Derivation of  $f(\theta, \phi)$ 

$f(\theta, \phi)$  gives the fractional off axis area of the detector exposed to a source at co-ordinates  $(\theta, \phi)$ . The relevant co-ordinate frame is shown in Figure A.1.1. Two effects are present; first, the off axis fall off in geometrical area; second, the reduced exposure due to the angle of the incident beam.

Consider Figure A.1.2 which shows the situation as viewed, from overhead, and side-on for an off axis source. The area GPF'Q is the actual detector area available for photons to fall on.

From the side view

$$O'O = b \tan \theta$$

where  $b$  is the mask to detector distance.

Required area = GPF'Q

$$= GP \cdot GQ$$

$$GP = a - PD$$

$$GQ = a - QE$$

$$PD = b \tan \theta \cos \psi$$

$$QE = b \tan \theta \sin \psi$$

Consider Figure A.1.3, which shows a close-up of triangle D'PD;

$$\phi + \psi + \pi/2 = \pi$$

$$\therefore \psi = \pi/2 - \phi$$

Now  $\cos \psi = \cos(\pi/2 - \phi)$

$$= \cos \pi/2 \cos \phi + \sin \pi/2 \sin \phi$$

$$= \sin \phi$$

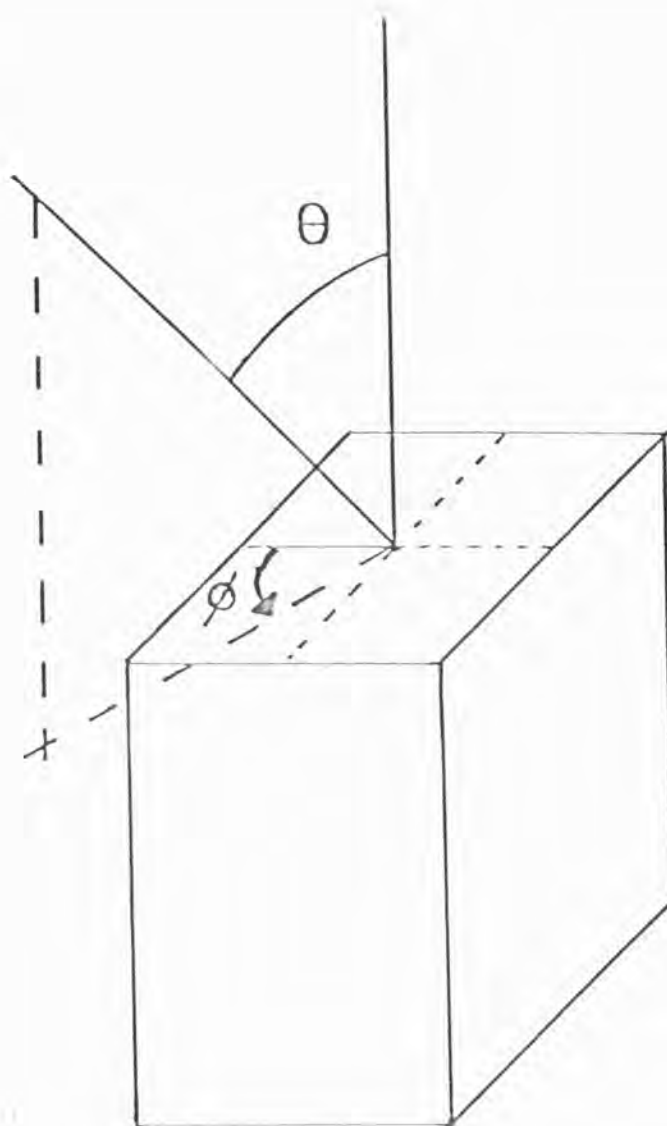


Figure A.1.1. Relevant co-ordinate frame for calculation of  $f(\theta, \phi)$ .  $\theta$  is angle of source from instrument view axis,  $\phi$  is azimuthal angle measured from midpoint of one side of camera.

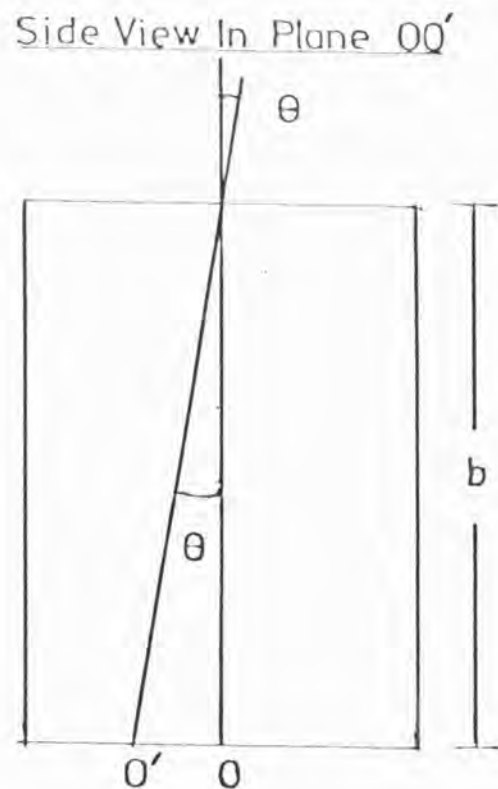
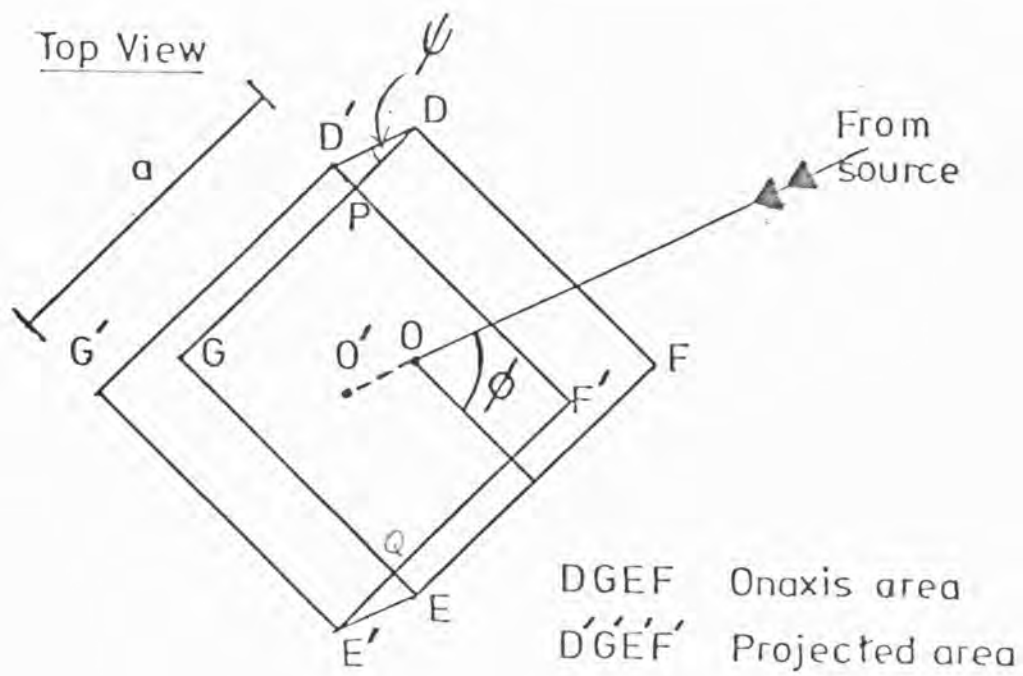


Figure A.1.2. Top and side view of shadow camera showing projected area for off-axis source at co-ordinates  $(\theta, \phi)$ . Co-ordinate frame as Figure A.1.1.  $a$  is length of one side of camera,  $b$  is mask to detector distance.

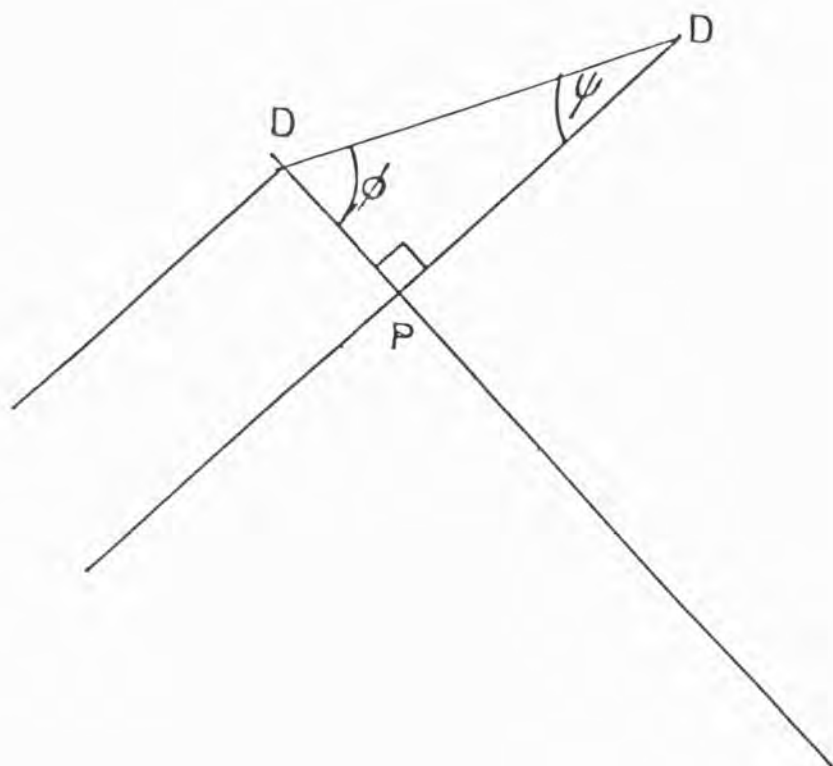


Figure A.1.3. Close up view of triangle  $D'PD$  from Figure A.1.2.



Now

$$\begin{aligned}\sin \psi &= \sin(\pi/2 - \phi) \\ &= \sin \pi/2 \cos \phi - \cos \pi/2 \sin \phi \\ &= \cos \phi\end{aligned}$$

Hence area GPF'Q

$$= [a - b \tan \theta |\sin \phi|][a - b \tan \theta |\cos \phi|]$$

The modulus signs are necessary as otherwise we have a problem in sign changes with the functions  $\sin$  and  $\cos$ , as area is always reduced, never increased, the absolute values must be used. As the X-ray beam enters at a zenith angle  $\theta$  it sees the area reduced by a  $\cos \theta$  term. Hence the overall fractional area is given by

$$f(\theta, \phi) = \cos \theta \left[ 1 - \frac{b}{a} \tan \theta |\cos \phi| \right] \left[ 1 - \frac{b}{a} \tan \theta |\sin \phi| \right]$$

#### A.2. Calculation of Effective Solid Angle

If  $\Omega$  = effective solid angle

$$\Omega = \iint f(\theta, \phi) \sin \theta \, d\theta \, d\phi$$

as  $\sin \theta \, d\theta \, d\phi = d\Omega$  the elemental solid angle.

Substituting for  $f(\theta, \phi)$  from above

$$\Omega = \iint \frac{\sin \theta \cos \theta}{a^2} (a - b \tan \theta |\sin \phi|)(a - b \tan \theta |\cos \phi|) d\theta d\phi$$

Let  $\phi$  run from 0 to  $\pi/2$ , so we do not require the modulus signs, the  $\theta$  integral becomes

$$\begin{aligned}&= -\frac{1}{4} \cos 2\theta - \frac{1}{2} \frac{b}{a} \left( \theta - \frac{1}{2} \sin 2\theta \right) (\sin \phi + \cos \phi) \\ &\quad + \frac{b^2}{a^2} \left( \frac{1}{2} \cos^2 \theta - \ln \cos \theta \right) \sin \phi \cos \phi\end{aligned}$$

The limits for  $\theta$  are 0 to  $\tan^{-1} \frac{a}{b \cos \phi}$  if  $0 \leq \phi \leq \pi/2$ . Substituting these and reducing we have

$$\frac{1}{2} - \frac{1}{2} \frac{b}{a} \left( \tan^{-1} \frac{a}{b \cos \phi} \right) (\sin \phi + \cos \phi) - \frac{b^2}{a^2} \sin \phi \cos \phi \ln \frac{b \cos \phi}{\sqrt{a^2 + b^2 \cos \phi}}$$

For the  $\phi$  integral, we integrate 0 to  $\pi/4$ . Normalising, after much mathematics (Primrose 1978, private communication) we obtain

$$\Omega = 4 \left[ \frac{\sqrt{a^2 + b^2}}{a} \tan^{-1} \frac{a}{\sqrt{a^2 + b^2}} - \frac{b}{a} \tan^{-1} \frac{a}{b} \right] + \frac{b^2}{a^2} \frac{\ln(a^2 + b^2)}{b^2 (2a^2 + b^2)}$$

### A.3. Calculation of Total Solid Angle

Figure A.3.1 shows the shadow camera and total solid angle viewed by the device. The total solid angle is calculated by considering a sphere centered on the intersection of the four corner lines. By integrating the elemental solid angle over the limits of  $\theta$  and  $\phi$  it can be shown (Primrose 1978, private communication) that

$$\Omega_{\text{TOTAL}} = 2\pi - 8 \sin^{-1} \frac{b}{\sqrt{2(a^2 + b^2)}}$$

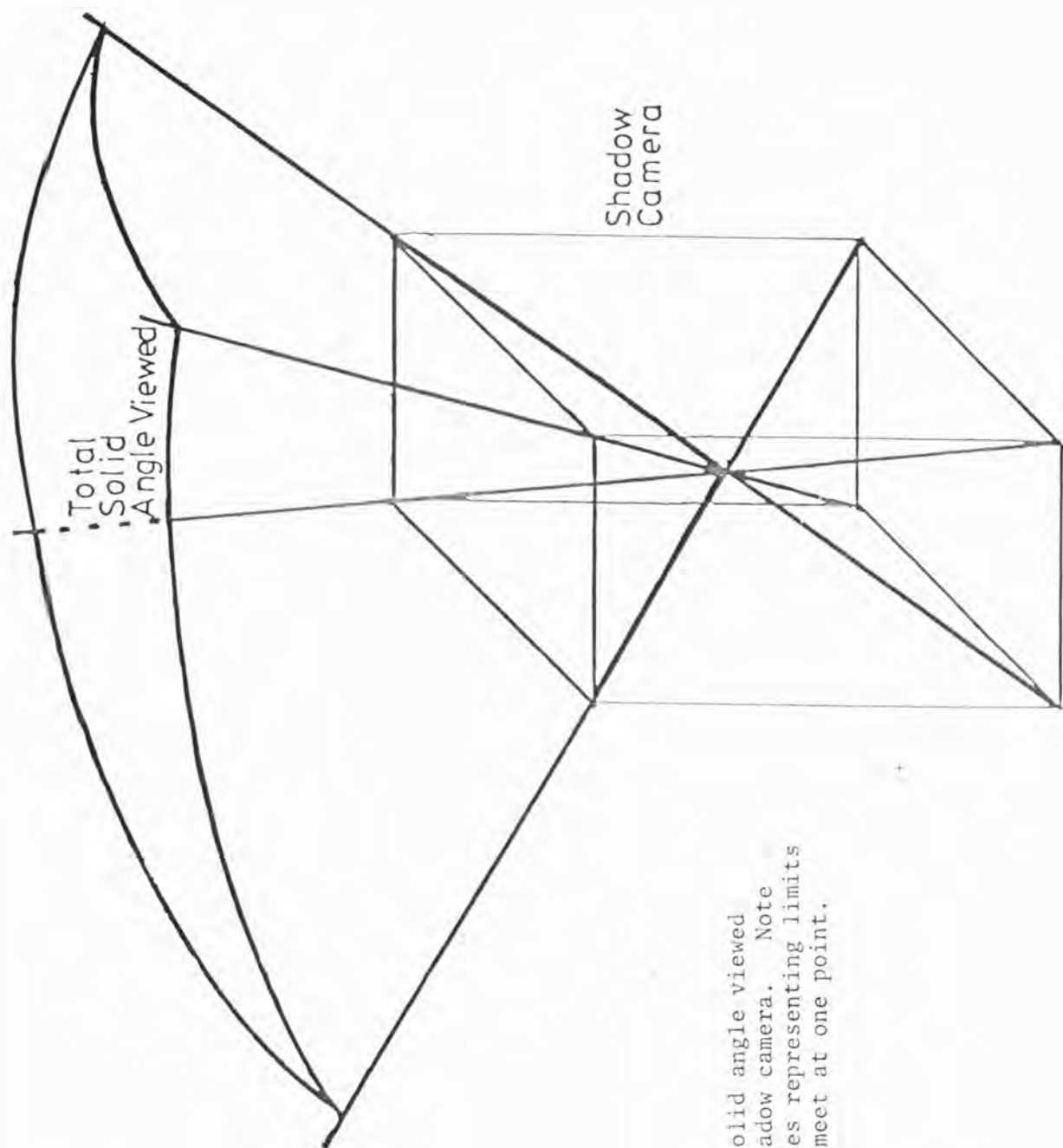


Figure A.3.1. Total solid angle viewed by a shadow camera. Note how lines representing limits of FOV meet at one point.

## APPENDIX B

## THE DETECTOR RESPONSE AND SAMPLING RATE

## REQUIRED FOR THE SHADOW CAMERA

This Appendix will discuss theoretically the effect of finite detector response and the required sample rate for the shadow camera.

B.1. Detector Response

Let us approximate the mask pattern to a random array of circular holes. This can then be represented mathematically by a convolution of a two-dimensional array of delta functions, one at each hole centre, with a single circular hole. The resulting recorded shadows from such a mask are blurred by the detector point response, which can be modelled by a convolution of the mask pattern with the response function. If we examine the recorded data in the Fourier domain, we have

$$D(\alpha, \beta) = \delta(\alpha, \beta) H(\alpha, \beta) R(\alpha, \beta)$$

where  $D(\alpha, \beta)$  is the FT of the data

$\delta(\alpha, \beta)$  is the FT of the delta function array

(chose  $|\delta(\alpha, \beta)| = \text{constant}$ )

$H(\alpha, \beta)$  is the FT of a single hole

$R(\alpha, \beta)$  is the FT of the detector point response

as convolutions become direct products in the Fourier Transform (FT) domain.

The FT of a circular hole is circularly symmetric and given by

$$H(k) = 2\pi a \frac{J_1(\omega, a)}{k}$$

where  $a$  is the hole radius

$J_1$  is the 1st order Bessel Function

$\omega$  is the wave number

The first zero of  $\bar{H}$  occurs when

$$\omega a = 3.832$$

Let the point response ( $r'(x,y)$ ) function of the detector be approximated by a two dimensional Gaussian

$$r'(r) = C \exp \left( -\frac{r^2}{2\sigma^2} \right)$$

$\sigma$  is the rms of point response function

Then the FT is given by

$$R(k) = C' \exp \left( -\frac{\omega^2 \sigma^2}{2} \right)$$

Figure B.1.1 shows schematically the FT of the detector point response and the FT of the hole. As the hole radius ( $a$ ) is decreased the value of  $\omega$  corresponding to the first zero increases. Similarly as the rms ( $\sigma$ ) of the detector response function is decreased the tail of the modulation transfer function of the detector is pushed farther away from the origin. If the width of the FT of the detector point response function is less than the width of the FT of the hole then the tail of the mask FT function is lost and hence the pattern will be degraded. We therefore require that

$$\frac{1}{\sigma} \geq \frac{3.832}{a}$$

If  $\sigma < \frac{a}{3.832}$  then the detector will record faithfully the shadow of the holes. Since for a Gaussian, the FWHM is given by

$$\text{FWHM} = 2.355 \sigma$$

and  $a = d/2$

where  $d$  is the diameter of a hole we have

$$\text{FWHM} \leq \frac{2.355 d}{2 \times 3.832}$$

that is for zero degradation

$$\text{FWHM} \leq \frac{1}{3} \text{ diameter of the holes}$$

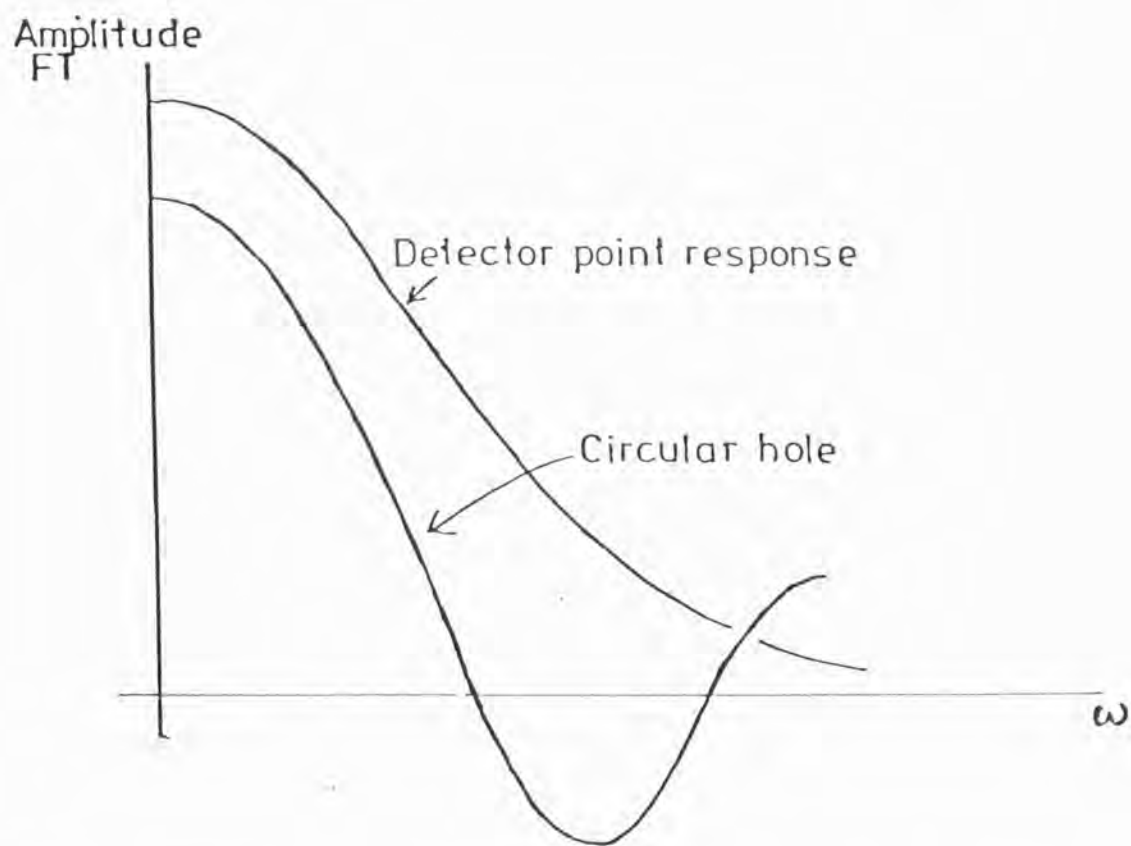


Figure B.1.1. Schematic amplitude of Fourier transform of detector point response and a circular hole as a function of frequency  $\omega$ .



## B.2 Required Sampling Rate

We require to sample the pattern recorded by the detector.

The upper cut off in  $\omega$  is naturally set by the first zero of the FT of the hole, using the Nyquist criterion

$$\omega_{\text{sample}} \geq 2 \times \frac{3.832}{a}$$

where  $\omega_{\text{sample}}$  is the sampling frequency, if  $\Delta x_{\text{sample}}$  is the sample size in the real domain

$$\Delta x_{\text{sample}} = \frac{2\pi}{\omega_{\text{sample}}}$$

Therefore

$$\frac{2\pi}{\Delta x_{\text{sample}}} \geq 2 \times \frac{3.832}{a}$$

$$\text{or } \Delta x \leq a$$

In summary, making the approximation of a mask consisting of randomly spaced holes, we require first that the FWHM of the detector response is less than the hole size in order that the recorded pattern is not degraded. Secondly, at least two samples must occur across each hole so that the pattern is faithfully recorded. This argument is adapted from Willingale 1981(b), private communication.

## APPENDIX C

## THE MAXIMUM ENTROPY METHOD OF DECONVOLUTION

Practical implementation of the maximum entropy method of deconvolution is covered in Willingale (1979, 1981). The principles only of the technique will be dealt with here. The following argument is adapted from Willingale (1979, 1981). Consider the following generalised situation

$$m_k = \sum_{i=0}^{N-1} f_i \varepsilon_i T_{k-i} + n_k$$

where  $m_k$  is recorded data (M points in total)  
 $f_i$  object field (N points in total)  
 $\varepsilon_i$  exposure  
 $T_{k-i}$  response function (transmission of mask)  
 $n_k$  noise

where all the above, object, image fields are stacked into vectors. One requires an estimate of the object field  $f_i$ , only using  $m_k$ ,  $\varepsilon_i$ , and  $T_{k-i}$  and a knowledge of  $n_i$ . If a maximum entropy solution is found for  $f_i$ , one has the distribution which can occur in the largest number of ways,  $f_i$  must of course be consistent with the data. The configurational entropy as defined by the following equation is used

$$H = - \sum_{i=0}^{N-1} \hat{f}_i \ln \hat{f}_i \quad (C.1)$$

where  $\hat{f}_i$  are the estimates of the pixel values. In order to test whether the estimate is consistent with the data, the  $\chi^2$  statistic was used

$$\chi^2 = \sum_{k=0}^{M-1} \frac{(m_k - \hat{m}_k)^2}{\sigma_k^2} \quad (C.2)$$

where 
$$\hat{m}_k = \sum_{i=0}^{N-1} \hat{f}_i \varepsilon_i \Gamma_{k-i}$$

$\hat{m}_k$  is of course the simulated data from  $\hat{f}_i$ . In the shadow camera the values of  $m_k$  are reasonably large ( $m_k > 10$ ) hence counting statistics are assumed i.e.  $\sigma_k^2 = m_k$ . In the case of very short integration times a different statistic must be used. For  $\hat{m}_k$  to be consistent with  $m_k$ , the actual data, then

$$\chi^2 \approx M$$

the number of data points. If  $\chi^2$  is too large  $\hat{f}_i$  does not adequately represent the object field, and if  $\chi^2$  is too small, the image will contain features due to noise, insignificant in the actual object field.

Combining equations (C.1) and (C.2) one can set up an objective function  $P$ , where  $\lambda$  plays the role of a Lagrangian multiplier in the maximisation of  $H$  under the constraint  $\chi^2 = M$

$$P = - \sum_{i=0}^{N-1} \hat{f}_i \ln \hat{f}_i - \lambda \sum_{k=0}^{M-1} \frac{(m_k - \hat{m}_k)^2}{\sigma_k^2}$$

$P$  is then maximised,  $\lambda$  is chosen such that  $\chi^2 = M$ , for a maximum

$$\frac{dP}{d\hat{f}_i} = 0$$

Solution of  $\frac{dP}{d\hat{f}_i}$  leads to a transcendental equation which must be solved iteratively, where  $\hat{f}_i$  is incremented until a solution is found, the goodness of fit being measured by the  $\chi^2$  statistic. The maximum entropy solution 'forces' the object field to fit the data using the known response function of the mask.

## REFERENCES

References to the same author in the same year are distinguished by letters (i.e. 80a, 80b or 80,80b)

1. Ables, J.G., Proc. Ast. Soc. Australia, 1, 172, 1968.
2. Allemand, R., & Thomas, G., Nucl. Instr. and Methd., 137, 141, 1976.
3. Anderson, D.F., Nucl. Instr. and Methd., 178, 125, 1980.
4. Anderson, D.F., IEEE Trans. Nucl. Sci., in press, 1981.
5. Andresen, R.D., Karlsson, L., Peacock, A., & Taylor, B.G., Astr. & Astrophys. 53, 309, 1976.
6. Anger, H.O., Rev. Sci. Instr., 29, 1, 27, 1958.
7. Anisimov, Yu. S., Chernenko, S.P., Ivanov, A.B., Peshekhonov, V.D., Rozhnyatovskaya, S.A., Zanevsky, Yu.V., Kheiker, D.M., Malakhova, L.F., & Popov., A.N., Nucl. Instr. and Methd. 179, 503, 1981.
8. Bateman, J.E., Waters, M.W., & Jones, R.E., Nucl. Instr. and Methd., 135, 235, 1976.
9. Bolon, C., Burns, R., Deutsch, M., Judy, P., Lanza, R., & Zimmerman, K., IEEE Trans. Nucl. Sci., NS-25, 661, 1978.
10. Borkowski, C.J., & Kopp, M.K., Rev. Sci. Instr., 39, 10, 1515, 1968.
11. Borkowski, C.J., & Kopp, M.K., IEEE Trans. Nucl. Sci., NS-19, 161, 1972.
12. Borkowski, C.J., & Kopp, M.K., Rev. Sci. Instr., 46, 8, 951, 1975.
13. Borkowski, C.J., & Kopp, M.K., IEEE Trans. Nucl. Sci., NS-24, 287, 1977.
14. Bradt, H.V., Doxsey, R.E., & Jernigan, J.E., X-ray Astronomy, Advances in Space Exploration Volume 3, Pergamon Oxford, 3, 1979.
15. Breare, J.M., Lightfoot, J.A., & Stubbs, R.J., Nucl. Instr. and Methd., 100, 281, 1972.
16. Breskin, A., Charpak, G., Demierre, C., Majewski, S., Policarpo, A., Sauli, F., & Santiard, J.C., Nucl. Instr. and Methd., 143, 29, 1977.
17. Breskin, A., & Zwong, N., IEEE Trans. Nucl. Sci., NS-25, 126, 1978.
18. Breskin, A., Charpak, G., Majewski, S., Melchart, G., Petersen, G., & Sauli, F., Nucl. Instr. and Methd., 161, 19, 1979.

19. Bronshtein, I.N., & Semendyayev, K.A., A Guide Book to Mathematics,  
Springer-Verlag, New York Inc., 427, 1973.
20. Campion, P.J., Int. J. Applied Radiation and Isotopes, 19, 219, 1968.
21. Carver, J.H., & Mitchell, P., Nucl. Instr. and Methd., 52, 130, 1967.
22. Charles, M.W., J. Phys. E., 5, 95, 1972.
23. Charles, M.W., & Cooke, B.A., Nucl. Instr. and Methd., 61, 31, 1968.
24. Charpak, G., Ann. Rev. Nucl. Sci., 20, 195, 1970.
25. Charpak, G., & Sauli, F., Phys. Lett., 78B, 523, 1978.
26. Charpak, G., & Sauli, F., Nucl. Instr. and Methd., 162, 405, 1979.
27. Chartres, M., & Li, F., IAU Circ. No.3154, 1977.
28. Christie, P.F., Mathieson, E., & Evans, K.D., J. Phys. E., 9, 673, 1976.
29. Christophorou, L.G., Maxey, D.V., McCorkle, D.L., & Carter, J.G.  
Nucl. Instr. and Methd. 171, 491, 1980.
30. Clark, G., & Chartres, M., IAU Circ. No.3208, 1978.
31. Cline, T.L., Desai, U.D., Pizzichini, G., Teegarden, B.J., Evans, W.D.,  
Klebesadel, R.W., Laros, J.G., Hurley, K., Niel, M., Vedrenne, G.,  
Estoolin, I.V., Kouznetsov, A.V., Zenchenko, V.M., Hovestadt, D.,  
& Cloeckler, G., Astrophys. J. Lett., 237, L1, 1980.
32. Cooke, B.A., Nature, 261, 195, 1976.
33. Cooley, J.W., & Tukey, J.W., Math. Comp., 19, 297, 1965.
34. Davelaar, J., Manzo, G., Peacock, A., Taylor, B.G., & Bleeker, J.A.M.,  
IEEE Trans. Nucl. Sci., NS-27, 196, 1980.
35. Dicke, R.H., Astrophys. J., Lett., 153, L101, 1968.
36. Diethorn, W., U.S. AEC. Report NY06629, 1956.
37. Elvis, M., Mon. Not. R. Astr. Soc., 177, 7P, 1976.
38. ESA Spectroscopy/Timing-Transient Mission in X-ray Astronomy,  
Sci(80) 5, Paris, June 1980.
39. Evans, W.D., Belian, R.D., & Conner, J.P., Astrophys. J. Lett., 159,  
L57, 1970.

40. Evans, W.D., Klebesadel, R.W., Laros, J.G., Cline, T.L., Desai, U.D., Pizzichini, G., Teegarden, B.J., Hurley, K., Niel, M., Vedrenne, G., Estoolin, I.V., Kouznetsov, A.V., Zenchenko, V.M., Kurt, V.G., *Astrophys. J. Lett.*, 237, 17, 1980.
41. Fano, U., *Phys. Rev.*, 72, 26, 1947.
42. Fischer, J., Okuno, H., & Walenta, A.J., *IEEE Trans. Nucl. Sci.*, NS-26, 794, 1978(a).
43. Fischer, J., Okuno, H., & Walenta, A.H., *Nucl. Instr. and Methd.*, 151, 451, 1978(b).
44. Franks, A., *Sci. Prog. Oxf.*, 64, 371, 1977.
45. Fraser, G.W., Ph.D. Thesis, University of Leicester, 1980.
46. Fraser, G.W., XRA Group, University of Leicester, private communication, 1981.
47. Friedman, H., *New Instrumentation for Space Astronomy, COSPAR Advances in Space Exploration Volume I*, Pergamon Oxford, 101, 1978.
48. Gatti, E., Okuno, H., & Artuso, M., *Nucl. Instr. and Methd.*, 167, 417, 1979.
49. Giaconni, R., Gursky, H., Paolini, F.R., & Rossi, B.B., *Phys. Rev. Lett.*, 9, 439, 1962.
50. Giles, B., *Appl. Opt.* submitted 1980.
51. Gilvin, P.J., Mathieson, E., & Smith, G.C., *Nucl. Instr. and Methd.*, 163, 279, 1979.
52. Gilvin, P.J., Mathieson, E., & Smith, G.C., *IEEE Trans. Nucl. Sci.*, NS-27, 101, 1980.
53. Gilvin, P.J., XRA Group, University of Leicester, private communication, 1980.
54. Gilvin, P.J., Mathieson, E., & Smith, G.C., *IEEE Trans. Nucl. Sci.*, in press, 1981.
55. Gilvin, P.J., Mathieson, E., & Smith, G.C., XRA Group, University of Leicester, private communication, 1981b.



56. Gorenstein, P., Perlman, D., Parsignault, D., & Burns, R., IEEE Trans. Nucl. Sci., NS-26, 502, 1979.
57. Grindlay, J., & Heise, J., IAU Circ. No.2879, 1975.
58. Grindlay, J., Gursky, H., Schnopper, H., Parsignault, D.R., Heise, J., Brinkman, A.C., & Schrijver, J., Astrophys. J. Lett., 205, L127, 1976.
59. Grove, R., Lee, K., Perez Mendez, V., & Sperinde, J., Nucl. Instr. and Methd., 89, 257, 1970.
60. Gull, S.F., & Daniell, G.J., Nature, 272, 636, 1978.
61. Gunson, J., & Polychronopulous, B., Mon. Not. R. Astr. Soc., 177, 485, 1976.
62. Harries, J.R., McCracken, K.G., Francey, R.J., & Fenton, A.B., Nature, 215, 38, 1967.
63. Harris, T.J., & Mathieson, E., Nucl. Instr. and Methd., 154, 183, 1978.
64. Hendricks, R.W., Nucl. Instr. and Methd., 102, 309, 1972.
65. Hoffman, J.A., Marshall, H.L., & Lewin, W.H.G., Nature, 271, 630, 1978.
66. Holt, S.S., Astrophys. Space. Sci., 42, 123, 1976.
67. Hudson, H.S., & Lin, R.P., Space. Sci. Instr., 4, 101, 1978.
68. Humphrey, A., Cabral, R., Brissette, R., Carroll, R., Morris, J., & Harvey, P., IEEE Trans. Nucl. Sci., NS-25, 445, 1978.
69. Inoue, H., Koyama, K., Makishima, K., Matsuoka, M., Murakami, T., Oda, M., Ōgawara, Y., Ohashi, T., Shibasaki, N., Tanaka, Y., Tawara, Y., Kondo, I., Hayakawa, S., Kunieda, H., Makino, F., Masai, K., Nagase, F., Miyamoto, S., Tsunemi, H., & Yamashita, K., Nature, 283, 358, 1980.
70. Jagoda, N., & Antrim, W.B., J.B.I.S., 28, 299, 1975.
71. Joss, P.C., Astrophys. J., 225, L123, 1978.
72. Joss, P.C., & Rappaport, S.A., Astron. Astrophys., 71, 217, 1979.
73. Kablitzer, S., & Meltzer, W., Nucl. Instr. and Methd., 56, 301, 1967.
74. Kaluzienski, L.J., Ph.D. Thesis, University of Maryland, 1977.
75. Kaluzienski, L.J., Robinson-Saba, J.L., Boldt, E.A., Holt, S.S., Mushotzsky, R.F., Rothschild, R.E., & Serlemitsos, P.J., HEAD Meeting San Diego, Sept.12-14, 1978, Bull.Amer.Astron.Soc.,10,516, 1978.

76. Kaplan, S.N., Kaufman, L., Perez Mendez, V., & Valentine, K., Nucl. Instr. and Methd., 106, 397, 1973.
77. Kaufman, L., Perez Mendez, V., Shames, D., & Stoker, G., IEEE Trans. Nucl. Sci., NS-12, 169, 1972.
78. Kikuchi, R., & Soffer, B.H., J. Op. Soc. Amer., 67, No.12, 1977.
79. Klebesadel, R.W., Strong, I.B., & Olson, R.A., Astrophys. J. Lett., 182, L85, 1973.
80. Klebesadel, R.W., & Strong, I.B., Review Article, Scient. Am., 1976.
81. Korff, S.A., Electron and Nuclear Counters, Princeton, M.J., Van Nostrand, 1955.
82. Ku, W.H.M., & Hailey, C.J., IEEE Trans. Nucl. Sci., in press, 1981
83. Lawrence, A., Mon. Not. R. Astr. Soc., 192, 83, 1980.
84. Lazewatsky, J., & Lanza, R., IEEE Trans. Nucl. Sci. NS-27, 519, 1980.
85. Leicester, MIT, 1978. Proposal to NASA for an All Sky Survey of Transient X-ray Sources, X-ray Bursts, and Flares on Spacelab Missions between 1981-1983. Submitted by the University of Leicester, Massachusetts Institute of Technology. In response to AO-OSS-2-78. High Energy Astrophysics.
86. Levine, A., Petre, R., Rappaport, S., Smith, G.C., Evans, K.D., & Rolf, D., Astrophys. J. Lett., 228, L99, 1979.
87. Lewin, W.H.G., & Joss, P.C., CSR-HEA-80-80 Preprint 1980. To be published in Space Science Reviews.
88. Li, F., Rappaport, S., Clark, G.W., & Jernigan, J.G., Astrophys. J., 228, 893, 1979.
89. Longhurst, R.S., Geometrical and Physical Optics (3rd Edition), Longman Group Ltd., London, 447, 1973.
90. Marshall, N., Mon. Not. R. Astr. Soc., to be published, 1981

( Marshall, N., XRA Group, University of Leicester, Private communication, 1981.)

91. Marshall, N., Warwick, R.S., & Pounds, K.A., Mon. Not. R. Astr. Soc.,  
to be published, 1981.
92. Mathieson, E., Nucl. Instr. and Methd., 97, 171, 1971.
93. Mathieson, E., Nucl. Instr. and Methd., 159, 29, 1979.
94. Mathieson, E., Physics Department, University of Leicester, private  
communication, 1980.
95. Mathieson, E., Physics Department, University of Leicester, private  
communication, 1980(b).
96. Mathieson, E., Physics Department, University of Leicester, private  
communication, 1981.
97. Mathieson, E., & Harris, T.J., Nucl. Instr. and Methd., 157, 563, 1978.
98. Mathieson, E., Smith, G.C., & Gilvin, P.J., Nucl. Instr. and Methd.,  
174, 221, 1980.
99. Mazets, E.P., et al., Akademiya Nauk USSR Ordena Lenina Fiziko-Tekhn  
Eskii Institut Im.A.F. IOFFE, 599, 1979(a).
100. Mazets, E.P., et al., Lebedev Institute preprint 610, 1979(b).
101. Mazets, E.P., et al., Lebedev Institute preprint 617, 1979(c).
102. McHardy, I.M., et al., in preparation, 1981.
103. McMaster, W.H., Kerr Del Grande, N., Mallet, J.H., Hubbell, J.H.,  
Compilation of X-ray Cross-sections, National Bureau of Standards,  
UCRL-50174 Sec.II Rev.1. Lawrence Radiation Laboratory, University  
of California Livermore, TLD-4500 UC-34 Physics, 1979.
104. Mertz, L., Transformations in Optics, Wiley, New York, 1965.
105. MIT, Leicester 1976. Proposal to NASA for a Wide Field Camera for  
X-ray Bursts and Transients submitted by Center for Space Research  
of the Massachusetts Institute of Technology and the University of  
Leicester in response to AO-OSS-2-76, 1976.
106. Miyamoto, S., Space Sci. Instrum., 3, 473, 1977.
107. Murray, S., Proc. Soc. Photo. Opt. Instr. Eng., 106, X-ray Imaging,  
8, 1977.

108. Naval Research Laboratory, University of Birmingham, and Los Alamos  
1978. High Resolution X-ray Observations with a Transform  
Telescope (TRANSTEL) Proposal to NASA in response to AO-OSS-2-78  
High Energy Astrophysics by Naval Research Laboratory, Washington,  
D.C., Department of Space Research, University of Birmingham,  
England, and Los Alamos Scientific Laboratory, Los Alamos NM.
109. Oda, M., *Applied Optics*, 4, 143, 1965.
110. Oda, M., *IAU Cir. No.3525*, 1980(a).
111. Oda, M., *IAU Cir. No.3527*, 1980(b).
112. Owen, R.B., Awcock, M.L., *IEEE Trans. Nucl. Sci.*, NS-15, 290, 1968.
113. Palladino, V., & Sadoulet, B., *Nucl. Instr. and Methd.*, 128, 323, 1975.
114. Palmieri, T.M., *Astrophys. Space. Sci.*, 20, 431, 1974.
115. Parker, S.I., Jones, R., Kadyk, J., Stevenson, L., Katsura, T.,  
Peterson, V., & Yount, D., *Bull. Amer. Phys. Soc. Series II*, 16,  
658, 1971.
116. Peacock, A., Andresen, R.D., Van Dordrecht, A., Leimann, E.A., Manzo,  
G., Taylor, B.G., Berthelsdorf, R., Culhane, J.L., Ives, J.C., &  
Sanford, P.W., *IEEE Trans. Nucl. Sci.*, NS-26, 486, 1979(a).
117. Peacock, A., Andresen, R.D., Leimann, E.A., Long, A., Manzo, G., &  
Taylor, B.G., *Nucl. Instr. and Methd.*, 169, 613, 1979(b).
118. Petersen, L.E., *Ann. Rev. Astron. Astrophys.*, 13, 423, 1975.
119. Petersen, L.E., Hudson, H.S., Hurford, G., & Schneible, D. Hard X-ray  
Imaging Facility for Space Shuttle. A Scientific and Conceptual  
Engineering Study by the Hard X-ray Imaging Facility Definition  
Team, Nov. 1976. Report for NASA Contract No,NAS5-22375, 1976.
120. Planinic, J., *Nucl. Instr. and Methd.*, 136, 165, 1976.
121. Policarpo, A., *Nucl. Instr. and Methd.*, 153, 389, 1978.
122. Pounds, K.A., *Comments in Astrophys. Sp. Sci.*, 6, 145, 1976.
123. Pounds, K.A., *Proceedings of the Fifth European Regional Meeting in  
Astronomy; Variability in Stars and Galaxies. Leige Belgium 28  
July-1 August 1980. Institut d'Astrophysique, Liege, 1980.*

124. Pounds, K.A., Paper presented at Uhuru Memorial Symposium, Goddard Space Flight Center, 13th December 1980, to be published in the Journal of Washington Academy of Sciences, 1981.
125. Primrose, E.G., Mathematics Department, University of Leicester, private communication, 1978.
126. Procter, R.J., Skinner, G.K., & Willmore, A.P., Mon. Not. R. Astr. Soc. 185, 745, 1978.
127. Procter, R.J., Skinner, G.K., & Willmore, A.P., Mon. Not. R. Astr. Soc. 187, 633, 1979.
128. Radeka, V., IEEE Trans. Nucl. Sci., NS-21, 51, 1974.
129. Rappaport, S., Joss, P.C., Bradt, H., Clark, G.W., & Jernigan, J.G., Astrophys. J., 208, 119, 1976(a).
130. Rappaport, S., Buff, J., Clark, G., Lewin, W.H.G., Matilsky, T., & McClintock, J., Astrophys. J. Lett., 206, L139, 1976(b).
131. Rappaport, S.A., Clark, G.W., Cominsky, L., Joss, P.C., & Li, F., Astrophys. J. Lett., 224, L1, 1978.
132. Rappaport, S., Petre, R., Kayat, M.A., Evans, K.D., Smith, G.C., & Levine, A., Astrophys. J., 227, 285, 1979.
133. Reid, P.B., Ku, W.H.M., Long, K.S., Novick, R., & Pisarki, R.L., IEEE Trans. Nucl. Sci., NS-26, 46, 1979.
134. Ricker, G., & Primini, F., IAU Circ. No.3078, 1977.
135. Ricketts, M.J., Turner, M.J.L., Page, C.G., & Pounds, K.A., Nature, 256, 631, 1975.
136. Ricketts, M.J., Cooke, B.A., & Pounds, K.A., Nature, 259, 546, 1976.
137. Ricketts, J.J., Cooke, B.A., & Pye, J.P., HEAD Meeting San Diego September 12-14, 1978. Bull.Am.Astron.Soc., 10, 516, 1978.
138. Ricketts, M.J., Gilvin, P.J., & Turner, M.J.L., XRA Group, University of Leicester, private communication 1981.
139. Roarke, R.J., & Young, W.C. Formula for Stress and Strain, McGraw Hill Kogakusha Ltd., 1973.



140. Rosenberg, F.D., Eyles, C.J., Skinner, G.J., & Willmore, A.P., *Nature*, 256, 628, 1975.
141. Rossi, B., Paper presented at Conference "Perspective of Fundamental Physics", Rome, September 7-9 1978. CSR-HEA-79-55 Preprint.  
To be published High Energy Physics.
142. Sanford, P.W., Mason, I.M., Dimmack, K., & Ives, J.C., *IEEE Trans. Nucl. Sci.*, NS-26, 169, 1979.
143. Schreier, E.J., New Instrumentation for Space Astronomy. COSPAR  
Advances in Space Exploration, Volume 1, Pergamon Oxford, 179, 1978.
144. Schwarz, D. A., X-ray Astronomy. COSPAR Advances in Space Exploration  
Volume 3, Pergamon Press, 453, 1979.
145. Sims, M.R., & Fraser, G.W., *IAU Circ. No.* 3339, 1979.
146. Sims, M., Turner, M.J.L., & Willingale, R., *Space Sci. Instrum.*, 5,  
109, 1980.
147. Sipila, H., *Acta Polytechnica Scandinavica, Applied Physics Series* 116,  
UDC 621.387.42:543.426, 1976(a).
148. Sipila, H., *Nucl. Instr. and Methd.*, 133, 251, 1976(b).
149. Smith, K.F., & Cline, J.E., *IEEE Trans. Nucl. Sci.*, NS-13, 468, 1966.
150. Snell, A.H., *Nuclear Instruments and their Uses. Volume 1*, John  
Wiley & Sons Inc., 1962.
151. Spiegel, M.R., *Mathematical Handbook of Formulae and Tables*, Schaum's  
Outline Series in Mathematics, McGraw-Hill, 1968.
152. Spragg, J., XRA Group, University of Leicester, private communication,  
1977.
153. Spragg, J., XRA Group, University of Leicester, private communication,  
1980.
154. Tabata, T., Ito, R., & Okable, S., *Nucl. Instr. and Methd.*, 103, 85, 1972.
155. Tananbaum, H., Peters, G., Forman, W., Giaconni, R., Jones, C., & Anvi,  
Y., *Astrophys. J.*, 223, 74, 1978.
156. Terell, J., Evans, W.D., Klebesadel, R.W., & Laros, J.G., *Nature*, 285,  
383, 1980.



157. Thomas, H.D., XRA Group, University of Leicester, private communication, 1981.
158. Tobin, R.A., Rev. Sci. Instr. 34, 1450, 1963.
159. Tomitani, T., Nucl. Instr. and Meth., 100, 179, 1972.
160. Trippe, T., CERN Internal Report 69-18, 1969.
161. Turner, J.A., Pickard, R.M., & Hoffman, C.R., J. Sci. Instr. 39, 26, 1962.
162. Turner, M.J.L., XRA Group, University of Leicester, private communication, 1977.
163. Turner, M.J.L., XRA Group, University of Leicester, private communication, 1978.
164. Van Atta, C.M., Vacuum Science and Engineering, McGraw-Hill, 1965.
165. Villa, G., Page, C.G., Turner, M.J.L., Cooke, B.A., Ricketts, M.J., & Pounds, K.A., Mon. Not. R. Astr. Soc., 176, 609, 1976.
166. Whitford, C.H., et al., to be published, 1981.
167. Wilkinson, P.J., & Johnston, H.L., J. Chem. Phys. 18, 2, 190, 1950.
168. Williams, A., & Sara, R.I., Int. J. Applied Radiation and Isotopes, 13, 229.
169. Williams, E.J., Proc. Roy. Soc. A., 130, 310, 1931.
170. Willingale, R., M.Sc., Project Report, University of Leicester, 1976.
171. Willingale, R., Ph.D. Thesis, University of Leicester, 1979.
172. Willingale, R., Mon. Not. R. Astr. Soc., 194, 35a, 1981.
173. Willingale, R., XRA Group, University of Leicester, private communication, 1981(b).
174. Wolff, R.S., Nucl. Instr. and Methd., 115, 461, 1974.
175. Zastawny, A., J. Sci. Instr., 43, 179, 1966.
176. Zombeck, M.V., SAO Special Report 386, Smithsonian Institution Astrophysical Observatory, Cambridge Massachusetts 92138, 1980,

## ERRATA TO REFERENCES

The following two references should be inserted into list at points noted.

Between 60 and 61

Gurman, S., Physics Department, University of Leicester,  
private communication, 1981.

Between 107 and 108

NASA report 1980

NASA Technical Memorandum

NASA TM - 78285

Advanced X-ray Astrophysics Facility (AXAF) - Science  
Working Group Report by Program Development Directorate  
May 1980

George C. Marshall Space Flight Center, Marshall Space  
Flight Center, Alabama.

This makes total number of references 178.

P 111 / 231 B.

## A WIDE FIELD CAMERA FOR X-RAY ASTRONOMY

M.R.SIMS

### ABSTRACT

The need for a wide field camera for X-ray astronomy is reviewed. The theory and practical design of one suitable instrument, the shadow or Dicke camera are discussed, and results and conclusions from computer simulation of the device are presented.

The basic principles and design of a suitable X-ray imaging detector, the Imaging Proportional Counter, are outlined. This is followed by the description of a small prototype detector filled with Xenon/Methane at 2 atmospheres pressure. Results from this detector are presented.

Finally some remarks on the performance and design of the shadow camera are made along with a discussion of future work required before a flight of a wide field shadow camera is made.